Volcanic Stratigraphy and Epithermal Mineralization of the La Coipa District, Maricunga belt, Chile

by

Sergio Gamonal

B.Sc. Universidad de Chile, 2007

A THESIS SUBMITTED IN PARTIAL FULFILLMENT OF

THE REQUIREMENTS FOR THE DEGREE OF

MASTER OF SCIENCE

in

THE FACULTY OF GRADUATE AND POSTDOCTORAL STUDIES

(Geological Sciences)

THE UNIVERSITY OF BRITISH COLUMBIA

(Vancouver)

August 2015

© Sergio Gamonal

Abstract

The La Coipa district is located in the northern part of the Oligocene-Miocene Maricunga belt, northern Chile. It consists of a cluster of high- to intermediate-sulfidation Ag-Au epithermal deposits that sustained one of the major producing mines within the region, otherwise dominated by gold-rich porphyry systems. The depletion of reserves led to a temporary mine closure in 2013, which highlights the necessity of a renewed effort to improve the district exploration model. Following this objective, this study is focused on a detailed district-scale geological characterization with emphasis on Tertiary magmatic rocks. Epithermal mineralization in La Coipa is hosted in an intra-arc Oligocene-Miocene basin that overlies rocks of Permian to Eocene age. The Oligocene-Miocene magmatic rocks have been divided into two groups: La Coipa Group (24-21 Ma) and Codocedo Group (21-16 Ma). A regional unconformity separates these groups. With the exception of the intermediate-sulfidation Purén deposit, the high-sulfidation systems are always associated with concentrically zoned advanced argillic alteration where economic grades are mainly associated with vuggy quartz and quartz+alunite core zones. Outer alteration zones are constituted by kaolinite ± dickite ± pyrophyllite, and illite ± kaolinite ± smectite. The Purén deposit is characterized by silicification and illite + kaolinite alteration. CA-ID-TIMS U-Pb (zircon) and $^{40}Ar/^{39}Ar$ (biotite) ages determined that Tertiary magmatic rocks range in age between ca. 37 and 16 Ma. $^{40}Ar/^{39}Ar$ alunite ages reveal multiple episodes of hydrothermal alteration and mineralization that range between 30 and 14 Ma, but with a main episode bracketed between 19 and 14 Ma. The prolonged history of epithermal mineralization at La Coipa requires a revised model for fertile metallogenic episodes for the Maricunga belt. These alunite ages indicate a more continuous distribution of mineralizing events, which contrasts previous models that indicated two fertile episodes limited to the 24-20 Ma and 14-13 Ma periods. Trace element ratios in Oligocene and Miocene igneous rocks commonly used as tectonic and porphyry fertility indicators (eg., La/Yb, Sr/Y) suggest that La Coipa is situated at the southern end of a domain characterized by a thickened crust that acted as a favorable place for emplacement of magmatic and hydrothermal fluids.

Preface

This thesis was supported and funded by Kinross Gold as part of a program of postgraduate studies for exploration geologists. The data collection, interpretation, and writing was done by the author, under the collaborative supervision of the committee members Thomas Bissig, Craig Hart, and James Scoates. Kinross supervisors were Jack Pritting, Darby Fletcher, and George Schroer. Fieldwork was done in June 2012, January-March 2013, and December 2013. The Kinross La Coipa Exploration Group supported it with logistics and field assistants.

This thesis has been divided into seven chapters plus discussion and conclusions. Chapter One summarizes the general concepts of La Coipa district, including the background description of epithermal deposits, the geological background of the study area and the mining history of this district. It also includes the justification for this study. Chapter Two contains a regional framework of the Maricunga, El Indio, and Los Pelambres-El Teniente metallogenic belts. Compilation of regional data included geological maps and geochemical analysis. Chapter Three explains the methodologies applied during this research.

The main body of the thesis is constituted by Chapter Four. Here, the La Coipa district scale geology is described based on the results of geological mapping, geochronology, geochemistry, isotopic-analysis, petrography, and complementary techniques. The author is responsible for the 1:10.000 scale geological map presented in this thesis. This map builds on company internal geological maps generated by the La Coipa Exploration Group (of which the author of this thesis was a member prior to 2012). All the rock samples considered for analysis mentioned before were processed by the author at the MDRU/UBC facilities. Petrographic thin-sections were prepared by Vancouver Petrographics. Geochronology was performed at the Pacific Centre for Isotopic and Geochemical Research (PCIGR) at UBC and at the Université de Genève. U-Pb analyses were conducted by Dr. Richard Friedman, and $^{40}Ar/^{39}Ar$ by Janet Gabites. At the Université de Genève, $^{40}Ar/^{39}Ar$ analyses were done by Richard Spikings. SEM, XRD, and Microprobe analyses were performed at the Electron Microbeam / X-ray Diffraction Facility at the Department of Earth, Ocean & Atmospheric Sciences at UBC, under the supervision of Dr. Mati Raudsepp. Sulfur isotopes were done at Queen's University by Christabel Jean.

Chapter Five includes the geochemical characterization of Tertiary magmatic rocks observed in La Coipa, and their context compared to regional geochemistry of rocks belonging to the Maricunga, El Indio and Los Pelambres-El Teniente belts. Whole-rock geochemical analyses were performed at the ACME laboratory, Vancouver. Chapters six and seven correspond to the discussion and conclusions respectively.

Table of Contents

Abstract..... ii

Preface..... iii

Table of Contents.....v

List of Tables.....x

List of Figures..... xi

List of Abbreviations.....xv

Acknowledgements.....xvi

Dedication.....xvii

Chapter 1: Introduction.....1

1.1 High-sulfidation epithermal systems.....2

1.2 Tectonic setting of the Maricunga belt.....4

1.3 La Coipa district.....5

Chapter 2: Geological Framework of the Maricunga belt.....11

2.1 Tectonics and magmatism of the Andean margin in Northern Chile.....11

2.2 Physiography.....14

2.3 The Maricunga belt.....14

2.3.1 Large scale structural control on magmatism and mineralization.....15

2.3.2 Paleozoic and Mesozoic basement rocks.....18

2.3.3 Regional magmatism and mineralization during the Oligocene-Miocene arc.....21

2.3.3.1 Volcanism and mineralization of the Maricunga belt for the 26 to 21 Ma period..22

2.3.3.2 Volcanism and mineralization of the Maricunga belt for the 21 to 17 Ma period..26

2.3.3.3 Volcanism and mineralization of the Maricunga belt for the 17 to 11 Ma period..29

2.3.3.4 Volcanism and mineralization of the Maricunga belt for the 11 to 4 Ma period....33

2.4 Magmatism and mineralization in areas to the south of the Maricunga belt: The El Indio and Los Pelambres-El Teniente belts.....37

2.4.1 The El Indio belt....38
2.4.2 The Los Pelambres-El Teniente belt....42
Chapter 3: Methodology....45
Chapter 4: Geology, Alteration and Mineralization of the La Coipa district....48
4.1 Paleozoic and Mesozoic basement rocks....48
4.1.1 Permian Granodiorite (Pzgd)....48
4.1.2 Estratos El Mono....56
4.1.2.1 Coarse conglomerates and quartz-rich sandstones (TrJem1)....56
4.1.2.2 Black Shales (TrJem2)....58
4.1.2.3 Quartz-rich sandstones and fine-grained conglomerates (TrJem3)....59
4.1.3 Montandón Formation (Jm)....60
4.1.4 Asientos Formation (Ja)....63
4.1.5 Estratos Quebrada Vicuñita (Jqv)....63
4.1.6 Pedernales Formation (JKp)....64
4.1.7 Quebrada Monardes Formation (Kqm)....65
4.1.8 Estratos de Cerro Los Carneros....66
4.1.9 Complejos Intrusivos (KSpa)....68
4.1.10 Codocedo Gabbro and Monzodioritic porphyritic dykes and stocks (KTgd)....68
4.2 Paleocene-Eocene rocks....71
4.2.1 Dacitic Porphyries (TPpd)....71
4.2.2 Rhyodacitic Porphyries and Dykes (TEpa) and Rhyolitic Domes (TEdrd)....71
4.2.3 Volcaniclastic Deposits (TEvd) and Dacitic Ignimbrite (TEdi)....74
4.2.4 Estratos de Huidobro (EOh)....76
4.3 Oligocene-Miocene volcanic arc....80
4.3.1 La Coipa Group....80
4.3.1.1 Ladera Tuffs (OMlc1)....80

4.3.1.2 Mina Vieja Domes (OMlc2).....82
4.3.1.3 Purén Domes (OMlc3).....84
4.3.1.4 Pompeya Pyroclastics (OMlc4).....86
4.3.2 Codocedo Group.....89
4.3.2.1 Azufrera Volcaniclastics (Mcd1).....89
4.3.2.2 Torito Dome (Mcd2).....91
4.3.2.3 Los Terneros Ignimbrite (Mcd3).....91
4.3.2.4 Vicuñita Domes (Mcd4).....94
4.3.2.5 Hematitized Sandstones and fine-grained Conglomerates (Mcd5).....98
4.3.2.6 Diatreme related base and surge deposits (Mcd6).....98
4.3.3 Breccia units.....98
4.3.3.1 Type 1 breccias: Tuffaceous matrix with hetherolitic fragments.....101
4.3.3.2 Type 2 breccias: Quartz+sulfide+alunite cement with hetherolitic fragments....101
4.3.3.3 Type 3 breccias: Iron oxide+quartz matrix with monolithic to hetherolitic fragments.....103
4.3.3.4 Type 4 breccias: Rock flour matrix and hetherolitic fragments.....104
4.4 Structural setting.....105
4.5 Hydrothermal alteration and mineralization.....107
4.5.1 High-sulfidation assemblages.....107
4.5.2 Intermediate-sulfidation assemblages.....111
4.5.3 Sericite-quartz.....113
4.6 Ore mineralogy.....113
4.7 Deposit characterization.....115
4.7.1 Ladera Farellón.....115
4.7.2 Can Can.....118
4.7.3 Coipa Norte.....121

4.7.4 Brecha Norte....121

4.7.5 Purén....126

4.8 Alunite geochronology....129

4.9 Sulfur Isotopes on alunite and adjacent sulfur-bearing minerals....143

Chapter 5: Whole-Rock Geochemistry of the La Coipa district....147

5.1 Major-element compositions....149

5.2 Trace-element compositions....154

5.3 Comparison with regional data....158

Chapter 6: Discussion....166

6.1 Regional distribution of magmatism through time and implications for tectonomagmatic evolution of the Pampean flat-slab....166

6.2 Petrogenesis of igneous rocks from La Coipa district and their context within the Maricunga belt....171

6.3 Metallogeny of La Coipa district and its regional context....174

6.4 Exploration model for La Coipa district and similar deposits in the Maricunga belt....177

Chapter 7: Conclusions....183

7.1 Exploration recommendations....185

7.2 Recommendations for future work....187

References....189

Appendices....206

Appendix A1: 1:20,000 scale geological map of the La Coipa district....207

Appendix A2: Location and analytical techniques applied to surface and drill-hole samples collected during the field mapping campaign. 209

Appendix A3: CA-ID-TIMS U-Pb Zircon Geochronology....223

Appendix A4: LA-ICP-MS U-Pb Zircon Geochronology....240

Appendix A5: $^{40}Ar/^{39}Ar$ Biotite Geochronology....245

Appendix A6: $^{40}Ar/^{39}Ar$ Alunite Geochronology....250

Appendix A7: Whole-Rock Geochemistry.....267

Appendix A8: QA/QC of whole-rock geochemistry: Precision.....276

Appendix A9: QA/QC of whole-rock geochemistry: Accuracy.....280

Appendix A10: Electron probe microanalysis (EPMA) of alunite samples.....286

List of Tables

Table 4.1: Summary of U-Pb ages on zircons obtained in the present study.....……55

Table 4.2: Summary of $^{40}Ar/^{39}Ar$ ages on biotite obtained in the present study…….....77

Table 4.3: Summary of $^{40}Ar/^{39}Ar$ ages on alunite obtained in the present study…….....130

Table 4.4: Summary of K/Ar ages on biotite obtained in previous studies…….....131

Table 4.5: $\delta^{34}S$ Isotopic composition of sulfur-bearing minerals analyzed in the present study….....144

List of Figures

Figure 1.1: Tectonic framework of Oligocene-Miocene metallogenic belts in northern and central Chile, and western Argentina…….....6

Figure 1.2: Location map of the La Coipa District, Atacama Region, Northern Chile…….....7

Figure 1.3: View of La Coipa and Esperanza districts with their mining operations (open pits and underground)…….....9

Figure 2.1: Distribution of the late Permian-Early Triassic Choiyoi magmatic province and Late Triassic-Early Jurassic extensional rift basins (bounded by normal faults) developed in the southern part of the South American continent …….....12

Figure 2.2: Geological map of the Maricunga belt. This map corresponds to the first model proposed for the magmatic and metallogenic evolution of the Maricunga belt….....16

Figure 2.3: Structural setting of the Domeyko Fault System (Eocene) at the latitude of La Coipa district…….....17

Figure 2.4: Geological map of the most important basement units cropping out in the Maricunga belt. It should be noted that the eastern part of the map is dominated by the Oligocene-Miocene and Pliocene arc…….....19

Figure 2.5: Chronostratigraphic scheme of basement units of the Maricunga belt…….....20

Figure 2.6: Volcanic and hypabyssal rocks and porphyry/epithermal deposits of the Maricunga Belt, 26 to 21 Ma…….....23

Figure 2.7: Volcanic and hypabyssal rocks and porphyry/epithermal deposits of the Maricunga belt, 21 to 17 Ma…….....27

Figure 2.8: Volcanic and hypabyssal rocks and porphyry/epithermal deposits of the Maricunga belt, 17 to 11 Ma…….....30

Figure 2.9: Volcanic and hypabyssal rocks and porphyry/epithermal deposits of the Maricunga Belt, 11 to 4 Ma…….....34

Figure 2.10: Geology and metallogeny of the El Indio belt…….....39

Figure 2.11: Geology and metallogeny of the Los Pelambres-El Teniente belt.....43

Figure 4.1: Topographic map of La Coipa district showing locations mentioned in the text….....49

Figure 4.2. A: Simplified geologic simplified map of La Coipa district.....……50

Figure 4.2. B: Legend of lithological units defined for the La Coipa district…….....51

Figure 4.3: Stratigraphic column proposed for the La Coipa district…….....52

Figure 4.4: Photographs and photomicrographs of the Permian Granodiorite….....53

Figure 4.5: Photographs of characteristic rocks of the Estratos El Mono unit.....57

Figure 4.6: Photographs of the Jurassic sedimentary and volcanic units….....61

Figure 4.7: Photographs of the Cretaceous rocks: Estratos Cerro Los Carneros (Ksecc2)….....67

Figure 4.8: Photographs and photomicrographs of the Cretaceous and Paleocene intrusive and hypabyssal rocks….....70

Figure 4.9: Photographs and photomicrographs of the Paleocene/Eocene hypabyssal rocks….....72

Figure 4.10: Photographs and photomicrographs of the Andesitic ignimbrite and volcaniclastic deposits (TEia and TEvd)…….....75

Figure 4.11: Photographs and microphotographs of the Estratos de Huidobro….....79

Figure 4.12: Photographs of the Ladera Tuffs (OMlc1) member of the La Coipa Group.....81

Figure 4.13: Photographs and photomicrographs of the Mina Vieja domes (OMlc2)….....83

Figure 4.14: Photographs and photomicrographs of the Purén domes (OMlc3)….....85

Figure 4.15. Photographs of the Pompeya Pyroclastics unit (OMlc4)….....87

Figure 4.16: Photographs and photomicrographs of the Azufrera volcaniclastics (Mcd1).....90

Figure 4.17: Photographs and photomicrographs of the Torito Dome (Mcd2).....92

Figure 4.18: Photographs and photomicrographs of the Los Terneros Ignimbrite (Mcd3)….....93

Figure 4.19: Photographs and photomicrographs of the Vicuñita domes (Mcd4)….....95

Figure 4.20: Photographs and photomicrographs of the Vicuñita domes (Mcd4)….....97

Figure 4.21: Photographs of the Hematitized sandstones and fine-grained conglomerate unit (Mcd5)….....99

Figure 4.22: Photographs of the Diatreme related base and surge deposits unit (Mcd6)….....100

Figure 4.23: Photographs and photomicrographs of the Breccia units….....102

Figure 4.24: Alteration map of La Coipa district. Alteration classes based on surface mapping, short-wave infrared spectroscopy (SWIR) using Terraspec® spectrometer, and hyperspectral data collected from an airborne survey done by Kinross in 2007….....108

Figure 4.25: Mineralogy of advanced argillic alteration phases…….....110

Figure 4.26: Photographs and photomicrographs of altered rocks in the Purén deposit and in the tailings area…….....112

Figure 4.27: Sulfides and oxidized ore minerals identified in the La Coipa district….....114

Figure 4.28: Representative NW-SE geological section through the Ladera Farellón deposit…….116

Figure 4.29: Representative NW-SE alteration and mineralization section through the Ladera Farellón deposit….....117

Figure 4.30: Representative NW-SE geological section through the Can Can deposit….....119

Figure 4.31: Representative NW-SE alteration and mineralization section through the Can Can deposit…….....120

Figure 4.32: Representative NW-SE geological section through the Coipa Norte deposit….....122

Figure 4.33: Representative NW-SE alteration and mineralization section through the Coipa Norte deposit….....123

Figure 4.34: Representative W-E geological section through the Brecha Norte deposit….....124

Figure 4.35: Representative W-E alteration and mineralization section through the Brecha Norte deposit….....125

Figure 4.36: Representative NW-SE geological section through the Purén deposit….....127

Figure 4.37: Representative NW-SE alteration and mineralization section through the Purén deposit….....128

Figure 4.38: Photographs of alunite samples dated by $^{40}Ar/^{39}Ar$ geochronology (Part I)….....132

Figure 4.39: Photographs of alunite samples dated by $^{40}Ar/^{39}Ar$ geochronology (Part II)….....133

Figure 4.40: $^{40}Ar/^{39}Ar$ results for alunite samples (Part I)…….....134

Figure 4.41: $^{40}Ar/^{39}Ar$ results for alunite samples (Part II)….....136

Figure 4.42: Scanning Electrom Microscopy (SEM) images of alunite samples….....138

Figure 4.43: $^{40}Ar/^{39}Ar$ geochronology for alunite samples (Part III)….....140

Figure 4.44: Summary of geochronological ages obtained at La Coipa district….....142

Figure 4.45: Sulfide-sulfate pairs of $\delta^{34}S$ for alunite and its associated sulfide minerals (pyrite or enargite) samples considered for $^{40}Ar/^{39}Ar$ geochronology…….....146

Figure 5.1: Location map of samples analyzed by whole-rock geochemistry….....148

Figure 5.2: Alteration Diagram (from Williams and Davidson, 2004) applied to whole-rock analysis of samples from La Coipa District….....150

Figure 5.3: R1-R2 Diagram (from De La Roche, 1980) for plutonic rocks from La Coipa district…151

Figure 5.4: K_2O vs. SiO_2 diagram (from Peccerillo and Taylor, 1976) for volcanic and hypabyssal rocks from La Coipa district….....152

Figure 5.5: TAS Diagram (from Le Maitre et al., 1989) for volcanic and hypabyssal rocks from La Coipa district….....153

Figure 5.6: Major elements Harker diagrams for La Coipa samples compared to Oligocene-Miocene volcanic and hypabyssal rocks of Maricunga, El Indio, and El Teniente-Los Pelambres belts…….....155

Figure 5.7: MORB-normalized trace element diagram (from Pearce, 1983) for Tertiary volcanic and hypabyssal rocks from La Coipa district…….....156

Figure 5.8: MORB-normalized REE diagram (from Sun and McDonough, 1989) for Tertiary volcanic and hypabyssal rocks…….....157

Figure 5.9: K_2O vs. SiO_2 diagram (from Peccerillo and Taylor, 1976) for volcanic and hypabyssal rocks of the Maricunga Belt…….....159

Figure 5.10: Sr/Y vs. SiO_2 wt% diagram (from Loucks, 2014) used to discriminate Cu and Cu-Au porphyry related rocks (region within red dashed line) from barren tholeiitic and calc-alkaline arc suites…….....160

Figure 5.11: La/Yb and Sm/Yb vs. Age and SiO_2 respectively. Samples from the Oligocene-Miocene volcanic arc…….....162

Figure 5.12: Dy/Dy* vs. Dy/Yb diagram. Samples from the Oligocene-Miocene volcanic arc with available geochemical data…….....164

Figure 5.13: Regional maps of petrogenetic indicators for Oligocene-Miocene rocks….....165

Figure 6.1: Review of Figure 1.1 highlighting the factors that contribute to the interpretation of a major discontinuity across the Andean margin.....….....167

Figure 6.2: Schematic geologic section of the La Coipa district…….....180

List of Abbreviations

Ag = Silver

Au = Gold

AuEq = Gold equivalent

°C = Celsius degree

Cm = Centimeter

CMLC = Compañia Minera La Coipa

E = East

g/t = Grams per ton

km = Kilometer

Lat = Latitutde

LOI = Lost of Ignition

Long = Longitude

M = Meter

mm = Milimeter

Ma = Million of years

MDO = Mantos de Oro

MORB = Mid-Ocean Ridge Basalt

Moz = million of ounces

N = North

REE = Rare Earth Elements

S = South

SWIR = Short-Wave Infrared

TVX = TVX Gold Inc.

W = West

Acknowledgements

The author would like to thank, in first place, the understanding of my wife and daughter, who accompanied me in this fructiferous odyssey that demanded incredible familiar efforts. Secondly, I would like to thank the support of Kinross Gold, in special to Jack Pritting and Graeme Davies that allowed this project to be developed. I also appreciate the discussion and edits of Darby Fletcher. The collection of rock samples was supported by two excellent field assistants, José Bugueño and Luis Romero.

The final product of this research has the remarkable contributions and expertise of my supervisors, Thomas Bissig, Craig Hart, and James Scoates. I am really greatful of your guidance. I also would like to thank the help of Arne and Curtis, who solved thousand of questions and problems during my stay at the MDRU.

Finally but not last, I am really thankfull of many friends that made our stay in Canada an unforgettable experience. Eddie, Myriam, Ricardo, Alejandra, Miguel, José, Irene, Paula, Matías, Antonio, Jaime, Alfonso, Hildebrando, Brian, Martín, and Agustín. I really enjoyed your friendship.

To Andrea and Leonor

Chapter 1: Introduction

The location of magmatic-hydrothermal ore deposits is controlled by the large-scale architecture of the lithosphere and is typically focused along sutures between different lithospheric blocks (e.g., Griffin et al., 2013). In the Central Andes, the boundaries between ancient lithospheric blocks are commonly obscured by younger volcanic or sedimentary rocks. However, it has been suggested that the location of some porphyry ore deposits of northern Chile is controlled by large scale basement discontinuities (e.g., Gow and Walshe, 2005). This thesis presents new geological, geochronological and geochemical data on the La Coipa district, where a cluster of high- to intermediate-sulfidation epithermal Ag-Au deposits is located near a major discontinuity at the western margin of the South American continent. The new data allow discussing possible basement controls on mineralization in the district and on the regional distribution of ore deposit types.

The La Coipa district has been the most productive high-sulfidation epithermal Ag-Au system of the Maricunga belt. This metallogenic belt (Sillitoe et al., 1991; Kay et al., 1994; Mpodozis et al., 1995) is characterized by a predominance of gold-rich porphyry systems that in most cases are overprinted by acid-sulfate alteration which is largely barren of epithermal mineralization (Vila and Sillitoe, 1991; Muntean and Einaudi, 2001). In the La Coipa district, in contrast, gold-silver mineralization is spatially associated with acid-sulfate alteration but there is no clear evidence for spatially and temporally related porphyry-style mineralization. Paradoxically, La Coipa is, together with the Maricunga mine (previously called Refugio; Muntean and Einaudi, 2000), the only major producing mine of the last three decades within the belt, and most gold-rich porphyry districts which define the metallogeny have not seen major gold or copper production (e.g., Cerro Maricunga, and Lobo, King, 1992; Caspiche, Sillitoe et al., 2013; and Cerro Casale, Hollings et al., 2014). Other mines that have seen sporadic production include the Esperanza and La Pepa high-sulfidation deposits and the Marte Au rich-porphyry (Vila, 1991; King, 1992; Muntean and Einuadi, 2001). La Coipa has, together with the nearby Esperanza district, the largest argillic and advanced argillic alteration footprint in the Maricunga belt. The only study in an international peer reviewed journal focused on La Coipa corresponds to the paper of Oviedo et al. (1991). These authors described the local geology and style of mineralization recognized during the early years of mining activity.

Despite its importance, exploration activities were limited in the last 25 years in the La Coipa district and increased exploration efforts were initiated in 2006. This was too late to prevent the mine from being put on care and maintenance in late 2013. The present thesis was funded by Kinross as part of a larger effort to improve the geological basis for district exploration. The main objective of this research is to generate a geological model that explains the genetic and temporal relationship between the volcanic stratigraphy, hypabyssal intrusive units and epithermal mineralization. To accomplish this objective, a series of methodologies such as geological mapping, U-Pb and $^{40}Ar/^{39}Ar$ geochronology, whole-rock geochemistry of igneous rocks, isotopic characterization of alunite and associated sulfide minerals, and characterization of each deposit were applied. For the contextualization of the Tertiary evolution at the La Coipa district, a regional overview of the Oligocene-Miocene magmatic arc that comprised the Andean margin between Lat. 25°S and 34°S is included in this study.

The outcomes of this study will provide the basis for applying the geological concepts of igneous host-rocks as an important criteria for exploration within the La Coipa district and also in grass-roots prospects along the Maricunga belt. This study describes the evolution of the magmatic history and related mineralization events, situating the La Coipa district into the temporal and tectonic framework that allowed it to become one of the most important mineralized centers of the Maricunga belt. As will be discussed later, the La Coipa high-sulfidation epithermal deposit has experienced a long history of episodic magmatic and hydrothermal activity of epithermal type that distinguishes this center from others located in the Maricunga metallogenic belt which is dominated by gold-rich porphyry systems.

1.1 High-sulfidation epithermal systems

Epithermal systems were first described in the early twentieth century (Lindgren, 1922; 1933). The term epithermal has its origin in the range of temperature and pressure of hydrothermal systems exposed to near-surface conditions, i.e., temperatures below 300°C and depths of formation less than 1.5 km (Simmons et al., 2005). However, genetic models for this type of deposits were not advanced until the late twentieth century (Sillitoe, 1977; Hayba et al., 1985; Bonham, 1986; Heald, 1987;

Hedenquist, 1987; Berger and Henley, 1989; White and Hedenquist, 1990; Sillitoe, 1993; Cooke and Simmons, 2000; Sillitoe and Hedenquist, 2003). These workers established the relationship between plate tectonics, magmatic and hydrothermal processes. Later, thanks to advances in analytical techniques, the fluid processes and vertical transition between Cu-Au-Mo porphyry and shallower epithermal systems were investigated (e.g., Heinrich et al., 1999; Heinrich, 2005; Pudack et al., 2009).

Epithermal deposits are commonly associated with volcanic rocks related to calc-alkaline to alkaline arc magmatism, either in intra-, near- or back-arc settings, as well as rift settings (Sillitoe and Hedenquist, 2003). Several classification schemes based on ore, gangue and alteration mineralogy, which reflect some aspects of fluid chemistry (pH, oxidation state and sulfidation state) have been proposed to group these deposits (e.g., Sillitoe, 1977; Hedenquist, 1987; White and Hedenquist, 1990; Cooke and Deyell, 2003; Simmons et al., 2005). The most widely used classification divides the deposits in high-, intermediate- and low-sulfidation types (Hedenquist et al., 2000).

High-sulfidation systems, which are formed by acid fluids with sulfide assemblages of high-sulfidation state, typically contain ore minerals like pyrite, enargite, luzonite, famatinite and covellite, and gangue minerals dominated by quartz, alunite, pyrophyllite, dickite, and kaolinite (Sillitoe and Hedenquist, 2003; Simmons et al., 2005). The alteration mineralogy shows a concentric zonation that reflects temperature gradients and degree of interaction with acid fluids, varying from a silica-rich center and haloes of advanced argillic alteration and more distal argillic and propylitic alteration assemblages (Hedenquist et al., 2000). La Coipa is considered a classic example of a high-sulfidation epithermal deposit (Oviedo et al., 1991).

1.2 Tectonic setting of the Maricunga belt

The current Andean margin of South America is characterized by a latitudinal segmentation with regions with active volcanism and Andean-type subduction, separated by aseismic non volcanic regions characterized by flat subduction (Ramos, 2009). A spatial correlation between flat-slab segments and occurrence of high-sulfidation epithermal systems found in this region has been documented along the Andean margin (Bissig et al., 2015, and references therein). The particularity of the Maricunga belt is that it is situated in a transition zone between a current flat-slab subduction segment without volcanism to the south, and the Central Volcanic Zone (CVZ) to the north (Figure 1.1), which is characterized by extensive Neogene volcanism and development of the Altiplano-Puna high plateau (Alonso & Viramonte, 1987; Allmendinger et al., 1997). The shallowing of the subducting slab in the current flat-slab region (27.5°-33°S) is considered a process that started 18 Ma ago (Kay et al., 1991; Walker et al., 1991). Now, the Nazca plate is subducting with an angle of ~30° below the CVZ, and a near-horizontal angle below the flat-slab region (Cahill & Isacks, 1992).

The northern limit of the flat-slab region is considered a major tectonic discontinuity of the Andean margin (Moore, 1979; Jordan et al., 1983; González-Ferrán et al., 1985; Walker et al., 1991). This volcanic discontinuity can be spatially correlated with other features that show segmentation at this latitude, such as geomorphological domains and basement blocks. According to Ramos (2009), the contact between the northern edge of the Famatina and Cuyania terranes and the southern edge of the Antofalla terrane is located in this region (Figure 1.1). Reflected in specific features observed in the upper plate (morphology, location of volcanic centers, seismic activity), this discontinuity is interpreted as a crustal scale feature (Moore, 1979; Jordan et al., 1983; Gonzalez-Ferran et al., 1985), indicating a possible suture boundary generated during the Paleozoic amalgamation of allochthonous and para-autochthonous terranes (Ramos, 2008).

The particular combination of tectonic and magmatic processes described at the Maricunga belt have made this region an excellent natural laboratory to understand the connection between magmatism, uplift and tectonics, and mineralizing processes (e.g., Bissig et al., 2015; Kay and Mpodozis, 2002). Moreover, the Maricunga belt is widely recognized as the first place where the gold-rich endmember porphyry systems were described (Vila and Sillitoe, 1991).

1.3 La Coipa district

The La Coipa district is located in the Atacama Region, northern Chile, approximately on latitude 26°49'6'' S and longitude 69°14'06'' W, between elevations of 3500 and 4700 m (Figure 1.2). The district contains a cluster of deposits distributed in a semi-circular array that include Ladera Farellón, Can-Can, Coipa Norte, Brecha Norte, Purén, and Pompeya (Figure 1.3). This district is situated in the northern segment of the Maricunga metallogenic belt, an Oligocene-Miocene volcano-magmatic province that hosts several gold-rich porphyry systems and high-sulfidation epithermal centers (Vila and Sillitoe, 1991; Mpodozis et al., 1995).

The geological context of La Coipa was first described in the early 1990s, during the first modern reconnaissance campaigns in the Maricunga belt (Oviedo et al., 1991; Sillitoe et al., 1991; Mpodozis et al., 1995). Since then, La Coipa has experienced a long history of mining and exploration that have dramatically increased the exposure and availability of geological data. For the present study, historic maps and exploration data were integrated with information collected during this research to provide a district scale geological exploration framework.

The first mining activities in the La Coipa district date back to 1876 (Zentilli, 1974), when a small underground operation at what now is known as La Coipa Vieja mine, was established 1.5 km southeast of the Ladera Farellón open pit (Figure 1.3). The discovery of the bonanza-style El Indio mine during the late 1970s, located 300 km south of La Coipa, led several companies to increase the exploration in the high Andes of northern Chile (Rivera, 1990).

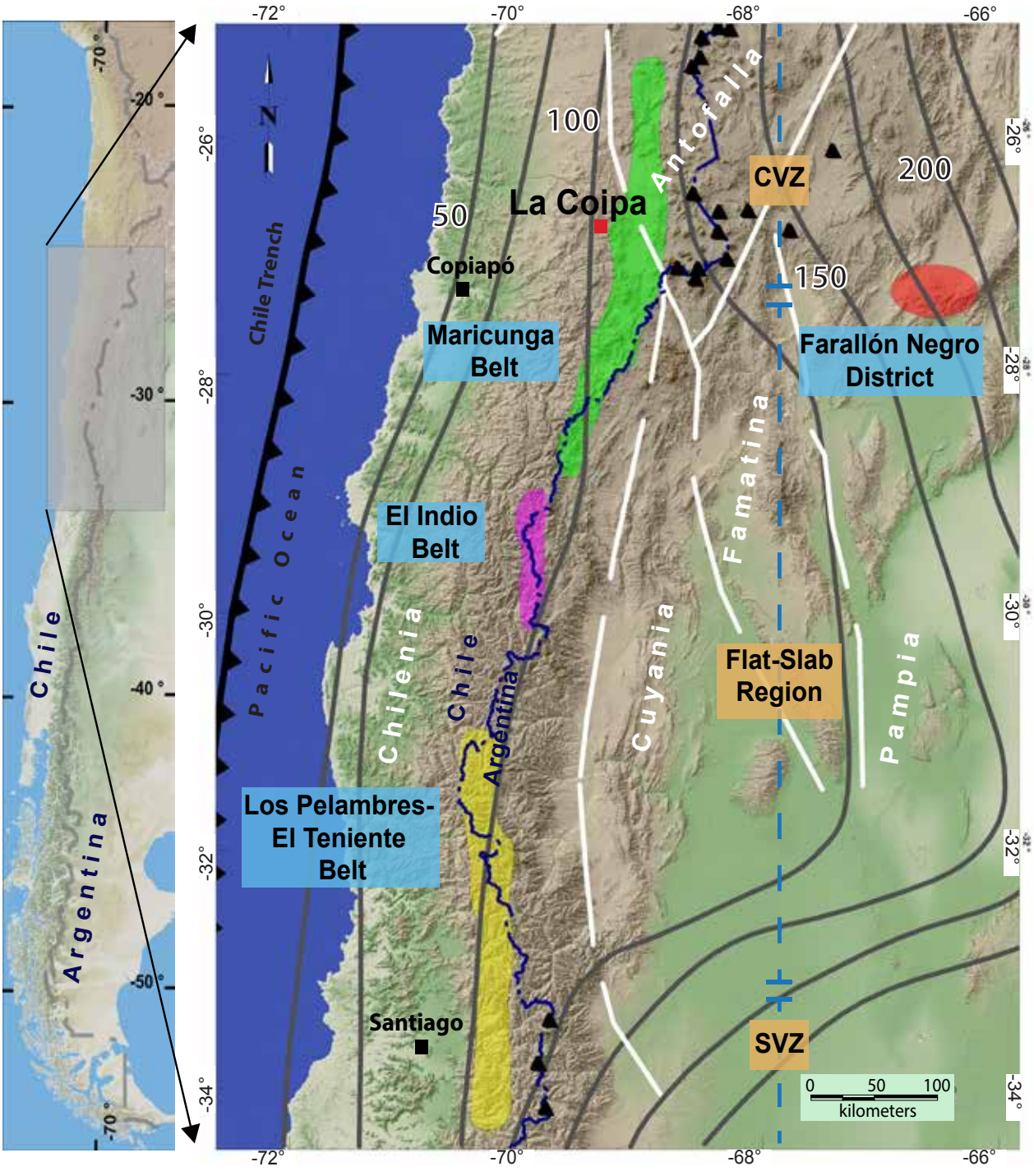

Figure 1.1. Tectonic framework of Oligocene-Miocene metallogenic belts in northern and central Chile, and western Argentina. Green field shows the position of the Maricunga Belt (with extension proposed in this study), pink field showing the El Indio Belt, yellow field showing the Los Pelambres-El Teniente Belt, and red box showing the Farellón Negro District. Solid grey lines show contours of the subducting Nazca plate with depths in kilometers to the Wadati-Benioff zone as modified from Mulcahy et al. (2010) and Mulcahy (2012) after Cahill & Isacks (1992). Solid black line indicates the Chile trench of the subducting Nazca plate. Black triangles indicate the active volcanic centers. Dashed blue lines show the distribution of the Central Volcanic Zone (CVZ), the flat-slab region, and the Southern Volcanic Zone (SVZ). White dashed line show the suture of terranes (named with white letters) proposed by Ramos (2009). Blue line representing the border between Chile and Argentina.

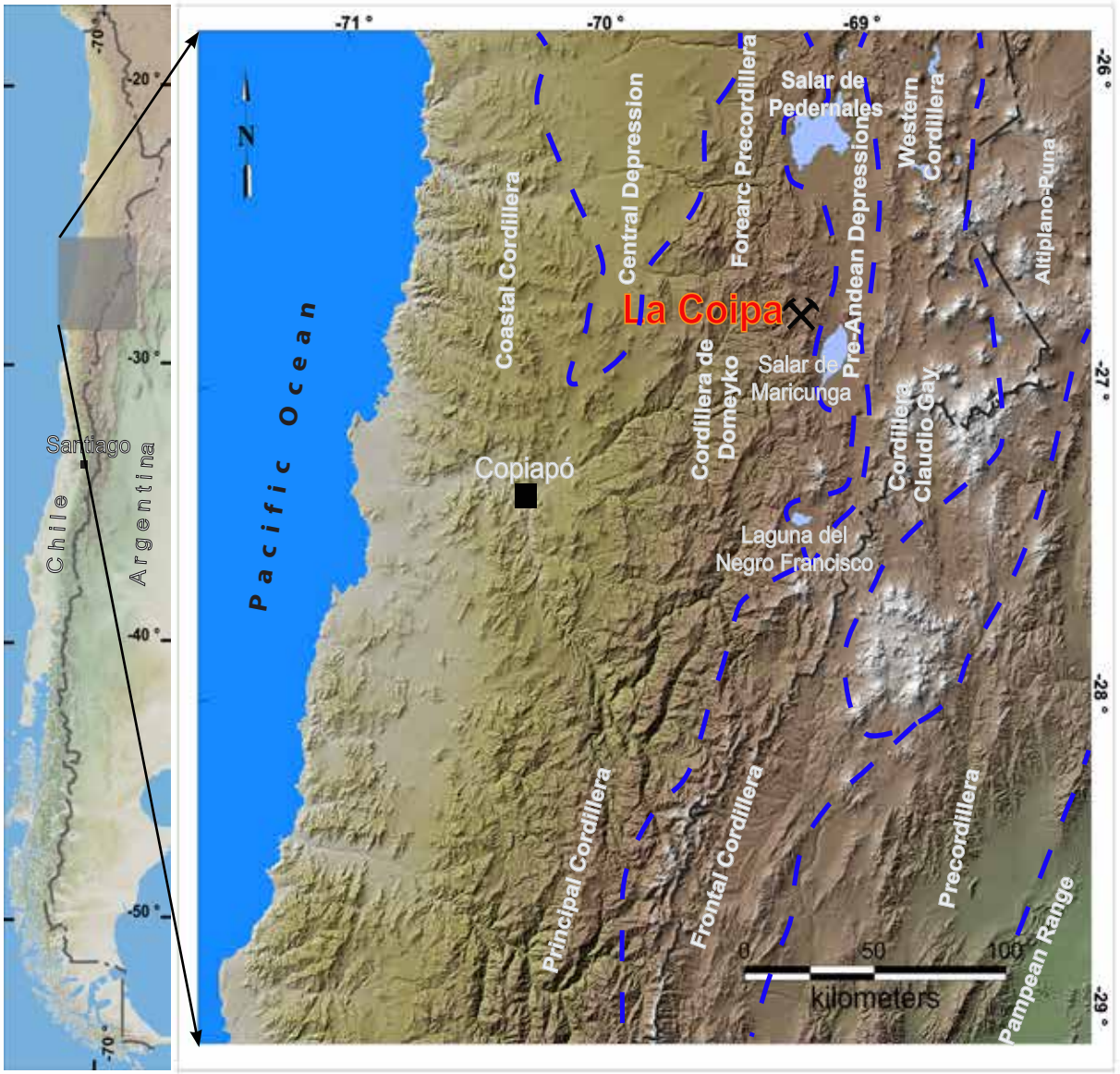

Figure 1.2. Location map of the La Coipa District, Atacama Region, Northern Chile: Digital Elevation Model (DEM) showing the main geomorphological domains of the Atacama Region. Domains taken from Riquelme et al., 2007; and Charrier et al., 2007.

The outcome of the identification of several color anomaly targets observed during reconnaissance flights in the Andean Cordillera in the Atacama region gave way to an aggressive exploration campaign carried out by companies such as Sierra Morena and Anglo American (Vila and Sillitoe, 1991). The La Coipa district was targeted by Sierra Morena during 1980. The following year, a talus-fines geochemical survey was executed, which led to the selection of three targets: Ladera Farellón, Don Eduardo, and Coipa Norte. During this year, Consolidated Goldfields acquired Sierra Morena. In 1982, the construction of roads and trenches led to the first signs of a new discovery, considering the attractive results of a 60 m long trench with 640 g/t Ag over what is now the Ladera Farellón orebody. Between 1983 and 1986, the first drilling campaign delineated these orebodies. During 1987, TVX Gold acquired the rights to the property, creating the Compañia Minera Nacional, changed two years later into the future operator during the entire life of mine: Compañia Minera Mantos de Oro (MDO). La Coipa started its production during 1989, operating a pilot plant with a 1.000 tons-per-day cyanide leach capacity. At this time, the mine was owned by two equal parties: TVX and Placer Dome. During 1991, the plant started to operate at full capacity, processing 15.000 ton-per-day with an agitation leach plant using the Merryl-Crowe methodology (Oviedo et al., 1991). Two open pits initiated at this time: Ladera Farellón and Coipa Norte. During 1997, lower prices of precious metals forced to MDO to negotiate the resources discovered by Anglo American at the Esperanza district (Figure 1.3), which yielded to MDO the rights to extract ore from the silver-rich breccia hosted Chimberos deposit (Figure 1.3; Vila, 1991). This material was shipped 25 km to La Coipa and was the only source that fed the plant during approximately two years.

The current owner of La Coipa, Kinross Gold, acquired the TVX owned part in 2003. In the same year, the Brecha Norte open pit initiated its operation. Up to now, the pits operating at La Coipa were discovered by surface expression of mineralization. Exploration of the eastern domain of the district, characterized by relatively smooth topography with colluvium and alluvium regolith covering the area, led to the discovery of the blind Purén deposit, which started its operation in 2006. During this year, Barrick acquired Placer Dome, and decided to sell its portion of La Coipa to Goldcorp. During 2007, Kinross acquired the Goldcorp owned portion of La Coipa, becoming the exclusive owner of the district.

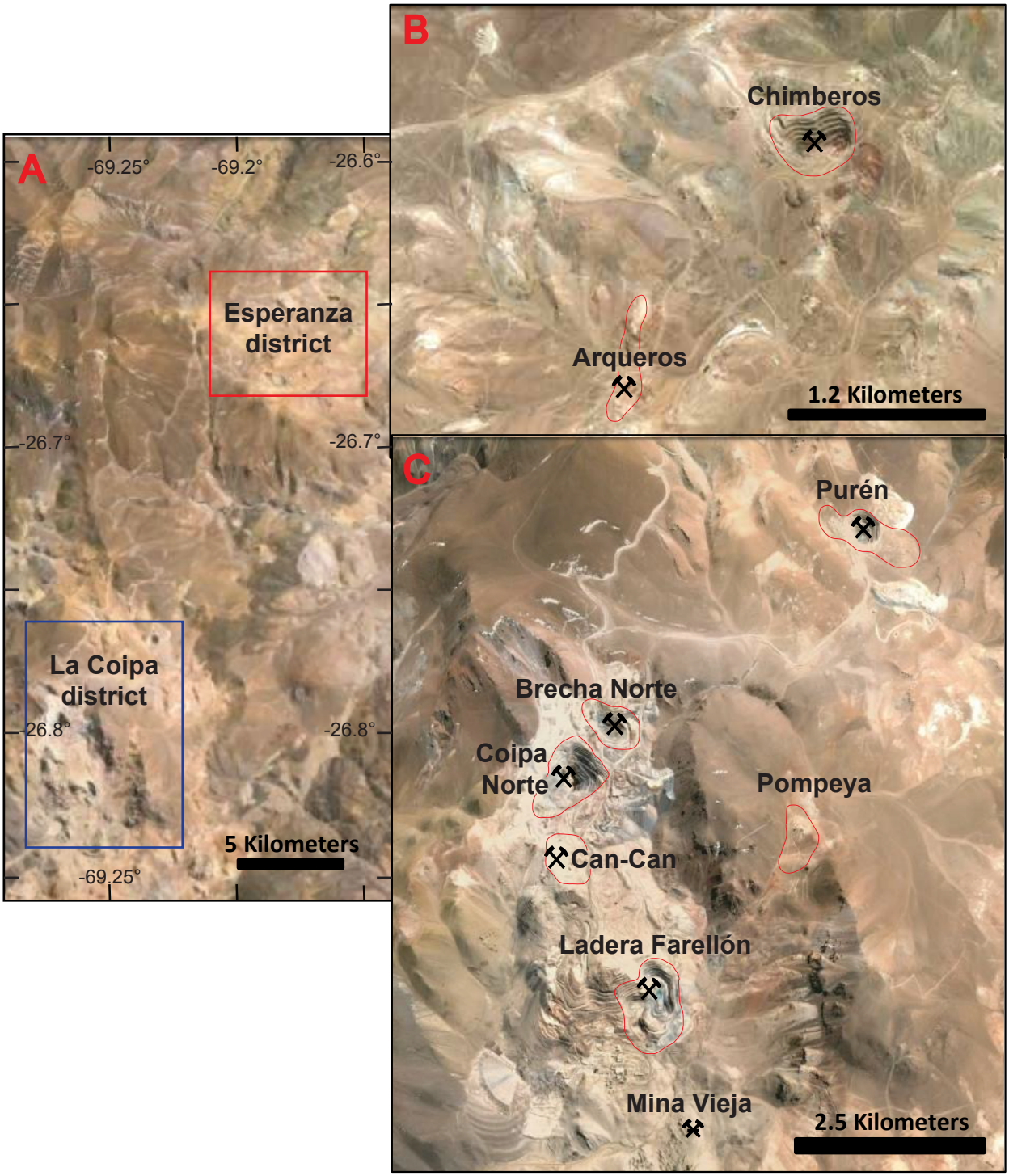

Figure 1.3. View of La Coipa and Esperanza districts with their mining operations (open pits and underground). A) Central-west segment of the Maricunga belt showing the location and distance between the La Coipa (blue rectangle) and Esperanza (red rectangle) districts. B) Esperanza district, showing the location of the Chimberos open-pit and the Arqueros underground operation. C) La Coipa district, showing the cluster of deposits that constitute the mined open pits, the historic artisanal underground operation at Mina Vieja, and the recent discovery of the Pompeya deposit. Base imagery: Google Earth for figures 1.3.A and 1.3.B, GeoEye satellite data for figure 1.3.C.

Considering the exploration potential of the area that surrounds the MDO mining concessions, in 2009 Kinross signed an agreement with Compañia Minera La Coipa (CMLC), to begin exploration over its property. Under this deal, the discovery of the Pompeya deposit during 2011 opened a new frontier in the district. Nevertheless, the mine is currently under care and maintenance, as of late 2013, mainly because of depletion of reserves. The mining of the >1Moz AuEq Pompeya deposit will permit the re-opening of the mine operation, but a decision to start the production has not been reached by Kinross. Prior to the temporary closure, the production of oxide reserves from La Coipa between 1991 and 2012 was approximately 230 Moz Ag and 3.5 Moz Au.

Chapter 2: Geological Framework of the Maricunga belt

2.1 Tectonics and magmatism of the Andean margin in Northern Chile

The orogeny of the western margin of the South American continent is very complex and has evolved through its lifetime with multiple variations of tectonic settings (Ramos, 2009). During the Phanerozoic, this active margin was characterized by subduction of the Nazca and precursor oceanic plates under the South American continental plate, generating arc magmatism that, since the Jurassic, built one of the most prominent orogenic landscapes on earth: the Andean Range.

Collision and accretion of allocthonous and/or para-autochthonous terranes characterized the western margin of South America during the late Proterozoic-late Paleozoic (Alvarez et al., 2013). The western margin of the Gondwana supercontinent became active at 530 Ma (Cawood, 2005), initiating its associated subduction related magmatism. Since then, magmatism along the active margin has been continuous. After the accretionary stage, a late Carboniferous-early Permian magmatic arc developed on the accreted terranes (Mpodozis and Cornejo, 2012). In the late Permian-Early Triassic, an episode of felsic volcanism and granitoid plutonism changed from subduction-related arc magmatism to a widespread extensional volcanism that gave rise to the extensive felsic Choiyoi Magmatic Province (Figure 2.1; Ramos, 2009), developed between the Salar de Atacama (Lat. 23°30'S) and northern Patagonia (Lat. 42°S). In the Late Triassic-Early Jurassic, NW-trending extensional rift basins with bimodal volcanism developed in response to the break-up of the Pangea supercontinent (Charrier et al., 2007). These regionally extensive rift basins and associated NW-trending faults are developed across the strike of the Andes and influenced the distribution of magmatism and ore deposits later in the Andean evolution (Richards, 2000).

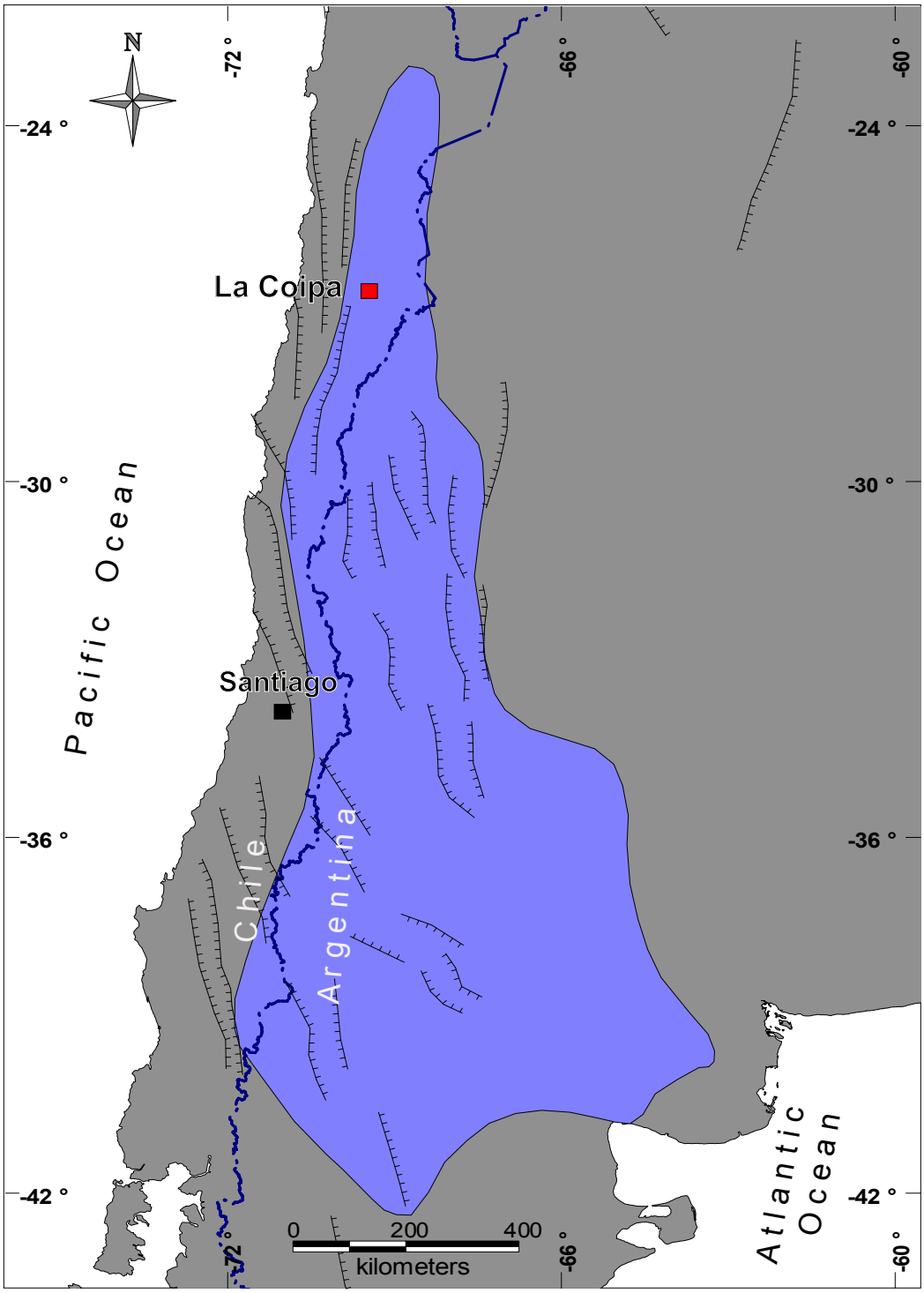

Figure 2.1. Distribution of the late Permian-Early Triassic Choiyoi magmatic province and Late Triassic-Early Jurassic extensional rift basins (bounded by normal faults) developed in the southern part of the South American continent (Modified from Ramos, 2009).

A reestablishment of subduction during the Early Jurassic initiated the present configuration of the Andean margin. Charrier et al. (2007) divided the Andean orogenesis along the margin of northern and central Chile into three stages. The first stage (late Early Jurassic to late Early Cretaceous) consisted of widely distributed volcanic activity along the arc (which central axis is in the present Coastal Cordillera) and the deposition of abundant marine and terrestrial sedimentary deposits in the contemporaneous back-arc basin to the east. The current absence of the forearc basin for this early magmatic arc, considering the relative migration of the South American continent to the west, is explained by progressive subduction-erosion of the continental margin (Charrier et al., 2007).

The second stage (late Early Cretaceous to early Paleogene) is characterized by migration of arc magmatism to the east, and the creation of a foreland basin instead of a back-arc basin. Abundant volcanic deposits of andesitic and dacitic to rhyolitic compositions were associated in most cases with caldera structures (Charrier et al., 2007). This period is defined by oblique subduction accompanied by extensive parallel to arc transtensional sinistral faulting developed on the present Central Depression and Forearc Precordillera. This setting is part of the Domeyko Fault System (DFS; Figure 2.2; Charrier et al., 2007; Niemeyer and Urrutia, 2009; Abels and Bischoff, 2009).

The third and last stage (late Paleogene-Present) is represented by the current configuration of the Andean margin. This period is characterized by intense uplift and shortening associated with an overall near-orthogonal subduction (Charrier et al., 2007). During this third stage, most of the copper, gold and silver deposits found at the western margin of the continent were emplaced. The intensity of shortening and thickening of the crust produced the second highest plateau on earth: the Altiplano-Puna, which also hosts the highest stratovolcanoes on earth (Ojos del Salado, Monte Pissis and Cerro Bonete Chico), and one of the largest concentration of felsic ignimbrites (Trumbull et al., 2006).

2.2 Physiography

The physiography of the western margin of the South American continent follows a longitudinal division of parallel to margin domains, which reflect the current tectonic setting for each segment of the Andean margin. In particular, the geomorphology of the Andean segment that encompasses the Maricunga belt reflects a major discontinuity observed at Lat. 27.5° S. North of this latitude, the Andean margin can be divided, from west to east, into the Coastal Cordillera, the Central Depression, the Forearc Precordillera, the Pre-Andean Depression, the Western Cordillera, the Altiplano-Puna and the Eastern Cordillera (Figure 1.2). In this region, the Forearc Precordillera is separated from the Western Cordillera (locally called Cordillera Claudio Gay) by the Pre-Andean Depression, which consists of internally drained basins filled by saline-playa sediments, that from north to south, constitute the Punta Negra, Pedernales, Maricunga and Laguna del Negro Francisco salares. The axis of the Western Cordillera hosts the active volcanic front. South of Lat. 27.5° S, the geomorphological domains are, from west to east, the Coastal Cordillera, the Principal Cordillera, the Frontal Cordillera, the Precordillera and the Pampean Range (Figure 1.2; Charrier et al., 2007). The Pre-Andean and Central Depressions are absent in this region.

In the northern segment of the Maricunga belt, the Oligocene-Miocene magmatic arc is hosted in the Forearc Precordillera and in the westernmost part of the Western Cordillera. Towards the south of the Lat. 27.5°S discontinuity, the Oligocene-Miocene magmatic arc is restricted to the Principal Cordillera.

2.3 The Maricunga belt

The Maricunga belt was defined as a 200x50 km north-oriented metallogenic belt of Oligocene-Miocene age that extends between latitudes 26° to 28°S along the Domeyko Cordillera and its southern prolongation onto the Principal Cordillera (Figure 2.2; Villa and Sillitoe, 1991). It hosts multiple centers of alteration and mineralization mostly discovered during the 1980s (e.g., Cerro Casale, Lobo-Marte, and Maricunga). Based on K-Ar geochronological ages of volcanic rocks and their respective

mineralized systems, Vila and Sillitoe (1991) defined a western sub-belt (24-20 Ma) and an eastern sub-belt (14-13 Ma), which locally overlap (Figure 2.2). However, recent regional geological mapping, geochronological data; much of it presented in this thesis, and new mineral discoveries, indicate a need for a new definition of dimensions, chronology, and distribution of magmatic and hydrothermal activity along the belt. Considering these multiple advances of geological knowledge, remarkable findings of new mineral resources could increase the first estimation of endowment of gold, silver and copper defined for this metallogenetic province. Examples of prospects discovered and delineated since 1991 include Maricunga, Lobo-Marte, Caspiche, Cerro Casale, Cerro Maricunga, Pompeya, and Caserones.

2.3.1 Large scale structural control on magmatism and mineralization

Transition periods between the different stages of the Andean orogeny are characterized by compressive tectonic events that inverted and deformed sedimentary basins that constituted the intra-arc, back-arc and later foreland basins developed during the evolution of arc magmatism that characterized each stage of the Andean formation (Charrier et al., 2007). During the Late Cretaceous, a generalized compressive episode deformed the Mesozoic sequences developed in a back-arc domain at the present Central Depression and Precordillera (Arévalo and Mpodozis, 1991). Later, during the Eocene, folding and thrusting occurred along the sinistral/dextral transpressional Domeyko Fault System (DFS), which includes the Potrerillos Fold and Thrust Belt (PFTB; Figure 2.3). The PFTB defines the axis of the Precordillera domain immediately north of La Coipa (Arriagada et al., 2006). According to these authors, the DFS comprises structures formed during the Jurassic extension, which were reactivated during the Late Cretaceous basin inversion and Early Tertiary compression, and the main Incaic tectonic event (45-35 Ma), leading to the deformation of the Cordillera de Domeyko. A second-order array of transpressive sinistral deformation, represented by left-lateral strike-slip subvertical NW-striking faults controlled in the eastern part of the Precordillera the emplacement of Eocene and Oligocene-Miocene hypabyssal units (Cornejo et al., 1993).

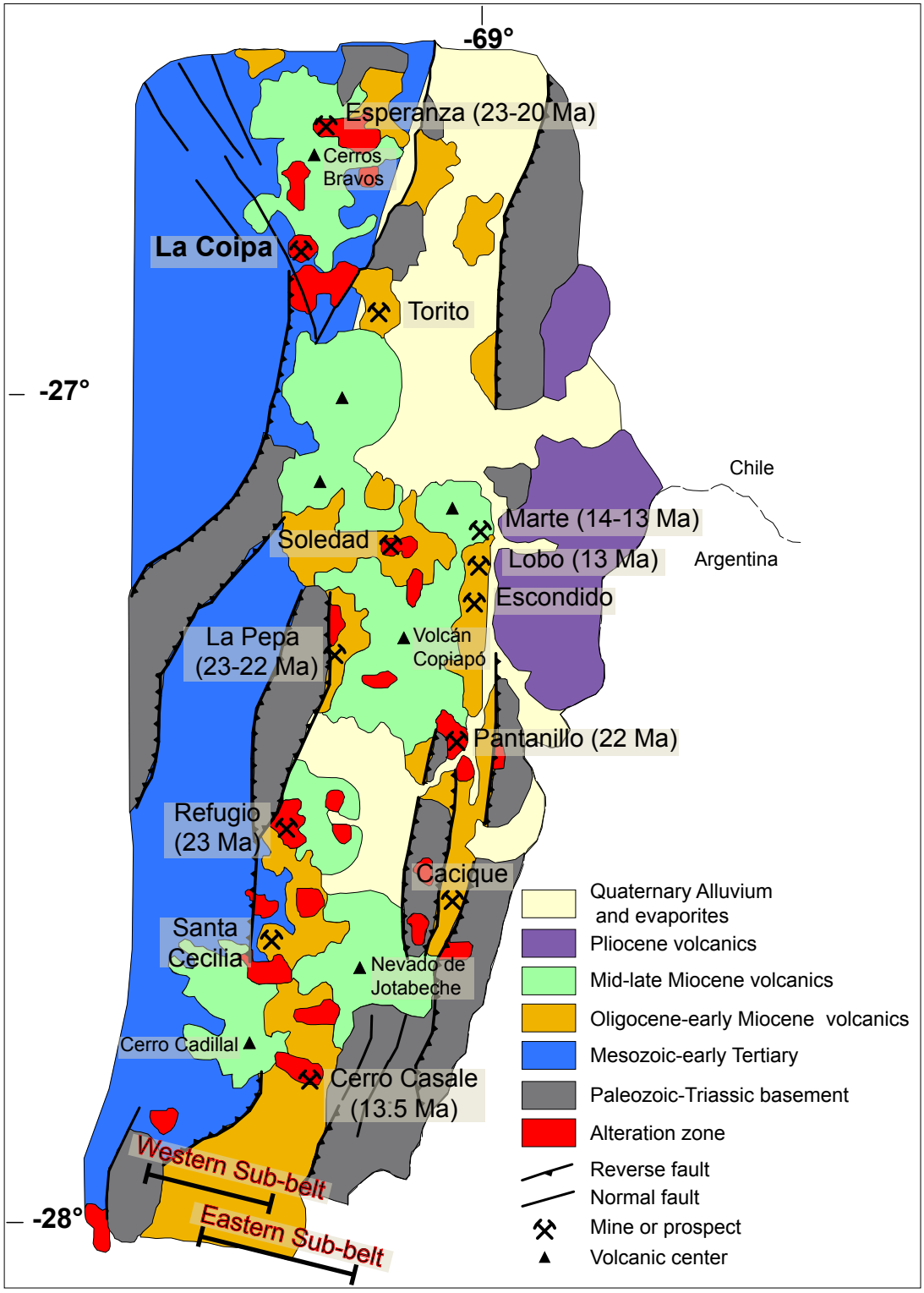

Figure 2.2. Geological map of the Maricunga belt. This map corresponds to the first model proposed for the magmatic and metallogenic evolution of the Maricunga belt. According to radiometric ages obtained at that time, the genesis of porphyry and epithermal system was divided into two periods: the Western sub-belt (24-20 Ma) and the Eastern sub-belt (14-13 Ma). Modified from Vila and Sillitoe, 1991. Note: Radiometric ages of these deposits published after 1991 were not considered in this figure in order to illustrate the integrity of this model.

Figure 2.3. Structural setting of the Domeyko Fault System (Eocene) at the latitude of La Coipa district. The southern domain is characterized by NW-oriented sinistral strike-slip faults. To the north of 26.5°S, the thin-skinned Potrerillos Fold and Thrust Belt (PFTB) is developed. Main deposits of this region correspond to the Eocene El Salvador and Potrerillos Cu-porhyries and the Miocene high-sulfidation epithermal districts of Esperanza and La Coipa. (Modified from Cornejo et al. (1993) and Abels and Bischoff (1999). Base imagery: Topographic map of Digital Elevation Model (DEM).

During the middle Eocene-early Oligocene, the Incaic tectonic event deformed the Andean margin of the Central Volcanic Zone, generating a major continental-scale discontinuity: the Arica oroclinal bend (whose axis is located 1000 km north of the La Coipa district; Mpodozis and Cornejo, 2012). This regional compressive event produced in-situ rotation of crustal blocks around vertical axes (Abels and Bischoff, 1999), which occurred clockwise in northern Chile and counterclockwise in southern Perú (Arriagada et al., 2006). During the early Miocene (20 to 17 Ma), a new compressive pulse of deformation affected rocks of the Oligocene-early Miocene arc and near back-arc domains, a period that coincided with a quiescence of arc volcanism (Kay et al., 2014). This event uplifted the western side of the Western Cordillera through high-angle reverse faults (Arriagada et al., 2006). South of the discontinuity at Lat. 27.5° S, this early Miocene compressive episode gave rise to high angle NS- to NNE-striking reverse faults that dissected Incaic anticlines. Such features were observed in the Frontal Cordillera domain in the flat-slab region (Lat. 27.5°-33° S; Moscoso and Mpodozis, 1988, in Arriagada et al., 2006).

The last pulse of compressional deformation recognized in the study area occurred during the middle Miocene (16 to 15 Ma) in the Pre-Andean Depression. This event is represented by syn-sedimentary deformation that caused progressive unconformities and intraformational folds developed on gravels interbedded with ignimbritic sheets (Mpodozis and Clavero, 2002).

2.3.2 Paleozoic and Mesozoic basement rocks

The basement to the Middle Tertiary volcanic rocks that constitute the Maricunga belt is formed by Paleozoic, Mesozoic and Early Tertiary rocks (Figures 2.4 and 2.5). The oldest rocks recognized in this region include Devonian-Carboniferous sedimentary and Permian volcanic rocks, represented by the Chinches and La Tabla Formations respectively (Cornejo et al., 1993). This sequence is intruded by Permian batholiths of the Choiyoi Group (Mpodozis et al., 1995). An unconformity separates these units from the continental (alluvial, fluvial and lacustrine) and marine sedimentary and bimodal volcanic rocks of the Late Triassic-Early Jurassic La Ternera (Brüggen, 1950), Agua Chica (Mercado,

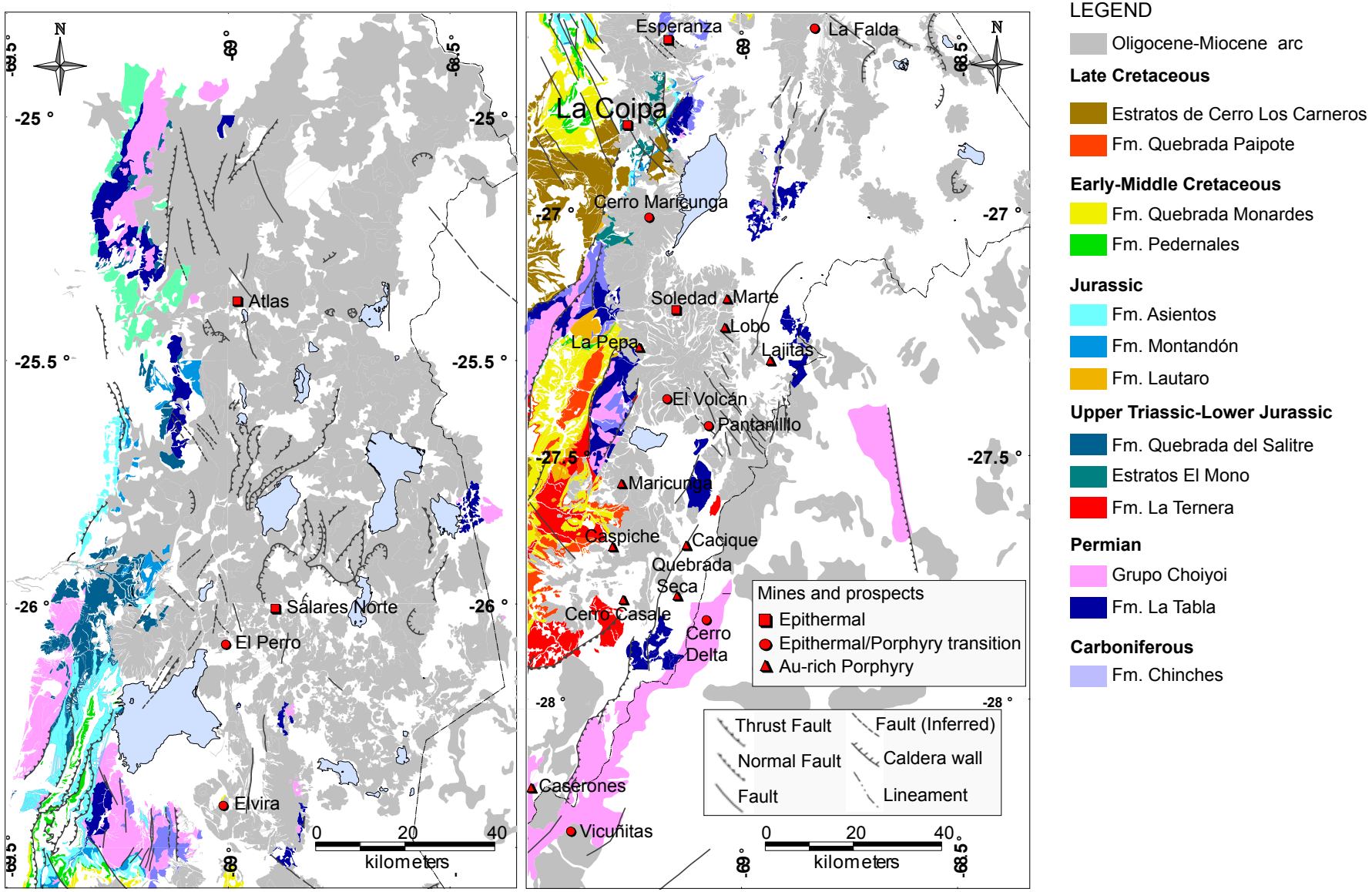

Figure 2.4. Geological map of the most important basement units cropping out in the Maricunga belt. It should be noted that the eastern part of the map is dominated by the Oligocene-Miocene and Pliocene arc. This is reflected in the more limited outcrops of basement units in the east compared to the west.

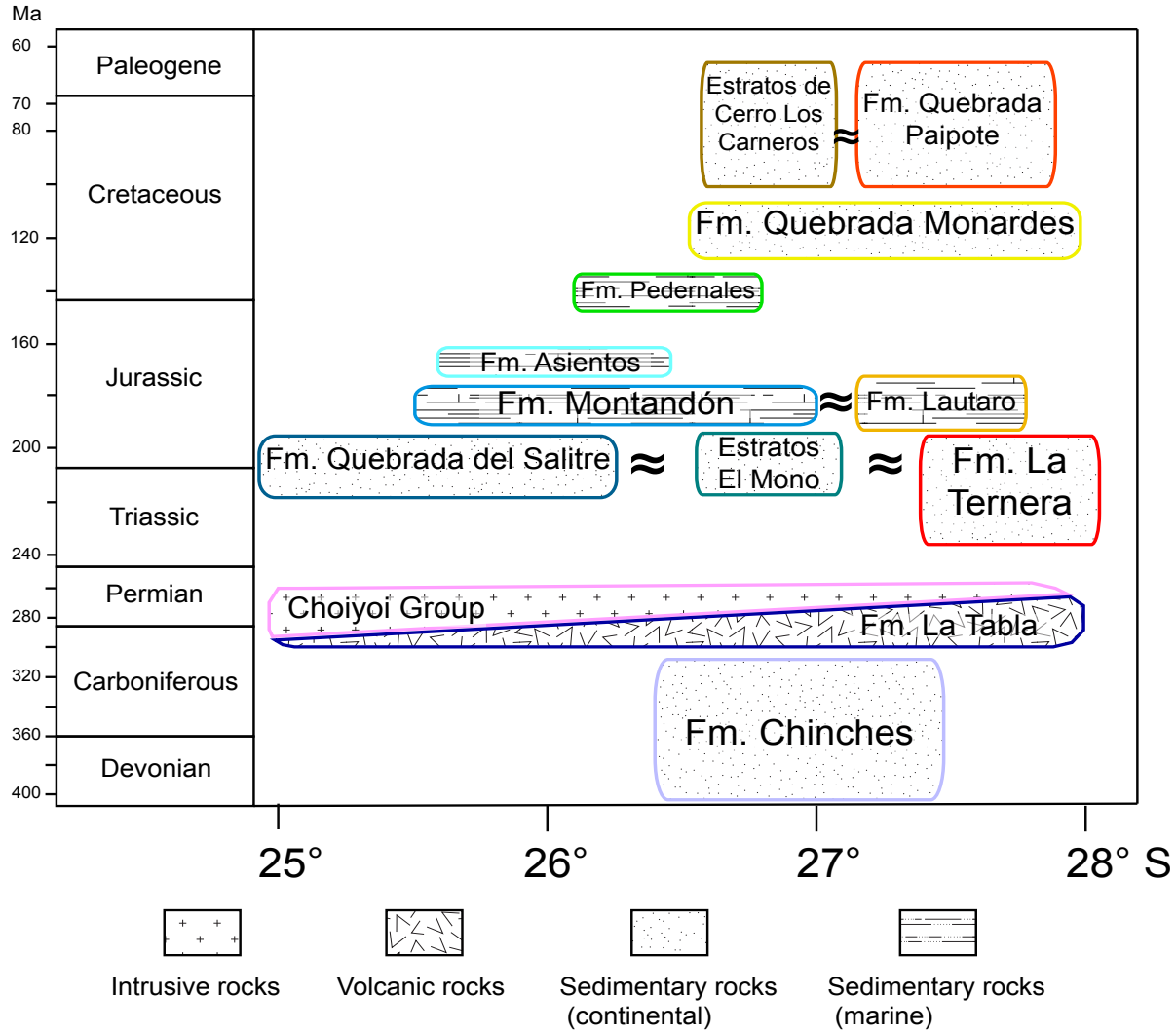

Figure 2.5. Chronostratigraphic scheme of basement units of the Maricunga belt. The color of each box is equivalent to the geological map of Figure 2.4. The width of these boxes represents the north-south distribution of the respective lithological unit, whereas the height represents the age. Units that can be correlated lithologically and temporarely are indicated by the "≈" symbol. Plutonic rocks of the Choiyoi Group intrude the La Tabla and Chinches formations.

1980), and Quebrada del Salitre (Naranjo and Puig, 1984) formations, which were deposited in NW-oriented rift basins (Cornejo et al., 1993). During the first cycle of the Andean orogeny, a back-arc basin of calcareous marine sediments, which include the Lautaro (Jensen and Vicente, 1976), the Montandón and the Asientos formations (Harrington, 1961), and younger clastic continental sediments (Quebrada Monardes (Muzzio, 1980) and Quebrada Paipote (Sepúlveda and Naranjo, 1982) formations). These units were deposited to the east of the Early Jurassic to Early Cretaceous arc, located at that time at the present Coastal Range (La Negra Formation; García, 1967). During the Middle to Late Cretaceous, an increase in the spreading rate along the mid-Atlantic ridge caused a westward migration of the South American continent, resulting in a compressional event that led to the closure of the back-arc basin and a subsequent tectonic inversion and uplift, which is considered the first major episode of the Andean orogenesis (Coira et al., 1982). Overlying this back-arc sedimentary sequence, calc-alkaline felsic volcanic and hypabyssal units were emplaced under extensional conditions from the Late Cretaceous to the early Eocene (Charrier et al., 2007).

2.3.3 Regional magmatism and mineralization during the Oligocene-Miocene arc

The Oligocene-Miocene magmatic arc initiated as a response to a reconfiguration of oceanic plates that were subducting under the South American continent, where the break-up of the Farallón plate at 26 Ma created the Cocos and Nazca plates, producing an east-west orthogonal and rapid convergence with strong coupling between the subducting Nazca plate and the South American continent at the latitude of the Central Andes (Somoza, 1998). A more oblique subduction was resumed during the middle Miocene (Pardo-Casas and Molnar, 1987). Magmatic reactivation along the western margin of South America produced voluminous Oligocene-Miocene volcanic, hypabyssal and intrusive rocks along, practically, the entire Andean margin. In the Maricunga belt region, Kay et al. (1994) and Mpodozis et al. (1995) proposed the first models of magmatic evolution. These authors identified two periods of mineralization: 26-21 Ma and 16-12 Ma.

Based on compiled literature data, a description of magmatic and hydrothermal centers of the Maricunga belt is discussed in the following section. The studied area includes the Oligocene-Miocene arc between Lat. 25°S and Lat. 28.5° S. The evolution of the Maricunga belt is divided into four periods: 26-21 Ma, 21-17 Ma, 17-11 Ma and 11-4 Ma. Regional distribution of magmatism and important ore deposits are illustrated in Figures 2.6, 2.7, 2.8, and 2.9 for each period respectively. To demonstrate the relationship between volcanic lithology and mineralogy and porphyry/epithermal mineralization, a brief description of each volcanic/plutonic center will be discussed starting from north to south.

2.3.3.1 Volcanism and mineralization of the Maricunga belt for the 26 to 21 Ma period

Magmatic activity developed during this period along this NS-oriented belt includes stratovolcanoes, dome complexes and pyroclastic deposits. The location of these centers was in most cases controlled by NW to WNW-striking faults (Kay et al., 1994). A common feature that characterizes these centers is the presence of hydrothermal alteration with epithermal and gold-rich porphyry mineralization (Vila and Sillitoe, 1991; Davidson and Mpodozis, 1991).

The northernmost centers that belong to this period are located at the eastern side of the Salar de Pedernales (Figure 2.6). Among them, the Complejo Volcánico El Perro (Cornejo et al., 1993) consists of domes and lavas with dacitic composition, together with pyroclastic deposits. The domes present a porphyritic texture with plagioclase, hornblende, pyroxene, biotite and quartz phenocrysts. Kat et al. (1994) reported a 22.5±0.7 Ma K-Ar age (whole rock) on one of these volcanic rocks. The pyroclastic sequence presents advanced argillic alteration overprinted by steam-heated alteration with opaline silica, native sulfur, alunite and kaolinite. Immediately to the north of the altered zone, the Pedernales massive magnetite body (Grez et al., 1991) stands out as the only iron deposit recognized in this region, which together with the El Laco deposit (e.g., Frutos et al., 1990; Rhodes et al., 1999), are the only occurrences of iron deposits observed in the Western Cordillera of northern Chile.

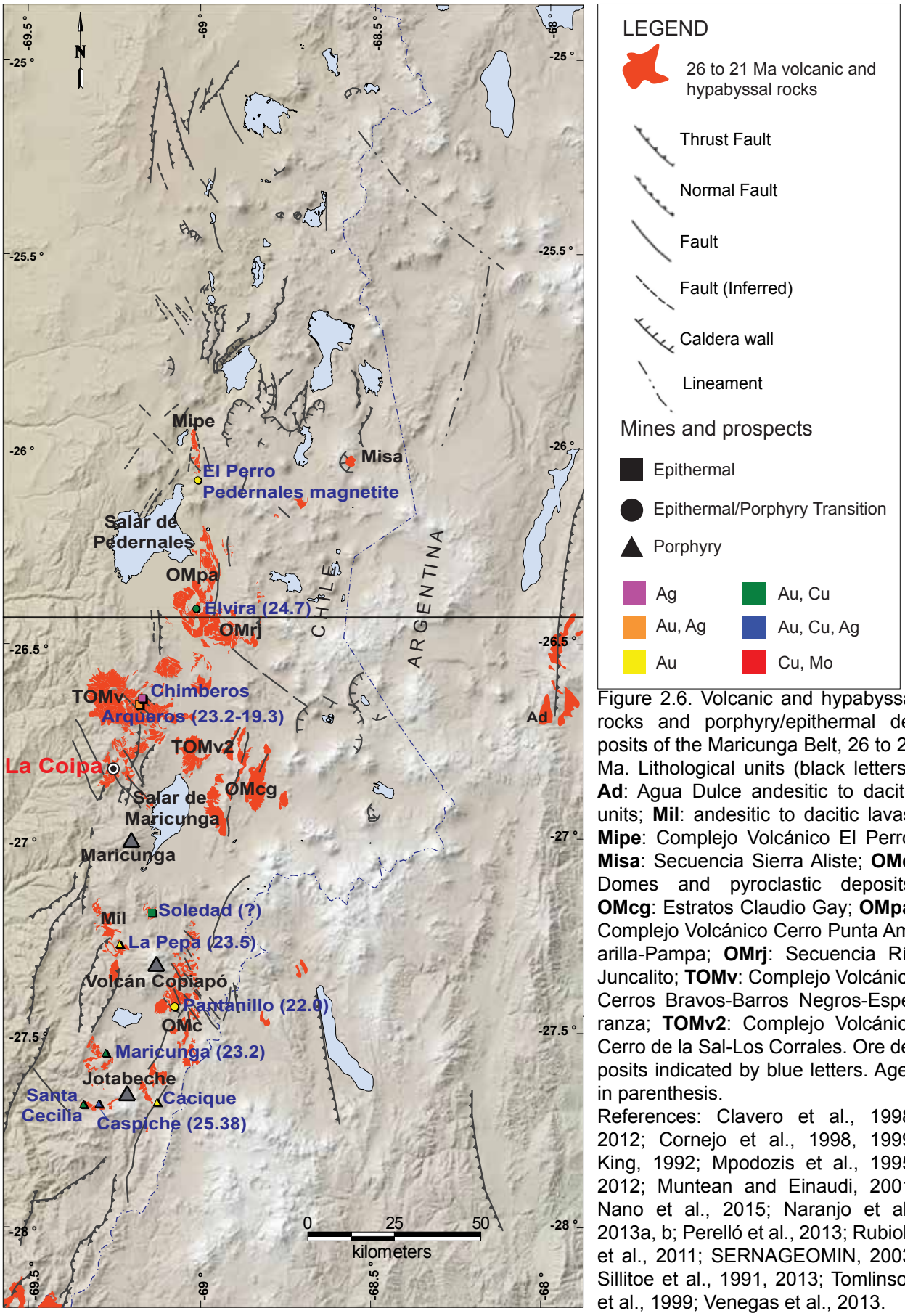

Figure 2.6. Volcanic and hypabyssal rocks and porphyry/epithermal deposits of the Maricunga Belt, 26 to 21 Ma. Lithological units (black letters), **Ad**: Agua Dulce andesitic to dacitic units; **Mil**: andesitic to dacitic lavas; **Mipe**: Complejo Volcánico El Perro; **Misa**: Secuencia Sierra Aliste; **OMc**: Domes and pyroclastic deposits; **OMcg**: Estratos Claudio Gay; **OMpa**: Complejo Volcánico Cerro Punta Amarilla-Pampa; **OMrj**: Secuencia Río Juncalito; **TOMv**: Complejo Volcánico Cerros Bravos-Barros Negros-Esperanza; **TOMv2**: Complejo Volcánico Cerro de la Sal-Los Corrales. Ore deposits indicated by blue letters. Ages in parenthesis.
References: Clavero et al., 1998; 2012; Cornejo et al., 1998, 1999; King, 1992; Mpodozis et al., 1995, 2012; Muntean and Einaudi, 2001; Nano et al., 2015; Naranjo et al., 2013a, b; Perelló et al., 2013; Rubiolo et al., 2011; SERNAGEOMIN, 2003; Sillitoe et al., 1991, 2013; Tomlinson et al., 1999; Venegas et al., 2013.

At the southeastern corner of the Salar de Pedernales, the Complejo Volcánico Cerro Punta Amarilla-Pampa (Figure 2.6) is reported as an eroded volcanic edifice with an extrusive dome in the center surrounded by a ring of pyroclastic deposits and lava flows. Lavas have porphyritic textures with plagioclase and hornblende phenocrysts. These units are intruded by unaltered dacitic porphyries with plagioclase, biotite, rounded quartz and hornblende phenocrysts (Cornejo et al., 1993). This center has hydrothermal alteration (Elvira prospect). Cornejo et al. (1993) reported a K-Ar alunite age of 24.7±4.3 Ma for the altered unit observed at the center of the system.

Located immediately to the north of La Coipa, the Cerros Bravos-Barros Negros-Esperanza Complex (Figure 2.6) has been described as the only center of this period where the stratovolcano edifices have not been eroded (Kay et al., 1994). The first phase of magmatic activity consisted, from oldest to youngest, of a rhyodacitic ignimbrite, pyroxene-(< hornblende) andesitic and hornblende-biotite dacite to andesite lavas, block and ash deposits, and hornblende-biotite dacitic domes, which were emplaced between 25 and 21 Ma (Cornejo et al., 1993). The second phase is represented by the Esperanza dome complex. These dacitic domes are flanked by rhyolitic crystal and lapilli tuffs. The Cerros Bravos-Barros Negros-Esperanza Complex is associated with WNW-trending sinistral strike-slip faults of Eocene age that were reactivated during the Oligocene (Cornejo et al., 1993). The Esperanza dome complex hosts a series of gold-silver deposits that form the Esperanza district, which includes, silicified veining and brecciated systems (Arqueros, Santa Rosa, Potosí and Huantajaya), a stratiform system (Arqueros), and a breccia emplaced on a NS-oriented reverse fault that juxtaposes Paleozoic sediments over Triassic quartzites (Chimberos; Cornejo et al., 1993). All these centers present intense advanced argillic hydrothermal alteration. Alunite ages range from 23.2±1.4 to 19.3±0.7 Ma (Sillitoe et al., 1991). The geology of volcanic units and hydrothermal alteration and mineralization of the Esperanza District has similarities to the La Coipa district, which is located 20 km southwest of the Esperanza district.

The southeastern prolongation of the Cerros Bravos-Barros Negros volcanic complex, at the northeastern margin of the Salar de Maricunga, is represented by the Complejo Volcánico Cerro de la Sal-Los Corrales and the Estratos Claudio Gay units (Figure 2.6), both located at the western

margin of the Western Cordillera. The Cerro de la Sal-Los Corrales complex consists of eroded stratovolcano edifices, with quartz-plagioclase-hornblende dacitic to rhyodacitic dykes and domes flanked by andesitic and dacitic hornblende-pyroxene lavas (Cornejo et al., 1993). These authors obtained a K-Ar biotite age of 23.0±0.7 Ma for a central dome.

Flanking by the east and underlying the well-preserved late Miocene Volcán Copiapó, dome complexes and pyroclastic units are present at different localities stratigraphically below the younger rocks of the Volcán Copiapó (Figure 2.6). These domes and pyroclastic rocks are controlled by NW-NNW-striking faults (Kay et al., 1994). Towards the east and southeast, a NS corridor of volcanic and hypabyssal units can be found between the Marte deposit and the Pantanillo prospect. The Pantanillo prospect (Figure 2.6; Gamonal, 2007) corresponds to a group of five dacitic domes and porphyries that host porphyritic-style gold mineralization. Kay et al., (1994) reported a K-Ar whole rock age of 22.6±1.1 Ma for a dome, while a K-Ar alunite age of 22.0±0.6 was published by Sillitoe et al. (1991). Located 10 km to the west of the Volcán Copiapó, the La Pepa system is characterized by NW-oriented gold bearing veins hosted in dacitic domes and quartz diorite porphyries, the latter developing potassic alteration and hosting low-grade Au mineralization (Muntean and Einaudi, 2001). Hydrothermal alteration was dated by the $^{40}Ar/^{39}Ar$ method on alunite between 23.5±0.06 Ma and 23.47±0.12 Ma and on biotite at 23.81±0.08 Ma (Muntean and Einaudi, 2001). Located 11 km north of the Volcán Copiapó, the Soledad prospect (Figure 2.6) is characterized by dacitic domes and their respective pyroclastic deposits (Mpodozis et al., 1995).

The southern part of the Maricunga Belt is represented by several dome and pyroclastic sequences in the Maricunga (Refugio) deposit and in the Jotabeche area (Figure 2.6). At the Maricunga gold-rich porphyry deposit, a sequence of dacitic to andesitic lavas and breccias and dacitic porphyry domes, were intruded by quartz-diorite porphyries stocks and breccia pipes (Muntean and Einaudi, 2000). A $^{40}Ar/^{39}Ar$ age on hydrothermal biotite of 23.22±0.06 Ma and two $^{40}Ar/^{39}Ar$ ages on magmatic biotite (23.27±0.06 and 23.28±0.06 Ma) demonstrated a coeval and rapid emplacement of dacitic domes and associated hydrothermal fluids (Muntean and Einaudi, 2001).

At the western side of the Jotabeche summit, a group of domes and associated deposits constitute the Santa Cecilia Complex (Mpodozis et al., 1995), which hosts the Santa Cecilia and the large Caspiche deposit. Located 15 km south of the Maricunga deposit, the Caspiche Au-Cu porphyry is hosted by a composite dioritic to quartz-dioritic porphyritic stock that intruded a subhorizontal sequence of hornfelsed sandstones and siltstones overlain by a volcanic breccia (Sillitoe et al., 2013). A U-Pb age of 24.7±0.7 Ma on the volcanic breccia and a Re/Os molybdenite age of 25.38±0.09 Ma indicate a close temporal relationship between volcanic host rocks and mineralized porphyritic systems (Sillitoe et al., 2013).

2.3.3.2 Volcanism and mineralization of the Maricunga belt for the 21 to 17 Ma period

During this period, the magmatic activity was concentrated in the northern part of the belt, notwithstanding a poorly defined group of volcanic rocks in the southern area may also be assigned to this period. Only minor occurrences are present in the central region (Figure 2.7). The geologic models proposed for the Maricunga belt consider the 21-17 Ma period as a magmatic lull in the middle of the two major episodes of volcanic activity described in this region (26-21 Ma and 17-11 Ma; Kay et al., 1994; Mpodozis et al., 1995).

In the northern segment of the Maricunga belt, the early Miocene magmatic arc is represented by lava flows and extensive ignimbritic covers. The oldest unit recognized in this region corresponds to the Volcanes del Mioceno Inferior Unit (Figure 2.7), which is constituted by pyroxene (minor hornblende and biotite) andesitic lavas and pyroclastic rocks (Naranjo et al., 2013a). Several K-Ar ages obtained in this unit (whole rock and biotite) bracket the age between 18 and 21 Ma, including also a couple of alunite ages obtained in hydrothermally altered volcanic centers (Naranjo et al., 2013a, b; Clavero et al., 1998; Tomlinson et al., 1999).

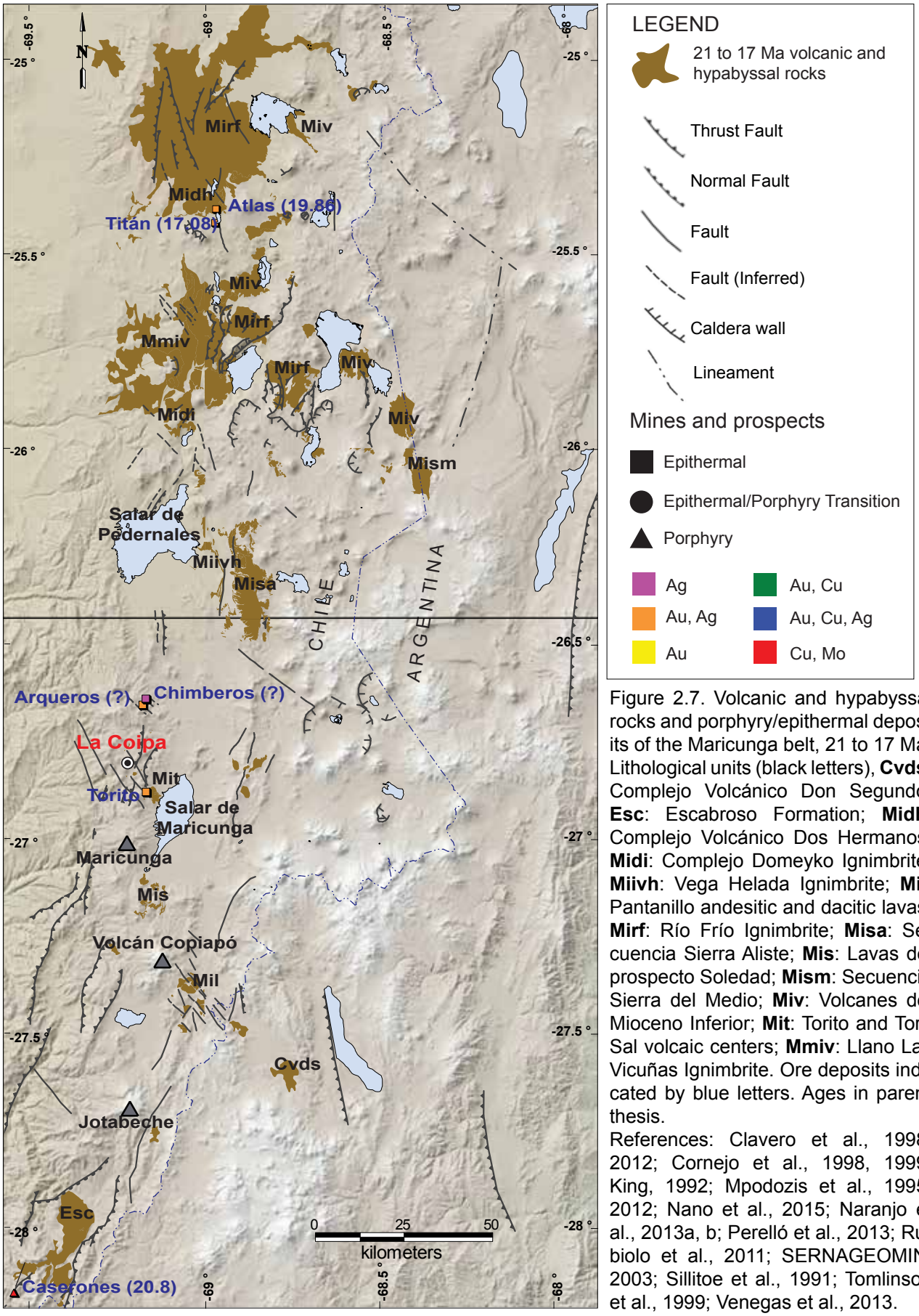

Figure 2.7. Volcanic and hypabyssal rocks and porphyry/epithermal deposits of the Maricunga belt, 21 to 17 Ma. Lithological units (black letters), **Cvds**: Complejo Volcánico Don Segundo; **Esc**: Escabroso Formation; **Midh**: Complejo Volcánico Dos Hermanos; **Midi**: Complejo Domeyko Ignimbrite; **Miivh**: Vega Helada Ignimbrite; **Mil**: Pantanillo andesitic and dacitic lavas; **Mirf**: Río Frío Ignimbrite; **Misa**: Secuencia Sierra Aliste; **Mis**: Lavas del prospecto Soledad; **Mism**: Secuencia Sierra del Medio; **Miv**: Volcanes del Mioceno Inferior; **Mit**: Torito and Toro Sal volcaic centers; **Mmiv**: Llano Las Vicuñas Ignimbrite. Ore deposits indicated by blue letters. Ages in parenthesis.

References: Clavero et al., 1998; 2012; Cornejo et al., 1998, 1999; King, 1992; Mpodozis et al., 1995, 2012; Nano et al., 2015; Naranjo et al., 2013a, b; Perelló et al., 2013; Rubiolo et al., 2011; SERNAGEOMIN, 2003; Sillitoe et al., 1991; Tomlinson et al., 1999; Venegas et al., 2013.

Located at Lat. 25.4°S, the Complejo Volcánico Dos Hermanos (Figure 2.7) is the northernmost volcanic edifice of lower Miocene age (Venegas et al., 2013). This center is constituted by two andesitic volcanic edifices with dacitic and andesitic hornblende-bearing lava flows (Venegas et al., 2013). To the southeast and south of the Complejo Volcánico Dos Hermanos, alunite from the Atlas and Titán high-sulfidation epithermal prospects were dated by $^{40}Ar/^{39}Ar$ at 19.86±0.04 and 17.08 Ma (Figure 2.7; Nano et al., 2015).

Unconformably overlying the Volcanes del Mioceno Inferior and the Complejo Volcánico Dos Hermanos, the Río Frío Ignimbrite Unit covers an extensive region (Figure 2.7), forming a plateau that is overlain by younger stratovolcanoes. Naranjo et al. (2013a) obtained a $^{40}Ar/^{39}Ar$ age of 17.93±0.17 Ma (hornblende) for this unit. The Río Frio Ignimbrite is correlated with other ignimbrites of the northern Maricunga belt, including the Llano Las Vicuñas Ignimbrite, and the Complejo Domeyko Ignimbrite (Naranjo et al., 2013a).

To the east of the Salar de Pedernales, the Secuencia Sierra Aliste unit (Figure 2.7) includes block-and-ash pyroclastic deposits intergrown and covered by sedimentary sequences. The block-and-ash sequence is characterized by rounded blocks (up to 2 m) of hornblende-pyroxene- and clinopyroxene-orthopyroxene-phyric dacite (Clavero et al., 1998). A K-Ar age of 20.7±0.8 Ma (whole rock) is considered the most representative age for this unit (Clavero et al., 1998). The Sierra de Aliste Unit is covered by the Vega Helada Ignimbrite (Figure 2.7), a 1 to 3 (locally up to 25-30) m thick unit characterized by a vitric black-colored level at its base. Its age is constrained between 18.7±0.7 and 19.1±0.7 Ma (K-Ar, whole rock; Clavero et al., 1998).

To the southeast of La Coipa district, the Torito and Toro Sal volcanic centers (Figure 2.7) are composed of hornblende-biotite-plagioclase-quartz dacitic domes surrounded by pyroclastic deposits (Cornejo et al., 1993). The Torito dome has a K-Ar whole rock age of 18.6±1.3 Ma, whereas a K-Ar hornblende age of 17.6±4.3 Ma is assigned to the Toro Sal dome (Kay et al., 1994). The Torito and Toro Sal dome are spatially associated with pyroclastic rocks intensely altered to advanced argillic minerals such as alunite, kaolinite, opaline silica, and quartz.

At the Complejo Volcánico Copiapó, volcanic rocks from this period are found at the Soledad and Pantanillo prospects (Figure 2.7). At the Soledad prospect, andesitic lava flows have been dated by K-Ar (whole rock) at 20.1±0.9 Ma and 20.7±1.3 Ma (Kay et al., 1994). In the Pantanillo area, andesitic to dacitic lava flows present a marked NW-striking alignment that extends these units onto the Argentinian side of the Western Cordillera, constituting the Complejo Volcánico Don Segundo (Figure 2.7), characterized by dacitic lavas, volcanic breccias and tuffs (Rubiolo et al., 2001).

In the southern Maricunga belt, volcanism of this period is represented by the andesitic to basaltic lavas of the Escabroso Formation (included by Moscoso et al. (2010) in the Doña Ana Group). This unit has been defined in the El Indio belt (see Chapter 2.4.1). Units mapped in the Argentinian side are similar to the Escabroso Formation defined on the Chilean side of the Andes. At the southern terminus of the Maricunga Belt, the Caserones Cu-Mo porphyry deposit is the only known occurrence of mineralization can be assigned to this period (Figure 2.7). The Caserones porphyry system is characterized by quartz-plagioclase-hornblende-biotite bearing dacitic porphyry stocks and dikes, dated at 20.8±0.8 Ma (K-Ar, whole rock; Perelló et al., 2003).

2.3.3.3 Volcanism and mineralization of the Maricunga belt for the 17 to 11 Ma period

In the middle Miocene, a reactivation of volcanic activity is recorded by multiple centers along the entire belt, represented in most cases by composite stratovolcanoes (Figure 2.8; Kay et al., 1994). These volcanic centers are mainly distributed in the northern and southern parts of the belt, presenting reduced activity between the Salar de Pedernales and the Salar de Maricunga. The more explored southern part of the Maricunga belt contains the majority of deposits; in most cases gold-rich porphyries.

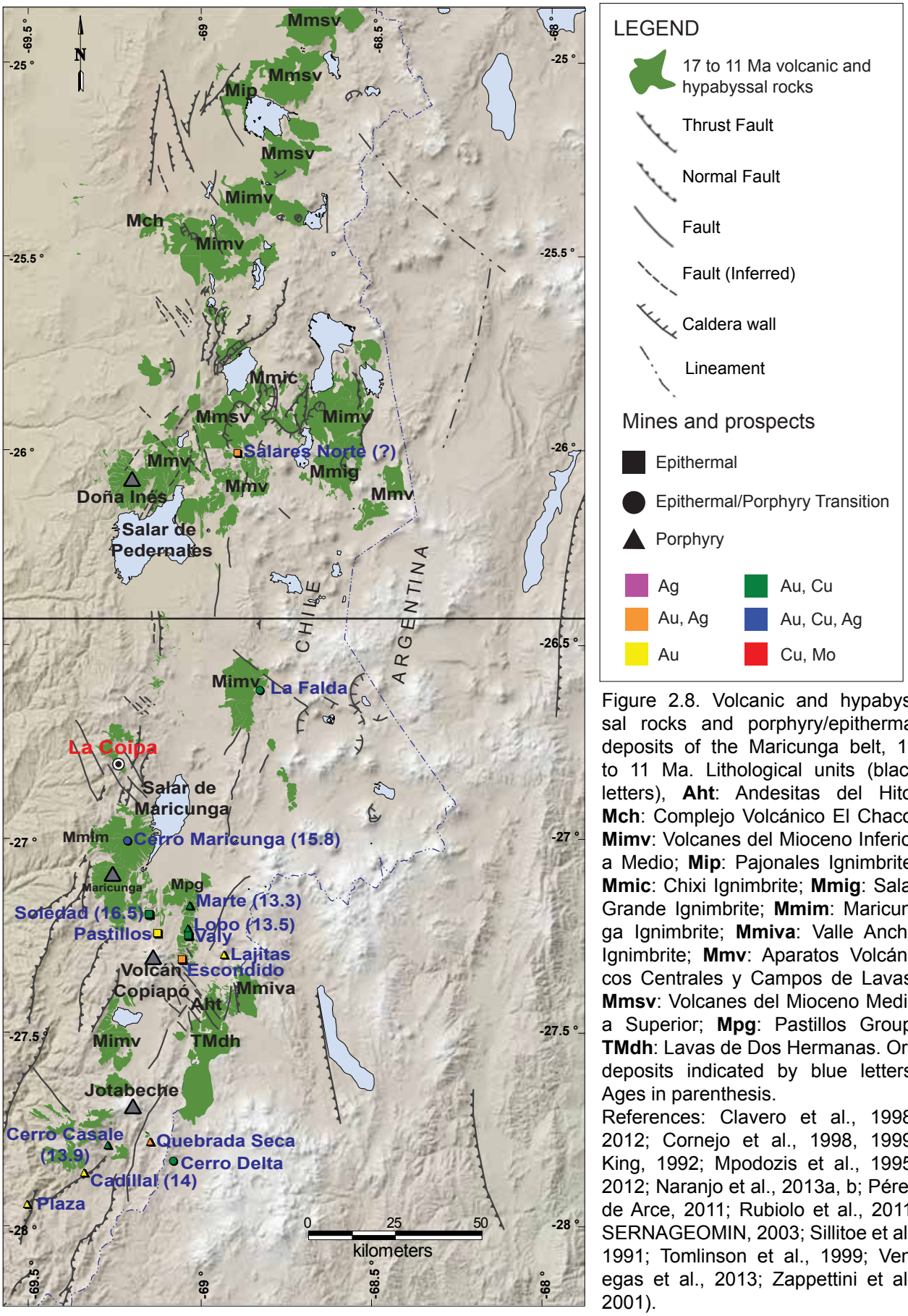

Figure 2.8. Volcanic and hypabyssal rocks and porphyry/epithermal deposits of the Maricunga belt, 17 to 11 Ma. Lithological units (black letters), **Aht**: Andesitas del Hito; **Mch**: Complejo Volcánico El Chaco; **Mimv**: Volcanes del Mioceno Inferior a Medio; **Mip**: Pajonales Ignimbrite; **Mmic**: Chixi Ignimbrite; **Mmig**: Salar Grande Ignimbrite; **Mmim**: Maricunga Ignimbrite; **Mmiva**: Valle Ancho Ignimbrite; **Mmv**: Aparatos Volcánicos Centrales y Campos de Lavas; **Mmsv**: Volcanes del Mioceno Medio a Superior; **Mpg**: Pastillos Group; **TMdh**: Lavas de Dos Hermanas. Ore deposits indicated by blue letters. Ages in parenthesis.
References: Clavero et al., 1998; 2012; Cornejo et al., 1998, 1999; King, 1992; Mpodozis et al., 1995, 2012; Naranjo et al., 2013a, b; Pérez de Arce, 2011; Rubiolo et al., 2011; SERNAGEOMIN, 2003; Sillitoe et al., 1991; Tomlinson et al., 1999; Venegas et al., 2013; Zappettini et al., 2001).

In the northern part of the Maricunga belt, the Volcanes del Mioceno Inferior a Medio Unit comprises a set of moderately eroded stratovolcanoes (Figure 2.8). This unit includes lava flows, volcanic breccias, and ash-fall pyroclastic rocks. Lavas have andesitic to dacitic composition and contain plagioclase, pyroxene and lesser hornblende and biotite phenocrysts (Naranjo et al., 2013a). K-Ar biotite ages and one $^{40}Ar/^{39}Ar$ whole-rock age constrain this unit between 17 and 15 Ma (Naranjo et al., 2013a, b). The Complejo Volcánico El Chaco (Figure 2.8) stands out as one of the most prominent volcanic edifices of the northern Maricunga belt. It is composed of pyroxene-hornblende bearing andesitic and hornblende-pyroxene bearing dacitic lavas, as well as andesitic domes with hydrothermal alteration (Venegas et al., 2013). Several K-Ar whole-rock dates established a 17 to 15 Ma age for this unit, and a K-Ar age on alunite established a 15.6±0.7 Ma age for hydrothermal alteration at El Chaco (Venegas et al., 2013). The Volcanes del Mioceno Inferior a Medio Unit can be correlated with other volcanic centers defined by other authors in the Salar de Pedernales area. This is the case for the Aparatos Volcánicos Centrales y Campos de Lavas (Figure 2.8) that include the Doña Inés and Gemelos-Fortuna stratovolcanoes. These centers include basaltic andesite to dacitic and andesitic lava flows (most of them hornblende bearing), dacitic to andesitic domes, pyroclastlic block-and-ash deposits, and welded ignimbrites (Tomlinson et al., 1999). Several K-Ar ages (whole rock and biotite) obtained in this units indicate a 17 to 14 Ma period of emplacement (Tomlinson et al., 1999; Cornejo et al., 2009; and Clavero et al., 1998). The younger group of volcanic centers is represented by the Volcanes del Mioceno Medio a Superior Unit (Figure 2.8). This unit is characterized by well-preserved volcanic edifices formed by lava-domes, caldera related debris flows, and ash-fall pyroclastic deposits. Lava units range from basaltic andesites to dacites. Andesites and basalts are constituted by pyroxene- and lesser hornblende- and biotite-phyric (Naranjo et al., 2013a). Ages obtained by K-Ar (biotite and whole-rock) and $^{40}Ar/^{39}Ar$ (groundmass) range between 14.5 and 10.5 Ma (Naranjo et al., 2013a, b).

Several ignimbritic units are present in the northern segment of the Maricunga belt. Between them, the Pajonales ignimbrite (Figure 2.8) overlies the older Río Frío ignimbrite, and is also intecalated with the Volcanes del Mioceno Inferior a Medio Unit. A recent $^{40}Ar/^{39}Ar$ date on biotite indicates a 16.5 Ma age for this unit (Naranjo et al., 2013a, b). Overlying the Pajonales ignimbrite, local ignimbritic units are distributed in this region. These include the Chixi and Salar Grande ignimbrites (Figure 2.8).

K-Ar whole-rock ages on fragments and rocks overlying the Chixi ignimbrite, assign it an age range between 14.7 and 13.2 Ma (Naranjo et al., 2013a; Naranjo and Cornejo, 1992). For the Salar Grande Ignimbrite, K-Ar ages on biotite are distributed between 12.3 and 11.2 Ma (Naranjo and Cornejo, 1992).

On the southwestern margin of the Salar de Maricunga, the Maricunga (also known as Ojos de Maricunga) is one of the best-preserved stratovolcanoes. In the Cerro Maricunga prospect (Figure 2.8), located at the top of this edifice, several subvolcanic intrusive phases that include a dacite to andesitic porphyry (plagioclase, hornblende and lesser biotite), andesitic dykes and plugs, dacitic to andesitic coarse hornblende-bearing porphyries, a quartz-eyes porphyry, a rhyodacitic holocrystalline porphyry (plagioclase, biotite and quartz), mingled porphyries and phreatomagmatic breccias are exposed (Magri, 2012). Some of these host porphyry gold mineralization controlled by NW-striking faults. Flanks of the stratovolcano are covered by a rhyodactic ignimbrite. K-Ar ages of hypabyssal and volcanic rocks obtained on biotite and hornblende indicate a range between 14.3 and 16.2 Ma (Mpodozis et al., 1995; and references therein). South of the Maricunga center, a series of volcanic centers include the Santa Rosa, Cerro Lagunillas, Pastillitos, and Cerro Las Cluecas (Kay et al., 1994), all of them emplaced at the same time as Cerro Maricunga (Kay et al., 1994; Mpodozis et al., 1995).

To the southeast of the Salar de Maricunga, a belt of younger volcanic centers defined as the Pastillos Group (Figure 2.8), is characterized by a series of gold-rich porphyry systems (Kay et al., 1994). The arc magmatism in this region has been divided, from oldest to youngest, into four units: a Lower Volcanic Unit, a hypabyssal unit of porphyries and domes, an Intermediate Volcanic Unit, and the Upper Volcanic Unit (King, 1992). The Lower Volcanic Unit is composed of andesite-dacite flows, breccias and agglomerates, with a maximum exposed thickness of 250 m. This unit is intruded by quartz diorite to diorite porphyries, and dacite domes and sills, intrusions characterized by plagioclase, hornblende, occasional quartz and biotite phenocrysts. Au-Cu deposits associated with these porphyritic systems include the Marte, Lobo, Valy, and Escondido prospects. The Intermediate Volcanic Unit is formed by extensive pyroclastic deposits and volcanic breccias, rocks

that are partially affected by hydrothermal alteration. This unit is pre- to syn-mineralization (King, 1992). Unconformably overlying this sequence, the Upper Volcanic Unit is constituted by plagioclase-hornblende bearing andesites, whose thickness range between 350 and 150 m (King, 1992). The entire sequence of extrusive volcanic rocks, hypabyssal domes and porphyries, and their respective gold-copper mineralization took place in a short period of time between 13 and 11 Ma (based on K-Ar dates on biotite, hornblende and hypogene alunite; González-Ferrán et al., 1985; Sillitoe et al., 1991; Zentilli et al., 1991; King, 1992; and Mpodozis et al., 1995).

The emplacement of gold-rich porphyry systems between 14-11 Ma is also important to the south of the Laguna del Negro Francisco basin, where Cerro Casale, the largest Au-Cu porphyry of this region (1300 Mt @ 0.7 g/t Au and 0.35% Cu; Barrick Technical Report, 2009) is located (Figure 2.8). In the Cerro Casale district, dioritic to granodioritic plutons intruded Oligocene volcanic rocks of andesitic composition (Hollings et al., 2013). The mineralized diorite has a U-Pb age of 13.9±1.1 Ma, which is part of a series of otherwise only weakly mineralized to barren intrusions that range in age between 28 and 14 Ma (Hollings et al., 2013). In this region, straddling the border of Chile and Argentina, the Valle Ancho ignimbrite and the Dos Hermanas and Andesitas del Hito lava flows cover an extensive area of the Western Cordillera (Figure 2.8; Rubiolo et al., 2001).

2.3.3.4 Volcanism and mineralization of the Maricunga belt for the 11 to 4 Ma period

The Oligocene to early Pliocene is characterized by an eastward migration and widening of the arc. The 11 to 4 Ma volcanic arc is centered at the position of the current arc. Nevertheless, there are isolated centers emplaced in this period that overlap with older units of the Maricunga belt, as is the case for the Copiapó and Jotabeche volcanic complexes (Figure 2.9).

The northernmost group of late Miocene to Pliocene volcanic centers is represented by the Volcanes del Mioceno Superior-Plioceno Unit (Figure 2.9), which is defined by stratovolcanoes and

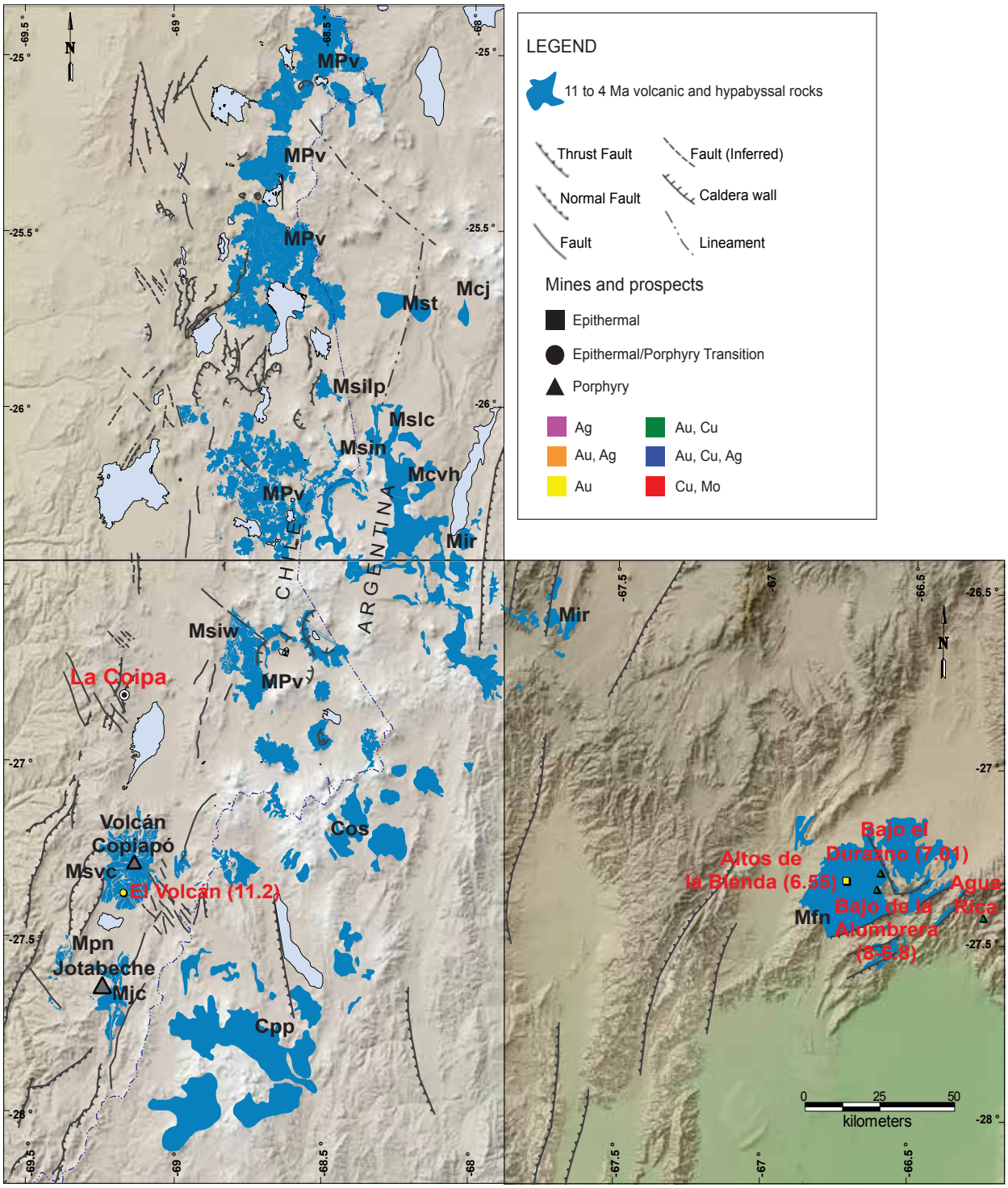

Figure 2.9. Volcanic and hypabyssal rocks and porphyry/epithermal deposits of the Maricunga Belt, 11 to 4 Ma. Lithological units (black letters), **Cos**: Complejo basal Ojos del Salado; **Cpp**: Complejo basal Pissis-Los Patos; **Mcj**: Cajeros Ignimbrite; **Mcvh**: Complejo Volcánico La Hoyada; **Mfn**: Distrito Farallón Negro; **Mir**: Rosada Ignimbrite; **Mjc**: Jotabeche Complex; **Mpn**: Domos y lavas de Pircas Negras; **MPv**: Volcanes del Mioceno Superior-Plioceno; **Msilp**: Las Parinas Ignimbrite; **Msin**: Narnia Ignimbrite; **Msiw**: Wheelwright Ignimbrite; **Mslc**: Los Colorados Ignimbrite; **Mst**: Tamberías Ignimbrite; **Msvc**: Complejo Volcánico Copiapó. Ore deposits indicated by blue letters. Ages in parenthesis.
References: Clavero et al., 1998; 2012; Cornejo et al., 1998, 1999; Halter et al., 2004; Harris et al., 2004; Lehman, 2007; Mpodozis et al., 1995, 2012; Naranjo et al., 2013a, b; Rubiolo et al., 2011; Sasso and Clark, 1998; Schnurr et al., 2007; SERNAGEOMIN, 2003; Tomlinson et al., 1999; Venegas et al., 2013.

scoria cones distributed in a NS-oriented corridor north of Lat. 27°S, presenting a NNE arcuate strike in the northern segment. Lava flows consist of plagioclase, pyroxene, hornblende and lesser biotite-phyric andesites, with minor basaltic andesites and dacites. Several K-Ar (whole-rock, biotite, and hornblende) and $^{40}Ar/^{39}Ar$ (hornblende) dates define an age range between 8.3 and 3.7 Ma for this unit (Naranjo et al., 2013a, b).

Several ignimbritic units can be recognized in this region as well. Located adjacent to the border with Argentina, the Narnia Ignimbrite (Figure 2.9) has at least two flow units, which have been dated by K-Ar (whole-rock) between 8.6±0.5 and 9.8±0.8 Ma (Clavero et al., 1998). To the south, the up to 50 m thick Las Parinas Ignimbrite (Figure 2.9) has been dated by K-Ar on biotite between 5.3±0.5 and 5.1±0.4 Ma (Naranjo et al., 2013b). On the Argentinian side of the Western Cordillera, extensive fields of ignimbrites have been grouped into several rhyodacitic to rhyolitic units (Figure 2.9), such as the Rosada (6.3 Ma), Los Colorados (7.8 Ma), Cajeros (8.7-8.4 Ma), and Tambería (9.8-10.7 Ma) ignimbrites (Schnurr et al., 2007).

East of the Salar de Maricunga, the Wheelwright Ignimbrite has an age of 5.5±0.8 Ma (K-Ar, biotite; Clavero et al., 2012). Two of the most prominent Pleistocene volcanic edifices, the Ojos del Salado and Pissis-Los Patos, were constructed on late Miocene andesitic to dacitic lava-flows and pyroclastic sequences (Figure 2.9; Rubiolo et al., 2001). Some of these centers have hydrothermal alteration (Naranjo et al., 2013a).

The westernmost centers of this period are restricted to two areas: the Complejo Volcánico Copiapó and the Jotabeche center. The Complejo Volcánico Copiapó covers a 200 km^2 area (Figure 2.9) and its activity has been divided into two stages: 11 to 10 Ma and 8 to 7 Ma (Kay et al., 1994). The first stage (11-10 Ma) is constituted by two stratovolcanoes located in the southern part of the complex: Azufre and Azufre Norte. These edifices consist of hornblende-bearing dacitic flows and block-and-ash pyroclastic deposits, which were intruded by dacitic porphyries. K-Ar biotite and whole rock ages from these centers range between 11.9 and 10.5 Ma (Kay et al., 1994; Mulja, 1986). At the same time, extensive pyroclastic deposits covered the northern and western part of the complex.

These ignimbrites, named Copiapó I and Copiapó II, have been dated by K-Ar (whole rock) between 11±2.2 Ma and 9.6±0.8 Ma (Kay et al., 1994). The second stage was centered on the Copiapó stratovolcano, formed by hornblende and biotite bearing dacitic lavas and domes, which have been dated between 8.4±0.4 Ma and 6.9±1.1 Ma (Kay et al., 1994).

In the southern part of this center, the El Volcán epithermal gold system (Figure 2.9) is the only known occurrence of mineralization in this period. A Re/Os age on molybdenite of 11.2±0.2 Ma, a $^{40}Ar/^{39}Ar$ age on hydrothermal K-feldspar of 11.39±0.48 Ma, and two $^{40}Ar/^{39}Ar$ alunite ages of 11.24±0.7 and 11.1±0.32 Ma situate this deposit in the first stage of the Azufre stratovolcano (Lehman, 2007).

South of the Laguna del Negro Francisco, the Jotabeche volcanic center is one of the last expressions of volcanism in the Maricunga belt before the arc migrated to the east. The Jotabeche Complex (Figure 2.9) is formed by thick sequences of rhyodacitic lavas, tuffs, pyroclastic breccias and rhyolitic domes (Kay et al., 1994). A basal ignimbrite, considered the first rock unit erupted from this center, has a K-Ar (biotite) age of 8.6±2 Ma (Kay et al., 1994). The core of the Jotabeche volcano was built between 6.2 and 5.9 Ma (K-Ar on biotite, Kay et al., 1994; McKee et al., 1994). Coeval with the eruptions of the Jotabeche center, dacitic, andesitic and basaltic lava flows erupted by fissures along faults at different points of the southern Maricunga belt. These are named Pircas Negras flows (Figure 2.9; Mpodozis et al., 1995). These lava flows are characterized by absence of plagioclase phenocrysts (Kay et al., 1994). K-Ar ages on whole rock determined a range between 6.7 and 5.2 Ma (Kay et al., 1991; 1994).

During the middle to late Miocene (between 12.5 and 5 Ma), a remarkable widening of the magmatic arc is represented by large volcanic centers that erupted as far as 200 km east of the current arc (which roughly follows the political division between Chile and Argentina). This is the case for the Farallón Negro district (Figure 2.9; Sasso, 1997). This volcanic complex is formed by a group of stocks and dikes that intruded a basal sequence of basalts, basaltic andesites and dacites that were covered later by andesites and dacite lava-flows and pyroclastic breccias (Sasso and Clark, 1998). Volcanic activity lasted between 9.7 and 6.1 Ma (Sasso, 1997; Halter et al., 2004). The Farallón Negro

District is characterized by multiple centers of mineralization of Cu-Au porphyry and epithermal style (Figure 2.9). The most important deposit is the Bajo La Alumbrera porphyry system (Proffett, 2003), considered one of the largest gold-rich copper porphyries of the Andes. Mineralization at Bajo La Alumbrera is associated with dacitic porphyries that intruded between 8.02±0.14 and 6.83±0.07 Ma (U-Pb on zircon and $^{40}Ar/^{39}Ar$ on biotite; Harris et al., 2004; Sasso and Clark, 1998). Other examples of porphyritic systems include the Agua Rica (Franchini et al., 2011) and Bajo el Durazno systems, while at the same time, low-sulfidation epithermal veins were generated at the Farallón Negro and Altos de la Blenda centers (Sasso and Clark, 1998).

In summary, the Maricunga belt is characterized by several high-sulfidation and Au-rich porphyry systems emplaced during multiple episodes of hydrothermalism and magmatism associated with episodic crustal thickening and uplift that marks the northern transition of the Pampean flat-slab segment (Kay et al., 1994; Mpodozis et al., 1995).

2.4 Magmatism and mineralization in areas to the south of the Maricunga belt: The El Indio and Los Pelambres-El Teniente belts

As has been described for the entire history of the Andean orogenic cycle, the Oligocene-Miocene magmatic arc also showed a segmented evolution. South of the Maricunga belt, two metallogenic provinces present a remarkable metal endowment: the El Indio Au-Ag belt and the Los Pelambres-El Teniente Cu-Mo belt (Figure 1.1).

2.4.1 The El Indio belt

Located to the south of the Maricunga belt, the El Indio belt (Lat. 29°-30° S) is characterized by gold-silver epithermal systems of which El Indio, Pascua-Lama and Veladero stand out as the largest deposits discovered in this region (Figure 2.10). Since the discovery of the high-grade El Indio epithermal system, several authors have documented the geological evolution of this metallogenic province (Maksaev et al., 1984; Martin et al., 1995; Bissig et al., 2001).

The basement in the El Indio belt is constituted by metamorphic, sedimentary and igneous rocks that range in age from Devonian to Jurassic and include the voluminous granitoids of the Choiyoi province and age equivalent volcanic rocks (Martin et al., 1995). During the Eocene-Oligocene, the Bocatoma Group of calc-alkaline dioritic to granodioritic stocks intruded in the northern part of the belt. These have been dated by $^{40}Ar/^{39}Ar$ (hornblende) between 35.9 and 30 Ma (Bissig et al., 2001). Locally, a dioritic unit located 10 km south of Pascua-Lama, is associated with sericite-biotite alteration, corroborated by two $^{40}Ar/^{39}Ar$ ages of 36.2±1.2 Ma (sericite) and 36.1±1.3 Ma on hydrothermal biotite (Bissig et al., 2001).

The Oligocene-Miocene magmatic activity started in this region with an up to 1200 m thick sequence of dacitic, and less abundant andesitic and rhyolitic tuffs, associated volcaniclastic sedimentary rocks and subordinate andesitic lava flows, included in the Tilito Formation which was originally included in the Doña Ana Group (Maksaev et al., 1984; Martin et al., 1995). The Tilito Formation is widely distributed on both the Argentinian and Chilean side of the international border and was emplaced in an extensional setting (Winocur et al., 2014). Volcanic rocks are characterized by plagioclase and biotite phenocrysts, with variable proportions of quartz, augite, hornblende and sanidine (Bissig et al., 2001). This unit has been dated by $^{40}Ar/^{39}Ar$ (biotite) between 25.1±0.4 and 23.1±0.4 Ma (Bissig et al., 2001). No significant hydrothermal alteration contemporaneous with the Tilito Formation has been documented.

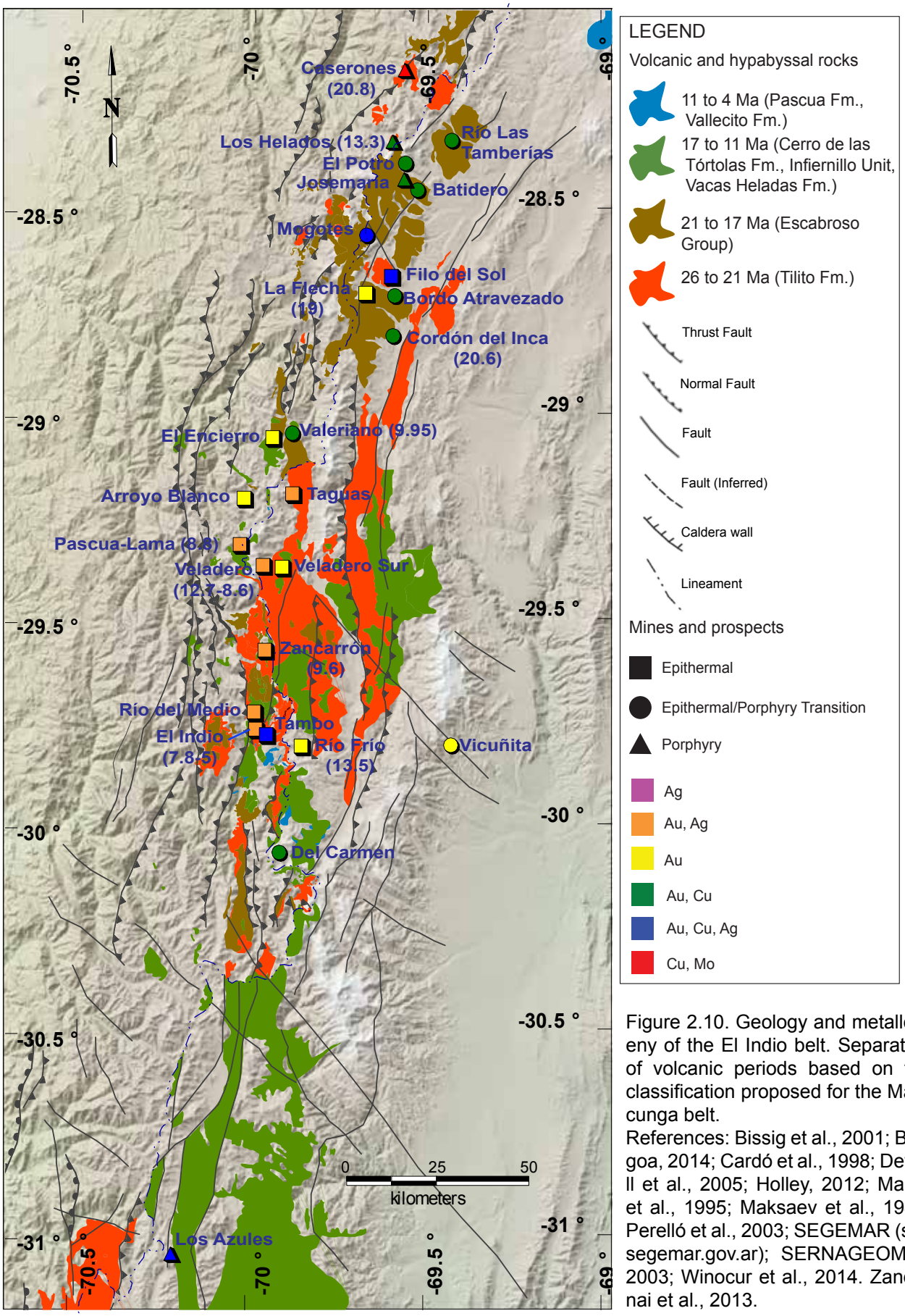

Figure 2.10. Geology and metallogeny of the El Indio belt. Separation of volcanic periods based on the classification proposed for the Maricunga belt.
References: Bissig et al., 2001; Burgoa, 2014; Cardó et al., 1998; Deyell et al., 2005; Holley, 2012; Martin et al., 1995; Maksaev et al., 1984; Perelló et al., 2003; SEGEMAR (sig.segemar.gov.ar); SERNAGEOMIN, 2003; Winocur et al., 2014. Zandonai et al., 2013.

After a period of contractional deformation, the Escabroso Group, originally also included in the Doña Ana Group (Maksaev et al., 1984), was unconformably deposited on the Tilito Formation. The Escabroso Group consists of andesitic to dacitic lava flows, hypabyssal intrusive bodies, dacitic ash-flow tuffs, and volcaniclastic sedimentary rocks (Bissig et al., 2001; Deyell et al., 2004). The lava flows comprise plagioclase and augite as mayor phenocrysts, with minor hornblende and biotite (Bissig et al., 2001). Ages for this group range between 22.1 and 17.6 Ma ($^{40}Ar/^{39}Ar$ ages on biotite, hornblende, and plagioclase). Hydrothermal alteration is associated with shallow-level intrusions, exhibiting different assemblages such as sericite, and locally pyrophyllite, zunyite and topaz, as well as rare alunite (Bissig et al., 2001). Ages of alteration range between 20.1±1.2 Ma and 17.2±0.2 Ma ($^{40}Ar/^{39}Ar$, alunite; Bissig et al., 2001).

A new unconformity separates the Escabroso Group from the overlying Cerro de las Tórtolas Formation and its coeval intrusive Infiernillo Unit (Martin et al., 1995). The Cerro de las Tórtolas Formation consists of biotite, augite, hornblende, and plagioclase bearing andesitic lava flows which differ from the Escabroso group in the greater proportion of hornblende phenocrysts (Bissig et al., 2001). The Infiernillo intrusives are constituted by granodioritic and dioritic porphyries and equigranular bodies with hornblende and biotite as the main mafic phases, with augite as a subordinate component (Bissig et al., 2001). Ages for the Cerro Las Tórtolas Formation and the Infiernillo Group are restricted to the 17 to 14 Ma interval (Bissig et al., 2001). Several centers of hydrothermal alteration developed during this period, such as the Libra system (silicification, potassic and phyllic alteration and local presence of andalusite), a site in the upper Rio Apolinario (silicification, advanced argillic), and the Lama Central area, characterized by silicification, alunite, and steam-heated horizons (Bissig et al., 2001).

After the Cerro Las Tórtolas Formation, erupted magma volumes decreased markedly. Isolated dacitic ignimbrites, with local domes and block-and-ash deposits, constitute the 11 and 12.8 Ma Vacas Heladas Formation (Bissig et al., 2001). Pyroclastic rocks of this formation have hornblende, quartz, biotite and plagioclase as dominant phenocrysts phases (Bissig et al., 2001). Several occurrences of alunite alteration are associated with this event (Filo Federico, Veladero Sur, Fabiana, Tambo and

El Indio), although age equivalent mineralization has only been recognized at Veladero (Bissig et al., 2001; Holley, 2012).

Hydrothermal activity and most gold-silver mineralization developed shortly after the eruption of the Vacas Heladas Formation. The largest concentration of metals corresponds to the Pascua-Lama deposit (15.3 Moz @ 0.6 gr/ton Au, www.barrick.com), a high-sulfidation epithermal deposit hosted by several hydrothermal breccias (Deyell et al., 2004; Chouinard et al., 2005), estimating the main pulse of mineralization at 8.8±0.6 Ma ($^{40}Ar/^{39}Ar$ on alunite; Deyell et al., 2005). The El Indio system, a high-grade vein-hosted system with assemblages either of high- and intermediate-sulfidation (Deyell et al., 2004), has been dated between 7.8 and 5 Ma (Bissig et al., 2001; Deyell et al., 2004; Bissig et al., 2015). In the case of the high-sulfidation Veladero system, a wider range of ages, determined between 12.7±0.02 and 8.58±0.17 Ma ($^{40}Ar/^{39}Ar$ on alunite and jarosite respectively), has been considered as evidence for multiple pulses of hydrothermal alteration (Holley, 2012).

Cropping out 12 km north of the Pascua deposit, the Pascua Formation has been defined for an ignimbritic deposit and its intrusive equivalent dacitic dike that crosscut the breccia-hosted orebody at the Pascua deposit. This dike is characterized by biotite, quartz and plagioclase phenocrysts. A $^{40}Ar/^{39}Ar$ analysis on biotite established a 7.8±0.3 Ma age (Bissig et al., 2001) whereas the dacitic tuff north of Pascua has a K-Ar biotite age of 7.6±0.7 Ma (Martin et al., 1995).

Rhyolitic tuffs and volcaniclastic sedimentary rocks cropping out in the Valle del Cura area, with local occurrences in the El Indio area, are grouped in the Vallecito Formation. The tuffs are biotite, sanidine, quartz, and plagioclase-phyric (Bissig et al., 2001). Ages for this unit ($^{40}Ar/^{39}Ar$ on sanidine, biotite, and plagioclase) range between 5.5±0.1 and 6.0±0.3 Ma (Bissig et al., 2001). The most recent volcanic activity in this region corresponds to the Cerro de Vidrio rhyolitic dome; a vitreous plagioclase, quartz, sanidine and biotite-phyric dome that crops out 15 km southeast of the Pascua deposit. This dome has an age between 2.1±0.5 and 2.0±0.2 Ma ($^{40}Ar/^{39}Ar$ on biotite and glass, respectively; Bissig et al., 2002).

In summary, the El Indio belt contains exclusively high-sulfidation epithermal deposits which were emplaced after a marked reduction in erupted magma volumes and during major uplift of the Andean Cordillera. Reduction in magma volumes and uplift as well as epithermal mineralization are attributed to the onset of flat subduction in the region (Bissig et al, 2002; 2015).

2.4.2 The Los Pelambres-El Teniente belt

The Oligocene-Miocene-early Pliocene magmatic arc at Chile central (Figure 2.11; Lat. 31-34°S) has been extensively studied due to an exceptional concentration of supergiant Cu-Mo deposits that make this region the best endowed in Cu of the world (Toro et al., 2012). The host-rock volcanic to intrusive sequence has been divided into two units: the Abanico (and its local equivalents Coya-Machalí, and Cura-Maullín Formations) and the Farellones Formations.

The Abanico Formation consists of a 2000 m thick sequence of volcanic, pyroclastic, volcaniclastic and sedimentary deposits, as well as abundant subvolcanic intrusions (Charrier et al., 2007). Ages at the latitude of Santiago range between 35 and 21 Ma (Muñoz et al., 2006). This sequence was deposited in an extensional-basin that was tectonically inverted after and during the late episodes of this unit, approximately between 21 and 16 Ma (Charrier et al., 2007). An unconformity separates this sequence from the younger Farellones Formation, a ca. 2400 m thick succession of andesitic to rhyolitic lavas, volcaniclastic deposits, and reduced sedimentary deposits (Charrier et al., 2007, and references therein). Ages for the Farellones Formation range between 25 and 2 Ma (Parada et al., 2007).

Oligocene-Miocene plutons are widely scattered across the Central Depression and Principal Cordillera. Parada et al. (2007) grouped these bodies into the Intrusives I Unit, which includes microgabbros, dolerites, basalts and pyroxene-bearing andesites. Their ages range between 34 and 20 Ma. A younger group, called Intrusives II Unit is constituted by andesitic to rhyolitic porphyries. Their ages range between 21 and 14 Ma (Parada et al., 2007).

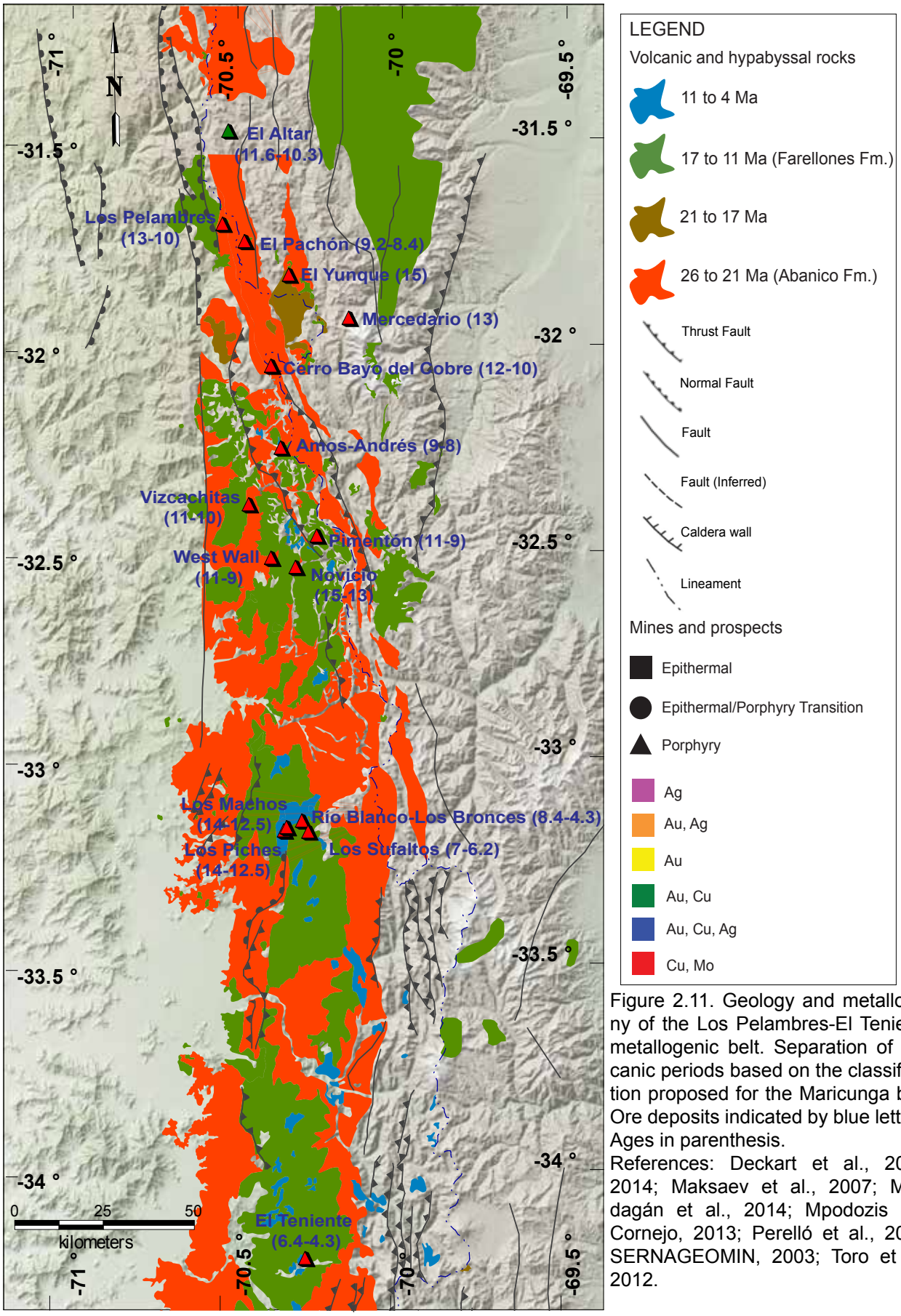

Figure 2.11. Geology and metallogeny of the Los Pelambres-El Teniente metallogenic belt. Separation of volcanic periods based on the classification proposed for the Maricunga belt. Ore deposits indicated by blue letters. Ages in parenthesis.
References: Deckart et al., 2013, 2014; Maksaev et al., 2007; Maydagán et al., 2014; Mpodozis and Cornejo, 2013; Perelló et al., 2013; SERNAGEOMIN, 2003; Toro et al., 2012.

During the late Miocene, a series of magmatic centers generated the Cu-Mo porphyritic systems. These porphyries are associated with multiphase stocks and a variety of hydrothermal breccia bodies (Charrier et al., 2007, and references therein). The composition of these intrusions varies from quartz diorite to quartz monzonite (Maksaev et al., 2007). Three world-class Cu-Mo districts stand out in this region: Los Pelambres, Rio Blanco-Los Bronces, and El Teniente (Figure 2.11). The age of emplacement of mineralized porphyritic systems at Río Blanco-Los Bronces ranges between 8.49 and 4.3 Ma (Deckart et al., 2013; 2014), whereas, at El Teniente, the magmatic-hydrothermal activity lasted between 6.46 and 4.37 Ma (Maksaev et al., 2007, and references therein). The Los Pelambres center was developed earlier, between 13 and 10 Ma (Bertens et al., 2003; Perelló et al., 2012). In addition to these supergiant deposits, other centers with Cu-Mo mineralization, albeit currently sub-economic, were emplaced earlier than these deposits. The oldest centers range between 15 to 13 Ma, as for example, Novicio (15-13 Ma), Los Machos (14-12.5 Ma), and Los Piches (14-12.5 Ma; Mpodozis and Cornejo, 2012). A second group of porphyry centers, located north of Lat.33°S, were emplaced between 12 and 8 Ma, as is the case of Los Azules, Rincones de Araya, Altar (11.6-10.3 Ma; Maydagán et al., 2014), El Pachón, Vizcachitas, Amos-Andrés, Pimentón, Novicio and West-Wall (Mpodozis and Cornejo, 2012; and references therein).

The Los Pelambres-El Teniente belt contains an enormous Cu-Mo endowment concentrated mainly in three behemothian porphyry deposits that were emplaced during an episode of crustal thickening and lack of coeval volcanism, together with a temporal relationship with the subduction of the Juan Fernández Ridge below this segment of the Andean margin (Hollings et al., 2005; Maksaev et al., 2007).

Chapter 3: Methodology

To establish an integrated model of the geological evolution at La Coipa district, a characterization of surface geology through the updating of the geological mapping, complemented by drill core logging at each deposit, was done during two field campaigns. Selected samples collected during this time were studied petrographically and analyzed by U-Pb and $^{40}Ar/^{39}Ar$ geochronology, whole-rock geochemistry, X-ray diffraction (XRD), scanning electron microscopy (SEM), and for sulfur isotopes.

Geological mapping at a 1:10.000 scale covered an area of 243 km^2, using a GeoEye satellite image as a base. The coordinate system used is Universal Transverse Mercator (UTM), with the Provisional South American 1956 (PSAD 56) datum, Zone 19 South. The purpose was to provide a district geological map containing more detail than the 1:100.000 scale Hoja Salar de Maricunga Chilean Geological Survey (Sernageomin) map (Cornejo et al., 1998), and the district-scale geological maps prepared by MDO and Kinross exploration geologists. Coding nomenclature of lithological units was taken from the above mentioned regional map where possible, adding modifications to the Tertiary units based on the present study. Logging of diamond drill-core was performed on selected holes, prioritizing those located in representative sections of each deposit or prospect. Hand samples were taken during mapping and logging. For alteration mapping, these samples were analyzed by short wave infrared spectroscopy (SWIR) using a Terraspec® spectrometer, interpreting the occurrence of alteration minerals and quantification of spectral parameters with the TSG (The Spectral Geologist) software.

In total, 23 radiometric ages were obtained, including 11 $^{40}Ar/^{39}Ar$ alunite ages, two $^{40}Ar/^{39}Ar$ biotite ages, eight zircon U-Pb ages by chemical abrasion-isotope dilution-thermal ionization mass spectrometry (CA-ID-TIMS), and two zircon U-Pb ages by laser ablation-inductively coupled plasma-mass spectrometry (LA-ICP-MS). All radiometric dating was performed at the Pacific Centre for Isotopic and Geochemical Research (PCIGR) at the University of British Columbia, Vancouver, Canada. In addition, two $^{40}Ar/^{39}Ar$ duplicates of alunite samples dated at PCIGR were also dated at the Isotope Geochemistry, Geochronology and Thermochronology Unit, Université de Genève, Switzerland.

For $^{40}Ar/^{39}Ar$ geochronology, step-heating analyses were done on handpicked grains of alunite and biotite, ranging between 0.59 and 0.29 mm grain-size. The grains were selected using a binocular microscope, picking the most pure and homogeneous grains from crushed rock material. Grains analyzed at the PCIGR were wrapped in aluminum foil and irradiated through intermediate speed neutrons at the McMaster Nuclear Reactor in Hamilton, Canada. Samples were intercalated with the Fish Canyon Tuff sanidine neutron flux monitor, which has an age of 28.201±0.046 Ma (Kuiper et al., 2008).

For CA-ID-TIMS U-Pb dating (Scoates and Friedman, 2008), zircons grains were separated under standard mineral separation procedures, selecting four to five crack-and-inclusion free grains, which were chemically abraded, dissolved and homogenized with an isotope tracer (EARTHTIME ET535), to be finally thermally ionized, obtaining the isotopic ratios that can be used to calculate the Concordia diagrams and subsequent ages, a process that was performed with the Isoplot software (Ludwig, 2003).

Zircons analyzed by the LA-ICP-MS method followed the procedure established by Tafti et al. (2009). After a standard separation, zircon grains greater than 50 microns were mounted in an epoxy puck, accompanied by some zircons grains obtained from two standards: Plešovice and Temora2. Line scans were run on each zircon, selecting an area free of alteration, inclusions, or inherited cores. For the two samples presented in this work, 15 and 18 unknown zircon grains were analyzed respectively. Interpretation and plotting of data was performed using the Isoplot software (Ludwig, 2003).

As a complement to radiometric dating, alunite was characterized by X-ray diffraction, SEM and Electron Microprobe techniques. Prior to the separation of alunite for radiometric dating, a mineralogical characterization using X-ray diffraction of a powdery subsample was performed with the aim of identification of secondary mineral phases that could alter the geochronological analysis. In addition, a polished thin section of the alunite domain considered for geochronology was analyzed by SEM and Electron Microprobe. A grain size image and X-ray mineral mapping of selected

elements by SEM was obtained for each sample. Selected alunite grains were analyzed by electron microprobe for major elements. The analysis was performed on a small area 15 by 15 μm scanned by the microbeam to prevent excessive loss of K or Na. These analyses were performed at the Electron Microbeam / X-ray Diffraction Facility at the Department of Earth, Ocean & Atmospheric Sciences at UBC. Alunite grains were also analyzed for sulfur stable isotopes (Rainbow et al., 2005), accompanied by analysis of sulfides in those samples were pyrite or enargite was intergrown with alunite. These isotopic analyses were performed at the Queen´s Facility for Isotope Research, Queen´s University, Kingston, Canada.

A set of 22 samples was analyzed by whole-rock geochemistry, including major, trace and rare earth elements (REE). These samples were analyzed by a combination of ICP emission spectrometry and mass spectrometry at the Acme Analytical Laboratories Ltda., Vancouver, Canada. The analytical package, called 4A-B, considered a total digestion after a lithium-borate fusion. For petrographic characterization, 80 thin-and polished-sections were prepared at Vancouver Petrographics and studied for detailed characterization of most important lithological units.

Chapter 4: Geology, Alteration and Mineralization of the La Coipa district

The objective of the present chapter is to describe the geological framework of the La Coipa district, including the lithological characterization of igneous and sedimentary rocks, the structural setting, and the hydrothermal alteration and mineralization. A map showing the geographic features, locations and key areas is illustrated in Figure 4.1. A 1:10.000 scale geological map of the La Coipa district covering a 196 km^2 surface is presented in this study (Appendix A1), of which a simplified version is illustrated in Figure 4.2. The stratigraphic units are described below and a schematic stratigraphic column is presented in Figure 4.3. A new nomenclature for Oligocene-Miocene units is proposed based on stratigraphic and geochronological data obtained in this study.

4.1 Paleozoic and Mesozoic basement rocks

4.1.1 Permian Granodiorite [Pzgd]

Age: Permian

Reference: This study

The Permian Granodiorite (Pzgd) is an intrusive unit that crops out north of the Brecha Norte open pit (200x200 m in outcrop; Figure 4.2). This unit has also been exposed by mining in the Brecha Norte and Coipa Norte open pits. Core logging suggests that it is a single stock, overlain by younger units and displaced by normal faults. A nonconformity separates this intrusive unit from the overlying quartz-rich sandstone and black shale members of the Estratos El Mono Unit (see below). The base of the Permian Granodiorite unit has not been observed.

The outcrops of this unit (Figure 4.4.A) have a reddish to greenish appearance. The rock contains coarse-grained (up to 3 mm) equigranular euhedral quartz, K-feldpar and biotite. In the Brecha Norte deposit, a fine-grained xenolith with a similar composition (Fig. 4.4.B) indicates that least two textural varieties make up this intrusive unit. A set of thin sections indicate that this unit consists of coarse

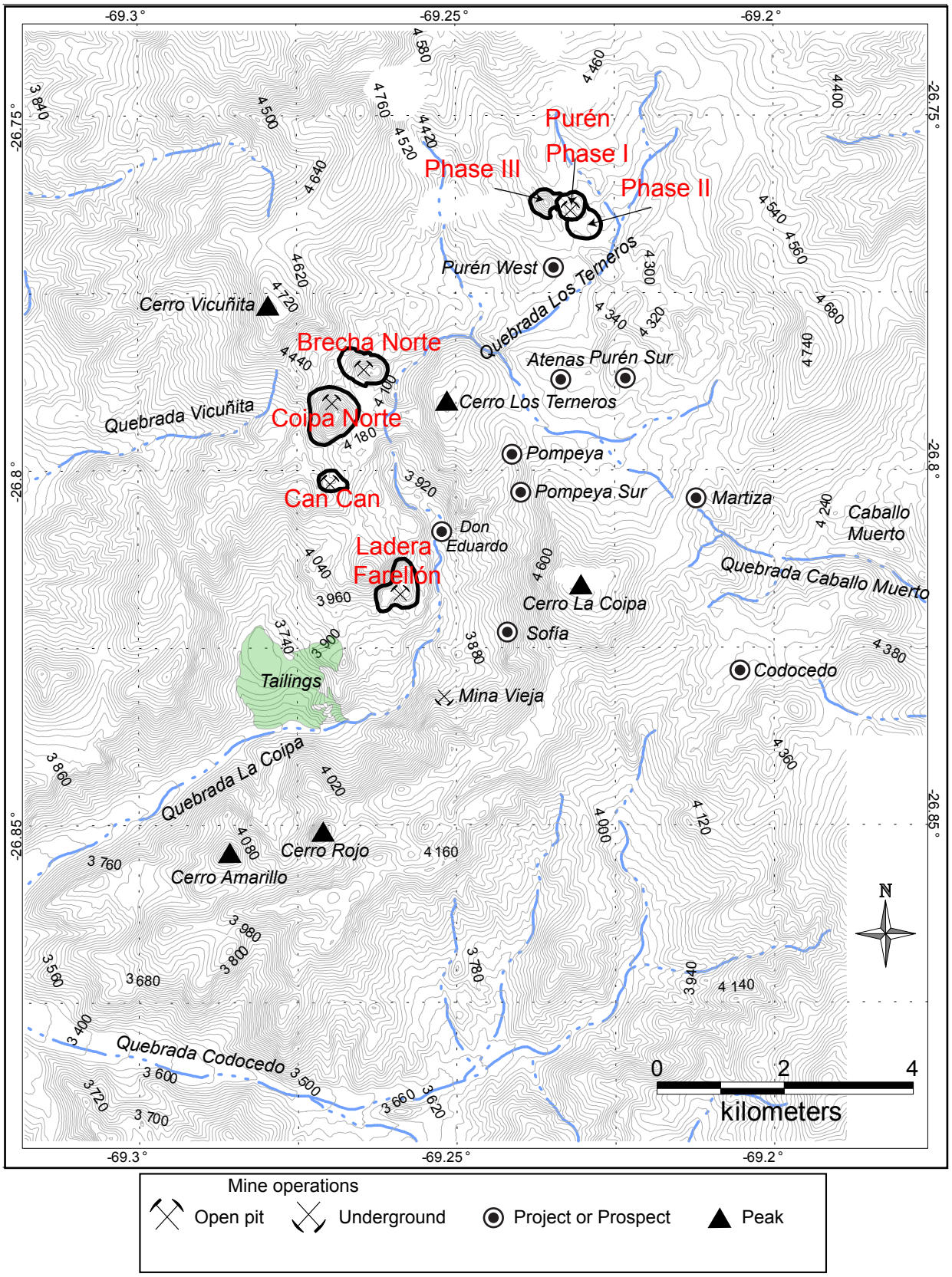

Figure 4.1. Topographic map of La Coipa district showing locations mentioned in the text. Mines, prospects, peaks and creeks are labelled.

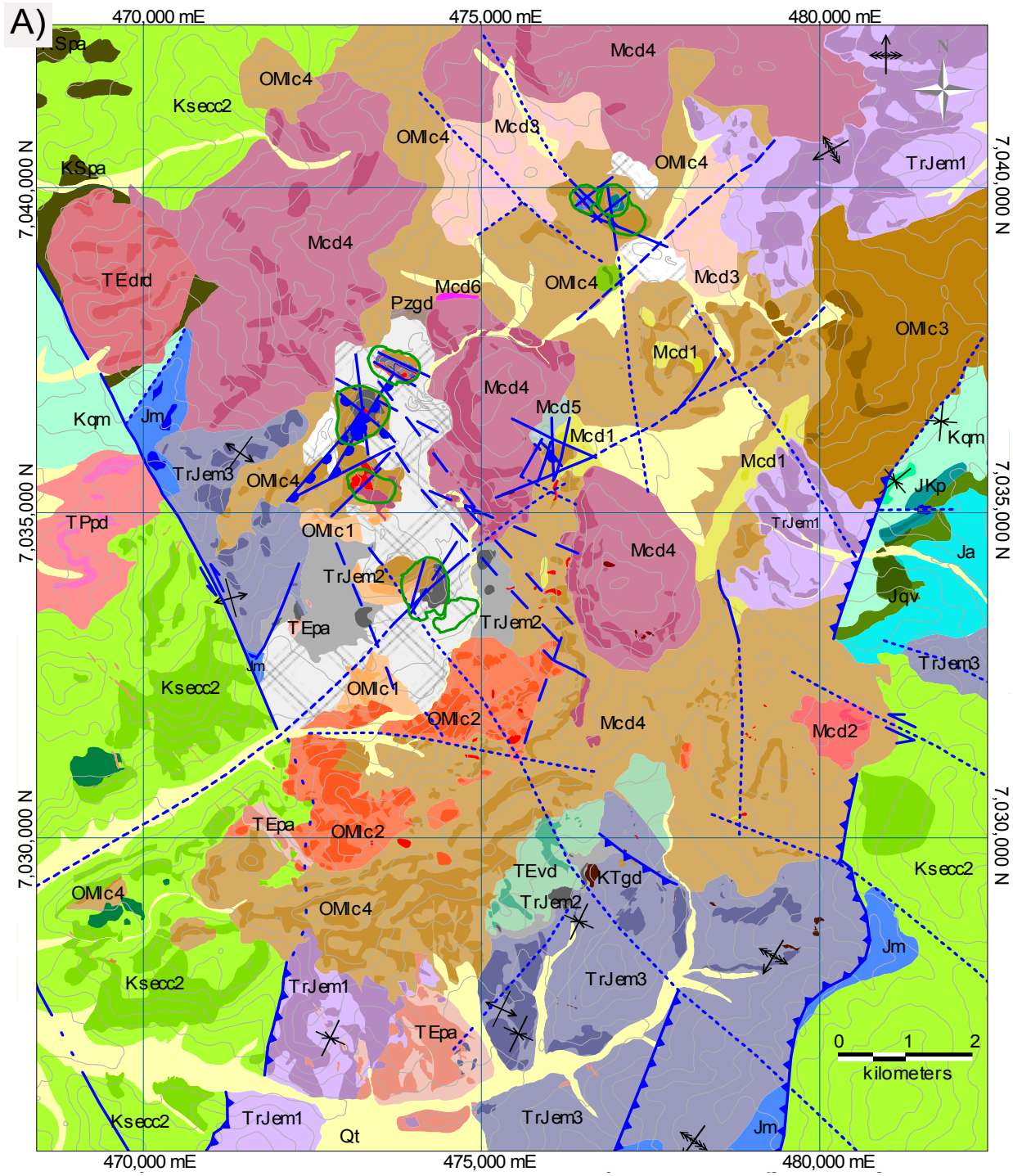

Figure 4.2. A) Simplified geologic map of La Coipa district. For detailed map see Appendix A1.
B) Legend of lithological units defined for the La Coipa district (contiguous page). Boxes painted according to the outcrop mapping (inner box) and the interpretation polygon for each lithological unit (outer box).

B) **LEGEND**

Holocene
Alluvial and colluvial deposits

Qt — Unconsolidated gravels, breccias, sands and silts

Middle Miocene

Mbx — Phreatomagmatic to phreatic breccias

Codocedo Group

Mcd6 — Base and surge deposits

Mcd5 — Hematitized volcaniclastic sandstones and breccias

Mcd4 — Vicuñita domes

Mcd3 — Los Terneros ignimbrite

Mcd2 — Torito dome

Mcd1 — Azufrera volcaniclastics

Oligocene -early Miocene
La Coipa Group

OMlc4 — Pompeya pyroclastics

OMlc3 — Purén domes

OMlc2 — Mina Vieja domes

OMlc1 — Ladera tuffs

Eocene - Oligocene

EOh — Estratos de Huidobro

Eocene

TEdi — Dacitic ignimbrite

TEvd — Volcaniclastic deposits

Middle Eocene - late Eocene

TEpa — Rhyodacitic porphyries and dikes

TEdrd — Rhyolitic domes

Paleocene - early Eocene

TPpd — Dacitic Porphyries

Late Cretaceous- early Paleocene

KTgb — Monzogabbroic stocks

KSpa — Andesitic and microdioritic porphyries

Estratos de Cerro Los Carneros

Ksecc2b — Ocoitic sills

Ksecc2 — Andesitic lavas

Early Cretaceous

Quebrada Monardes Formation

Kqm — Brown-reddish sandstones

Late Jurassic - Early Cretaceous

Pedernales Formation

JKp — Limestones and calcareous sandstones

Estratos de Quebrada Vicuñita

Jqv — Andesitic to basaltic lavas

Middle Jurassic

Asientos Formation

Ja — Fossiliferous limestones

Early Jurassic - Middle Jurassic

Montandón Formation

Jm — Fossiliferous limestones and calcareous shales

Late Triassic - Early Jurassic

Estratos El Mono Unit

TrJem3 — Quartz-rich sandstones and fine grained conglomerates

TrJem2 — Black shales

TrJem1 — Coarse conglomerates and quartz-rich sandstones

Permian

Pzgd — Permian Granodiorite

Structures

Fault (Undifferentiated)

Thrust Fault

Normal Fault

Fault (Inferred)

Fault (Covered)

Lineament

Sincline

Anticline

Anticline (overturned)

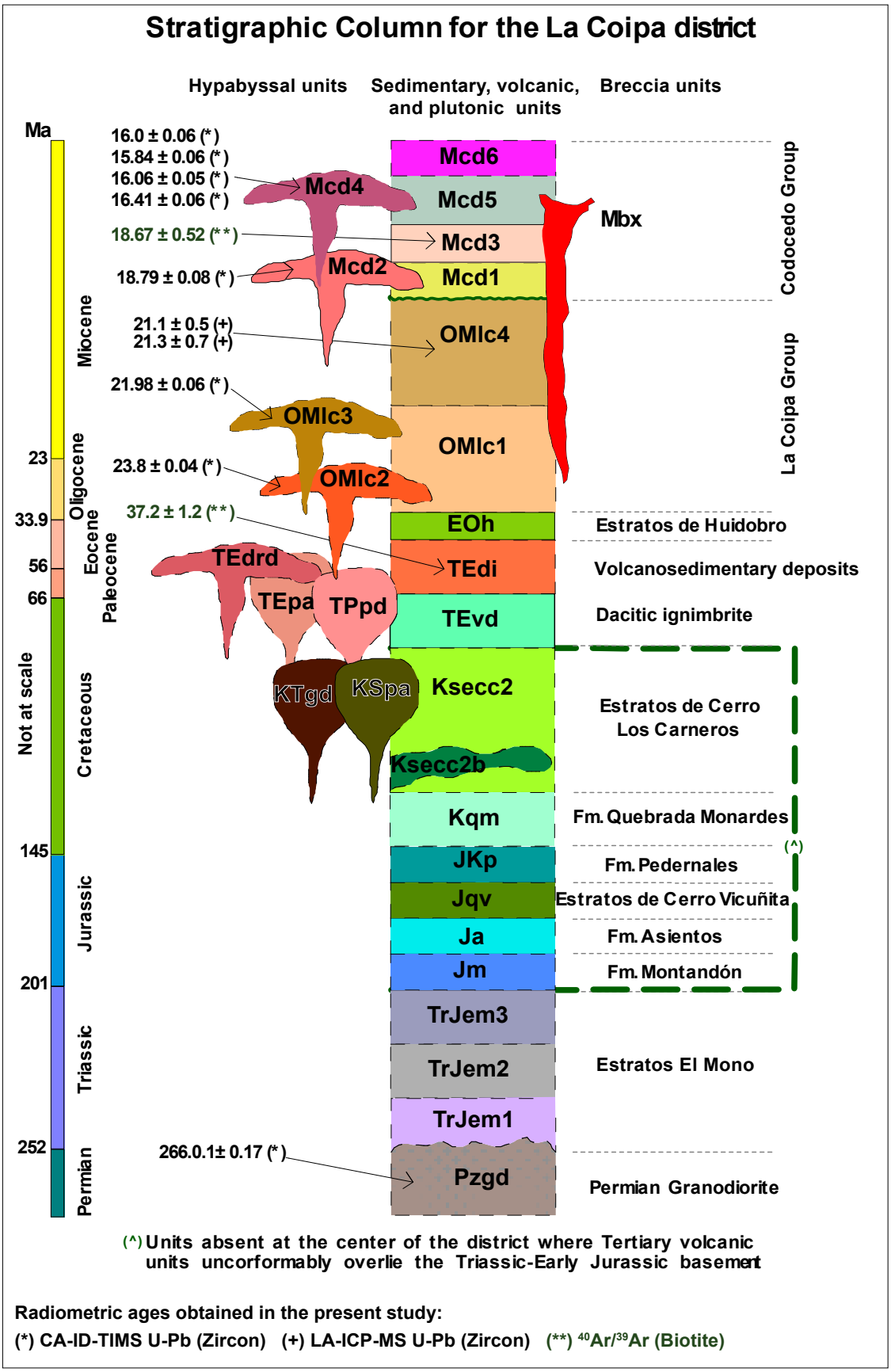

Figure 4.3. Stratigraphic column proposed for the La Coipa district. A green wavy line between the OMlc4 and Mcd1 units indicates an unconformable contact.

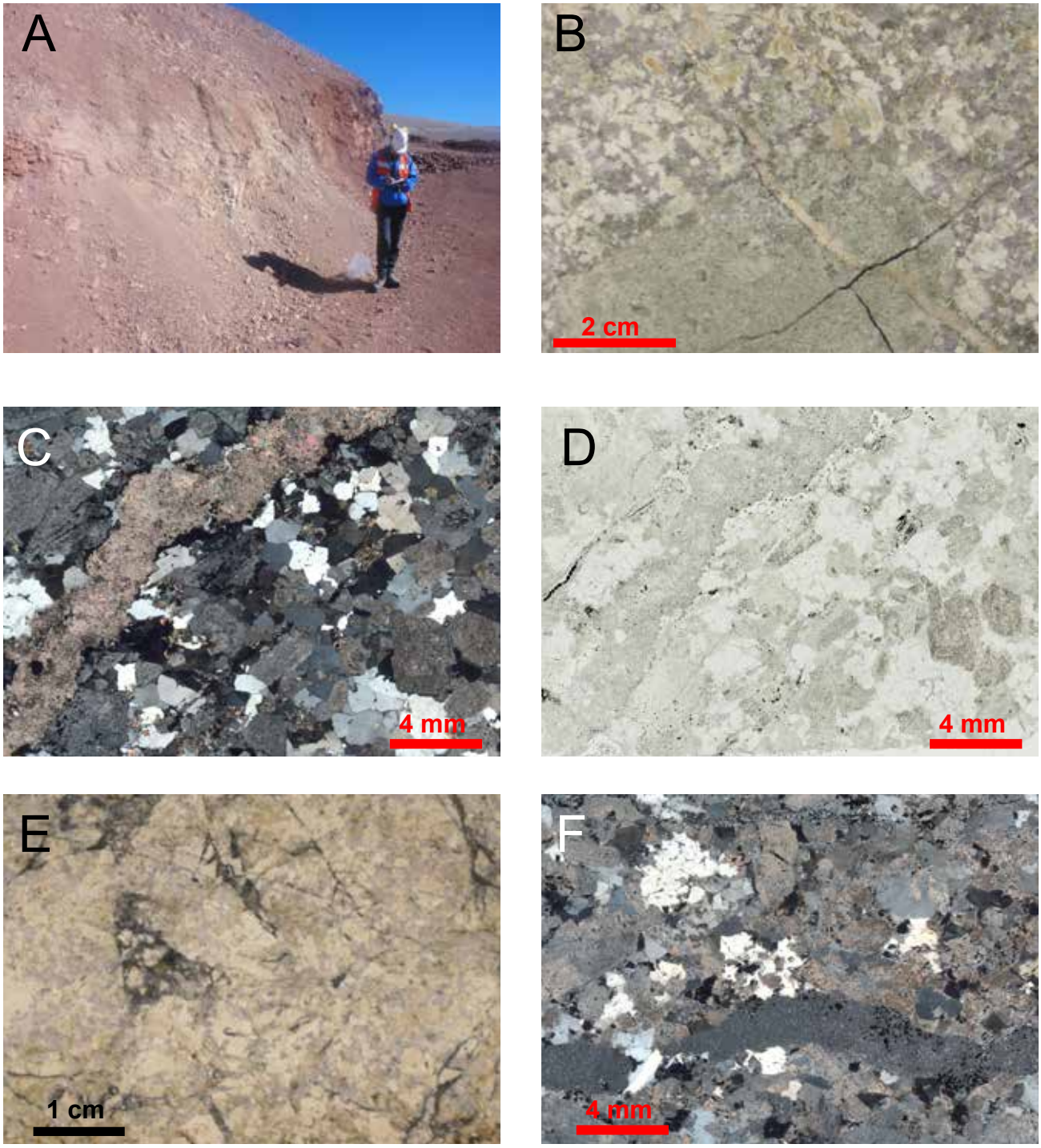

Figure 4.4. Photographs and photomicrographs of the Permian Granodiorite. **(A)** View of the moderately weathered outcrop of the Permian Granodiorite, located to the north of the Brecha Norte open pit. **(B)** Photograph of sample SG16263 (Drill-hole BND-011, 293.1 m, Brecha Norte deposit). A fine-grained xenolith of a fine-grained facie of the Permian Granodiorite is observed at the bottom of the imagen. Rock is cross-cut by a calcite vein. **(C)** Photomicrograph taken under cross-polarized light of sample SG16263 showing the hollocristaline texture of this unit. Plagioclase phenocrysts are replaced by clay minerals. A calcite vein is cross-cutting this sample. **(D)** Photomicrograph taken under plane-polarized light of sample SG16263. A pseudo-porphyritic texture is observed with tabular plagioclase phenocrysts inmersed in an anhedral intergrowth of quartz and K-feldspar. **(E)** Photograph of sample SG16261 (Drill-hole CND-241, 588.45 m, Coipa Norte deposit). This rock is cross-cut by quartz veinlets producing local brecciation. **(F)** Photomicrograph taken under cross-polarized light of sample SG16261. Plagioclase and K-feldspar crystals are replaced by sericite. Rock is cross-cut by a quartz-alunite-pyrite vein.

subhedral tabular plagioclase (up to 3.5 mm) and biotite (up to 1 mm) phenocrysts immersed in a fine grained matrix of anhedral quartz and K-feldspar (Figures 4.4.C, D and F).

The Permian Granodiorite is the oldest unit described in the La Coipa district. Cornejo et al. (1993) assigned it a Paleozoic age, which was later changed to a Cretaceous age (Cornejo et al., 1998). During this study, a CA-ID-TIMS U-Pb zircon age of 266.01±0.17 Ma was obtained for a sample collected in the Brecha Norte open pit (sample SG16263, Drill-hole BND-011, 293.1 m. See Table 4.1 and Appendix A3), confirming the original age assignment by Cornejo et al. (1993). Furthermore, inherited zircons from Oligocene-Miocene lapilli tuffs dated by U-Pb LA-ICP-MS showed ages ranging between 265 and 266 Ma (Samples SG050315P5 and SG190213P16, see Appendix A4), suggesting that this unit also underlies other areas of the district.

Due to the proximity of the mineralized systems at Brecha Norte and Coipa Norte, this unit is variably altered and mineralized. Alteration varies from illite-sericite replacing plagioclase and biotite crystals to pervasive alunite (Figure 4.4.E and F). The Permian Granodiorite is cross-cut by quartz+pyrite±enargite±alunite, sericite and calcite veins, presenting also disseminated sulfides such as pyrite and enargite. Fragments of the Permian Granodiorite observed in Tertiary pyroclastic rocks cropping out in the eastern part of the district have no hydrothermal alteration.

The Permian Granodiorite can be correlated with the Pedernales and Sierra Castillo batholiths (Cornejo et al., 1993), both located in the northern Maricunga belt. The Quebrada Caballo Muerto monzogranite (Cornejo et al., 1998) is located 12 km east of La Coipa (outside of the study area). It has been dated at 265±8 Ma (K-Ar, biotite; Cornejo et al., 1998). In the Caballo Muerto area, a block of Late Paleozoic intrusive and volcanic rocks is overthrusted by Triassic and Mesozoic units by the west-vergent Caballo Muerto reverse fault, which crops out in the eastern part of the study area. These batholiths and stocks, together with the Permian Granodiorite, form part of the late Carboniferous-Permian plutonic Choiyoi Group (Figure 2.1), which constitutes a large proportion of the basement of the Maricunga and El Indio belts (Cornejo et al., 1993; Martin et al., 1999).

Table 4.1: Summary of U-Pb ages on zircons obtained in the present study

Sample no	Location	Unit	Method	UTM North / UTM East or Drill-Hole		Age (Ma) (± 2σ)	MSWD
SG13358	Co Los Terneros	Mcd4	CA-ID-TIMS	7034983	474888	16.00±0.06	0.062
SG13363	Co La Coipa	Mcd4	CA-ID-TIMS	7035060	476614	15.84±0.06	0.5
SG13364	Co Los Terneros	Mcd4	CA-ID-TIMS	7034661	475228	16.06±0.05	1.12
SG13365	Co La Coipa	Mcd4	CA-ID-TIMS	7032983	476738	16.405±0.056	0.52
SG210213_P5	Codocedo	Mcd2	CA-ID-TIMS	7031688	480696	18.79±0.08	0.29
SG050213_P5	W of Co Amarillo	OMlc4	LA-ICP-MS	7029091	469591	21.1±0.5	0.58
SG190213_P16	S of Mina Vieja	OMlc4	LA-ICP-MS	7031226	475799	21.3±0.7	0.75
SG16305	Purén Sur	OMlc3	CA-ID-TIMS	DPU-243, 547.32m.		21.98±0.06	1.01
SG13351	Sofía	OMlc2	CA-ID-TIMS	7032650	475924	23.8±0.04	1.19
SG16263	Brecha Norte	Pzgd	CA-ID-TIMS	BND-011, 293.1m.		266.01±0.17	1.13

4.1.2 Estratos El Mono

Age: Late Triassic-Early Jurassic.

Reference: Mercado, 1982.

The Estratos El Mono sequence, defined by Mercado (1982) as a member of the La Ternera Formation, comprises a sedimentary sequence of lacustrine, fluvial and alluvial deposits. This unit comprises three members, that from bottom to top, correspond to: Coarse conglomerates and quartz-rich sandstones (TrJem1), Black shales (TrJem2), and Quartz-rich sandstones and fine-grained conglomerates (TrJem3). These members are described below.

4.1.2.1 Coarse conglomerates and quartz-rich sandstones [TrJem1]

The most widely distributed member of the Estratos El Mono unit consists of coarse conglomerates interbedded with coarse-grained sandstones (Figure 4.5.A). This unit can be found in three separate domains in the eastern, northeastern, and south-central areas of the district (Figure 4.2). A common feature between these three domains is that they are thrusted over younger rocks by regional reverse faults. In the southern area, this unit is thrusted over the Cretaceous Estratos de Cerro Los Carneros (see below) unit by the west vergent NNE high-angle Vega la Junta reverse fault. The eastern blocks are thrusted over Mesozoic sedimentary sequences by the east vergent NE Portezuelo Codocedo fault. The TrJem1 unit is uncorfomably overlain by Tertiary volcanic rocks of the La Coipa and Codocedo Groups (see below). Besides, the southern block is intruded by a rhyodacitic porphyry (TEpa) of Eocene age. No contacts between the TrJem1 and the other two upper members of this unit (TrJem2 and TrJem3, see below) have been identified in the field. The TrJem1 member is folded by a NE-oriented anticline (southern block) and a N- to NE-oriented syncline (northeastern block). The eastern block is characterized by NE-striking strata dipping 20° to 70° degrees to the southeast. Suárez et al., (1995) estimated a 200 m thickness for the coarse-conglomerate member in the southern area.

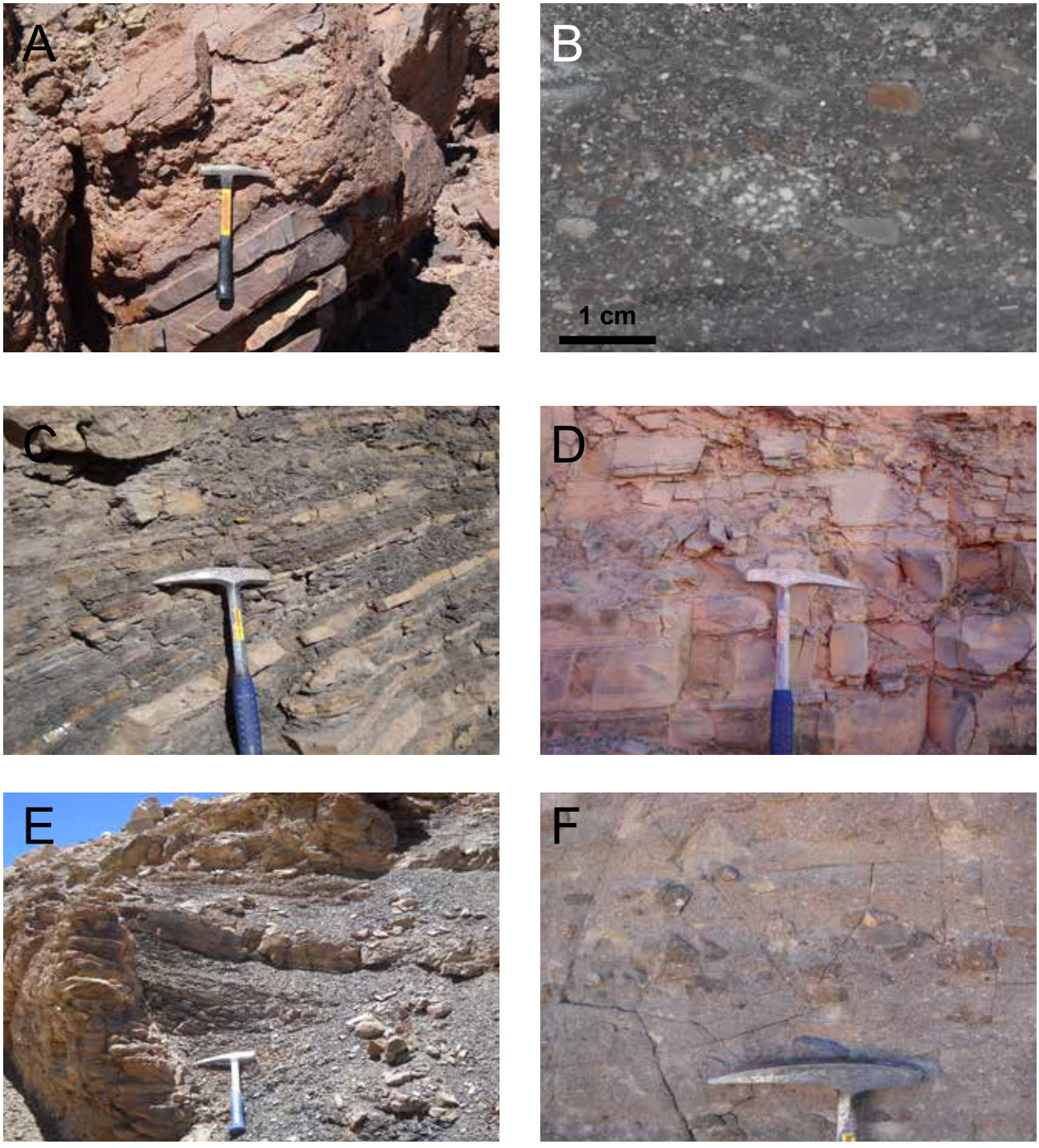

Figure 4.5. Photographs of characteristic rocks of the Estratos El Mono unit. **(A)** TrJem1 member: Conglomerates interbedded with coarse-grained sandtones, Maritza area. **(B)** TrJem1 member: Hand sample from the Maritza area, showing a conglomerate altered to intense silicification and dissemination of fine-grained pyrite (sample SG210213_P6). **(C)** TrJem2 member: Black Shales member, carbonaceous black shales, tailings area (sample SG050313P_5). **(D)** TrJem2 member: Black shales cropping out to the south of the Cerro Los Terneros (sample SG040213_P2) **(E)** Contact between a black shale lense and coarse-grained sandstones, outcrop located to the north of the Codocedo Creek. **(F)** TrJem3 member: quartz-rich sandstones interbedded with fine-grained conglomeratic levels with subhorizontal-oriented clasts, outcrop located to the east of the Indagua Fault, tailings area (sample SG050313_P1).

This basal member is characterized by up to 2 m thick strata of polymictic well sorted conglomerates (clasts of andesitic volcanic rocks, intrusive rocks, metasediments, and limestones), clast- to matrix-supported, with up to 80 cm diameter rounded clasts. The rock is cemented by calcite. The conglomerates are interbedded with quartz-rich coarse-grained sandstones. A thin section obtained from a sample taken in the Maritza area shows that these conglomerates contain sub-rounded heterolithic clasts of quartz-rich metasediments, limestones, plagioclase-phyric porphyritic volcanic rocks, hypabyssal plagioclase-rich trachytic fragments, together with up to 2 mm angular crystals of quartz, supported in a calcite-epidote cemented matrix. These conglomerates are interbedded with quartz-rich sandstones characterized by angular crystals of quartz (up to 2 mm, 60% of the total volume rock), plagioclase (up to 0.3 mm, 5% of the total volume), and lithics (up to 3 mm, 20% of the total volume) of similar lithologies observed as in the conglomerates. The matrix is cemented by calcite. The most characteristic alteration of this unit is propylitic, i.e., chlorite-epidote-calcite. Locally, at the eastern margin of the Maritza target, pyrite+sericite and strong silicification are indicating a hydrothermal overprint (Figure 4.5.B).

4.1.2.2 Black shales [TrJem2]

The TrJem2 member of the Estratos El Mono unit is constituted by carbonaceous black shales interbedded with minor levels of mudstones and sandstones. This unit can be found in the central area between the Quebrada La Coipa and the tailings area, and is also recognized at the Brecha Norte, Coipa Norte, Can-Can and Ladera Farellón open pits (Figure 4.5.C and D). A thinner package of black shales crops out in the southern area, north of the Quebrada Codocedo. West of the Ladera Farellón open pit, near the tailings area, a transitional concordant gradation to quartz-rich sandstones is observed. Here, layers of sandstones are becoming thicker (from centimetric to metric scale) and more continuous in the stratigraphically higher portions. Where this member is not in contact with the upper member of quartz-rich sandstones, the black shales are unconformably overlain by Tertiary volcaniclastic deposits of the TEvd unit and volcanic rocks of the La Coipa Group. The base of the black shales member has only been observed in the Brecha Norte pit, where it directly overlies the Permian granodiorite.

Outcrops of the black shales member consist of very thinly laminated carbonaceous black or dark grey shales rich in organic matter, locally interbedded with mudstones and fine to medium-grained sandstones (Figure 4.5.E). Deformation with local and district scale folds caused highly variable bedding orientations of these black shales. Proximal to the epithermal Au-Ag deposits, the black shales are altered to alunite + pyrophyllite + scorodite + jarosite, while distal occurrences are devoid of visible alteration. The black shales member presents biostratigraphic markers, such as *Estherias* (a fresh-water crustacean), plant fossils, *Diplodon* (a fresh water bivalve), oncolites and Hybodontid shark teeth (Suárez et al., 1995), determining a Late Triassic-Early Jurassic age for this unit.

4.1.2.3 Quartz-rich sandstones and fine-grained conglomerates [TrJem3]

The upper member of the Estratos El Mono unit is formed by quartz-rich coarse-grained sandstones interbedded with fine-grained conglomerates (Figure 4.5.F). This unit can be found in three localities: to the east of the Indagua Fault, in the southern part of the district (south of the Codocedo area), and in the Brecha Norte and Coipa Norte open pits (Figure 4.2). The TrJem3 member concordantly overlies the TrJem2 member, while an unconformity separates this member from the overlying pyroclastic rocks of the La Coipa Group. A series of sub-parallel NE-oriented anticlines and synclines deformed the NE-striking strata of the TrJem3 member, resulting in bedding dips that range between 20 to 80 degrees to the southeast or northwest.

Outcrops of this unit are defined by coarse- to medium-grained sandstones with quartz and lesser feldspar grains interbedded with fine-grained conglomerates, which have hetherolithic sub-rounded to sub-angular clasts (coming from fine-grained sandstones, rhyolites, and from intrusive rocks). A thin section obtained from a sample collected near the western part of the tailings area (sample SG0503013_P1) reveals a clast-supported texture with angular quartz (up to 1.5 mm, 70% of the total volume), plagioclase (up to 1 mm, 5% of the total volume), and lithics (up to 7 mm, 20% of the total volume), which are supported by a calcite+iron oxide cemented matrix. To the east of the Indagua Fault, the TrJem3 member is characterized by silicification, while the sequence observed in

the Brecha Norte open pit is pervasively altered to quartz-alunite. The sedimentary sequence of the Estratos El Mono unit at the La Coipa area has been defined as a distal member of the La Ternera Formation (Aguilar, 1984), or as La Coipa Beds (Suárez & Bell, 1991). Defined by Brüggen (1950) in the Precordillera of the Atacama Region, southeast of La Coipa, La Ternera Formation consists of Triassic continental clastic sediments intercalated with andesitic to basaltic volcanic rocks.

The Estratos El Mono unit can also be correlated with the Quebrada del Salitre Formation (Naranjo & Puig, 1984), which consists of conglomerates, sandstones, siltstones, and intercalations of marine limestones. The Quebrada del Salitre Formation crops out at the Salar de Pedernales (Suárez & Bell, 1992), north of the study area. The Estratos el Mono unit, considering its three members, was deposited in a continental setting, characterized by lacustrine, fluvial and alluvial deposition (Bell & Suarez, 1991; Suárez et al., 1995). This unit was part of NW-oriented subparallel marine and continental rift basins that according to Charrier (1979), characterized the Late Triassic-Early Jurassic period in the southern part of the South American continent. The Estratos El Mono unit is an important ore host in the Brecha Norte, Coipa Norte, Can Can and Ladera Farellón deposits.

4.1.3 Montandón Formation [Jm]

Age: Early Jurassic-Middle Jurassic.

Reference: Harrington, 1961.

In the study area, the Montandón Formation (Jm) is characterized by a sequence of limestones and carbonaceous fossiliferous shales. The Jm unit is distributed in two domains: in the southeastern region of the study area, and in the western area, bounded to the west by a segment of the Indagua Fault (Figures 4.2 and 4.6.A). In the southeastern area, outcrops of this unit are spatially associated with the Portezuelo Codocedo thrust fault. In this area, the strata are concordantly overlying the quartz-rich sandstones member (TrJem3) of the Estratos El Mono unit. Here, the Montandón Formation is unconformably overlain by the Estratos de Cerro Los Carneros unit. The western outcrops are

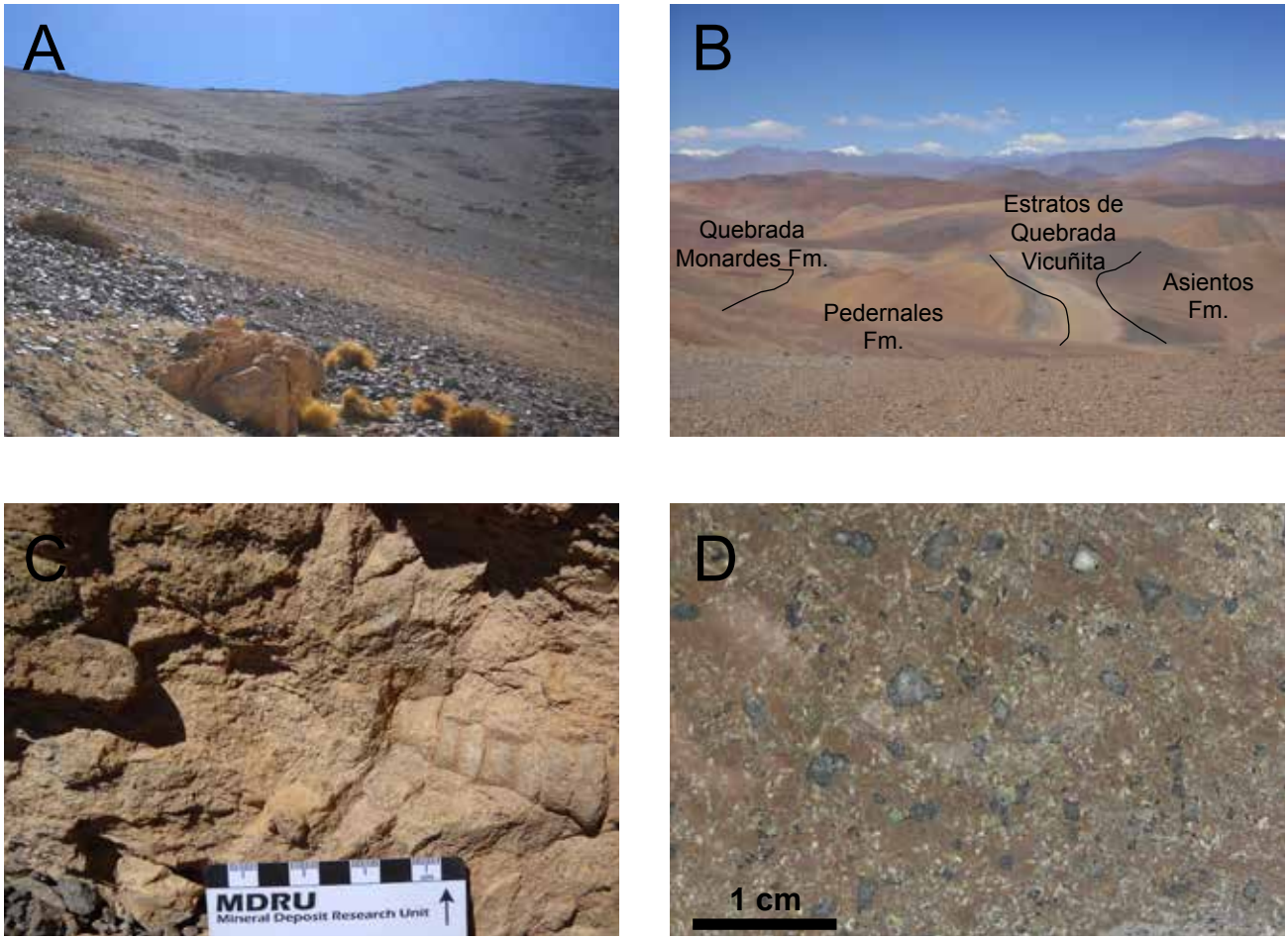

Figure 4.6. Photographs of the Jurassic sedimentary and volcanic units. **(A)** View of a Montandón Formation limestone outcrop located to the west of the tailings area, just over the trace of the Indagua Fault. Upper units correspond to the Estratos Cerro Los Carneros unit. (foto 1352 050313P2) **(B)** Panoramic view of a sequence of Jurassic marine and terrestrial sediments (Asientos, Pedernales, and Quebrada Monardes Formations) and the Estratos de Quebrada Vicuñita volcanic unit (foto 1206 2100113p6) **(C)** Fossiliferous limestone of the Asientos Formation. this rock is constituted by univalves, bivalves, and cephalopods. (foto 1203 210113P4) **(D)** Hand sample SG210213_P3. porphyritic andesite of the Estratos Quebrada Vicuñita unit showing a high content of vesicles filled by calcite, quartz, and chlorite.

associated with the sinistral strike-slip Indagua Fault, presenting intensely deformed near-vertical folded strata. According to Abels & Bischoff (1999), the thrusting of the Indagua and Sierra Amarga Faults, both belonging to the Domeyko Fault System, was focused along incompetent sequences of limestones, explaining narrow and highly deformed outcrops of the Montandón Formation in the hanging wall of the fault. The southeastern domain has a thickness of approximately 300 m, while the western domain reaches a thickness of 100 m (Cornejo et al., 1993).

Only outcrops located west of the tailings area were mapped during this study. Here, rocks of the Montandón Formation comprise re-crystallized and auto-brecciated white limestones. These rocks have intense goethite oxidation. North of these outcrops, Cornejo et al. (1993) described the Montandón Formation as a succession of grey limestones with bivalve and ammonite fossils. According to these authors, the southeastern domain is formed by alternating limestones and carbonaceous shales with a basal level of quartz-rich conglomerates. Rocks of the Montandón Formation in the study area are neither altered nor mineralized.

Fossils markers give a deposition age for the Montandón Formation between the Pliensbachian and middle Bajocian (Cornejo et al., 1993). This unit can be correlated with the basal member of the Sierra Fraga Formation (Sepúlveda & Naranjo, 1982), located to the west of the La Coipa district. It should be noted that in the study area, the Montandón Formation is also known as the Lautaro Formation (Aguilar, 1984). The marine character of this formation indicates the deepening of the Triassic continental rift basins developed in this region, marking a period defined by marine transgressions that affected the back-arc region of northern Chile (Charrier et al., 2007).

4.1.4 Asientos Formation [Ja]

Age: Middle Jurassic.

Reference: Harrington, 1961.

A fossiliferous sequence of marine limestones observed in the eastern margin of the study area is assigned to the Asientos Formation (Figures 4.2 and 4.6.B). In its type locality, the Quebrada Asientos (55 km northwest of the study area), this unit was defined as a thickly bedded unit of fossiliferous limestones interbedded with calcareous sandstones and volcanic sandtones (Müller & Perelló, 1982). Cropping out at both sides of the Quebrada Caballo Muerto, this unit is conformably overlying the TrJem3 member of the Estratos El Mono Unit. The strata of the Asientos Formation keep a NE-strike orientation, dipping 15° to 50° to the northwest. Cornejo et al. (1993) estimated a 400 m thickness for the Asientos Formation in this area.

Rocks of this unit are characterized by light-brown limestones with a high content of several species of marine fossils (univalves, bivalves and cephalopods; Figure 4.6.C). This unit presents thick homogeneous strata (>1 m). No hydrothermal alteration has been observed in this unit. Based on fossil ages of *Reineckeia* and *Macrocephalites*, García (1967) established a Calovian age for the Asientos Formation.

4.1.5 Estratos Quebrada Vicuñita [Jqv]

Age: Late Jurassic.

Reference: Cornejo et al., 1993.

The Estratos Quebrada Vicuñita (Jqv) unit is composed of andesitic to basaltic lavas. This unit was proposed by a Field Geology Course of the University of Chile (1990). The Jqv unit crops out in the eastern area of the district (Figure 4.2), on both sides of the Caballo Muerto Creek (Figure 4.6.B).

The Jqv unit is conformably overlying the Asientos Formation. In the study area, the Jqv unit reaches a maximum thickness of 140 m.

These strata are dark green to brown color andesitic to basaltic porphyritic lavas with abundant vesicles (Figure 4.6.D). Lavas are characterized by plagioclase and pyroxene(?) phenocrysts immersed in an aphanitic brown groundmass. Vesicles are filled by chlorite, calcite, and quartz. Phenocrysts are completely altered to chlorite, epidote, and montmorillonite. Due to its stratigraphic position between the limestone sequences of the Asientos and Pedernales Formations, the age of the Estratos Quebrada Vicuñita unit is constrained between the Calovian and Titonian.

4.1.6 Pedernales Formation [JKp]

Age: Late Jurassic-Early Cretaceous.

Reference: Harrington, 1961.

The Pedernales Formation (JKp) is represented in the study area by a marine sedimentary sequence of limestones and carbonaceous sandstones. At its type locality (Quebrada Asientos, 55 km northwest of La Coipa), this unit includes a 150-300 m thick sequence of green sandstones, and ocoitic and bioclastic limestones (Müller and Perelló, 1982). This unit has been identified at the eastern border of the district, north of the Quebrada Caballo Muerto (Figure 4.6.B). In this region, the JKp unit is conformably overlying the Estratos Quebrada Vicuñita unit.

This unit is represented by alternating grey and light-brown fine-grained limestones. At the visited outcrop, the strata of the JKp unit are strike to the NE and dip between 25° and 10° to the NW. Thickness of this unit is approximately 100 m. This unit is cross-cut by an EW sinistral strik-slip fault that displaces the sequence 250 m. No alteration was identified within this unit. Based on fossil markers, which include several types of *Trigonidae* (Cornejo et al., 1993), the age for the Pedernales Formation is assigned to the Titonian-Valanginian. The Pedernales Formation represents a high-

energy coastal environment, beginning the transition from marine sequences developed during the Jurassic to continental sedimentary sequences developed during the Cretaceous.

4.1.7 Quebrada Monardes Formation [Kqm]

Age: Early Cretaceous.

Reference: Muzzio, 1980.

The Quebrada Monardes Formation (Kqm) is constituted by red sandstones and siltstones. This unit can be found at the eastern (Figure 4.6.B) and western margins of the district. The eastern occurrence, on both sides of the Quebrada Caballo Muerto, is conformably overlying the Pedernales Formation and the Estratos Quebrada Vicuñita unit. The upper contact is limited by the Portezuelo Caballo Muerto thrust fault, putting this unit in contact with the hanging wall represented by the TrJem1 member of the Estratos El Mono unit and by pyroclastic rocks of the La Coipa Group (see below). At the western margin of the study area, the easternmost occurrence of a thick sequence of the Kqm unit (extended in a NS-oriented 35x10 km belt) is observed along the western domain of the Indagua Fault. In the eastern region, strata of this unit strike NE to ENE, dipping 8° to 20° to the NW. Here, a minimum thickness of 100 m is estimated due to the limit with the Portezuelo Caballo Muerto Fault. In turn, the western outcrops present a NW-strike, dipping 30° to the NE.

Mapped during this study in the eastern region, this unit consists of a succession of dark green medium- to coarse-grained sandstones. This unit has no visible hydrothermal alteration. Based on stratigraphic relationships (lower contact with the Pedernales Formation) and fossils (Muñoz, 1984), the maximum age for the Kqm unit is Early Cretaceous. Equivalents of the Kqm unit include the Agua Helada Formation (García, 1967), which crops out to the northwest of the Salar de Pedernales. The Quebrada Monardes Formation marks the end of the marine episode that is represented in the Precordillera in northern Chile. Its rocks have been interpreted as deposited in a coastal environment, with braided rivers and sand dunes (Suárez and Bell, 1985).

4.1.8 Estratos de Cerro Los Carneros

Age: Late Cretaceous-early Paleocene.

Reference: Muñoz, 1982.

A sequence of andesitic lavas interbedded with conglomerates and intruded by andesitic sills is assigned to the Estratos de Cerro Los Carneros unit (Ksecc2, see below). Defined by Muñoz (1982), this unit was described as a succession of three members that from base to top, comprise a lower pyroclastic sequence of rhyolitic tuffs and volcanosedimentary deposits, a middle member of andesitic to basaltic andesite lavas and ocoitic sills, and an upper member of pyroclastic deposits, dacitic lavas and volcanosedimentary agglomerates. In the study area, the middle member is the only one observed. This unit crops out in three domains: in the northwest, southwest and southeast areas of the La Coipa district (Figures 4.2, 4.7.A, E and F). The Ksecc2 unit is unconformably overlying the Quebrada Monardes Formation (southwest domain) and the TrJem3 member of the Estratos El Mono unit (southeast domain). Distribution of the Ksecc2 unit is controlled by the Indagua, Vega La Junta, and Portezuelo Caballo Muerto faults. This unit is intruded by NW-oriented rhyodacitic porphyries and dikes of Eocene age. Subhorizontal strata dominate at the southwestern region, while they are slightly tilted in the eastern and northwestern regions, with dips ranging between 10° to 20° to the northeast and south respectively. In the southwestern region of the study area this unit reaches a maximum thickness of 700 m.

The andesitic lavas of the Ksecc2 member are dark lavas with plagioclase and pyroxene(?) phenocrysts inmersed in a fine-grained greenish groundmass (Figure 4.7.C). In the southern wall of the Quebrada La Coipa, south of the tailings area, a level of conglomerates is characterized by heterolithic (fragments of sedimentary rocks, andesites, intermediate composition intrusive rocks, and limestones) rounded clasts (up to 80 cm), clast-soported, imbricated and with poorly sorted texture (Figure 4.7.D). This unit is altered to chlorite, epidote, carbonates and pumpellyite, minerals that alter the groundmass and phenocrysts and fill vesicles and fractures. The ocoitic andesitic sills (Ksecc2b) intrude the volcanic sequence of the Ksecc2 member at the south-western area of the district

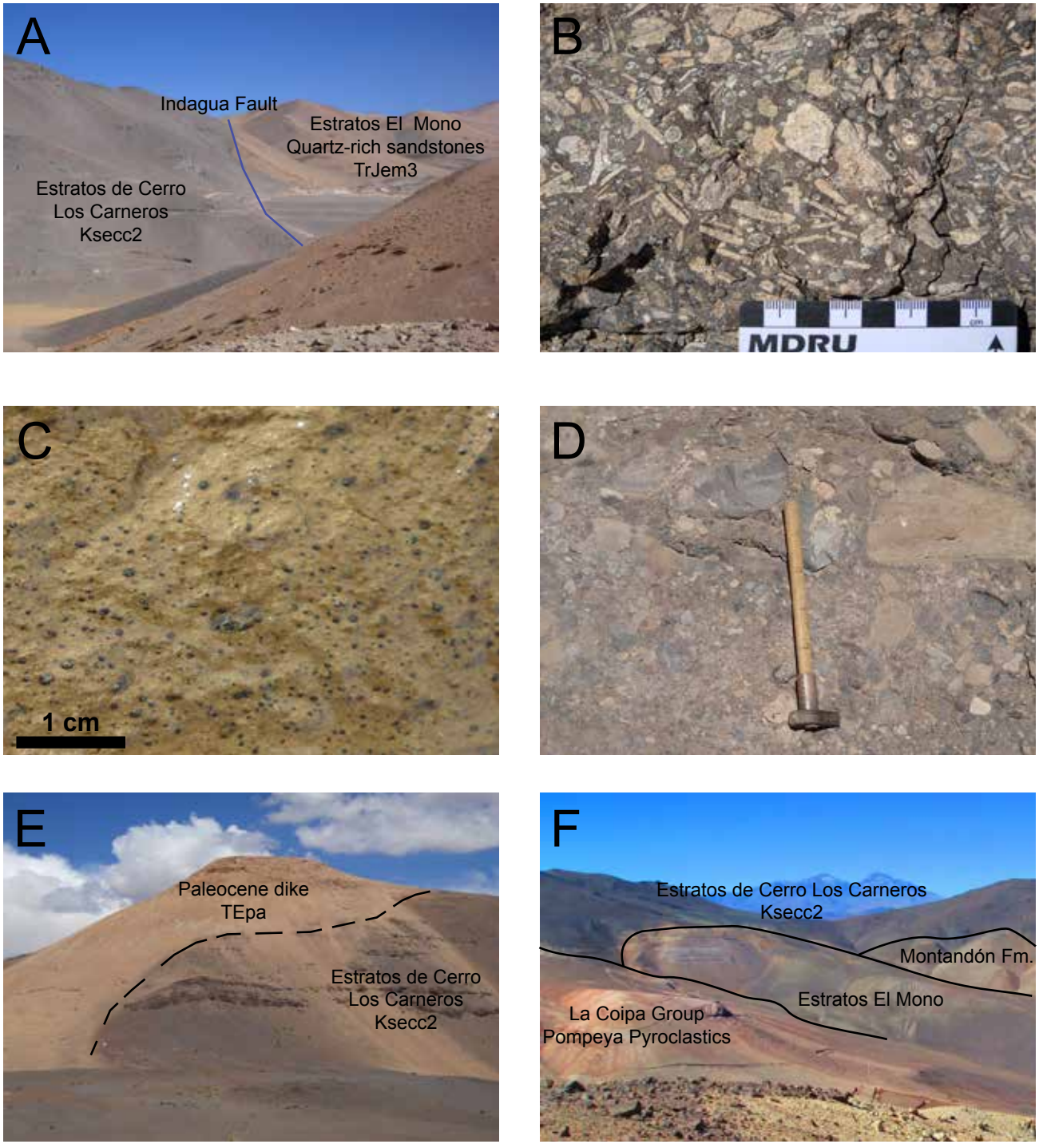

Figure 4.7. Photographs of the Cretaceous rocks: Estratos Cerro Los Carneros (Ksecc2). **(A)** Panoramic view looking north. The western block of the Ksecc2 unit occupies the foot-wall of the Indagua Fault. **(B)** Ocoitic sill (Ksecc2b) with coarse plagioclase phenocrysts. (sample 050213P4). **(C)** Photograph of an andesite sample outcropping to the south of the Quebrada La Coipa (Sample 080113P1). **(D)** Conglomeratic level observed at the Quebrada La Coipa (Sample 050113_P1). **(E)** A Paleocene rhyodacitic sill intruding the Ksecc2 unit, south of the Quebrada La Coipa. **(F)** Panoramic view looking east (south of the Codocedo area), eastern block of the Ksecc2 unit. Photograph taken by Rodolfo Lagos.

(Figure 4.7.B). These sills are characterized by coarse (up to 4 cm) tabular plagioclase phenocrysts. Alteration of groundmass and vesicles is represented by chlorite-phrenite-pumpellyite. Cornejo et al. (1993) published K-Ar ages for the Estratos de Cerro Los Carneros unit ranging between 70 and 65 Ma, establishing a Late Cretaceous formation age that could have extended to the lower Paleocene. This unit can be correlated with the Quebrada Paipote Formation (Mercado, 1982), which crops out in the southern Maricunga belt.

4.1.9 Complejos Intrusivos [KSpa]

Age: Late Cretaceous

Reference: Cornejo et al., 1998.

Represented by andesitic and microdioritic porphyries (KSpa), the Complejos Intrusivos unit crops out at the northwestern margin of the study area (Figure 4.2). In this area, this unit intrudes the volcanic sequence of the Estratos de Cerro Los Carneros (Ksecc2), and is, in turn, intruded by rhyolitic domes (TEdrd) of Eocene age. During this research, outcrops of this unit were not visited and the following description is taken from Cornejo et al. (1998). These authors defined this unit as black to greenish porphyritic sills of andesitic and basaltic-andesitic composition characterized by plagioclase, clinopyroxene, and lesser amphibole or olivine phenocrysts. The basaltic andesitic sills present an aphanitic texture. K-Ar ages obtained on whole rock range between 69 and 75 Ma (Cornejo et al., 1998).

4.1.10 Codocedo Gabbro and Monzodioritic porphyritic dykes and stocks [KTgd]

Age: Late Cretaceous-early Paleocene.

Reference: This study

A group of intrusive rocks consisting of a gabbro (380x220 m) and a series of small dikes and/ or stocks (less than 10 m width) are defined at the present study as the Codocedo Gabbro and Monzodioritic porphyritic dykes and stocks (KTgd) unit (Figure 4.2). The nomenclature is based

on the Intrusives unit defined by Cornejo et al. (1998) for Late Cretaceous-early Paleocene age. These authors defined the Codocedo stock as a monzodioritic rock, but based on the classification of plutonic rocks by De la Roche et al. (1980), a gabbroic composition is interpreted in the present study (see chapter 5.1). This unit can be found in the south-central area of the district, intruding the TrJem2 and TrJem3 members of the Estratos El Mono unit (Figure 4.8.A).

The Codocedo Gabbro consists of a black coarse-grained equigranular holocrystalline unit with plagioclase, pyroxene and biotite crystals. A thin section (sample SG200213_P4) indicates a porphyritic texture with up to 3 mm octahedral pyroxene phenocrysts (10% of the volume rock) standing out from a plagioclase+biotite+pyroxene aggregate (Figure 4.8.B). Weak argillization is present on biotite and plagioclase crystals.

The Monzodioritic dykes and stocks crop out as green-colored porphyritic rocks with plagioclase phenocrysts inmersed in a fine-grained aphanitic groundmass (Figure 4.8.C). Microscopically, the dikes are characterized by porphyritic to cumuloporphyritic textures with pyroxene and plagioclase phenocrysts immersed in a plagioclase-rich crystalline groundmass (Figure 4.8.D). Cornejo et al. (1993) published two K-Ar ages for monzodioritc/gabbroic rocks of this unit that range between 66±1 Ma (biotite) and 64±2 Ma (aggregate of plagioclase and K-feldspar).

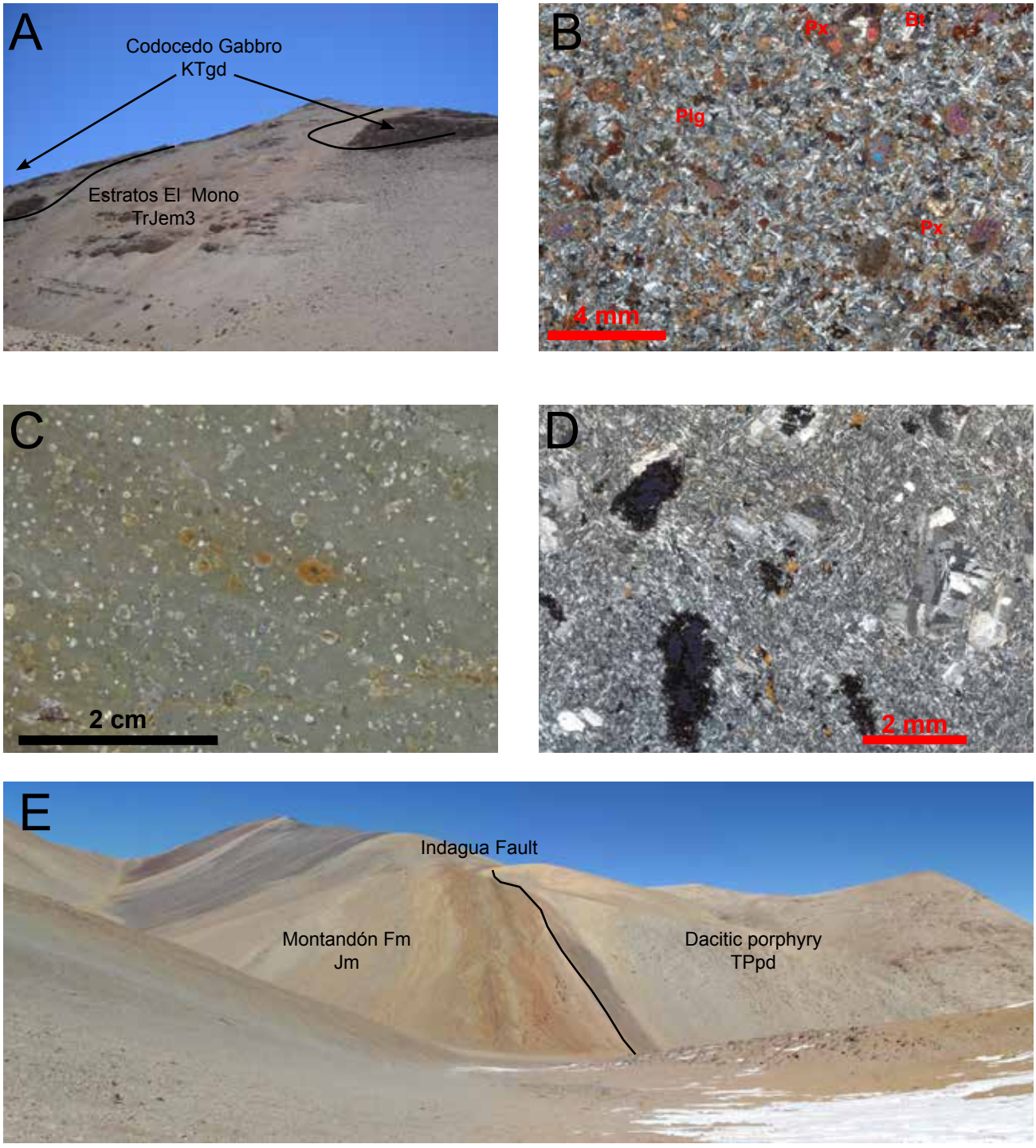

Figure 4.8. Photographs and photomicrographs of the Cretaceous and Paleocene intrusive and hypabyssal rocks. **(A)** Outcrop of the Codocedo Gabbro (KTgd) intruding sedimentary rocks of the Estratos El Mono unit, southern part of the study area. **(B)** Photomicrograph taken under cross-polarized light of the Codocedo Gabbro, sample SG200213_P4. Minerals: Pyroxene (Px), Plagioclase (Plg) and Biotite (Bt) crystals. **(C)** Photograph of the monzodioritic dike (sample SG200213_P8), south of the Codocedo area. **(D)** Photomicrograph taken under cross-polarized light of sample SG200213_P8. Pyroxene phencrysts inmersed in a plagioclase-rich groundmass. **(E)** TPpd dacitic porphyry in contact with the limstones of the Montandón Formation (Jm) through the Indagua Fault (Photgraph taken by Rodolfo Lagos).

4.2 Paleocene-Eocene rocks

Paleocene-Eocene magmatic activity is represented by hypabyssal porphyries and dikes, and pyroclastic and volcaniclastic sequences.

4.2.1 Dacitic Porphyries [TPpd]

Age: Paleocene.

Reference: Cornejo et al., 1998.

Located at the western margin of the La Coipa district (Figures 4.2 and 4.8.E), a porphyritic stock has been assigned to the Dacitic Porphyries unit (TPpd) defined by Cornejo et al. (1998). This stock intrudes red sandstones of the Quebrada Monardes Formation and conglomeratic rocks of the Estratos de Cerro Los Carneros unit. Also, the sinistral strike-slip Indagua Fault puts this unit in contact with limestones of the Montandón Formation.

Not mapped during this study, outcrops of this unit are characterized by grey porphyritic rocks with plagioclase, biotite, hornblende and lesser quartz phenocrysts immersed in an aphanitic groundmass of fine-grained quartz+K-feldspar (Cornejo et al., 1993). This unit is altered to quartz-sericite. Cornejo et al. (1993) obtained a K-Ar biotite age of 64±2 Ma for this unit.

4.2.2 Rhyodacitic Porphyries and Dikes [TEpa] and Rhyolitic Domes [TEdrd]

Age: Eocene.

Reference: Cornejo et al., 1998.

This unit includes a group of felsic porphyries, dikes, and domes that were emplaced during the Eocene. The TEpa unit comprises a porphyritic stock and NW-striking dikes, all of them with rhyodacitic composition. The porphyritic stock is located in the southern area of the La Coipa district (Figure 4.9.B). This stock intruded the TrJem1 and the TrJem3 members of the Estratos El Mono unit. The TEpa stock is characterized by white rocks with porphyritic texture with plagioclase, biotite and

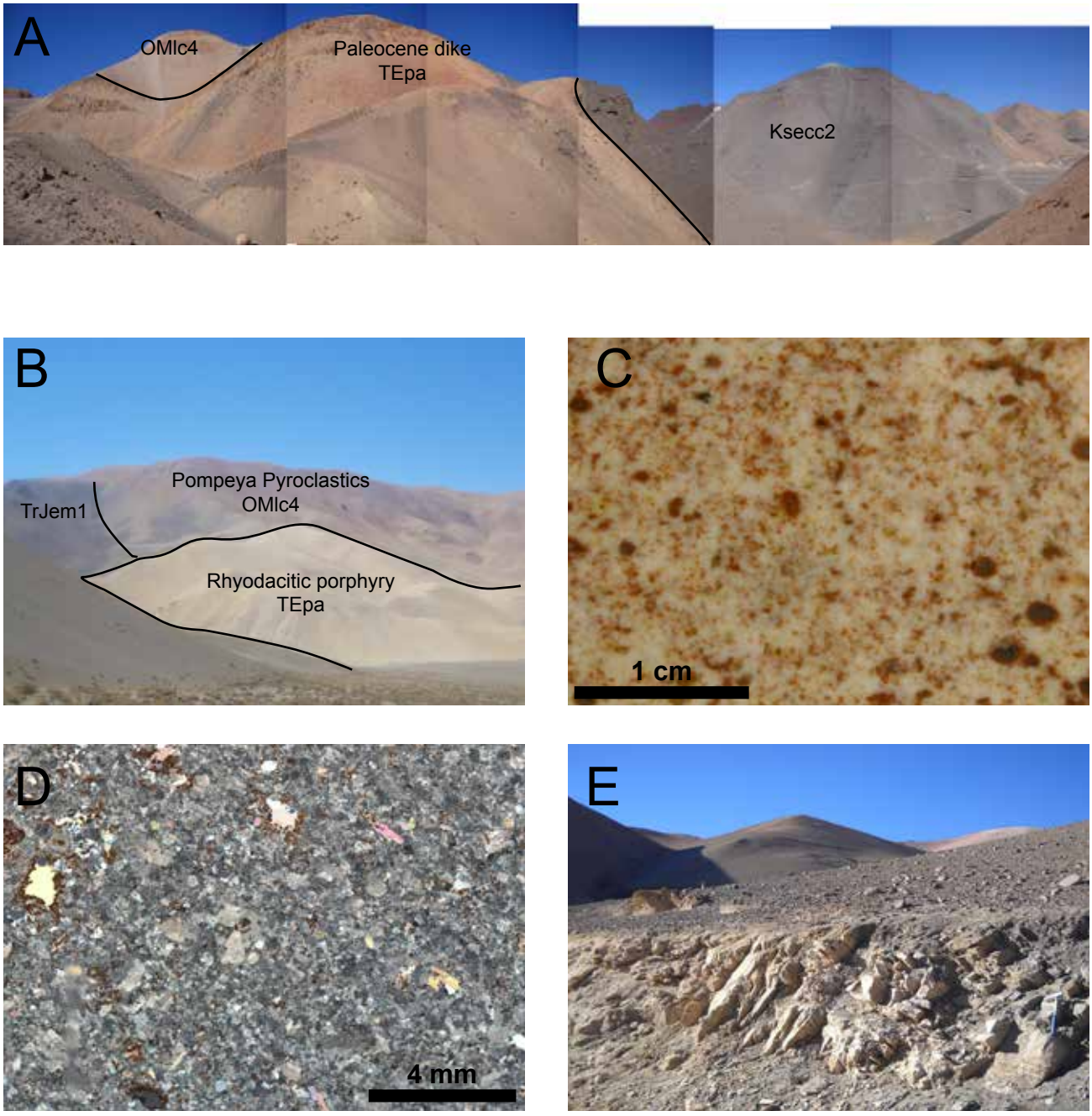

Figure 4.9. Photographs and photomicrographs of the Paleocene/Eocene hypabyssal rocks. **(A)** Panoramic view from south to north (left to right) of the rhyodacitic dike (TEpa) that intrudes the Estratos Cerro Los Carneros unit and is overlain by Miocene volcanic rocks (OMlc4). **(B)** Panoramic view looking north, rhyodacitic porphyry (TEpa) outcropping at the Quebrada La Codocedo area. **(C)** Photograph of a hand sample (SG200213_P10) taken from the rhyodacitic porphyry (4.9.B) **(D)** Photomicrograph taken under cross-polarized light of sample SG200213_P10. **(E)** Stock of a rhyodacitic pophryry outcropping at the Tailings area and intruding the Estratos El Mono Unit. (sample 050313P8).

rounded quartz phenocrysts, the former two being replaced by sericite (Figures 4.9.C and D). These phenocrysts are immersed in a fine-grained groundmass altered pervasively to quartz-sericite. A microscopic characterization of the TEpa unit (samples SG200213_P10 and SG050313_P8) reveals a holocrystalline texture with a felsitic aggregate of equigranular plagioclase, K-feldspar and quartz, and tabular phenocrysts (up to 0.8 mm) of plagioclase and biotite completely replaced to muscovite-sericite-goethite(?). Alteration is represented by sericite-muscovite, quartz, calcite, and albite (the latter being recognized by XRD analysis in sample SG050313_P8).

The NW-striking dikes of the TEpa unit are constituted by a large body (maximum thickness of 170 m) cropping out to the south of the Quebrada La Coipa (Figures 4.2 and 4.9.A), and smaller (up 10 m diameter) dikes that extend north of the Quebrada La Coipa. These dikes cross-cut volcanic rocks of the Estratos de Cerro Los Carneros unit. A small outcrop (200x300 m) of this unit is intruding the TrJem2 member of the Estratos El Mono unit in the tailings area (Figure 4.9.E). Macroscopically and microscopically, these rocks are similar to the porphyritic stock.

The Rhyolitic dome unit (TEdrd) is emplaced along the trace of the Indagua Fault, intruding red sandstones of the Quebrada Monardes Formation and andesites of the Estratos de Cerro Los Carneros unit. The TEdrd dome unit is a white porphyritic and partially banded and aphanitic dome. The porphyritic texture includes fine-grained plagioclase, biotite and quartz phenocrysts, immersed in a devitrified groundmass with relicts of spherulitic texture (Cornejo et al., 1993). Cornejo et al., (1993) interpreted the TEpa and TEdrd units as part of a group of felsic domes, porphyries, dykes and tuffs that were emplaced during the middle to late Eocene (41 to 39 Ma) along faults associated with the Domeyko Fault System.

4.2.3 Volcaniclastic Deposits [TEvd] and Dacitic Ignimbrite [TEdi]

Age: Eocene

Reference: This study

This unit comprises a sequence consisting of a lower member of volcanosedimentary breccias and sandstones and an upper member of a welded dacitic ignimbrite. The volcaniclastic deposits (TEvd) are observed between the Cerro La Coipa and the Quebrada Codocedo, and also in the Purén and Ladera Farellón open pits (Figure 4.2). With the exception of the Purén mine occurrence where this unit is the stratigraphically lowest lithology exposed by mining, the TEvd unit unconformably overlies the TrJem2 member of the Estratos El Mono unit. A 100 m thickness is estimated in the outcropping area south of the Cerro La Coipa.

South of the Cerro La Coipa, the TEvd unit is a semi-consolidated sequence of grey subhorizontal breccias interbedded with layers of coarse-grained sandstones (Figures 4.10.A and B). Breccias are formed by up to 10 cm heterolithic angular clasts (derived from sedimentary rocks, porphyritic domes, and intrusive rocks). In this area, the base of this unit is composed of a 2 m thick clast-supported conglomerate level (Figure 4.10.A). In the Ladera Farellón and Purén pits, the Volcaniclastic Deposits are characterized by grey to yellow fragmental rocks consisting of lapilli to block-size subangular to subrounded hetherolithic fragments (up to 15 cm) derived from older tuffs, porphyritic domes, black shales and sandstones. Sedimentary fragments are more abundant at the bottom of the unit. These rocks are moderately argillized to smectitic minerals (montmorillonite and nontronite).

The Dacitic Ignimbrite (TEdi) does not crop out in the study area. This unit has only been observed in drill core between the Purén, Pompeya, Pompeya Sur, and at the western slope of Cerro La Coipa. A roughly constant thickness of 200 to 250 m is estimated for this unit. In the Purén area, the TEdi unit conformably overlies the TEvd unit. At Pompeya and at the Cerro La Coipa, the Dacitic Ignimbrite unconformably overlies the TrJem2 member of the Estratos El Mono unit. In the Pompeya Sur area, this unit overlies a dacitic porphyritic dome of unknown age.

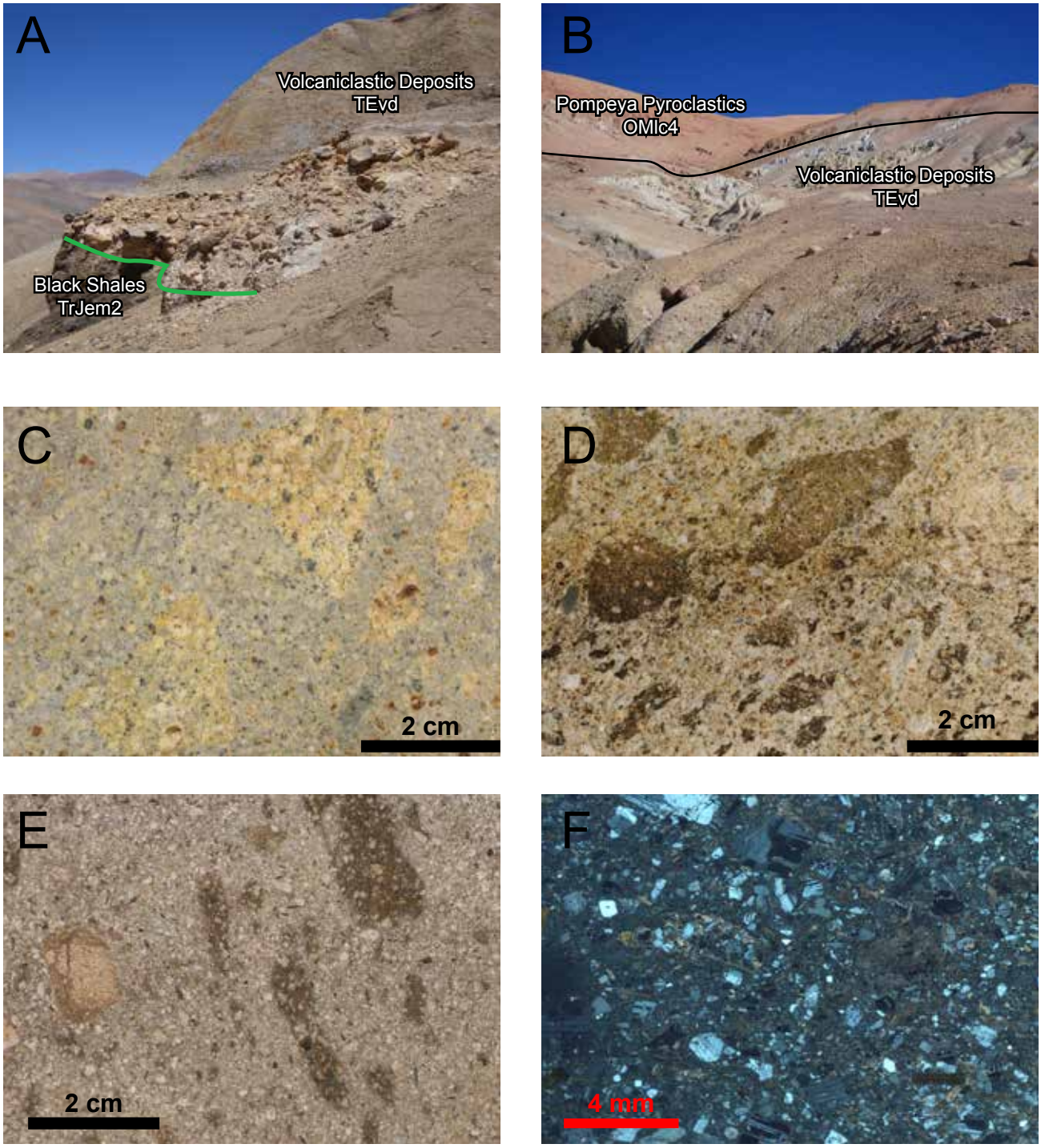

Figure 4.10. Photographs and photomicrographs of the Andesitic ignimbrite and volcaniclastic deposits (TEia and TEvd). **(A)** Unconformity between the underlying Estratos El Mono black shales and a basal conglomeratic level of a volcaniclastic deposit of Eocene age (TEvd), north of the Codocedo Creek. **(B)** TEvd semiconsolidated volcaniclastic deposits underlying pyroclastic rocks of the La Coipa Group. **(C)** Hand sample SG16297, Drill-Hole DPUW-011, 243.52 mts. **(D)** Hand sample SG16280, Drill-Hole PUM-154, 254.1 mts, Purén Phase III. **(E)** Photograph of the andesitic ignimbrite (TEia), sample SG16294, Drill-Hole DPMP-113, 101.75 mts, Pompeya Sur. **(F)** Photomicrograph taken under cross-polarized light of sample SG16294.

The Dacitic Ignimbrite (TEdi) is characterized by eutaxitic texture with lithic and juvenile fragments (20% of the rock volume) and crystals (60% of the rock volume) immersed in an aphanitic groundmass (Figures 4.10.C, D, E, and F). Fragments are represented by juvenile pumice and accessories (rocks from Cretaceous units). Crystals are mostly broken and include plagioclase, biotite, and quartz. Plagioclase and biotite crystals are partially replaced by sericite.

A 37.2±1.2 Ma $^{40}Ar/^{39}Ar$ biotite age obtained for a sample collected in the Pompeya Sur area (sample SG16294, Drill-hole DPMP-113, 101.75 m, see Table 4.2 and appendix A5) revealed the age of the Dacitic Ignimbrite. This age can be considered the minimum age for the Volcaniclastic Deposits (TEvd). On a regional scale, the TEvd unit can be correlated with the volcaniclastic and sedimentary Estratos Cerro El Buitre, defined by Tomlinson et al. (1999) in the Potrerillos area (42 km northwest of La Coipa district). These authors estimated a 38-37 Ma age for this unit. This Eocene age represents a newly recognized volcanic event that was not described in previous studies from La Coipa district.

4.2.4 Estratos de Huidobro [EOh]

Age: Eocene.

Reference: Clavero et al., 2012.

This unit comprises a sedimentary and volcanosedimentary sequence of finely banded carbonaceous siltstones and shales interbedded with ash-tuffs and volcaniclastic breccias and sandstones. This unit crops out in the Purén West and Atenas prospects (Figure 4.2), and is also observed in drill core between Purén Phase II and Purén West. In the Purén area this unit conformably overlies the Dacitic Ignimbrite. At Atenas, the base of this unit has not been observed. Between Purén Phase II and Purén West, the thickness of the Estratos de Huidobro increases to the southeast from ~40 m to ~180 m.

Table 4.2: Summary of $^{40}Ar/^{39}Ar$ ages on biotite obtained in the present study

Sample no	Location	UTM North / UTM East or Drill-Hole	Domain	Plateau Age (Ma) (± 2σ)	Inverse Isochron Age (Ma) (± 2σ)
SG040213_P8	N of Purén West	7039537 475978	Phenocryst	18.67±0.52	18.7±0.82
SG16294	Pompeya Sur	DPMP-113, 101.75m.	Phenocryst	37.2±1.2	37.0±1.2

The Estratos de Huidobro unit can be divided into three members: a lower and an upper member of banded carbonaceous siltstones and shales, both with a thickness of approximately 30 to 40 m, and an intermediate member of volcaniclastic breccias and sandstones with variable thickness. The shales of the lower member are represented by layers of anoxic black shales and layers of grey shales (Figure 4.11.A). The black shales from this unit are generally brecciated. An evaporitic level of massive gypsum has been observed at Purén West and Atenas within the lower member (Figure 4.11.B). This massive gypsum likely represents an evaporate horizon during its deposition. The volcaniclastic breccia of the intermediate member (Figure 4.11.C) is characterized by heterolithic up to 20 cm subangular to subrounded matrix-supported clasts, which occupy a wide range of rock volume (30 to 70%). Fragments are derived from previous breccias, tuffs, porphyritic domes, black shales and fine-grained sediments, presenting a zoning with different relative abundance between them. In general, sedimentary fragments are more abundant at the bottom of the unit. Volcaniclastic sandstones (Figure 4.11.D) are characterized by matrix-supported quartz and plagioclase crystals (replaced by clays) and lithic clasts (mainly from rocks hydrothermally altered to sericite ± quartz). Observed in the upper member, finely-banded carbonaceous siltstones are characterized by greenish and grey rocks that are characterized by alternating irregular bands of coarse- to fine- grained silt-size fragments that in the case of coarse layers are constituted by up to 0.1 mm lithic clasts and angular quartz crystals (Figures 4.11.E and F).

The Estratos de Huidobro unit is affected by syn-sedimentary and secondary brecciation, together with hydrothermal alteration and mineralization. Secondary brecciation includes Miocene Type 2 and Type 3 breccias (see below). Hydrothermal alteration is represented by silicification, argillization (illite, kaolinite, smectite), and locally by alunite.

The Estratos de Huidobro unit was defined by Clavero et al. (2012) in the Cordillera Claudio Gay (38 km southeast of La Coipa). The Estratos de Huidobro unit defined by these authors can be correlated with the Estratos de Llano los Gases Blancos defined by Tomlinson et al. (1999) in the southeastern corner of the Salar de Pedernales. Together with the TEvd and the TEdi units, the Estratos de Huidobro are part of previously unrecognized Eocene rocks at the La Coipa district.

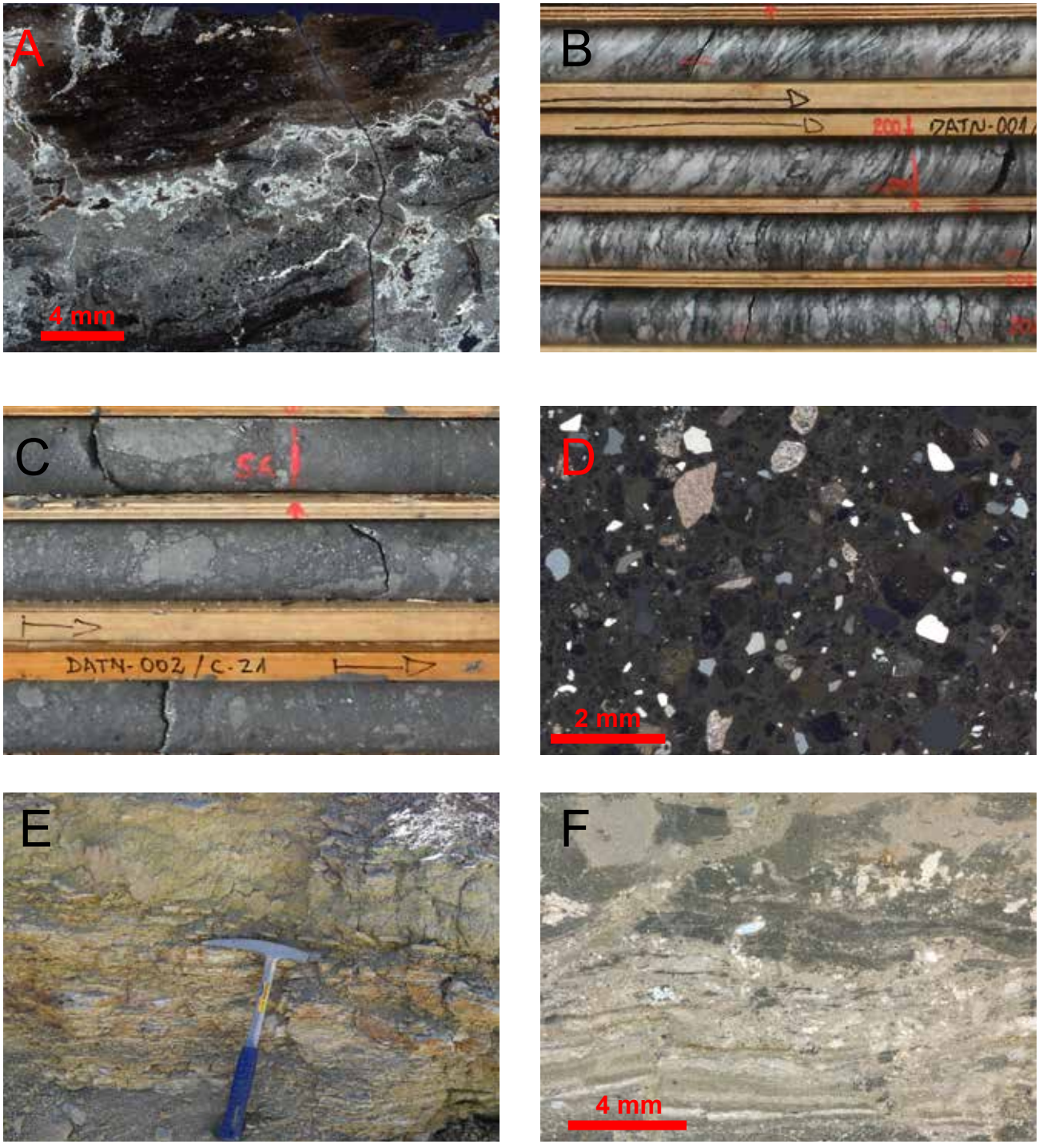

Figure 4.11. Photographs and microphotographs of the Estratos de Huidobro. **(A)** Photomicrograph taken under cross-polarized light of the intensely silicified black shales basal member (sample SG16281, Purén Phase II, drill-hole DPU-06, 163.5 mts). **(B)** Massive level of gypsum developed in the basal member (Atenas prospect, drill-hole DATN-001. 200 m). **(C)** Silicified volcaniclastic breccias from the intermediate member (Atenas prospect, drill-hole DATN-002, 56 m). **(D)** Volcaniclastic sandstones from the intermediate member (Atenas prospect, sample SG13372). **(E)** Outcrop of carbonaceous siltstones (Purén West prospect, sample 040213_P11). **(F)** Photomicrograph taken under cross-polarized light of sample 040213_P11 showing the carbonaceous siltstones with synsedimentary deformation.

4.3 Oligocene-Miocene volcanic arc

The Oligocene-Miocene volcanic stratigraphy at La Coipa can be divided into two major groups defined in this study: the La Coipa Group (24-21 Ma), and the Codocedo Group (21-15 Ma). A series of different types of hydrothermal and phreatomagmatic breccias cut these units and play an important role in mineralizing processes. They will be described in a subsequent section.

4.3.1 La Coipa Group

The La Coipa Group comprises a sequence of volcanic pyroclastic tuffs and hypabyssal domes that constitute the main host-rock unit for mineralization in the La Coipa district. This Group has been divided into the following units:

4.3.1.1 Ladera Tuffs [OMlc1]

The Ladera Tuffs member comprises a pyroclastic sequence that is considered the basal member of the La Coipa Group. It consists of crystal tuffs and fine-grained lapilli tuffs. This member has been recognized in the southern part of the Can Can open pit, in the Ladera Farellón open pit, at the western side of the Ladera Farellón open pit, and to the east of the tailings area (Figure 4.2). The Ladera Tuffs are unconformably overlying the TrJem2 and TrJem3 members of the Estratos El Mono unit. The WNW-striking Ladera Tuffs strata are moderately tilted, dipping 15° to 30° to the SW. A 150 m thickness is estimated from the outcrop exposure southwest of the Ladera Farellón open pit as well as from drill-core intercepts in the Sofía area.

East of the tailings area, the outcrops of this unit are characterized by grey crystal tuffs with plagioclase and biotite crystals immersed in a fine-grained groundmass (Figures 4.12.A and B). These crystal tuffs present less than 5% of lithic clasts (up to 2 cm). South of the Can Can open pit, a road-cut shows a normally graded and poorly sorted lapilli tuff with heterolithic angular lithic blocks

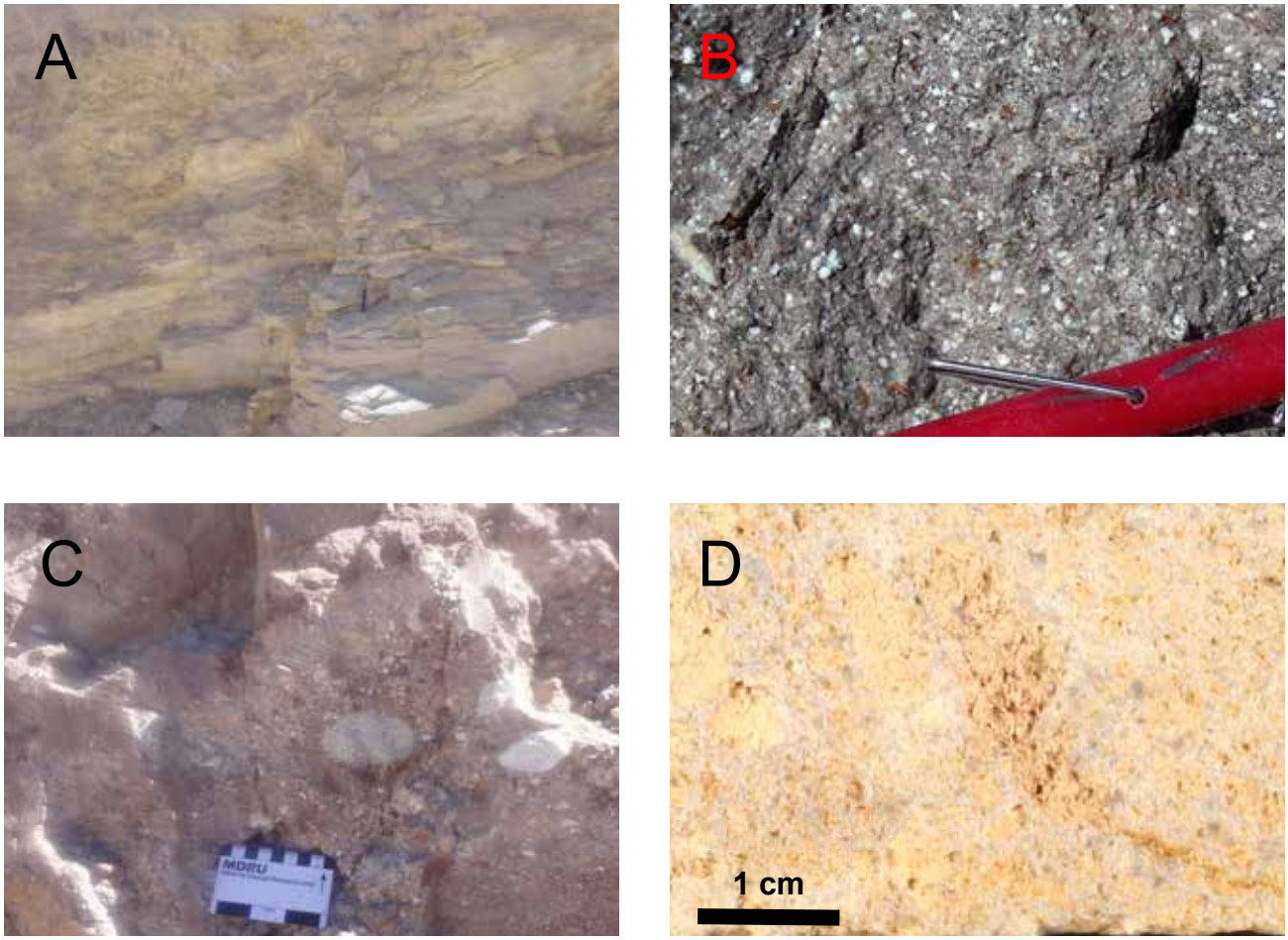

Figure 4.12. Photographs of the Ladera Tuffs (OMlc1) member of the La Coipa Group. **(A)** Outcrop of crystal tuffs of the Ladera Tuffs unit, east of the tailings area. **(B)** Hand sample of crystal tuff taken from the outcrop mentioned in Figure 4.12.A. **(C)** Outcrop of crystal tuffs interbedded with lapilli tuffs, south of the Can Can open pit. **(D)** Crystal tuff altered to alunite+quartz **(**Hand sample SG16253, Ladera Farellón, Drill-hole CUM-006, 11.1 m).

(up to 1 m), which grades upwards to crystal tuffs (Figure 4.12.C). Alteration of this unit depends on the proximity to mineralized centers. In the Can Can area, rocks are argillized and hematitized, whereas, in the Ladera Farellón deposit these rocks are altered to alunite + quartz (Figure 4.12.D). K-Ar biotite ages of 24.7±0.7 Ma and 24.0±1 Ma indicate a late Oligocene age for this unit (Cornejo et al., 1993). The Ladera tuffs are therefore temporally related to the emplacement of the Mina Vieja dacitic domes (OMlc2, see below).

4.3.1.2 Mina Vieja Domes [OMlc2]

This unit has been defined as a group of several subvolcanic to extrusive dacitic domes that are distributed to the south of the Ladera-Farellón open pit (Figure 4.2), with local occurrences in the Brecha Norte open pit. North of the Quebrada La Coipa, a dome belonging to this unit is cross-cutting the Ladera Tuffs. South of the Sofía prospect, a dome characterized by vertical columnar joints is considered the source of a lava-flow level that outflowed to the west. The lava unconformably overlies the TrJem2 member of the Estratos El Mono unit (Figure 4.13.A). Another massive dome characterized by an intense red color gives the name to the Cerro Rojo (Figure 4.13.B). Between the Cerro Rojo and the Sofía prospect, several dome bodies have hydrothermal alteration represented by argillic and advanced argillic phases.

Outcrops of these domes are characterized by porphyritic texture with plagioclase, hornblende, biotite and rounded quartz phenocrysts immersed in a devitrified aphanitic grey groundmass. Petrographically, these domes present porphyritic to cumuloporphyritic texture, with 40% to 60% of the rock volume formed by plagioclase, biotite, hornblende and quartz phenocrysts, immersed in a groundmass formed by microliths and glass (Figures 4.13.C, D, E, and F). Phenocrysts are constituted by plagioclase (20 to 50% of the rock volume, up to 7 mm), biotite (4 to 8% of the rock volume), hornblende (5% to 10% of the rock volume), and rounded quartz (2% to 8% of the rock volume). Groundmass is characterized by plagioclase+hornblende microliths and volcanic glass that in some samples is replaced by devitrification.

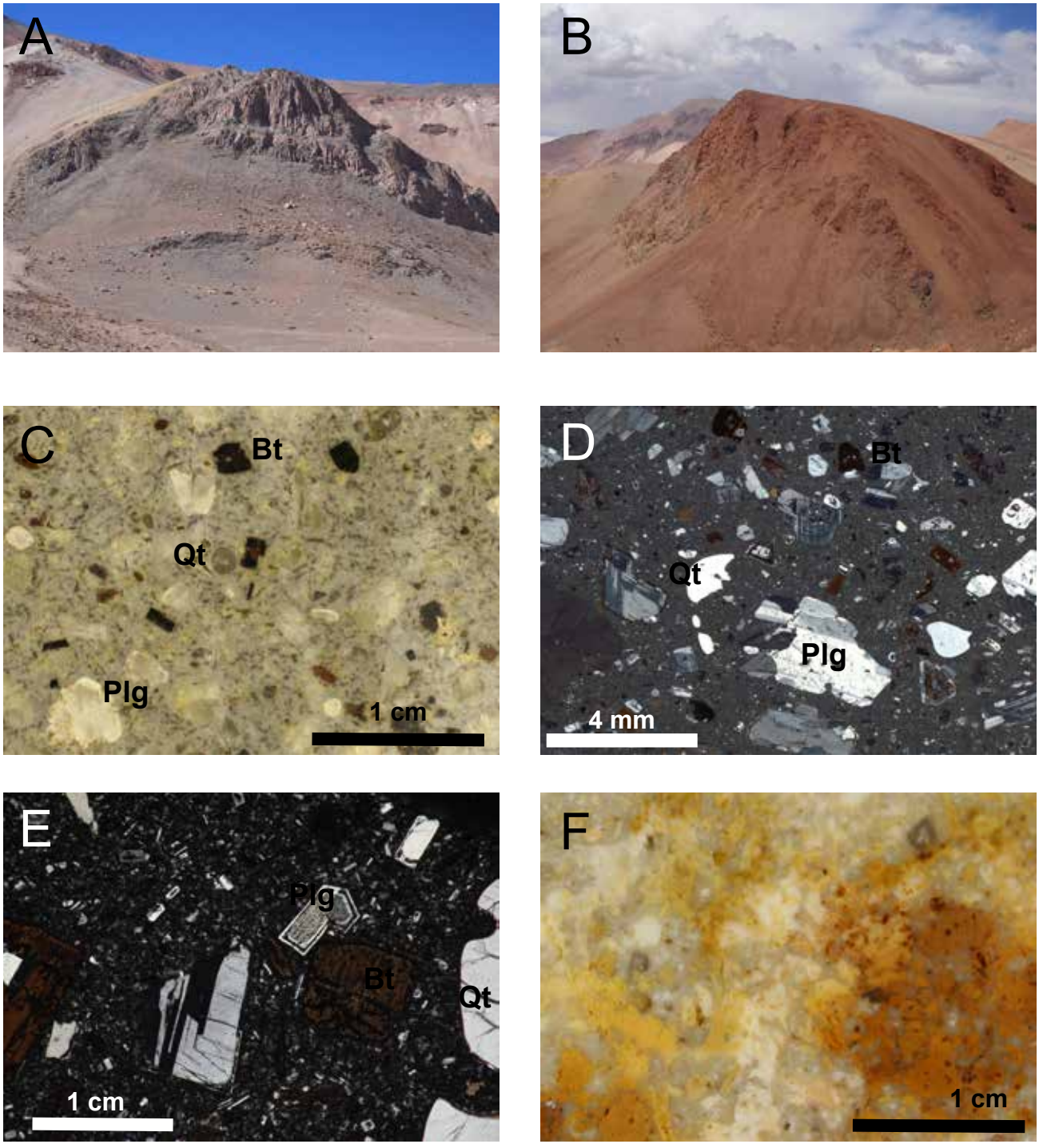

Figure 4.13. Photographs and photomicrographs of the Mina Vieja domes (OMlc2). **(A)** Vertical columnar joints, south of the Sofía prospect (sample SG13351). **(B)** Red colored fresh unit of a dacitic dome at the Cerro Rojo (sample SG190213_P1). **(C)** Porphyritic texture with plagioclase, biotite, and quartz inmersed in an aphanitic groundmass. Photograph of a hand-sample from the outcrop described in Figure 4.13.A. (sample SG13351). **(D)** Photomicrograph taken under cross-polarized light of a dacitic dome at the Cerro Rojo (sample SG190213_P1). Porphyritic to cumuloporphyritic texture with plagioclase phenocrysts inmersed in an aphanitic groundmass. **(E)** Photomicrograph taken under cross-polarized light of sample SG13351. Plagioclase (with reabsorption texture), biotite, and anhedral quartz phenocrysts inmersed in a plagioclase-rich microlithic groundmass. **(F)** Porphyritic dome altered to alunite, dickite, kaolinite, quartz, and jarosite. East of the Cerro Rojo (sample SG050213_P6).
Abbreviations: (Plg) plagioclase, (Bt) biotite, (Qt) quartz.

The Mina Vieja domes are altered to advanced argillic phases (alunite, dickite, kaolinite) and argillic phases (kaolinite, montmorillonite, illite and local chlorite), although there are some plugs with no alteration (Cerro Rojo, Sofía prospect). In some localities, Iron oxides (hematite and goethite) are replacing mafic phenocrysts. Hematite veins are also observed to the north of the Cerro Rojo. South of Mina Vieja; an intense overprint of black manganese oxides characterizes these outcrops.

The age for this unit is based on a zircon CA-ID-TIMS U-Pb date of 23.8±0.04 Ma obtained in this study near the Sofía prospect (sample SG13351, table 4.1, appendix A3), and a previous date of 23.4±0.7 Ma (K-Ar on biotite) obtained from the same place by Sillitoe et al. (1991). According to Cornejo et al. (1993), the emplacement of these domes was favored by the crustal weakness produced by the intersection of the sinistral Indagua Fault and the reverse Vega La Junta Fault (Figure 4.2).

4.3.1.3 Purén Domes [OMlc3]

This unit, defined in the present study, includes dacitic domes that are outcropping at the eastern margin of the district, to the northeast of the Purén Sur area, and below the Pompeya Pyroclastics (see below) unit in the Purén Sur area (Figure 4.2). In the eastern area (north of the Maritza prospect), the Purén Domes are intruding the TrJem1 member of the Estratos El Mono unit (Figure 4.14.A). Here, the hypabyssal unit is thrusted over the Quebrada Monardes Formation by the east-vergent Portezuelo Codocedo Fault.

Outcrops of this unit are characterized by light grey porphyritic rocks with plagioclase, hornblende, biotite, and quartz phenocrysts immersed in a fine-grained groundmass (Figures 4.14.B and C). In surface outcrops, this unit is generally unaltered, while in the Purén Sur drill-cores is intensely altered to alunite+quartz+native sulfur (Figures 4.14.D, E, and F). At microscopic scale, these domes are characterized by porphyritic textures with 60% to 70% phenocrysts of tabular plagioclase (40% of

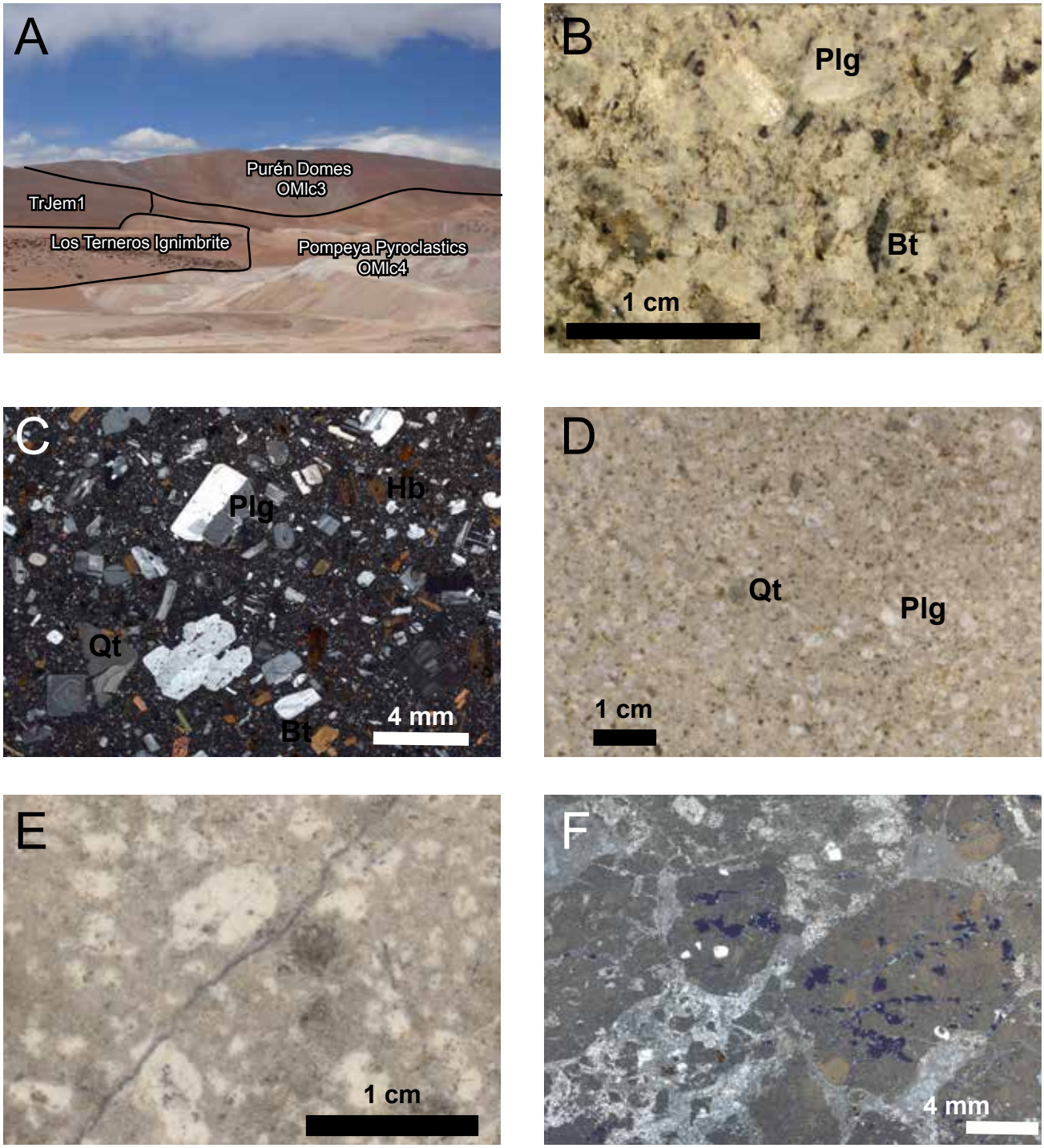

Figure 4.14. Photographs and photomicrographs of the Purén domes (OMlc3). **(A)** Panoramic view looking east of the Purén Domes outcropping at the eastern part of the study area. This unit is intruding the TrJem1 member of the Estratos El Mono unit. **(B)** Photograph of sample SG13366. Porphyritic texture with plagioclase and biotite phenocrysts. **(C)** Photomicrograph taken under cross-polarized light of sample SG13366. Plagioclase, hornblende, biotite, and quartz phenocrysts inmersed in an aphanitic/microlithic groundmass. **(D)** Photograph of a porphyritic dome altered to quartz+alunita and mineralized with fine-grained disseminated pyrite (sample SG16305, drill-hole DPU-243, 547.32 m). **(E)** Enargite+pyrite vein cross-cutting an altered porphyritic (pyrophyllite+dickite+quartz) (sample SG16309, Pompeya prospect, drill-hole DPMP-050, 514.24 m) **(F)** Photomicrograph taken under cross-polarized light of sample SG020213_P7. Autobrecciated porphyritic dome intensely silicified (locally with vuggy quartz texture, as indicated by blue patches within plagioclase phenocrysts) and altered to alunite+kaolinite (Purén Sur prospect). Abbreviations: (Bt) biotite, (Hb) hornblende, (Plg) plagioclase, (Qt) quartz.

total volume, up to 4 mm, polysynthetic and carlsbad twinning), rhombohedric hornblende (15% of the total volume, up to 2mm), tabular and prismatic biotite (7% of the total volume, up to 1 mm), and anhedral quartz (7% of the total volume, up to 3.5 mm, embayment texture). These phenocrysts are immersed in a groundmass comprised of microliths and glass.

A U-Pb zircon age obtained in the Purén Sur area (sample SG16305, Drill-Hole DPU-243, 547.32 m) reveals a 21.98±0.06 Ma age for this unit (Table 4.1, Appendix A3). Similar K-Ar biotite ages of 21.97±0.9 Ma and 22.3±0.9 Ma were obtained by Cornejo et al. (1993) in the eastern part of the study area. Here, these authors mapped this unit as part of the Volcanes Cerros Bravos-Barros Negros unit, widely exposed to the north of the La Coipa district in the Cerros Bravos region.

4.3.1.4 Pompeya Pyroclastics [OMlc4]

The Pompeya Pyroclastics, defined by coarse-grained lapilli tuffs and lesser ash and crystal tuffs, are widely distributed over the district, especially in the eastern and central part of the study area (Figure 4.2), but are confined between the Indagua and Portezuelo Codocedo Faults (Figure 4.2). This sequence unconformably overlies the three members of the Estratos El Mono unit. In the southern area, a paraconformity separates this unit from the underlying Eocene Volcanosedimentary Deposits (TEvd) and andesitic lavas of the Estratos de Cerro Los Carneros (Ksecc2). The Pompeya pyroclastics are also underlain by the Mina Vieja (OMlc2) and Purén Domes (OMlc3). This pyroclastic sequence presents subhorizontal to moderately tilted strata, reaching at the Pompeya prospect dips of 40° to the SW and NW due to a NE-striking syncline that deformed these strata (Figure 4.15.A).

This unit is characterized by a thick sequence (up to 200 m in the eastern margin of the Cerro Amarillo) of weakly welded pyroclastic deposits formed by lithic tuffs interbedded with crystal tuffs. Lithic tuffs contain hetherolithic fragments (20 to 60 % of rock volume) of dacitic domes, fine-grained sedimentary units, granodioritic intrusive rocks and pervasively silicified rocks. Flow-banded ash-

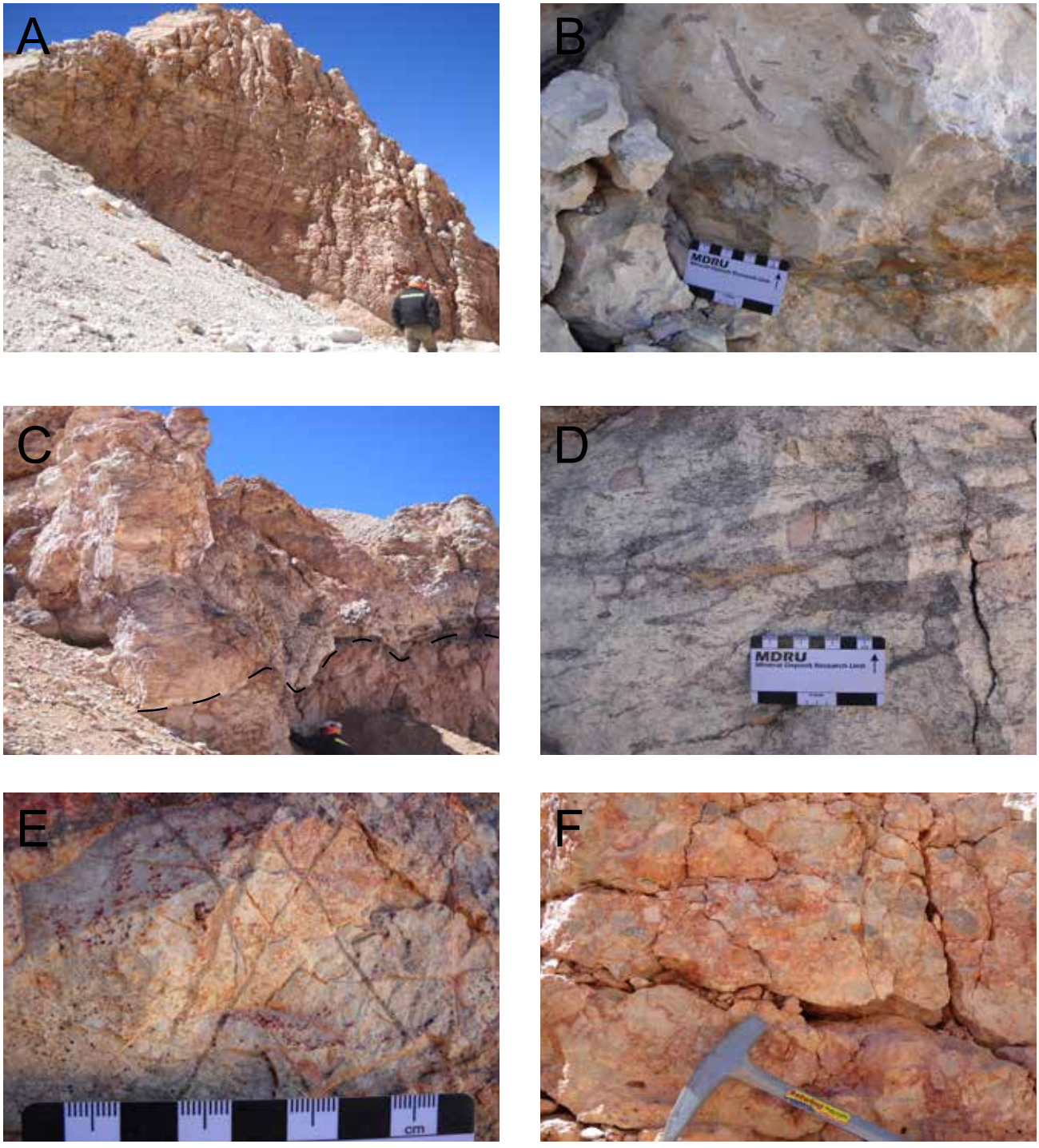

Figure 4.15. Photographs of the Pompeya Pyroclastics unit (OMlc4). **(A)** Lapilli tuffs outcropping at the Pompeya prospect. **(B)** ash-size crystal tuff with dark cylindric fragments of flow-banded juvenile fine-ash rocks. (sample SG070113_P1). **(C)** Two packages of lapilli tuffs separated by a sedimentary horizon of a basal conglomeratic level (dashed line). **(D)** Fiame-bearing ignimbrite overlying the conglomeratic level described on Figure 4.15.C. (sample SG270113_P5). **(E)** Quartz-stockwork fragment observed at the conglomeratic level mentioned in Figures 4.15.C. and D. **(F)** Lapilli tuff intensely altered to quartz+alunite+kaolinite, Purén West prospect.

sized juvenile fragments are observed in the Sofía area prospect (Figure 4.15.B). Lithic clasts have average sizes between 3 and 6 cm, reaching in the Pompeya area sizes up to 60 cm; they are sub-rounded to sub-angular, and generally poorly sorted. In the Purén Sur area, a distinctive 3 to 4 m thick fiamme-bearing monolithic ignimbritic sequence with a 2 m thick basal conglomerate separates two packages of lapilli tuff units (Figure 4.15.C and D). The particularity of this conglomeratic level is its abundance of fragments with veining of crystalline quartz potentially derived from a porphyry related stockwork (Figure 4.15.C and E).

Petrography of the Pompeya Pyroclastics member reveals different grain sizes and compositional types of fragments. Samples SG050213_P5 and SG020213_P1, considered as representatives of the least altered rocks of this unit, are characterized by crystals (60% to 70% of the rock volume) of plagioclase, quartz, and biotite. Lithic fragments (derived from fine-grained quartz-sericite altered rocks and from porphyritic domes) occupy 20% to 30% of the rock volume. The rest (~10% of the rock volume) is constituted by a glassy groundmass. Some samples (SG230113_P6 and SG190213_P16) evidence a higher proportion of lithic fragments (60 to 80% of the volume rock), which are accompanied by 10% to 30% of crystals (quartz and plagioclase) immersed in a glassy groundmass. Different types and intensities of alteration are recognized in the Pompeya Pyroclastics. Hydrothermal alteration varies from advanced argillic phases (alunite + kaolinite; Figure 4.15.F), to steam-heated (opaline silica + alunite), and argillic alteration (montmorillonite + kaolinite ± nontronite). Distal outcrops (in the southern area) have weak argillic alteration.

LA-ICP-MS U-Pb ages on zircon grains obtained during this study established the age of the Pompeya Pyroclastics unit between 21.1±0.5 Ma (sample SG050213_P5, see Appendix A4) and 21.3±0.7 Ma (sample SG190213_P16, see Appendix A4). Previous ages for this unit include two K-Ar biotite ages of 21±1.1 Ma (Cornejo et al., 1993) and 22.5±1.2 Ma (Moscoso et al., 1991).

4.3.2 Codocedo Group

The Codocedo Group is constituted by a sequence of volcaniclastic deposits, dacitic domes, ignimbritic sequences, and base and surge deposits. This group has been divided in the following units:

4.3.2.1 Azufrera Volcaniclastics [Mcd1]

Identified in the central area of the district (Figure 4.2), this unit is formed by volcaniclastic sandstones and ash tuffs. The Azufrera Volcaniclastics unit is distributed in the central and eastern parts of the study area, between the Purén West, Pompeya and Maritza prospects. In the central area, this sequence unconformably overlies the Pompeya Pyroclastics, while distal facies in the eastern area unconformably overly Triassic basement (TrJem3 member). Rocks of the Azufrera volcaniclastics are characterized by subhorizontal stratification. The unit is characterized by a fine-grained banded sequence of ash-size air fall deposits and finely laminated volcaniclastic medium- to fine-grained sandstones (Figures 4.16.A, B, and C). Locally, volcanosedimentary breccias with lapilli sized clasts and a conglomeratic level are observed in the upper part of the Pompeya prospect (Figure 4.16. D).

Thin sections from Pompeya and Purén West reveal that this unit is characterized by layers of ash-size (<2 mm) juvenile, lithics, and crystal grains that in the case of Pompeya, are interbedded with a lapilli-size (<7 mm) juvenile clast-bearing layer. Crystals are formed mainly by angular quartz grains, with lesser argillized plagioclase. Juvenile clasts are represented by welded pumice fragments and lithics that are mostly made-up of quartz-sericite replaced fragments. This unit is mainly altered to advanced argillic and argillic facies (alunite, kaolinite and montmorillonite; Figure 4.16.E).

Age estimates for this unit are based on the stratigraphic control of underlying and overlying units. In the Pompeya area, this unit is overlying the 21 Ma Pompeya Pyroclastics; whereas, in the Purén

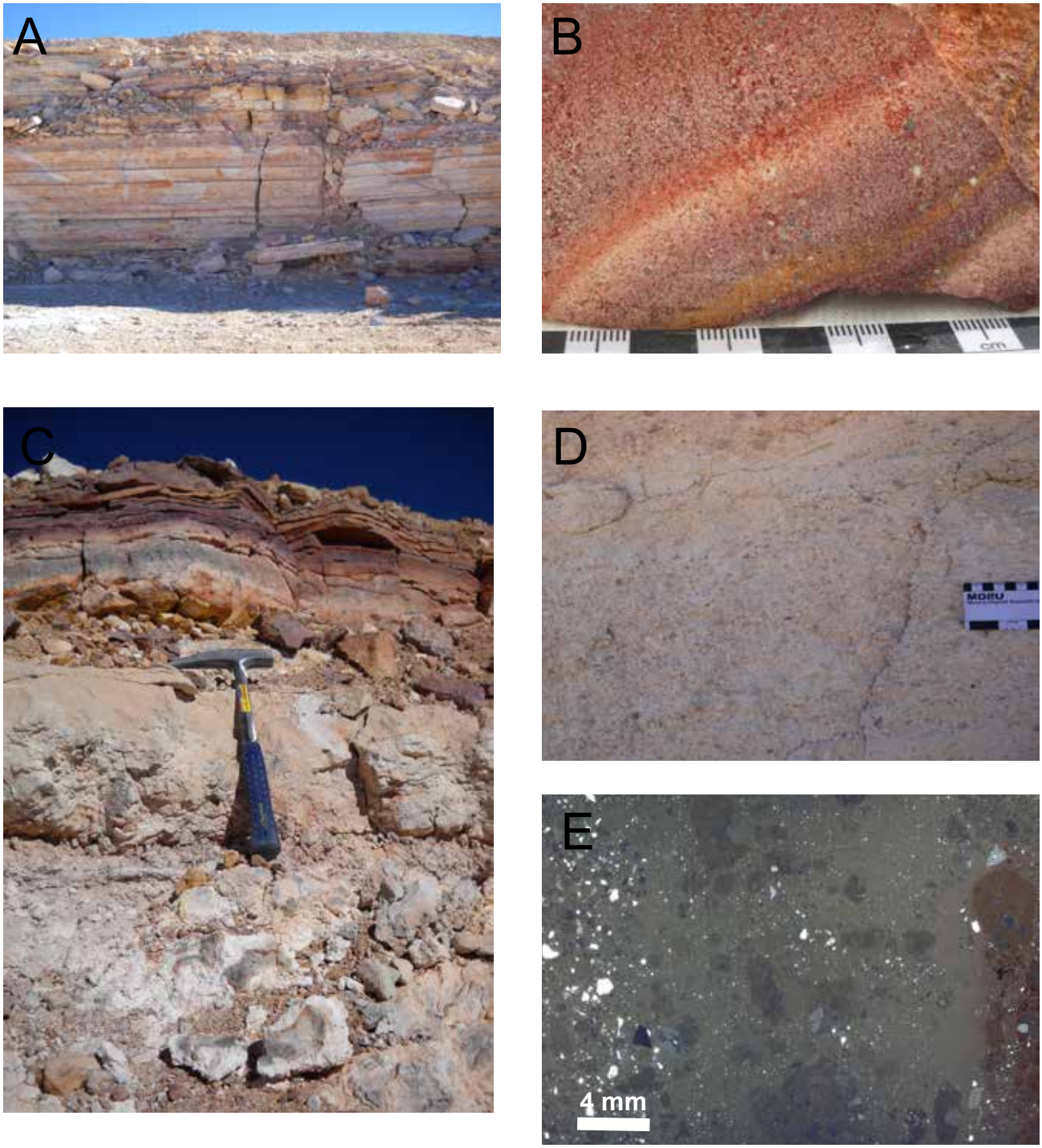

Figure 4.16. Photographs and photomicrographs of the Azufrera volcaniclastics (Mcd1). **(A)** Subhorizontal strata of ash-size air fall deposits, Pompeya prospect. **(B)** Volcaniclastic sandstones constituted by <0.3 mm quartz and plagioclase crystals and lithics of dome units (sample SG090313P5). **(C)** Finely-banded hematitized ash-size tuffs overlying a steam-heated horizon at the Purén Sur prospect. **(D)** Conglomeratic level with steam-heated alteration, Pompeya prospect. **(E)** Photomicrograph taken under cross-polarized light of a banded fine-grained lapilli and crystal tuff altered to kaolinite and alunite (sample 040213_P4).

area, this unit is underlying the Los Terneros Ignimbrite (18.64 Ma, see below), so that a 21 to 19 Ma age is inferred for this unit.

4.3.2.2 Torito Dome [Mcd2]

The Torito Dome corresponds to a dacitic dome that crops out at the Codocedo prospect (Figure 4.2 and 4.17.A). In this area, the Torito Dome intrudes and overlies the Pompeya Pyroclastics. The outcrop of the Torito Dome is characterized by an unaltered red colored porphyritic rock with plagioclase, hornblende, biotite and lesser quartz phenocrysts, which are immersed in a red fine-grained groundmass (Figures 4.17.B). Hornblende and biotite are oxidized to hematite. At microscopic scale, rocks of this unit are characterized by porphyritic texture with tabular euhedral plagioclase (up to 3.2 mm, 60% of the rock volume, carlsbad and polysynthetic twinning), tabular biotite (up to 2 mm, 8% of the rock volume), and rhombohedric hornblende (up to 1 mm, 5% of the rock volume). These phenocrysts are immersed in a fine-grained microlithic groundmass composed of the same mineral species (Figure 4.17.C).

A CA-ID-TIMS U-Pb zircon analysis gave an 18.79±0.08 Ma age for this unit (Sample SG210213_P5, see table 4.1, Appendix A3). Cornejo et al. (1993) obtained a K-Ar whole-rock age of 18.6±1.3 Ma for this dome. Located to the southeast of the Torito dome, the Toro Sal dome was dated by Cornejo et al., (1998) at 19.6±0.9 Ma (K-Ar, biotite) and 17.6±4.3 Ma (K-Ar, hornblende).

4.3.2.3 Los Terneros Ignimbrite [Mcd3]

The Los Terneros Ignimbrite (Mcd3) corresponds to a pyroclastic unit that crops out in the northern part of the district (Figure 4.2 and 4.18.A), overlying the Pompeya Pyroclastics (OMlc4) and Azufrera Volcaniclastics (Mcd1). Subhorizontal stratification characterizes this unit. Outcrops of

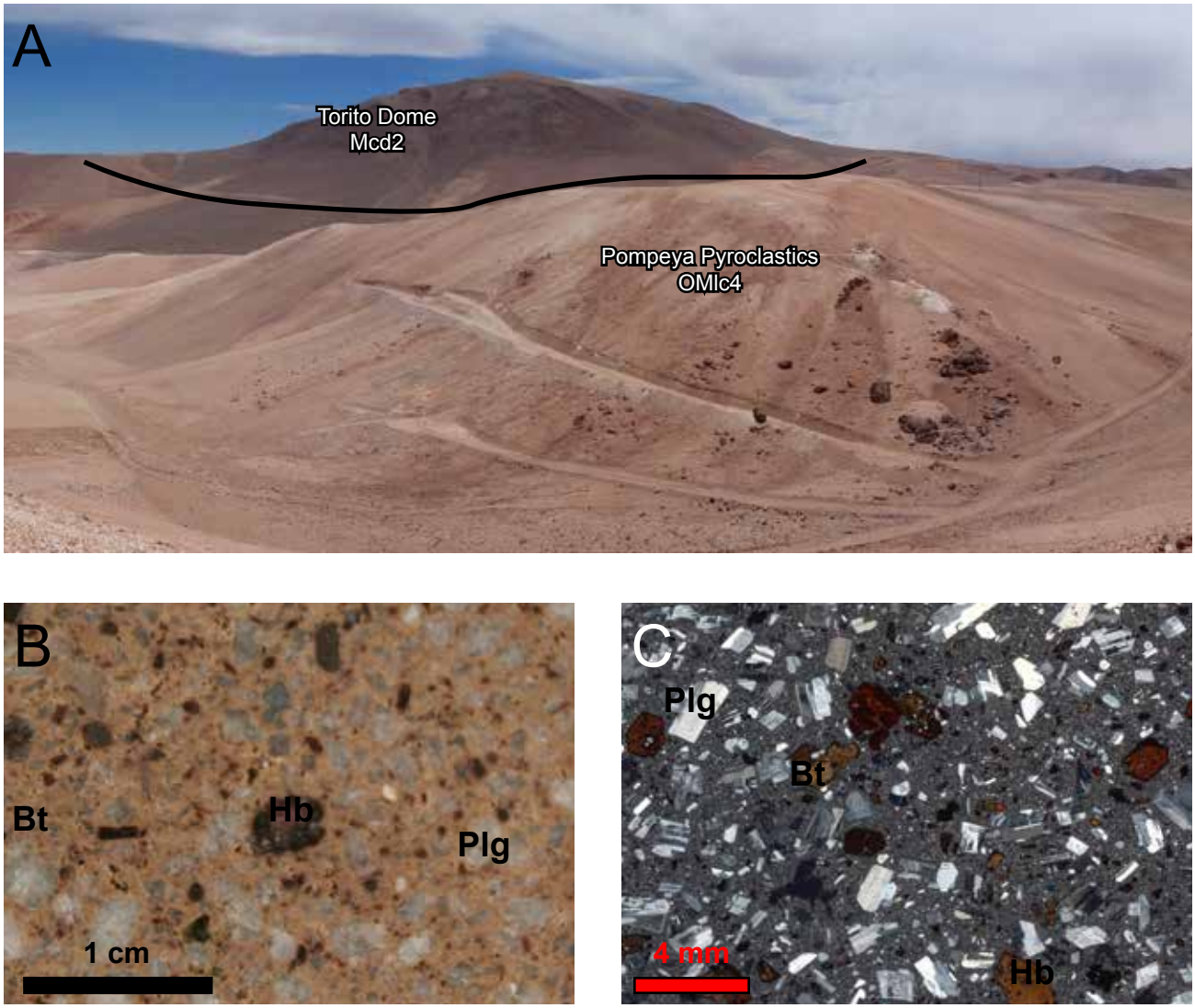

Figure 4.17. Photographs and photomicrographs of the Torito Dome (Mcd2). **(A)** Panoramic view looking east to the Codocedo Area. The Torito dacitic dome is intruding pyroclastic rocks of the Pompeya Pyroclastics unit **(B)** Photograph of sample SG210213_P5, illustrating a porphyritic texture with plagioclase, hornblende, and biotite phenocrysts inmersed in an aphanitic groundmass. **(C)** Photomicrograph taken under cross-polarized light of sample SG210213_P5. Red color hornblende phenocrysts are characterisitc of the Torito Dome unit. Abbreviations: (Bt) biotite, (Hb) hornblende, (Plg) plagioclase.

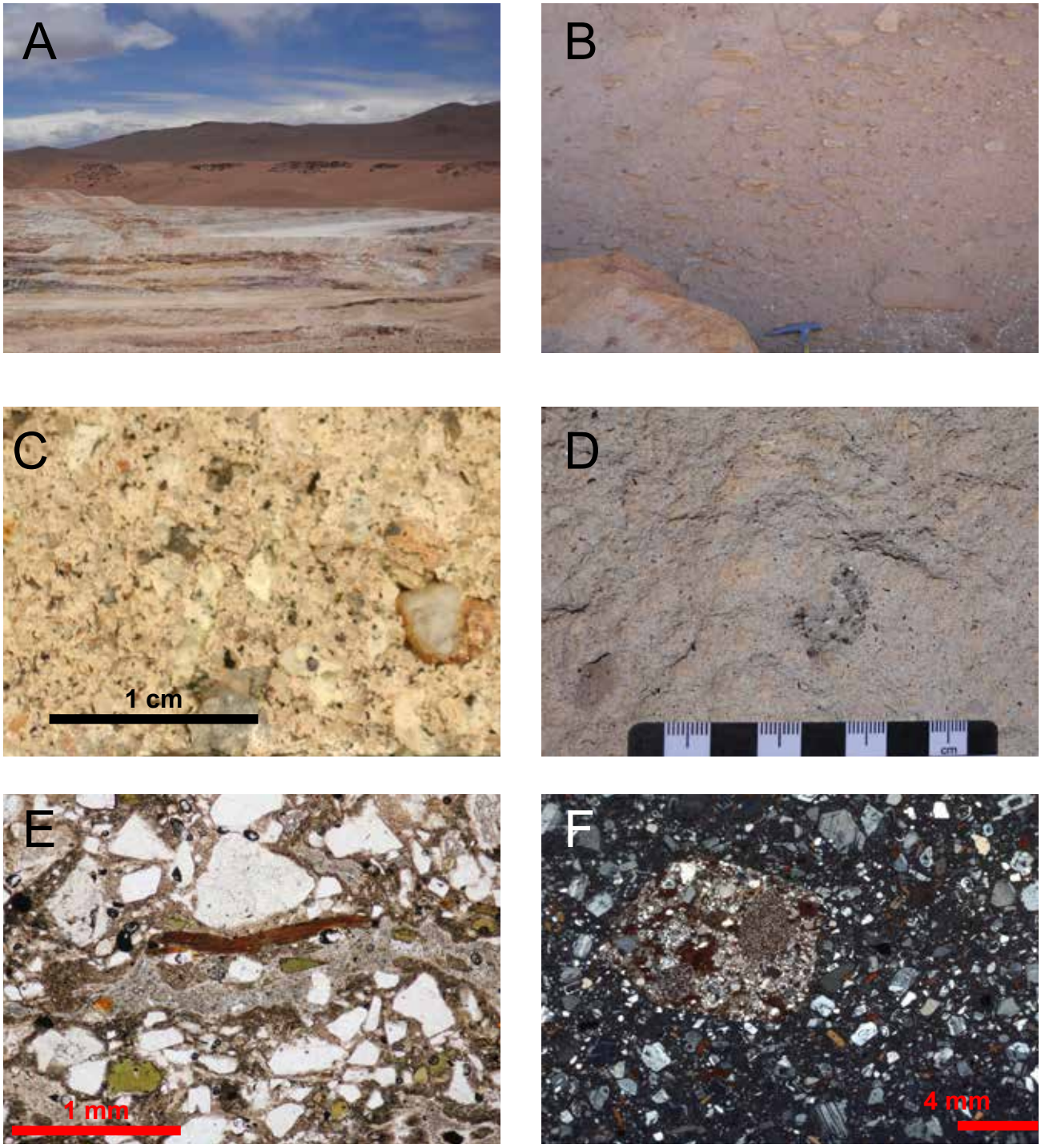

Figure 4.18. Photographs and photomicrographs of the Los Terneros Ignimbrite (Mcd3). **(A)** panoramic view looking east of a pyroclastic ignimbritic sequence, southeast of the Purén Phase II open pit **(B)** Sub-horizontal hetherolithic fragments in a non-welded ignimbritic sequence. **(C)** Photograph of a crystal-rich ignimbritic rock taken from the outcrop described in Figure 4.18.B. (sample SG13369). **(D)** Granodioritic accesory fragment immersed in a non-welded crystal-rich matrix. Purén West prospect, sample SG040213_P8. **(E)** Photomicrograph taken under plane-polarized light showing eutaxitic texture in a plagioclase, hornblende, and biotite crystal phyric rock, together with deformed biotite (sample SG13369). **(F)** Photomicrograph taken under cross-polarized light of a crsytal-rich ignimbrite with plagioclase, biotite, hornblende, and quartz crystals, together with a lithic fragment of an older ignimbritic rock (sample SG040213_P8).

this unit are characterized by non-welded pink pyroclastic deposits with lithics and crystals (Figures 4.18.B, C, and D). Subrounded to subangular fragments (40 to 60% of the rock volume) are largely represented by juvenile pumice clasts and subordinate clasts of granodiorite, porphyritic subvolcanic rocks, pyroclastic rocks, and fine grained-sedimentary rocks.

Thin sections of the Los Terneros Ignimbrite reveal a fragmental texture with lithic and juvenile fragments (20% of the rock volume) and crystals (60% of the rock volume) immersed in a vitric groundmass (Figures 4.18, E and F). Crystals are composed of plagioclase (35% of the rock volume, generally broken, polysynthetic and concentric twinning), hornblende (12% of the rock volume, euhedral to anhedral, green color), biotite (5% of the rock volume, subhedral, with some deformed crystals), and quartz (3% of the rock volume, rounded and resorbed). Lithic fragments are represented by previous pyroclastic rocks, and by microcrystalline aggregates of hydrothermal quartz. Pumice fragments show intense flow texture. Leaving aside the fragments of hydrothermal quartz, the Los Terneros Ignimbrite has no visible hydrothermal alteration. A $^{40}Ar/^{39}Ar$ biotite age of 18.67±0.52 Ma (sample SG040213_P8) obtained in the present study (see Table 4.2 and Appendix A5) confirms a previous K-Ar biotite age of 19.0±1.8 Ma obtained by Cornejo et al. (1993).

4.3.2.4 Vicuñita Domes [Mcd4]

The Vicuñita Domes unit covers the northern and central region of the La Coipa district (Figure 4.2). This unit is formed by dacitic extrusive domes and their respective lateral lava-flows. These domes and flows intrude and cover respectively the La Coipa Group, stratigraphically older rocks of the Codocedo Group, and basement rocks of the Estratos El Mono unit. At the Cerro Los Terneros, a massive outcrop of ~200 m in the vertical extent suggests a vertical conduit that fed a more extensive lateral flow, which according to geological and geophysical evidence includes Cerro La Coipa (Figure 4.19.A and B). In some localities, autobrecciation of marginal facies (carapace-type) indicates the primary borders of these flows (Figure 4.19.C). Even though flow-banding is observed locally (Figure 4.19.D), isotropic textures dominate outcrops of this unit.

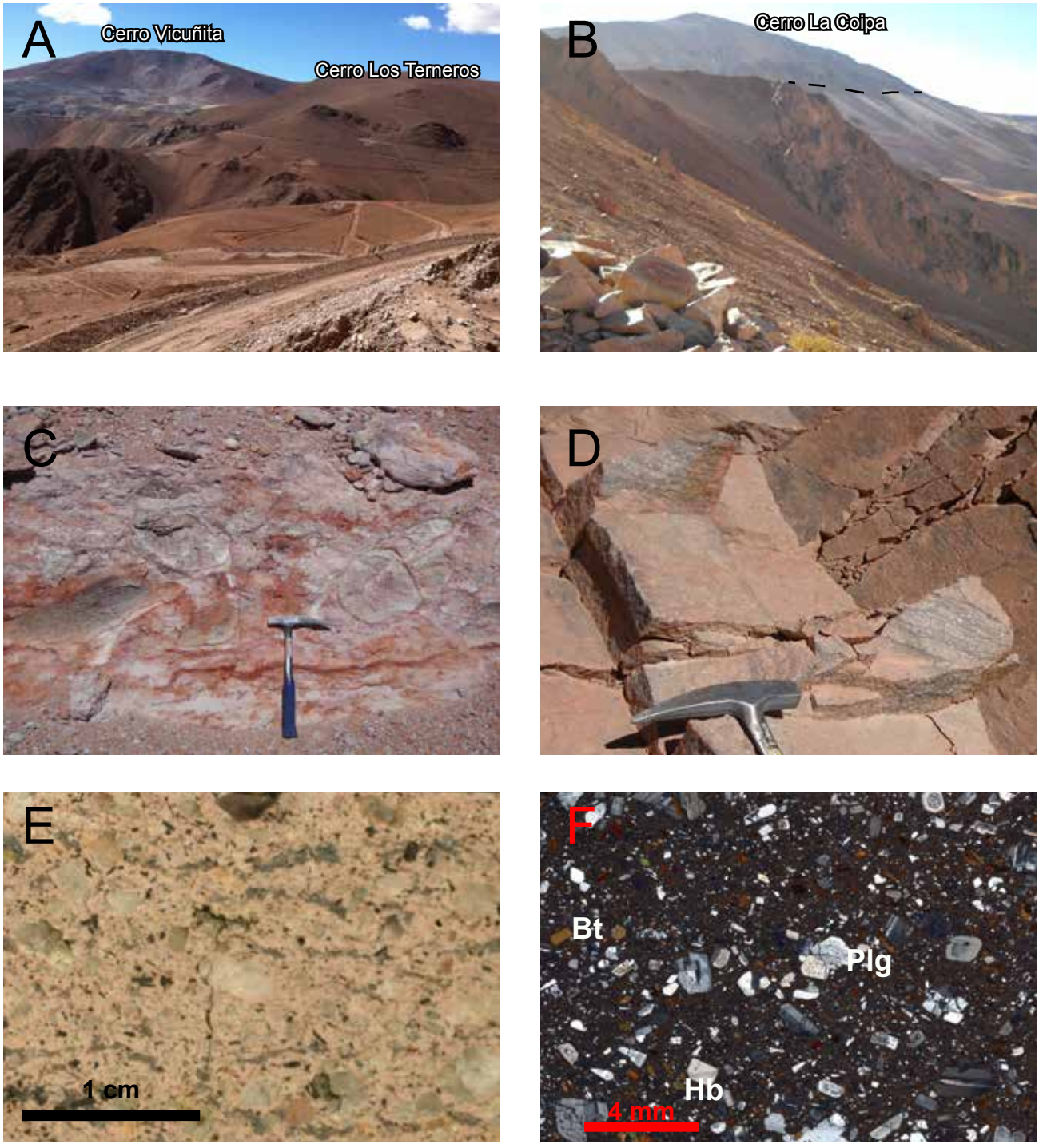

Figure 4.19. Photographs and photomicrographs of the Vicuñita domes (Mcd4). **(A)** Panoramic view looking northwest of two of the main elevations at the La Coipa district: the Cerros Vicuñita and Los Terneros, both formed by dacitic domes of the Mcd4 unit. **(B)** Panoramic view looking southeast of the Cerro La Coipa, peak characterized by a dacitic lava-flow at its top (dashed line). **(C)** Autobrecciation in a margin of a dome outcrop at the Pompeya prospect. **(D)** Flow-bandind of a Vicuñita dome unit observed at the Cerro Los Terneros.| **(E)** Photograph of a pink color porphyritic dome with plagioclase and lesser biotite phenocrysts. (Cerro La Coipa, sample SG13362). **(F)** Photomicrograph taken under cross-polarized light of sample SG13362, showing the plagioclase, biotite, and hornblende inmersed in a glassy groundmass.
Abbreviations: (Bt) biotite, (Hb) hornblende, (Plg) plagioclase.

Outcrops of the Vicuñita Domes are characterized by grey, red, or black porphyritic domes with plagioclase, biotite and hornblende phenocrysts, immersed in an aphanitic and locally devitrified fine-grained groundmass. These domes are porphyritic rocks with phenocrysts of plagioclase, hornblende and biotite, with subordinate quartz, which are immersed in a vitric and microcrystalline ground mass, which in some samples presents a banded texture (Figure 4.19.E, and F). Thin sections of the Vicuñita Domes unit show a porphyritic to cumuloporhyritic texture (at some places with a seriate texture) with 60 to 80% of the rock volume of phenocrysts, including tabular plagioclase (25 to 45% of the rock volume, up to 5 mm, polysynthetic twinning), tabular and prismatic biotite (7 to 15% of the rock volume, up to 2 mm), rhombohedric and prismatic hornblende (3 to 15% of the rock volume, up to 4 mm; Figures 4.20.B to F). Some plagioclase phenocrysts show concentric zonation with reabsorption texture suggesting magma mixing (Figures 4.20.C and D). The phenocrysts are immersed in a microlithic and glassy groundmass. Samples with banded texture show bands with higher content of microlithic quartz and plagioclase crystals alternating with crystal poor bands.

Four CA-ID-TIMS U-Pb zircon ages were obtained in the present study (Figure 4.20.A, Table 4.1, and Appendix A3). Ages of 15.84±0.06 Ma (sample SG13363), 16.00±0.06 Ma (sample SG13358), 16.06±0.05 Ma (sample SG13364), and 16.405±0.056 Ma (sample SG13365) bracket the age of these domes. Previous ages of 16.2±0.8 Ma (K-Ar, biotite), 15.8±0.6 Ma (K-Ar, hornblende), and 15.4±1.4 (K-Ar, biotite), indicated a similar range for this unit (Cornejo et al., 1998). This unit was considered by Cornejo et al. (1993) as part of the Aparatos Volcánicos Centrales unit, defined as a group of volcanic centers that include the Cerros Bravos, La Coipa and Cerro Maricunga centers. These domes are not hydrothermally altered, presenting only subtle weathering. Nevertheless, heterolithic breccias of possible phreatic origin cross-cut this unit at the top of the Cerro La Coipa (see below), suggesting younger events of hydrothermal activity.

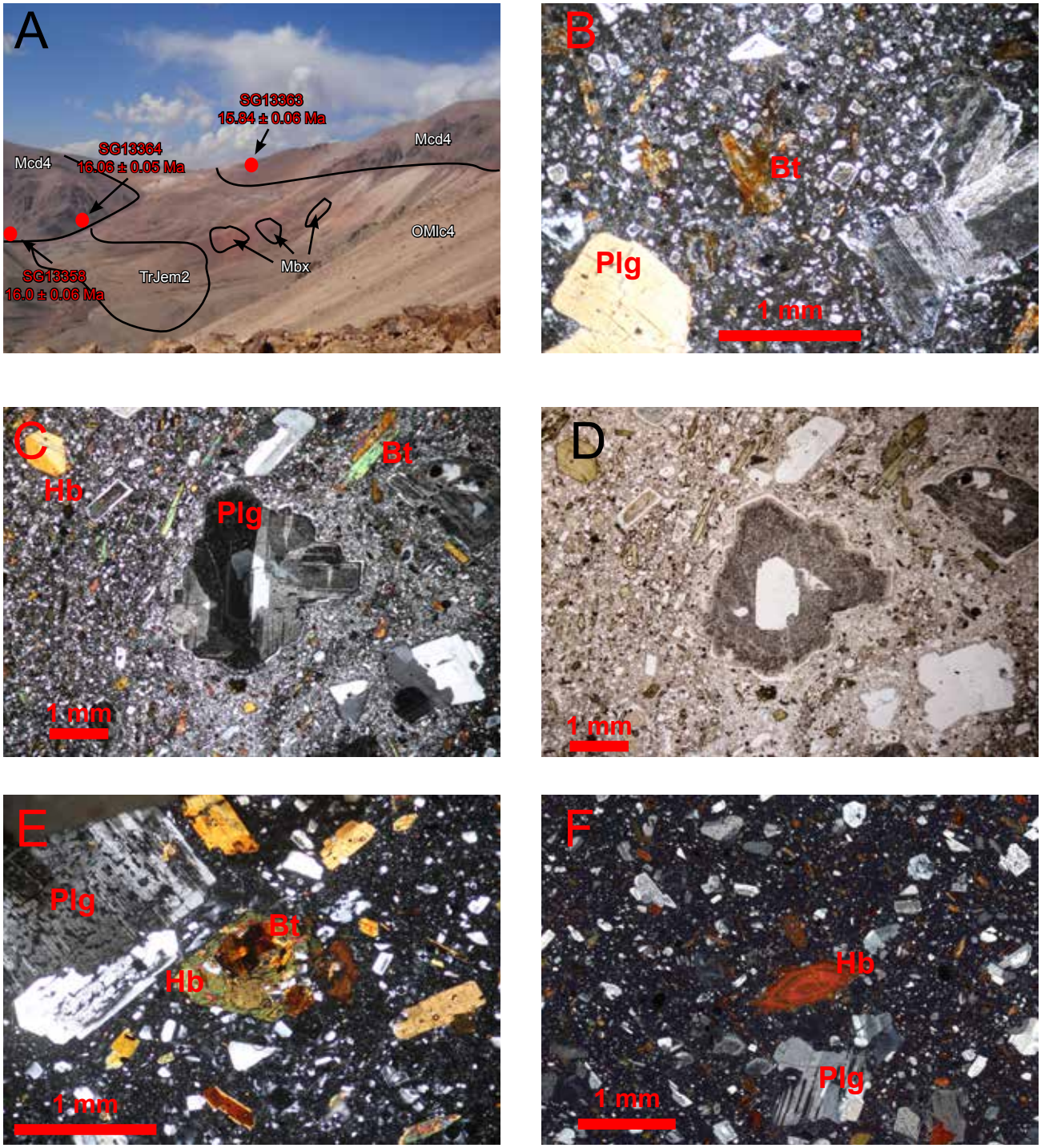

Figure 4.20. Photographs and photomicrographs of the Vicuñita domes (Mcd4). **(A)** Location of three of the four ID-TIMS U/Pb ziron ages obtained for the Vicuñita Domes unit, eastern slope of the Cerro La Coipa and southern slope of the Cerro Los Terneros. **(B)** Photomicrograph taken under cross-polarized light showing a porphyritic texture with plagioclase and biotite phenocrysts inmersed in a plagioclase-bearing microlithic groundmass. (sample SG13364). **(C and D)** Cumuloporphyritic texture on a plagioclase aggregate with concentric reabsorption. Photomicrographs taken under cross-polarized and plane-polarized light respectively (sample SG13358). **(E)** Photomicrograph taken under cross-polarized light of a disequilibrium texture with biotite crystals growing over a hornblende phenocryst (sample SG13365). **(F)** Photomicrograph taken under cross-polarized light illustrating porphyritic texture with plagioclase and hornblende phenocrysts inmersed in a glassy groundmass. In this case, an oxi-hornblende phenocrysts in observed at the center of the image (sample SG13363).
Abbreviations: (Bt) biotite, (Hb) hornblende, (Plg) plagioclase.

4.3.2.5 Hematitized Sandstones and fine-grained Conglomerates [Mcd5]

Distributed in the Pompeya prospect area (Figure 4.2), this unit comprises semi-consolidated strongly hematitized sandstones and conglomerates (Figures 4.21.A to D). This sequence contains lithic clasts and crystals eroded from the Vicuñita Domes. This sequence is characterized by subhorizontal stratification and cross-stratification is observed locally. A maximum age of 16 Ma is given for this unit by the clats derived from the Vicuñita Domes.

4.3.2.6 Diatreme related base and surge deposits [Mcd6]

Located in a road-cut between the Brecha Norte and Purén open pit, an outcrop of semi-consolidated base surge deposits cross-cut by phreatic breccias is interpreted as the upper level of a diatreme volcanic structure (Figure 4.2). Rocks of this unit are characterized by subhorizontally stratified volcanosedimentary deposits of sandstones and breccias (Figure 4.22.A). Levels of cross-stratification are also observed in sandstones (Figure 4.22.B). The source of the fragments and crystals is mostly originated from the Vicuñita domes unit. The Mcd6 unit is displaced by a series of NE-oriented normal faults (Figure 4.22.C) that have a maximum vertical displacement of 2 m. Besides, NNW-oriented Type 4 breccias (see chapter 4.3.3) cross-cut the Mcd6 unit (Figure 4.22.D). No hydrothermal alteration is observed on rocks of the Mcd6 unit.

4.3.3 Breccia units

Multiple styles of breccia units related to hydrothermal, magmatic, and phreatic processes are observed at the La Coipa district, commonly spatially associated with ore deposits. More than one episode of breccia emplacement and intense hydrothermal alteration make mapping of individual breccia types on a district scale impractical. Four types of breccia have been defined and are described below.

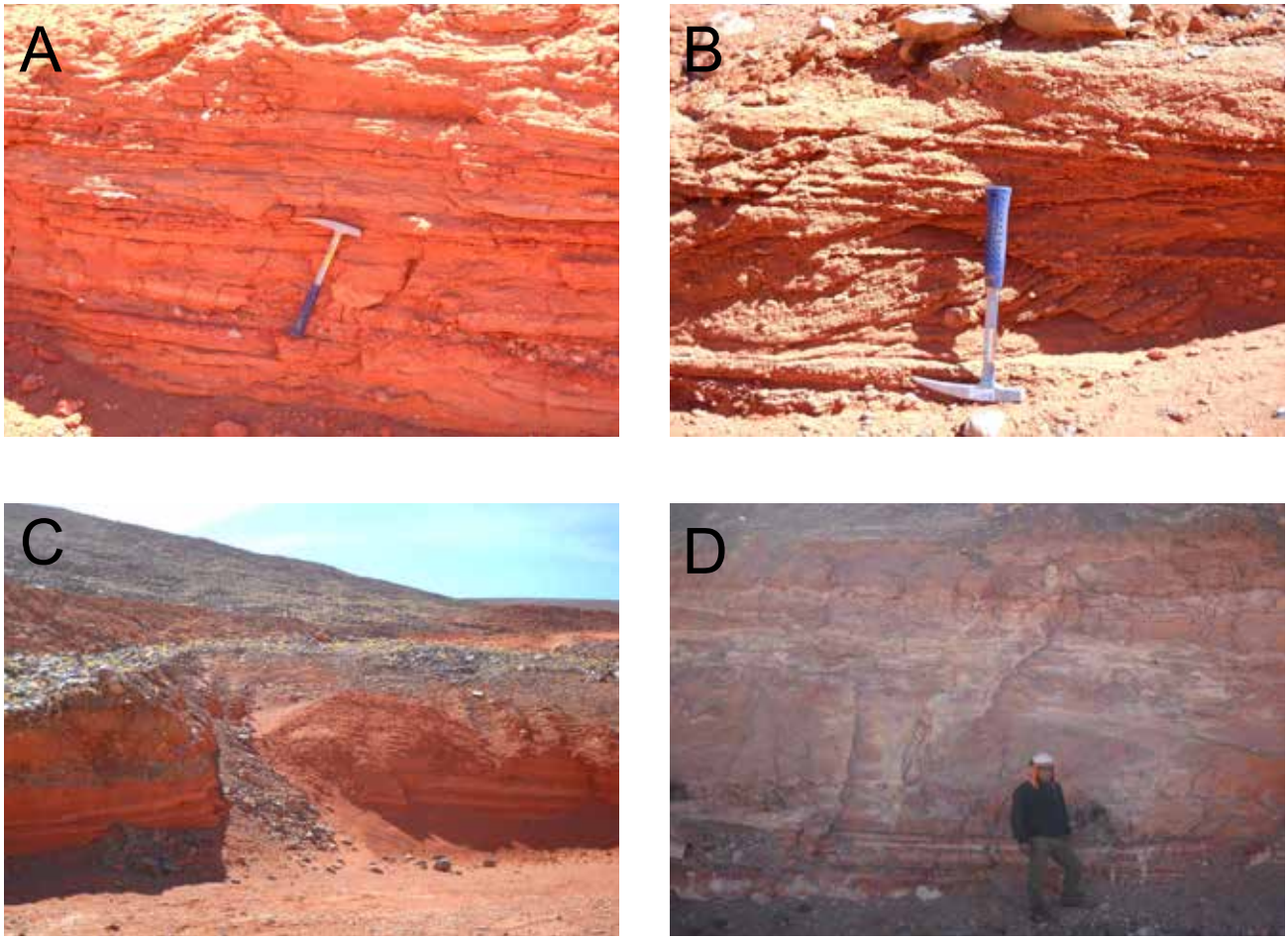

Figure 4.21. Photographs of the Hematitized sandstones and fine-grained conglomerates unit (Mcd5). **(A)** Sub-horizontal strata of semiconsolidated sandstones, Pompeya prospect. **(B)** Cross-stratification of coarse-grained sandstones, Pompeya prospect. **(C)** Semiconsolidated red sandstones at the eastern slope of the Cerro Los Terneros, Pompeya prospect. **(D)** Outcrop of sandstones interbedded with coarse conglomerates with up to 1 m fragments derived from dacitic domes of the Vicuñita Domes unit.

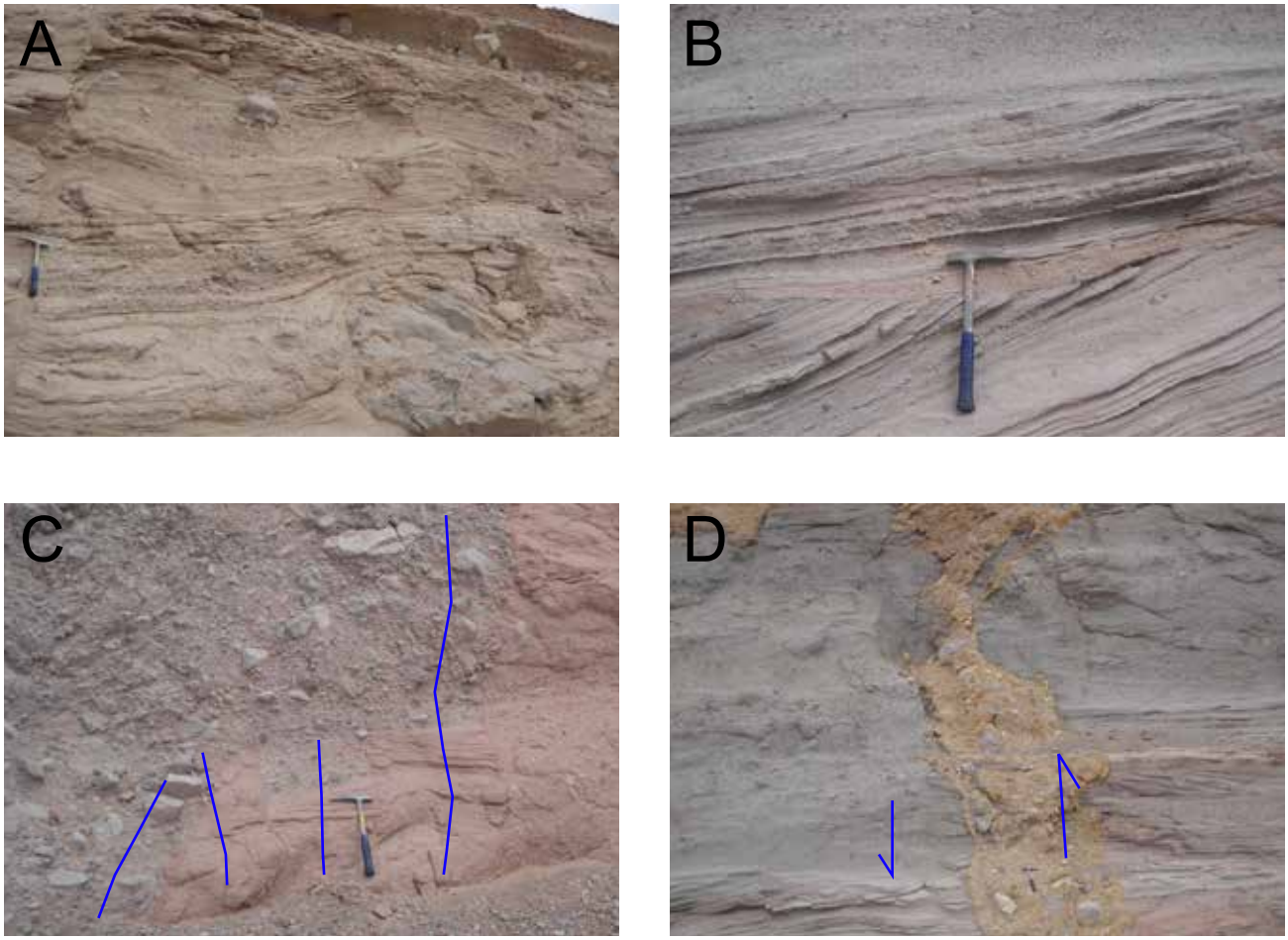

Figure 4.22. Photographs of the Diatreme related base and surge deposits unit (Mcd6). **(A)** Road-cut between the Purén and Brecha Norte open pits showing the stratified sandstones of the Mcd6 unit. **(B)** Cross-stratification. **(C)** Set of NE-oriented normal faults (blue lines) displacing the sandstones of the Mcd6 unit. **(D)** Type 4 breccia cross-cutting the Mcd6 unit. This structure is emplaced along a normal fault plane.

4.3.3.1 Type 1 breccias: Tuffaceous matrix with heterolithic fragments

These breccias are characterized by a tuffaceous matrix that varies from massive to fluidized texture. The matrix also contains plagioclase and quartz crystals. Fragments include juvenile material and wall-rock material. Juvenile fragments are characterized by irregular borders, showing in some cases reabsorption textures. Wall-rock fragments, ranging in size between 2 cm and 1 m, include porphyritic dacitic rocks, fine-grained silicified rock, vuggy quartz mineralized fragments, and black shale fragments. These breccias are matrix- to clast-supported, contain angular to rounded fragments, and are generally poorly sorted and chaotic. Contacts between these breccias and wall rocks are commonly sharp.

This type of breccia is observed in the Can Can open pit, in the Brecha Norte open pit, and in the Pompeya (Figure 4.23.A, B, and and C) and Sofia prospects. In the Can Can open pit, a funnel-shape breccia reached a maximum diameter of 250 m at the pre-mining surface. Type 1 breccias cross-cut basement rocks (Permian Granodiorite (Pzgd), Estratos El Mono (TrJem2), and the Dacitic ignimbrite (TEdi)) and rocks of the Pompeya Pyroclastics member of the La Coipa Group. In the Can Can open pit, Au and Ag mineralization is mostly hosted in this breccia. Type 1 breccias are intensely altered to vuggy quartz and quartz-alunite. According to the breccia texture and composition of matrix and fragments, the Type 1 breccias are interpreted as phreatomagmatic breccias. This type of brecciation occurred before the events of mineralization, acting as a favorable host-rock unit.

4.3.3.2 Type 2 breccias: Quartz+sulfide+alunite cement with heterolithic fragments

These breccias are characterized by pyrite ± enargite-bearing cement that also includes cryptocrystalline quartz ± alunite ± dickite ± barite ± pyrophyllite. Oxidized levels of these breccias are dominated by jarosite ± scorodite. The heterolithic fragments, ranging in size between a few centimeters and up to 2 m, are angular and poorly sorted. These breccias are matrix-to clast-supported. Fragments are from basement rocks such us the Permian Granodiorite, sediments from

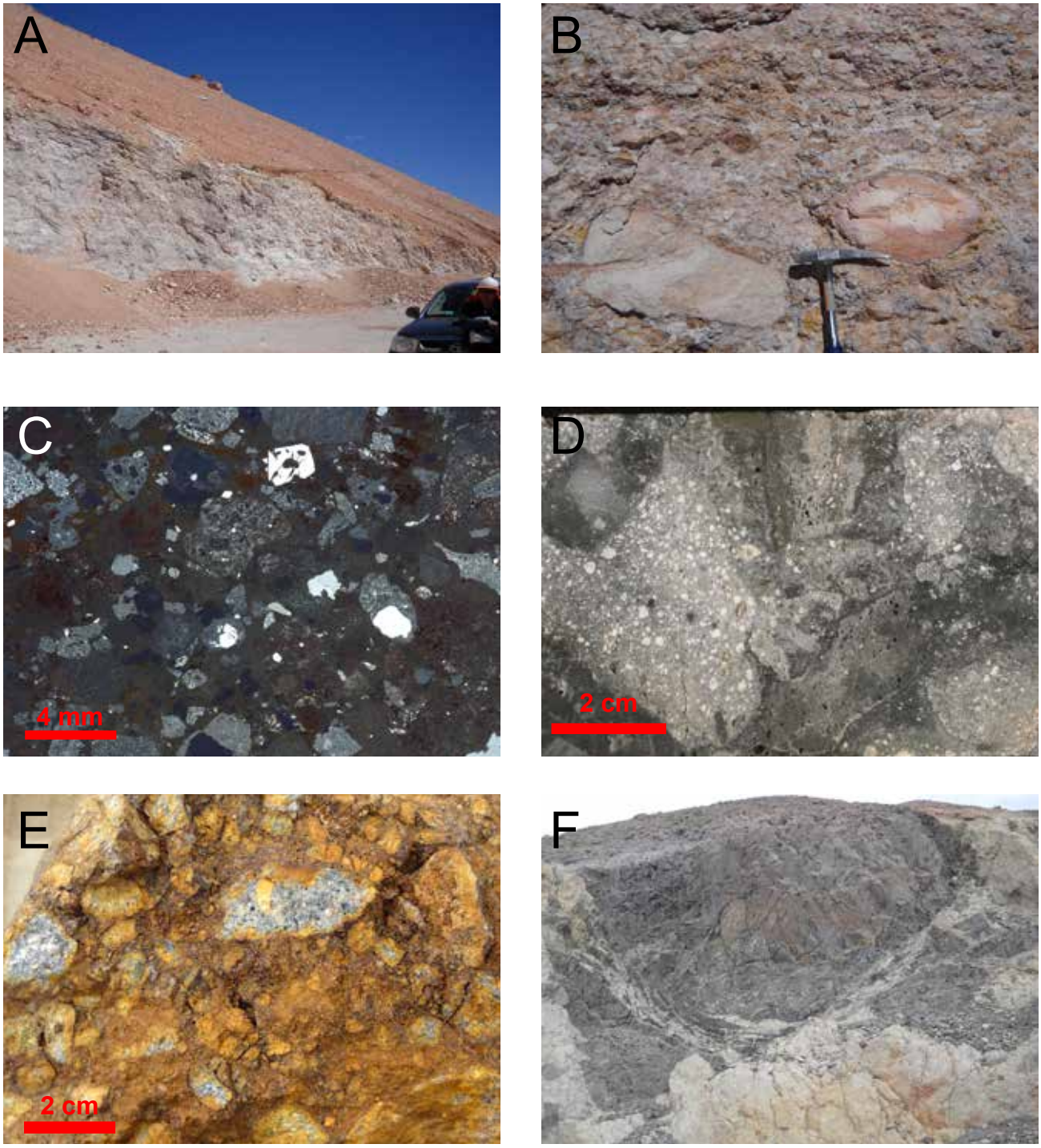

Figure 4.23. Photographs and photomicrographs of the Breccia units. **(A, B, and C)** Type 1 breccia at the Pompeya prospect. Hetherolithic fragments that include mineralized and altered vuggy-quartz clasts. Figure 4.23.C: sample SG240113_P17, photomicrograph taken under cross-polarized light. **(D)** Photograph of a Type 2 breccia characterized by a quartz+pyrite+dickite matrix supporting sub-rounded hetherolithic fragments (Purén Phase III open pit, drill-hole PUM-154, sample SG16286, 138.55 m). **(E)** Type 3 breccia defined by monomictic porphyritic dome sub-rounded fragments of the Mina Vieja Domes unit. Clasts supported by a quartz+iron oxides (hematite+goethite) matrix. **(F)** Type 4 breccia at the top of the cerro La Coipa. In the picture, a metric-scale in-situ brecciated fragment of a porphyritic dome (Vicuñita Domes unit). A hammer at the center of the picture is shown for scale.

the Estratos El Mono unit, and porphyritic domes. Fragments of brecciated massive pyrite±enargite indicate at least two episodes of brecciation in some of these occurrences. Size of breccia conduits are highly variable, ranging from a few centimeters to 80 m diameter at the Purén Phase III deposit (Figure 4.23.D). The fracturing that originated these breccias was favored by the rheologic contrast observed between sedimentary and volcanic rocks. Structurally controlled narrow massive sulfide-bearing feeder dikes (average diameter <10cm) hosted in sedimentary rocks change to Type 2 breccias at the contact with Tertiary volcanics. Due to the sulfide content, these breccias are highly mineralized.

Type 2 breccias are observed in different deposits, such as Coipa Norte, Can Can, Pompeya, Brecha Norte, Purén Phase I, II, and III. They crosscut basement rocks and volcanic rocks of the La Coipa Group. Most of these breccias are hosted by Type 1 breccias. Based on composition of matrix and fragments, and their spatial and temporal relationship with mineralization, the Type 2 breccias are interpreted as magmatic-hydrothermal breccias.

4.3.3.3 Type 3 breccias: Iron oxide+quartz matrix with monolithic to heterolithic fragments

The Type 3 breccias comprise several centimetric to metric scale bodies that crop out throughout the district with different types of fragments. The common feature for these breccias is the predominance of iron oxides (hematite or goethite) and quartz cementing the matrix. A variety of fragments ranging from monolithic to hetherolithic types are included in this group. In the Sofía prospect, a monolithic breccia with subrounded clasts of the Mina Vieja Domes (Figure 4.23.E) crops out intruding the Black shales member of the Estratos El Mono unit. Diameter of these breccia bodies varies from a few centimeters to up to 100 m. Contacts with wall rocks are not sharp.

These breccias cross-cut different lithologies, including basement rocks (black shales, and dacitic ignimbrites from the TEvd unit) and Tertiary volcanic units such as the Mina Vieja domes and the Pompeya Pyroclastics. No mineralization is observed in these breccias. The composition of the matrix and the origin of fragments, with absence of juvenile fragments, indicate a phreatomagmatic origin for Type 4 breccias.

4.3.3.4 Type 4 breccias: Rock flour matrix and heterolithic fragments

The type 4 of breccias comprises hetherolithic fragments that are immersed in a rock flour matrix characterized by fine sand-size angular lithic fragments and quartz, plagioclase, and lesser biotite crystals. Fragments range in size between 0.1 mm and 2 m. They are subrounded to subangular, poorly sorted, chaotic and matrix-supported. These fragments comprise hydrothermally altered rocks (quartz aggregates, sericite-quartz altered rocks, quartz-alunite altered rocks, welded tuffs, porphyritic domes, and metasandstones). Crystals are dominated by angular quartz (up to 1.5 mm). This type of breccia has only been observed at surface, at the top of the Cerro La Coipa and in a road-cut between the Puren and Brecha Norte open pits (Figure 4.2).At the top of the Cerro la Coipa, two bodies of Type 4 breccias cross-cut the 16 Ma Vicuñita Domes (Figure 4.23.F). The diameter of these breccias ranges between 100 to 200 m. Type 4 breccias in the road-cut between Purén and Brecha Norte are formed by up to 2 m NW-oriented breccia-dikes that cross-cut the diatreme related base and surge unit (Mcd6).

At both sites, brecciated rocks are altered to clay minerals (smectite, nontronite, illite, and kaolinite). Fragments altered to advanced argillic minerals are locally observed. These breccias, at least in the Cerro La Coipa, locally contain elevated Au due to the presence of hydrothermally altered clasts. Type 4 breccias are considered the youngest event of brecciation, and according to cross-cutting relationships, a maximum age of 16 Ma is estimated for this unit. The Type 4 breccias are interpreted as phreatic breccias based on their spatial distribution, composition of matrix and fragments.

4.4 Structural setting

Structures observed at La Coipa district comprise major regional faults and local faults. Local faults are divided into subsidiary faults parallel to major faults and nearly orthogonal transfer faults. Folding is observed in rocks of the Triassic Estratos El Mono Unit.

The Oligocene-Miocene volcanic La Coipa and Codocedo groups, which host most of the mineralization in the La Coipa district, are mostly underlain by sedimentary rocks of the Estratos El Mono Unit. The Estratos El Mono unit, as well as the Oligocene-Miocene volcanic rocks, is bounded by major faults that in the central and northern part of the district, on a plan-view, show a V-shape geometry, limited to the west by the Indagua Fault, and to the east by the Portezuelo Codocedo Fault (Figure 4.2). In the southern part of the study area, a more N to NNE orientation of these faults (in the western margin the Indagua Fault merges with the Vega La Junta Fault) coincides with the regional orientation of high-angle reverse faults that control the distribution of Paleozoic basement outcrops along the Maricunga belt (Mercado, 1982).

The Indagua Fault, located at the western margin of the district, is part of a NW-striking left-lateral and high-angle reverse system of faults that was active between 42 and 39 Ma (Cornejo et al., 1993). The trace of the Indagua Fault has a length of 30 km, with its southern tail ending at the Quebrada La Coipa. According to Cornejo et al. (1993), the lateral displacement was larger than the vertical movement (the maximum vertical displacement was around 500 m, compared with a maximum left-lateral displacement of 3.5 km). Abels and Bischoff (1999) determined that the vertical displacement was younger than the left-lateral displacement. In the study area, the west-vergent Indagua Fault puts the TrJem3 member of the Estratos El Mono unit in the hanging-wall domain in contact with younger Mesozoic rocks of the Montandón Formation and the Estratos de Cerro Los Carneros unit in the foot-wall domain. Abels and Bischoff (1999) suggested that these NW-oriented faults used pre-Andean mid-to-deep crustal level structural weakness zones, which according to the paleotectonic reconstruction of the South American continent, correspond to the orientation of marine

and continental rift basins developed during the Triassic (Charrier, 1979). The Estratos El Mono unit represents such a rift basin depocenter in the study area.

The Indagua Fault merges towards the south with the NNE-striking west vergent high angle Vega La Junta thrust fault. The transition zone between these faults is covered by undeformed rocks of the Pompeya Pyroclastics unit. The temporal relationship with the Pompeya Pyroclastics, together with the occurrence of NW-oriented Eocene dikes limited by the Vega La Junta Fault, suggests that the deformation along this fault took place between 39 and 21 Ma (Abels & Bischoff, 1999). In the study area, this fault puts the Late Triassic-Early Jurassic TrJem1 member of the Estratos El Mono unit in the hanging-wall in contact with Cretaceous lavas of the Estratos de Cerro Los Carneros unit in the foot-wall (Figure 4.2). Prolonged towards the south of the study area for approximately 27 km (Mercado, 1982), the Vega La Junta Fault is part of a regional system of NNE-striking high-angle dipping thrust faults that uplifted Paleozoic basement blocks along the Maricunga belt (Abels and Bischoff, 1999; Cornejo et al., 1993).

In the eastern part of the study area, the NNE-striking high-angle east-vergent Portezuelo Codocedo thrust fault puts rocks of the Estratos El Mono unit in the hanging-wall in contact with younger Mesozoic rocks in the foot-wall. This fault, discontinuously exposed over 27 km from the north to the south of the study area, is covered by Tertiary rocks of the Pompeya Pyroclastics unit. NW-oriented left-lateral strike-slip faults observed in this area suggest a left-lateral offset of the Portezuelo Codocedo Fault, a relationship that can be observed south of the study area (Cornejo et al., 1998).

Local structures are represented by NW, NNW, NE, and NS-oriented faults. Most of these structures are mapped as high-angle faults with vertical displacements either with normal or reverse movement, presenting in some cases evidence that suggest both types of movements during reactivation periods. The most widely distributed set of faults corresponds to the NW-oriented structures. These faults are associated with the Eocene strike-slip left lateral system, which was reactivated through a series of sub-parallel faults during the emplacement of the La Coipa Group (late Oligocene-early Miocene). In

this second period, vertical movements were predominant. A brief description of most important faults at the deposit scale will be discussed in Chapter 4.6.

Major folding is observed only in Mesozoic sedimentary sequences. A contractional event of probable Early Cretaceous age affected these sedimentary rocks, especially the less competent TrJem2 and TrJem3 members of the Estratos El Mono unit. District scale NE-oriented anticlines and synclines mark the main deformation of these rocks (Figure 4.2). According to Arriagada et al. (2013), asymmetric folds that terminate in high-angle reverse faults; which were observed on the TrJem2 member, are indicators for Early Cretaceous inversion of Jurassic-Triassic basins.

4.5 Hydrothermal alteration and mineralization

The La Coipa district is characterized by intense hydrothermal alteration spread over a large proportion of the rocks that constitute the study area. Associated with Au-Ag Oligocene-Miocene epithermal mineralization, assemblages of alteration minerals include high-sulfidation and intermediate-sulfidation styles. Of secondary importance is quartz-sericite alteration related to Eocene hypabyssal units. Figure 4.24 shows an alteration map of the study area.

4.5.1 High-sulfidation assemblages

With the exception of the Purén Phase II and Purén West projects, the deposits and prospects that constitute the La Coipa district are classified as high-sulfidation epithermal systems. A common feature between these deposits is the concentric zoning from proximal to distal alteration surrounding ore shoots. As it has been described for high sulfidation epithermal systems (White and Hedenquist, 1995; Hedenquist et al., 2000), the zonation at La Coipa grades from vuggy quartz to quartz+alunite, alunite±pyrophyllite+dickite, dickite±kaolinite, kaolinite+illite, and illite+smectite.

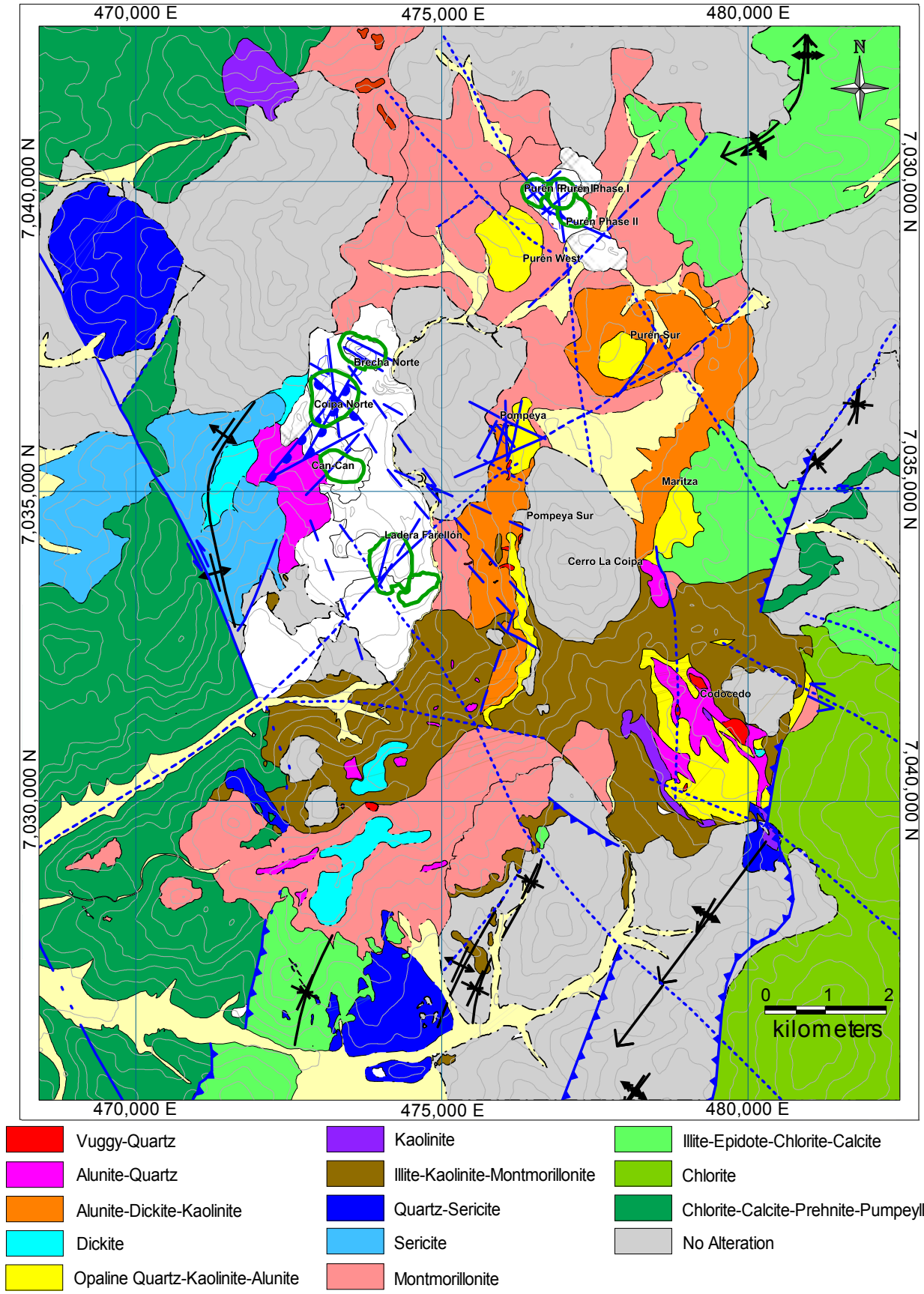

Figure 4.24. Alteration map of La Coipa district. Alteration classes based on surface mapping, short-wave infrared spectroscopy (SWIR) using Terraspec® spectrometer, and hyperspectral data collected from an airborne survey done by Kinross in 2007. White areas represent mine operation, tailings and waste rock dumps.

The most proximal alteration to the higher-grade ore shoots is vuggy quartz. This type of highly acidic alteration obliterates the primary mineralogy leaving a porous rock consisting of residual plus added hydrothermal quartz (Arribas, 1995). Vugs remain at the sites of plagioclase phenocrysts or juvenile pumice fragments, but the original intermediate igneous composition of the matrix is replaced entirely by quartz. The volume of rocks altered to vuggy quartz zones varies from a few centimeters in haloes of pyrite+enargite veins to lithologically controlled breccia units or permeable fragmental volcanic to volcaniclastic units. The occurrence of shallow levels of barren vuggy quartz alteration with open cavities and deeper levels filled with alunite or sulfides suggests that the vuggy quartz alteration is a first-stage prograde event that allowed to this rock to act as a favourable host-rock for later depositional stages of metals-bearing hydrothermal fluids under less acid conditions (Figures 4.25.A, B). This situation can be observed in Pompeya and Purén Sur.

Volumetrically, the most dominant alteration observed at La Coipa district is the advanced argillic alteration. Peripheral to the vuggy quartz alteration, the alunite+quartz assemblage is also associated with Au and Ag mineralization (Figure 4.25.C) and replaces the host rock pervasively to selectively; i.e., alunite replacing plagioclase phenocrysts selectively. All types of host rocks are affected by this alteration. Mineralization associated with quartz-alunite alteration is represented by quartz+pyrite+enargite veins and dissemination (Figure 4.25.E). Local occurrences of barite, diaspore and zunyite have been identified inside this type of alteration. The alunite samples collected in the present study for geochronology are described in Chapter 4.7.

The alunite+quartz assemblage grades outward to alunite+pyrophillite, alunite+dickite, dickite+kaolinite, and kaolinite associations. Considered a mineral formed under high temperature conditions of advanced argillic alteration phases, the occurrence of pyrophyllite in the La Coipa district is associated with deeper levels of some deposits. In the Ladera Farellón open pit, an amoeboid texture with rounded nodules with pyrite-rich rims (Figure 4.25.D), developed in fine-grained sediments of the Estratos El Mono unit, is considered to represent the deeper part of the advanced argillic lithocap (Sillitoe, 2010). Upper levels of the deposits which reflect originally lower temperature hydrothermal conditions are characterized by dickite and kaolinite assemblages.

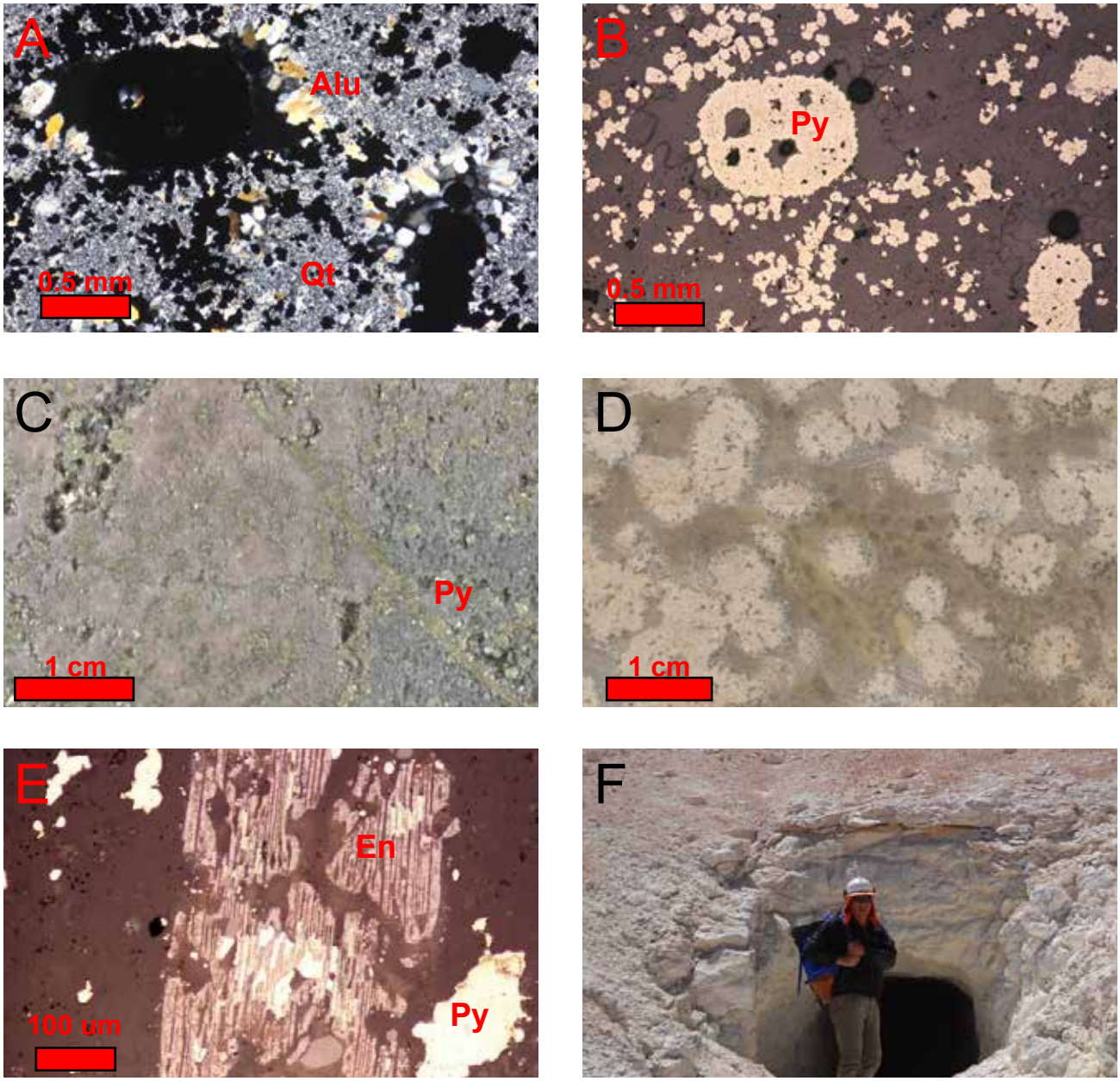

Figure 4.25. Mineralogy of advanced argillic alteration phases. **(A, B)** Vugs originated by a primary event of vuggy quartz alteration that latter were filled by pyrite and alunite. Photomicrograph taken under cross-polarized and reflected light respectively. Sample SG16312, Pompeya prospect, drill-hole DPMP-033, 187 m). **(C)** Strong quartz+alunite alteration with veins and dissemination of pyrite @1.03 ppm Au and 10 ppm Ag (Ladera Farellón, sample SG16251, drill-hole LRD-033, 96.15m) **(D)** Amoeboid texture with rounded nodules of pyrophyllite+alunite and pyrite rims (Ladera Farellón, sample SG16252, drill-hole LRD-033, 200.9 m). **(E)** Photomicrograph taken under reflected light showing lamellar texture for an enargite crystal growing over pyrite grains (sample SG16313, Pompeya prospect, drill-hole DPMP-064, 91 m) **(F)** Steam-heated alteration level. Picture taken from an artisanal sulfur mine (Purén Sur area).
Abbreviations: (Alu) alunite (En) enargite, (Py) pyrite, (Qt) quartz.

The most distal assemblages are represented by minerals such as illite and smectite, which are stable under neutral to weakly acidic pH. This type of alteration varies from pervasive to selective, in the latter case replacing the plagioclase phenocrysts and groundmass microliths. Weak and spotty occurrences of chlorite and calcite veins which are observed in distal units and locally in areas such as Purén and deeper parts of the Brecha Norte deposit, suggest that the propylitic halo which developed peripherally to the advanced argillic alteration was generally weak and very restricted over the district.

Only minimal to moderate erosion affected the La Coipa district since the Oligocene and is exemplified by the preservation of steam-heated horizons in the eastern part of the district and in the upper levels of the Coipa Norte and Can Can deposits. The steam-heated alteration is represented by opaline silica+kaolinite±alunite±native sulfur. Corbett (1998) recognized cinnabar in a hand sample of the steam-heated level. Strongly acidic conditions typical of this alteration are reflected with intense leaching of upper levels of this horizon, where powdery opaline silica is the only relict of an intensely altered primary lithology. The bottom level of the steam-heated zone is characterized by massive opaline to chalcedonic silica and interpreted as a paleo-water table level. This steam-heated zone is well developed at the western margin of the Cerro La Coipa, in the Purén Sur area (Figure 4.25.F), in the Pompeya and Pompeya Sur prospects, and in the Codocedo area.

4.5.2 Intermediate-sulfidation assemblages

A distinctive signature of ore and alteration minerals has been identified in the Purén deposit and the Purén West area (Figure 4.2). Hydrothermal alteration is represented by silicification and argillic alteration. Even though present in all host rocks, silicification is more intense in the permeable sedimentary and volcaniclastic deposits of the Estratos de Huidobro unit (Figure 4.26.A). Argillic alteration, developed around the silicified rocks, is characterized by kaolinite, illite and smectite. Rhodocrosite+quartz veins have also been observed in this area (Figure 4.26.B).

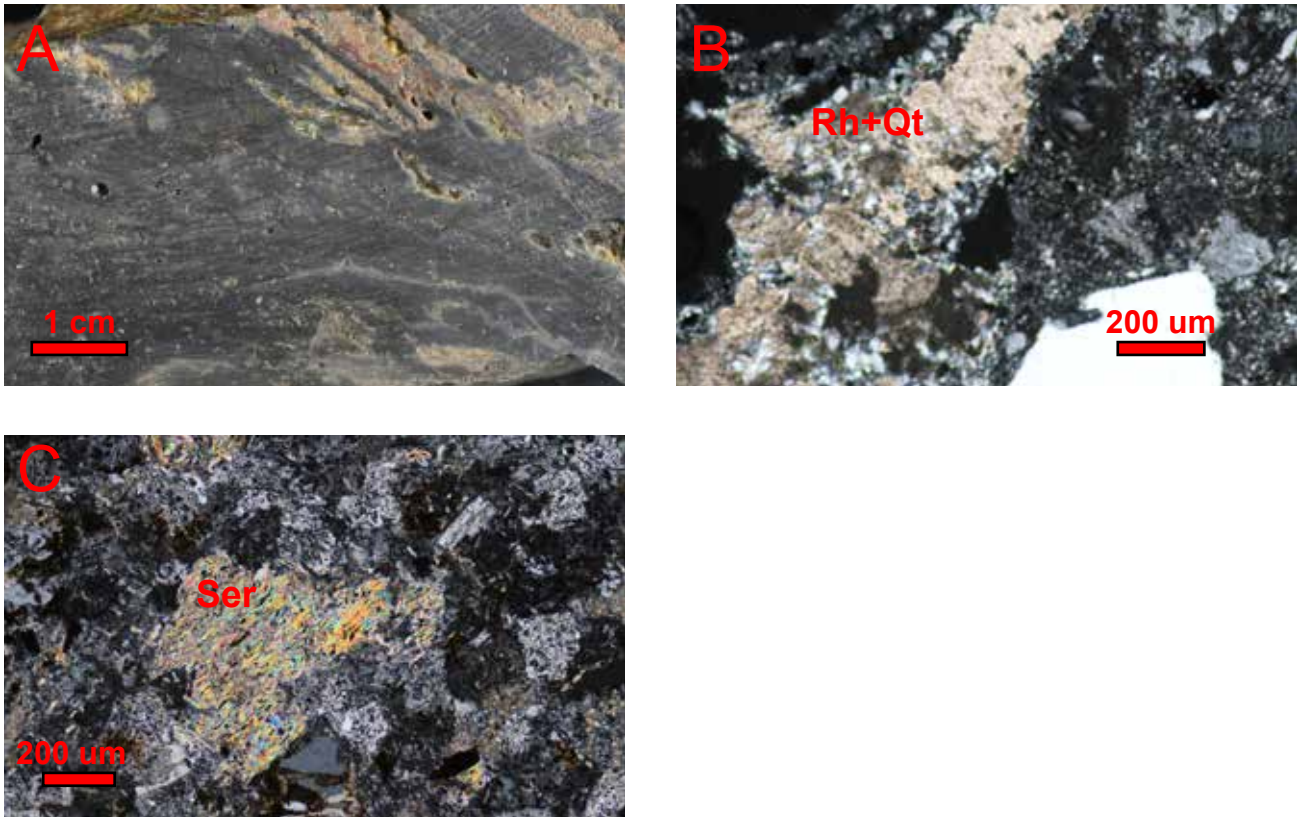

Figure 4.26. Photographs and photomicrographs of altered rocks in the Purén deposit and in the tailings area. **(A)** Strongly silicified fine-grained sediments of the Estratos de Huidobro unit (sample SG16281, drill-hole DPU-06, 270.5 m). **(B)** Photomicrograph taken under cross-polarized light of a quartz+rhodochrosite vein cross-cutting a fragmental pyroclastic rock (sample SG16283, Purén Phase II, drill-hole DPU-06, 331.74 m). **(C)** Photomicrograph taken under cross-polarized light of coarse-grained sericite alteration replacing plagioclase crystals of a rhyodacitic stock of the TEpa unit (sample SG050313_P8, tailings area).
Abbreviations: (Qt) quartz, (Rh) rhodocrosite (Ser) sericite.

4.5.3 Sericite-quartz

An intense episode of sericite+quartz+pyrite+(goethite)±albite±kaolinite alteration is spatially associated with the Eocene rhyodacitic to rhyolitic hypabyssal units. Rocks of the TEpa unit, cropping out mainly in the southern part of the study district (including a small stock observed in the tailings area), are pervasively altered to this assemblage (Figure 4.26.C). Sericite replaced mafic phases as indicated by relicts of hornblende and biotite. Calcite in veins and cavities is also observed in these rocks. The potential association of sericite-quartz alteration with gold, silver or copper mineralization remains undetermined.

4.6 Ore mineralogy

The most abundant unoxidized ore minerals associated with the advanced argillic alteration correspond to pyrite and enargite (Figure 4.27.A, B). Less abundant minerals include covellite and chalcosite. Local occurrences of chalcopyrite, bornite, tetrahedrite, tennantite, galena and sphalerite have also been reported (Figure 4.27.C; Oviedo et al., 1991). Sulfide minerals associated with the intermediate-sulfidation system observed in the Purén deposit are represented by pyrite, sphalerite, and galena (Figure 4.27.D).

According to Oviedo et al. (1991), silver ore minerals identified in oxidized mineralization at Ladera Farellón consist of cerargyrite (AgCl), native silver, embolite (Ag[Cl,Br]), iodargirite (AgI), electrum, argentite (Ag_2S), and argentojarosite ($Ag_3Fe_3[SO_4]_2[OH]_6$). In the Ladera Farellón and Coipa Norte open pits, gold is present in its native form and as electrum (Oviedo et al., 1991). Both, gold and silver, are generally present as free grains, but in some places they are encapsulated in quartz (Ceccioni & Dick, 1992). Sulfide minerals are present in veinlets, disseminated, or cementing breccia units. In the finely banded shales and siltstones of the Estratos El Mono unit, veins of enargite+pyrite+quartz developed along this sedimentary banding, utilized these weakness zones to discharge mineralized

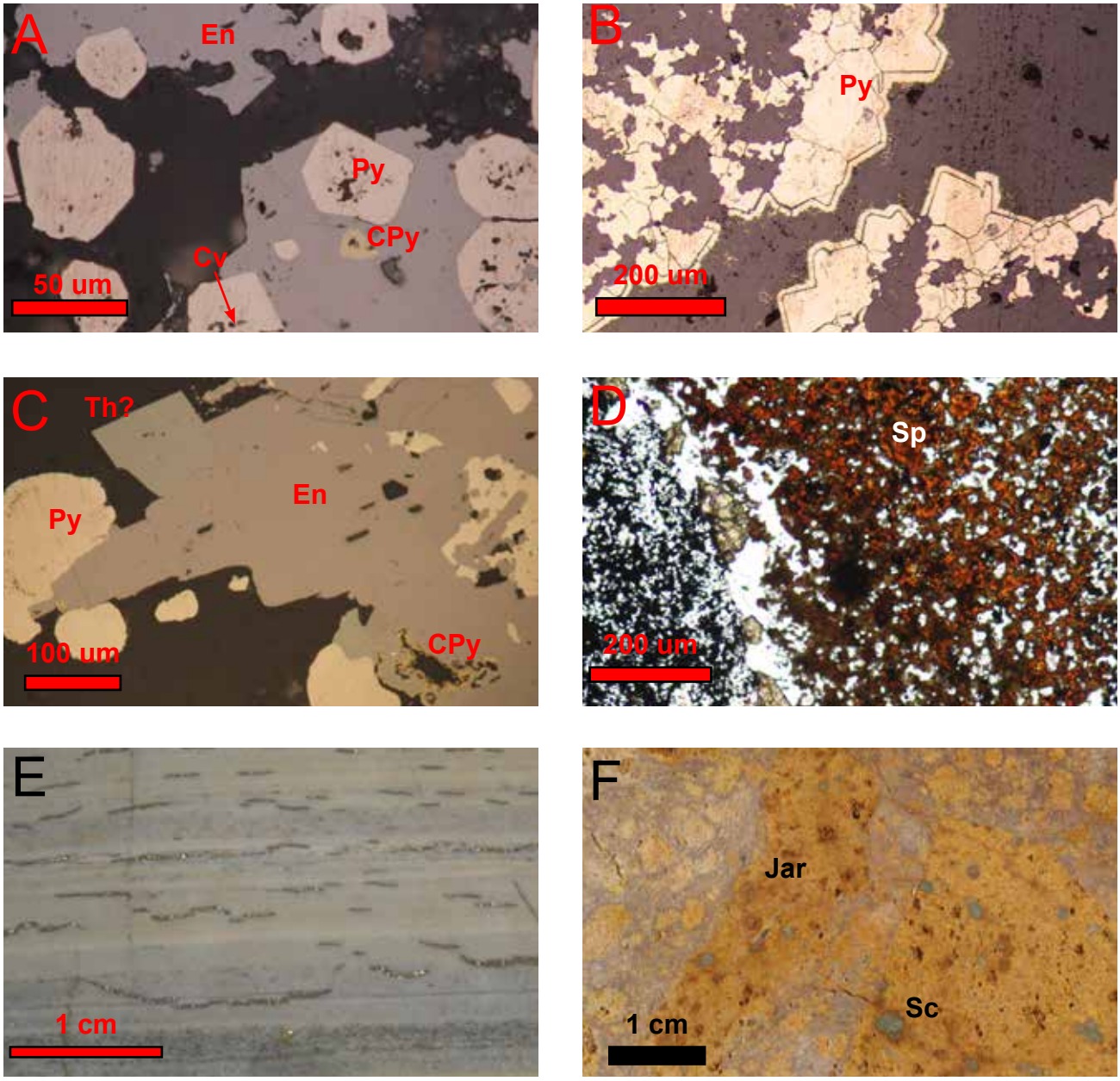

Figure 4.27. Sulfides and oxidized ore minerals identified in the La Coipa district. **(A)** Subhedral pyrite grains growing over enargite. Traces of chalcopyrite are also observed (Mina Vieja, sample SG050113_P12, photomicrograph taken under reflected light). **(B)** Two events of pyrite mineralization indicated by rims of pyrite around primary pyrite grains (sample SG16313, Pompeya prospect, drill-hole DPMP-064, 91 m, photomicrograph taken under reflected light). **(C)** Vein of enargite+pyrite+chalcopyrite+tetraheditre(?) (sample SG16274, Can Can, drill-hole CCD-01, 385.3 m, photomicrograph taken under reflected light). **(D)** Photomicrograph taken under cross-polarized light of a red sphalerite vein cross-cutting fine-grained of the Estratos de Huidobro unit. Host-rock mineralized to disseminated pyrite (sample SG16296, Purén West prospect, drill-hole DPUW-011, 143.15 m). **(E)** parallel to stratificaion discontinuous pyrite veins hosted in fine-grained siltstones sediments of the Estratos El Mono unot (Can Can open pit, drill-hole CCD-01, 330 m).**(F)** Oxidized jarosite+scorodite ore minerals associated with advanced argillic alteration of alunite+quartz (sample SG16258, Coipa Norte, drill-hole CND-241. 203.3 m).
Abbreviations: (CPy) chalcopyrite, (Cv) covellite, (En) enargite, (Jar) jarosite, (Py) pyrite, (Sc) scorodite, (Sp) sphalerite (Th) tetrahedrite.

fluids originated in oblique-to-strata sub-vertical feeder conduits (Figure 4.27.E). Oxidized levels are characterized by patches, fractures or veins filled by jarosite and scorodite, considered as the oxidation products of pyrite and enargite respectively (Figure 4.27.F). Orpiment and realgar are also observed locally.

4.7 Deposit characterization

As every deposit has its particularity, a brief description of each one will be discussed below. It should be noted that the ore mined at La Coipa to-date included completely and partially oxidized mineral zones, whereas hypogene sulfide ore has not been mined.

4.7.1 Ladera Farellón

The Ladera Farellón deposit was the first open pit developed in the La Coipa district. Lithological units observed in this deposit consist of a massive basement domain of the Black shale member of the Estratos El Mono unit, which is overlain by the Ladera Tuffs and by the Pompeya Pyroclastics members of the La Coipa Group (Figure 4.28). Main structures observed in the open pit include NNE- to NE-striking high-angle normal faults. These faults control the Au-Ag mineralization, which occurs as two N-striking orebodies developed in the upper and more permeable volcanic domain. In the lower Black shales member, economic mineralization is restricted to subvertical feeders, veinlets, and local stockworks, whereas once these same feeders reach the overlying Tertiary volcanic units they blossom out into disseminated mineralization. Economic silver grades are restricted to the upper volcanic sequence, whereas economic gold grades are distributed in both domains (Figure 4.29). It should be noted that although mineralization in the Black shales member is controlled by subvertical structures, it´s common to observe enargite+pyrite+quartz veins parallel to stratification. The orebodies show a concentric zonation of alteration with vuggy quartz and quartz+alunite±pyrophyllite in the centrally mineralized rocks and distal kaolinite+illite in the upper sequence of volcanic rocks.

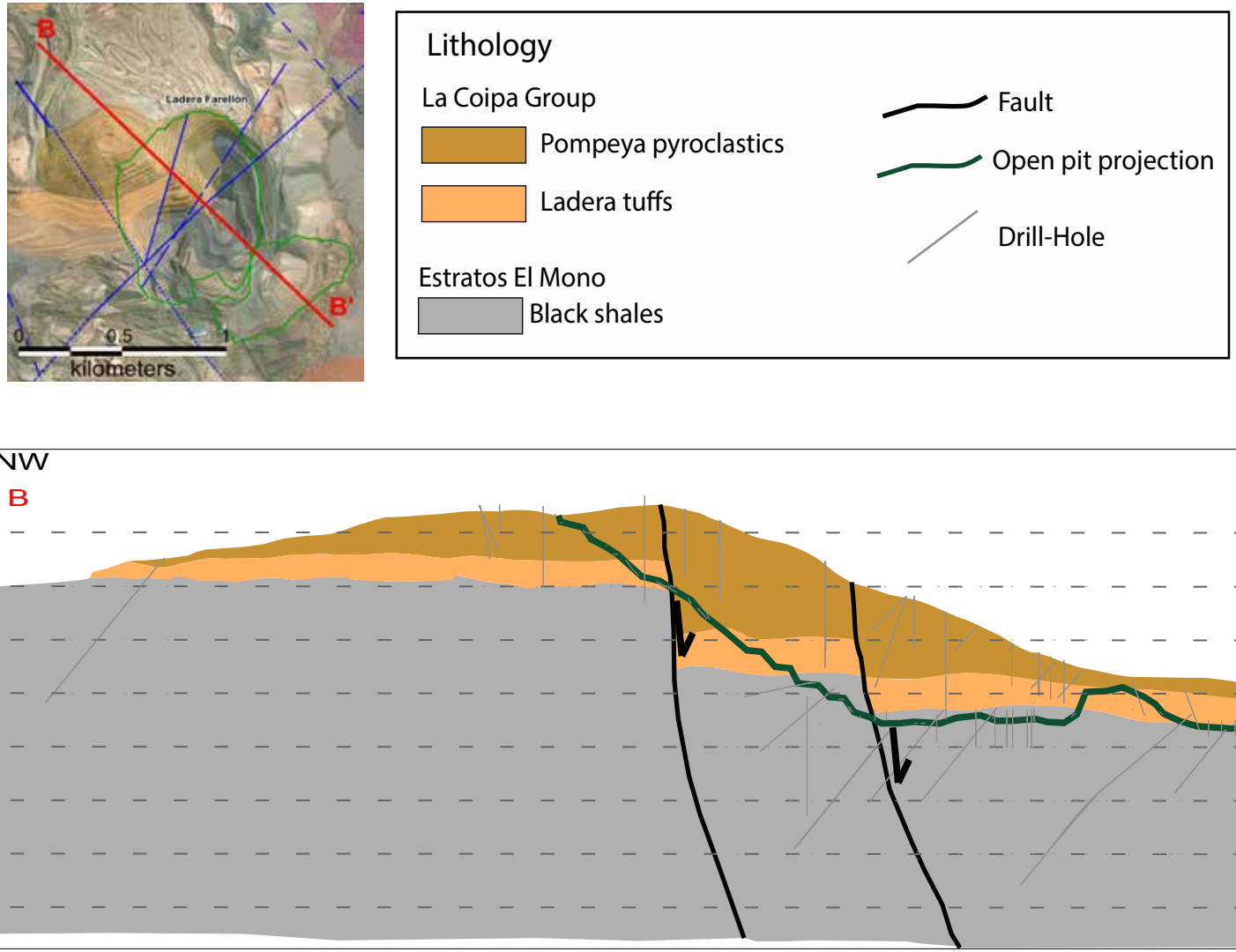

Figure 4.28. Representative NW-SE geological section through the Ladera Farellón deposit. Lithological units based on selected core-logging done at the present study and geological models ellaborated by mine geologists. Section line is shown in the upper left of the figure.

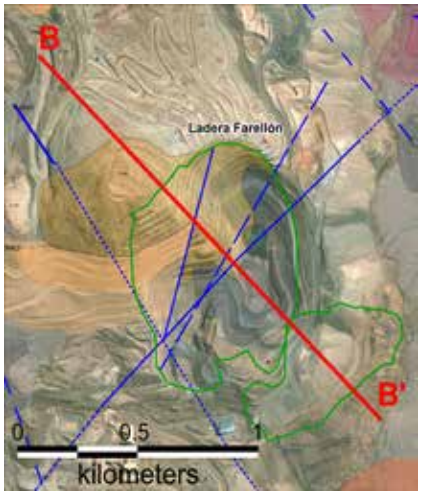

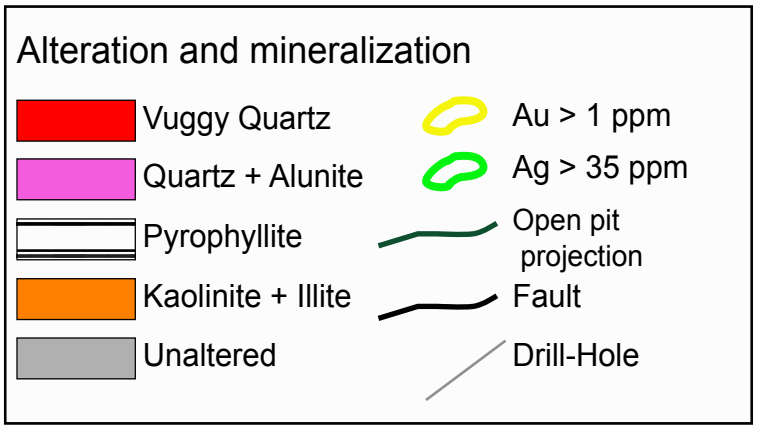

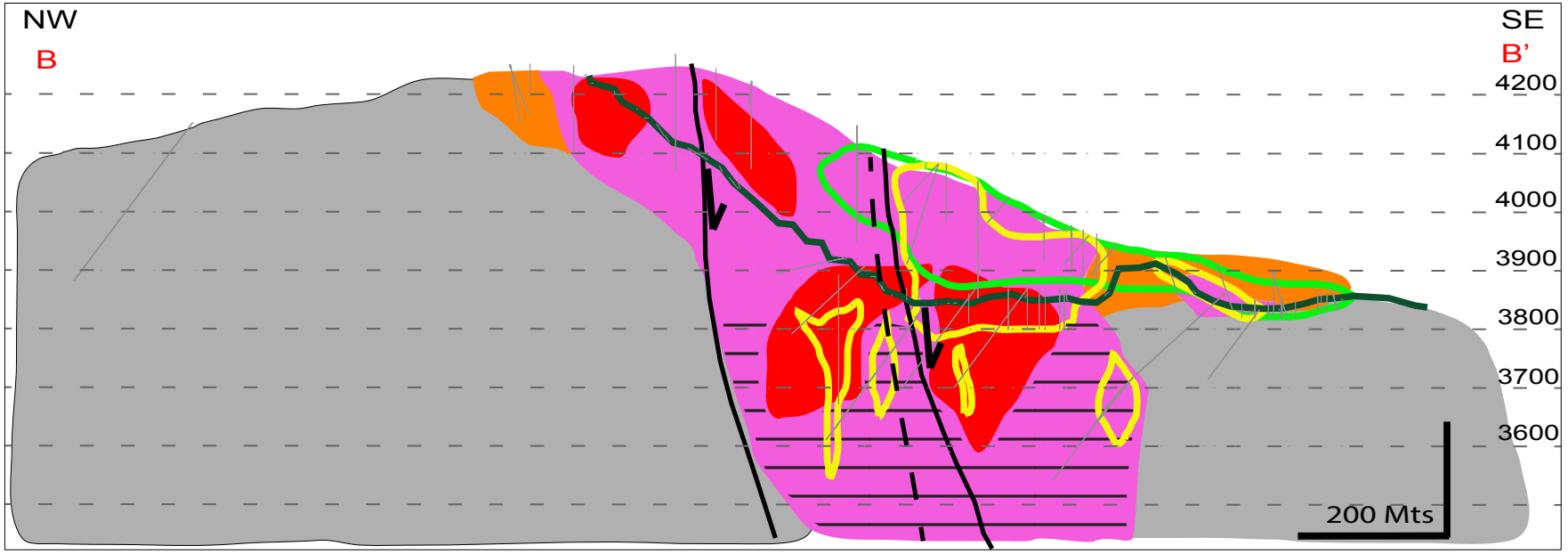

Figure 4.29. Representative NW-SE alteration and mineralization section through the Ladera Farellón deposit. Alteration model based on Terraspec sampling done in this study and alteration models ellaborated by mine geologists. Section line is shown in the upper left of the figure.

The oxidation level, which roughly coincides with the contact between volcanic and sedimentary rocks, marks the bottom of the ore mined in this open pit.

4.7.2 Can Can

Can Can was mined during its first stage as an underground operation along high-grade feeder structures hosted in the underlying Triassic sedimentary units, and there was a subsequent open pit phase developed in disseminated mineralization hosted in the overlying Tertiary volcanic sequence. The Can Can deposit consists of a vertical orebody steeply east dipping, which is spatially associated with a phreatomagmatic breccia that acted as a favorable host-rock for later hydrothermal breccias and fractures that carried mineralized fluids. This second episode is characterized by black-silica+alunite stockwork and veinlets (Ceccioni & Dick, 1992). The phreatomagmatic breccia, controlled by two NE-striking normal faults, increases in diameter once it reaches the upper level of the Ladera Tuffs and Pompeya Pyroclastics units (Figure 4.30). The western NE-striking fault presents also a strike-slip left-lateral movement. Secondary structures with NS orientation are also observed in this deposit (Ceccioni & Dick, 1992). The hydrothermal alteration includes a vuggy quartz domain in the more permeable phreatomagmatic breccia, which concentrated a high proportion of the mineralization. At the bottom level of the Pompeya Pyroclastics unit, a subhorizontal lense-type domain with gold and silver mineralization which was developed in a more permeable fragmental unit is observed. Hydrothermal alteration is widely developed in the upper volcanic domain, with subhorizontal variations of alunite, dickite, or kaolinite-illite as the dominant species for each level of this intense advanced argillic alteration (Figure 4.31). SWIR measurements performed on the Black shales member the Estratos El Mono showed only weak to minimal alteration.

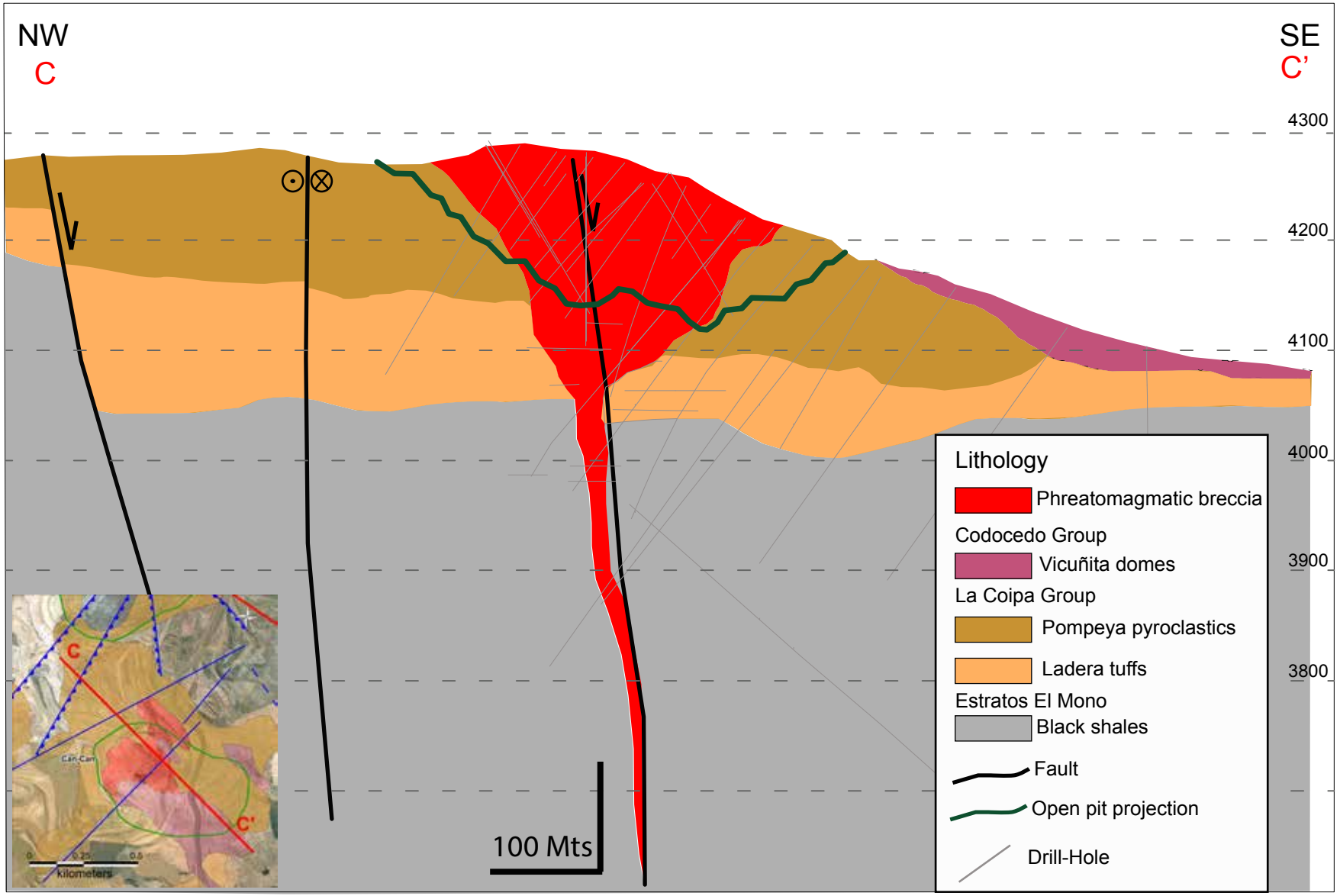

Figure 4.30. Representative NW-SE geological section through the Can Can deposit. Lithological units based on selected core-logging done at the present study and geological models ellaborated by mine geologists. Section line is shown in the bottom of the figure.

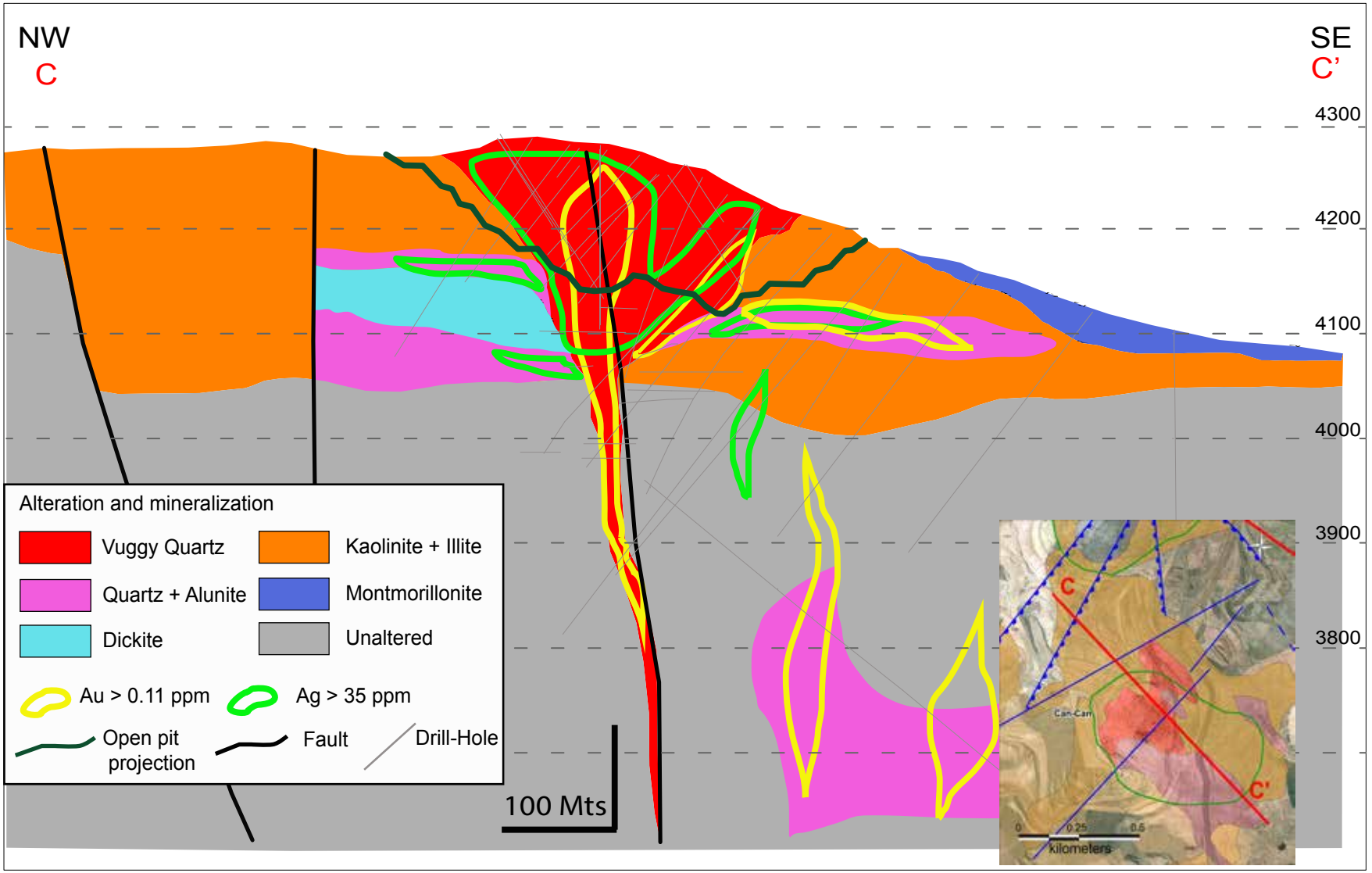

Figure 4.31. Representative NW-SE alteration and mineralization section through the Can Can deposit. Alteration model based on Terraspec sampling done at the present study and alteration models ellaborated by mine geologists. Section line is shown in the bottom right of the figure.

4.7.3 Coipa Norte

The Coipa Norte deposit is characterized by a breccia-hosted subvertical orebody controlled by two sub-parallel steeply dipping NE-striking normal faults. Steeply dipping normal faults with NW and NNW-strikes are also observed in this pit. With a similar lithology to the Can Can deposit, in the Coipa Norte deposit a phreatomagmatic breccia acted as a favorable conduit for later mineralizing fluids that precipitated gold and silver in multiple and narrow (centimeter scale) hydrothermal breccias cemented by quartz+sulfides+alunite. The phreatomagmatic breccia, which intruded the TrJem2 member of the Estratos El Mono unit and the Pompeya Pyroclastics member of the La Coipa Group (Figure 4.32), is altered to pervasive vuggy quartz and alunite+quartz. Proximal-to-ore rocks of the sedimentary basement are altered to alunite+pyrophyllite in the western domain, whereas kaolinite+illite are more abundant in the eastern domain. Volcanic rocks in the upper level are altered to montmorillonite. High-grade mineralization shows a subvertical cylindrical shape with silver concentrated in the upper level and gold distributed homogeneously along the orebody. Smaller phreatomagmatic breccias (diameter <10m) observed in the eastern part are not mineralized (Figure 4.33).

4.7.4 Brecha Norte

The Brecha Norte deposit shows a complex distribution of rock units, which display deformation and displacement along two sub-parallel steeply dipping NW-striking normal faults. The bottom part of the Brecha Norte open pit is occupied by the Permian granodiorite, which is overlain by the TrJem2 and TrJem3 members of the Estratos El Mono unit. Dacitic domes with abundant quartz phenocrysts intruding this sequence are assigned to the Mina Vieja unit (Figure 4.34). The NW-oriented faults originated a graben that controlled the emplacement of a phreatomagmatic breccia that, as has been observed in the other deposits, acted as a favorable host-rock for later mineralized fluids. The phreatomagmatic breccia, hosting the richest and most continuous Au and Ag mineralization, is altered to vuggy quartz. Moderately mineralized rocks of the Estratos El Mono unit and the Permian Granodiorite are altered to alunite+quartz. Lower parts of the Permian Granodiorite are altered selectively to illite+kaolinite (Figure 4.35).

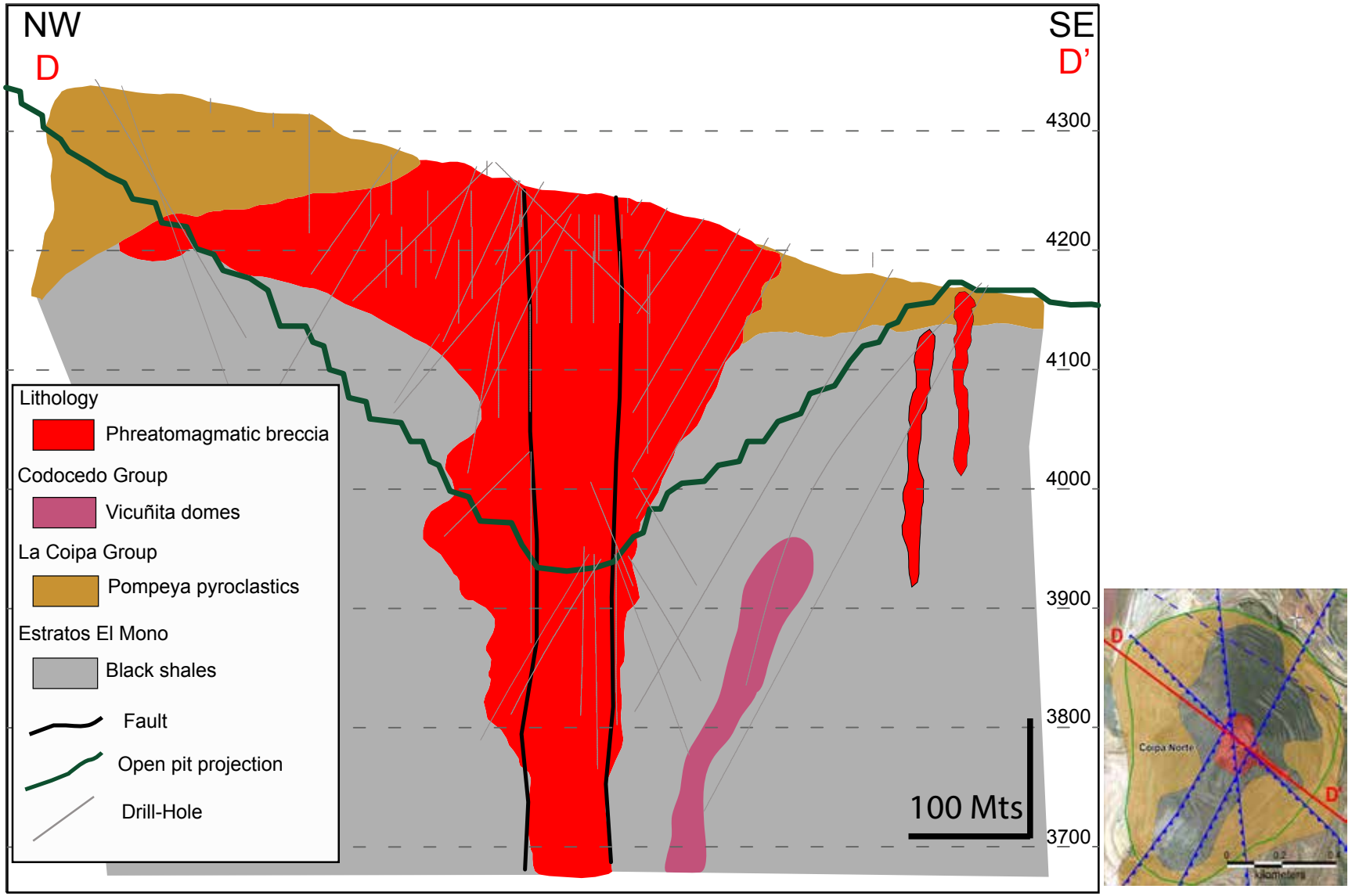

Figure 4.32. Representative NW-SE geological section through the Coipa Norte deposit. Lithological units based on selected core-logging done at the present study and geological models ellaborated by mine geologists. Section line is shown in the bottom right of the figure (faults illustrated in this figure correspond to normal faults).

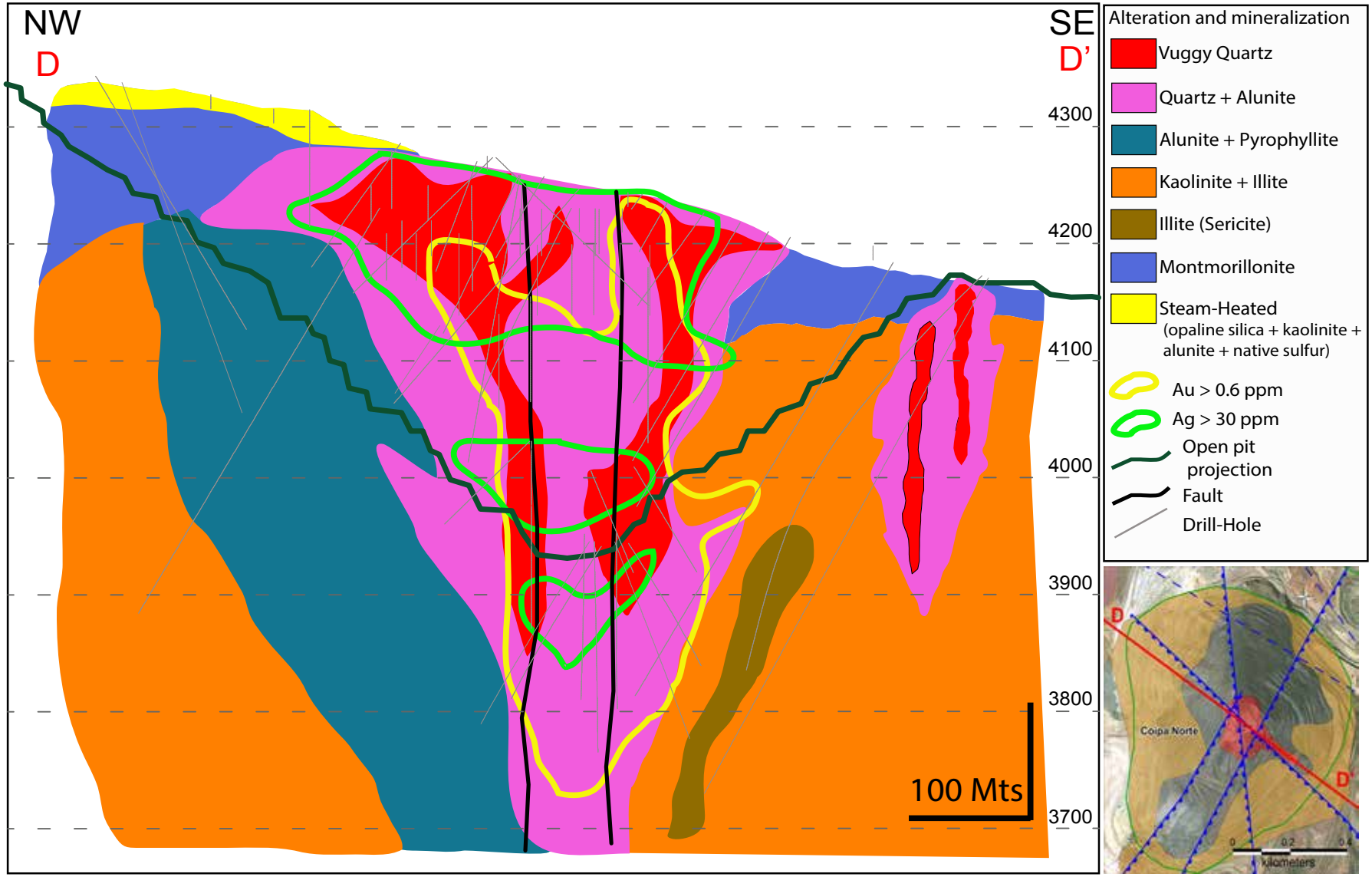

Figure 4.33. Representative NW-SE alteration and mineralization section through the Coipa Norte deposit. Alteration model based on Terraspec sampling done at the present study and alteration models ellaborated by mine geologists. Section line is shown in the bottom right of the figure.

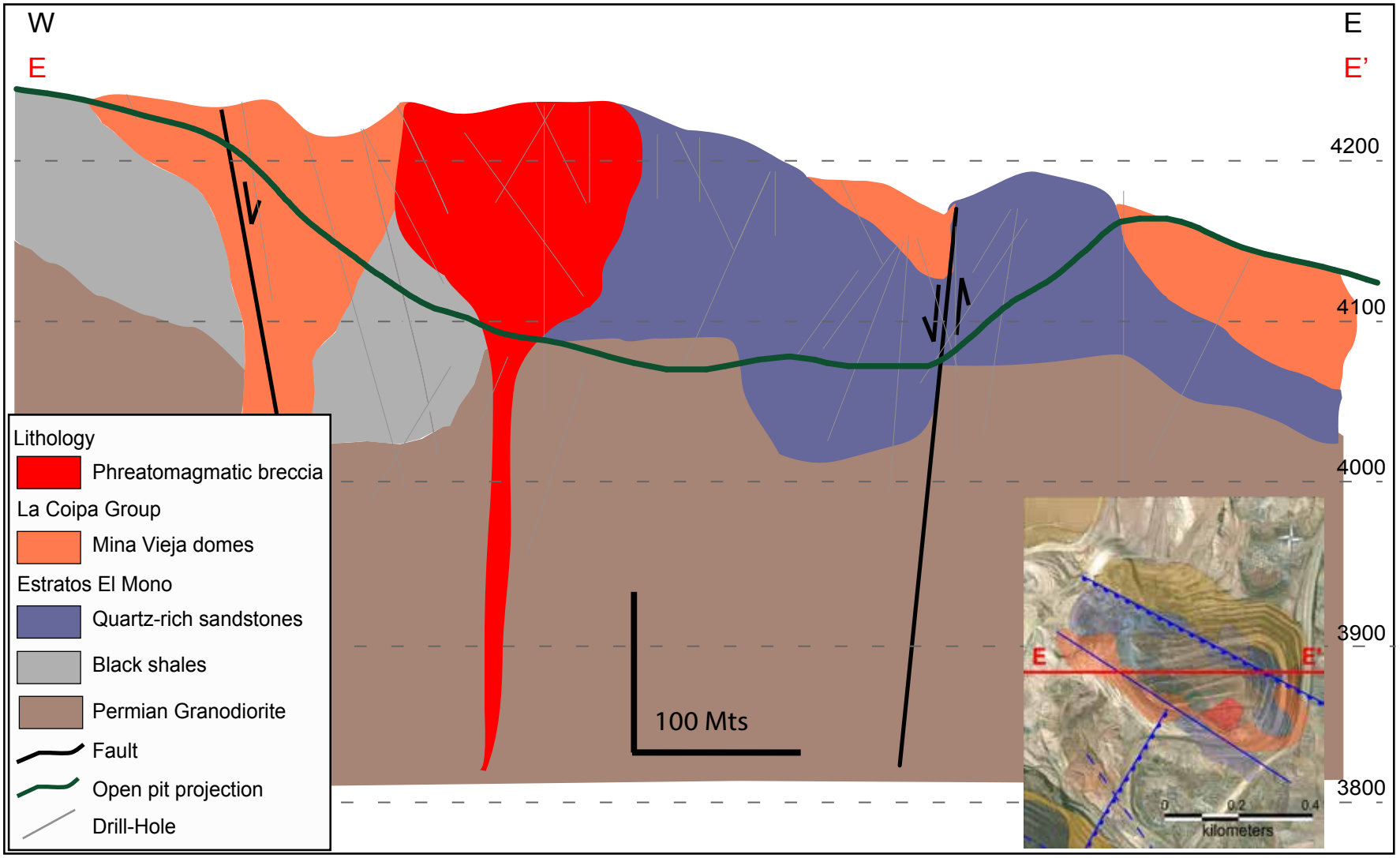

Figure 4.34. Representative W-E geological section through the Brecha Norte deposit. Lithological units based on selected core-logging done at the present study and geological models ellaborated by mine geologists. Section line is shown in the bottom right of the figure.

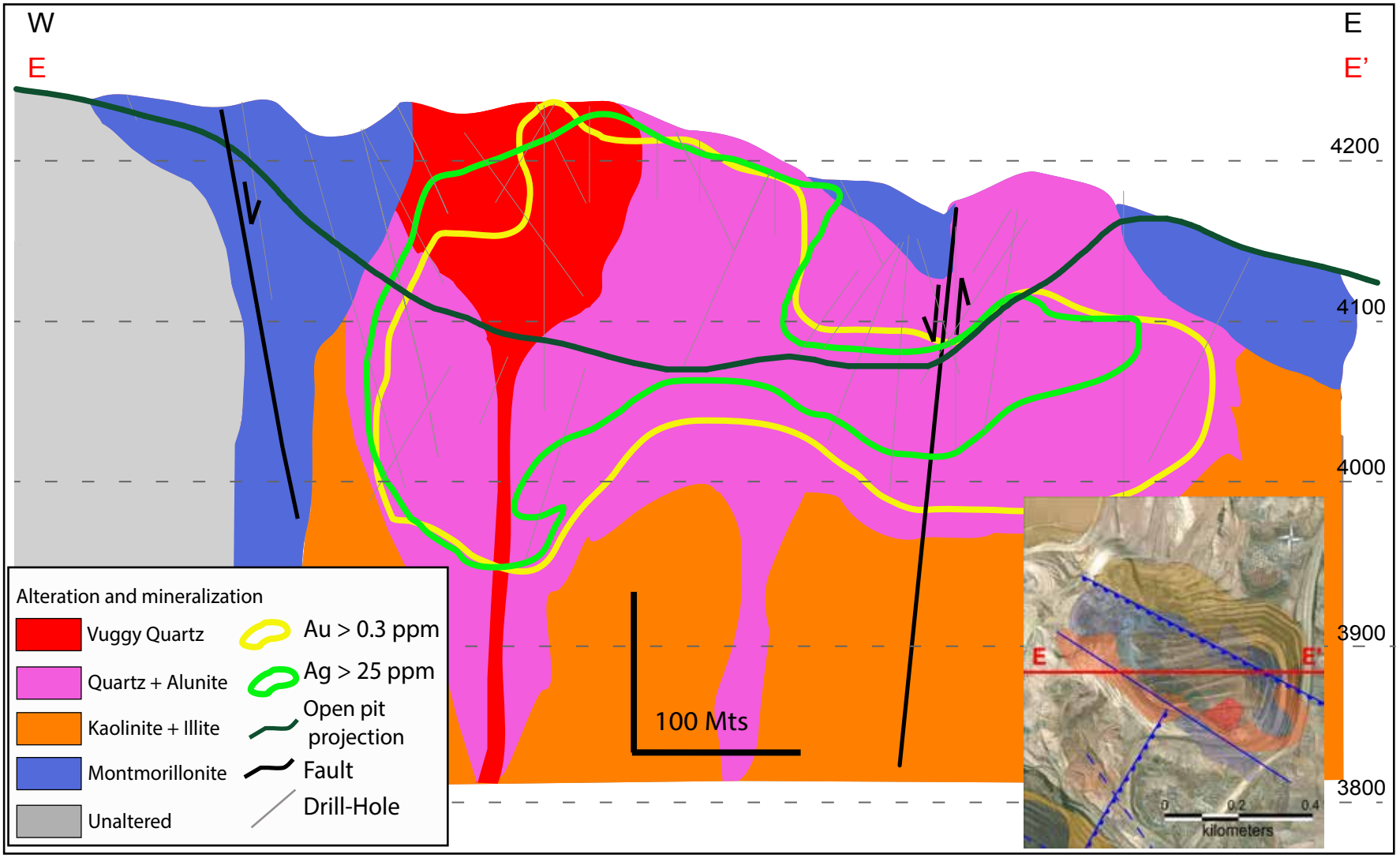

Figure 4.35. Representative W-E alteration and mineralization section through the Brecha Norte deposit. Alteration model based on Terraspec sampling done at the present study and alteration models ellaborated by mine geologists. Section line is shown in the bottom right of the figure.

4.7.5 Purén

The Purén deposit comprises three phases from which two (Phase I and Phase III) have been exploited to-date. Structures observed in these deposits consist of steeply-dipping NW-, NS-, and NE-striking faults, from which normal movements seems to control the emplacement of rocks of the Eocene Estratos de Huidobro unit and subsequently younger units. Rocks of the Purén deposit are represented by a subhorizontal sequence that, from bottom to top, consists of volcaniclastic deposits, a 200 m thick dacitic ignimbrite, fine-grained sedimentary rocks, volcaniclastic breccia, fine-grained sediments and an upper lapilli-tuff unit (Figure 4.36).

This sequence is intruded by hydrothermal breccias that were best developed in the Phase III open pit. Here, the dominant alteration is vuggy quartz+dickite. Surrounding these breccia bodies, quartz and quartz+illite are the characteristic alteration of volcanic and volcaniclastic units. A more reactive level that is interpreted for the lower fine-grained sediments of the Estratos de Huidobro unit allowed the development of lenses with stratiform Zn-Pb-Ag mineralization characterized by a black silica and fine-grained sulfides, mostly pyrite (marcasite) in addition to sphalerite and galena. Distal host-rocks are altered to kaolinite in the upper part and montmorillonite in the lower part. The upper part of these deposits is covered by steam-heated alteration associated spatially with the lapilli tuffs. This acidic horizon is interpreted by geochronology and cross-cutting relationships as product of pre-mineral lateral fluid-flow which probably originated in the Purén Sur area, and which acted as a trap for subsequent hydrothermal fluids. The steam-heated level is characterized by opaline silica+alunite+kaolinite (Figure 4.37).

Mineralization in the Purén deposits indicates two different styles: a structurally controlled breccia-hosted domain in the Phase III open pit, and a more disseminated and lithologically controlled style in the Phase I and II sectors (Figure 4.37). In the first case, sulfides are pyrite and local occurrences of enargite. In the second case, pyrite accompanied by sphalerite and galena are dominant.

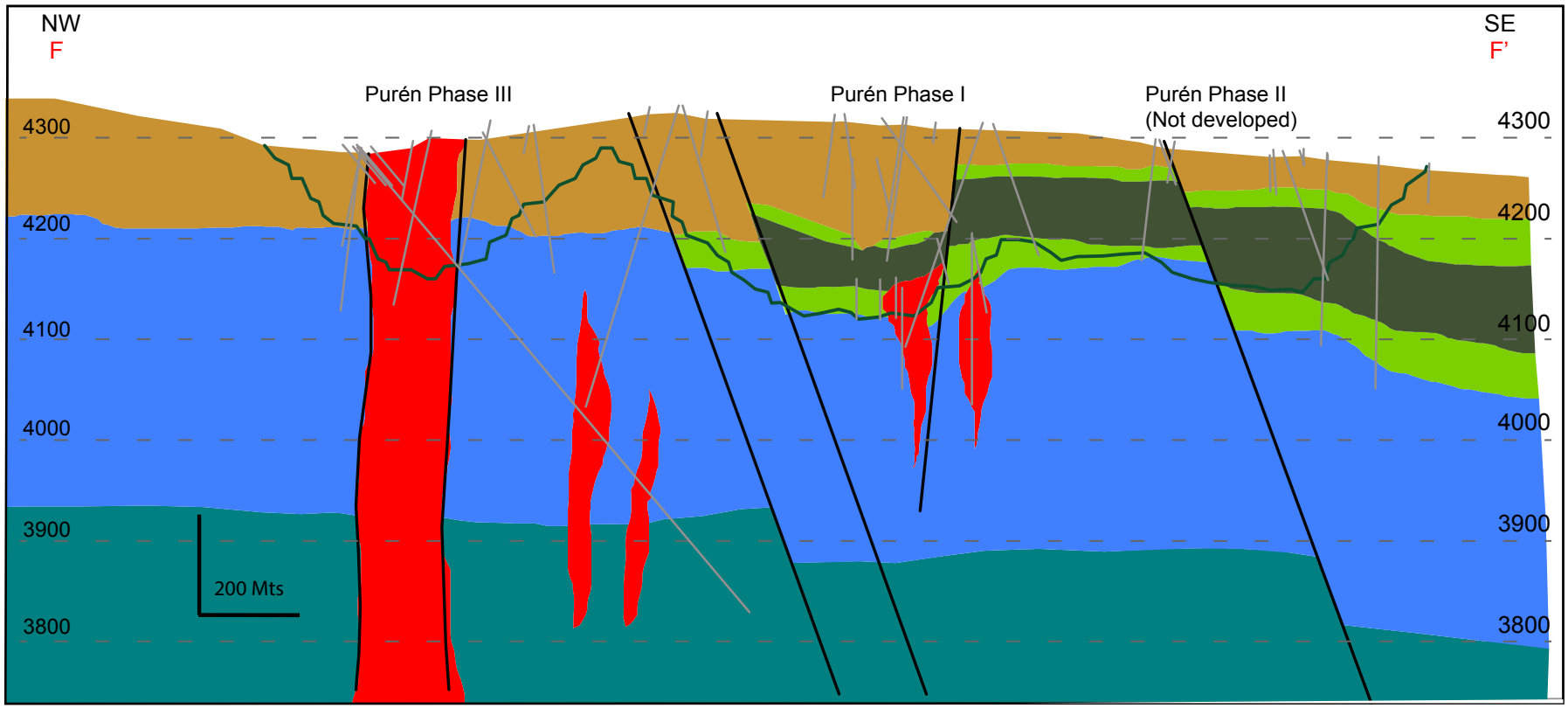

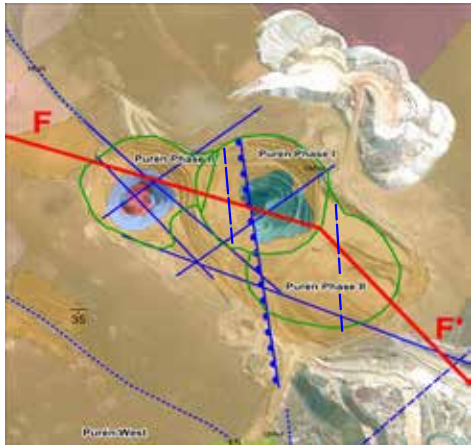

Figure 4.36. Representative NW-SE geological section through the Purén deposits. Lithological units based on selected core-logging done at the present study and geological models ellaborated by mine geologists. Section line is shown in the bottom center of the figure.

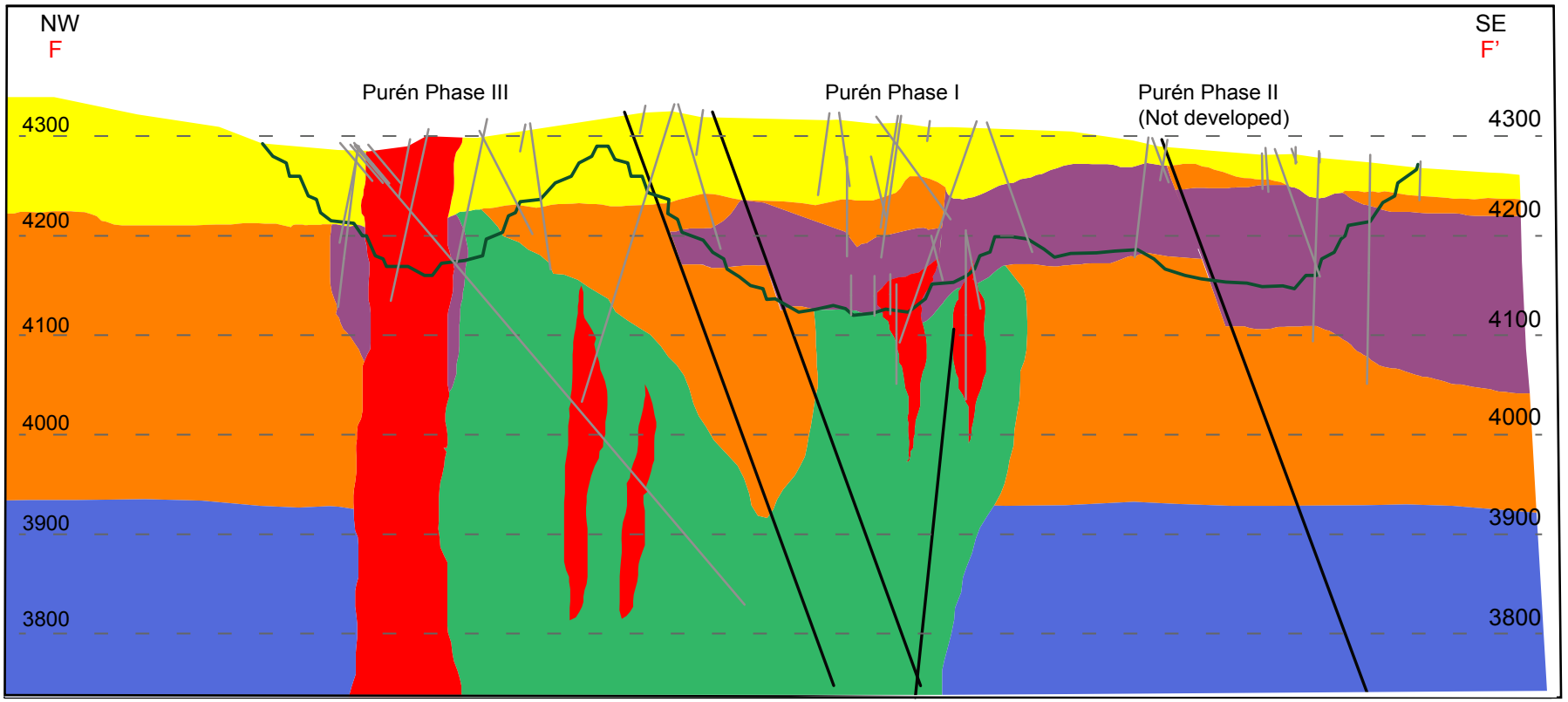

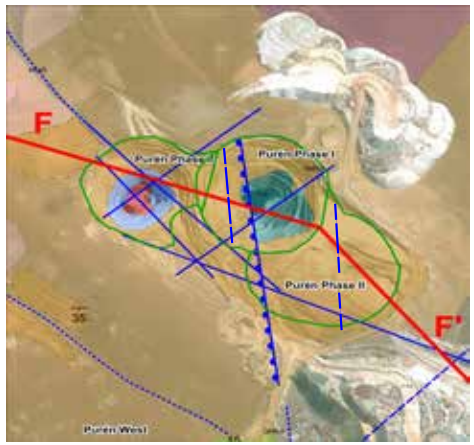

Figure 4.37. Representative NW-SE alteration and mineralization section through the Purén deposits. Alteration model based on Terraspec sampling done at the present study and alteration models ellaborated by mine geologists. Section line is shown in the bottom center of the figure.

4.8 Alunite geochronology

Alunite is widely distributed throughout the La Coipa District. In the present study, a total of 11 samples of alunite were dated by $^{40}Ar/^{39}Ar$ at the PCIGR facilities (Table 4.3 and Figures 4.38 and 4.39). Two of these samples were also analyzed at the Université de Genève as part of a quality control. Previous K-Ar alunite ages from La Coipa district are summarized in Table 4.4. The analytical results for each sample dated are described below, starting with the oldest. Analytical data are included in Appendix A6. Plateau ages were calculated according to the Isoplot criteria (Ludwig, 2003) unless indicated otherwise.

Pompeya Sur (Sample SG16293)

The alunite for this sample was taken from a ~3 cm thick alunite+pyrite+enargite vein (Figure 4.38.A). This vein cross-cuts a crowed plagioclase-porphyritic rock of unknown age. Two aliquots of this sample have been analyzed. The first run gave a 30.42±0.88 Ma plateau age constituted by five steps containing 90% of the ^{39}Ar (Figure 4.40.A). Normal and inverse isochron ages of 31.1±1.5 Ma and 31.2±1.6 Ma yielded slightly older values. The second run yielded a 31.38±0.78 Ma plateau age constituted by 5 steps that include 97.5% of the ^{39}Ar released (Figure 4.40.B). This second analysis revealed a 31.7±1.3 Ma normal isochron age and a 31.7±1.3 Ma inverse isochron age. Considering that both plateau ages overlap within the error of each other and the ages of isochrons, the more precise second plateau of **31.38±0.78 Ma** is considered the preferred age for this sample.

Purén (Sample SG16290)

This sample was collected from the steam-heated blanket that covered the mined shallow level of the Purén Phase I open pit (Figure 4.38.B). This steam-heated zone is constituted by fine-grained white alunite, which is intergrown with quartz and kaolinite. This alunite yielded a poorly defined (according to the Isoplot criteria) plateau age of 18.01±0.57 Ma (including 69.6% of the ^{39}Ar released), constituted by three steps from which the first two showed younger ages as a consequence of argon loss (Figure 4.40.C). Slightly older ages of 18.8±1.3 and 18.9±1.2 Ma were obtained through normal

Table 4.3: Summary of $^{40}Ar/^{39}Ar$ ages on alunite obtained in the present study

Sample no	Location	UTM North / UTM East or Drill-Hole		Domain	Plateau Age (Ma) (± 2σ)	Inverse Isochron Age (Ma) (± 2σ)
SG090313_P3	Codocedo	7030304	478720	Pervasive	12.3±3.4	10.8±6.2
SG090313_P4	Maritza	7033653	478590	Pervasive	15.04±0.81	15.03±0.8
SG250113_P4	Sofía	7033633	476292	Pervasive		
SG14161	Ladera Farellón	7034077	474332	Vein	2.0±1.7	17.7±2.2
SG14166	Pompeya	DPMP-032, 402.42 m.		Vein	16.44±0.27	16.34±0.25
SG16257	Coipa Norte	CND-219, 299.55 m.		Vein	13.76±0.27	13.72±0.34
SG16271	Brecha Norte	BND-01, 156.6 m.		Pervasive	14.64±0.7	14.1±1.3
SG16274	Can Can	CCD-01, 385.3m.		Vein	17.47±0.32	17.17±0.34
SG16290	Purén Phase I	DPU-087, 31.7m.		Pervasive	18.01±0.57	18.9±1.2
SG16293	Pompeya Sur	DPMP-113, 321.98m.		Vein	30.42±0.88	31.2±1.6
SG16303	Purén Sur	DPU-243, 440m.		Vein	18.33±0.56	19.09±0.87

Table 4.4: Summary of K/Ar ages on alunite obtained in previous studies

Sample no	Location	K_2O (%)	$^{40}Ar^*$ (mole/g)	$^{40}Ar^*/\Sigma^{40}Ar$	Age (Ma) (± 2σ)	Ref.
MAAC-82-2	Ladera Farellón	2.92	8.54139×10^{-11}	57.7	20.2±1.2	(1)
MAAC-88-4	Brecha Norte	3.76	9.38430×10^{-11}	43.2	17.3±1.0	(1)
	Ladera Farellón				15.4±0.7	(2)
	Unknown				15.5±0.5	(2)
FD-14	Can Can	6.159 (K%)	4.418 (nl/g)		18.4±0.7	(3)
AK1339	Coipa Norte	4.771 (K%)	3.3841 (nl/g)		18.2±2.3	(4)
AK1331	Can Can	1.254 (K%)	0.6501 (nl/g)		13.3±2.0	(4)

(1) Sillitoe et al., 1991. (2) Oviedo et al., 1991. (3) Moscoso et al., 1992. (4) King, 1992.

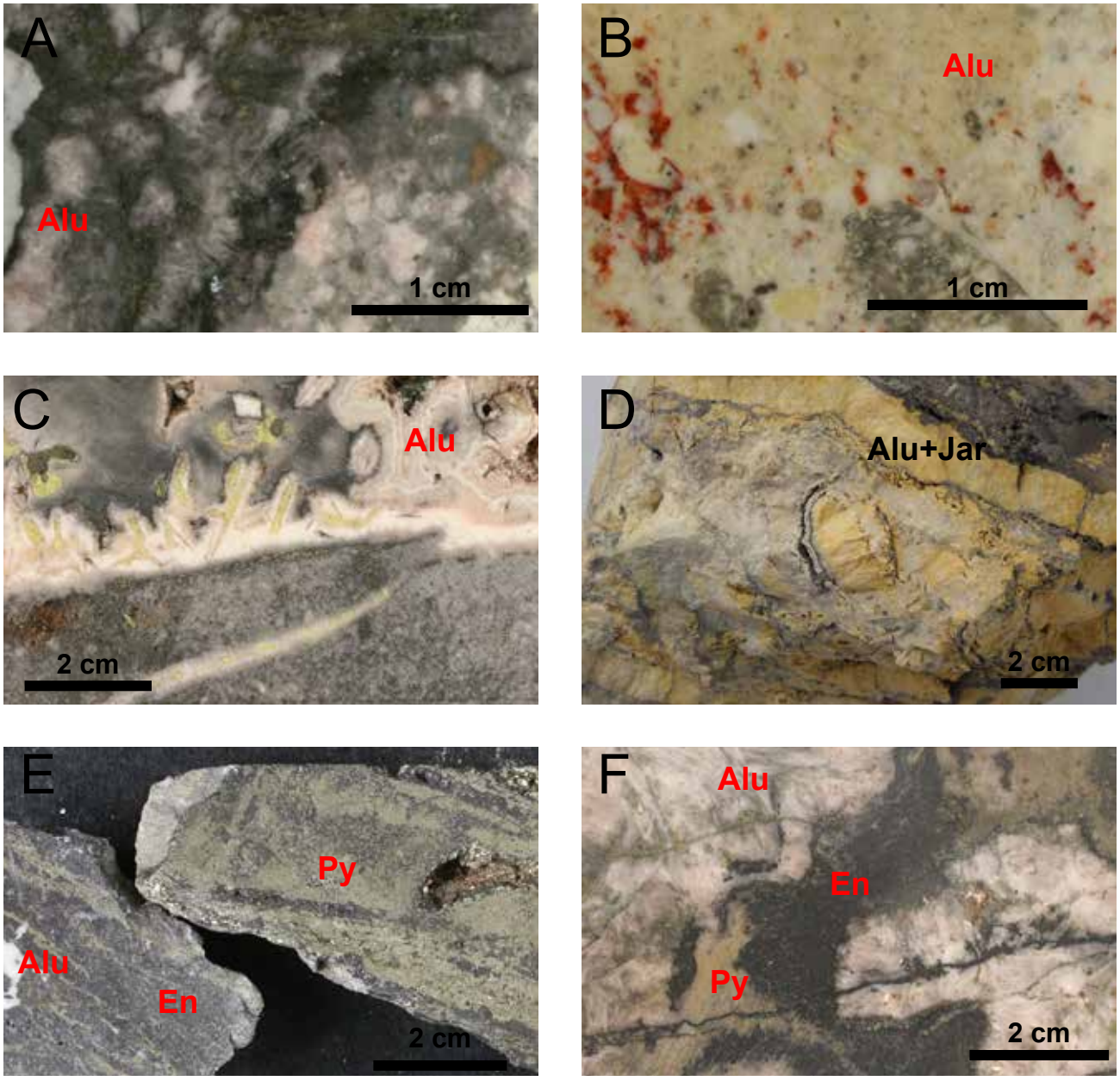

Figure 4.38. Photographs of alunite samples dated by $^{40}Ar/^{39}Ar$ geochronology (Part I). **(A)** sample SG16293, Pompeya Sur prospect. **(B)** sample SG16290, Purén Phase I. **(C)** sample SG16303, Purén Sur prospect. **(D)** sample SG14161, Ladera Farellón open pit. **(E)** sample SG16274, Can Can open pit. **(F)** sample SG14166, Pompeya prospect.
Abbreviations: (Alu) alunite, (En) enargite, (Jar) jarosite, (Py) pyrite.

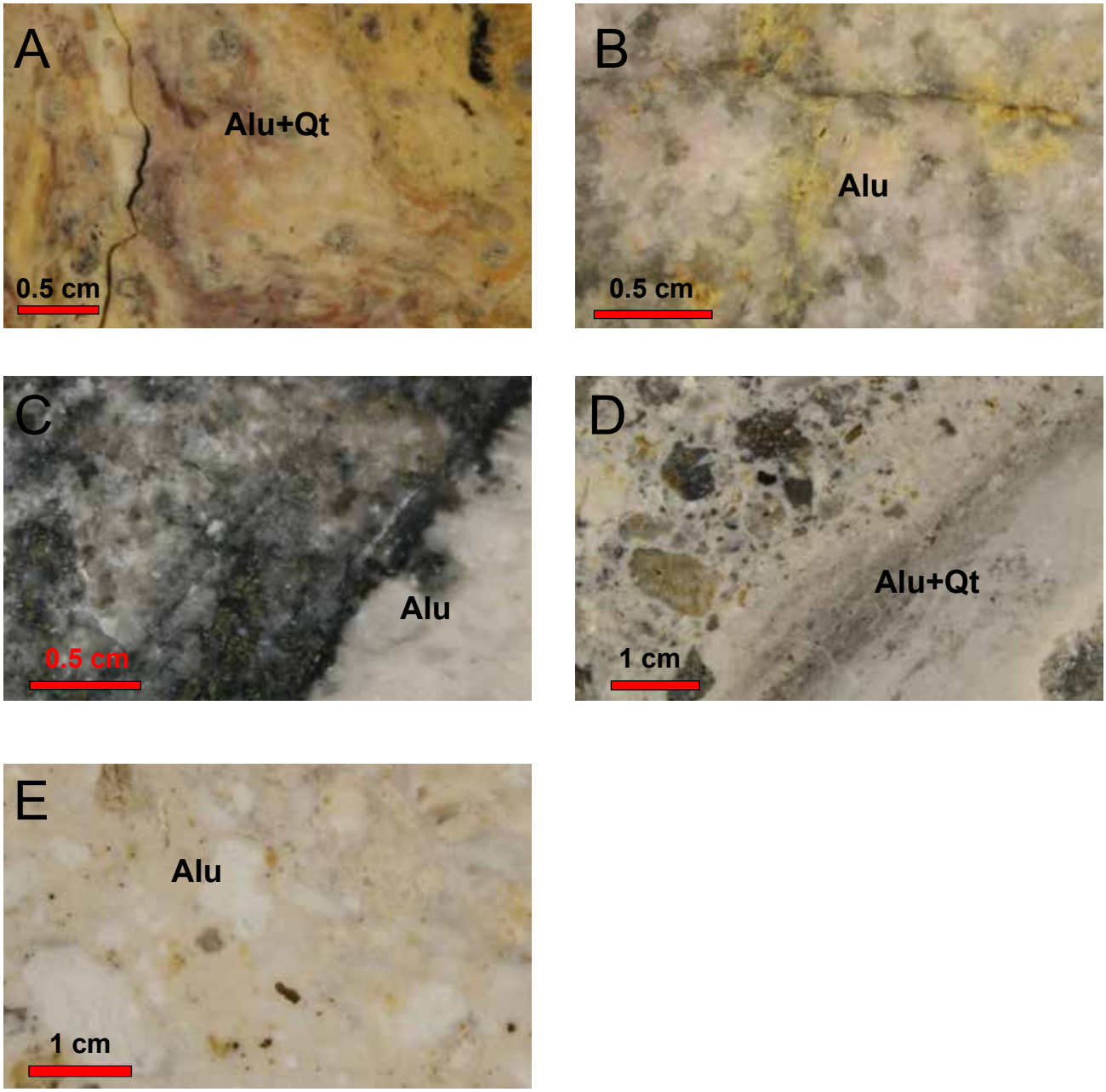

Figure 4.39. Photographs of alunite samples dated by $^{40}Ar/^{39}Ar$ geochronology (Part II). **(A)** sample SG090313_P4, Maritza prospect. **(B)** sample SG16271, Brecha Norte open pit. **(C)** sample SG16257, Coipa Norte open pit. **(D)** sample SG090313_P3, Codocedo area. **(E)** sample SG250113_P4, Sofía prospect.
Abbreviations: (Alu) alunite, (Qt) quartz.

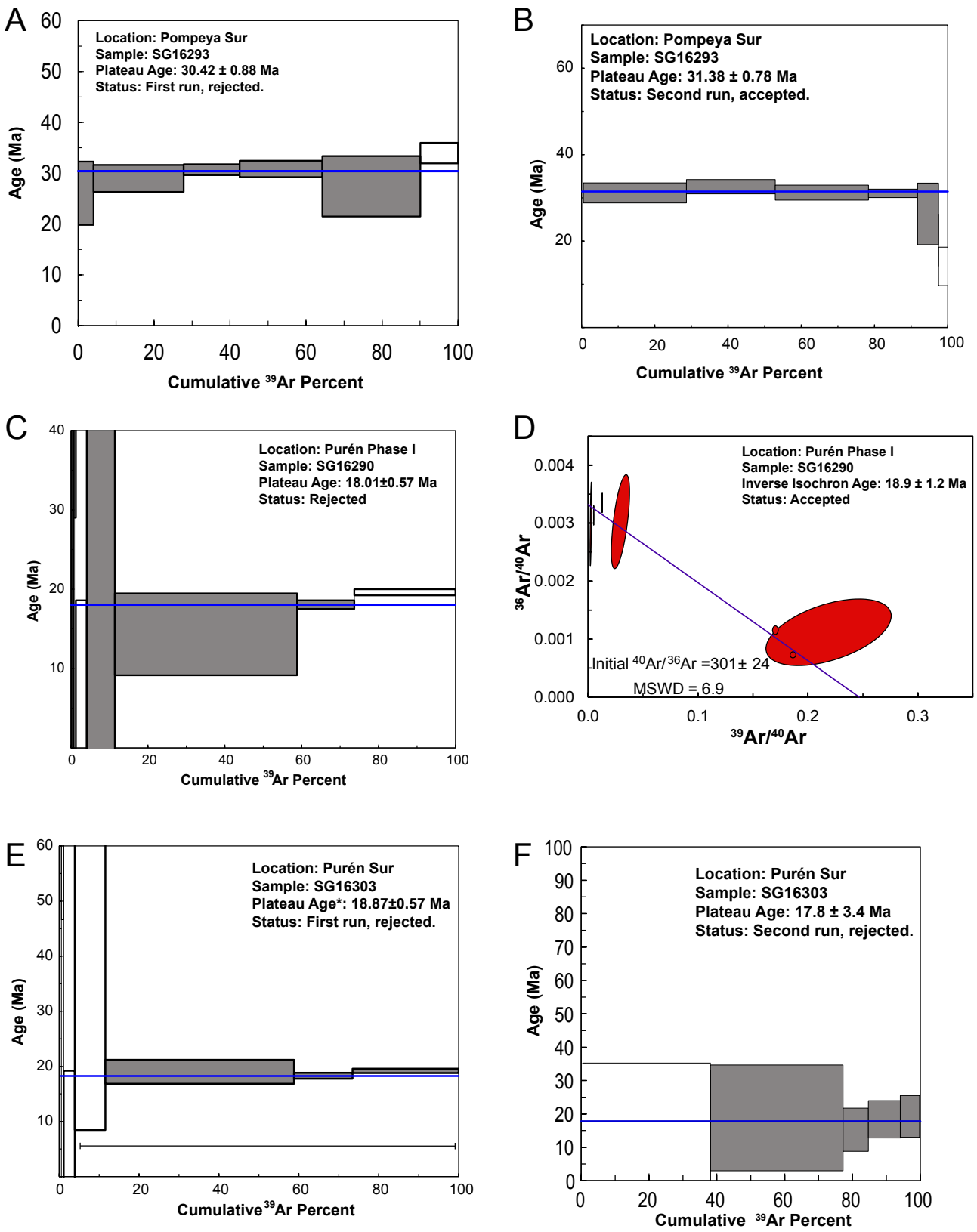

Figure 4.40. $^{40}Ar/^{39}Ar$ results for alunite samples (Part I). **(A)** Age plateau for sample SG16293 (first run). **(B)** Age plateau for sample SG16293 (second run). **(C)** Age plateau for sample SG16290. **(D)** Inverse Isochron age for sample SG16290. **(E)** Age plateau for sample SG16303 (first run). **(F)** Age plateau for sample SG16303 (second run).

and inverse scattered isochrons respectively. The inverse isochron age of **18.9±1.2 Ma** is considered the best estimate for this sample (Figure 4.40.D).

Purén Sur (Sample SG16303)

The alunite sample collected from the Purén Sur prospect is characterized by a coarse-grained crustiform pink alunite precipitated in an alunite+barite+quartz+pyrite+native sulfur vein (Figure 4.38.C). The host rock is altered to fine-grained quartz+alunite. Two runs were performed for this sample. According to the criteria used by Isoplot to calculate a plateau age, the two runs yielded imprecise ages of 18.33±0.56 and 17.8±3.4 Ma (Figures 4.40.E and F). The second run presented a very low ^{39}ArK volume, explaining the large uncertainty observed in this analysis. A second aliquot was analyzed at the Université de Genève. This run showed a highly variable plateau age of 22.03±0.57 Ma that considered only 30% of the ^{39}Ar (Figure 4.41.A). The rest of steps showed younger ages. The inverse isochron restricted to the last four steps yielded a 17.73±5.84 Ma age suggesting that the 22.03 Ma plateau age is older than the true age due to excess ^{40}Ar.

The divergent ages obtained between different runs and between the two labs can be partially explained by the presence of two domains of alunite differing in their relative Na and K content (Figure 4.42). The analytical uncertainty of disturbed plateau ages and the variability observed between each run, do not allow an interpreted age for this alunite sample.

Ladera Farellón (Sample SG14161)

This alunite sample was collected from the bottom of the Ladera Farellón deposit. Here, alunite+jarosite+scorodite veins are cross-cutting fine-grained sedimentary rocks of the Triassic Estratos El Mono unit (Figure 4.38.D). These rocks are altered to fine-grained alunite+quartz. Pale yellow coarse-grained alunite from one of these veins yielded a plateau age of 2.0±1.7 Ma (considering the lower temperature four steps; Figure 4.41.B). This younger age is interpreted as a

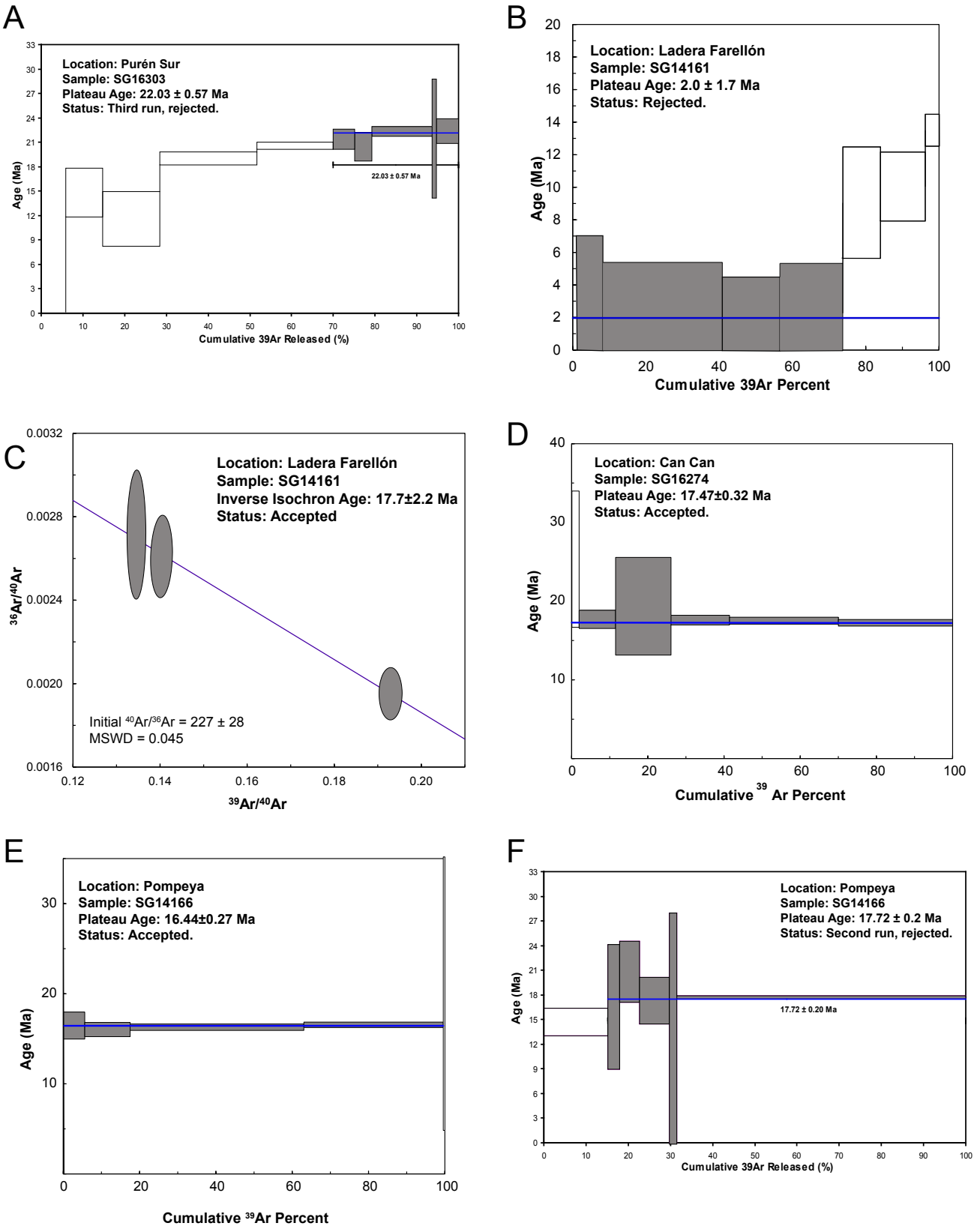

Figure 4.41. $^{40}Ar/^{39}Ar$ results for alunite samples (Part II). (A) Age plateau for sample SG16303 (third run). **(B)** Age plateau for sample SG14161. **(C)** Inverse Isochron age for sample SG14161. **(D)** Age plateau for sample SG16274. **(E)** Age plateau forsample SG14166 (first run). **(F)** Age plateau for sample SG14166 (second run).

weathering event evidenced by the presence of jarosite and scorodite. However, taking into account the last three steps (higher temperature), an inverse isochron age of **17.7±2.2 Ma** is considered the best estimate for the age of the coarse-grained alunite (Figure 4.41.C).

Can Can (sample SG16274)

In the Can Can deposit, an alunite sample was collected from a vein filled by alunite+quartz+pyrite+enargite (Figure 4.38.E). This alunite sample is characterized by white pseudo-cubic medium-grained alunite. This vein is cross-cutting quartz-rich sandstones (Estratos El Mono unit) altered to coarse-grained tabular alunite. This sample yielded a well-defined plateau age of **17.47±0.32 Ma** calculated with five steps that include 98% of the ^{39}Ar (Figure 4.41.D). The normal and inverse isochron both yielded a 17.17±0.34 Ma age, which is similar to the plateau age, although excess argon is suggested by the slightly elevated initial $^{40}Ar/^{36}Ar$ of 310±8.9. The plateau age is considered the best estimate for this sample.

Pompeya (sample SG14166)

The alunite sample collected at the Pompeya prospect corresponds to a coarse-grained pink alunite precipitated in a vein together with enargite and pyrite (Figure 4.38.F). This vein cross-cut s a fragmental volcanic rock. This sample yielded a well-defined plateau age of 16.4±0.27 Ma consisting of four steps that include 99.95% of the ^{39}Ar release (Figure 4.41.E). Normal and inverse isochrons showed a similar age that validate the plateau age as the best estimation for this sample. Alunite grains from the SG14166 sample were also analyzed at the Université de Genève. This run showed a plateau age of 17.7±0.2 Ma, slightly older than the first run (Figure 4.41.F). The plateau obtained at Université de Genève is more variable than the one obtained at PCIGR and the first two steps of this run showed younger ages around 16.5 Ma.

The analytical variability observed between the two laboratories can not be explained by heterogeneous alunite, as was the case for sample SG16303. The alunite from Pompeya is very homogeneous in composition and grain-size (Figure 4.42). Considering also that the normal and

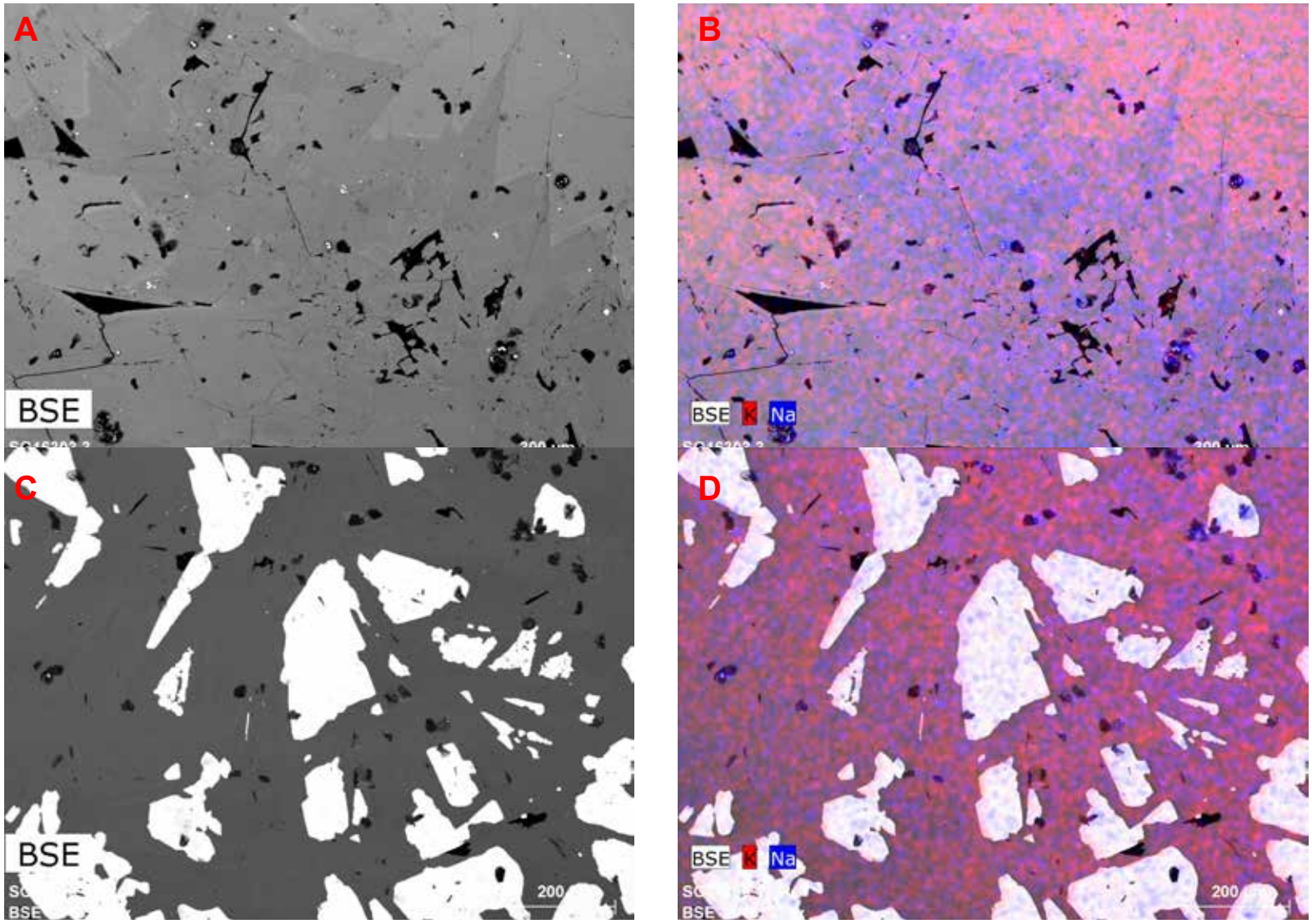

Figure 4.42. Scanning Electrom Microscopy (SEM) images of alunite samples. A) and B) Sample SG16303, Backscattered electron image and K-Na mineral mapping. Coarser crystals at the top and left side of the image show higher K content compared to the center of the image. C) and D) Sample SG14166, BSE image and element map showing homogeneous composition of tabular alunite crystals.

inverse isochrons of the first run match the well defined plateau age closely, the **16.4±0.27 Ma** age of the first run is considered the best estimate for this sample.

Martiza (sample SG090313_P4)

At the Maritza prospect, a surface sample of alunite collected in a fine-grained volcaniclastic rock altered intensely to pervasive alunite+quartz (Figure 4.39.A) was analyzed in two runs. The first run yielded a three steps plateau age of 15.04±0.81 Ma, from which only the middle step released 67.63% ^{39}Ar (Figure 4.43.A). The outermost steps showed less precise but similar ages. Normal and inverse isochrons both yielded a 15.03±0.8 Ma age. The second run revealed an argon loss at the low temperature steps, leaving a plateau age of 14.62±0.37 Ma consisting of the higher temperature four steps (Figure 4.43.B). Normal and inverse isochron showed slightly older ages of 14.93±0.8 and 14.96±0.84 Ma respectively. The preferred age for this unit corresponds to the **15.04±0.81 Ma** plateau age obtained for the first run.

Brecha Norte (sample SG16271)

At Brecha Norte, the alunite sample is characterized by a medium-grained pink alunite which is replacing plagioclase phenocrysts in a quartz-plagioclase sandstone rock of the Triassic Estratos El Mono unit (Figure 4.39.B). This sample yielded a plateau age of 14.64±0.7 Ma, which is constituted by eight steps that include 99.97% of the ^{39}Ar release (Figure 4.43.C). Normal and inverse isochrons showed slightly younger ages of 14.0±1.3 and 14.0±1.3 Ma respectively. The preferred age corresponds to the **14.64±0.7 Ma** plateau age.

Coipa Norte (sample SG16257)

The alunite from the Coipa Norte open pit consists of a medium-grained pseudo-cubic white alunite precipitated in a vein of quartz+alunite (Figure 4.39.C). This vein cross-cuts sandstones of the Estratos El Mono unit. These rocks are also moderately altered to pervasive alunite. Two runs were performed for this sample. The first analysis yielded a 13.76±0.27 plateau age consisting of

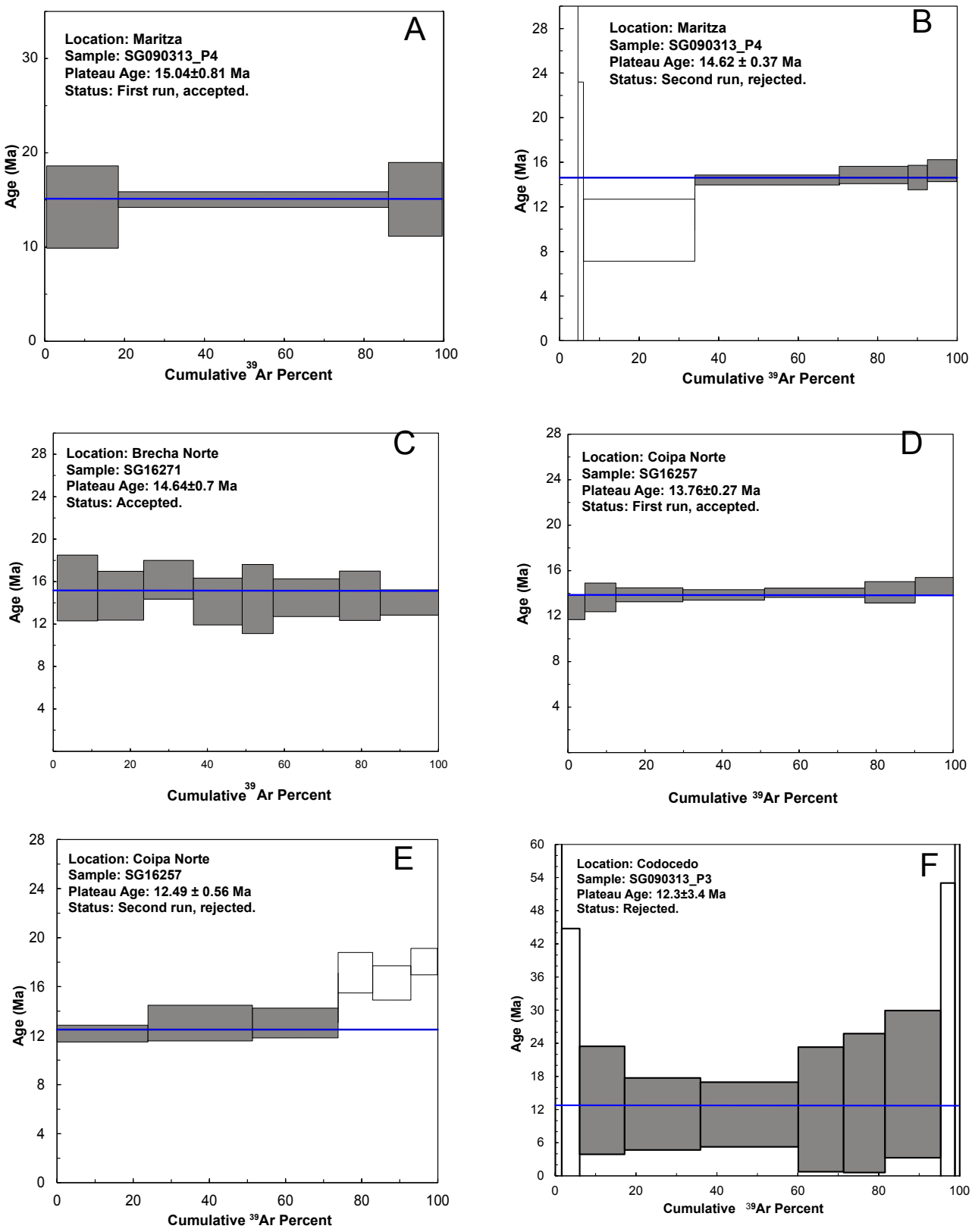

Figure 4.43. $^{40}Ar/^{39}Ar$ geochronology for alunite samples (Part III). **(A)** First plateau run for sample SG090313_P4 **(B)** Second plateau run of sample SG090313_P4. **(C)** Plateau age for sample SG16271. **(D)** First plateau run of sample SG16257. **(E)** Second plateau run for sample SG16257. **(F)** Plateau age of sample SG090313_P3.

seven steps that encompass 100% of the ^{39}Ar release (Figure 4.43.D). A similar age of 13.72±0.34 Ma was obtained with the normal and inverse isochron. The second run gave younger ages for the high temperature steps. Using an initial $^{40}Ar/^{36}Ar$ ratio of 280±21, the plateau age calculated yielded a 12.49±0.56 Ma age consisting of three steps that include 73.9% of the ^{39}Ar release (Figure 4.43.E). The plateau age of **13.76±0.27 Ma** from the first run is considered the best estimate for this sample.

Codocedo (sample SG090313_P3)

The alunite sample from the Codocedo prospect was collected from a volcaniclastic unit of the Pompeya pyroclastics, which is pervasively altered to quartz+alunite (Figure 4.39.D). This sample yielded an imprecise plateau age of 12.3±3.4 Ma (Figure 4.43.F). The initial $^{40}Ar/^{36}Ar$ of 246.6±6.2 suggests possible analytical issues with significantly higher atmospheric 36Ar. The age estimated for this sample is not considered a geologically meaningful age.

Sofía (sample SG250113_P4)

An alunite sample from a pervasively altered pyroclastic rock of the Pompeya Pyroclastics (Figure 4.39.E) unit from the Sofía prospect was attempted but no meaningful result was obtained.

Figure 4.44 summarizes the U-Pb and $^{40}Ar/^{39}Ar$ radiometric ages obtained in the present study, illustrating the wide variation of ages interpreted for La Coipa district, including the ages of magmatism and hydrothermal alteration.

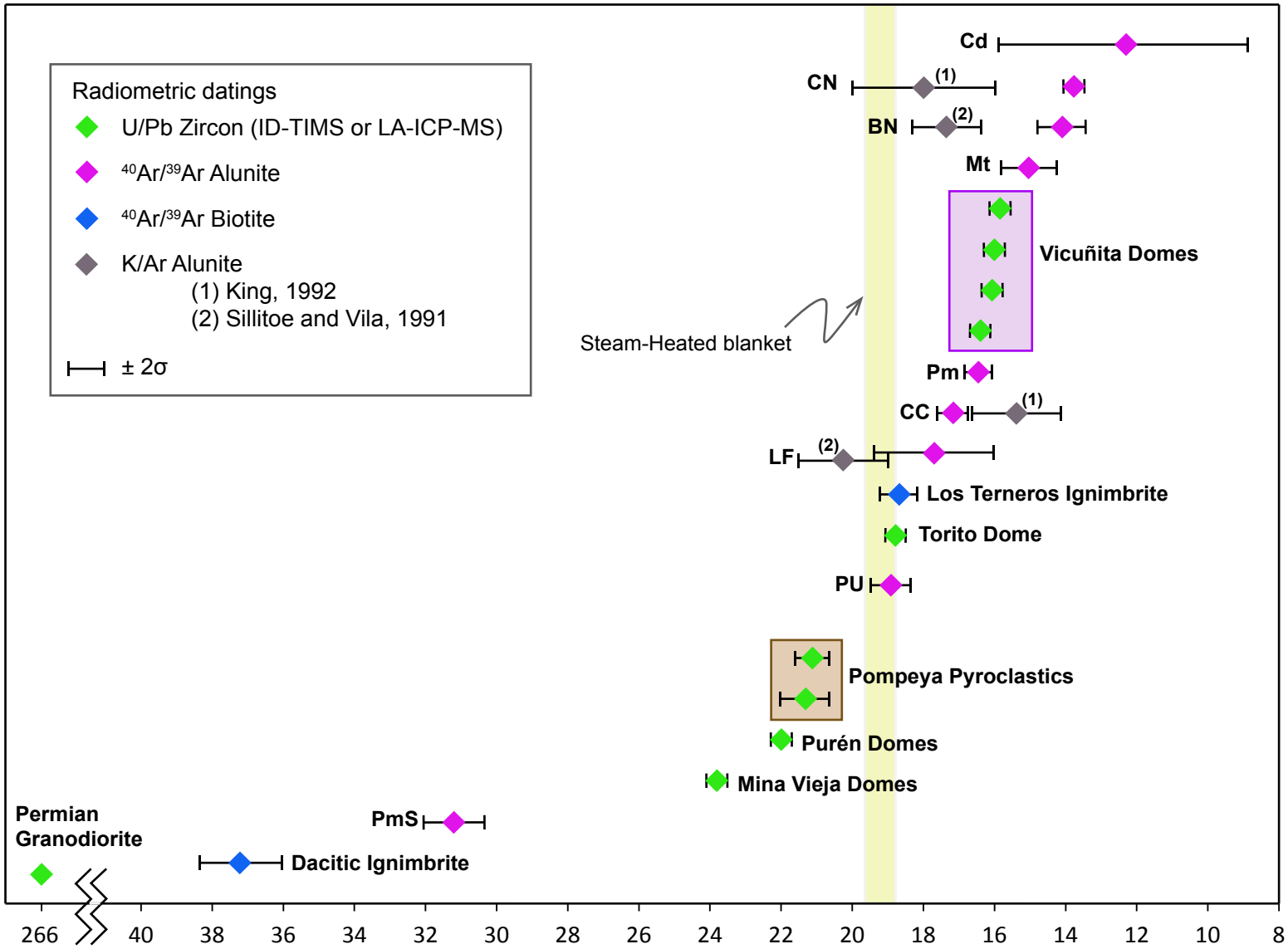

Figure 4.44. Summary of geochronological ages obtained at La Coipa district. Previously published ages are also included. Yellow box indicates the steam-heated age range obtained by 40Ar/39Ar on alunite from the Purén Phase I area.
Abbreviations: BN: Brecha Norte; CC: Can Can; Cd: Codocedo; CN: Coipa Norte; Mt: Maritza; Pm: Pompeya; PmS: Pompeya Sur; PU: Purén Phase I.

4.9 Sulfur Isotopes on alunite and adjacent sulfur-bearing minerals

According to the classification of Rye et al., (1992), alunite can precipitate within four environments: magmatic-hydrothermal, magmatic-steam, steam-heated, and supergene. Isotopically, it will be shown that the four types of alunite proposed by Rye et al. (1992) have been recognized between the samples analyzed by $^{40}Ar/^{39}Ar$ geochronology.

For those samples analyzed by $^{40}Ar/^{39}Ar$ alunite geochronology, handpicked grains of alunite and adjacent sulfur-bearing minerals such as pyrite, enargite, and native sulfur were analyzed for their $\delta^{34}S$ composition. Alunite shows a wide variation of $\delta^{34}S$ values that range between 0.6 and 26.3‰ (see table 4.5). Pyrite and enargite yielded $\delta^{34}S$ values that range between -8.9 and 1.2‰. The single sample of native sulfur yielded a $\delta^{34}S$ value of -7.9‰ (see Table 4.5).

Coarse-grained pink alunites precipitated within veins or replacing crystals and matrix yielded $\delta^{34}S$ values between 15.1 and 26.3‰. This group includes samples from Pompeya, Pompeya Sur, Purén Sur, Brecha Norte, Maritza, and Codocedo. For those samples with coexisting sulfides (Pompeya, Pompeya Sur, and Purén Sur), pyrite has the most negative values of $\delta^{34}S$, ranging between -0.4 and -8.9‰. A second group is formed by pseudo-cubic medium-grained white alunite precipitated in veins with pyrite+enargite (Can Can) or with quartz (Coipa Norte). Both alunite samples are characterized by lower $\delta^{34}S$ values that range between 0.6 and 3.7‰. Sulfides adjacent to these alunite samples have barely negative to positive $\delta^{34}S$ values that vary between -0.2 and 1.2‰. A third group is constituted by alunite samples collected from the steam-heated level. Samples taken from the Purén Phase I and the Sofía prospect are characterized by fine-grained alunite intergrown with quartz and kaolinite. These samples are characterized by lower values of $\delta^{34}S$, ranging between 1.8 and 2.6‰. No sulfides were present in these samples. A distinctive value was obtained in the Ladera Farellón alunite. Here, the $\delta^{34}S$ showed an 8.6‰ value.

Table 4.5: $\delta^{34}S$ Isotopic composition of sulfur-bearing minerals analyzed in the present study.

Sample no	Location	$\delta^{34}S$ ‰ vs VCDT			
		Alunite	Pyrite	Enargite	Native Sulfur
SG090313_P3	Codocedo	15.1			
SG090313_P4	Maritza	18.7			
SG250113_P4	West side Cerro La Coipa	1.8			
SG14161	Ladera Farellón	8.6			
SG14166	Pompeya	26.3	-0.4		
SG16257	Coipa Norte	0.6	1.2		
SG16271	Brecha Norte	21.3			
SG16274	Can Can	3.7		-0.2	
SG16290	Purén	2.6			
SG16293	Pompeya Sur	20.9	-8.9		
SG16303	Purén Sur	17.5	-6.8		-7.9
SG16320_Alu	Duplicate of SG16257	0.9			

The variation of $\delta^{34}S$ values obtained from alunite samples corroborates the textural variations observed in the field and the origin interpreted for each sample. The most abundant group corresponds to the coarse-grained pink alunites, which are characterized by $\delta^{34}S>15$ ‰, indicating a magmatic-hydrothermal origin (Rye et al., 1992). The group of pseudo-cubic white alunite, which is precipitated in veins, has $\delta^{34}S$ values that indicate a magmatic steam origin. The alunites collected from the steam-heated level have $\delta^{34}S$ values that belong to the steam-heated field proposed by Rye et al. (1992). Finally, the intermediate $\delta^{34}S$ value obtained from the Ladera Farellón open pit suggests a combination of supergene and hypogene processes.

The isotopic signature of sulfide-sulfate pairs can be represented in a $\delta^{34}S_{sulfate}$- $\delta^{34}S_{sulfide}$ diagram created to interpret the isotopic exchange between sulfur-bearing minerals (Fifarek, 2003; Fifarek and Rye, 2005). In this diagram, isotherms of equilibration between alunite and pyrite are represented by straight lines with negative slopes. These isotherms vary between 200 and 400°C (Fifarek and Rye, 2005), besides a theoretical upper temperature limit isotherm that gathers those pairs where the sum of the $\delta^{34}S$ values for coexisting species is zero (Rye, 2005). Ohmoto and Rye (1979) established a formula to calculate the equilibrium temperature (Equation 5.1), where the temperature is expressed in Kelvin units, and $\alpha_{alun(SO_4)\text{-}H_2S} = (\delta^{34}S_{sulfate} + 1000)/(\delta^{34}S_{sulfide} + 1000)$.

$$10^3 \ln \alpha_{alun(SO_4)\text{-}H_2S} = 5.26 \times 10^6 T^{-2} + 6.0 \quad \text{(Eq. 5.1)}$$

Sulfide-sulfate pairs from La Coipa District are plotted in Figure 4.45. Oxidized samples of alunite without sulfides are also included in this diagram at the top for comparison. Magmatic-hydrothermal alunite/pyrite pairs from Pompeya and Pompeya Sur gave temperatures of 234°C and 197°C respectively, whereas the alunite/pyrite pair from Purén Sur has a calculated equilibrium temperature of 264°C. The application of this equation to the samples from Coipa Norte and Can Can is not feasible due to the lower difference of the $\delta^{34}S$ value between alunite and pyrite which would yield temperatures above the theoretical stability limit for alunite. Isotopic disequilibrium is assumed for these.

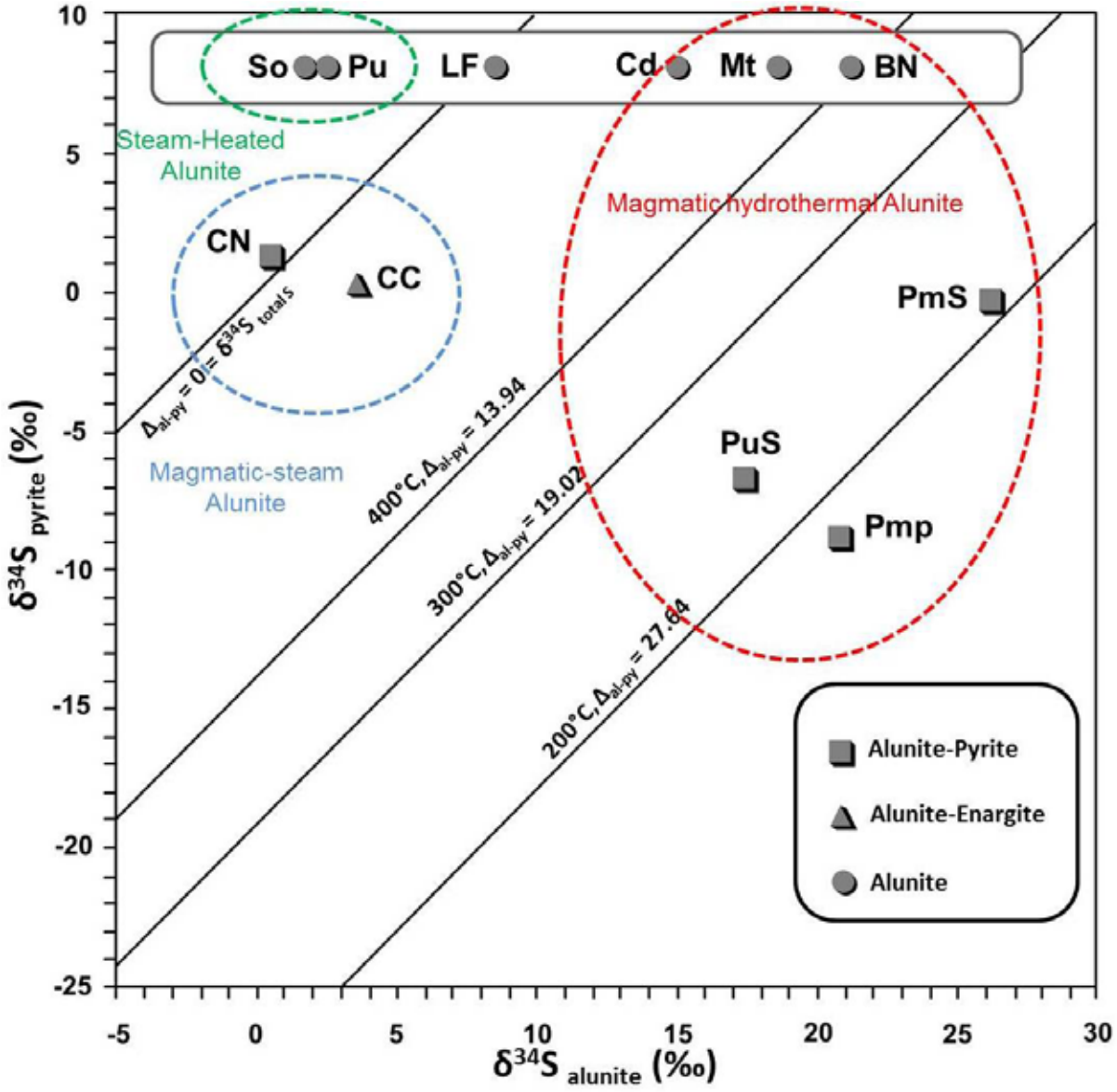

Figure 4.45. Sulfide-sulfate pairs of $\delta^{34}S$ for alunite and its associated sulfide minerals (pyrite or enargite) samples considered for $^{40}Ar/^{39}Ar$ geochronology. Oxidized samples are plotted at the top of the diagram to illustrate the value of the $\delta^{34}S$ for alunites.

Chapter 5: Whole-Rock Geochemistry of the La Coipa district

A total of 22 analyses of whole-rock geochemistry were performed on volcanic, hypabyssal and intrusive rocks representative of the most important magmatic episodes recorded in the study area (see Appendices A7, A8, and A9). Samples were collected from unaltered rocks where possible, or from the least altered outcrops in case of lithological units with hydrothermal alteration. Figure 5.1 shows the location of surface and drill-core samples considered for whole-rock geochemistry.

To exclude significantly altered rocks from the petrogenetic interpretation, a combination of two numeric indexes defined to quantify hydrothermal alteration was used. Figure 5.2 shows an alteration diagram proposed by Williams and Davidson (2004), which plots the Advanced Argillic Alteration Index (AAAI) versus the Alteration Index (AI), which are calculated according to Equations 5.1 and 5.2 respectively.

$$AAAI = 100x\frac{SiO_2}{SiO_2 + (10xMgO) + (10xCaO) + (10xNa_2O)} \quad \text{(Eq. 5.1)}$$

$$AI = 100\ x\ \frac{K_2O + MgO}{K_2O + Na_2O + CaO + MgO} \quad \text{(Eq. 5.2)}$$

The AAAI illustrates the type and intensity of advanced argillic alteration associated with hydrothermal systems with high-sulfidation characteristics, such as a type of volcanic-hosted massive sulfide (VHMS) and epithermal deposits (Williams and Davidson, 2004). The AI value was defined to quantify the intensity of sericitic and chloritic alteration, besides the CaO and Na_2O depletion associated with the feldspar destruction (Ishikawa et al., 1976). This diagram indicates the trend estimated from unaltered distal rocks (box in the middle of the diagram), passing through the kaolinite and muscovite zone (upper right of the diagram), finishing in the pyrophyllite+quartz zone (upper left of the diagram), the latter commonly being related to mineralization (Williams and Davidson, 2004). Geochemical data from the present study plotted in this alteration diagram reveal that three samples are outside the field defined for the least altered rocks (Figure 5.2). These samples (SG190213_P16, SG16305, and SG16263) will not be considered in the following analysis.

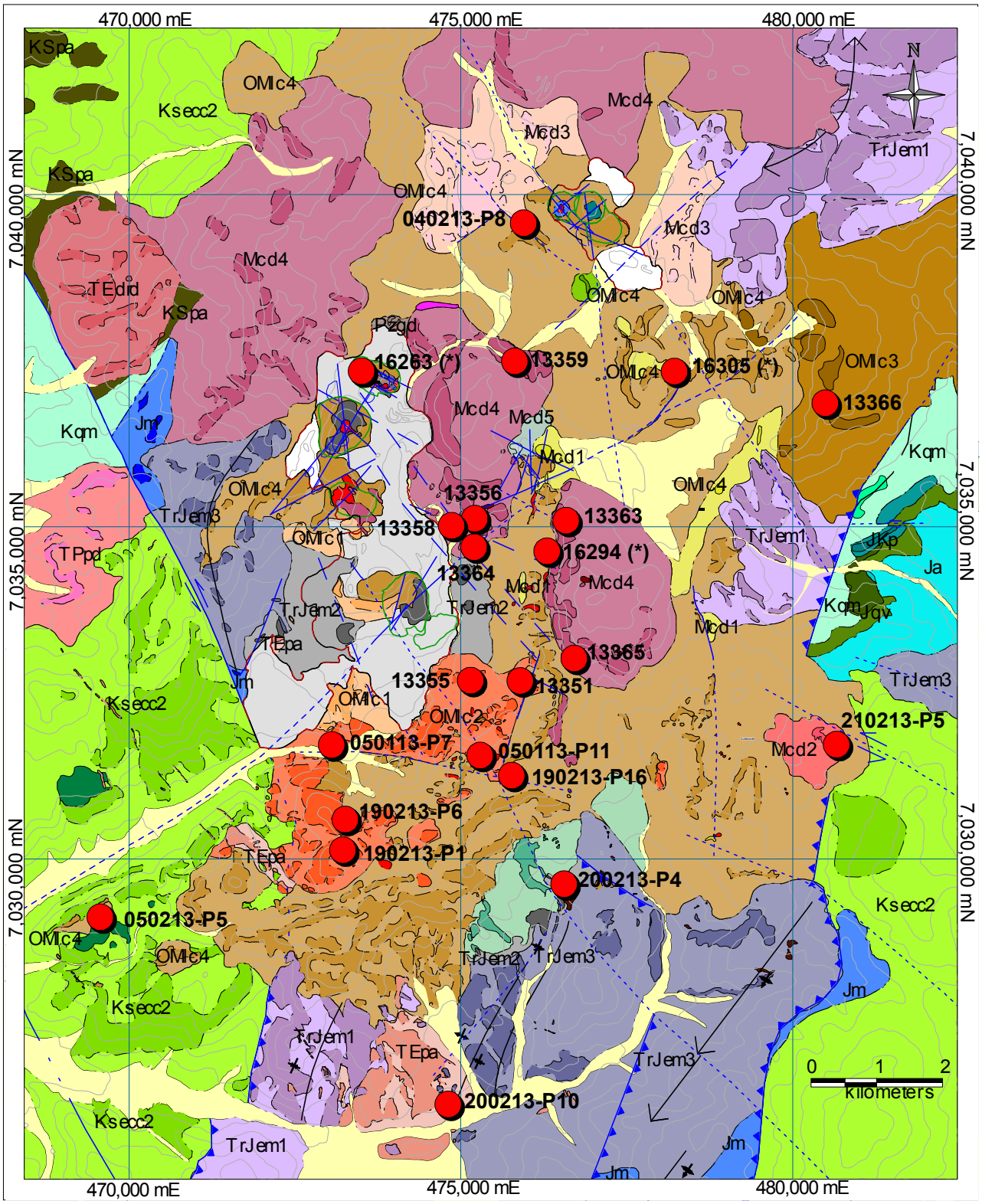

Figure 5.1. Location map of samples analyzed by whole-rock geochemistry. Drill-hole samples indicated by the (*) symbol.

5.1 Major-element compositions

The composition of two basement igneous rocks was determined using the R1-R2 diagram for plutonic rocks (De la Roche et al., 1980; Figure 5.3). The sample from the Permian Granodiorite (SG16263), which plots along the boundary between the granite and granodiorite fields, is considered a granodiorite for consistency with the nomenclature given by mine geologists. The Late Cretaceous-early Paleocene Codocedo Gabbro (KTgb) is the most mafic rock identified in the study area (SiO_2 = 53.74 wt. %).

According to the classification of K_2O vs. SiO_2 (Peccerillo and Taylor, 1976), the Tertiary hypabyssal and pyroclastic rocks belong to the calc-alkaline to high-K calc-alkaline series (Figure 5.4). Two Eocene samples from the Dacitic Ignimbrite (TEdi) and the Rhyodacitic Porphyry (TEpa) units belong to the calc-alkaline field, where also the Purén Domes (OMlc3) and Pompeya Pyroclastics (OMlc4) plot. Among the units of the La Coipa Group, some of the Mina Vieja Domes (OMlc2) plot in the calc-alkaline and high-K calc-alkaline fields, the other units being restricted to the calc-alkaline field. Similarly, among the units of the Codocedo Group, samples from the Vicuñita Domes (Mcd4) are mostly high-K calc-alkaline, whereas other units of the Codocedo Group such as the Torito Dome (Mcd2) and the Los Terneros Ignimbrite belong to the calc-alkaline field (Figure 5.4).

Based on the TAS diagram for volcanic rocks (Le Maitre et al., 1989), hypabyssal and pyroclastic Tertiary rocks show a predominance of dacitic compositions (64.77 wt. % < SiO_2 < 70.71 wt.%; Figure 5.5). Samples with SiO_2 >70wt.% present weak to moderate silicification, which together with a petrographic criteria, suggest a primary dacitic to rhyodacitic composition of these samples.

Major elements are shown in a series of Harker diagrams and compared to approximately a thousand of published analyses from the Maricunga, El Indio and El Teniente-Los Pelambres belts (Figure 5.6). Considering the samples from La Coipa, K_2O (1.8 - 4.7 wt. %) is the only element that

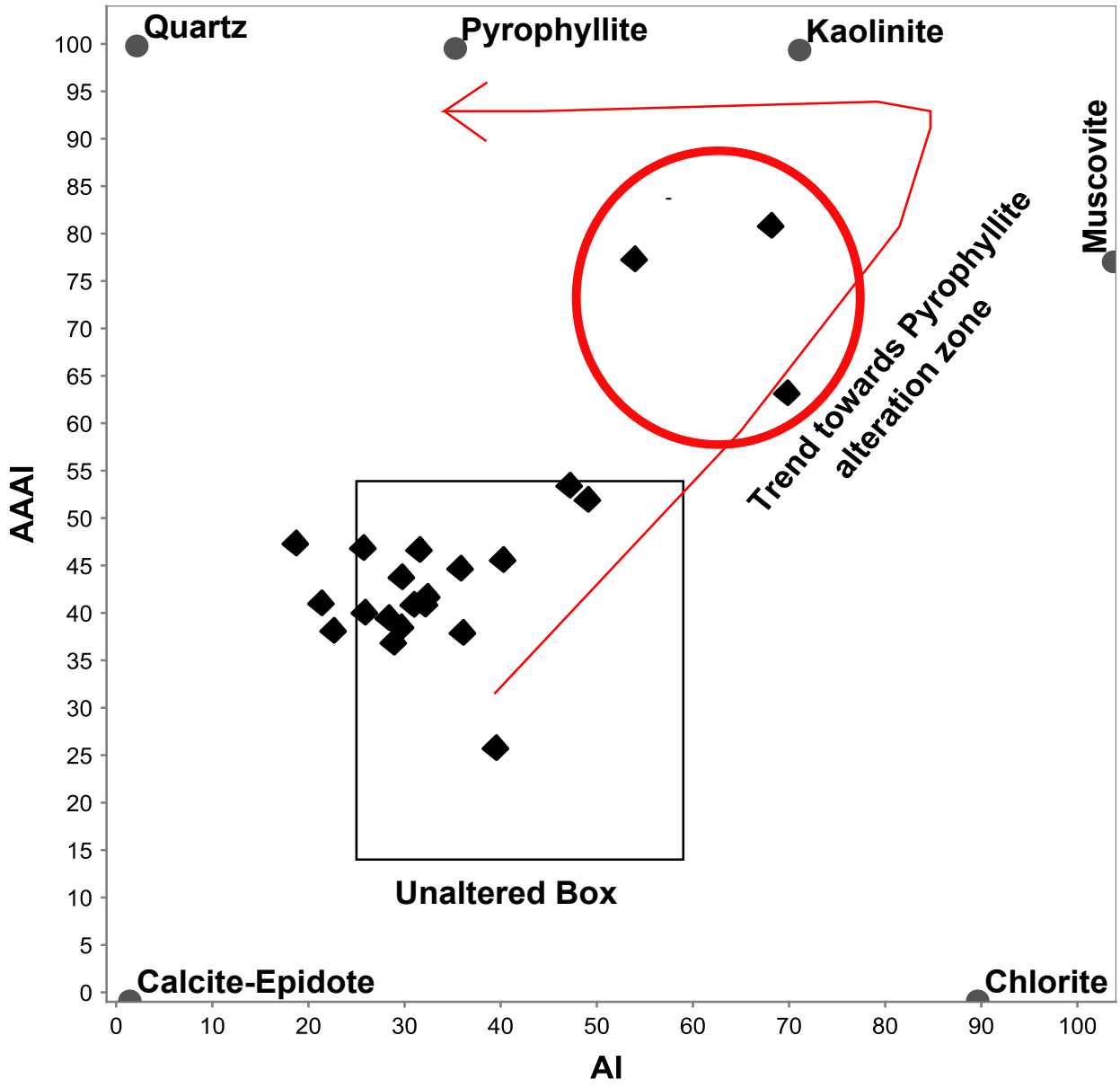

Figure 5.2. Alteration Diagram (from Williams and Davidson, 2004) applied to whole-rock analysis of samples from La Coipa District. This diagram utilizes the AAAI (Advanced argillic alteration Index; Williams and Davidson, 2004) v/s the AI (Alteration Index, Ishikawa et al., 1976). Samples that fall into or near the unaltered box are considered for later geochemical interpretations. Samples within the red circle are considered altered and not used in following diagrams.

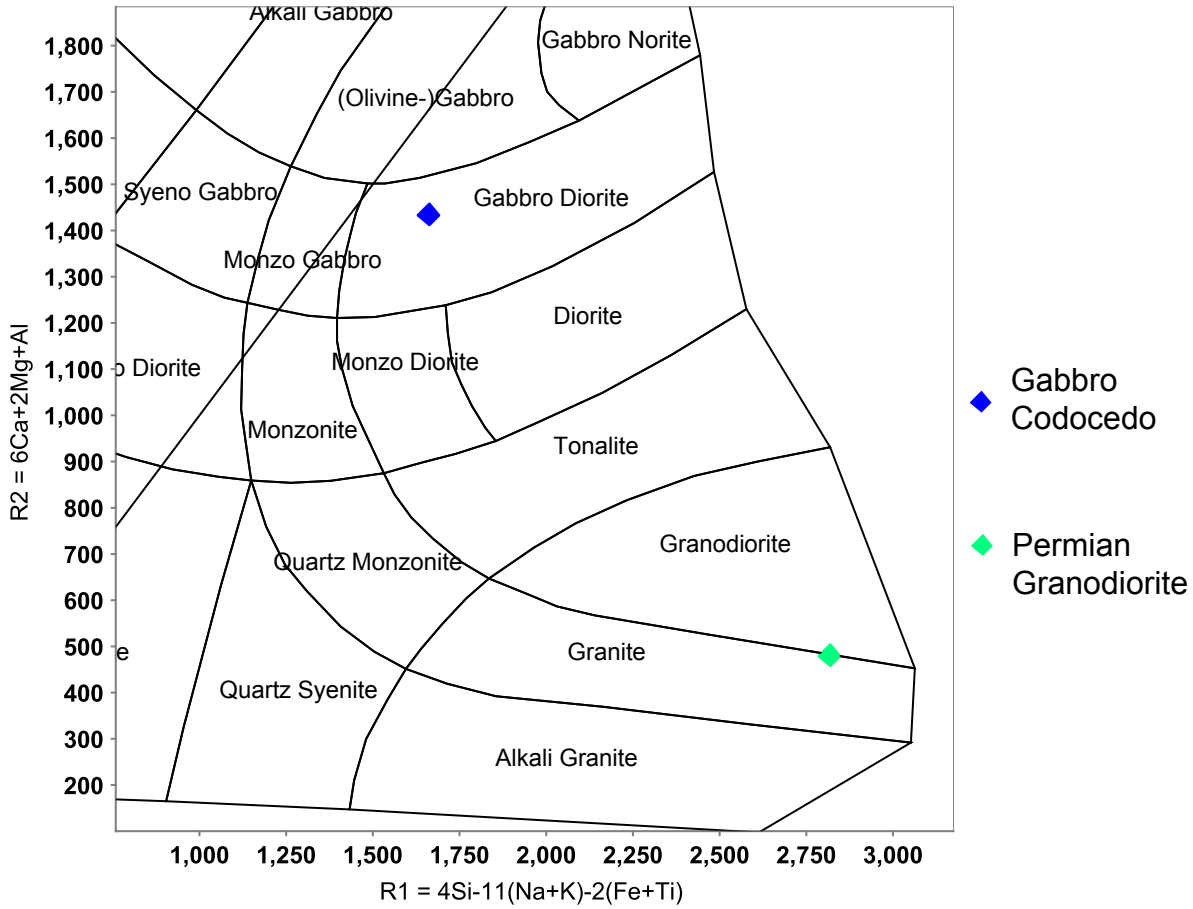

Figure 5.3. R1-R2 Diagram (from De La Roche, 1980) for plutonic rocks from La Coipa district.

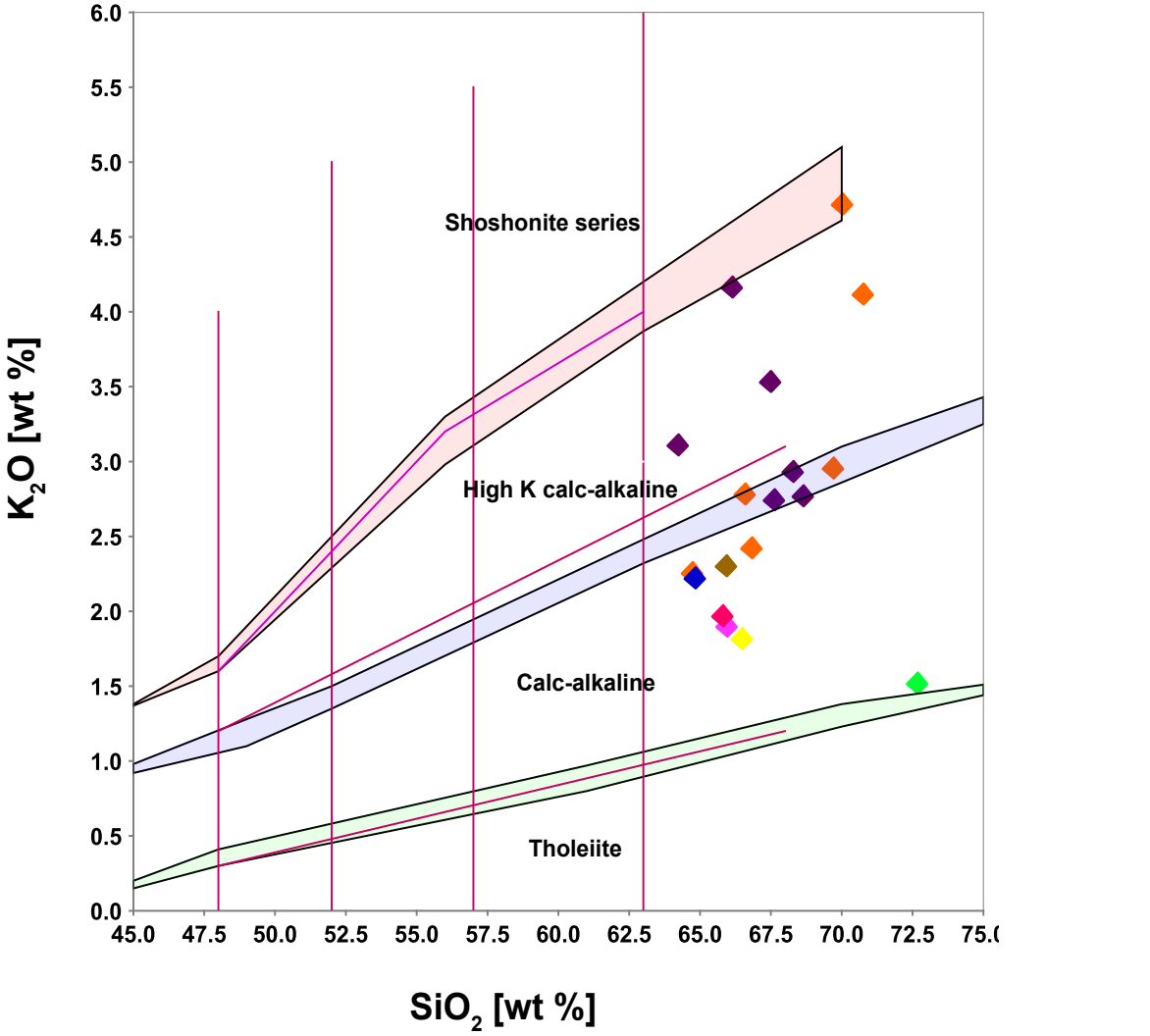

Figure 5.4. K2O vs. SiO2 diagram (from Peccerillo and Taylor, 1976) for volcanic and hypabyssal rocks from La Coipa district.

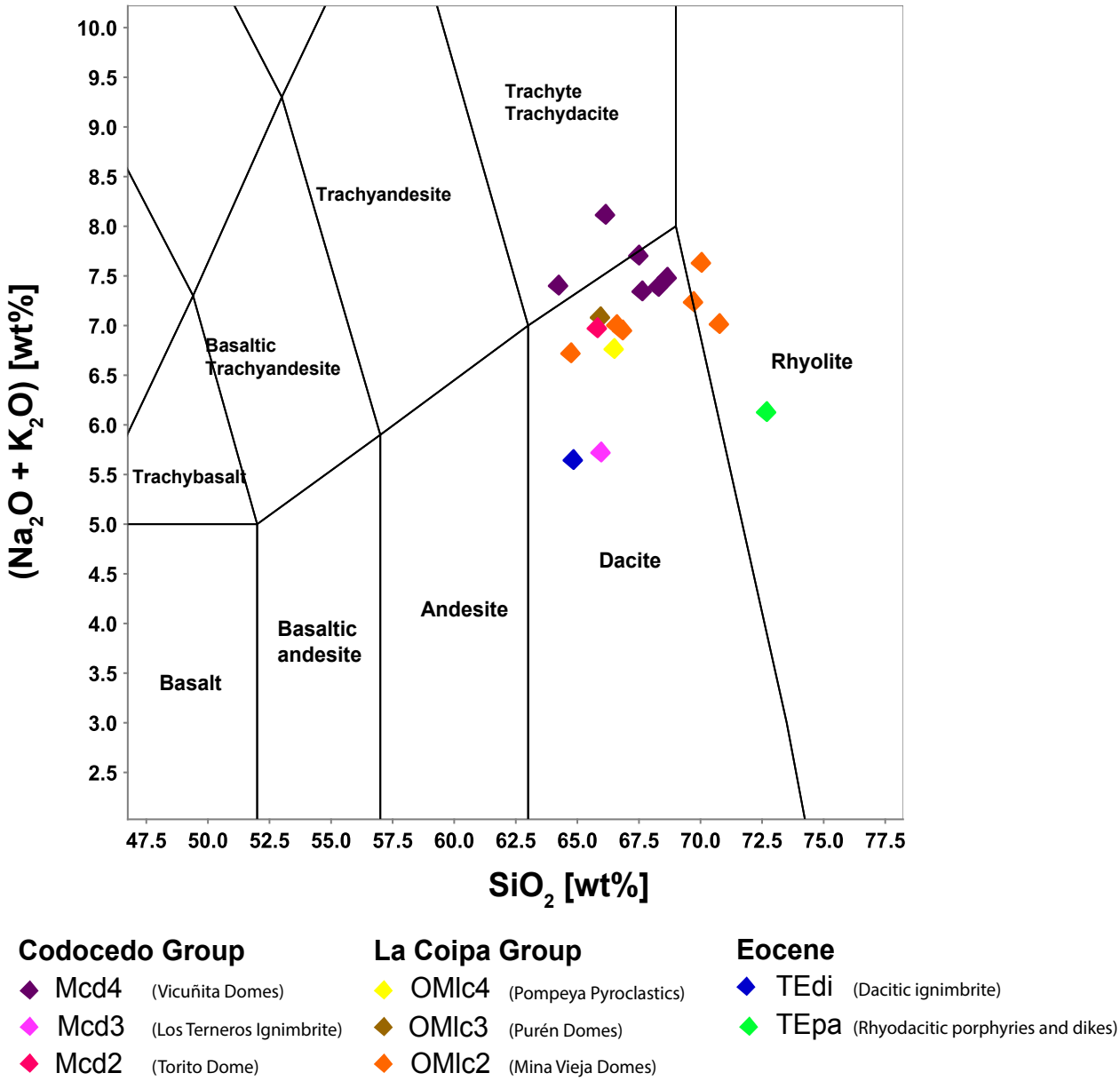

Figure 5.5. TAS Diagram (from Le Maitre et al., 1989) for volcanic and hypabyssal rocks from La Coipa district.

increases with increasing SiO_2 content. On the other hand, TiO_2 (0.4 - 0.6 wt. %), Al_2O_3 (15.9 - 18.2 wt. %), Fe_2O_3 (1.9 - 3.9 wt. %), MgO (0.4 - 1.7 wt. %), and CaO (2.5 – 5.3 wt. %) decrease with increasing SiO_2 content, which can be explained by crystal fractionation of mineral species such as amphibole and plagioclase. The MnO (0.01 – 0.14 wt. %), Na_2O (2.9 – 5.0 wt. %), and P_2O_5 (0.15 – 0.21 wt. %) contents show a wider variation for a fixed SiO_2 content. Compared to regional data (Figure 5.6), samples from La Coipa are among the most differentiated with the lowest concentrations of TiO_2, Al_2O_3, Fe_2O_3, MgO, and CaO. According to Longo et al., (2010), this wide variation for MgO and P_2O_5 is indicative of processes more complex than fractionated crystallization of a single mafic parent. The low slope of Al_2O_3 content suggests relatively incompatible behavior and lack of feldspar fractionation.

5.2 Trace-element compositions

The compositional variation of trace elements is shown in Figure 5.7. Here, a MORB-normalized trace element plot (Pearce, 1983) for Tertiary units reveals a relative depletion of Nb and Ta, together with a relative enrichment of Rb, Ba, Th, and Ce. Elements such as Nb and Ta are not mobilized by arc subduction processes (Richards, 2003), explaining the depletion of these elements in the arc-related magmatic rocks of the La Coipa district. Pattern of trace elements from the La Coipa Group are quite homogeneous (Fig. 5.7.A). This is different for samples from the Codocedo Group (Figure 5.7.B), which is characterized by higher variation of concentration of elements such as Y and Yb. From this group, the sample from the Los Terneros Ignimbrite (Mcd3) shows a distinctive pattern with relative depletion of Ce, P, Sm, and Y. The Eocene sample of the Dacitic Ignimbrite (TEdi) shows a similar pattern to the La Coipa Group samples (Figure 5.7.C). A higher variability in the sample from the Rhyodacitic Porphyry (TEpa) is attributed to some degree of hydrothermal alteration (Figure 5.7.C).

MORB-normalized pattern of REE (from Sun and McDonough, 1989) is shown in Figure 5.8. In general, the patterns of REE show a relative enrichment of light REE (LREE) and a relative depletion of heavy REE (HREE). In general, the patterns are relatively smooth, and lack negative

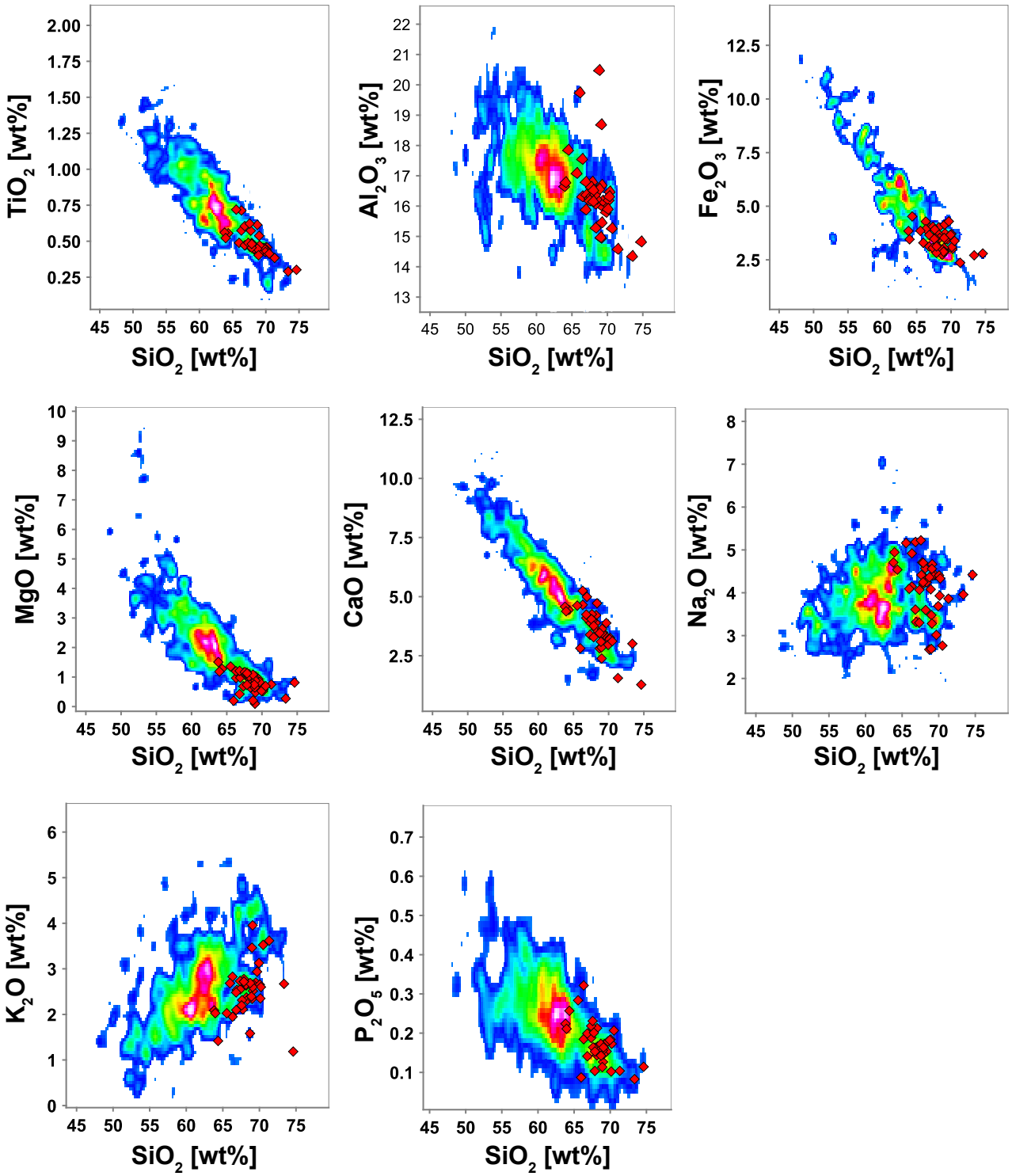

Figure 5.6. Major elements Harker diagrams for La Coipa samples (red rhombus) compared to Oligocene-Miocene volcanic and hypabyssal rocks of Maricunga, El Indio, and El Teniente-Los Pelambres belts. Regional samples plotted as spatial density of points with a progressive scale of colors (from blue to pink). (n = 969 samples; References: Bello, 2012; Bissig, 2001; Charchaflie, 2003; Cornejo et al., 1993; Goss and Kay, 2009; Goss et al., 2013; Halter et al., 2004; Hollings et al., 2005; Kay and Gordillo, 1994;
Kay et al., 1988, 1991, 1999, 1994; Litvak et al., 2007; Maydagán et al., 2011, 2014; Mpodozis et al., 1995; Muntean, 2000; Naranjo et al., 2013a, b; Sasso, 1997; Schnurr et al., 2007;
Siebel et al., 2001; Titler, 1995; Trumbull et al., 1999; Walker et al., 1991; Winocur et al., 2014).

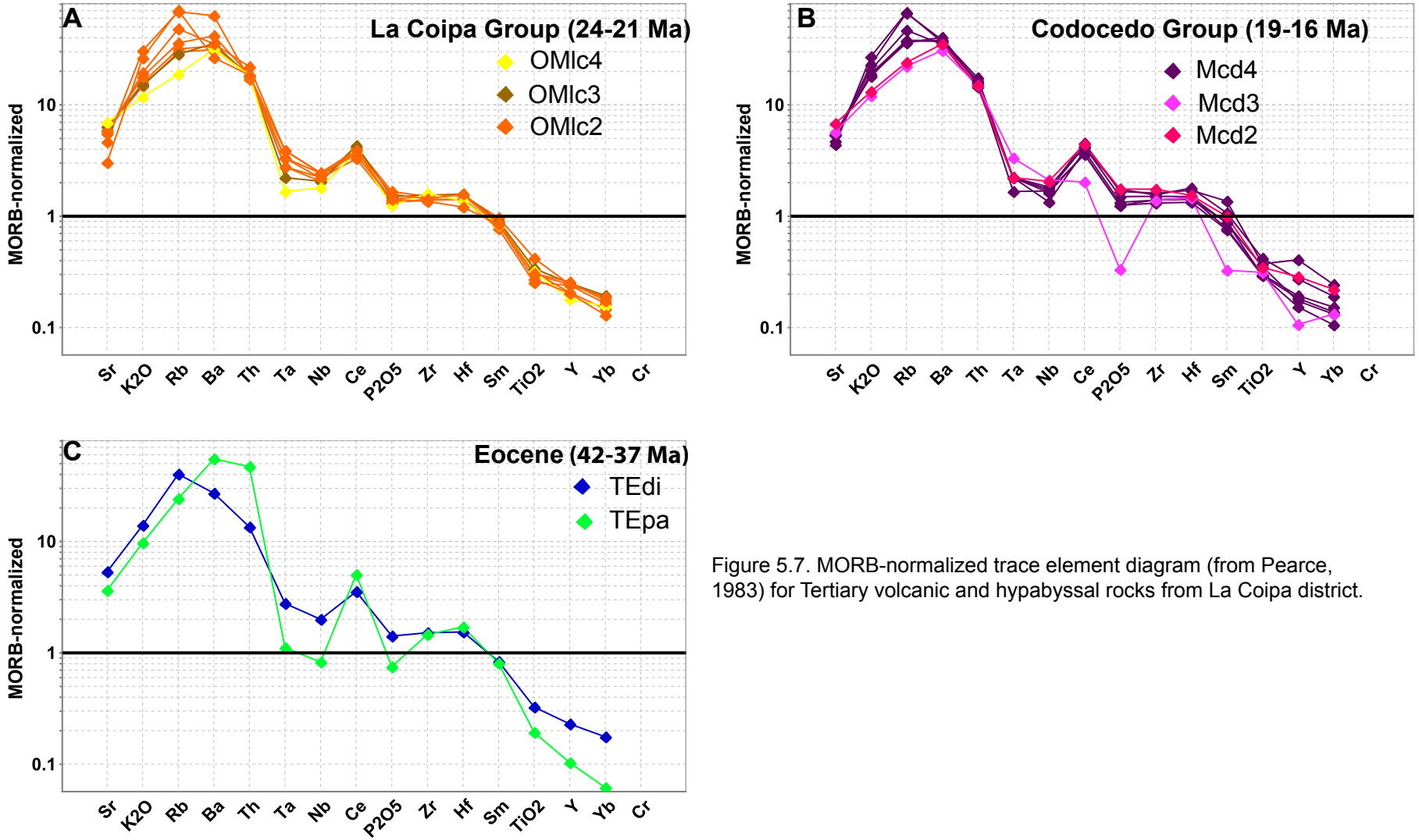

Figure 5.7. MORB-normalized trace element diagram (from Pearce, 1983) for Tertiary volcanic and hypabyssal rocks from La Coipa district.

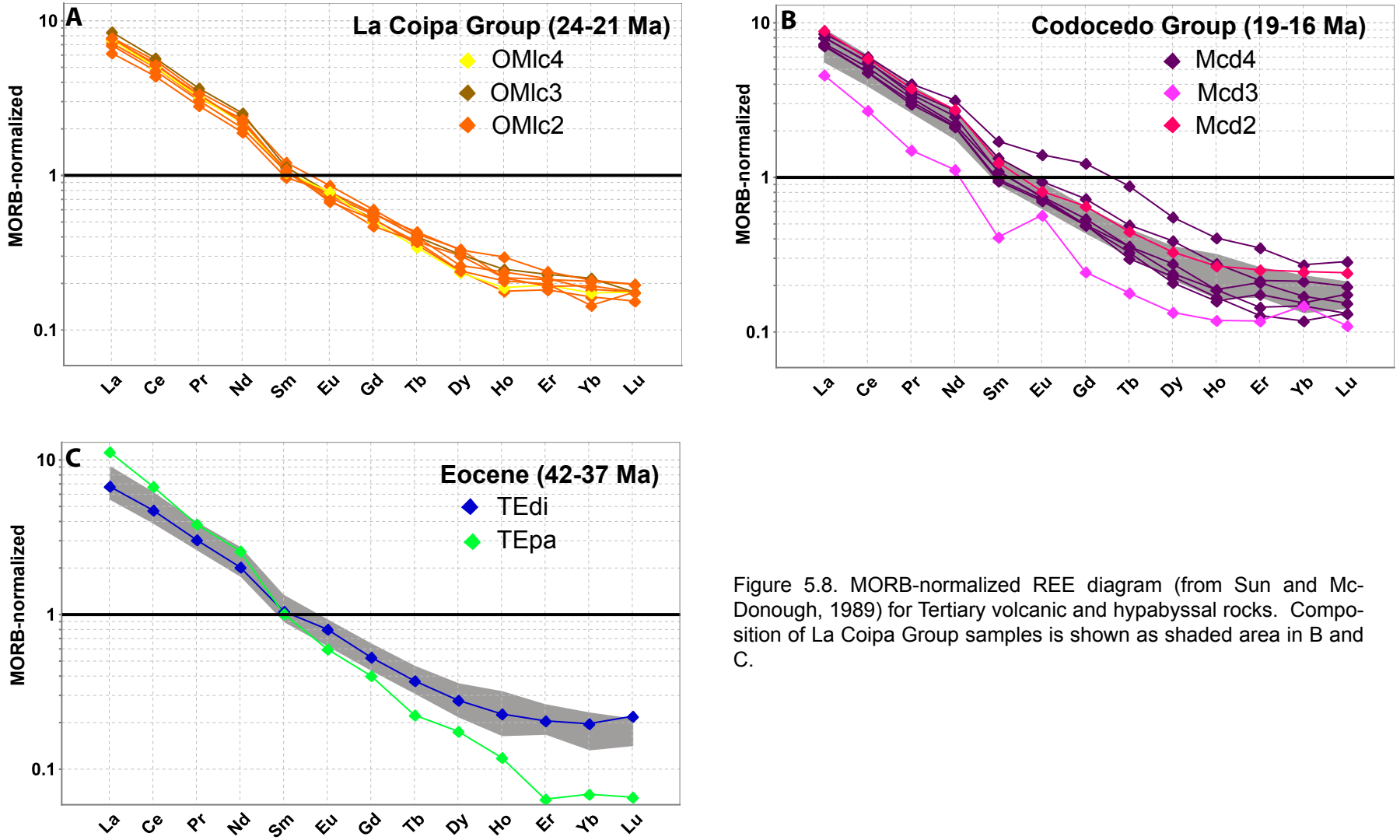

Figure 5.8. MORB-normalized REE diagram (from Sun and McDonough, 1989) for Tertiary volcanic and hypabyssal rocks. Composition of La Coipa Group samples is shown as shaded area in B and C.

Eu anomalies. Samples from La Coipa Group are homogeneous (Figure 5.8.A), whereas, patterns from the Codocedo Group are more scattered, especially in the HREE content (Figure 5.8.B). The Eocene Dacitic Ignimbrite (TEdi) shows a similar pattern to the La Coipa Group rocks (Figure 5.8.C). The fractionated HREE and the slope of the patterns of Eocene to Miocene rocks is attributed to a combined residual phase of amphibole and garnet. The sample from the Los Terneros Ignimbrite (Mcd3) shows a distinctive pattern with positive Eu anomaly, together with a concave-up shape of MREE to HREE. This pattern is attributed to residual amphibole.

5.3 Comparison with regional data

One of the most important characteristics of the Tertiary magmatic rocks of the La Coipa District is their high SiO_2 content compared to Oligocene-Miocene magmatic rocks of northern and central Chile (Figure 5.6). Considering the main units defined in the Maricunga belt, similar elevated and narrow ranges of SiO_2 are only observed in the Río Frío Ignimbrite, and in the Jotabeche and Copiapó volcanic centers, whereas andesitic compositions dominate for the remaining lithological units (Figure 5.9).

Global comparative studies (e.g., Loucks, 2014) suggest that $Sr/Y > 25$ at $SiO_2 > 55$ wt%, indicate magmatic suites fertile for porphyry deposits. These are distinct from barren suites which have values of $Sr/Y < 50$ and SiO_2 values that range between 50 and 75 wt% (Loucks, 2014). This fertility is usually attributed to high H_2O content in the magmas (Richards, 2011). Rocks from La Coipa plot inside the fertile field of Loucks (2014; Figure 5.10). Other magmatic centers along the Oligocene-Miocene arc that share this behavior include intrusive rocks from the Altar Cu-porphyry in the Los Pelambres-El Teniente belt (Maydagán et al., 2011), the Vallecito and Vacas Heladas Formations of the El Indio belt (Bissig et al., 2003; Figure 5.10), and the Jotabeche volcanic center in the Maricunga belt (Kay et al., 1994).

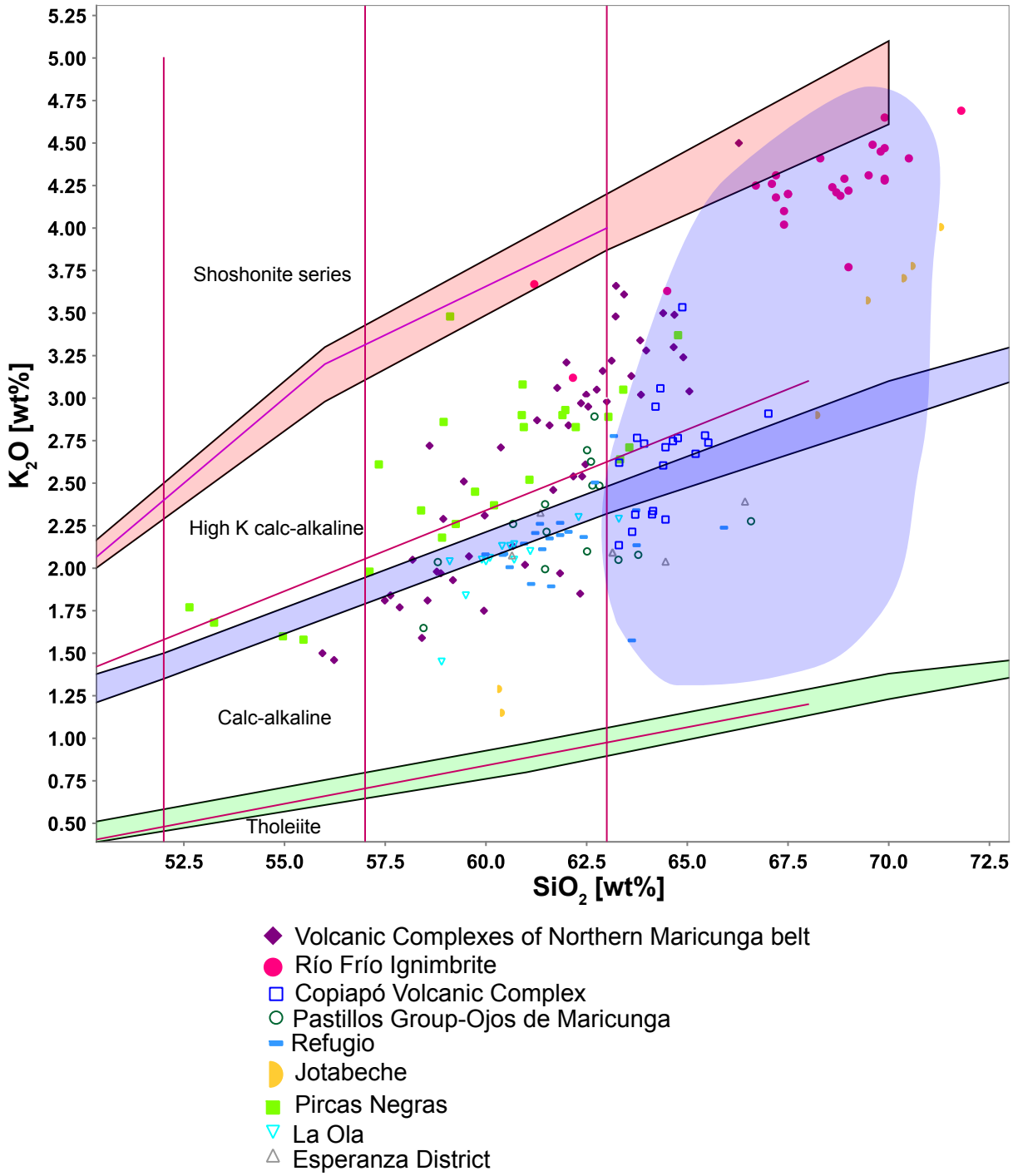

Figure 5.9. K2O vs. SiO2 diagram (from Peccerillo and Taylor, 1976) for volcanic and hypabyssal rocks of the Maricunga Belt. The blue shaded region corresponds to La Coipa district samples analyzed at the present study and samples from Bello, 2012. References of regional geochemistry: Cornejo et al., 1993; Goss and Kay, 2009; Goss et al., 2013; Kay et al., 1991, 1994, 1999; Mpodozis et al., 1995; Naranjo et al., 2013a, b; Schnurr et al., 2007; Walker et al., 1991.

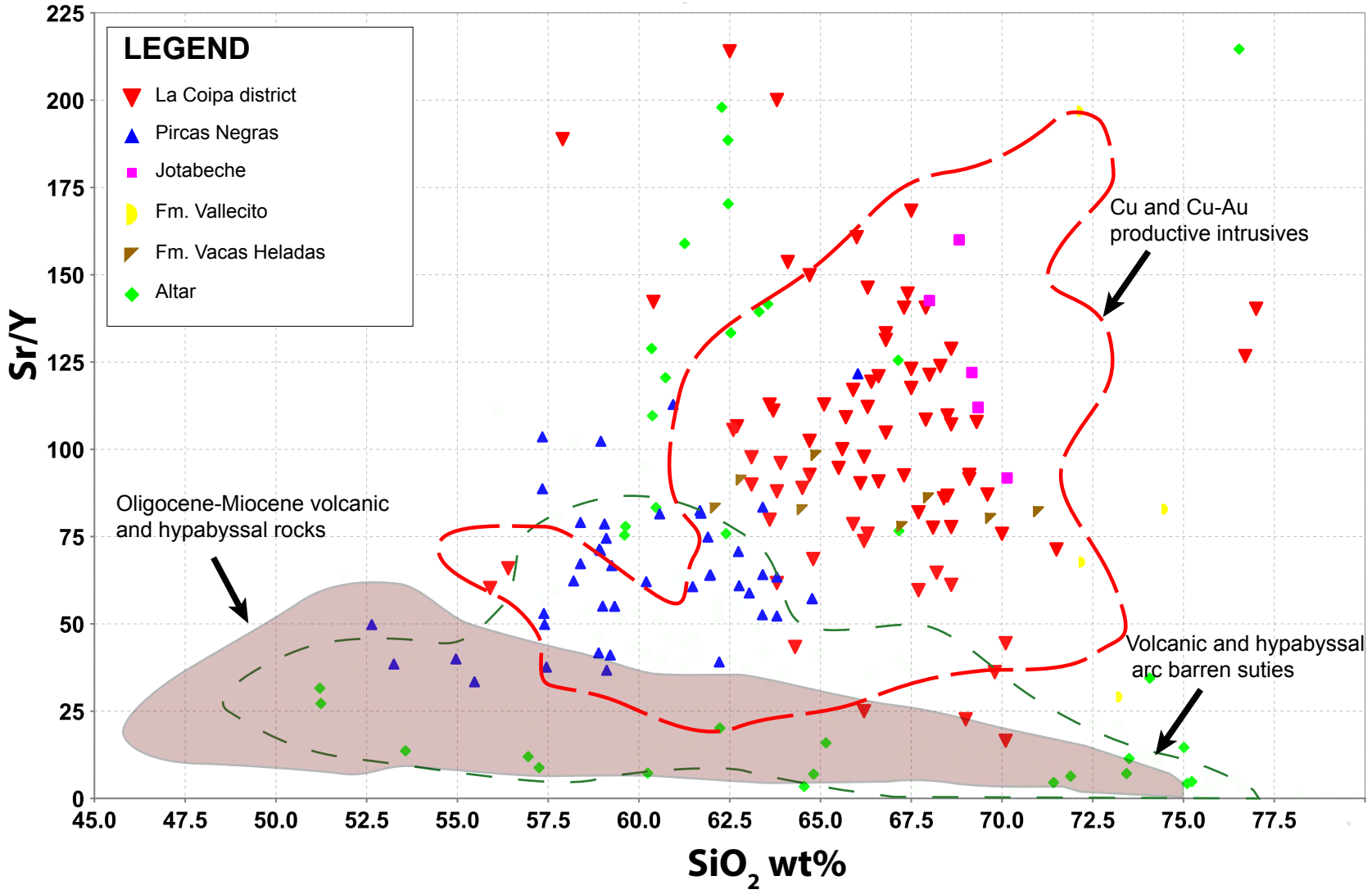

Figure 5.10. Sr/Y vs. SiO2 wt% diagram (from Loucks, 2014) used to discriminate Cu and Cu-Au porphyry related rocks (region within red dashed line) from barren tholeiitic and calc-alkaline arc suites (green dashed line). The Oligocene-Miocene volcanic and hypabyssal rocks from the Maricunga, El Indio and El Teniente-Los Pelambres belts fall within the region filled by reddish color . Samples that fall within the porphyry-related field are plotted by individual symbols, highlighting in red triangles samples from La Coipa district. References of the Oligocene-Miocene rocks cited in Figure 5.6.

Besides the Sr/Y ratio, the fertility of porphyry and epithermal-related magmatic rocks has been correlated with other trace element geochemical signatures which are commonly referred to as adakite-like signature (Kay, 1978; Defant and Drummond, 1990; Richards and Kerrich, 2007). An example of this signature is the La/Yb ratio. Figure 5.11 shows the variation of the La/Yb with the age and the SiO_2 content for rocks of the Maricunga, El Indio, and Los Pelambres-El Teniente belts. Having La/Yb ratios that range between 25 and 50, samples from La Coipa show the highest ratio of La/Yb within rocks older than 13 Ma. The most similar signature corresponds to the ~16 Ma Cerro Las Tórtolas Formation, which has La/Yb values equivalent to the Vicuñita Domes (Mcd4; Figure 5.11). For a given SiO_2 content, rocks from La Coipa show a ratio similar to rocks from the Complejo Volcánico Copiapó, the Vacas Heladas Formation, the Vallecito Formation, and the Pascua Formation. Units with higher than La Coipa La/Yb ratios include the Teniente Porphyry, the Complejo Volcánico Jotabeche, and the Negro Francisco Ignimbrite (Kay et al., 1994; Kay et al., 1999).

Another indicator of HREE depletion is the Sm/Yb ratio. This value is utilized to discriminate the residual mineralogy left in the source region during the generation of magmatic rocks. High values of this ratio indicate garnet ± hornblende in the residual phase whereas low values correspond to pyroxene+plagioclase residual phase (Rollinson, 1993). Similar to the La/Yb ratio, the Sm/Yb ratios for La Coipa magmatic rocks are the highest among all rocks older than 13 Ma within the Oligocene-Miocene arc (Figure 5.11).

Davidson et al., (2013) proposed a numeric approach to plot large datasets, quantifying the curvature of the REE pattern through the Dy/Dy* ratio (Eq. 5.3), where the N subindex indicates the chondrite normalized values for each element.

$$\frac{Dy}{Dy*} = \frac{Dy_N}{La_N^{\frac{4}{13}} * Yb_N^{\frac{9}{13}}} \qquad \text{(Eq. 5.3)}$$

Plotting the Dy/Dy* against the Dy/Yb ratio, which is an indicator of the gradient for the REE pattern, it is possible to discriminate the residual phase during the evolution of magmatic rocks. Using this diagram, samples from La Coipa district show a trend that reflects a HREE depletion that has

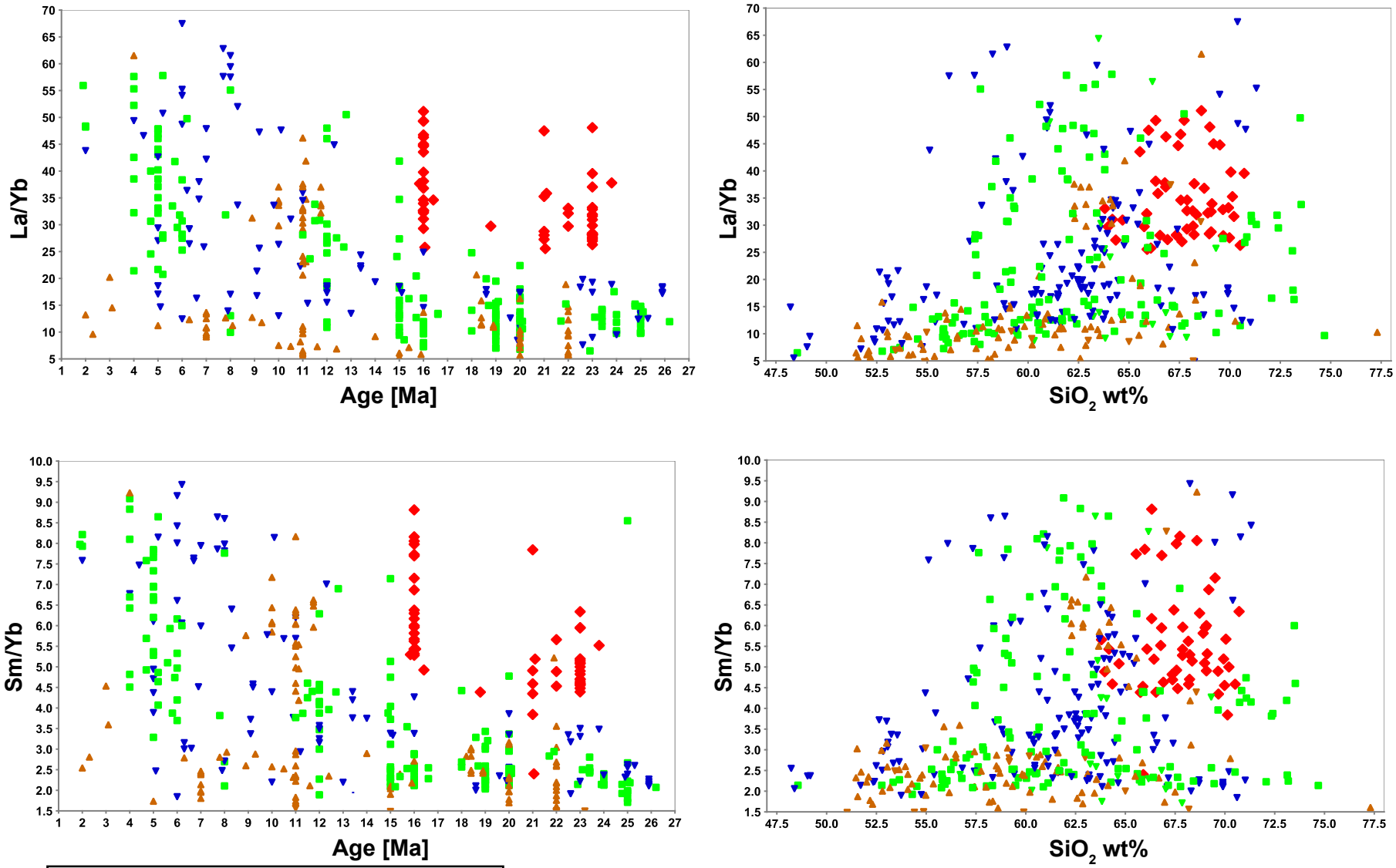

Figure 5.11. La/Yb and Sm/Yb vs. Age and SiO2 respectively. Samples from the Oligocene-Miocene volcanic arc. References of regional samples cited in Figure 5.6.

been interpreted as a signal of garnet as residual phase (Figure 5.12). Samples from the Oligocene-Miocene volcanic arc outside La Coipa that are characterized by this signature include the Pircas Negras lavas, the Rosada Ignimbrite, the Vacas Heladas and Vallecito Formations, and the Altar volcanic rocks (Figure 5.12).

The spatial distribution of porphyry fertility indicators of trace elements can be illustrated along the Maricunga, El Indio and Los Pelambres-El Teniente metallogenetic belts (Figure 5.13). Using the La/Yb, Sm/Yb, Dy/Yb, Sr/Y, Eu/Eu*, and Al_2O_3/TiO_2 ratios, a segmentation of the Oligocene-Miocene arc is evident. La Coipa district is located in the northern part of a segment that extends between 26.5° and 28.5°S. This segment hosts the highest values of these chemical indicators (ie., the most “fertile” signatures), evidencing a marked contrast with the northward contiguous segment that extends between 25° and 26.5°S, which is characterized by lower values of these indicators. Low values of these chemical indicators are also observed in the southern segment between 31° and 34°S.

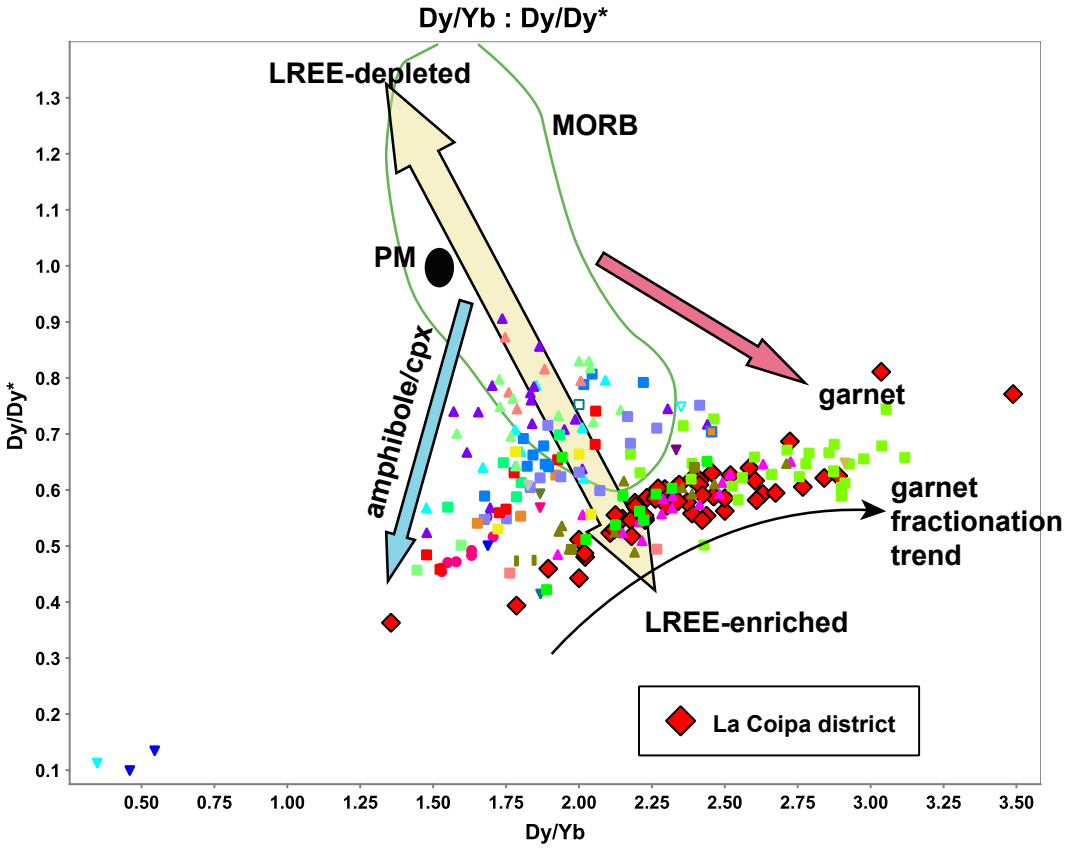

	MARICUNGA BELT	EL INDIO BELT	LOS PELAMBRES-EL TENIENTE BELT
11- 4 Ma	Volcán Rodrigo Parinas Dos Cráteres Pircas Negras Rosada Ign. Vn. Copiapó San Andrés	Vallecito Pascua	Fm. Farellones
17- 11 Ma	Plato Ign. Doña Inés Loma Doña Inés La Ola Ign.	Fm. Vacas Heladas Infiernillo Intrusives Fm. Cerro de las Tórtolas	Altar Upper Subvolcanic Unit Altar Fm. Salamanca
21 - 17 Ma	Colorado de Azufre León Muerto Ign. Río Frío 2 Ign.	Fm. Escabroso	Altar Lower Volcanic Complex
26 - 21 Ma	Río Frío 1 Ign.	Fm. Tilito	Fm. Abanico
36 - 26 Ma		Bocatoma Fm. Valle del Cura	

Figure 5.12. Dy/Dy* vs. Dy/Yb diagram. Samples from the Oligocene-Miocene volcanic arc with available geochemical data (modified from Davidson et al., 2013). References cited in Figure 5.6.

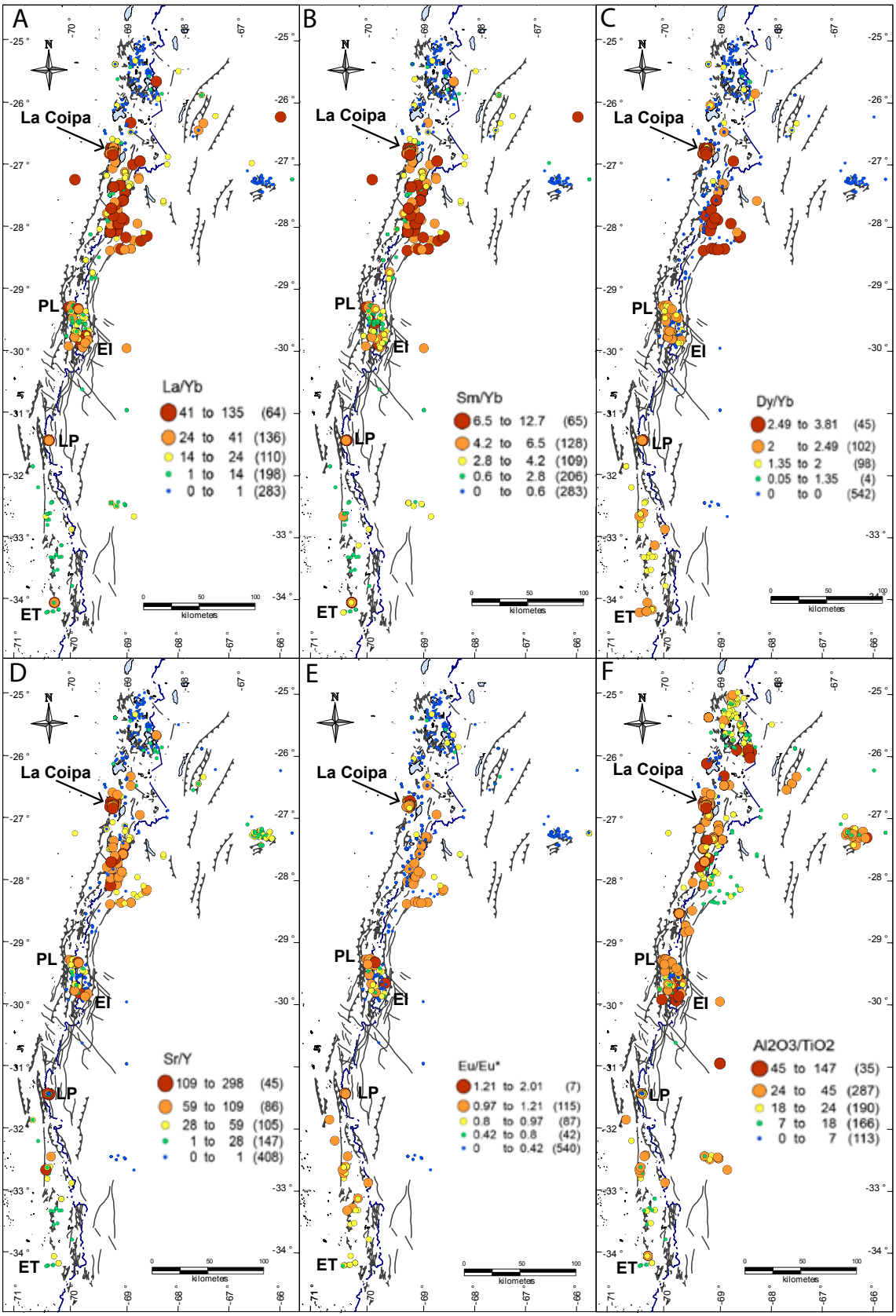

Figure 5.13: Regional maps of petrogenetic indicators for Oligocene-Miocene rocks.
Abbreviations: EI: El Indio; PL: Pascua-Lama; LP: Los Pelambres; ET: El Teniente. References of regional samples cited in Figure 5.6.

Chapter 6: Discussion

To understand the evolution of magmatism and hydrothermalism at La Coipa it is necessary to contextualize the district into a regional scale. The La Coipa district is located near a major discontinuity across the western margin of the South American continent (Figure 6.1), reflecting changes in lithospheric basement blocks, angle of subduction, style of volcanism, and geomorphological domains. This discontinuity also separates the Maricunga belt into two segments, putting La Coipa into the southern part of the northern segment. NW-oriented lineaments illustrated in Figure 6.1 are considered a major control of Tertiary magmatic and hydrothermal activity observed at la Coipa. This NW-oriented lineaments controlled the Late Triassic-early Jurassic rift basins in which the Estratos El Mono unit was deposited. The presence of these deep structures, together with the crustal weakness interpreted for the discontinuity at the latitude of La Coipa district, is interpreted to have played a crucial role for the emplacement of magmas and the precious-metal bearing fluids derived thereof.

6.1 Regional distribution of magmatism through time and implications for tectonomagmatic evolution of the flat-slab subduction

Oligocene magmatism at La Coipa began approximately at 24 Ma, a period in which volcanism along the present flat-slab segment (Lat. 28°S to 33°S) was reactivated after a reconfiguration of tectonic plates within the Pacific oceanic realm (Pardo-Casas et al., 1987). This is fairly evident in the Maricunga and El Indio belts, where volcanic activity started at ~26 Ma following a period of magmatic quiescence between 26 and 30 Ma. Muñoz et al. (2006) established that magmatism was voluminous in the middle Oligocene but started earlier, at 35 Ma, in the Los Pelambres-El Teniente belt, based on an age that was obtained from the basal level of the ca. 2000 m thick Abanico Formation.

Voluminous sequences of volcanic and volcaniclastic rocks characterized the 26-21 Ma arc in the El Indio and Los Pelambres-El Teniente belts (Winocur et al., 2014; Bissig et al., 2001; Mpodozis and Cornejo, 2012), whereas magmatism in the Maricunga belt was restricted to isolated volcanic centers, as is the case of the La Coipa Group in the La Coipa district. Volcanic and hypabyssal

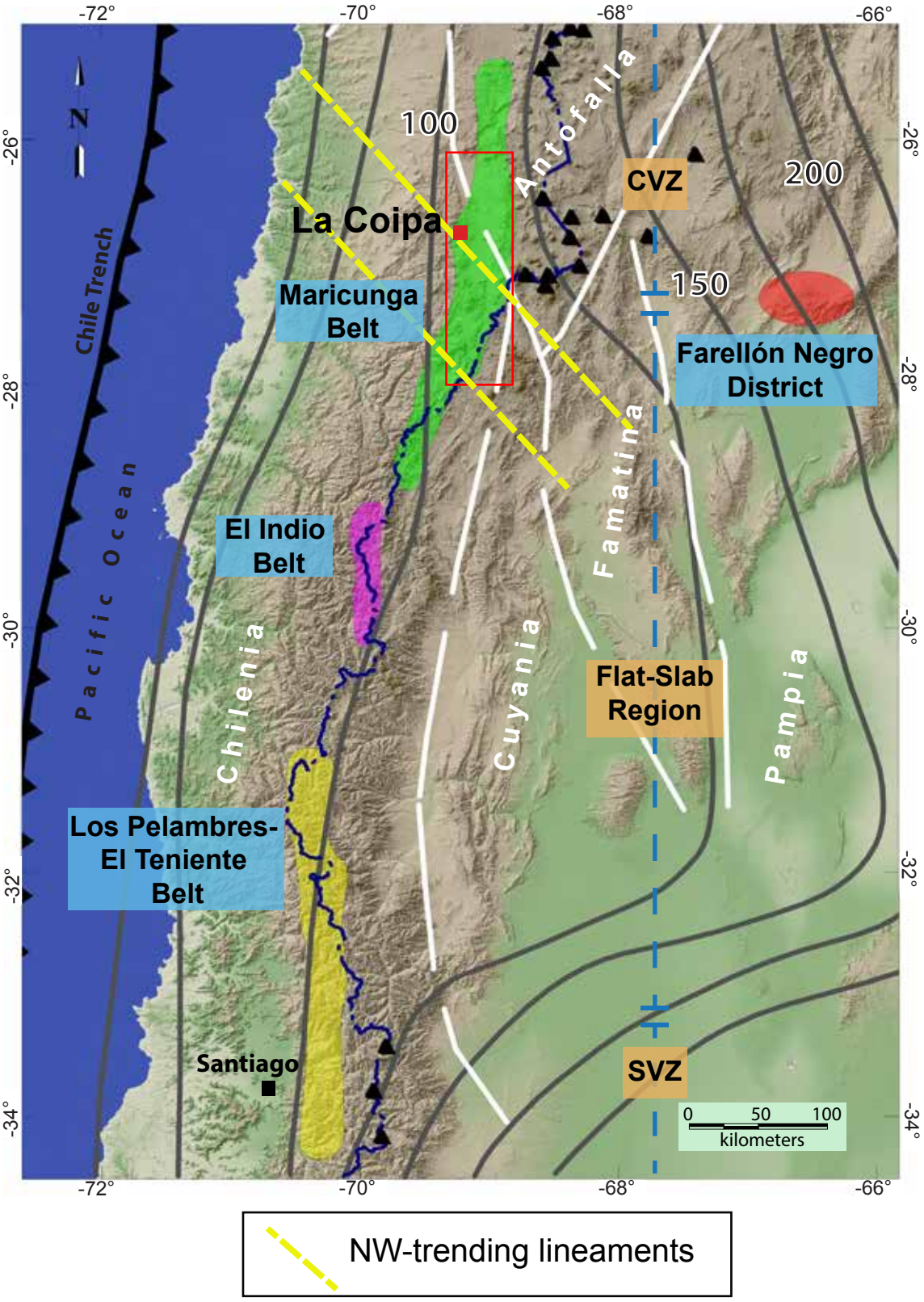

Figure 6.1: Review of Figure 1.1 highlighting the factors that contribute to the interpretation of a major discontinuity across the Andean margin. NW-oriented lineaments (taken from Abels and Bischoff, 1999) mark the transition between the northern and southern Maricunga belt. The northern lineament is considered the first-order control of magmatism and hydrothermalism observed at La Coipa. The red box indicates the original definition of the Maricunga belt (Vila and Sillitoe, 1991).

rocks have a mainly dacitic composition in the Maricunga and El Indio belts, whereas a more basic andesitic composition dominates in lavas of the Los Pelambres-El Teniente belt. The difference of distribution and composition of volcanic rocks along the flat-slab segment may be attributed to variations in the stress regime and crustal thickness, with more extensional conditions and thicker volcanic sequences towards the south, and more contractional conditions towards the north, reflected in a reduced volume of volcanism in the Maricunga belt (Kay and Mpodozis, 2002; Charrier et al., 2002; Parada et al., 2007).

Previous studies and evolution models of the Maricunga belt considered that after the 26-21 Ma period a volcanic lull related to a more contractional regime dominated between 21 and 17 Ma (Kay et al., 1994; Mpodozis et al., 1995). However, in spite of the volcanic lull described for the 21-17 Ma period, extensive ignimbrites covering the Maricunga belt north of Lat. 26.5°S erupted (Río Frío Ignimbrite, Llano Las Vicuñas Ignimbrite, the Complejo Volcánico Dos Hermanos, and the Volcanes del Mioceno Inferior unit). More restricted volcanic volumes distributed along NW-oriented lineaments covered the southern part of the Maricunga belt, suggesting a segmentation in basement architecture near Lat. 26.5°S. Thus, the style of volcanism in the northern Maricunga belt changed from isolated stratovolcanoes to extensive felsic ignimbritic fields around 21 Ma. In the El Indio belt, this transitional period is marked by the angular unconformity between the 26-23 Ma dacitic to andesitic Tilito Formation and the 22-17 Ma andesitic Escabroso Formations. In the Los Pelambres-El Teniente belt, the 25-2 Ma andesitic to rhyolitic Farellones Formation unconformably overlies the 35-21 Ma andesitic Abanico Formation. Godoy (2011) established that the tectonic inversion in the Los Pelambres-El Teniente belt migrated from north to south, being older and more intense in the northern part of this belt. In the La Coipa district, volcanic and hypabyssal units from the Codocedo Group, deposited and emplaced between 19 and 16 Ma, unconformably overlie volcanic rocks of the 24-21 Ma La Coipa Group. Therefore, the unconformity that separates the La Coipa Group from the overlying Codocedo Group can broadly be correlated with the discontinuity between the Tilito and Escabroso Formations and between the Abanico and Farellones Formations.

This unconformity along the Miocene arc is the result of compressional deformation and the tectonic inversion of the intra-arc basin in which middle Oligocene volcanic rocks were deposited. This compressional diachronic event observed along the entire arc indicates a period of considerable uplift of the Andean Cordillera, which occurred through several stages of contractile deformation bracketed between 23 and 16 Ma. It should be noted that this tectonic inversion has been widely discussed for the El Indio and Los Pelambres-El Teniente belts (Martin et al., 1995; Bissig et al., 2001; Fuentes et al., 2002; Godoy, 2011; Jara and Charrier, 2014; Winocur et al., 2014), whereas scarce publications have documented this process in the Maricunga belt (Charrier et al., 2009).

In the Maricunga belt, Kay and Mpodozis (2002) estimated that during the 20-16 Ma period a extensional or transtensional regime transitioned into a contractional one. In the El Indio belt, the unconformity between the Tilito and Escabroso Formations was restricted to the 23-21 Ma period. In this belt, a major event of deformation associated with reverse faults, folds, and uplift between 17 and 16 Ma was documented (Bissig et al., 2001, 2002; Martin et al., 1995) . For the northern part of the Los Pelambres-El Teniente belt, Jara and Charrier (2014) estimated a 21 to 18 Ma period of deformation and tectonic inversion. Moreover, Gatzoubaros et al. (2014) established that at ~20Ma a change from extension to compression characterized the Altar Cu-Mo porphyry region. A similar process of deformation was estimated for the El Teniente region between 20 and 18 Ma (Kurtz et al., 1997; Godoy et al., 1999). The overlapping of ages of deformation indicated for each of these regions suggests that similar tectonic changes occurred between the Maricunga, El Indio, and Los Pelambres-El Teniente belts. Another aspect to consider is the style of deformation related to the tectonic inversion. Jara and Charrier (2014) documented that in the northern part of the Los Pelambres-El Teniente belt the eastern margin of the Abanico basin concentrated the majority of the deformation associated to the basin inversion. Similarly, in the La Coipa district, this tectonic inversion is characterized by intensely deformed Mesozoic rocks cropping out to the east of the Oligocene-Miocene intra-arc basin, compared to subhorizontal Mesozoic strata cropping out to the west of the basin.

The contractional deformation discussed above is associated to tectonic processes such as slab flattening. Based on changes in magma chemistry suggestive of crustal thickening, the beginning of the flat-slab subduction was estimated by Kay et al. (1987, 1991, 1999) around 18 Ma for the Maricunga belt. Although the flat subduction is widely attributed to the subduction of the Juan Fernandez Ridge, the subduction of this aseismic ridge in the Maricunga belt did not initiate until 14 Ma (Yañez et al., 2001). Even though there is a spatial correlation between aseismic ridge subduction and flat-slab subduction, several authors point out that other factors could explain these processes without ridge subduction (Skinner and Clayton, 2013; Kay and Mpodozis, 2002). Skinner and Clayton (2013; and references therein) indicate that large magmatic addition combined with ductile thickening of the lower crust are the result of crustal shortening, as documented for the southern Puna plateau (~Lat. 26°S). Other authors (Manea et al., 2012), suggested that a relative westward motion of the South American plate accompanied by slab retreat caused the lower angle of subduction. In conclusion, a regional tectonic change occurred before the proposed mechanism of flat slab subduction and ridge underplating.

Following contractional deformation and volcanic lull, volcanism resumed more vigorously in the Maricunga belt between 16-11 Ma (Mpodozis et al., 1995). Here, a broadening of the arc whose axis partially migrated towards the east can be observed. A series of Au-Cu porphyry systems were emplaced at different centers such as the Lobo-Marte region (King, 1992), the Cerro Casale district (Hollings et al., 2014), and the Doña Inés and Maricunga volcanic centers (Kay et al., 1994). In the El Indio belt, the Infiernillo Intrusives constituted the main event of hypabyssal/plutonic activity (Bissig et al., 2001). In the Los Pelambres-El Teniente belt, a series of porphyries grouped into the Intrusive II Unit were emplaced between 21 and 14 Ma (SERNAGEOMIN, 2003). At La Coipa, this event is coeval with the ca. 16 Ma Vicuñita Domes unit, which is considered the youngest magmatic epidose recorded in the district.

According to the paleo-reconstruction of the subduction of the Juan Fernández Ridge, which migrated from north to south (Lat. 19°S at 22 Ma to Lat. 33°S at 3 Ma), it is established that it passed beneath the northern Maricunga belt at 14 Ma and beneath the southern Maricunga belt at 12 Ma

(Yañez et al., 2001). Kay and Mpodozis (2002) argued that the age of the pass of the ridge beneath the Maricunga belt coincided with a change of widespread andesitic stratovolcanoes to volumetrically restricted dacitic dome centers. This was also observed in the El Indio belt by 12-10 Ma with the isolated eruption of the dacitic Vacas Heladas Formation and the termination of the andesitic Cerro de las Tórtolas Formation. This waning of volcanism in the El Indio belt has been temporally associated to the flattening of the slab, which on the basis of petrochemical data (Bissig et al., 2003), began ca. 14 Ma. This tectonomagmatic evolution indicates that the 14-11 Ma gold-rich porphyries of the southern Maricunga belt were emplaced just before the arrival of the subducting ridge, a situation that also was observed later in the Los Pelambres-El Teniente belt (Deckart et al., 2013).

The youngest period of the Miocene volcanism (11-4 Ma) is characterized by an eastward migration of the volcanic front. This migration of the volcanic front is most evident at the latitude of the Maricunga belt. During this period, the voluminous volcanic activity was restricted to the Maricunga and Los Pelambres-El Teniente belts, whereas volcanism at the El Indio belt was drastically reduced but is represented by isolated domes and small ignimbrite deposits emplaced periodically until 2 Ma (Bissig et al., 2001). The scarce volcanic activity in the El Indio belt can be explained by the flat subduction that characterized the Andean margin at this time (e.g., Kay and Mpodozis, 2002).

6.2 Petrogenesis of igneous rocks from La Coipa district and their context within the Maricunga belt

The relationship between magmatic host-rock and ore deposits along the Oligocene-Miocene arc is generally manifested in the chemistry and mineralogy of volcanic and hypabyssal rocks. A characteristic of the magmatic rocks from La Coipa is the relatively constant Si-content from the Eocene through the Miocene, which puts the volcanic and hypabyssal units emplaced during this time into a dacitic compositional field. Kay et al. (1994) observed a similar pattern in the Esperanza district. According to these authors, the constant dacitic composition is a consequence of magmas hosted in a thick crust that difficults the path to extrusion and causing assimilation and contamination

of crustal material. The Esperanza magmatic and high-sulfidation epithermal system was developed approximately at the same time as the La Coipa district (Vila and Sillitoe, 1991), and mineralization styles are also similar. Kay et al. (2014) observed a major discontinuity in the character of igneous rocks at Lat. 27.5°S (coinciding with the Valle Ancho lineament). Regional geochemical data compiled during this study show that north of this latitude there are multiple centers with Si>63 wt. %, contrasting with the predominance of Si<63 wt.% rocks towards the south.

Petrography of volcanic rocks throughout the Maricunga belt shows that the occurrence of ore deposits is in most cases related to hornblende-bearing host rocks. For the Maricunga belt, Kay and Abbruzzi (1996) concluded that ore-bearing magmatic rocks are homogeneous in composition, carry hydrous minerals, and are rich in hornblende; a situation that is also observed in La Coipa within Oligocene-Miocene magmatic rocks. Pyroxene-bearing rocks are generally barren, as was shown by Gatzoubaros et al., (2014) for the Altar Cu-porphyry and its Abanico Formation host-rocks characteristic of the northern part of the Los Pelambres-El Teniente belt. In the El Indio belt, a change from pyroxene-bearing rocks of the Escabroso Formation to pyroxene- and hornblende-bearing Cerro de las Tórtolas Formation and finally to the hornblende- and biotite-bearing Vacas Heladas has been documented (Bissig et al., 2001). Mpodozis and Cornejo (2012) described also the connection between hydrous mineral-bearing rocks and ore deposits during the middle Eocene to early Pliocene in northern and central Chile. Moreover, they established that fertile rocks of this period have the following geochemical signatures: SiO_2 > 56 wt. %, Sr > 400 ppm, high Sr/Y ratios (>40), low HREE contents, and high La/Yb ratios (>20).

The Sr/Y ratio is expected to increase with rising SiO_2 in more hydrous magmatic differentiation series (Loucks, 2014), due to the Y depletion associated with hornblende or garnet partition in residual melts. Oligocene-Miocene rocks from La Coipa district are characterized by relatively high Sr/Y ratios, with practically all samples obtained in the present study plotting inside the Cu-Au productive field (Loucks, 2014). This high ratio is explained by strong Y depletion values accompanied by relatively elevated Sr values compared to regional samples from the Maricunga, El Indio, and Los Pelambres-El Teniente belts. Meanwhile, REE are used to interpret petrogenetic processes due to

the systematic variation of distribution coefficients and partition of these elements into the different crystallizing minerals, indicating partial melting and fractional crystallization processes (Davidson et al., 2012). Tertiary rocks from the La Coipa district are characterized by straight REE normalized patterns where HREE are strongly depleted compared to LREE, suggesting that garnet was a residual phase in the melting source region, implying a thick crust. The partition of garnet in the residual melt is also supported by the Y depletion observed in these rocks (Loucks, 2014). Petrogenetic indicators obtained from REE such as the La/Yb and Sm/Yb ratios are also higher in igneous rocks of La Coipa district compared to regional samples >15 Ma in age and jointly suggest the presence of residual minerals (garnet, hornblende) indicative of high pressure and hydrous conditions at the lower crustal site of magma evolution.

Previous authors (Goss and Kay, 2006, 2009; and Kay and Mpodozis, 2002) suggested that the depleted HREE and high Sr/Y geochemical signature was established at 9 Ma for the Lat. 27°-28.5°S region during the initiation of an eastward arc migration and crustal thickening. This contrasts the results of the present study obtained at La Coipa, which yielded similar trace element signatures for rocks ranging between 23.8 and 16 Ma. The anomalously high values of La/Yb and Sr/Y obtained at La Coipa could be explained by higher water content of fractionated magmas, by a more felsic composition, and/or by a thicker crust (Richards and Kerrick, 2007). For a given Si-content, the La/Yb and Sr/Y ratios are higher in rocks from La Coipa compared to rocks from the Maricunga belt, discarding that the anomaly of these ratios is a consequence of the more felsic composition (Figure 5.11).

The tectonic evolution models of the flat-slab segment indicate that during the 26-21 Ma period, more evolved volcanism towards the north is a consequence of a thicker crust, especially in the northern part of the Maricunga belt, enough to stabilize garnet in the lower crust (Haschke et al., 2002, and references therein). Normal subduction occurring along the entire arc has been interpreted for the 26-21 Ma period (Bissig et al., 2003; Kay et al., 2014), although a shallower slab characterized the Maricunga belt, especially its northern segment north of Lat. 27.5°S at that time (Kay et al., 1994). Within the Maricunga belt, the northern segment was characterized by more contractional

conditions related to the NW-sinistral system that was part of the Domeyko Fault System, which was reactivated during the late Oligocene. Lavas from the 26-21 Ma period were calc-alkaline in the northern Maricunga belt, whereas a tholeiitic signature was common in the southern Maricunga belt. Calc-alkaline rocks characterized the El Indio and the Los Pelambres-El Teniente belts (Kay and Mpodozis, 2002), the latter presenting also tholeiitic rocks typical of a thin crust (Kay et al., 2005). For the 21-17 Ma period, a transition to the high-K- calc-alkaline field is observed in the entire flat slab segment, and an increase of crustal thickness is interpreted for the Maricunga belt (Parada et al., 2007). During the 21-17 Ma period, a thicker crust with garnet as a residual phase was reached along the southern part of the Maricunga belt, the El Indio and the Los Pelambres-El Teniente belts, but estimating a decrease of thickness towards the south (Parada et al., 2007). In conclusion, during the Oligocene-Miocene the Maricunga belt was characterized by a thicker crust than the southern El Indio and Los Pelambres-El Teniente belts.

Situating La Coipa into this tectonic setting, it is suggested that a thick crust below the Maricunga belt, especially in its northern segment, explains the geochemical signature of elevated Sr/Y and La/Yb Oligocene-Miocene rocks. This tectonic setting, accompanied by the generation of hydrous magmas and evolved rocks, acted as optimal conditions for epithermal mineralization.

6.3 Metallogeny of La Coipa district and its regional context

The economic endowment of Au, Ag, Cu, and Mo expressed in multiple occurrences of epithermal and porphyry deposits has led to several authors to study the metallogenesis of this province. The Oligocene-Miocene arc of the flat-slab segment (Lat. 28°S to 33°S) hosts, from north to south, the Maricunga, El Indio, and Los Pelambres-El Teniente belts (Sillitoe et al., 1991; Bissig et al., 2001; Mpodozis and Cornejo, 2012). In general terms, gold-rich porphyry systems dominate in the Maricunga belt, high-sulfidation deposits characterize the El Indio belt, and Cu-Mo porphyry systems define the Los Pelambres-El Teniente belt. However, La Coipa is an exception within the Maricunga belt since it is of high-sulfidation type. It is somewhat distinct from porphyry Cu-Au deposits in that it

is spatially associated with more felsic magmas. A common characteristic of the Oligocene –Miocene arc is that ore deposits were formed during fertile episodes and not throughout the entire period of magmatic activity, even though data from this and compiled studies indicate that mineralization events are more continuous in the Maricunga belt.

Within the flat-slab segment, the age of mineralization becomes younger from north to south, even though there is evidence for multiple episodes of hydrothermal alteration through time along the belt. The oldest deposits have been recognized in the Maricunga belt. Formed between 26 and 22 Ma in the late Oligocene, deposits such as Caspiche, Maricunga, and La Pepa, were grouped into the western sub-belt (Sillitoe et al., 1991). La Coipa and Esperanza high-sulfidation Ag-Au deposits were originally assigned to this group as well (Sillitoe et al., 1991), but new $^{40}Ar/^{39}Ar$ data for alunite, together with limited published K-Ar data (Sillitoe et al., 1991) indicate that these deposits are younger and formed between 21 and 15 Ma. Recently published ages for high-sulfidation epithermal systems in the northern Maricunga belt (Atlas and Titán prospects; Nano et al., 2015), together with the ca. 20.8 Ma Caserones Cu-porphyry (Perelló et al., 2003), suggest that substantial mineralization occurred in the early Miocene in the Maricunga belt, especially between the 19-16 Ma period. Although hydrothermal alteration did also occur in the El Indio belt in the early Miocene, these centers are apparently devoid of significant mineralization (Bissig et al., 2001).

The youngest episode of mineralization for the Maricunga belt (Mpodozis et al., 1995) is characterized by Au-rich porphyry systems that were emplaced between 15 and 13 Ma (Cerro Maricunga, Marte, Lobo, and Cerro Casale), besides the youngest ca. 9 Ma Volcán deposit. The recently discovered Los Helados porphyry deposit, located in the southern Maricunga belt at Lat. 28.34°S has also been dated at 13 Ma (Kapusta, 2012). These deposits were included in the eastern sub-belt (Sillitoe et al., 1991). Geochronological data from alunite obtained in the present study indicate a middle episode of mineralization that occurred in the Maricunga belt, suggesting that multiple fertile episodes occurred between 26 and 9 in different places within the belt.

In the El Indio belt, the fertile period was restricted between 9.5 - 5 Ma (El Indio, Pascua-Lama, Tambo), with the exception of the older Veladero deposit (12.7-10.3 Ma; Holley, 2012, Bissig et al., 2015). In the southern segment, several Cu-Mo porphyry deposits range in age between 15 and 4.6 Ma (Mpodozis and Cornejo, 2012). The three largest deposits, Los Pelambres, Río Blanco-Los Bronces and El Teniente have been widely studied by geochronology. At Los Pelambres mineralization was restricted to 11.8-10.1 Ma (Perelló et al., 2012). In the Río Blanco-Los Bronces district, the main mineralization event spanned from 8.5 to 4.3 Ma, preceded by a less endowed period of hydrothermal activity that ranged between 14.8 and 12.3 Ma (Toro et al., 2012; Deckart et al., 2013, 2014). Located at the southern part of the southern segment, the El Teniente porphyry-system consisted of several mineralized pulses that ranged between 6.5 and 4.6 Ma (Mpodozis and Cornejo, 2012), even though the evidence of high-sulfidation epithermal systems as older as 13.61 ±0.16 Ma ($^{40}Ar/^{39}Ar$ on alunite; Pardo and Kovacic, 2012) suggests a more prolonged hydrothermal activity, overlapping with the youngest ages of mineralization described for the Maricunga belt.

The Maricunga belt was originally defined for a volcanomagmatic arc that hosted several epithermal and porphyry deposits located between the Esperanza district and the Cerro Casale deposit (Lat. 26.6° to 27.8° S; Vila and Sillitoe, 1991). This definition was based on first modern exploration campaigns carried out at this latitude of the Andean Cordillera, using the K-Ar technique to obtain the age of these deposits. However, based on regional data compiled in the present study with the geological mapping, the geochronological ages and the geological interpretation established for La Coipa district, it is suggested that this metallogenic province covers a more extensive area between Lat. 25° and 28.3°S (360 km length), including the northernmost prospects of Atlas and Titán to the southernmost Caserones (ca. 20.8 Ma) and Los Helados (ca. 13.1 Ma) Cu-porphyries (Nano et al., 2015; Perelló et al., 2002; Kapusta, 2012).

Another aspect to consider is the distribution of porphyry and epithermal systems. The different levels of exposure of magmatic-hydrothermal deposits along the Oligocene-Miocene arc, expressed in well-preserved shallow epithermal systems in the northern segment and more deeply eroded porphyry systems in the southern segment, can be explained by the increasing degree of erosion

towards the south related to the increasingly wetter climate towards the south. Increasing rates of erosion towards the south are expressed on deeply eroded younger deposits found in the southern segment (i.e., El Teniente and Río Blanco-Los Bronces). However, the dominance of porphyry over epithermal deposits cannot simply be attributed to higher level of erosion. Thus, in the El Indio belt economic mineralization is exclusively hosted in high-sulfidation deposits despite the more southerly latitude and wetter climate than in the porphyry Au-Cu Maricunga belt. Besides the erosion level, there are fundamental differences in volcanic and physiographic settings between the epithermal and porphyry mineralization styles (Bissig et al., 2015). In conclusion, the combination of magmatism and volcanic setting (represented by the depth of batholith intrusion and fluid evolution; Murakami et al., 2010; Bissig et al., 2015) allowed that at certain places of the Oligocene-Miocene arc porphyry deposits were generated through the time from the oldest Caserones deposit to the youngest El Teniente world-class Cu-Mo porphyry.

6.4 Exploration model for La Coipa district and similar deposits in the Maricunga belt

A unique configuration of basement blocks, regional structures, and prolonged magmatic and hydrothermal activity, played an important role in the generation of this important Ag-Au district. Oligocene-Miocene magmatism at La Coipa district is represented by pyroclastic sequences and hypabyssal domes that covered a surface of 10x20 km^2 and up to 800 m of vertical thickness. Radiometric ages revealed that domes and pyroclastic rocks were emplaced between ca. 24 Ma and ca. 15 Ma in several pulses. A common feature of these magmatic rocks is the fairly constant dacitic composition expressed in a homogeneous mineralogy dominated by plagioclase, biotite, and hornblende. The principal difference observed between these rocks is the presence or absence of anhedral embayed quartz phenocrysts. The youngest group of domes (Vicuñita and Torito units) is characterized by a very low abundance of quartz phenocrysts (< 0.5% of the rock volume), compared to the oldest Mina Vieja and Purén domes (up to 8% of the rock volume).

The style of volcanism observed at La Coipa is characterized by multiple hypabyssal domes and their associated pyroclastic flows. Dacitic domes were emplaced throughout the Oligocene-Miocene (Mina Vieja, Purén, Torito, and Vicuñita domes). Mineralogy and texture of these dome units are fairly similar, difficulting the age interpretation for these units. Differences in vertical thickness of these bodies suggest that thinner units should constitute lateral lava-flow sequences originated during the dome collapse, whereas thicker bodies constitute the conduits from which these hypabyssal units are emplaced or erupted. As has been observed in contemporaneous volcanic eruptions, volcanic activity in La Coipa was constituted by dome collapses which triggered plinian eruptions with pumice-bearing ignimbritic flows (Cas and Wright, 1996).

The presence of multiple breccia bodies, in most cases associated spatially to dome occurrences, suggests that phreatic activity could have occurred at the moment of the contact between the growing dome and the paleo-water table, eruption that also could have generated pyroclastic flows not necessarily with presence of juvenile fragments (Cas and Wright, 1996).

Hydrothermal fluids exploit permeability networks. The development of phreatomagmatic breccias in La Coipa district generated the permeable rocks for hydrothermal fluid flow. A characteristic of the high- to intermediate-sulfidation in La Coipa deposits is the occurrence of pre-mineral breccia units, which acted as favorable conduits for late ore-bearing hydrothermal fluids. Within La Coipa district, the Can Can, Coipa Norte, Brecha Norte, and Purén deposits have breccia bodies hosting most or a major part of ore. Other epithermal systems of the flat-slab segment hosted in phreatomagmatic to phreatic breccias include the Pascua-Lama, Veladero, Tambo, Cerro Maricunga, Río Blanco-Los Bronces, and El Teniente deposits, indicating the importance of brecciation processes associated to epithermal and porphyry systems (Bissig et al., 2002; Cannell et al., 2005; Chouinard et al., 2005; Holley, 2012; Magri, 2012; and Toro et al., 2012).

Besides the control of breccia units, economic mineralization at La Coipa is spatially associated with the contact zone between the underlying Triassic sedimentary basin and the Tertiary volcanic units. Rheological and chemical contrasts between black shales and quartz-rich sandstones are

considered an important factor for pathways and traps of mineralizing fluids. According to Arriagada et al. (2013), the anticline folding of Triassic basement acted as favorable domains for later magmatic rocks and hydrothermal fluids. Another aspect to consider is the emplacement of pre-, syn-, and late-mineralization hypabyssal domes along the same structures that controlled the mineralized fluids (Figure 6.2). This explains the spatial association between dome units and ore deposits, even though some of these bodies present no visual hydrothermal alteration, and may pre or post date hydrothermal activity.

Although some alunite samples presented analytical challenges when using for $^{40}Ar/^{39}Ar$ dating technique, the results overall allow constraining the temporal evolution of high-sulfidation mineralizing events at La Coipa. It should be noted that the results of applying the $^{40}Ar/^{39}Ar$ technique to alunite samples are considered an estimation of a cooling age (Chiaradia et al., 2013), which is related to the closure temperature of the mineral dated (approximately 280°C for alunite; Love et al., 1998). Because the closure temperature is higher than the formation temperature calculated by sulfur isotopes formation temperature, alunite ages presented in this study are considered formation ages. Coupled with precise U-Pb zircon ages, the magmatic-hydrothermal evolution of the Oligocene-Miocene La Coipa district can be estimated more accurately than previous results based on K-Ar ages (Oviedo et al., 1991). These authors estimated that the magmatic/hydrothermal La Coipa district formed between 24 and 20 Ma. This interpretation was based on radiometric ages of hypabyssal units belonging to the Mina Vieja unit, which acted as host-rocks for alteration and mineralization. Alunite ages obtained during the present study indicate multiple mineralizing events, which mostly took place between 19 and 16 Ma.

The ca. 30.4 Ma alunite age obtained in the Pompeya Sur prospect suggests an older event of hydrothermal alteration that pre-dated the most important Oligocene-Miocene mineralizing events. The presence of the ca. 37 Ma dacitic ignimbrite (TEdi) and the Estratos de Huidobro suggest that magmatism and hydrothermalism was active during the Eocene-early Oligocene. The distinctive intermediate-sulfidation epithermal mineralization observed in the Purén deposit may be temporarily associated to the 30.4 Ma age of the Pompeya Sur alunite but further study is necessary to confirm that.

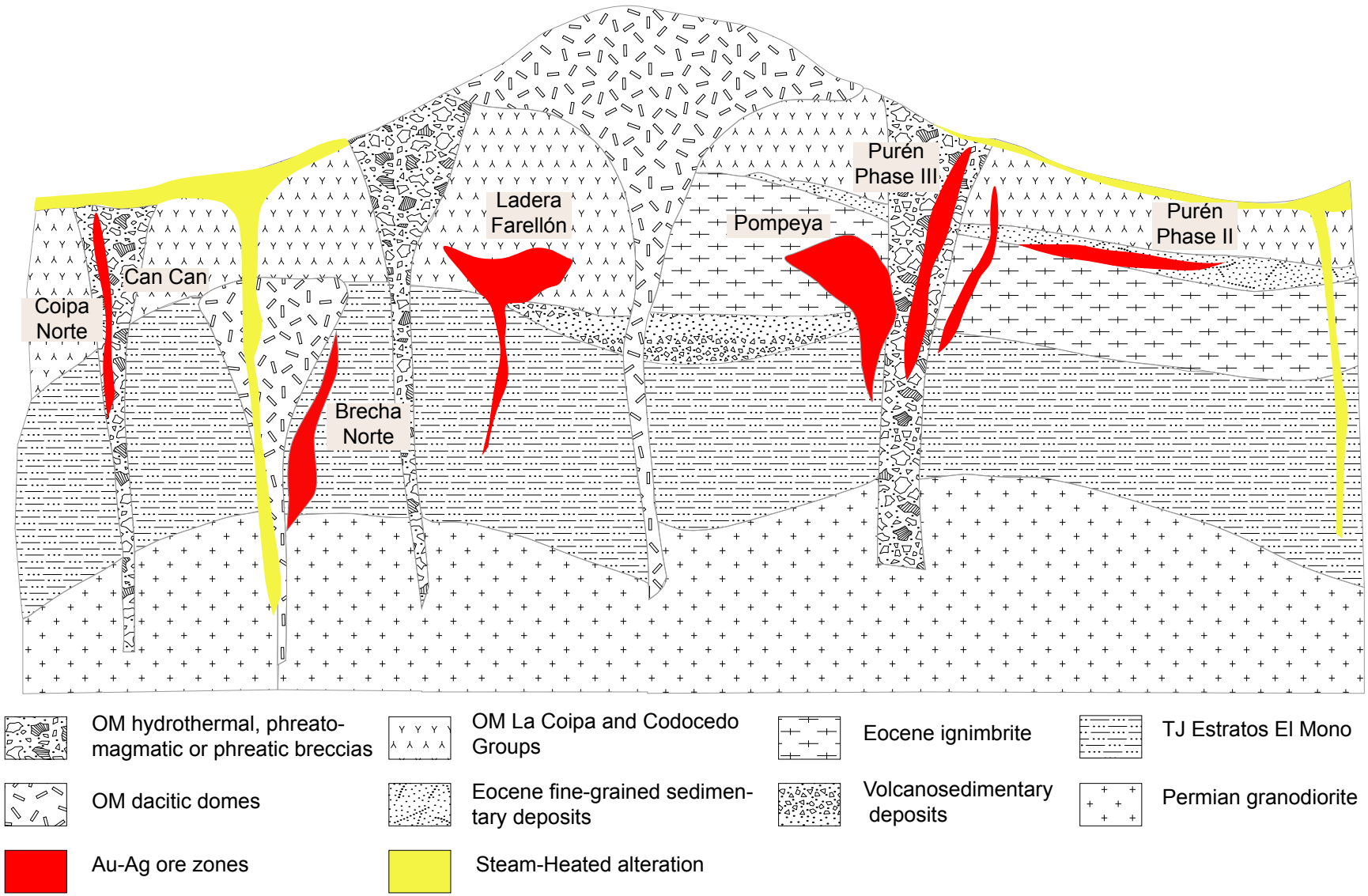

Figure 6.2. Schematic geologic section of the La Coipa district. Main deposits found in the district are represented by Au-Ag ore zones and their location is aproximately situated over the principal host rock lithologies. Abbreviations: OM = Oligocene-Miocene; TJ: Late Triassic-Early Jurassic.

The mineralization events observed in La Coipa are not coeval with pyroclastic volcanic activity. This was described also for the El Indio belt (Bissig et al., 2015). Notwithstanding the time lapse between the Oligocene-Miocene magmatic rocks and the mineralization events, the magmatic and hydrothermal activity occurred episodically over an approximately 10 Ma period (ca. 24 to 14 Ma). This prolonged history of activity has been described for other epithermal districts such as the Yanacocha district (ca. 19.5 to 8.4 Ma; Longo et al., 2010) and the Cerro Casale district (ca. 28 to 13.8 Ma; Hollings et al., 2014).

Situating the formation of ore deposits at La Coipa district into a regional framework, it should be noted that mineralization within the district occurred after and maybe during a regional contractional event that characterized the Andean margin during the late Oligocene-early Miocene. In the Maricunga belt (Lat. 25°-28°S), Arriagada et al. (2006) concluded that block rotation originated during the Eocene as a consequence of deformation of the Precordillera terminated before 18 Ma, in which the non-rotated Río Frío Ignimbrite was deposited. These paleomagnetic results can be used to estimate the minimum age for the compressive event discussed above. According to Tosdal and Richards (2001), changes of the stress regime are an important factor for ore deposits formation and porphyry deposits in the Andes are generally thought to have been emplaced during contractional tectonic events (e.g., Niemeyer and Munizaga, 2008; Mpodozis and Cornejo, 2012). This tectonic setting was described for epithermal and porphyry systems emplaced during the late Eocene along the Domyeko Fault System. These deposits (including the El Hueso and the Guanaco epithermal systems, and the giant Chuquicamata, Escondida, and Collahuasi Cu-porphyries) were emplaced during the Incaic orogen, characterized by slab flattening, crustal thickening and volcanic lull (Mpodozis and Cornejo, 2012).

The metallogeny of the Andean margin in northern Chile and northwestern Argentina is strongly influenced by NW-oriented deep structures and lineaments that controlled the location of porphyry and epithermal systems (Chernicoff et al., 2002). In the La Coipa district, the NW-oriented faults are manifested in a branch of the Eocene Domeyko Fault System characterized by strike-slip left-lateral faults that during the Oligocene-Miocene were reactivated as thrusts and/or normal faults.

The La Coipa district is located near a transition zone described for the Maricunga belt, more specifically, in the southern part of the northern domain. The northern domain is characterized by felsic volcanism and high-sulfidation epithermal systems, developed above a thick crust that implied hydrous magmas that were emplaced through deep NW-oriented structures. It is worth mentioning the Eocene El Salvador porphyry system is considered one of the Cu-porphyry deposits with highest Au grades along the Domeyko Fault System (Tosdal et al., 1999). Further geochronological studies are necessary to investigate the genetic link between the Eocene El Salvador porphyry deposit, the Eocene El Hueso epithermal district, and the Eocene ages for magmatic and hydrothermal activity obtained in the present study.

Chapter 7: Conclusions

The Maricunga belt hosts a series of gold-rich porphyry and high-sulfidation epithermal systems that were emplaced during multiple mineralizing events between 26 and 9 Ma. According to major tectonic changes along the subduction margin, the spatial distribution, intensity, and style of volcanism active during the Oligocene-Miocene arc indicate an evolution divided into four periods: 26-21 Ma, 21-17 Ma, 17-14 Ma, and 11-4 Ma. Volcanic activity was intense during 26-21 Ma and 17-14 Ma, whereas a volcanic lull affected the southern part of the belt between 21 and 17 Ma but not the northern part (north of Lat. 26.5°S). The youngest period, 11-4 Ma, is characterized by a broadening of the arc and an eastward migration of the volcanic front.

Mineralizing events occurred during all these periods, with no clear spatial segregation as was previously suggested by Vila and Sillitoe (1991). A decrease of hydrothermal activity occurred in the arc during the 11-4 Ma period, but the generation of the Farallón Negro volcanic complex further east is correlated with the eastward migration of the arc front. About the latitudinal spread of the Maricunga belt, it is proposed during this study that volcanism and hydrothermal activity proper of this metallogenic province occurred between Lat. 25°S and 28.3°S. The Maricunga belt was developed in a transition zone of the Andean margin where slab-flattening and crustal thickening processes were part of important tectonic changes along the Oligocene-Miocene arc.

To the south of the Maricunga belt segment, the El Indio and the Los Pelambres-El Teniente belts are characterized by multiple Au-Ag high-sulfidation epithermal and Cu-Mo porphyry systems respectively. These belts share with the Maricunga belt a similar history of volcanic evolution and tectonic setting, although a migration from north to south of tectonic events such as crustal thickening and slab-flattening, together with younger ages of mineralizing events, control the evolution of these highly endowed metallogenic provinces. A common feature of some of the main deposits along these three provinces is the prolonged history of volcanic and hydrothermal events through time.

Located in the middle Maricunga belt, the La Coipa Au-Ag epithermal deposit is considered one of the largest high-sulfidation systems developed in this Oligocene-Miocene metallogenic province. The large alteration footprint that characterizes the La Coipa district is the reflection of multiple episodes of volcanism, alteration and mineralization that ranged between 24 and 14 Ma. $^{40}Ar/^{39}Ar$ radiometric ages of alunite obtained in the present study indicate multiple episodes of alteration/mineralization that ranged between 19 and 14 Ma. An older event recorded at Pompeya Sur revealed a ca. 30 Ma alunite age that suggests a newly recognized fertile episode of mineralization.

The La Coipa district is formed by a cluster of high- to intermediate-sulfidation epithermal deposits hosted in Oligocene-Miocene volcanic and hypabyssal units, Eocene ignimbrite and volcaniclastic sequences, Late Triassic-Early Jurassic sedimentary rocks, and Permian granodioritic intrusive units. Based on the stratigraphic column presented in this study, the Oligocene-Miocene magmatic units have been divided into two groups separated by an unconformable contact: The La Coipa (24-21 Ma) and the Codocedo (21-15 Ma) groups. Volcanic and hypabyssal units of both groups are characterized by dacitic rocks composed of plagioclase, hornblende, biotite, and lesser quartz phenocrysts. These rocks are the main host of mineralization and alteration, and temporally linked to the mineralizing events. Ore zones are, in most cases, spatially associated to breccia units. These breccias acted as permeable host rocks for later hydrothermal fluids that in some cases re-brecciated the host rock units.

The Au-Ag mineralization in the La Coipa district is mainly associated to high-sulfidation epithermal systems, characterized by concentric zonation of advanced argillic alteration that grades concentrically from inner vuggy quartz to quartz+alunite, alunite±pyrophyllite+dickite, dickite±kaolinite, kaolinite+illite, and illite+smectite. Most of the mineralization, associated to pyrite+enargite and their related oxidized products, is hosted in the vuggy quartz and quartz+alunite phases. The intermediate-sulfidation Purén deposit is distinguished by intense silicification and kaolinite+illite+smectite argillic alteration. Ore mineralogy in Purén is dominated by pyrite ± sphalerite.

The $\delta^{34}S$ isotopic signature of alunite samples dated by $^{40}Ar/^{39}Ar$ geochronology indicates four styles of precipitation of this mineral in La Coipa district: magmatic-hydrothermal, magmatic steam, steam-heated, and supergene. The $\delta^{34}S$ composition of equilibrated pairs of sulfate (alunite) and sulfides (pyrite or enargite) allowed an estimation of magmatic-hydrothermal alunite temperature formation between 197°C and 264°C. The least altered Eocene to Miocene igneous rocks from La Coipa district are characterized by a geochemical signature that includes elevated La/Yb, Sm/Yb, and Sr/Y ratios, and depleted HREE compared to LREE. This signature indicates a thick crust with garnet or hornblende as residual phases in the deep crust source of magmatic rocks.

In conclusion, the La Coipa district is located in a transition zone of the Maricunga belt, where deep-crustal structures allowed several pulses of magmatic and hydrothermal activity, explaining the development of a cluster of epithermal deposits of high- to intermediate-sulfidation style. The already known deposits, together with the high potential for new resources encountered through systematic exploration carried out in the last years, make La Coipa the most important epithermal system of the Maricunga belt.

7.1 Exploration recommendations

The recurrence and overlapping of multiple episodes of magmatic and hydrothermal activity in La Coipa district generated favorable conditions for the development of Au-Ag deposits that through geologically oriented exploration may increase the resources hosted in concealed deposits within the district. Ideas and conclusions obtained in the present study are presented herein:

- The Au-Ag epithermal system developed in La Coipa district is formed by a series of deposits distributed within an Oligocene-Miocene intra-arc basin characterized by an intense hydrothermal alteration footprint of advanced argillic alteration. These deposits were emplaced as multiple events that range between 19 and 14 Ma, in addition to a 30 Ma event that could increase the potentially

prospective host rock units. The most important event of mineralization is restricted to the 19-16 Ma period. Any exploration decision making within the district must consider this period as key during the selection of high-priority areas or prospects.

- The steam-heated blanket that covers an extensive part of the district, especially in the eastern part, present physical and geochronological evidences that suggest that it represents the paleosurface of hydrothermal systems. Dated at ca. 19 Ma, the steam-heated level pre-dated the main event of mineralization (19-17 Ma), but it bears potential for finding new deposits buried under the almost uneroded surface.

- Hydrothermal fluids used the same pathways as hypabyssal domes, explaining their spatial relationship to epithermal mineralization. The structural setting of the study area and the distribution of dome units suggest that NW-oriented deep structures, reaching lower crustal depths, channeled the magmas from which the hydrothermal fluids were exsolved. Deposits and domes were emplaced at the structural intersection of NW-oriented regional structures and N- to NE-striking local faults.

- The intermediate-sulfidation Purén deposit is partially hosted in reactive carbonaceous sediments of the Estratos de Huidobro unit. The Purén deposit is characterized by an overlap of stratiform polymetallic mineralization within this unit and breccia-hosted gold-rich vertical conduits. The stratiform mineralization may present a broader lateral distribution around the known orebody, improving the prospectivity of this area for Ag-Au and certainly Zn-Pb mineralization.

- On a regional scale, the Maricunga belt hosted multiple epithermal and gold-rich porphyry systems. Radiometric ages obtained in the present study, besides recently published results, suggest a more continuous period of fertile events ranging from 26 to 9 Ma, changing the evolution models proposed during the early stage of reconnaissance of this metallogenic province. The northern part of the Maricunga belt north of La Coipa exhibit the most favorable conditions for the development of high-sulfidation epithermal systems.

7.2 Recommendations for future work

La Coipa district is a good example of high-sulfidation epithermal mineralization and alteration that has not been fully studied, considering the recent improvements of analytical techniques that have not been applied to this district. A list of recommendations for future research is presented herein:

- Considering a regional perspective, the Maricunga belt is a not well studied metallogenic province that requires new models involving the temporal evolution of magmatism and its associated hydrothermal activity. Radiometric ages using precise techniques such as $^{40}Ar/^{39}Ar$, U-Pb, and Re/Os undoubtedly help to understand the history of this region better. Coupled with whole-rock geochemistry, a regional study focused on areas with poor availability of geological data is recommended to validate or modify previous studies.

- The La Coipa district is characterized by multiple events of magmatic activity, which began during the Permian and ended during the middle Miocene. Precise geochronology of these units is strongly recommended to improve the geological mapping of the district either at surface as well as at subsurface through core logging of mine areas and exploration prospects. The reconnaissance of Eocene units proposed in the present study, modified the stratigraphic column determined in previous studies. Furthermore, the lithology of Eocene units exhibits a similar composition and mineralogy as Oligocene-Miocene units, implying the necessity of detailed mapping throughout the entire district.

- The origin of the intermediate-sulfidation mineralization and alteration observed in the Purén deposit is still unclear. The absence of suitable minerals for geochronological techniques considered in the present study imply the evaluation of further techniques to incorporate this system into the district model. Characterized by a predominance of illite+kaolinite clays, an attempt to obtain a crystalline sericite suitable for $^{40}Ar/^{39}Ar$ dating using XRD was not successful. The application of the Re/Os technique on sulfide minerals such as pyrite should be evaluated to restrict the age of

formation of this deposit.

- Deposit-scale description of lithology, alteration, and mineralization of exploited pits is still necessary to understand the controls of mineralization, which can be applied to district-scale exploration of similar deposits. With the aim of improve the knowledge of these deposits, petrography of ore minerals and their related gangue minerals, detailed mapping of lithology and structures, systematic alteration mapping using a short-wave infrared spectrometer, and the study of the role of basement sedimentary rocks of the Estratos El Mono unit as reactive rocks that channeled, concentrated or trapped hydrothermal fluids, are different aspects that can be applied in the district.

References

Abels, A., and Bischoff, L., 1999, Clockwise block rotations in northern Chile: Indications for a large-scale domino mechanism during the middle-late Eocene. Geology, v.27, N°8, p.751-754.

Aguilar, A., 1984, Geología de los cuadrángulos Cerro Vicuñita y Salar de Maricunga, III Región de Atacama, Chile. Unpublished B.Sc. thesis, Universidad Católica del Norte, Antofagasta, Chile.

Allmendinger, R.W., Jordan, T.E., Kay, S.M., and Isacks, B.L., 1997, The evolution of the Altiplano–Puna plateau of the Central Andes. Annual Reviews in Earth and Planetary Science Letters 25, p. 139–174.

Alonso, R.N., and Viramonte, J.G., 1987, Geología y metalogenia de la Puna. Estudios Geológicos, v. 43, p. 393-407.

Alvarez, J., Mpodozis, C., Blanco-Quintero, I., García-Casco, A., Arriagada, C., and Morata, D., 2013, U/Pb ages and metamorphic evolution of the La Pampa Gneisses: Implications for the evolution of the Chilenia Terrane and Permo-Triassic tectonics of north Central Chile. Journal of South American Earth Sciences, v.47, p.100-115.

Arévalo, C., and Mpodozis, C., 1991, Tectónica del Grupo Chañarcillo: una franja de cabalgamientos con vergencia al oeste en el valle del río Copiapó, Región de Atacama, Chile. *In* Congreso Geológico Chileno, N° 6, Actas, p. 81-83, Viña del Mar.

Arriagada, C., and Becerra, J., 2013, Estudio modelo geológico-estructural 3D distrito La Coipa. Kinross Internal Report (unpublished).

Arriagada, C., Roperch, P., Mpodozis, C., and Fernandez, R., 2006, Paleomagnetism and tectonics of the southern Atacama Desert (25–28°S), northern Chile. Tectonics, v.25, p. 1-26.

Arribas Jr., A., 1995, Characteristics of high-sulfidation epithermal deposits and their relation to magmatic fluid. *In* Thompson, J.F.H., (ed.), Magmas, Fluids, and Ore Deposits, Mineral Association of Canada Short Course, v. 23, p. 419-454.

Barrick, 2009, Technical Report. www.barrick.com.

Bell, C.M. and Suárez, M., 1991, Late Triassic fluvial and marine shelf succession, Quebrada Doña Inés Chica, Atacama region, northern Chile. Journal of South American Earth Sciences, v. 4, N°4, p. 287-293.

Bello, E., 2012, El Complejo volcánico del distrito La Coipa, franja de Maricunga: geoquímica, petrología y alteración. Unpublished B.Sc. thesis, University of Chile, Santiago, Chile, 162 p.

Berger, B.R., and Henley, R.W., 1989, Advances in understanding of epithermal gold-silver deposits,

with special reference to the western United States. Economic Geology Monograph 6, p. 405–423.

Bertens, A., Deckart, K., and González, A., 2003, Geocronología U-Pb, Re-Os y $^{40}Ar/^{39}Ar$ del pórfido Cu-Mo Los Pelambres, Chile central. *In* 10° Congreso Geológico Chileno (Concepción) CD Rom.

Bissig, T., 2001, Metallogenesis of the Miocene El Indio-Pascua gold-silver-copper belt, Chile/ Argentina: Geodynamic, geomorphological and petrochemical controls on epithermal mineralisation. Unpublished Ph.D. thesis, Queen´s University, Kingston, Canada, 531 p.

Bissig, T., Lee, J.K.W., Clark, A.H., and Heather, K.B., 2001, The Cenozoic history of volcanism and hydrothermal alteration in the Central Andean flat-slab region: new ^{40}Ar-^{39}Ar constraints from the El Indio-Pascua Au (-Ag, Cu) belt, 29°20' - 30° 30´S. International Geology Reviews, v. 43, p. 312-340.

Bissig, T., Clark, A.H., and Lee, J.K., 2002, Cerro de Vidrio rhyolitic dome: evidence for Late Pliocene volcanism in the central Andean flat-slab region, Lama–Veladero district, 29 20′ S, San Juan Province, Argentina. Journal of South American Earth Sciences, v.15, p. 571–576.

Bissig. T., Clark, A.H., Lee, J.K.W., and von Quadt, A., 2003, Petrogenetic and metallogenetic responses to Miocene slab flattening: new constraints from the El Indio-Pascua Au–Ag–Cu belt, Chile/Argentina. Mineralium Deposita, v. 38, p. 844-862.

Bissig, T., Clark, A.H., Rainbow, A., and Montgomery, A., 2015, Physiographic and tectonic settings of high-sulfidation epithermal gold-silver deposits of the Andes and their controls on mineralizing processes. Ore Geology Reviews, v. 65, p. 327-364.

Bonham, H.F. Jr., 1986, Models for volcanic-hosted epithermal precious metal deposits: A review. *In* International Volcanological Congress, Symposium 5, Hamilton, New Zealand, 1986, Proceedings, p. 13-17.

Burgoa, C., 2014, The Valeriano porphyry. Deep exploration below a lithocap. Chile Explore Congress 2014, Santiago, Chile.

Brüggen, H. 1950, Fundamentos de la Geología de Chile, Instituto Geográfico Militar, Santiago, Chile.

Cahill, T.A., and Isacks, B.L., 1992, Seismicity and shape of the subducted Nazca Plate. Journal of Geophysical Research, v. 97, p. 503-517.

Cannell, J., Cooke, D.R., Walshe, J.L., and Stein, H., 2005, Geology, mineralization, alteration, and structural evolution of the El Teniente porphyry Cu-Mo deposit. Economic Geology, v. 100, p. 979-1003.

Cardó, R, Díaz, I., Cegarra, M., Rodríguez, R., Heredia, N., and Santamaría, G., 1998, Hoja Geológica 2969-III.Malimán. Escala 1:250.000. Servicio Geológico Minero Argentino, 70 p., Buenos Aires.

Cas, R.A.F., and Wright, J.V., 1996, Volcanic Successions Modern and Ancient A geological approach to processes, products and successions. Chapman and Hall, London, 528 p.

Cawood, P.A., 2005, Terra Australis orogen: Rodinia breakup and development of the Pacific and Iapetus margins of Gondwana during the Neoproterozoic and Paleozoic. Earth-Science Reviews, v.69, p. 249-279.

Cecioni, A.J., and Dick, L.A., 1992, Geología del yacimiento epitermal de oro y plata Can Can, Franja de Maricunga, Precordillera de Copiapó, Chile. Revista Geológica de Chile, v. 19, N°1, p. 3-17.

Charchaflie, D., 2003, Geological, structural and geochronological framework of the Veladero North área, Cordillera Frontal, Argentina. Unpublished M.Sc. thesis, University of British Columbia, Vancouver, Canada, 125 p.

Charrier, R., 1979, El Triásico en Chile y regiones adyacentes de Argentina: Una reconstrucción paleogeográfica y paleoclimática. Comunicaciones, Departamento de Geología, Universidad de Chile, Santiago, v. 26, p. 1-47.

Charrier, R., Pinto, L., and Rodríguez, M.P., 2007, Tectonostratigraphic evolution of the Andean orogen in Chile, *in* Moreno, T., and Gibbons, W., eds., The Geology of Chile: London, Geological Society of London, p. 21–114.

Charrier, R., Farías, M., and Maksaev, V., 2009, Evolución tectónica, paleogeográfica y metalogénica durante el Cenozoico en los Andes de Chile norte y central e implicaciones para las regiones adyacentes de Bolivia y Argentina. Revista de la Asociación Geológica Argentina, v. 65, N°1, p. 5-35.

Chernicoff, C., Richards, J.P., and Zappettini, E., 2002, Crustal lineament control on magmatism and mineralization in northwestern Argentina: geological, geophysical, and remote sensing evidence. Ore Geology Reviews, v. 21, p. 127-155.

Chiaradia, M., Schaltegger, U., Spikings, R., Wotzlaw, J.F., and Ovtcharova, M., 2013, How Accurately Can We Date the Duration of Magmatic-Hydrothermal Events in Porphyry Systems?—An Invited Paper. Economic Geology, v.108, p.565-584.

Chouinard. A., Williams-Jones, A.E., Leonardson, R.W., Hodgson, C.J., Silva, P., Tellez, C., Vega, J., and Rojas, F., 2005, Geology and Genesis of the multistage High-Sulfidation epithermal Pascua Au-Ag-Cu deposit, Chile and Argentina. Economic Geology, v. 100, p. 463-490.

Clavero, J., Gardeweg, M., and Mpodozis, C., 1998, Mapa Geológico Preliminar del Area del Salar de Piedra Parada, Región de Atacama. Servicio Nacional de Geología y Minería (Chile). Mapas Geológicos N°, Escala 1:100.000.

Clavero, J., Mpodozis, C., Gardeweg, M., and Valenzuela, M., 2012, Geología de las áreas Laguna Wheelwright y Paso San Francisco, Región de Atacama. Servicio Nacional de Geología y Minería, Carta Geológica de Chile, Serie Geología Básica 139-140 p. 1 mapa escala 1:100.000. Santiago.

Coira, B., Davidson, J., Mpodozis, V., and Ramos, V., 1982, Tectonic and magmatic evolution of the Andes of Northern Argentina and Chile, Earth-Science Reviews, v.18, p. 303-332.

Cooke, D.R., and Simmons, S.F., 2000, Characteristics and genesis of epithermal gold deposits. Reviews in Economic Geology, v. 13, p. 221–244.

Cooke, D.R., and Deyell, C.L., 2003, Descriptive names for epithermal deposits: Their implications for genetic classifications and inferring ore fluid chemistry. *In* Eliopoulos, D. *et al.*, eds., Mineral exploration and sustainable development: Rotterdam, Millpress. Proceedings of the Seventh Biennial SGA Meeting on Mineral Exploration and Sustainable Development, Athens, Greece, August 24–28, Volume 1 (Rotterdam, Millpress Science Publishers), p. 457–460.

Corbett, G., 1998, Comments on the geology of the La Coipa silver-gold and regional projects Maricunga belt, Chile. Kinross Internal Report (unpublished).

Cornejo, P., Mpodozis, C., Ramirez, C.F., and Tomlinson, A., 1993, Estudio Geológico de la Región de Potrerillos y El Salvador (26°–27°S), Servicio Nacional de Geología y Minería-CODELCO, Informe Registrado IR-93-01, 12 cuadrángulos escala 1:50,000 y texto, 258 pp., Santiago, Chile.

Cornejo, P., Mpodozis, C., and Tomlinson, A. J., 1998, Hoja Salar de Maricunga, Región de Atacama, Mapas Geológicos, 7, escala 1:100,000, Servicio Nacional de Geología Y Minería, Santiago.

Cornejo, P., Mpodozis, C., Rivera, O., and Matthews, S. 2009. Carta Exploradora, Regiones de Antofagasta y Atacama. Servicio Nacional de Geología y Minería. Carta Geológica de Chile, Serie Geología Básica 119, 99 p. 1 mapa escala 1:100.000. Santiago.

Davidson, J., and Mpodozis, C., 1991, Regional geologic setting of epithermal gold deposits, Chile. Economic Geology, v. 86, p. 1174–1186.

Davidson, J., Turner, S., and Plank, T., 2013, Dy/Dy*: Variations arising from mantle sources and petrogenetic processes. Journal of Petrology, v. 54, N° 3, p. 525-537.

De la Roche, H., Leterrier, J., Grandclaude, P., and Marchal, M., 1980, A classification of volcanic and plutonic rocks using R1,R2 diagrams and major element analysis-its relationships with current nomenclature. Chemical Geology, v. 29, p. 183-210.

Defant, M.J., and Drummond, M.S., 1990, Derivation of some modern arc magmas by melting of young subducted lithosphere. Nature, v. 347, p. 662-665.

Deyell, C.L., Bissig, T., and Rye, R., 2004, Isotopic Evidence for Magmatic-Dominated Epithermal Processes in the El Indio-Pascua Au-Cu-Ag Belt and Relationship to Geomorphologic Setting. *In*: Sillitoe, R.H., Perelló, J., Vidal, C.E., (eds), Andean Metallogeny: New discoveries, concepts, and updates. Society of Economic Geologists Special Publication 11, p. 55-74.

Deyell, C.L., Leonardson, R., Rye, R.O., Thompson, J.F.H., Bissig, T., and Cooke, D.R., 2005, Alunite in the Pascua–Lama high-sulfidation deposit: Constraints on alteration and ore deposition using stable isotope geochemistry. Economic Geology, v. 100, p. 131–148.

Deckart, K., Clark, A., Cuadra, P., and Fanning, M., 2013, Refinement of the time–space evolution of

the giant Mio-Pliocene Río Blanco–Los Bronces porphyry Cu–Mo cluster, Central Chile: new U–Pb (SHRIMP II) and Re–Os geochronology and $^{40}Ar/^{39}Ar$ thermochronology data. Mineralium Deposita, v.48, p. 57–79.

Deckart, K., Silva, W., Spröhnle, C., and Vela, I., 2014, Timing and duration of hydrothermal activity at the Los Bronces porphyry cluster: an update. Mineralium Deposita, v.49, p. 535-546.

Fifarek, R.H., 2003, Using δ- δ diagrams to interpret sulfide-sulfate sulfur isotopic data for magmatic hydrothermal systems. Abstract Programs-Geological Society of America, 35, 231 p.

Fifarek, R.H., and Rye, R.O., 2005, Stable-isotope geochemistry of the Pierina high-sulfidation Au–Ag deposit, Peru: influence of hydrodynamics on SO_4^{2-} –H_2S sulfur isotopic exchange in magmatic-steam and steam-heated environments. Chemical Geology, v. 215, p. 253-279.

Franchini. M., Impiccini, A., Lentz, D., Ríos, F.J., O´Leary, S., Pons, J., and Schalamuk, A.I., 2011, Porphyry to epithermal transition in the Agua Rica polymetallic deposit, Catamarca, Argentina: An integrated petrologic analysis of ore and alteration parageneses. Ore Geology Reviews, v. 41, p.49-74.

Frutos, J., Oyarzún, J., Shiga, Y., and Alfaro, G., 1990, The El Laco magnetite lava flow deposits, northern Chile: An up-to-date review and new data. *In*: Fontboté, L., Amstutz, G.C., Cardozo, M., Cedillo, E., and Frutos, J., (eds), Stratabound ore deposits in the Andes. Berlin, Germany, Springer-Verlag, p. 681-690.

Fuentes, F., Vergara, M., Aguirre, L., and Feraud, G., 2002, Relaciones de contacto de unidades volcánicas terciarias de los Andes de Chile central (33°S): una reinterpretación sobre la base de dataciones $^{40}Ar/^{39}Ar$. Revista Geológica de Chile, v. 29, p. 207-225.

Gamonal, S., 2007, Exploración minera del distrito Pantanillo, Franja de Maricunga, Región de Atacama, Chile. Unpublished B.Sc. thesis, University of Chile, Santiago, Chile, 113 p.

García, F., 1967, Geología del Norte Grande de Chile. Sociedad Geológica de Chile, Santiago, Simposio sobre el Geosinclinal Andino, Publicación 3, 318 p.

Gatzoubaros, M., von Quadt, A., Gallhofer, D., and Rey, R., 2014, Magmatic evolution of pre-ore volcanics and porphyry intrusives associated with the Altar Cu-porphyry prospect, Argentina. Journal of South American Earth Sciences, v. 55, p. 58-82.

Gonzalez-Ferrán, O., Baker, P.E., and Rex, D.C., 1985, Tectonic-volcanic discontinuity at latitude 27°S, Andean Range, associated with Nazca plate subduction. Tectonophysics, v. 112, p. 423-441.

Godoy, E., 2011, Las Formaciones Abanico y Farellones: nuevos datos hacia fines de una larga controversia. *In* XVIII Congreso Geológico Argentino, Neuquén, Argentina.

Godoy, E., Yañez, G., and Vera, E., 1999, Inversion of an Oligocene volcano-tectonic basin and uplifting of its superimposed Miocene magmatic arc in the Chilean Central Andes: first seismic and

gravity evidences. Tectonophysics, v. 306, p. 217-236.

Goss, A.R., and Kay, S.M., 2006, Steep REE patterns and enriched Pb isotopes in southern Central American arc magmas: Evidence for fore-arc subduction erosion?. Geochemistry, Geophysics, Geosystems, v. 7.

Goss, A.R., and Kay, S.M., 2009, Extreme high field strength element (HFSE) depletion and near-chondritic Nb/Ta ratios in Central Andean adakite-like lavas (~28°S, ~68°W). Earth and Planetary Science Letters, v. 279, p. 97-109.

Goss, A.R., Kay, S.M., and Mpodozis, C., 2013, Andean adakite-like high-Mg andesites on the northern margin of the Chilean-Pampean flat-slab (27-28.5°S) associated with frontal arc migration and fore-arc subduction erosion. Journal of Petrology, v. 54, N° 11, p. 2193-2234.

Gow, P.A., and Walshe, J.L. 2005. The role of preexisting geologic architecture in the formation of giant porphyry-related Cu±Au deposits: Examples from New Guinea and Chile. Economic Geology, v.100(5), p. 819-833.

Grez, E., Aguilar, A., Henríquez, F., and Nyström, J.O., 1991, Magnetita Pedernales: A new magmatic iron deposit in northern Chile. Economic Geology, v. 86, p.1346-1349.

Griffin, W.L., Begg, G.C., and O'Reilly, S.Y. 2013. Continental-root control on the genesis of magmatic ore deposits. Nature Geoscience, v. 6(11), p. 905-910.

Halter, W.E., Bain, N., Becker, K., Heinrich, C.A., Landtwing, M., Von Quadt A.,Clark, A.H., Sasso, A.M., Bissig, T., and Tosdal, R.M., 2004, From andesitic volcanism to the formation of a porphyry Cu-Au mineralizing magma chamber: the Farallón Negro volcanic complex, northwestern Argentina: Journal of Volcanology and Geothermal Research, v. 136, p. 1–30.

Harrington, H. H., 1961, Geology of parts of Antofagasta and Atacama Provinces of Northern Chile. AAPG Bulletin, 45, p. 168–197.

Harris, A.C., Allen, C.M., Bryan, S.E., Campbell, I.H., Holcombre, J., and Palin, J.M., 2004, ELA-ICP-MS U–Pb zircon geochronology of regional volcanism hosting the Bajo de la Alumbrera Cu–Au deposit: implications for porphyry-related mineralization. Mineralium Deposita, v. 39, p. 46-67.

Hayba, D.O., Bethke, P.M., Heald, P., and Foley, N.K., 1985, Geologic, mineralogic, and geochemical characteristics of volcanic-hosted epithermal precious metal deposits. Reviews in Economic Geology, v. 2, p. 129–167.

Heald, P., Foley, N.K., and Hayba, D.O., 1987, Comparative anatomy of volcanic-hosted epithermal deposits: Acid sulfate and adularia-sericite types. Economic Geology, v. 82, p. 1–26.

Hedenquist, J.W., 1987, Mineralization associated with volcanic-related hydrothermal systems in the Circum-Pacific Basin. *In* Horn, M.K., ed., Circum Pacific Energy and Mineral Resources Conference, 4th, Singapore, l986, Transactions. American Association of Petroleum Geologists, p. 5l3–524.

Hedenquist, J.W., Arribas R. A., and Gonzalez-Urien, E., 2000, Exploration for epithermal gold deposits. Reviews in Economic Geology, v. 13, p.245-277.

Heinrich, C.A., 2005, The physical and chemical evolution of low-salinity magmatic fluids at the porphyry to epithermal transition: a thermodynamic study. Mineralium Deposita, v. 39, p. 864–889.

Heinrich, C.A., Günther, D., Audétat, A., Ulrich, T., and Frischknecht, R., 1999, Metal fractionation between magmatic brine and vapor, determined by microanalysis of fluid inclusions. Geology, v. 27, p. 755–758.

Holley, E.A., 2012, The Veladero High-sulfidation Epithermal Au–Ag deposit, Argentina: Volcanic Stratigraphy, Alteration, Mineralization, and Quartz Paragenesis. PhD. Thesis, Colorado School of Mines, Golden, Colorado, p. 226.

Hollings. P., Cooke, D.R., and Clark, A., 2005, Regional geochemistry of Tertiary igneous rocks in Central Chile: Implications for the geodynamic environment of giant porphyry copper and epithermal gold mineralization. Economic Geology, v. 100, p. 887-904.

Hollings, P., Chen, H., and Cooke, D.R., 2013, Tectonic evolution of the Cerro Casale Cu-porphyry system, Chile: Implications for mineralization. *In* 2013 Goldschmidt Conference.

Hollings, P., Chen, H., and Cooke, D.R., 2014, Tectonic evolution of the Cerro Casale Au-Cu-porphyry system, Chile: using igneous geochemistry for exploration targeting. *In* 2014 SEG Conference, Keystone, Colorado.

Ishikawa, Y., Sawaguchi, T., Iwaya, S., and Horiuchi, M., 1976, Delineation of prospecting targets for Kuroko deposits based on modes of volcanism of underlying dacite and alteration halos. Mining Geology, v. 26, p. 105-117.

Itaya, T., Arribas, Jr., A., and Okada, T., 1996, Argon release systematics of hypogene and supergene alunite based on progressive heating experiments from 100 to 1000 °C. Geochimica et Cosmochimica Acta, v. 60, N°22, p. 4525-4535.

Jara, P., and Charrier, R., 2014, Nuevos antecedentes estratigráficos y geocronológicos para el Meso-Cenozoico de la cordillera Principal de Chile entre 32° y 32°30'S: implicancias estructurales y paleogeográficas. Andean Geology, v. 41, p. 174-209.

Jensen, O., and Vicente, J.C., 1976, Estudio geológico del área de "Las Juntas" del rio Copiapó (Provincia de Atacama-Chile). Asociación Geológica Argentina, Revista, 21(3), p. 145–173.

Jordan, T.E., Isacks, B.L., Allmendinger, R.W., Brewer, J.A., Ramos, V.A., and Ando, C.J., 1983, Andean tectonics related to geometry of subducted Nazca plate. Geological Society of America Bulletin 94, p. 341-361.

Kapusta, K., 2011, Los Helados / Re-Os Dating Result. JOGMEC Report, NGEX (unpublished).

Kay, S.M., 1978, Aleutian magnesian andesites: melts from subducted Pacific ocean crust. Journal

of Volcanology and Geothermal Research, v. 4, p. 117-132.

Kay, S.M., and Gordillo, C.E., 1994, Pocho volcanic rocks and the melting of depleted continental lithosphere above a shallowly dipping subduction zone in the Central Andes. Contributions to Mineralogy and Petrology, v. 117, p. 25-44.

Kay, S.M., and Abbruzzi, J.M., 1996, Magmatic evidence for Neogene lithospheric evolution of the Central Andean flat-slab between 30°S and 32°S. Tectonophysics, v. 259, p. 15-28.

Kay, S.M., and Mpodozis, C., 2002, Magmatism as a probe to the Neogene shallowing of the Nazca plate beneath the modern Chilean flat-slab. Journal of South American Earth Sciences, v. 15, p. 39-57.

Kay, S.M., Maksaev, V., Moscoso, R., Mpodozis, C., and Nassi, C., 1987, Probing the evolving Andean lithosphere; mid-late Tertiary magmatism in Chile (29°-30°30') over the modern zone of subhorizontal subduction. Journal of Geophysical Research, v. 92, p. 6173-6189.

Kay, S.M., Maksaev, V., Moscoso, R., Mpodozis, C., Nasi, C., and Gordillo, C.E., 1988, Tertiary Andean magmatism in Chile and Argentina between 28° S and 33°S: Correlation of magmatic chemistry with a changing Benioff zone. Journal of South American Earth Sciences, v. 1, pp. 21-38.

Kay. S.M., Mpodozis, C., Ramos, V.A., and Munizaga, F., 1991, Magma source variations for mid-late Tertiary magmatic rocks associated with a shallowing subduction zone and a thickening crust in the central Andes (28 to 33°S). Geological Society of America Special paper, v. 265, p. 113-137.

Kay, S.M., Mpodozis, C., Tittler, A., and Cornejo, P., 1994, Tertiary magmatic evolution of the Maricunga mineral belt in Chile. International Geology Review, v. 36, p. 1079–1112.

Kay, S.M., Mpodozis, C., and Coira, B., 1999, Neogene magmatism, tectonism and mineral deposits of the Central Andes (22-23° S Latitude). *In*: Skinner, B.J., (ed.), Geology and Ore Deposits of the Central Andes, Society of Economic Geologists Special Publication 7, pp. 27–59.

Kay, S.M., Godoy, E., and Kurtz, A., 2005, Episodic arc migration, crustal thickening, subduction erosion, and magmatism in the south-central Andes. Geological Society of America Bulletin, v. 116, p. 67-88.

Kay. S.M., Mpodozis, C., and Gardeweg, M., 2014, magma sources and tectonic setting of Central Andean andesites (25.5-28°S) related to crutal thickening, forearc subduction erosion and delamination. *In*: Gómez-Tuena, A., Straub, S.M., and Zellmer, G.F., (eds.), Orogenic andesites and crustal growth, Geological Society of London, Special Publication, 385, p. 303-334.

King, A.R., 1992, Magmatism, Structure and Mineralization in the Maricunga Belt N Chile. Unpublished Ph.D. thesis, Imperial College London, University of London, 395 p.

Kuiper, K.F., Deino, A., Hilgen, F.J., Krijgsman, W., Renne, P.R., and Wijbrans, J.R., 2008, Synchronizing rock clocks of earth history. Science, v. 320, p. 500-504.

Kurtz, A., Kay, S.M., Charrier, R., and Farrar, E., 1997, Geochronology of Miocene plutons and exhumation history of the El Teniente region, Central Chile (34-35°S). Revista Geológica de Chile, v. 24, p. 75-90.

Le Maitre, R.W., Bateman, P., Dudek, A., Keller, J., Le Bas, M.J., Sabine, P.A., Schmid, R., Sorensen, H., Streckeisen, A., Woolley, A.R., and Zanettin, B., 1989, A Classification of Igneous Rocks and Glossary of Terms. Blackwell, Oxford.

Lehman, B., 2007, Reconnaissance ore mineralogy, geochemistry and isotope dating (Re-Os, Ar-Ar) of the Dorado Oeste zone of the El Volcán gold deposit, Maricunga belt, northern Chile. Internal report prepared for Andina Minerals Limitada by Bernd Lehman, Institute of Mineralogy and Mineral Resources, Technical University of Clausthal, Clausthal-Zellerfeld, Germany, 4 July 2007.

Lindgren, W., 1922, A suggestion for the terminology of certain mineral deposits. Economic Geology, v. 17, p. 292-294.

-1933, Mineral deposits: New York, McGraw Hill, 4th ed., 930 p.

Litvak, V.D., Poma, S., and Kay, S.M., 2007, Paleogene and Neogene magmatism in the Valle del Cura region: New perspective on the evolution of the Pampean flat slab, San Juan province, Argentina. Journal of South American Earth Sciences, v. 24, p. 117-137.

Longo, A.A., Dilles, J.H., Grunder, A.L., and Duncan, R., 2010, Evolution of calc-alkaline volcanism and associated hydrothermal gold deposits at Yanacocha, Perú. Economic Geology, v. 105, p. 1191-1241.

Loucks, R.R., 2014, Distinctive composition of copper-ore-forming arc magmas. Australian Journal of Earth Sciences, v. 61, p. 5-16.

Love, D.A., Clark, A.H., Hodgson C.J., Mortensen, J.K., Archibald, D.A., and Farrar, E., 1998, The timing of adularia-sericite-type mineralization and alunite-kaolinite-type alteration, Mount Skukum epithermal gold deposit, Yukon Territory, Canada: ^{40}Ar-^{39}Ar and U-Pb geochronology: Economic Geology, v. 93, p. 437−462.

Ludwig, K.R., 2003, Isoplot 3.0 A geochronological toolkit for Microsoft Excel. Berkeley Geochronology Center. Special Publication 4, Berkeley, 71 p.

Magri, E., 2012, Technical Report on the Cerro Maricunga gold Project Region III Chile. Atacama Pacific Gold Corporation Technical Report.

Manea, V.C., Pérez-Gussinyé, M., and Manea, M., 2012, Chilean flat slab subduction controlled by overriding plate thickness and trench rollback. Geology, v. 40, N°1, p. 35-38.

Maksaev, V., Moscoso, R., Mpodozis, C., and Nasi, C., 1984, Las unidades volcánicas y plutónicas del Cenozoico Superior en la alta cordillera del norte chico (29°-31°S): Geología, alteración hidrotermal y mineralización. Revista Geológica de Chile, N°21, p.11-51.

Maksaev, V., Townley, B., Palacios, C., and Camus, F., 2007, Metallic ore deposits. *In* Moreno, T., and Gibbons, W., eds., The Geology of Chile: London, Geological Society of London, p. 179–199.

Martin, M., Clavero, J., Mpodozis, C., and Cutiño, L., 1995, Estudio geológico regional de la franja El Indio. Cordillera de Coquimbo: Informe registrado IR-95-6. Servicio Nacional de Geología y Minería, Chile, and Compañía Minera San José.

Martin, M.W., Clavero, J., and Mpodozis, C., 1999, Late Paleozoic to Early Jurassic tectonic development of the high Andean Principal Cordillera, El Indio Region, Chile (29-30°S). Journal of South American Earth Sciences, v. 12, p. 33-49.

Maydagán, L., Franchini, M., Chiaradia, M., Pons, J., Impiccini, A., Toohey, J., and Rey, R., 2011, Petrology of the Miocene igneous rocks in the Altar region, main Cordillera of San Juan, Argentina: A geodynamic model within the context of the Andean flat-slab segment and metallogenesis. Journal of South American Earth Sciences, v.32, p. 30-48.

Maydagán, L. Franchini, M., Chiaradia, M., Dilles, J., and Rey, R., 2014, The Altar porphyry Cu-(Au-Mo) deposit (Argentina): A complex magmatic-hydrothermal system with evidence of recharge processes. Economic Geology, v. 109, p. 621-641.

McKee, E. H., Robinson, A.C., Rybuta, J.J., Cuitiño, L., and Moscoso, R.D., 1994, Age and Sr isotopic composition of volcanic rocks in the Maricunga Belt, Chile: implications for magma sources. Journal of South American Earth Sciences, v. 7, N°2, p. 167-177.

Mercado, M., 1980, Geología del área Pan de Azúcar, Región de Atacama. Servicio Nacional de Geología y Minería, Santiago, Carta Geológica de Chile, 37, 1:100.000.

Mercado, M., 1982, Hoja Laguna del Negro Francisco, Región de Atacama. Servicio Nacional de Geología y Minería, Carta Geológica de Chile, N° 56, 73 p. Santiago.

Moore, N.D., 1979, The geology and geochronology of the Arequipa segment of the Coastal Batholith of Peru. Unpublished Ph.D. thesis, University of Liverpool, Liverpool, England.

Moscoso, R., and Mpodozis, C., 1988, Estilos estructurales en el Norte Chico de Chile. Revista Geológica de Chile, v. 15, p. 151-166.

Moscoso, R., Díaz, F., Cuitiño, L., and Maksaev, V., 1991, Mineralización de metales preciosos y volcanismo Neógeno en los Andes del norte de Chile (26°-28°S): El prospecto Esperanza. *In*: Seminario-Taller “Procesos Formadores de Depósitos Minerales en Ambientes Volcánicos”: INGEMMET, Lima, Perú.

Moscoso, R., Mpodozis, C., Nassi, C., Ribba, L., and Arévalo, C., 2010, Geología de la Hoja El Tránsito, Región de Atacama. Servicio Nacional de Geología y Minería, Serie Preliminar 7: 3 anexos, 1 mapa escala 1:250.000. Santiago.

Mpodozis. C., Cornejo, P., Kay, S.M., and Titler, A., 1995, La Franja de Maricunga: síntesis de la

evolución del Frente Volcánico Oligoceno-Mioceno de la zona sur de los Andes Centrales. Revista Geológica de Chile, v. 21, N°2, p. 273-313.

Mpodozis, C., and Clavero, J., 2002, Tertiary tectonic evolution of the southwestern edge of the Puna Plateau: cordillera Claudio Gay (26°–27°S). 5th Symposium on Andean Geodynamics, Toulouse (France), p. 445–448.

Mpodozis, C., and Cornejo, P., 2012, Cenozoic Tectonics and Porphyry Copper Systems of the Chilean Andes. *In*: Hedenquist, J.W., Harris, M., Camus, F. (Eds.), Geology and Genesis of Major Copper Deposits and Districts of the World: A Tribute to Richard H. Sillitoe. Society of Economic Geologists Special Publication 16, pp. 329–360.

Mulcahy, P., 2012, The southern Puna seismic experiment: seismicity and the morphology of the subduction zone. Unpublished M.Sc. thesis, Cornell University, United States, 88 p.

Mulcahy, P., Chen, C., Kay, S.M., Brown, L.D., Alvarado, D., Sandoval, E., Calixto, F., Heit, B., and Xiaohui, Y., 2010, The Southern Puna seismic experiment: shape of the subducting Nazca Plate, areas of concentrated mantle and crustal earthquakes, and crustal focal mechanisms. Transactions of the American Geophysical Union (AGU) 91, Fall Meeting Suppl., T11A-2050.

Mulja, T., 1986, Hydrothermal alteration, gold distribution and geochronology of epithermal gold mineralization in the Copiapó volcanic complex, Chile. B.Sc. Thesis (Unpublished), Dalhousie University, Halifax, Nova Scotia, Canada, 156 p.

Müller, G.M., and Perelló, L.J., 1982, Geología regional y bioestratigrafía del Jurásico marino al occidente del Salar de Pedernales (26°15' – 26°24'S. 69°15' – 69°30'W). Región de Atacama, Chile. B.Sc., Departamento de Geología y Geofísica, Universidad de Chile, Santiago, Chile.

Muntean, J.L., and Einaudi, M.T., 2000, Porphyry gold deposits of the Refugio district, Maricunga belt, northern Chile. Economic Geology, v. 95, p. 1445-1472.

Muntean. J.L., and Einaudi, M.T., 2001, Porphyry-Epithermal Transition: Maricunga Belt, Northern Chile. Economic Geology, v. 96, p. 743-772.

Muñoz, J., 1984, Geología de la hoja Salar de Maricunga (1:100,000): informe de avance de la hoja El Salvador (1:250,000), región de Atacama, Chile. Servicio Nacional de Geología y Minería, Informe inédito, p. 1-30, Santiago, Chile.

Muñoz, M., Fuentes, F., Vergara, M., Aguirre, L., Nyström, J. O., Feraud, G. and Demant, A., 2006, Abanico East Formation: petrology and geochemistry of volcanic rocks behind the Cenozoic arc front in the Andean Cordillera, central Chile (33º50´S). Revista Geológica de Chile, 33(1), p. 109–140.

Murakami, H., Seo, J.H., and Heinrich, C.A., 2010, The relation between Cu/Au ratio and formation depth of porphyry-style Cu-Au ± Mo deposits. Mineralium Deposita, v. 45, p. 11-21.

Muzzio, G., 1980, Geología de la región comprendida entre el Cordón de Varillar y Sierra Las Viscachas, Precordillera de Atacama, Chile. Unpublished B.Sc. thesis, Universidad de Chile, Santiago.

Nano, S., Nunn, D., Heenan, T., Echavarría, L., Nerach, M., and Frutos, P., 2015, Atlas gold/silver Project: A new generation precios metal project in the Mio-Pliocene volcanic arc of northern Chile. AME bc Roundup, 2015.

Naranjo, J. A. and Puig, A., 1984, Hojas Taltal y Chañaral. Servicio Nacional de Geología y Minería, Santiago, Carta Geológica de Chile, 62–63.

Naranjo, J.A., and Cornejo, P., 1992, Hoja Salar de la Isla. Servicio Nacional de Geología y Minería, Carta Geológica de Chile, No. 72, escala 1:250.000.

Naranjo, J.A.; Villa, V.; and Venegas, C., 2013, (a) Geología de las áreas Salar de Pajonales y Cerro Moño, regiones de Antofagasta y Atacama. Servicio Nacional de Geología y Minería, Carta Geológica de Chile, Serie Geología Básica, N° 153-154, 1 mapa escala 1:100.000. Santiago.

-(b) 2013. Geología de las áreas Salar de Aguilar y Portezuelo del León Muerto, Región de Atacama. Servicio Nacional de Geología y Minería, Carta Geológica de Chile, Serie Geología Básica, N° 151-152, 1 mapa escala 1:100.000. Santiago.

Niemeyer, H., and Munizaga, R., 2008, Structural control of the emplacement of the Potrerillos porphyry copper, central Andes of Chile. Journal of South American Earth Sciences, v. 26, p. 261-270.

Niemeyer, H., and Urrutia, C., 2009, Transcurrencia a lo largo de la Falla Sierra de Varas (Sistema de fallas de la Cordillera de Domeyko), norte de Chile. Andean Geology, v. 36, p. 37-49.

Ohmoto, H., and Rye, R.O., 1979, Isotopes of sulfur and carbon. *In*: Barnes, H.L., (ed.), Geochemistry of hydrothermal ore deposits, 2nd ed., New York, Wiley Interscience, v.2, p. 509-567.

Oviedo, L., Fuster, N., Tschischow, N., Ribba, L., Zuccone, A., Grez, E., and Aguilar, A., 1991, General Geology of La Coipa Precious Metal Deposit, Atacama, Chile. Economic Geology, v. 86, p.1287-1300.

Parada, M.A., López-Escobar, L., Oliveros, V., Fuentes, F., Morata, D., Calderón, M., Aguirre L., Féraud, G., Espinoza, F., Moreno, H., Figueroa, O., Muñoz Bravo, J., Troncoso Vásquez, R., and Stern, C.R., 2007, Andean magmatism. *in* Moreno, T., and Gibbons, W., eds., The Geology of Chile: London, Geological Society of London, p. 115–146.

Pardo, R., and Kovacic, P., 2012, Geología y potencial de exploración del distrito El Teniente. Andes Centrales, VI Región del Libertador Bernardo O'Higgins, Chile. In XIII Congreso Geológico Chileno, Antofagasta, Chile.

Pardo-Casas, F., and Molnar, P., 1987, Relative motion of the Nazca (Farallón) and South American plates since late Cretaceous time, Tectonics, v. 6, p. 233-248.

Peccerillo, R., and Taylor, S., 1976, Geochemistry of Eocene calc-alkaline volcanic rocks from the

Kastamonu area, northern Turkey. Contributions to Mineralogy and Petrology, v. 58, p. 63-81.

Perelló, J., Mpodozis, C., and Urzúa, F., 2003, Late Oligocene-early Miocene porphyry Cu-Mo and Au-Cu mineralization, Pulido cluster, Atacama Region, northern Chile. *In* 10° Congreso Geológico Chileno, Concepción, Chile.

Perelló, J., Sillitoe, R.H., Mpodozis, C., Brockway, H., and Posso, H., 2012, Geologic setting and evolution of the porphyry copper-molybdenum and copper-gold deposits at Los Pelambres, Central Chile. Society of Economic Geologists Special Publication N° 16, p. 79-104.

Proffett. J.M., 2003., Geology of the Bajo de la Alumbrera Porphyry Copper-Gold Deposit, Argentina. Economic Geology, v.98, p. 1535-1574.

Pudack, C., Halter, W.E., Heinrich, C.A., and Pettke, T., 2009, Evolution of magmatic vapor to gold-rich epithermal liquid: the porphyry to epithermal transition at Nevados de Famatina, Northwest Argentina. Economic Geology, v. 104, p. 449–477.

Rainbow. A., Clark, A.H., Kyser, T.K., Gaboury, F., and Hodgson, C.J., 2005, The Pierina epithermal Au–Ag deposit, Ancash, Peru: paragenetic relationships, alunite textures, and stable-isotope geochemistry. Chemical Geology, v. 215, p. 235-252.

Ramos, V. A., 2009, Anatomy and global context of the Andes: Main geologic features and the Andean orogenic cycle. *In* Kay, S.M., Ramos, V.A., and Dickinson, W.R., eds., Backbone of the Americas: Shallow subduction, plateau uplift, and ridge and terrane collision: Geological Society of America Memoir 204, p. 31-65.

Ramos, Victor A., 2008, The Basement of the Central Andes: The Arequipa and Related Terranes. Annual Review of Earth and Planetary Sciences, v. 36, p. 289-324.

Rhodes, A.L., Oreskes, N., and Sheets, S.A., 1999, Geology and rare earth element geochemistry of magnetite deposits at El Laco, Chile. *In*: Skinner, B.J., ed., Geology and ore deposits of the central Andes. Littleton, Colorado, Society of Economic Geologists Special Publication N° 7, p. 299-332.

Richards, J.P., 2000, Lineaments revisited. Society of Economic Geologists Newsletter, v. 42, p. 13-20.

- 2003, Tectono-magmatic precursors for porphyry Cu-(Mo-Au) deposit formation. Economic Geology, v. 98, p. 1515−1533.

- 2011, Magmatic to hydrothermal metal flux in convergent and collided margins. Ore Geology Reviews, v. 40, p. 1-26.

Richards, J.P., and Kerrich, R., 2007, Adakite-like rocks: their diverse origins and questionable role in metallogenesis. Economic Geology, v. 102, p. 537-576.

Riquelme, R., Hérail, G., Martinod, J., Charrier, R., and Darrozes, J., 2007, Late Cenozoic geomorphological signal of Andean forearc deformation and tilting associated with the uplift and

climate changes of the Southern Atacama Desert (26°S-28°S). Geomorphology, v. 86, p. 283-306.

Rivera, S., 1990, La Exploración del yacimiento epitermal de plata-oro La Coipa, Chile: antecedentes históricos y geológicos de un caso real. *In* Yacimientos minerales, técnicas de estudio-tipos-evaluación metalogénica-exploración. Lunar, R., and Oyarzún, R., eds., Editorial Centro de Estudios Ramón Areces. S.A., Madrid, España, 938 p.

Rollinson, H., 1993, Using Geochemical Data: Evaluation, Presentation, Interpretation. Longman, 352 p.

Rubiolo. D., 2001, Mapa de la Hoja Geológica 2769-IV Fiambalá, provincias de Catamarca y La Rioja. Boletín 361, Programa Nacional de Cartas Geológicas 1:250,000.

Rye, R.O., 2005, A review of the stable isotope geochemistry of sulfate minerals in selected igneous environments and related hydrothermal systems. Chemical Geology, v. 215, p. 5-36.

Rye, R.O., Bethke, P.M., and Wasserman, M.D., 1992, The stable isotope geochemistry of acid sulfate alteration. Economic Geology, v. 87, p. 225–262.

Sasso, A.M., 1997, Geological evolution and metallogenetic relationships of the Farallón Negro volcanic complex, NW Argentina. Unpublished Ph.D. thesis, Queen's University, Ontario, Canada, 842 p.

Sasso, A.M., and Clark, A.H., 1998, The Farallón Negro group, northwest Argentina: magmatic hydrothermal and tectonic evolution and implications for Cu-Au metallogeny in the Andean backarc, Society of Economic Geology Newsletter 34, 18 p.

Schnurr, W.B.W., Trumbull, R.B., Clavero, J., Hahne, K., Siebel, W., and Gardeweg, M., 2007, Twenty-five million years of silicid volcanism in the southern central volcanic zone of the Andes: Geochemistry and magma genesis of ignimbrites from 25 to 27° S, 67 to 72° W. Journal of Volcanology and Geothermal Research, v. 166, p. 17-46.

Scoates, J.S., and Friedman, R.M., 2008, Precise age of the platiniferous Merensky Reef, Bushveld Complex, South Africa, by the U-Pb zircon chemical abrasion ID-TIMS technique. Economic Geology, v. 103, p. 465-471.

SEGEMAR, sig.segemar.gov.ar

Sepúlveda, P., and Naranjo, J.A., 1982, Hoja Carrera Pinto. Servicio Nacional de Geología y Minería, Carta Geológica de Chile, 53, Escala 1:100,000.

SERNAGEOMIN, 2003. Mapa Geológico de Chile: versión digital. Servicio Nacional de Geología y Minería, Publicación Geológica Digital, N° 4 (CD-ROM, versión 1.0, 2003). Santiago.

Siebel, W., Schnurr, W.B.W., Hahne, K., Kraemer, B., Trumbull, R.B., van den Bogaard, P., and Emmermann, R., 2001, Geochemistry and isotope systematics of small- to medium-volume Neogene-Pleistocene ignimbrites in the southern central Andes: evidence for derivation from andesitic magma sources. Chemical Geology, v. 171, p. 213-237.

Sillitoe, R.H., 1977, Metallic mineralization affiliated to subaerial volcanism: A review. *In* Volcanic processes in ore genesis, London, Institution of Mining and Metallurgy and Geological Society, p. 99-116.

-1993, Epithermal models: Genetic types, geometrical controls and shallow features. Geological Association of Canada Special Paper 40, p. 403-417.

-2010, Porphyry Copper Systems., Economic Geology, v.105, p. 3-41.

Sillitoe, R.H., McKee, E.H., and Vila, T., 1991, Reconnaissance K-Ar geochronology of the Maricunga gold-silver belt, northern Chile. Economic Geology, v. 86, p. 1261-1270.

Sillitoe, R.H., and Hedenquist, J.W., 2003, Linkages between volcanotectonic settings, ore-fluid compositions, and epithermal precious metal deposits. Economic Geology Special Publication 10, p. 315-343.

Sillitoe. R.H., Tolman, J., and Van Kerkvoort, G., 2013, Geology of the Caspiche Porphyry Gold-Copper Deposit, Maricunga Belt, Northern Chile., Economic Geology, v. 108, p. 585-604.

Simmons, S.F., White, N.C., and John, D.A., 2005, Geological characteristics of epithermal precious and base metal deposits. Economic Geology, 100th Anniversary Volume, p. 485-522.

Skinner, S.M., and Clayton, R.W., 2013, The lack of correlation between flat slabs and bathymetric impactors in South America. Earth Planetary Science Letter, v. 371, p. 1-5.

Somoza, R., 1998, Updated Nazca (Farallón) -South America relative motions during the last 40 m.y. implications for mountain building in the central Andean region. Journal of South American Earth Sciences, v. 11, p. 211-215.

Suarez., and Bell. C.M., 1985, Sabkhas continentales y costeros en el Triásico Superior-Cretácico Inferior de Atacama, Chile. Revista Geológica de Chile, v. 25-26, p. 145-153.

Suárez, M., and Bell, C.M., 1991, Sedimentos lacustres de probable edad triásica, en el área de La Coipa, Región de Atacama, Chile. Actas 6 Congreso Geológico Chileno, Viña del Mar, p. 660-663.

Suarez, M., Bell, C. M., and Hutter, T., 1995, Lower Triassic lacustrine sediments in La Coipa area, Atacama, Chile. Journal of South American Earth Sciences, v. 8, p. 9–15.

Titler, A., 1995, The chemistry of Miocene Andean volcanic rocks from the “flat-slab” to central volcanic zone transition, Chile, 26° to 28° S. Unpublished M.Sc. thesis, Cornell University, United States, 142 p.

Tomlinson, A.J., Cornejo, P., and Mpodozis, C., 1999, Hoja Potrerillos, Región de Atacama, Servicio Nacional de Geología y Minería (Chile), Mapas Geológicos N° 14, 1 mapa escala 1:100.000, Santiago.

Toro, J.C., Ortúzar, J., Zamorano, J., Cuadra, P., Hermosilla, J., and Spröhnle, C., 2012, Protracted magmatic-hydrothermal history of the Río Blanco-Los Bronces district, Central Chile: Development of world´s greatest known concentration of copper. Society of Economic Geologists Special Publication N° 16, p. 105-126.

Tosdal, R.M., and Richards, J.P., 2001, Magmatic and structural controls on the development of porphyry Cu ± Mo ± Au deposits. Reviews in Economic Geology, v. 14, p. 157−181.

Tosdal, R.M., Wooden, J.L., and Bouse, R.M., 1999, Pb Isotopes, Ore deposits, and Metallogenic Terranes. *In*: Lambert, D.D., Ruiz, J., (eds.), Application of Radiogenic Isotopes to Ore Deposit Research and Exploration. Reviews in Economic Geology 12, p. 1-28.

Trumbull, R.B., Wittenbrink, R., Hahne, K., Emmermann, R., Büsch, W., Gerstenberger, H., and Siebel, W., 1999, Evidence for late Miocene to Recent contamination of arc andesites by crustal melts in the Chilean Andes (25-26°S) and its geodynamic implications. Journal of South American Earth Sciences, v. 12, p. 135-155.

Trumbull, R.B., Riller, U., Oncken, O., Scheuber, E., Munier, K., and Hongn, F., 2006, The time-space distribution of Cenozoic arc volcanism in the Central Andes: a new data compilation and some tectonic implications. *In*: Oncken, O., Chong, G., Franz, G., Giese, P., Götze, H.-J., Ramos, V.A., Strecker, M.R., Wigger, P. (Eds.), The Andes – Active Subduction Orogeny. Frontiers in Earth Sciences, v. 1, Springer-Verlag, Berlin, p. 29–43.

Venegas, C., Cervetto, M., Astudillo, N., Espinoza, F., Cornejo, P., Mpodozis, C., and Rivera, O., 2013, Carta Sierra Vaquillas Altas, Región de Antofagasta. Servicio Nacional de Geología y Minería, Carta Geológica de Chile, Serie Geología BásicaNo. 159, 1 mapa escala 1:100.000.

Vila, T., 1991, Epithermal silver-gold mineralization at the Esperanza area, Maricunga belt, high Andes of Northern Chile. Revista Geológica de Chile, v. 18, p. 37-54.

Vila. T., and Sillitoe, R.H., 1991, Gold-rich porphyry systems in the Maricunga belt, northern Chile. Economic Geology, v. 86, p. 1238-1260.

Walker, J.A., Moulds, T.N., Zentilli, M., and Feigenson, M.D., 1991, Spatial and temporal variations in volcanics of the Andean Central Zone (26° to 28° S). Geological Society of America Special Paper, v. 265, p. 139-155.

White, N.C., and Hedenquist, J.W., 1990, Epithermal environments and styles of mineralization – variations and their causes, and guidelines for exploration. Journal of Geochemical Exploration, v. 36, p. 445-474.

White, N.C., and Hedenquist, J. W., 1995, Epithermal gold deposits of the southwest Pacific. Society

of Economic Geologists Newsletter, v. 54, p. 87-136.

Williams, N.C., and Davidson, G.J., 2004, Possible submarine advanced argillic alteration at the Basin Lake prospect, Western Australia. Economic Geology, v. 99, p. 987-1002.

Winocur, D.A., Litvak, V.D., Ramos, V.A., 2014. Magmatic and tectonic evolution of the Oligocene Valle del Cura basin, Main Andes of Argentina and Chile: evidence for generalized extension. Geological Society of London Special Publication N° 399.

Yañez, G.A., Ranero, C.R., von Huene, R., and Díaz, J., 2001, Magnetic anomaly interpretation across the southern central Andes (32°-34°S): The role of the Juan Fernandez Ridge in the late Tertiary evolution of the margin. Journal of Geophysical Research, v.106, p. 6325-6345.

Zappettini, E., Miranda-Angeles, V., and Rodríguez, C., 2001, Mapa metalogénico de la región fronteriza entre Argentina, Bolivia, Chile y Perú (14°S-28°S). Servicio Nacional de Geología y Minería, Chile, Publicación Multinacional 2, 1:1,000,000.

Zentilli, M., 1974, Geological evolution and metallogenetic relationships in the Andes of northern Chile between 26° and 29° south. Unpublished Ph.D. thesis, Queen´s University, Ontario, Canada, 394 p.

Zentilli, M., Stark, A., Reynolds, P.H., Mulja, T., Walker, J.A., and Ulriksen, C., 1991, Native Sulphur deposits as The Crown of epithermal systems? Isotopic and geochronological data on the Copiapó Complex, Maricunga, Northern Chile. *In* Congreso Geológico Chileno N° 6, Actas, p. 616-620, Viña del Mar.

Appendices

Appendix A1. 1:20,000 scale geological map of the La Coipa district.

KINROSS

Appendix A1. 1:20,000 SCALE GEOLOGICAL MAP OF THE LA COIPA DISTRICT

UBC

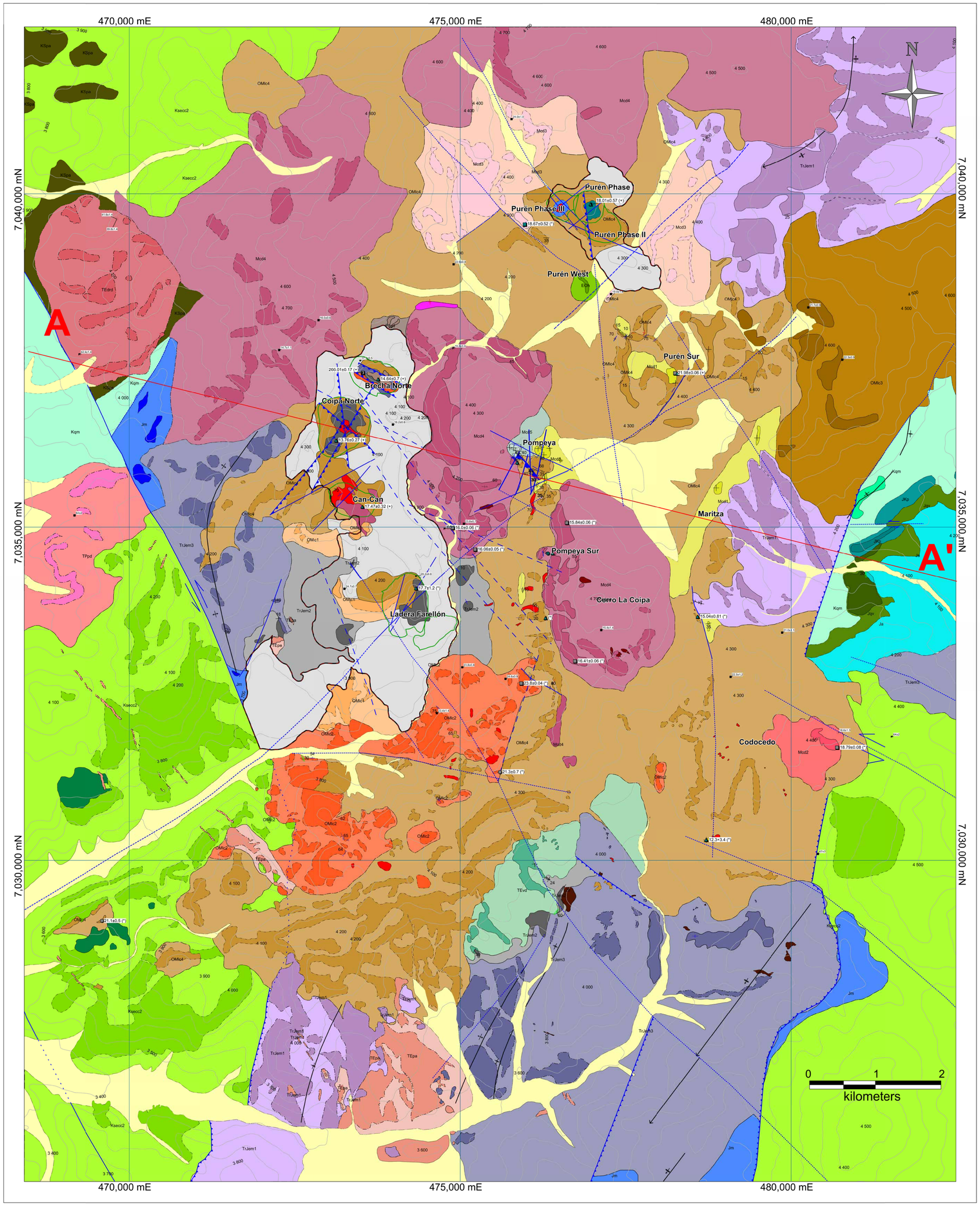

LEGEND

Holocene

Alluvial and colluvial deposits
- Qt — Unconsolidated gravels, breccias, sands and silts

Middle Miocene
- Mbx — Phreatomagmatic to phreatic breccias

Codocedo Group
- Mcd6 — Base and surge deposits
- Mcd5 — Hematitized volcaniclastic sandstones and breccias
- Mcd4 — Vicuñita domes
- Mcd3 — Los Terneros ignimbrite
- Mcd2 — Torito dome
- Mcd1 — Azufrera volcaniclastics

Oligocene -Lower Miocene

La Coipa Group
- OMlc4 — Pompeya pyroclastics
- OMlc3 — Purén domes
- OMlc2 — Mina Vieja domes
- OMlc1 — Ladera tuffs

Eocene - Oligocene
- EOh — Estratos de Huidobro

Eocene
- TEdi — Dacitic ignimbrite
- TEvd — Volcaniclastic deposits

Middle Eocene - Upper Eocene
- TEpa — Rhyodacitic porphyries and dikes
- TEdrd — Rhyolitic domes

Paleocene - Lower Eocene
- TPpd — Dacitic Porphyries

Upper Cretaceous- Lower Paleocene
- KTgb — Monzogabbroic stocks
- KSpa — Andesitic and microdioritic porphyries

Estratos de Cerro Los Carneros
- Ksecc2b — Ocoitic sills
- Ksecc2 — Andesitic lavas

Lower Cretaceous

Quebrada Monardes Formation
- Kqm — Brown-reddish sandstones

Upper Jurassic - Lower Cretaceous

Pedernales Formation
- JKp — Limestones and calcareous sandstones

Estratos de Quebrada Vicuñita
- Jqv — Andesitic to basaltic lavas

Middle Jurassic

Asientos Formation
- Ja — Fossiliferous limestones

Lower Jurassic - Middle Jurassic

Montandón Formation
- Jm — Fossiliferous limestones and calcareous shales

Upper Triassic - Lower Jurassic

Estratos El Mono Unit
- TrJem3 — Quartz-rich sandstones and fine grained conglomerates
- TrJem2 — Black shales
- TrJem1 — Coarse conglomerates and quartz-rich sandstones

Permian
- Pzgd — Permian Granodiorite

Structures
- Fault (Undifferentiated)
- Thrust Fault
- Normal Fault
- Fault (Inferred)
- Fault (Covered)
- Lineament
- Structure orientation
- Stratigraphical orientation (stratification, banding)
- Sub-horizontal stratification
- Veins and hydrothermal breccia orientation
- Lithological contact orientation
- Fold: Syncline, Anticline, Anticline (overturned)
- Perturbed surface by mining
- Mine Area

Geochronology

This study
(*) Surface sample (+) Drill-Hole sample
- ID-TIMS U/Pb zircon
- Laser Ablation U/Pb zircon
- $^{40}Ar/^{39}Ar$ Alunite
- $^{40}Ar/^{39}Ar$ Biotite

Previous K/Ar datings
(Cornejo and Mpodozis, 1993; Sillitoe et. al., 1991)
- Biotite
- Whole Rock
- Hornblende
- Alunite

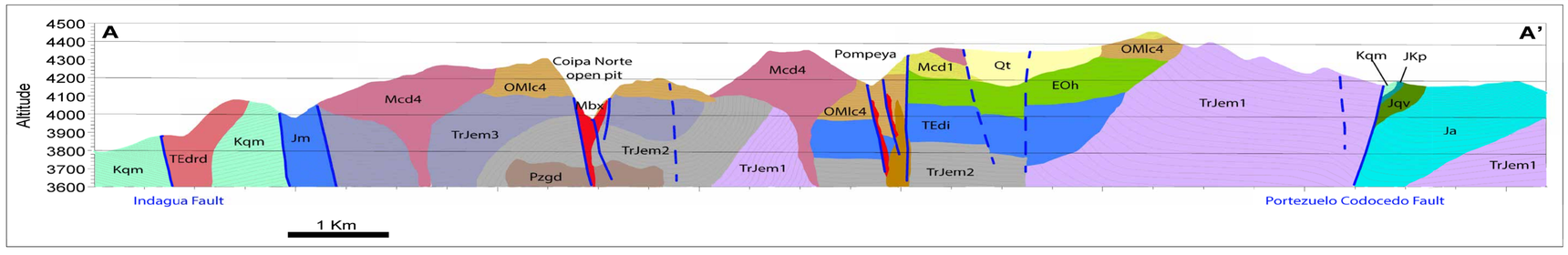

Base Map Information

Topography: Instituto Geográfico Militar Chile
Servicio Nacional de Geología y Minería - Hoja Salar de Maricunga

Imagery: Geoeye Image, 2012. GIS Consultores.

Projection: UTM Coordinates, Provisional South American Datum, Zone 19 South

References

Cornejo, P., Mpodozis, C., Ramírez, C.F., and Tomlinson, A.J. 1993. Estudio geológico de la región de Potrerillos y El Salvador (26° - 27° Lat.S). Servicio Nacional de Geología y Minería and CODELCO, Informe registrado (IR-93-01); 2 V. 258 p.

Cornejo, P., Mpodozis, C., and Tomlinson, A.J. 1998. Hoja Salar de Maricunga, Región de Atacama. Servicio Nacional de Geología y Minería. Mapas geológicos N°7, CD-ROM version 1.0, 1999. Escala 1:100.000. Santiago.

Kinross La Coipa. 2011. Mapa geológico del distrito La Coipa. Kinross Internal Report.

Kinross La Coipa. 2012. Modelos estructurales de rajos mina La Coipa. Kinross Internal Report.

Sillitoe, R.H., McKee, E.H., and Vila, T. 1991. Recconnaisance K-Ar geochronology of the Maricunga gold-silver belt, Northern Chile. Economic Geology, v.86, p. 1261-1270.

Appendix A2. Locations and analytical techniques applied to surface and drill-hole samples collected during the field mapping campaign.

Station/Sample	Unit	Sector	UTM N	UTM E	Elevation [m]	Petrography	Geochemistry	Geochronology
13351 (SG180712_P1)	OMlc2	Sofía	7032650	475925	4040	TS	WR	U/Pb
13352 (SG180712_P2)	OMlc2	Sofía	7032704	475776	3970	TS		
13353 (SG180712_P3)	OMlc2	Sofía	7032795.1	475332.48	3896	TS		
13354 (SG180712_P4)	OMlc2	Sofía	7032743	475229	3904			
13355 (SG180712_P5)	OMlc2	Sofía	7032652.67	475176.38	3865	TS	WR	
13356 (SG180712_P6)	Mcd4	Co. Los Terneros	7035091.13	475236.02	4169	TS	WR	
13357 (SG180712_P7)	Mcd4	Qda. Los Terneros	7035269.45	474517.03	3928	TS		
13358 (SG180712_P8)	Mcd4	Qda. Los Terneros	7034983.83	474888.78	3909	TS	WR	U/Pb
13359 (SG220712_P1)	Mcd4	Co. Los Terneros	7037458.42	475843.76	4214	TS	WR	
13360 (SG220712_P2)	Mcd4	Co. Los Terneros	7037528.76	475834.82	4243	TS		
13372 (SG220712_P3)	Mcd1(?)	Atenas	7037224	477068	4345	TS		
13361 (SG220712_P4)	Mcd4	Co. Los Terneros	7036074.62	474950.38	4388	TS		
13362 (SG220712_P5)	Mcd4	Co. La Coipa	7034493.49	476779.72	4593	TS		
13363 (SG220712_P6)	Mcd4	Co. La Coipa	7035061	476614	4479	TS	WR	U/Pb
13364 (SG220712_P7)	Mcd4	Co. Los Terneros	7034661.01	475228.98	3953	TS	WR	U/Pb
13365 (SG230712_P1)	Mcd4	Co. La Coipa	7032983.83	476738.28	4423	TS	WR	U/Pb
13366 (SG230712_P2)	OMlc3	Maritza North	7036829.02	480525.49	4678	TS	WR	
13367 (SG230712_P3)	TrJem1	Purén NE	7039691.92	479939.05	4547	TS		
13367B (SG230712_P3)	TrJem1	Purén NE	7039691.09	479938.64	4547	TS		
13368 (SG230712_P4)	Mcd4	Purén N	7041238.47	476982.51	4490	TS		
13369 (SG230712_P5)	Mcd3	Purén NE	7039937.04	478586.25	4394	TS		
13370 (SG230712_P6)	UN	Brecha Norte	7037174	473603	4215	TS		
13371 (SG230712_P7)	UN	Brecha Norte	7037176	474023	4166	TS		
SG050113_P1	Ksecc2	Domos Sur	7031482.19	472086.58	3575			
SG050113_P2	OMlc2	Domos Sur	7031065.17	471917.08	3582			

TS: Thin Section; PTS: Polished Thin Section; WR: Whole-Rock Geochemistry.

Station/Sample	Unit	Sector	UTM N	UTM E	Elevation [m]	Petrography	Geochemistry	Geochronology
SG050113_P3	OMlc2	Domos Sur	7031524.14	472840.45	3594			
SG050113_P4	OMlc2	Domos Sur	7031533.66	472766.05	3598			
SG050113_P5	OMlc2	Domos Sur	7031525.19	472605.26	3594			
SG050113_P6	OMlc2	Domos Sur	7031533.17	472623.44	3573			
SG050113_P7	OMlc2	Domos Sur	7031682.15	473079.95	3607	PTS	WR	
SG050113_P8	OMlc2	Domos Sur	7032080.63	475660.06	4049			
SG050113_P9	OMlc2	Domos Sur	7032029.15	475575.51	4067			
SG050113_P10	OMlc2	Domos Sur	7031876	475597	4075			
SG050113_P11	OMlc2	Domos Sur	7031527.84	475321.19	4145	TS	WR	
SG050113_P12	OMlc2	Antigua Mina La Coipa	7031956.24	474857.28	3983	PTS		
SG060113_P1 (SG14161)	TrJem2	Ladera Farellón	7034078	474333	3816	TS/PTS		Ar/Ar (Al)
SG060113_P2	TrJem2	Ladera Farellón	7033570	474267	3899	PTS		
SG060113_P3	Mbx	Can Can	7035485	473189	4060			
SG060113_P4	OMlc2	Can Can	7035499	473362	4200			
SG060113_P5	OMlc2	Can Can	7035481	473298	4187			
SG070113_P1	OMlc4	Ladera W Co La Coipa	7032590.13	476350.15	4154	TS		
SG070113_P2	OMlc4	Ladera W Co La Coipa	7032701.08	476425.98	4221			
SG070113_P3	OMlc4	Ladera W Co La Coipa	7032639.13	476398	4214			
SG070113_P4	OMlc4	Ladera W Co La Coipa	7032566.07	476411.89	4212			
SG080113_P1	Ksecc2	Domos Sur	7030603.09	472108.55	3680			
SG090113_P1	TrJem1	Maritza	7033851.37	478641.89	4391			
SG090113_P2	TrJem1	Maritza	7033870.03	478606.56	4382			
SG090113_P3	TrJem1	Maritza	7033887	478546	4379			
SG090113_P4	OMlc4	Maritza	7033854	478495	4380			
SG090113_P5	Mbx	Maritza	7033760.72	478538.53	4348			

TS: Thin Section; PTS: Polished Thin Section; WR: Whole-Rock Geochemistry.

Station/Sample	Unit	Sector	UTM N	UTM E	Elevation [m]	Petrography	Geochemistry	Geochronology
SG220113_P1	Mcd5	Pompeya	7036193.03	475745.98	4236			
SG220113_P2	Mcd5	Pompeya	7036186.86	475809.02	4238			
SG220113_P3	Mcd5	Pompeya	7036095.84	475795.94	4238			
SG220113_P4	Mcd4	Pompeya	7036036.45	475787.24	4242			
SG220113_P5	Mcd4	Pompeya	7035611.19	475337.59	4277			
SG220113_P6	Mcd4	Pompeya	7035604.15	475368.58	4264			
SG220113_P7	Mcd4	Pompeya	7035960.09	475778.3	4226			
SG220113_P8	Mcd5	Pompeya	7036233.56	475823.33	4230			
SG220113_P9	Mcd5	Pompeya	7036147.24	475839.15	4231			
SG220113_P10	Mcd5	Pompeya	7036050.69	475815.4	4215			
SG220113_P11	Mcd5	Pompeya	7036163.5	475851.57	4227			
SG220113_P12	Mcd4	Pompeya	7036016.49	475829.69	4209			
SG220113_P13	Mcd4	Pompeya	7035961.32	475838.53	4207			
SG220113_P14	Mcd4	Pompeya	7035638.05	475579.57	4210			
SG230113_P1	Mcd4	Pompeya	7036134.04	475637.76	4293			
SG230113_P2	Mcd5	Pompeya	7036199.84	475917.37	4200			
SG230113_P3	Mcd5	Pompeya	7036137	475897	4180			
SG230113_P4	OMlc4	Pompeya	7036050.59	475913.46	4203			
SG230113_P5	OMlc4	Pompeya	7036010.71	475936.6	4197			
SG230113_P6	OMlc4	Pompeya	7035952.33	475935.07	4177	TS		
SG230113_P7	OMlc4	Pompeya	7035902.28	475936.28	4179			
SG230113_P8	OMlc4	Pompeya	7035919.97	475886.77	4201			
SG230113_P9	Mbx	Pompeya	7035304.02	475429.23	4171			
SG230113_P10	Mcd4	Pompeya	7035565.32	476606.28	4384			
SG230113_P11	Mcd4	Pompeya	7035561.66	476549.87	4380			

TS: Thin Section; PTS: Polished Thin Section; WR: Whole-Rock Geochemistry.

Station/Sample	Unit	Sector	UTM N	UTM E	Elevation [m]	Petrography	Geochemistry	Geochronology
SG230113_P12	OMlc4	Pompeya	7035508.01	476393.71	4353			
SG230113_P13	OMlc4	Pompeya	7035445.01	476380.72	4348			
SG230113_P14	OMlc4	Pompeya	7035371.45	476385.71	4335			
SG230113_P15	Mcd4	Pompeya	7035187.08	476413.19	4353			
SG230113_P16	OMlc4	Pompeya	7035362.06	476261.94	4324			
SG230113_P17	OMlc4	Pompeya	7035407.65	476255.11	4309			
SG230113_P18	OMlc4	Pompeya	7035462.08	476262.97	4306			
SG230113_P19	OMlc4	Pompeya	7035524	476285	4276			
SG230113_P20	Mcd1	Pompeya	7035731.19	476278.97	4305			
SG230113_P21	Mcd1	Pompeya	7036003.97	476509.9	4277			
SG230113_P22	OMlc4	Pompeya	7035842.14	476235.84	4281			
SG240113_P1	OMlc4	Pompeya	7035847	476172	4266			
SG240113_P2	OMlc4	Pompeya	7035952.57	476301.41	4264			
SG240113_P3	Mcd1	Pompeya	7036083	476265	4240			
SG240113_P4	Mcd1	Pompeya	7036176.18	476176.2	4247	TS		
SG240113_P5	Mcd1	Pompeya	7036194.96	476226.41	4267			
SG240113_P6	Mcd1	Pompeya	7036180.98	476349.22	4283			
SG240113_P7	OMlc4	Pompeya	7035891.97	476129.01	4246			
SG240113_P8	OMlc4	Pompeya	7035893.38	476074.22	4234			
SG240113_P9	Mcd1	Pompeya	7036077.58	476181.62	4234	TS		
SG240113_P10	OMlc4	Pompeya	7036040	476129	4248			
SG240113_P11	OMlc4	Pompeya	7035996.37	476045.61	4190			
SG240113_P12	OMlc4	Pompeya	7035848.27	476046.92	4190			
SG240113_P13	OMlc4	Pompeya	7035757.56	476155.81	4224			
SG240113_P14	Mcd1	Pompeya	7035641.98	476166.41	4218			

TS: Thin Section; PTS: Polished Thin Section; WR: Whole-Rock Geochemistry.

Station/Sample	Unit	Sector	UTM N	UTM E	Elevation [m]	Petrography	Geochemistry	Geochronology
SG240113_P15	Mcd1	Pompeya	7035521.19	476152.62	4217			
SG240113_P16	Mbx	Pompeya	7035426	476097	4180			
SG240113_P17	Mbx/OMlc4	Pompeya	7035187.58	476071.21	4189	TS (2)		
SG250113_P1	OMlc4	Sofía	7033670	476091	4228			
SG250113_P2	OMlc4	Sofía	7033677	476141	4252			
SG250113_P3	OMlc4	Sofía	7033646	476209	4300			
SG250113_P4	OMlc4	Sofía	7033633	476292	4346	TS/PTS		Ar/Ar (Al)
SG250113_P5	OMlc4	Sofía	7033771	476194	4278			
SG250113_P6	Mbx	Sofía	7033766	476157	4250			
SG250113_P7	Mbx	Sofía	7033819	476069	4210			
SG250113_P8	Mbx	Sofía	7033757	475925	4110	PTS		
SG260113_P1	Mbx	Sofía	7033728	476129	4230			
SG260113_P2	OMlc4	Sofía	7033677	476112	4234			
SG260113_P3	Mbx	Sofía	7034077	475984	4192			
SG260113_P4	Mbx	Sofía	7034085	476034	4216			
SG260113_P5	UN	Sofía	7034056	475942	4166			
SG260113_P6	Mbx	Sofía	7033757	475925	4110			
SG260113_P8	OMlc4	Sofía	7033643	475886	4090			
SG260113_P9	Mbx	Sofía	7033529	475852	4078			
SG260113_P10	Mcd4	Pompeya Sur	7034405	476287	4286			
SG260113_P11	Mcd4	Pompeya Sur	7034600	476255	4288			
SG260113_P12	Mcd4	Pompeya Sur	7034684	476287	4282			
SG260113_P13	UN	Pompeya Sur	7034348	476249	4274			
SG270113_P1	OMlc4	Atenas	7037828	477339	4324			
SG270113_P2	OMlc4	Atenas	7037909	477386	4356			

TS: Thin Section; PTS: Polished Thin Section; WR: Whole-Rock Geochemistry.

Station/Sample	Unit	Sector	UTM N	UTM E	Elevation [m]	Petrography	Geochemistry	Geochronology
SG270113_P3	OMlc4	Atenas	7037961	477381	4365			
SG270113_P4	OMlc4	Atenas	7037909	477440	4382			
SG270113_P5	OMlc4	Atenas	7037860	477500	4374	TS		
SG270113_P6	OMlc4	Atenas	7037840	477508	4372			
SG270113_P7	OMlc4	Atenas	7037734	477513	4374			
SG270113_P8	OMlc4	Atenas	7037255	477239	4386			
SG270113_P9	Mcd1(?)	Atenas	7037232	477163	4386			
SG270113_P10	OMlc4	Atenas	7037172	477424	4402			
SG020213_P1	OMlc4	Purén Sur	7036562	478421	4406	TS		
SG020213_P2	OMlc4	Purén Sur	7037664	478754	4438			
SG020213_P3	OMlc4	Purén Sur	7038058	478923	4430			
SG020213_P4	OMlc4	Purén Sur	7037274	479239	4426			
SG020213_P5	OMlc4	Purén Sur	7037492	479381	4442			
SG020213_P6	OMlc4	Purén Sur	7037460	479386	4448			
SG020213_P7	OMlc3	Purén Sur	7037888	479340	4386	TS		
SG020213_P8	OMlc3	Purén Sur	7037989	479338	4392			
SG020213_P9	OMlc4	Purén Sur	7037660	479586	4412			
SG020213_P10	OMlc3	Purén Sur	7037807	479607	4426			
SG020213_P11	OMlc3	Purén Sur	7038223	480175	4554			
SG020213_P12	OMlc3	Purén Sur	7037607	480144	4524			
SG020213_P13	OMlc3	Purén Sur	7037857	480093	4480			
SG020213_P14	TrJem1	Purén	7039053	479129	4442			
SG020213_P15	OMlc4	Purén	7038991	478976	4422			
SG020213_P16	TrJem1	Purén	7038671	479043	4396			
SG020213_P17	OMlc4	Purén Sur	7038203	478352	4324			

TS: Thin Section; PTS: Polished Thin Section; WR: Whole-Rock Geochemistry.

Station/Sample	Unit	Sector	UTM N	UTM E	Elevation [m]	Petrography	Geochemistry	Geochronology
SG030213_P1	OMlc4	Purén Sur	7037060	478222	4442			
SG030213_P2	OMlc4/Mcd1	Purén Sur	7037160	478254	4442			
SG030213_P3	OMlc4	Purén Sur	7037467	477508	4458			
SG030213_P4	OMlc4	Purén Sur	7037811	477943	4386			
SG030213_P5	OMlc4	Purén Sur	7037872	477803	4390			
SG030213_P6	OMlc4	Purén Sur	7037915	477775	4390	TS		
SG030213_P7	OMlc4	Purén Sur	7038144	477852	4382			
SG030213_P8	OMlc4	Purén Sur	7038029	477712	4390			
SG030213_P9	OMlc4	Purén Sur	7037909	477605	4372			
SG030213_P10	Mcd1	Maritza	7036338	479486	4506			
SG030213_P11	Mcd1	Maritza	7035587	478868	4486			
SG030213_P12	OMlc4	Maritza	7034632	478834	4470			
SG040213_P1	Mcd4	Co. Los Terneros	7035574	474711	4102			
SG040213_P2	TrJem2	Don Eduardo	7034323	474981	3886			
SG040213_P3	TrJem2	Don Eduardo	7033879	475093	3890			
SG040213_P4	Mbx	Sofía	7033823	475795	4086			
SG040213_P5	Mbx	Sofía	7033847	475464	4012			
SG040213_P6	Mbx	Sofía	7033827	475376	3986			
SG040213_P7	OMlc4	Purén	7039339	476301	4344			
SG040213_P8	Mcd3	Purén	7039537	475978	4358	TS/PTS	WR	Ar/Ar (Bt)
SG040213_P9	Mcd3	Purén	7039878	475644	4382			
SG040213_P10	OMlc4	Purén	7039329	476034	4338			
SG040213_P11	EOh	Purén West	7038759	476803	4292	TS		
SG040213_P12	EOh	Purén West	7038464	476823	4286			
SG040213_P13	EOh	Purén West	7038613	476809	4294			

TS: Thin Section; PTS: Polished Thin Section; WR: Whole-Rock Geochemistry.

Station/Sample	Unit	Sector	UTM N	UTM E	Elevation [m]	Petrography	Geochemistry	Geochronology
SG050213_P2	OMlc4	Pompeya	7035861	476128	4276			
SG050213_P3	Mbx	Pompeya	7035302	476101	4234			
SG050213_P4	Ksecc2b	Domos Sur	7028999	469718	3736			
SG050213_P5	OMlc4	Domos Sur	7029091	469591	3761	TS	WR	U/Pb
SG050213_P6	OMlc2	Domos Sur	7030618	473979	4164	TS		
SG190213_P1	OMlc2	Domos Sur	7030103	473252	4064	TS	WR	
SG190213_P2	OMlc2	Domos Sur	7030205	473285				
SG190213_P3	OMlc2	Domos Sur	7030309	473274				
SG190213_P4	OMlc2	Domos Sur	7030372	473217		TS		
SG190213_P5	OMlc2	Domos Sur	7030654	473106				
SG190213_P6	OMlc2	Domos Sur	7030565	473285	4043	PTS	WR	
SG190213_P7	OMlc2	Domos Sur	7030492	473290	4058			
SG190213_P8	OMlc2	Domos Sur	7030267	473463	4077			
SG190213_P9	OMlc2	Domos Sur	7030314	473628	4110			
SG190213_P10	OMlc2	Domos Sur	7030406	473467				
SG190213_P11	OMlc2	Domos Sur	7029752	474383				
SG190213_P12	OMlc2	Domos Sur	7030327	474494	4136			
SG190213_P13	OMlc2	Domos Sur	7030900	474683	4182			
SG190213_P14	OMlc2	Domos Sur	7031324	475573	4240			
SG190213_P15	OMlc2	Domos Sur	7031321	475602	4240			
SG190213_P16	OMlc4	Domos Sur	7031226	475799	4250	PTS	WR	U/Pb
SG190213_P17	OMlc2	Domos Sur	7031996	475157	3943			
SG190213_P18	OMlc4	Domos Sur	7032105	475297	3941			
SG190213_P19	OMlc2	Domos Sur	7032321	475475	3931			
SG190213_P20	OMlc2	Domos Sur	7032420	475633	3916			

TS: Thin Section; PTS: Polished Thin Section; WR: Whole-Rock Geochemistry.

Station/Sample	Unit	Sector	UTM N	UTM E	Elevation [m]	Petrography	Geochemistry	Geochronology
SG190213_P21	OMlc2	Domos Sur	7032289	474668	3784			
SG200213_P1	TEdrdb	Basamento Sur	7029754	476263	3883			
SG200213_P2	TEdrdb	Basamento Sur	7029943	476125	3909			
SG200213_P3	TrJem2	Basamento Sur	7029715	476337	3867			
SG200213_P4	KTgb	Basamento Sur	7029588	476588	3883	TS	WR	
SG200213_P5	TrJem2	Basamento Sur	7029605	476569	3883			
SG200213_P6	TrJem2/TrJem3	Basamento Sur	7029229	476453	3799			
SG200213_P7	TrJem2 and TEdrdb	Basamento Sur	7028642	475212	3834			
SG200213_P8	Ksecc2	Codocedo Sur	7028977	478419	3825	TS		
SG200213_P9	TrJem3	Codocedo Sur	7028862	478547	3855			
SG200213_P10	TEpa	Basamento Sur	7026275	474839	3600	TS	WR	
SG200213_P11	TrJem3	Basamento Sur	7025835	474983	3595			
SG200213_P12	TrJem3	Basamento Sur	7025849	475036	3597			
SG200213_P13	TrJem1	Basamento Sur	7025634	473898	3568			
SG210213_P1	Kqm	Margen E	7035339	480983	4259			
SG210213_P2	JKp	Margen E	7034680	480901	4173			
SG210213_P3	Jqv	Margen E	7034530	480965	4187			
SG210213_P4	Ja and Jqv	Margen E	7034297	481125	4162			
SG210213_P5	Mcd2	Codocedo	7031688	480696	4403	TS	WR	U/Pb
SG210213_P6	TrJem1	Maritza	7034250	479239	4424	PTS		
SG210213_P7	OMlc4	Codocedo	7032415	478431	4195			
SG050313_P1	TrJem3	Tailings	7033472	471486	3861	TS		
SG050313_P2	Jm	Tailings	7032823	471569	3772			
SG050313_P3	Ksecc2	Tailings	7033023	471372				
SG050313_P4	TrJem3	Tailings	7033898	472203				

TS: Thin Section; PTS: Polished Thin Section; WR: Whole-Rock Geochemistry.

Station/Sample	Unit	Sector	UTM N	UTM E	Elevation [m]	Petrography	Geochemistry	Geochronology
SG050313_P5	TrJem3	Tailings	7033597	472269	3794			
SG050313_P6	TrJem3	Tailings	7033628	472254				
SG050313_P7	TrJem2	Tailings	7033523	472258	3788			
SG050313_P8	TEpa	Tailings	7033337	472313	3785	TS		
SG090313_P1	OMlc4	Codocedo	7030602	479213	4196			
SG090313_P2	Mbx	Codocedo	7030349	478843	4072	PTS		
SG090313_P3	Mcd1	Codocedo	7030304	478720	4084	TS (2)/PTS		Ar/Ar (Al)
SG090313_P4	OMlc4	Maritza	7033653	478590	4351	TS (B)/PTS		Ar/Ar (Al)
SG090313_P5	Mcd1	Maritza	7033552	478749	4347			
SG090313_P6	Mbx	Purén	7038376	474543				
SG090313_P7	Mcd6	Purén	7038363	474463				
SG090313_P8	Mcd4	Co. La Coipa	7034131	476830	4639			
SG090313_P9	Mbx	Co. La Coipa	7034172	476853	4644	PTS		
SG070413_P1	TrJem1	Maritza	7035413	479229	4466			
SG141213_P1	Omlc1	Mine plant	7032627	473572	3849			

TS: Thin Section; PTS: Polished Thin Section; WR: Whole-Rock Geochemistry.

Station/Sample	Unit	Sector	Drill-Hole Name	From	To	Elevation	Petrography	Geochemistry	Geochronology
SG14166	Alunite vein	Pompeya	DPMP-032	402.52	402.82	3813.386424	PTS		Ar/Ar (Al)
		Pompeya	DPMP-032	402.38	402.52	3813.508906			
SG14167	Sulfides	Pompeya	DPMP-063	264.6	264.72	3910.826884			
SG16251	TrJem2	Ladera Farellón	LRD-033	96.15	96.28	3804.171657			
SG16252	TrJem2	Ladera Farellón	LRD-033	200.9	201.1	3713.455496	PTS		
SG16253	OMlc1	Ladera Farellón	CUM-006	11.1	11.26	3852.69668			
SG16254	OMlc1 (?)	Ladera Farellón	CUM-006	24	24.2	3842.756063			
SG16255	Mbx	Coipa Norte	CND-219	149.35	149.72	4120.463108			
SG16256	Mbx	Coipa Norte	CND-219	319.5	319.9	3977.637851			
SG16257	Mbx	Coipa Norte	CND-219	299.55	300	3994.463104	PTS		Ar/Ar (Al)
SG16258	OMlc4	Coipa Norte	CND-241	203.3	203.68	4025.659211			
SG16259	Mbx	Coipa Norte	CND-241	514.05	514.35	3717.933409			
SG16260	Mbx	Coipa Norte	CND-241	561.7	562	3670.747135			
SG16261	Pzgd	Coipa Norte	CND-241	588.45	588.75	3644.257465	PTS		
SG16262	Mbx	Brecha Norte	BND-011	49	49.4	4031.80155			
SG16263	Pzgd	Brecha Norte	BND-011	293.1	293.5	3831.846536	PTS	WR	U/Pb
SG16264	Pzgd	Brecha Norte	BND-011	290.2	290.4	3834.222077			
SG16265	TrJem3	Brecha Norte	BND-03	55.25	55.5	4087.182096			
		Brecha Norte	BND-03	66.35	66.6	4077.569214			
SG16266	Pzgd	Brecha Norte	BND-03	229.63	229.83	3936.164587			
SG16267	Pzgd	Brecha Norte	BND-03	224.15	224.45	3940.910406			
SG16268	Pzgd	Brecha Norte	BND-03	176.45	176.65	3982.219818			
SG16269	TrJem3	Brecha Norte	BND-01	106.5	106.8	4095.168294			
SG16270	Pzgd	Brecha Norte	BND-01	202.15	202.5	4012.332965			
SG16271	Pzgd	Brecha Norte	BND-01	156.6	156.95	4051.780422	TS/PTS		Ar/Ar (Al)
SG16272	TrJem2	Can Can	CCD-01	197.5	198	3830.598342			

Station/Sample	Unit	Sector	Drill-Hole Name	From	To	Elevation	Petrography	Geochemistry	Geochronology
SG16273	TrJem3	Can Can	CCD-01	380.65	381	3709.404424			
SG16274	TrJem2	Can Can	CCD-01	385.3	386	3706.292966	PTS		Ar/Ar (Al)
SG16275	TrJem2	Can Can	CCD-01	441.25	441.4	3668.855109			
		Can Can	CCD-01	443.2	443.45	3667.550304			
		Can Can	CCD-01	443.9	444.15	3667.081913			
SG16276	OMlc2 (?)	Can Can	CCD-21	95	96	4125.167979			
SG16277	TrJem3	Can Can	CCD-07	398.2	398.5	3686.688253			
		Can Can	CCD-07	400.6	401.6	3685.045			
SG16278	TrJem3	Can Can	CCD-07	28	29	3939.164046	PTS		
SG16279	Mbx	Purén F2	DPU-06	48.5	48.75	4261.983152			
SG16280	TEdi	Purén F2	DPU-06	151.76	152	4177.330685			
SG16281	EOh	Purén F2	DPU-06	163.5	163.8	4167.597784	PTS		
SG16282	Mbx	Purén F2	DPU-06	270.55	271.15	4078.795849			
SG16283	EOh (?)	Purén F2	DPU-06	331.74	332	4027.477597	PTS		
SG16284	Mbx	Purén F2	PUM-082	196.15	196.47	4113.059117			
SG16285	Mbx	Purén F3	PUM-154	39.75	40.15	4260.289733			
		Purén F3	PUM-154	40.8	40.9	4259.485387			
SG16286	Mbx	Purén F3	PUM-154	138.55	138.95	4184.604542	PTS		
SG16287	TEdi	Purén F3	PUM-154	254.1	254.32	4096.088107	PTS		
SG16288	Mbx	Purén F3	PUM-154	280.3	280.55	4076.017743			
SG16289	Steam-heated	Purén F1	DPU-075	15.2	15.5	4303.429578			
SG16290	Steam-heated	Purén F1	DPU-087	31.7	31.9	4301.833818	TS/PTS		Ar/Ar (Al)
SG16291	Mbx	Purén F1	DPU-087	61	61.2	4274.479911	TS		
SG16292	EOh (?)	Purén F1	DPU-087	256.68	256.88	4092.180688			
		Purén F1	DPU-087	257.47	257.6	4091.443159			
SG16293	Dome	Pompeya Sur	DPMP-113	321.98	322.28	3951.165587	PTS		Ar/Ar (Al)

Station/Sample	Unit	Sector	Drill-Hole Name	From	To	Elevation	Petrography	Geochemistry	Geochronology
SG16294	TEdi	Pompeya Sur	DPMP-113	101.75	102	4159.975247	PTS	WR	Ar/Ar (Bt)
SG16295	Mcd1	Purén West	DPUW-011	53.05	53.3	4198.376068			
SG16296	EOh	Purén West	DPUW-011	143.15	143.4	4120.045988	PTS		
SG16297	TEdi	Purén West	DPUW-011	243.52	243.75	4032.855241			
SG16298	EOh	Purén West	DPUW-006	120.24	120.52	4135.828086			
SG16299	TEdi	Purén West	DPUW-006	157.16	157.4	4102.410232			
SG16301	OMlc4	Purén Sur	DPU-243	70.78	71.04	4289.198005	TS		
SG16302	OMlc3	Purén Sur	DPU-243	182.1	182.4	4184.079581			
SG16303	Alunite vein	Purén Sur	DPU-243	440	440.2	3939.548567	PTS		Ar/Ar (Al)
SG16304	OMlc3 (?)	Purén Sur	DPU-243	777.4	777.78	3618.496444	PTS		
SG16305	OMlc3 (?)	Purén Sur	DPU-243	547.32	547.86	3837.506877	PTS	WR	U/Pb
SG16306	OMlc3 (?)	Purén Sur	DPU-244	374.55	374.85	3991.42677			
SG16307	Dome	Pompeya	DPMP-073	398.1	398.65	3811.263569	TS		
SG16308	Sulfides	Pompeya	DPMP-037	326.55	326.9	3887.556355	PTS		
SG16309	Dome	Pompeya	DPMP-050	514.24	514.38	3766.742487	PTS		
SG16310	Steam-Heated	Pompeya	DPMP-059	14.2	14.45	4196.31554			
SG16311	Steam-Heated	Pompeya	DPMP-048	12	12.15	4215.53447			
SG16312	Alunite	Pompeya	DPMP-033	187	187.1	4000.558237	PTS		
SG16313	Alunite	Pompeya	DPMP-064	91	91.1	4069.175912	PTS		
SG16314	Alunite	Pompeya	DPMP-064	107.9	108	4052.811614	PTS		

Appendix A3. CA-ID-TIMS U-Pb Zircon Geochronology

Appendix A3. CA-ID-TIMS U-Pb on Zircon, Sample SG13351

		Compositional Parameters								Radiogenic Isotope Ratios							
Sample	Wt. mg	U ppm	Pb ppm	Th/U	$^{206}Pb^*$ x10^{-13} mol	mol % $^{206}Pb^*$	Pb^*/Pb_c	Pb_c (pg)	$^{206}Pb/^{204}Pb$	$^{208}Pb/^{206}Pb$	$^{207}Pb/^{206}Pb$	% err	$^{207}Pb/^{235}U$	% err	$^{206}Pb/^{238}U$	% err	corr. coef.
(a)	(i)	(j)	(j)	(b)	(c)	(c)	(c)	(c)	(d)	(e)	(e)	(f)	(e)	(f)	(e)	(f)	
SG13351																	
A	0.0036	192	0.9	0.497	0.1059	93.85%	5	0.57	301	0.159	0.046264	3.433	0.023551	3.622	0.003692	0.313	0.632
B	0.0038	203	1.0	0.470	0.1186	93.12%	4	0.72	269	0.143	0.043814	4.153	0.022330	4.376	0.003696	0.374	0.624
C	0.0032	164	0.8	0.542	0.0808	92.03%	4	0.57	232	0.176	0.046925	3.670	0.023967	3.886	0.003704	0.288	0.767
D	0.0032	200	1.0	0.544	0.0984	91.63%	3	0.74	222	0.174	0.046108	6.885	0.023572	7.282	0.003708	0.469	0.855

	Isotopic Ages					
Sample	$^{207}Pb/^{206}Pb$	±	$^{207}Pb/^{235}U$	±	$^{206}Pb/^{238}U$	±
(a)	(g)	(f)	(g)	(f)	(g)	(f)
SG13351						
A	11.41	82.43	23.64	0.85	23.76	0.07
B	-121.11	102.27	22.42	0.97	23.78	0.09
C	45.44	87.56	24.05	0.92	23.83	0.07
D	3.29	165.57	23.66	1.70	23.86	0.11

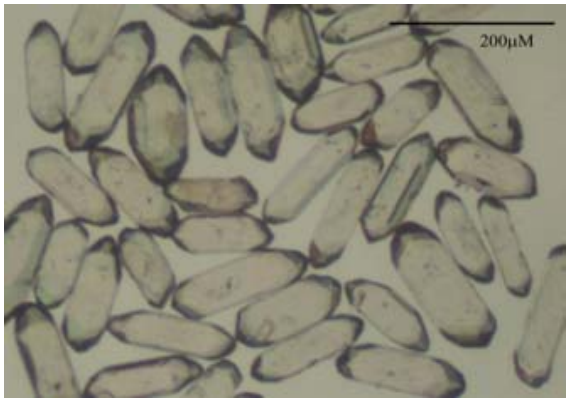

(a) A, B etc. are labels for fractions composed of single zircon grains or fragments; all fractions annealed and chemically abraded after Mattinson (2005) and Scoates and Friedman (2008).

(b) Nominal fraction weights estimated from photomicrographic grain dimensions, adjusted for partial dissolution during chemical abrasion.

(c) Nominal U and total Pb concentrations subject to uncertainty in photomicrographic estimation of weight and partial dissolution during chemical abrasion.

(d) Model Th/U ratio calculated from radiogenic $^{208}Pb/^{206}Pb$ ratio and $^{207}Pb/^{235}U$ age.

(e) Pb* and Pbc represent radiogenic and common Pb, respectively; mol % $^{206}Pb^*$ with respect to radiogenic, blank and initial common Pb.

(f) Measured ratio corrected for spike and fractionation only. Mass discrimination of 0.25%/amu based on analysis of NBS-982; all Daly analyses.

(g) Corrected for fractionation, spike, and common Pb; up to 0.5 pg of common Pb was assumed to be procedural blank: $^{206}Pb/^{204}Pb$ = 18.50 ± 1.0%; $^{207}Pb/^{204}Pb$ = 15.50 ± 1.0% (all uncertainties 1-sigma). Excess over blank was assigned to initial common Pb with S-K model Pb composition at 24 Ma.

(h) Errors are 2-sigma, propagated using the algorithms of Schmitz and Schoene (2007) and Crowley et al. (2007).

(i) Calculations are based on the decay constants of Jaffey et al. (1971). $^{206}Pb/^{238}U$ and $^{207}Pb/^{206}Pb$ ages corrected for initial disequilibrium in $^{230}Th/^{238}U$ using Th/U [magma] = 3. Isotopic dates are calculated the decay constants l238=1.55125E-10 and l235=9.8485E-10 (Jaffey et al. 1971).

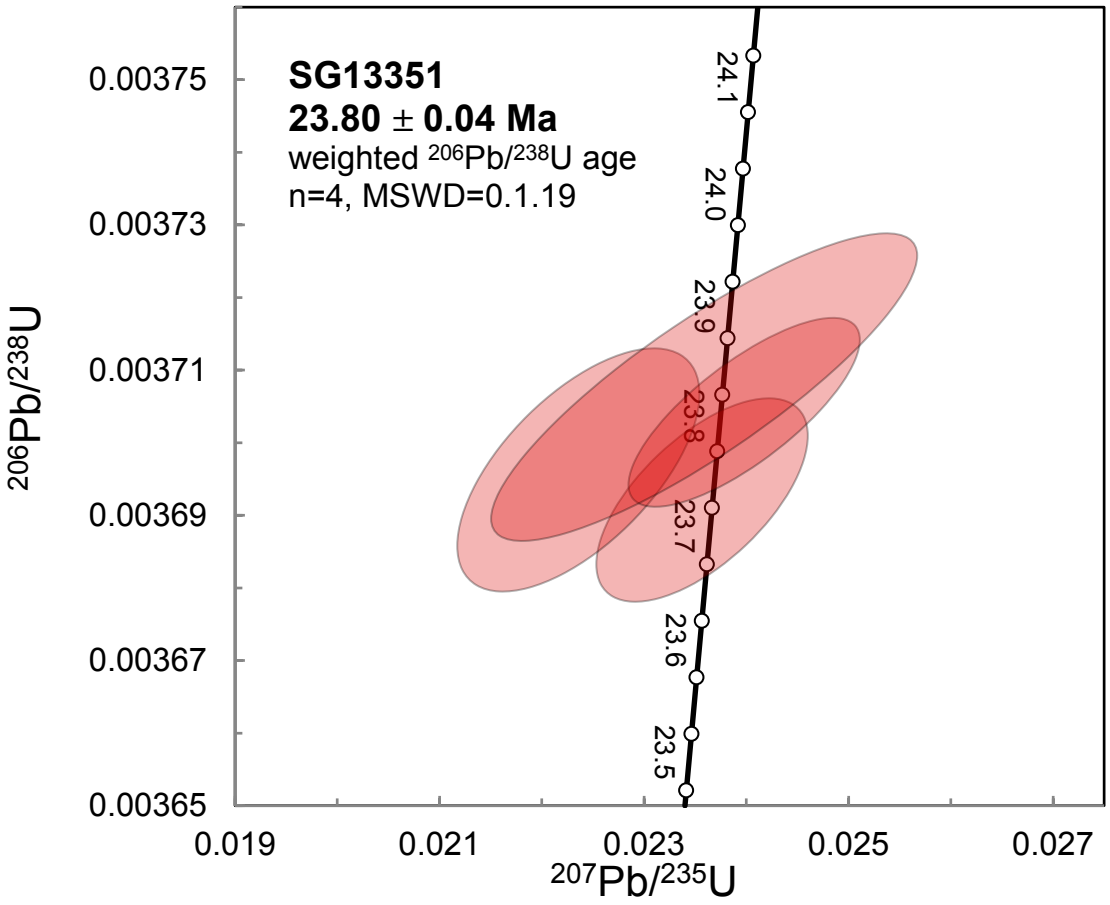

box heights are 2 σ

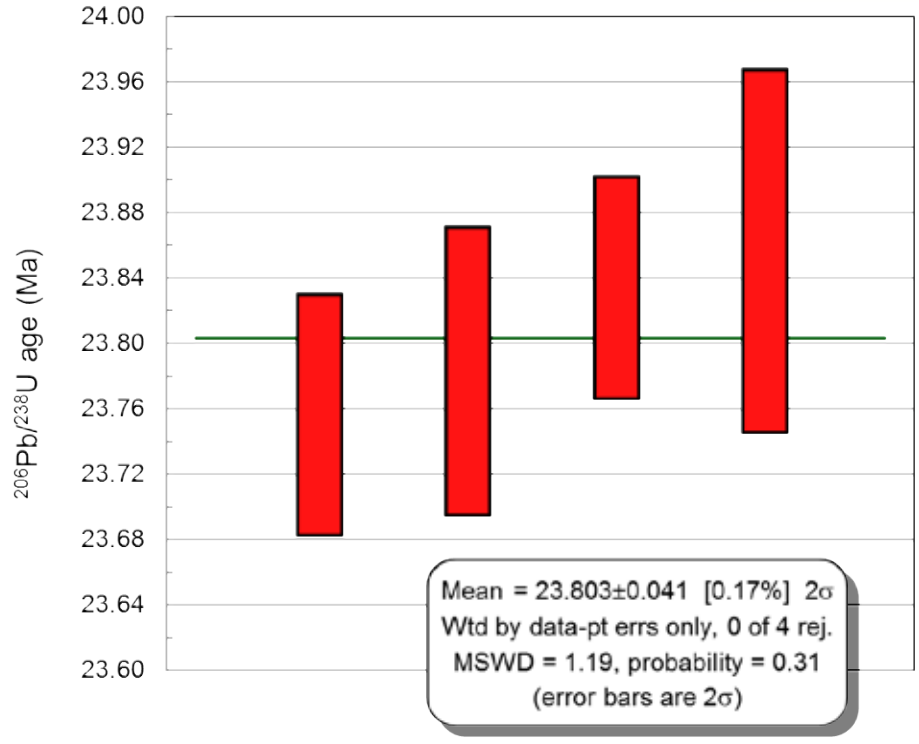

Appendix A3. CA-ID-TIMS U-Pb on Zircon, Sample SG13358

		Compositional Parameters								Radiogenic Isotope Ratios							
Sample	Wt. mg	U ppm	Pb ppm	Th/U	$^{206}Pb^*$ x10^{-13} mol	mol % $^{206}Pb^*$	Pb^*/Pb_c	Pb_c (pg)	$^{206}Pb/^{204}Pb$	$^{208}Pb/^{206}Pb$	$^{207}Pb/^{206}Pb$	% err	$^{207}Pb/^{235}U$	% err	$^{206}Pb/^{238}U$	% err	corr. coef.
(a)	(i)	(j)	(j)	(b)	(c)	(c)	(c)	(c)	(d)	(e)	(e)	(f)	(e)	(f)	(e)	(f)	
SG13358																	
A	0.0038	105	0.461	0.3	0.0425	92.90%	4	0.27	261	0.161	0.05006	6.14	0.0177	6.50	0.00256	0.46	0.800
B	0.0026	192	0.633	0.6	0.0514	94.24%	5	0.26	321	0.195	0.04431	5.50	0.0152	5.76	0.00249	0.52	0.538
C	0.0041	102	0.781	0.4	0.0430	92.06%	4	0.30	233	0.252	0.04637	7.01	0.0159	7.38	0.00248	0.56	0.665
D	0.0029	404	0.169	1.6	0.1413	88.03%	2	1.57	155	0.051	0.04348	5.64	0.0174	5.94	0.00290	0.37	0.800

	Isotopic Ages					
Sample	$^{207}Pb/^{206}Pb$	±	$^{207}Pb/^{235}U$	±	$^{206}Pb/^{238}U$	±
(a)	(g)	(f)	(g)	(f)	(g)	(f)
SG13358						
A	197.59	142.35	17.78	1.15	16.47	0.08
B	-93.44	134.61	15.31	0.87	16.01	0.08
C	16.90	168.10	16.00	1.17	15.99	0.09
D	-139.87	139.39	17.53	1.03	18.69	0.07

(a) A, B etc. are labels for fractions composed of single zircon grains or fragments; all fractions annealed and chemically abraded after Mattinson (2005) and Scoates and Friedman (2008).

(b) Nominal fraction weights estimated from photomicrographic grain dimensions, adjusted for partial dissolution during chemical abrasion.

(c) Nominal U and total Pb concentrations subject to uncertainty in photomicrographic estimation of weight and partial dissolution during chemical abrasion.

(d) Model Th/U ratio calculated from radiogenic $^{208}Pb/^{206}Pb$ ratio and $^{207}Pb/^{235}U$ age.

(e) Pb* and Pbc represent radiogenic and common Pb, respectively; mol % $^{206}Pb^*$ with respect to radiogenic, blank and initial common Pb.

(f) Measured ratio corrected for spike and fractionation only. Mass discrimination of 0.25%/amu based on analysis of NBS-982; all Daly analyses.

(g) Corrected for fractionation, spike, and common Pb; up to 0.5 pg of common Pb was assumed to be procedural blank: $^{206}Pb/^{204}Pb$ = 18.50 ± 1.0%; $^{207}Pb/^{204}Pb$ = 15.50 ± 1.0% (all uncertainties 1-sigma). Excess over blank was assigned to initial common Pb with S-K model Pb composition at 24 Ma.

(h) Errors are 2-sigma, propagated using the algorithms of Schmitz and Schoene (2007) and Crowley et al. (2007).

(i) Calculations are based on the decay constants of Jaffey et al. (1971). $^{206}Pb/^{238}U$ and $^{207}Pb/^{206}Pb$ ages corrected for initial disequilibrium in $^{230}Th/^{238}U$ using Th/U [magma] = 3. Isotopic dates are calculated the decay constants l238=1.55125E-10 and l235=9.8485E-10 (Jaffey et al. 1971).

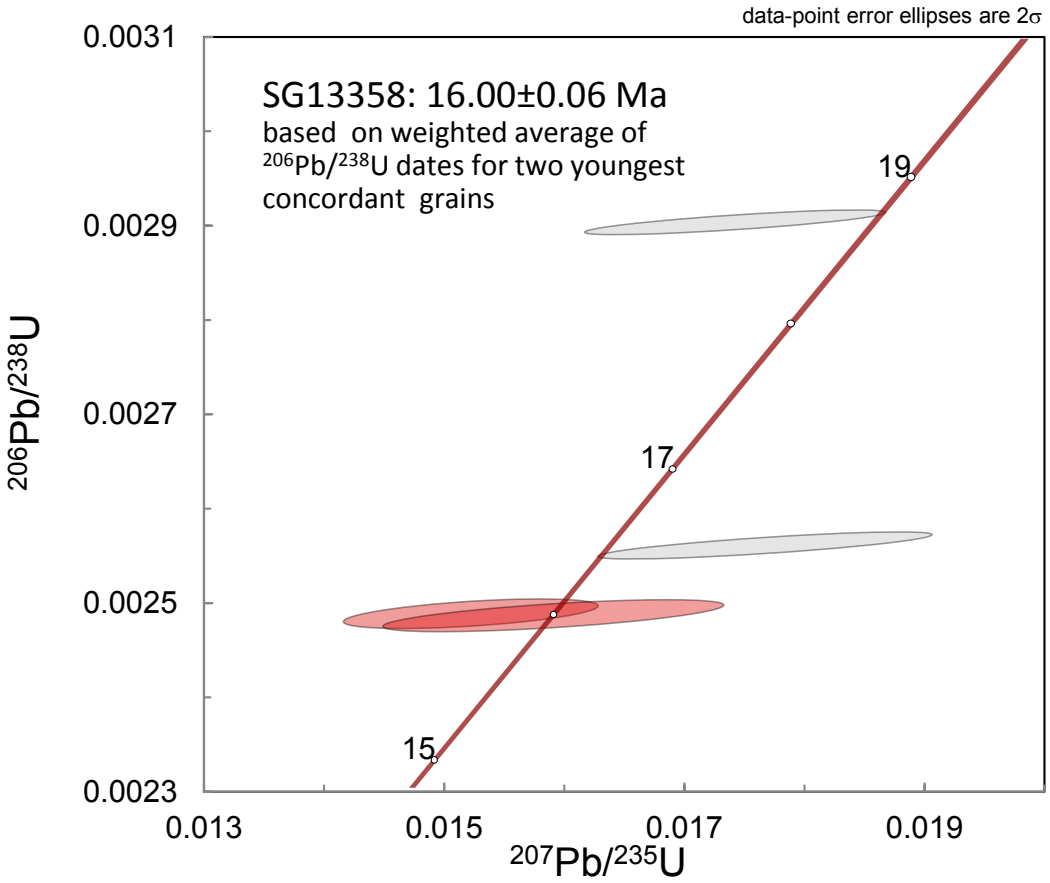
data-point error ellipses are 2σ
SG13358: 16.00±0.06 Ma
based on weighted average of
206Pb/238U dates for two youngest
concordant grains
19
17
15
0.0031
0.0029
0.0027
0.0025
0.0023
0.013
0.015
0.017
0.019
206Pb/238U
207Pb/235U

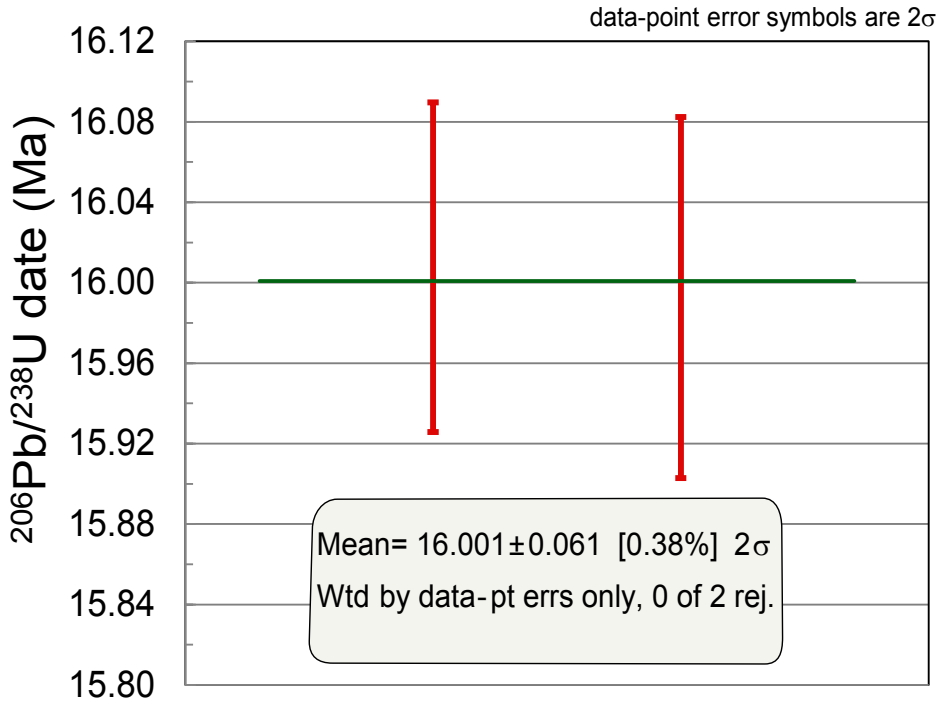
data-point error symbols are 2σ
16.12
16.08
16.04
16.00
15.96
15.92
15.88
15.84
15.80
206Pb/238U date (Ma)
Mean= 16.001±0.061 [0.38%] 2σ
Wtd by data-pt errs only, 0 of 2 rej.

Appendix A3. CA-ID-TIMS U-Pb on Zircon, Sample SG13363

		Compositional Parameters								Radiogenic Isotope Ratios							
Sample	Wt. mg	U ppm	Pb ppm	Th / U	$^{206}Pb^*$ x10^{-13} mol	mol % $^{206}Pb^*$	Pb^*/Pb_c	Pb_c (pg)	$^{206}Pb/^{204}Pb$	$^{208}Pb/^{206}Pb$	$^{207}Pb/^{206}Pb$	% err	$^{207}Pb/^{235}U$	% err	$^{206}Pb/^{238}U$	% err	corr. coef.
(a)	(i)	(j)	(j)	(b)	(c)	(c)	(c)	(c)	(d)	(e)	(e)	(f)	(e)	(f)	(e)	(f)	
SG13363																	
A	0.0028	241	0.968	1.0	0.0688	85.33%	2	0.97	126	0.314	0.04654	9.24	0.0158	9.61	0.00246	0.44	0.836
B	0.0028	208	0.658	0.8	0.0610	87.22%	2	0.73	145	0.241	0.05268	9.91	0.0183	10.46	0.00252	0.62	0.906
C	0.0032	137	0.447	0.8	0.0466	73.04%	1	1.41	69	0.166	0.05336	14.28	0.0189	14.96	0.00257	0.88	0.789
E	0.0023	252	0.505	1.0	0.0593	86.22%	2	0.77	134	0.167	0.04753	11.80	0.0161	12.39	0.00246	0.59	0.997

	Isotopic Ages					
Sample	$^{207}Pb/^{206}Pb$	±	$^{207}Pb/^{235}U$	±	$^{206}Pb/^{238}U$	±
(a)	(g)	(f)	(g)	(f)	(g)	(f)
SG13363						
A	25.91	221.29	15.89	1.52	15.82	0.07
B	315.01	224.85	18.40	1.91	16.21	0.10
C	344.24	322.45	19.00	2.82	16.53	0.14
E	75.87	279.78	16.27	2.00	15.87	0.09

(a) A, B etc. are labels for fractions composed of single zircon grains or fragments; all fractions annealed and chemically abraded after Mattinson (2005) and Scoates and Friedman (2008).

(b) Nominal fraction weights estimated from photomicrographic grain dimensions, adjusted for partial dissolution during chemical abrasion.

(c) Nominal U and total Pb concentrations subject to uncertainty in photomicrographic estimation of weight and partial dissolution during chemical abrasion.

(d) Model Th/U ratio calculated from radiogenic $^{208}Pb/^{206}Pb$ ratio and $^{207}Pb/^{235}U$ age.

(e) Pb* and Pbc represent radiogenic and common Pb, respectively; mol % $^{206}Pb^*$ with respect to radiogenic, blank and initial common Pb.

(f) Measured ratio corrected for spike and fractionation only. Mass discrimination of 0.25%/amu based on analysis of NBS-982; all Daly analyses.

(g) Corrected for fractionation, spike, and common Pb; up to 0.5 pg of common Pb was assumed to be procedural blank: $^{206}Pb/^{204}Pb$ = 18.50 ± 1.0%; $^{207}Pb/^{204}Pb$ = 15.50 ± 1.0% (all uncertainties 1-sigma). Excess over blank was assigned to initial common Pb with S-K model Pb composition at 24 Ma.

(h) Errors are 2-sigma, propagated using the algorithms of Schmitz and Schoene (2007) and Crowley et al. (2007).

(i) Calculations are based on the decay constants of Jaffey et al. (1971). $^{206}Pb/^{238}U$ and $^{207}Pb/^{206}Pb$ ages corrected for initial disequilibrium in $^{230}Th/^{238}U$ using Th/U [magma] = 3. Isotopic dates are calculated the decay constants l238=1.55125E-10 and l235=9.8485E-10 (Jaffey et al. 1971).

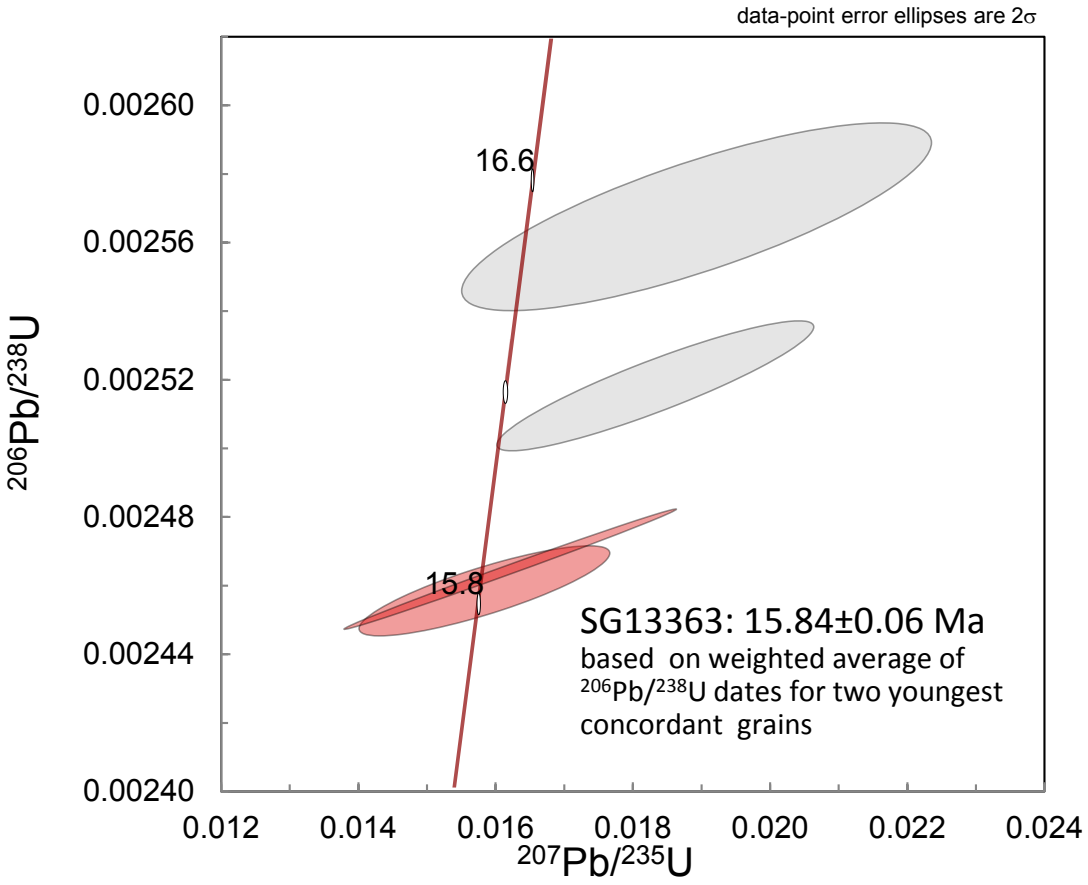
data-point error ellipses are 2σ
0.00260
0.00256
0.00252
0.00248
0.00244
0.00240
206Pb/238U
16.6
15.8
SG13363: 15.84±0.06 Ma
based on weighted average of
206Pb/238U dates for two youngest
concordant grains
0.012
0.014
0.016
0.018
0.020
0.022
0.024
207Pb/235U

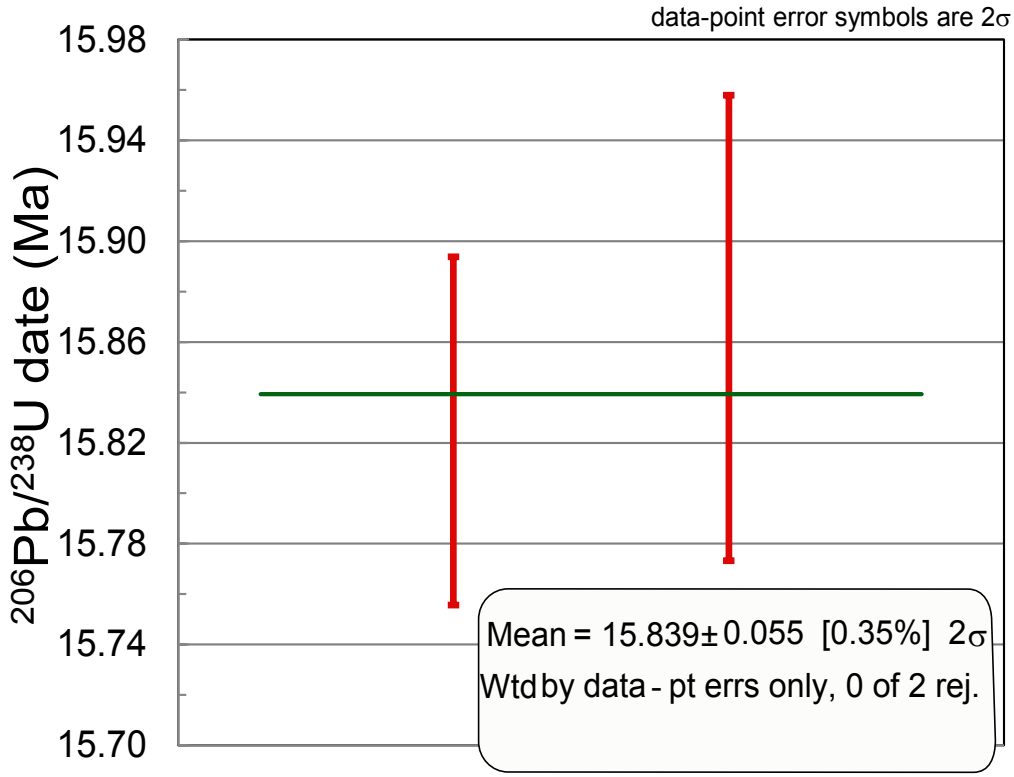
data-point error symbols are 2σ
15.98
15.94
15.90
15.86
15.82
15.78
15.74
15.70
206Pb/238U date (Ma)
Mean = 15.839± 0.055 [0.35%] 2σ
Wtd by data - pt errs only, 0 of 2 rej.

Appendix A3. CA-ID-TIMS U-Pb on Zircon, Sample SG13364

		Compositional Parameters								Radiogenic Isotope Ratios							
Sample	Wt. mg	U ppm	Pb ppm	Th/U	$^{206}Pb^*$ x10^{-13} mol	mol % $^{206}Pb^*$	Pb^*/Pb_c	Pb_c (pg)	$^{206}Pb/^{204}Pb$	$^{208}Pb/^{206}Pb$	$^{207}Pb/^{206}Pb$	% err	$^{207}Pb/^{235}U$	% err	$^{206}Pb/^{238}U$	% err	corr. coef.
(a)	(i)	(j)	(j)	(b)	(c)	(c)	(c)	(c)	(d)	(e)	(e)	(f)	(e)	(f)	(e)	(f)	
SG13364																	
A	0.0035	194	0.567	0.7	0.0702	87.04%	2	0.86	143	0.172	0.04347	11.40	0.0149	12.00	0.00249	0.79	0.779
B	0.0030	220	0.448	0.9	0.0687	85.19%	2	0.98	125	0.177	0.05671	12.95	0.0197	13.82	0.00252	1.19	0.753
C	0.0053	144	0.595	3.3	0.6535	98.53%	21	0.80	1262	0.201	0.05163	1.10	0.1466	1.15	0.02059	0.24	0.330
E	0.0059	151	0.501	0.6	0.0923	88.42%	2	0.99	160	0.168	0.04811	5.95	0.0165	6.33	0.00249	0.39	0.959

	Isotopic Ages					
Sample	$^{207}Pb/^{206}Pb$	±	$^{207}Pb/^{235}U$	±	$^{206}Pb/^{238}U$	±
(a)	(g)	(f)	(g)	(f)	(g)	(f)
SG13364						
A	-140.71	281.50	15.05	1.79	16.04	0.13
B	480.39	285.45	19.78	2.71	16.19	0.19
C	268.89	25.12	138.90	1.49	131.41	0.32
E	104.86	140.26	16.65	1.04	16.05	0.06

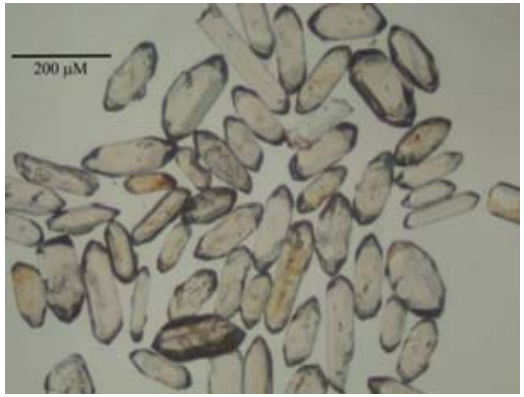

(a) A, B etc. are labels for fractions composed of single zircon grains or fragments; all fractions annealed and chemically abraded after Mattinson (2005) and Scoates and Friedman (2008).

(b) Nominal fraction weights estimated from photomicrographic grain dimensions, adjusted for partial dissolution during chemical abrasion.

(c) Nominal U and total Pb concentrations subject to uncertainty in photomicrographic estimation of weight and partial dissolution during chemical abrasion.

(d) Model Th/U ratio calculated from radiogenic $^{208}Pb/^{206}Pb$ ratio and $^{207}Pb/^{235}U$ age.

(e) Pb* and Pbc represent radiogenic and common Pb, respectively; mol % $^{206}Pb^*$ with respect to radiogenic, blank and initial common Pb.

(f) Measured ratio corrected for spike and fractionation only. Mass discrimination of 0.25%/amu based on analysis of NBS-982; all Daly analyses.

(g) Corrected for fractionation, spike, and common Pb; up to 0.5 pg of common Pb was assumed to be procedural blank: $^{206}Pb/^{204}Pb$ = 18.50 ± 1.0%; $^{207}Pb/^{204}Pb$ = 15.50 ± 1.0% (all uncertainties 1-sigma). Excess over blank was assigned to initial common Pb with S-K model Pb composition at 24 Ma.

(h) Errors are 2-sigma, propagated using the algorithms of Schmitz and Schoene (2007) and Crowley et al. (2007).

(i) Calculations are based on the decay constants of Jaffey et al. (1971). $^{206}Pb/^{238}U$ and $^{207}Pb/^{206}P$ ages corrected for initial disequilibrium in $^{230}Th/^{238}U$ using Th/U [magma] = 3. Isotopic dates are calculated the decay constants l238=1.55125E-10 and l235=9.8485E-10 (Jaffey et al. 1971).

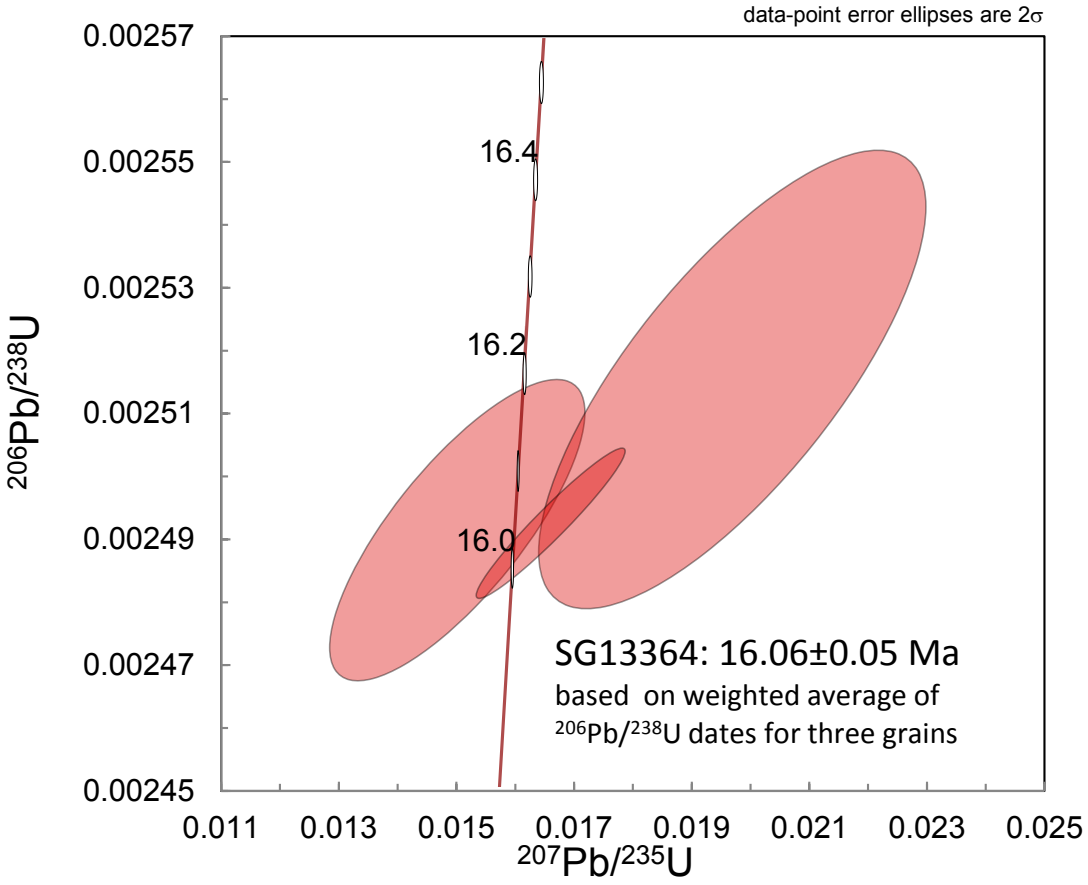
data-point error ellipses are 2σ
0.00257
0.00255
0.00253
0.00251
0.00249
0.00247
0.00245
206Pb/238U
16.4
16.2
16.0
SG13364: 16.06±0.05 Ma
based on weighted average of
206Pb/238U dates for three grains
0.011
0.013
0.015
0.017
0.019
0.021
0.023
0.025
207Pb/235U

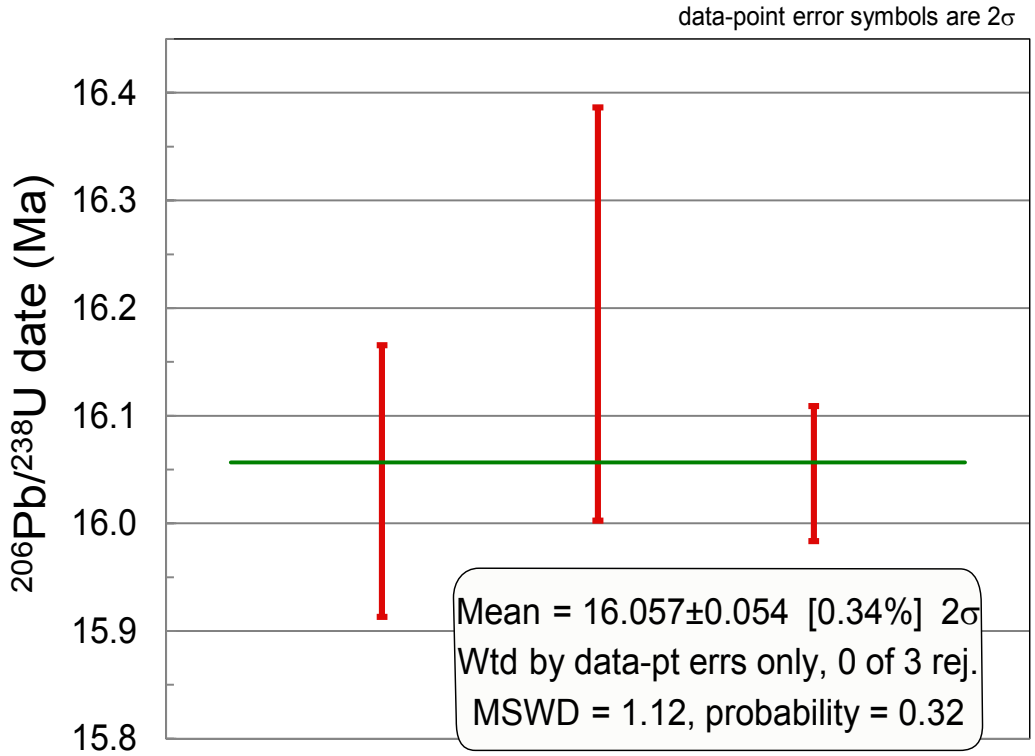
data-point error symbols are 2σ
206Pb/238U date (Ma)
16.4
16.3
16.2
16.1
16.0
15.9
15.8
Mean = 16.057±0.054 [0.34%] 2σ
Wtd by data-pt errs only, 0 of 3 rej.
MSWD = 1.12, probability = 0.32

Appendix A3. CA-ID-TIMS U-Pb on Zircon, Sample SG13365

		Compositional Parameters								Radiogenic Isotope Ratios							
Sample	Wt. mg	U ppm	Pb ppm	Th / U	$^{206}Pb^*$ x10^{-13} mol	mol % $^{206}Pb^*$	Pb^*/Pb_c	Pb_c (pg)	$^{206}Pb/^{204}Pb$	$^{208}Pb/^{206}Pb$	$^{207}Pb/^{206}Pb$	% err	$^{207}Pb/^{235}U$	% err	$^{206}Pb/^{238}U$	% err	corr. coef.
(a)	(i)	(j)	(j)	(b)	(c)	(c)	(c)	(c)	(d)	(e)	(e)	(f)	(e)	(f)	(e)	(f)	
SG13365																	
A	0.0035	174	0.619	0.6	0.0646	92.43%	4	0.44	244	0.216	0.05023	8.29	0.0177	8.69	0.00255	0.47	0.858
B	0.0036	267	0.768	1.0	0.1016	90.80%	3	0.85	201	0.253	0.04737	6.27	0.0166	6.64	0.00254	0.50	0.748
C	0.0032	94	0.715	0.4	0.0333	90.21%	3	0.30	189	0.296	0.05965	9.56	0.0220	10.25	0.00267	0.75	0.919
D	0.0031	215	0.488	0.9	0.0937	96.17%	8	0.31	483	0.174	0.05160	6.95	0.0241	7.37	0.00339	0.65	0.673
E	0.0029	193	0.572	3.7	0.3982	98.77%	25	0.41	1502	0.194	0.05122	1.03	0.1204	1.08	0.01705	0.22	0.327

	Isotopic Ages					
Sample	$^{207}Pb/^{206}Pb$	±	$^{207}Pb/^{235}U$	±	$^{206}Pb/^{238}U$	±
(a)	(g)	(f)	(g)	(f)	(g)	(f)
SG13365						
A	205.61	191.88	17.78	1.53	16.42	0.08
B	67.80	148.97	16.74	1.10	16.38	0.08
C	591.00	206.96	22.05	2.24	17.18	0.13
D	267.92	159.08	24.20	1.76	21.82	0.14
E	250.63	23.71	115.43	1.18	108.97	0.24

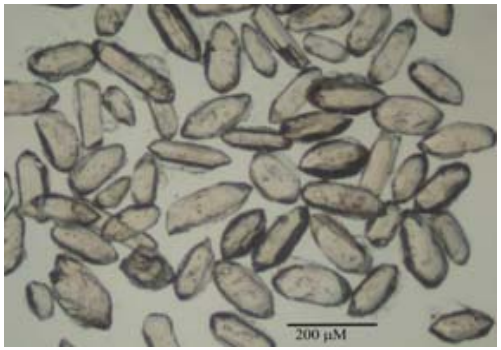

(a) A, B etc. are labels for fractions composed of single zircon grains or fragments; all fractions annealed and chemically abraded after Mattinson (2005) and Scoates and Friedman (2008).

(b) Nominal fraction weights estimated from photomicrographic grain dimensions, adjusted for partial dissolution during chemical abrasion.

(c) Nominal U and total Pb concentrations subject to uncertainty in photomicrographic estimation of weight and partial dissolution during chemical abrasion.

(d) Model Th/U ratio calculated from radiogenic $^{208}Pb/^{206}Pb$ ratio and $^{207}Pb/^{235}U$ age.

(e) Pb* and Pbc represent radiogenic and common Pb, respectively; mol % $^{206}Pb^*$ with respect to radiogenic, blank and initial common Pb.

(f) Measured ratio corrected for spike and fractionation only. Mass discrimination of 0.25%/amu based on analysis of NBS-982; all Daly analyses.

(g) Corrected for fractionation, spike, and common Pb; up to 0.5 pg of common Pb was assumed to be procedural blank: $^{206}Pb/^{204}Pb$ = 18.50 ± 1.0%; $^{207}Pb/^{204}Pb$ = 15.50 ± 1.0% (all uncertainties 1-sigma). Excess over blank was assigned to initial common Pb with S-K model Pb composition at 24 Ma.

(h) Errors are 2-sigma, propagated using the algorithms of Schmitz and Schoene (2007) and Crowley et al. (2007).

(i) Calculations are based on the decay constants of Jaffey et al. (1971). $^{206}Pb/^{238}U$ and $^{207}Pb/^{206}P$ ages corrected for initial disequilibrium in $^{230}Th/^{238}U$ using Th/U [magma] = 3. Isotopic dates are calculated the decay constants l238=1.55125E-10 and l235=9.8485E-10 (Jaffey et al. 1971).

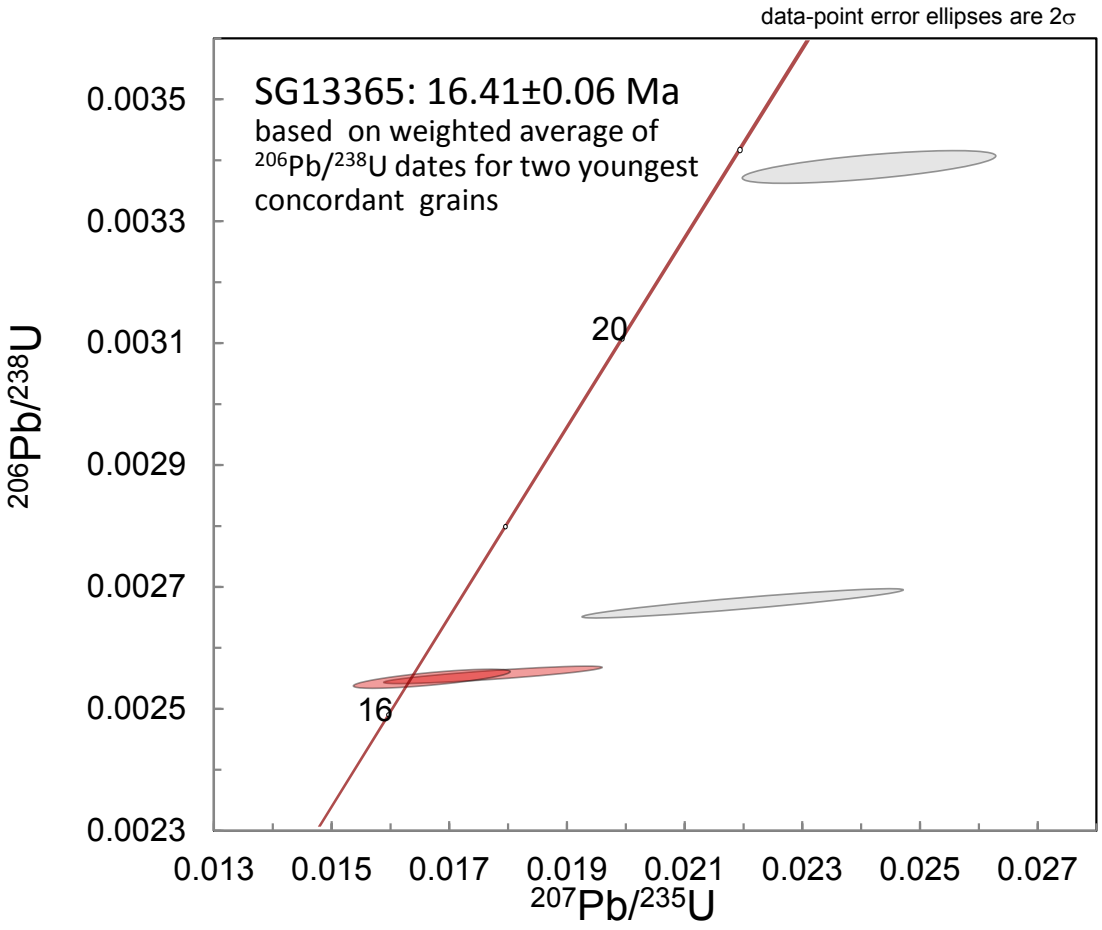
data-point error ellipses are 2σ
SG13365: 16.41±0.06 Ma
based on weighted average of
206Pb/238U dates for two youngest
concordant grains
20
16
0.0035
0.0033
0.0031
0.0029
0.0027
0.0025
0.0023
206Pb/238U
0.013
0.015
0.017
0.019
0.021
0.023
0.025
0.027
207Pb/235U

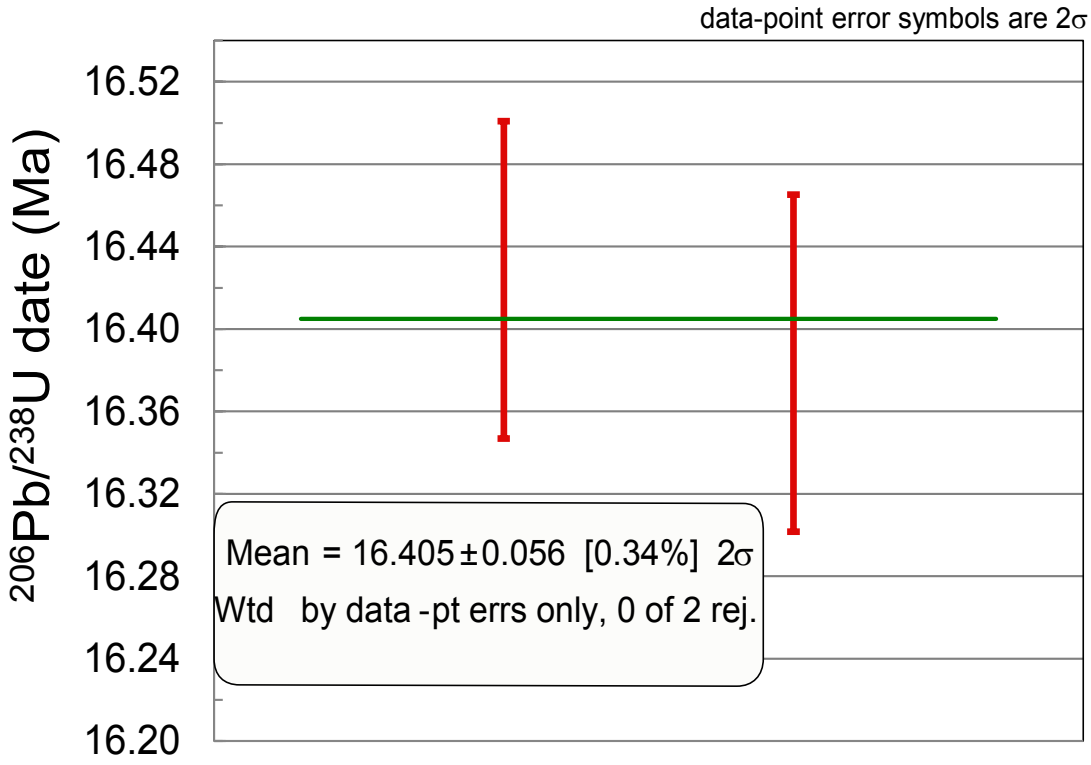
data-point error symbols are 2σ
16.52
16.48
16.44
16.40
16.36
16.32
16.28
16.24
16.20
206Pb/238U date (Ma)
Mean = 16.405±0.056 [0.34%] 2σ
Wtd by data-pt errs only, 0 of 2 rej.

Appendix A3. CA-ID-TIMS U-Pb on Zircon, Sample SG16263

		Compositional Parameters								Radiogenic Isotope Ratios							
Sample	Wt. mg	U ppm	Pb ppm	Th/U	$^{206}Pb^*$ x10^{-13} mol	mol % $^{206}Pb^*$	Pb^*/Pb_c	Pb_c (pg)	$^{206}Pb/^{204}Pb$	$^{208}Pb/^{206}Pb$	$^{207}Pb/^{206}Pb$	% err	$^{207}Pb/^{235}U$	% err	$^{206}Pb/^{238}U$	% err	corr. coef.
(a)	(i)	(j)	(j)	(b)	(c)	(c)	(c)	(c)	(d)	(e)	(e)	(f)	(e)	(f)	(e)	(f)	
SG16263																	
A	0.003	128	6.0	0.685	0.7180	99.33%	47	0.40	2767	0.217	0.051577	0.374	0.299885	0.430	0.042169	0.135	0.540
B	0.003	104	4.8	0.643	0.5676	99.46%	57	0.26	3402	0.204	0.051606	0.354	0.299754	0.406	0.042127	0.137	0.526
C	0.002	160	7.5	0.715	0.5887	99.38%	51	0.31	2980	0.227	0.051657	0.397	0.300008	0.441	0.042121	0.128	0.471
E	0.002	90	4.3	0.635	0.3624	98.32%	18	0.51	1100	0.201	0.051444	0.674	0.298602	0.734	0.042097	0.133	0.525

	Isotopic Ages					
Sample	$^{207}Pb/^{206}Pb$	±	$^{207}Pb/^{235}U$	±	$^{206}Pb/^{238}U$	±
(a)	(g)	(f)	(g)	(f)	(g)	(f)
SG16263						
A	266.71	8.59	266.31	1.01	266.27	0.35
B	267.99	8.12	266.21	0.95	266.01	0.36
C	270.28	9.10	266.41	1.03	265.97	0.33
E	260.78	15.48	265.31	1.71	265.82	0.34

(a) A, B etc. are labels for fractions composed of single zircon grains or fragments; all fractions annealed and chemically abraded after Mattinson (2005) and Scoates and Friedman (2008).

(b) Nominal fraction weights estimated from photomicrographic grain dimensions, adjusted for partial dissolution during chemical abrasion.

(c) Nominal U and total Pb concentrations subject to uncertainty in photomicrographic estimation of weight and partial dissolution during chemical abrasion.

(d) Model Th/U ratio calculated from radiogenic $^{208}Pb/^{206}Pb$ ratio and $^{207}Pb/^{235}U$ age.

(e) Pb* and Pbc represent radiogenic and common Pb, respectively; mol % $^{206}Pb^*$ with respect to radiogenic, blank and initial common Pb.

(f) Measured ratio corrected for spike and fractionation only. Mass discrimination of 0.25%/amu based on analysis of NBS-982; all Daly analyses.

(g) Corrected for fractionation, spike, and common Pb; up to 0.5 pg of common Pb was assumed to be procedural blank: $^{206}Pb/^{204}Pb$ = 18.50 ± 1.0%; $^{207}Pb/^{204}Pb$ = 15.50 ± 1.0% (all uncertainties 1-sigma). Excess over blank was assigned to initial common Pb with S-K model Pb composition at 24 Ma.

(h) Errors are 2-sigma, propagated using the algorithms of Schmitz and Schoene (2007) and Crowley et al. (2007).

(i) Calculations are based on the decay constants of Jaffey et al. (1971). $^{206}Pb/^{238}U$ and $^{207}Pb/^{206}P$ ages corrected for initial disequilibrium in $^{230}Th/^{238}U$ using Th/U [magma] = 3. Isotopic dates are calculated the decay constants l238=1.55125E-10 and l235=9.8485E-10 (Jaffey et al. 1971).

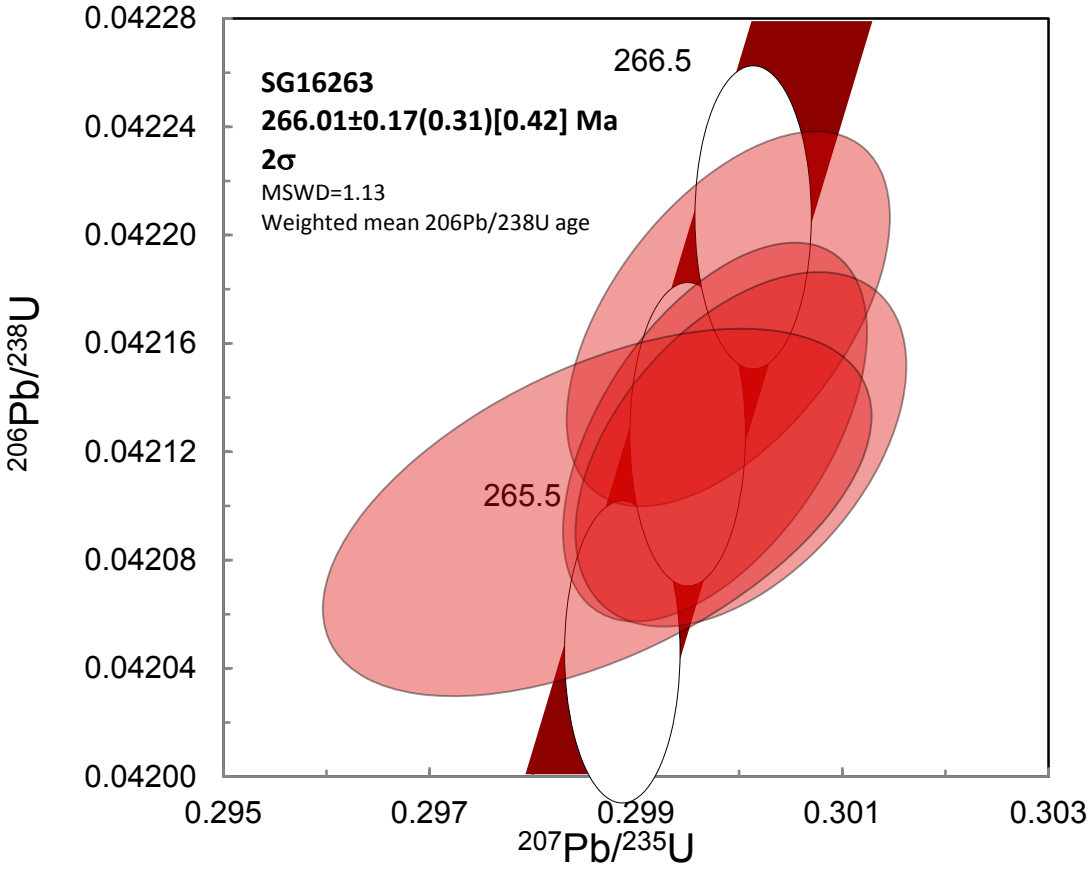
SG16263
266.01±0.17(0.31)[0.42] Ma
2σ
MSWD=1.13
Weighted mean 206Pb/238U age
266.5
265.5
0.04228
0.04224
0.04220
0.04216
0.04212
0.04208
0.04204
0.04200
206Pb/238U
0.295
0.297
0.299
0.301
0.303
207Pb/235U

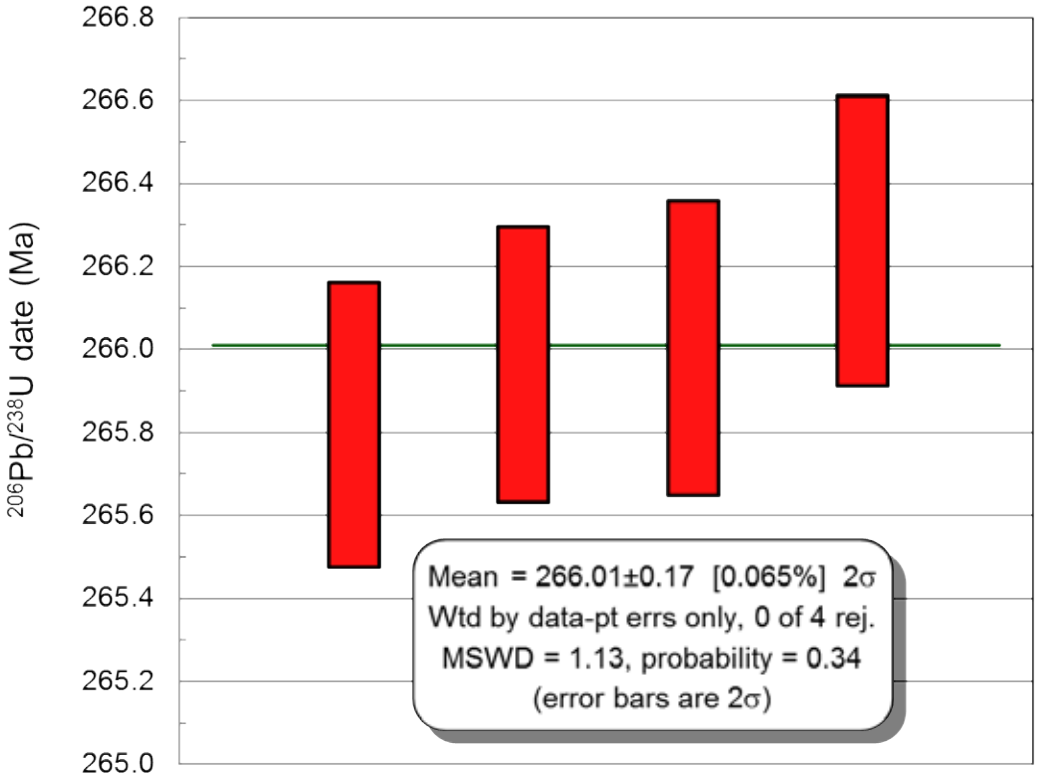
266.8
266.6
266.4
266.2
266.0
265.8
265.6
265.4
265.2
265.0
206Pb/238U date (Ma)
Mean = 266.01±0.17 [0.065%] 2σ
Wtd by data-pt errs only, 0 of 4 rej.
MSWD = 1.13, probability = 0.34
(error bars are 2σ)

Appendix A3. CA-ID-TIMS U-Pb on Zircon, Sample SG16305

		Compositional Parameters								Radiogenic Isotope Ratios							
Sample	Wt. mg	U ppm	Pb ppm	Th/U	$^{206}Pb^*$ x10^{-13} mol	mol % $^{206}Pb^*$	Pb^*/Pb_c	Pb_c (pg)	$^{206}Pb/^{204}Pb$	$^{208}Pb/^{206}Pb$	$^{207}Pb/^{206}Pb$	% err	$^{207}Pb/^{235}U$	% err	$^{206}Pb/^{238}U$	% err	corr. coef.
(a)	(i)	(j)	(j)	(b)	(c)	(c)	(c)	(c)	(d)	(e)	(e)	(f)	(e)	(f)	(e)	(f)	
SG16305																	
A	0.0020	591	21.4	0.505	1.6878	99.62%	80	0.53	4890	0.162	0.050989	0.434	0.240984	0.509	0.034277	0.198	0.546
B	0.0025	166	0.8	0.535	0.0591	89.69%	3	0.56	180	0.178	0.048013	5.274	0.022626	5.448	0.003418	0.291	0.614
C	0.0024	120	0.7	0.617	0.0407	84.04%	2	0.64	116	0.205	0.047970	6.954	0.022566	7.372	0.003412	0.449	0.935
D	0.0021	104	3.2	0.412	0.2358	95.10%	6	1.00	379	0.136	0.051451	0.982	0.184593	1.065	0.026021	0.157	0.576
E	0.0016	122	0.9	0.399	0.0276	74.21%	1	0.81	70	0.122	0.044238	13.771	0.020698	14.459	0.003393	1.033	0.686

	Isotopic Ages					
Sample	$^{207}Pb/^{206}Pb$	±	$^{207}Pb/^{235}U$	±	$^{206}Pb/^{238}U$	±
(a)	(g)	(f)	(g)	(f)	(g)	(f)
SG16305						
A	240.34	10.00	219.23	1.00	217.26	0.42
B	99.92	124.53	22.72	1.22	21.99	0.06
C	97.80	164.28	22.66	1.65	21.96	0.10
D	261.10	22.56	172.01	1.68	165.59	0.26
E	-97.45	337.52	20.80	2.98	21.84	0.22

(a) A, B etc. are labels for fractions composed of single zircon grains or fragments; all fractions annealed and chemically abraded after Mattinson (2005) and Scoates and Friedman (2008).

(b) Nominal fraction weights estimated from photomicrographic grain dimensions, adjusted for partial dissolution during chemical abrasion.

(c) Nominal U and total Pb concentrations subject to uncertainty in photomicrographic estimation of weight and partial dissolution during chemical abrasion.

(d) Model Th/U ratio calculated from radiogenic $^{208}Pb/^{206}Pb$ ratio and $^{207}Pb/^{235}U$ age.

(e) Pb* and Pbc represent radiogenic and common Pb, respectively; mol % $^{206}Pb^*$ with respect to radiogenic, blank and initial common Pb.

(f) Measured ratio corrected for spike and fractionation only. Mass discrimination of 0.25%/amu based on analysis of NBS-982; all Daly analyses.

(g) Corrected for fractionation, spike, and common Pb; up to 0.5 pg of common Pb was assumed to be procedural blank: $^{206}Pb/^{204}Pb$ = 18.50 ± 1.0%; $^{207}Pb/^{204}Pb$ = 15.50 ± 1.0% (all uncertainties 1-sigma). Excess over blank was assigned to initial common Pb with S-K model Pb composition at 24 Ma.

(h) Errors are 2-sigma, propagated using the algorithms of Schmitz and Schoene (2007) and Crowley et al. (2007).

(i) Calculations are based on the decay constants of Jaffey et al. (1971). $^{206}Pb/^{238}U$ and $^{207}Pb/^{206}Pb$ ages corrected for initial disequilibrium in $^{230}Th/^{238}U$ using Th/U [magma] = 3. Isotopic dates are calculated the decay constants l238=1.55125E-10 and l235=9.8485E-10 (Jaffey et al. 1971).

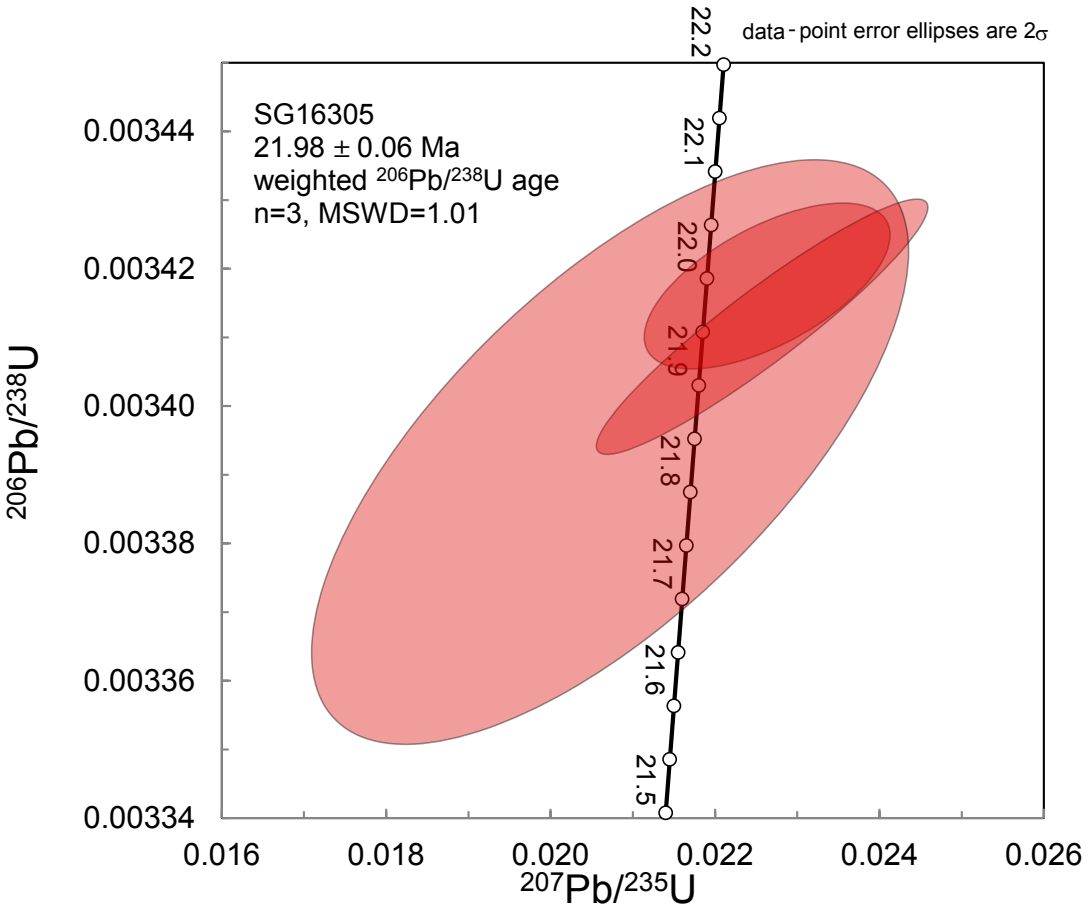
data-point error ellipses are 2σ
SG16305
21.98 ± 0.06 Ma
weighted 206Pb/238U age
n=3, MSWD=1.01
0.00344
0.00342
0.00340
0.00338
0.00336
0.00334
206Pb/238U
0.016
0.018
0.020
0.022
0.024
0.026
207Pb/235U
22.2
22.1
22.0
21.9
21.8
21.7
21.6
21.5

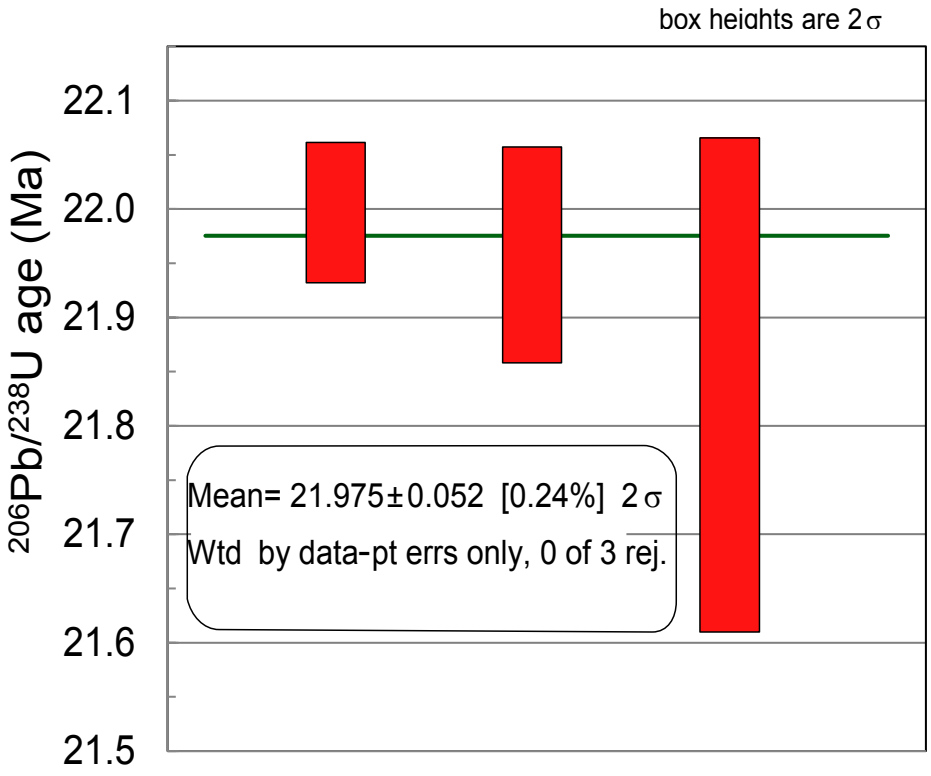
box heights are 2σ
206Pb/238U age (Ma)
22.1
22.0
21.9
21.8
21.7
21.6
21.5
Mean= 21.975±0.052 [0.24%] 2σ
Wtd by data-pt errs only, 0 of 3 rej.

Appendix A3. CA-ID-TIMS U-Pb on Zircon, Sample SG210213P5

		Compositional Parameters								Radiogenic Isotope Ratios							
Sample	Wt. mg	U ppm	Pb ppm	Th/U	$^{206}Pb^*$ x10^{-13} mol	mol % $^{206}Pb^*$	Pb^*/Pb_c	Pb_c (pg)	$^{206}Pb/^{204}Pb$	$^{208}Pb/^{206}Pb$	$^{207}Pb/^{206}Pb$	% err	$^{207}Pb/^{235}U$	% err	$^{206}Pb/^{238}U$	% err	corr. coef.
(a)	(i)	(j)	(j)	(b)	(c)	(c)	(c)	(c)	(d)	(e)	(e)	(f)	(e)	(f)	(e)	(f)	
SG210213P5																	
A	0.004	260	18.4	0.535	2.5247	99.70%	101	0.63	6091	0.171	0.056141	0.194	0.515841	0.239	0.066640	0.109	0.598
B	0.004	70	0.4	0.744	0.0311	86.19%	2	0.41	134	0.246	0.047741	22.996	0.020190	24.268	0.003067	1.358	0.940
C	0.001	272	1.4	0.618	0.0520	90.61%	3	0.44	197	0.199	0.046355	11.541	0.022649	12.178	0.003544	0.884	0.739
D	0.009	136	0.5	0.426	0.1502	95.53%	6	0.58	414	0.144	0.048670	5.848	0.019596	6.162	0.002920	0.445	0.725
E	0.004	75	0.3	0.560	0.0326	88.43%	2	0.35	160	0.183	0.046964	22.989	0.018835	24.276	0.002909	1.423	0.910

	Isotopic Ages					
Sample	$^{207}Pb/^{206}Pb$	±	$^{207}Pb/^{235}U$	±	$^{206}Pb/^{238}U$	±
(a)	(g)	(f)	(g)	(f)	(g)	(f)
SG210213P5						
A	457.95	4.31	422.37	0.82	415.88	0.44
B	86.47	544.36	20.30	4.88	19.74	0.27
C	16.11	276.86	22.74	2.74	22.80	0.20
D	131.97	137.21	19.71	1.20	18.80	0.08
E	47.38	548.04	18.95	4.56	18.72	0.26

(a) A, B etc. are labels for fractions composed of single zircon grains or fragments; all fractions annealed and chemically abraded after Mattinson (2005) and Scoates and Friedman (2008).

(b) Nominal fraction weights estimated from photomicrographic grain dimensions, adjusted for partial dissolution during chemical abrasion.

(c) Nominal U and total Pb concentrations subject to uncertainty in photomicrographic estimation of weight and partial dissolution during chemical abrasion.

(d) Model Th/U ratio calculated from radiogenic $^{208}Pb/^{206}Pb$ ratio and $^{207}Pb/^{235}U$ age.

(e) Pb* and Pbc represent radiogenic and common Pb, respectively; mol % $^{206}Pb^*$ with respect to radiogenic, blank and initial common Pb.

(f) Measured ratio corrected for spike and fractionation only. Mass discrimination of 0.25%/amu based on analysis of NBS-982; all Daly analyses.

(g) Corrected for fractionation, spike, and common Pb; up to 0.5 pg of common Pb was assumed to be procedural blank: $^{206}Pb/^{204}Pb$ = 18.50 ± 1.0%; $^{207}Pb/^{204}Pb$ = 15.50 ± 1.0% (all uncertainties 1-sigma). Excess over blank was assigned to initial common Pb with S-K model Pb composition at 24 Ma.

(h) Errors are 2-sigma, propagated using the algorithms of Schmitz and Schoene (2007) and Crowley et al. (2007).

(i) Calculations are based on the decay constants of Jaffey et al. (1971). $^{206}Pb/^{238}U$ and $^{207}Pb/^{206}Pb$ ages corrected for initial disequilibrium in $^{230}Th/^{238}U$ using Th/U [magma] = 3. Isotopic dates are calculated the decay constants l238=1.55125E-10 and l235=9.8485E-10 (Jaffey et al. 1971).

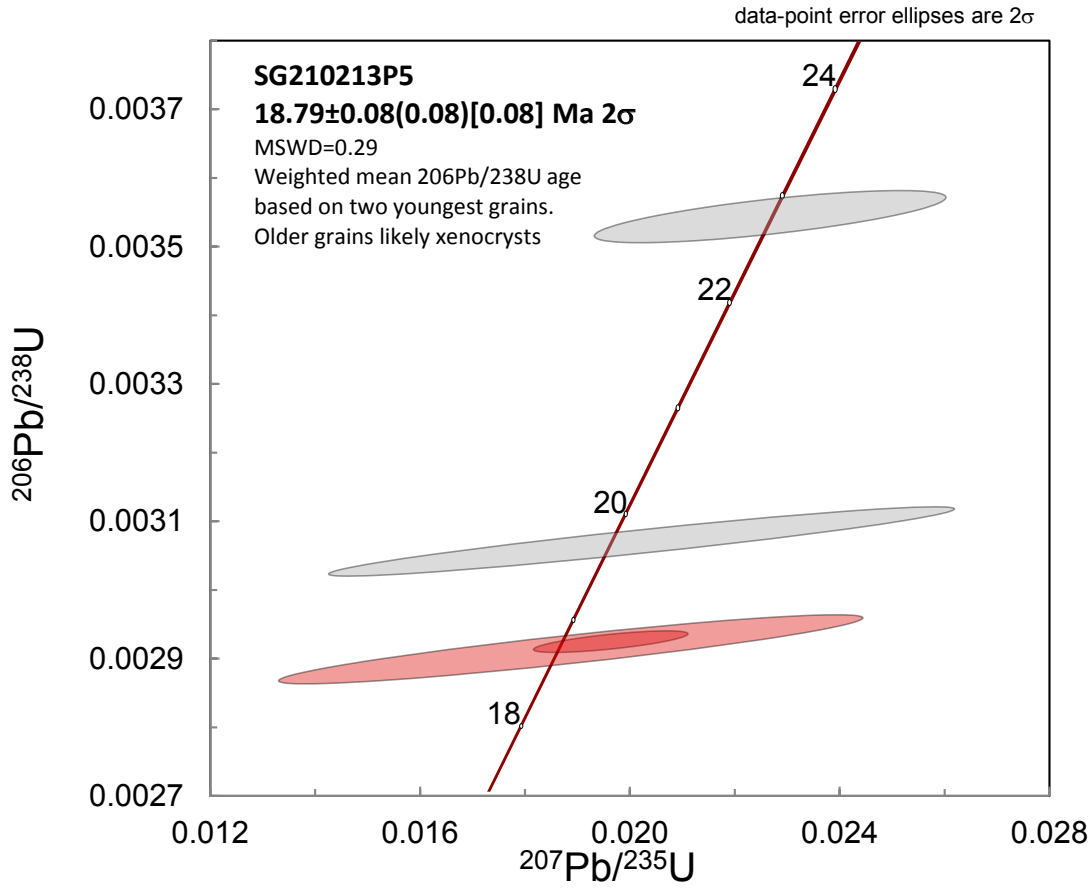
data-point error ellipses are 2σ
SG210213P5
18.79±0.08(0.08)[0.08] Ma 2σ
MSWD=0.29
Weighted mean 206Pb/238U age
based on two youngest grains.
Older grains likely xenocrysts
24
22
20
18
0.0037
0.0035
0.0033
0.0031
0.0029
0.0027
206Pb/238U
0.012
0.016
0.020
0.024
0.028
207Pb/235U

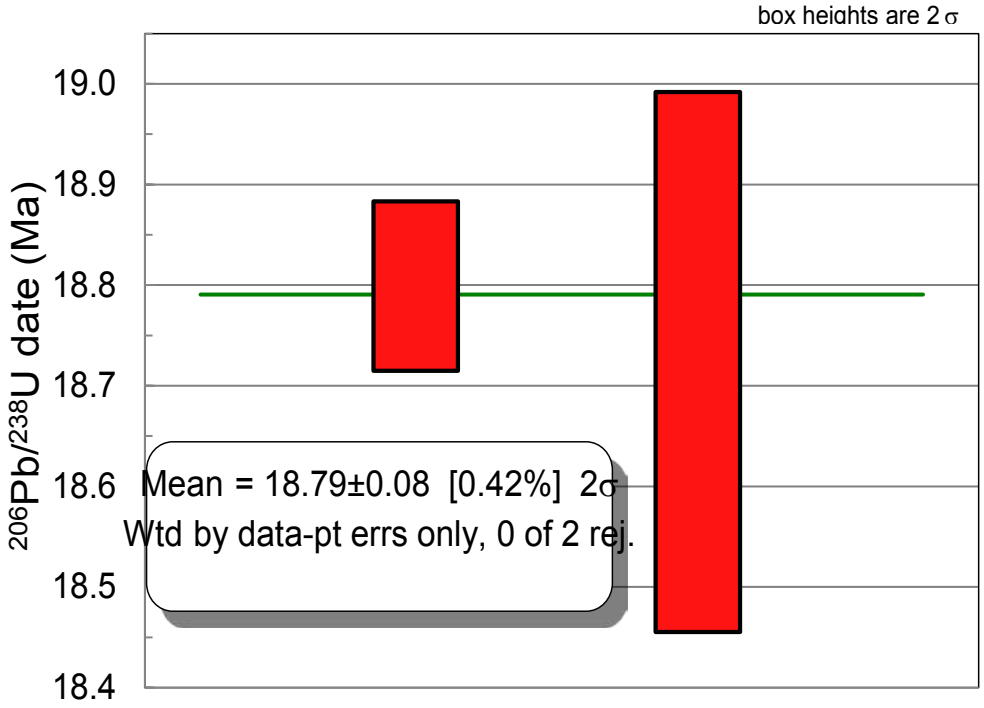
box heights are 2 σ
19.0
18.9
18.8
18.7
18.6
18.5
18.4
206Pb/238U date (Ma)
Mean = 18.79±0.08 [0.42%] 2σ
Wtd by data-pt errs only, 0 of 2 rej.

Appendix A4. LA-ICP-MS U-Pb Zircon Geochronology

Appendix A4. LA-ICP-MS U-Pb on Zircon, Sample SG050213P5

Sample Fraction	CL image	Radiogenic Isotope Ratios					Isotopic Ages						Background corrected mean counts per second at specified mass							
		$^{207}Pb/^{235}U$	%2σ	$^{206}Pb/^{238}U$	%2σ	corr. coef.	$^{207}Pb/^{206}Pb$	±2σ	$^{207}Pb/^{235}U$	±2σ	$^{206}Pb/^{238}U$	±2σ	^{202}Hg	^{204}Pb	^{206}Pb	^{207}Pb	^{208}Pb	^{232}Th	^{235}U	^{238}U
1	R1	0.019	0.0058	0.00318	0.0002	0.10066	0.065	0.017	18.1	5.8	20.5	1.3	8	24.6	400	15.8	41	26580	512	9.75E+04
2	R3	0.0198	0.0056	0.00324	0.0002	0.08325	0.049	0.015	19	5.5	20.8	1.4	-1	19.4	455	18.4	76	3.53E+04	528	1.02E+05
3	R4	0.017	0.0081	0.0036	0.0003	0.0449	0.048	0.025	15.3	7.9	23.2	1.8	7	14.9	333	12	27	20130	381	7.01E+04
4	R5	0.0252	0.0095	0.00313	0.0003	0.08598	0.07	0.032	23.1	9.3	20.1	1.6	4	19.2	227	14.3	23	11980	279	5.49E+04
5	R6	0.0233	0.0087	0.00377	0.0003	0.0038	0.073	0.033	21.3	8.6	24.3	2	6	17.9	281	14.7	34	12910	300	5.75E+04
6	R	0.0179	0.0077	0.00337	0.0003	0.05541	0.088	0.033	16	7.6	21.6	1.6	11	18.6	270	14.7	40	14870	320	6.19E+04
8	R9	0.0136	0.008	0.0032	0.0003	0.03489	0.049	0.029	12.4	8	20.6	1.7	6	18.5	268	6	20	14560	314	6.03E+04
9	R1	0.317	0.029	0.042	0.0014	0.35926	0.054	0.005	278	21	265	8.5	11	20.7	8450	460	3140	1.25E+05	824	1.56E+05
10	C1	0.0187	0.0066	0.00339	0.0002	0.13945	0.06	0.023	17.5	6.5	21.8	1.5	-7	17.1	314	10.6	32	14430	382	7.27E+04
11	C2	0.023	0.0043	0.00367	0.0002	0.02975	0.065	0.014	22.6	4.3	23.6	1.3	1	12.8	650	27.4	137	6.07E+04	711	1.35E+05
12	C3	0.352	0.035	0.0516	0.0016	0.10393	0.051	0.006	301	27	324	10	9	17.9	2610	129	451	13840	209	38720
13	C4	0.0253	0.0071	0.00328	0.0003	0.0188	0.074	0.028	24.2	7	21.1	1.7	8	16.4	364	19.5	37	2.34E+04	427	8.13E+04
14	C5	0.0211	0.0055	0.00334	0.0002	0.04055	0.06	0.019	20.3	5.5	21.5	1.3	6	19.9	389	19.7	49	3.01E+04	474	9.12E+04
15	C6	0.0259	0.0079	0.00359	0.0003	0.15365	0.061	0.023	25.5	7.8	23.1	1.8	-4	14	355	19.2	78	2.83E+04	401	7.98E+04
16	C8	0.0213	0.0054	0.00362	0.0002	0.0607	0.059	0.017	20.5	5.3	23.4	1.5	-8	17.5	452	21.9	85	4.06E+04	494	9.60E+04
17	C9	0.0227	0.0094	0.00364	0.0003	0.00462	0.096	0.039	20.1	9.1	23.4	2	4	14	247	10.5	33	11730	266	5.19E+04
19	L1	0.0189	0.0041	0.00336	0.0002	0.04912	0.054	0.013	19.1	4.1	21.6	1.3	3	16.4	520	21.8	90	3.69E+04	615	1.21E+05
20	L2	0.0213	0.0046	0.0033	0.0002	0.12502	0.053	0.014	21.2	4.5	21.2	1.2	3	19.9	551	24.6	110	5.38E+04	679	1.28E+05

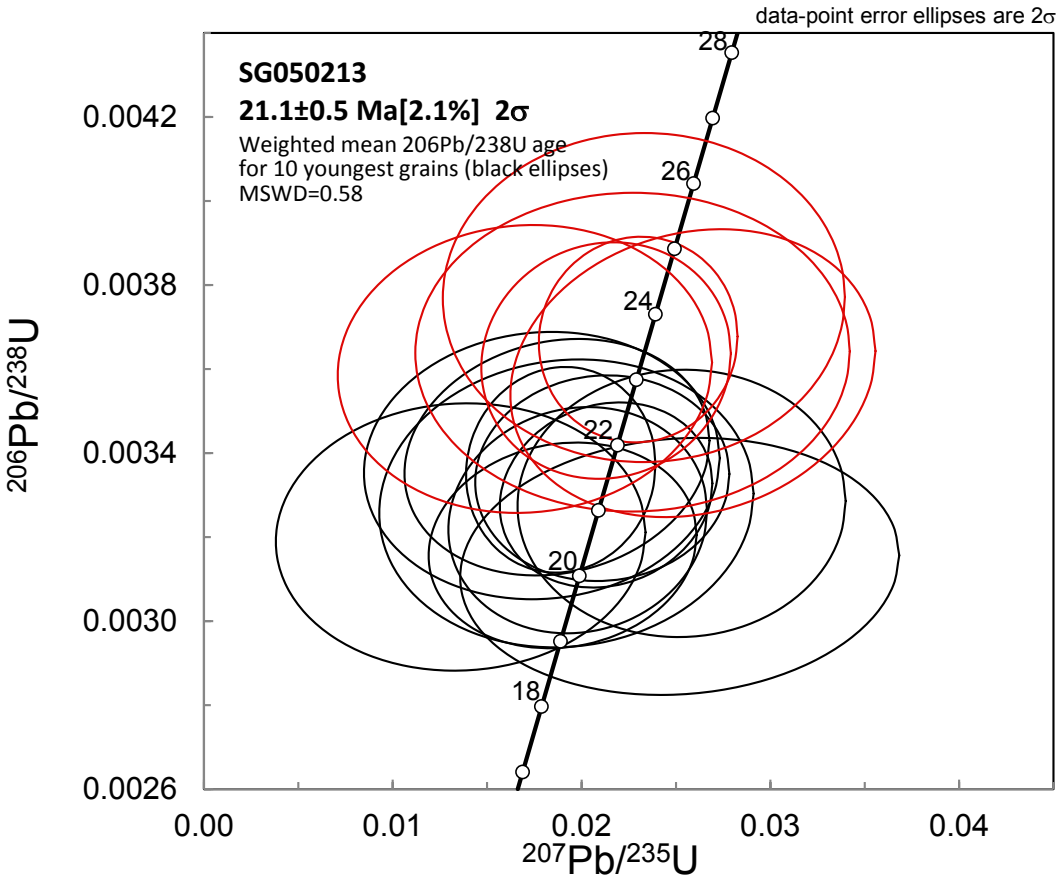
data-point error ellipses are 2σ
SG050213
21.1±0.5 Ma[2.1%] 2σ
Weighted mean 206Pb/238U age
for 10 youngest grains (black ellipses)
MSWD=0.58
28
26
24
22
20
18
0.0042
0.0038
0.0034
0.0030
0.0026
0.00
0.01
0.02
0.03
0.04
206Pb/238U
207Pb/235U

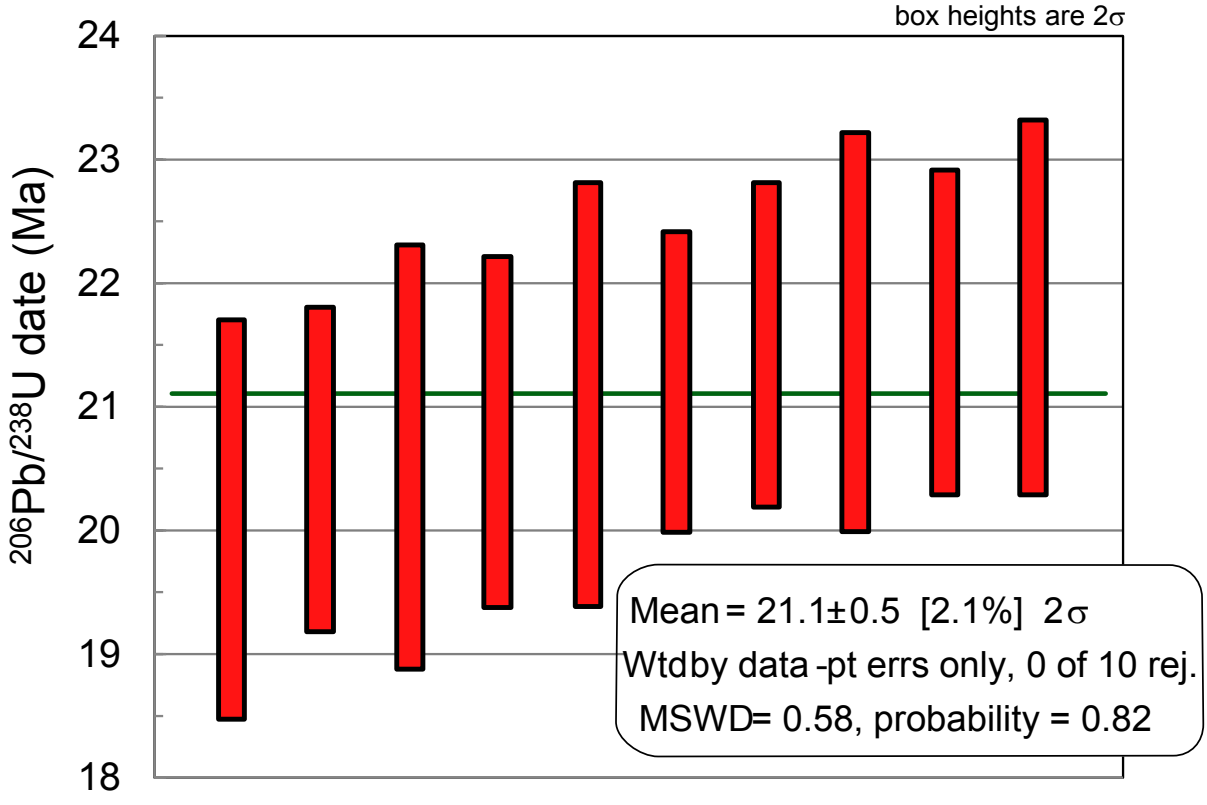
box heights are 2σ
24
23
22
21
20
19
18
206Pb/238U date (Ma)
Mean = 21.1±0.5 [2.1%] 2σ
Wtdby data-pt errs only, 0 of 10 rej.
MSWD= 0.58, probability = 0.82

Appendix A4. LA-ICP-MS U-Pb on Zircon, Sample SG190213P16

		Radiogenic Isotope Ratios					Isotopic Ages						Background corrected mean counts per second at specified mass							
Sample Fraction	CL image	$^{207}Pb/^{235}U$	%2σ	$^{206}Pb/^{238}U$	%2σ	corr. coef.	$^{207}Pb/^{206}Pb$	±2σ	$^{207}Pb/^{235}U$	±2σ	$^{206}Pb/^{238}U$	±2σ	^{202}Hg	^{204}Pb	^{206}Pb	^{207}Pb	^{208}Pb	^{232}Th	^{235}U	^{238}U
1	R1	0.0162	0.011	0.00336	0.0006	0.07818	0.049	0.013	15.8	10	21.6	3.7	11	15.4	504	19.7	22	12990	605	1.13E+05
5	R6	0.015	0.0097	0.00324	0.0002	0.04022	0.11	0.048	13.6	9.6	20.8	1.3	11	16.2	234	9.4	56	18010	280	5.43E+04
6	R8	0.018	0.0088	0.00357	0.0002	0.06801	0.081	0.034	16.7	8.7	23	1.3	12	14.2	272	11.8	66	24750	326	6.09E+04
7	R9	0.0182	0.0088	0.00329	0.0002	0.02462	0.065	0.029	16.3	8.7	21.2	1.3	11	15.5	220	11.7	58	17170	246	4.64E+04
8	R1	0.0172	0.01	0.00325	0.0003	0.0351	0.041	0.036	14.1	10	20.9	1.8	11	16.9	153	8	33.4	16690	195	38190
9	C1	0.0172	0.0066	0.00349	0.0002	0.04492	0.027	0.024	15.8	6.5	22.4	1.5	10	16.6	296	9.9	53	17830	372	6.82E+04
10	C2	0.031	0.011	0.00384	0.0004	0.06208	0.081	0.038	28	11	24.7	2.7	12	14.8	171	11.5	59	15890	184	36930
12	C3	0.0307	0.0091	0.00375	0.0004	0.02187	0.117	0.047	27.7	8.9	24.1	2.4	11	16	149	12.6	26.9	15190	207	38210
13	C6	0.266	0.027	0.042	0.0016	0.12971	0.054	0.005	232	21	265	9.8	12	17	2760	145	413	15880	319	6.01E+04
14	C7	0.027	0.01	0.0039	0.0004	0.15207	0.117	0.042	24	9.9	25.1	2.5	12	15.8	127	7.4	32.3	9960	160	30730
15	C8	0.0215	0.0089	0.00388	0.0006	0.00138	0.082	0.015	21.4	8.5	25.2	4	15	17.6	326	15.1	71	2.29E+04	373	6.71E+04
16	C9	0.0254	0.0065	0.00375	0.0003	0.02632	0.092	0.032	24	6.4	24.1	1.6	10	14.7	286	15.1	71	28660	357	6.59E+04
17	C1	0.0258	0.0061	0.00378	0.0003	0.05996	0.058	0.028	24.5	6	24.3	1.6	11	18.2	285	14.8	68	28140	339	6.60E+04
18	C1	0.037	0.011	0.00366	0.0003	0.01988	0.091	0.047	33	11	23.5	2.2	12	13.9	125	13.5	32.3	10930	176	33220
19	C1	0.017	0.0093	0.00406	0.0003	0.0144	0.086	0.05	14.2	9.1	26.1	2	11	14.6	173	3.7	52	15020	201	3.74E+04

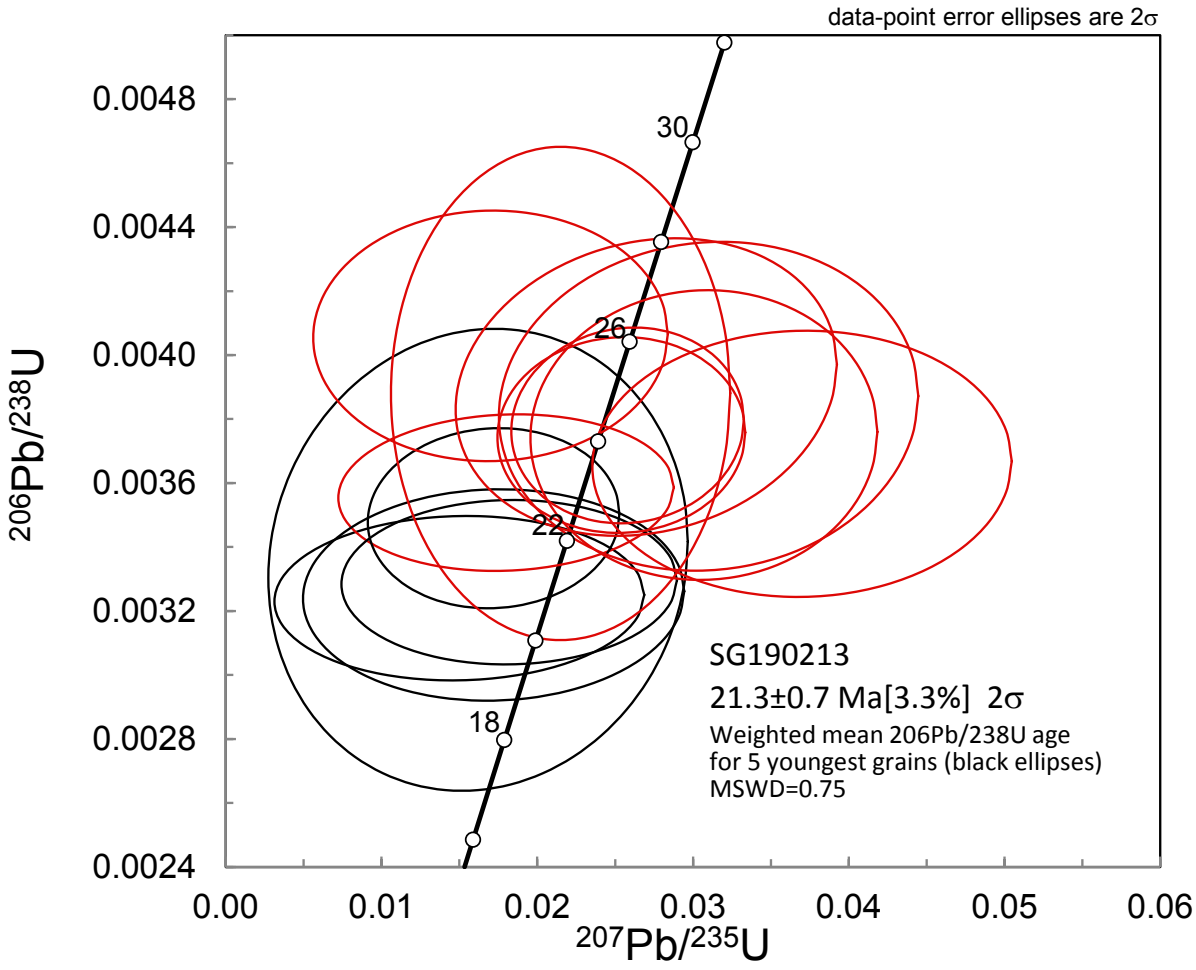
data-point error ellipses are 2σ
0.0048
0.0044
0.0040
0.0036
0.0032
0.0028
0.0024
206Pb/238U
30
26
22
18
SG190213
21.3±0.7 Ma[3.3%] 2σ
Weighted mean 206Pb/238U age
for 5 youngest grains (black ellipses)
MSWD=0.75
0.00
0.01
0.02
0.03
0.04
0.05
0.06
207Pb/235U

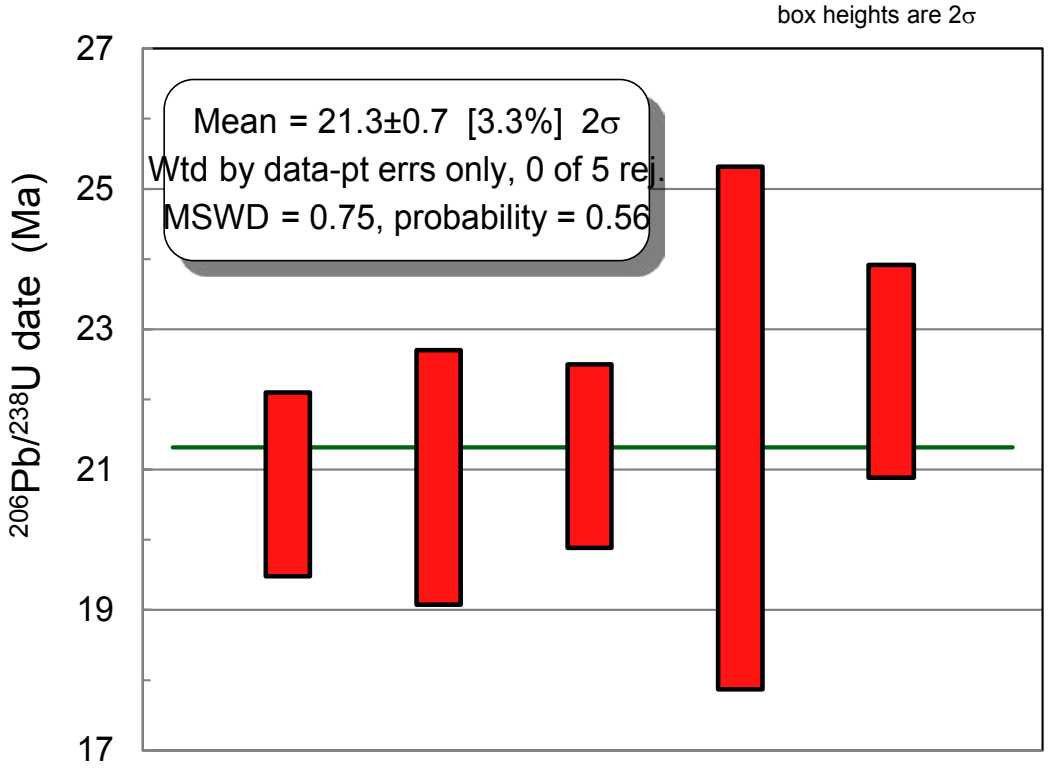
box heights are 2σ
Mean = 21.3±0.7 [3.3%] 2σ
Wtd by data-pt errs only, 0 of 5 rej.
MSWD = 0.75, probability = 0.56
27
25
23
21
19
17
206Pb/238U date (Ma)

Appendix A5. $^{40}Ar/^{39}Ar$ Biotite Geochronology

Appendix A5. $^{40}Ar/^{39}Ar$ Biotite, Sample SG040213P8

SG040213-P8 Biotite

Laser	*Isotope Ratios*										
Power(%)	*$^{40}Ar/^{39}Ar$*	*2σ*	*$^{36}Ar/^{40}Ar$*	*2σ*	*r.i.*	*Ca/K*	*%^{40}Ar atm*	*f ^{39}Ar*	*$^{40}Ar^*/^{39}ArK$*	*Age*	*2σ*
2.30	119.13	6.08	0.39	0.02	0.022	0.28	96.85	0.32	3.758	15.90	± 32.12
2.80	27.41	1.52	0.07	0.00	0.038	0.09	77.35	1.13	6.209	26.20	± 6.57
3.20	6.01	0.21	0.01	0.00	0.014	0.01	39.72	0.52	3.621	15.32	± 3.57
3.80	4.80	0.11	0.00	0.00	0.006	0.00	11.12	5.30	4.264	18.03	± 0.90
4.20	4.63	0.15	0.00	0.00	0.018	0.00	6.94	12.27	4.304	18.20	± 1.19
4.60	4.81	0.20	0.00	0.00	0.004	0.00	4.97	18.79	4.567	19.30	± 1.64
4.80	4.63	0.19	0.00	0.00	0.001	0.00	5.32	9.98	4.381	18.52	± 1.55
5.20	4.95	0.13	0.00	0.00	0.005	0.00	5.65	18.49	4.675	19.76	± 1.05
5.50	4.60	0.16	0.00	0.00	0.001	0.00	4.35	14.04	4.404	18.62	± 1.32
6.00	17.21	0.56	0.00	0.00	0.049	-0.01	1.39	6.60	16.966	70.70	± 4.51
7.00	8.98	0.24	0.00	0.00	0.001	-0.01	4.45	9.79	8.579	36.10	± 1.92
8.50	5.08	0.33	0.00	0.00	0.001	0.02	4.42	2.76	4.852	20.50	± 2.72

J = 0.00235000 ± 0.00001175 Volume 39A 0.137 x E-13 cm3 NPT

Integrated Date = 20.23 ± 0.46 Ma

Plateau age = 18.67 ± 0.52 Ma (2s, including J-error of MSWD = 1.5, probability=0.18 Includes 78.9% of the 39/ steps 4 through 9

Inverse isochron (correlation age) results, plateau steps: Model 1 Solution (±95%-conf.) on 10 points

Age = 18.70 ± 0.82 Ma Initial 40Ar/36Ar =305 ± 25 MSWD = 2.2 Probability = 0.03

Analysis by Janet Gabites
Pacific Centre for Isotopic and Geochemical Research,
Dept Earth and Ocean Sciences,
The University of British Columbia,
Vancouver, BC., Canada

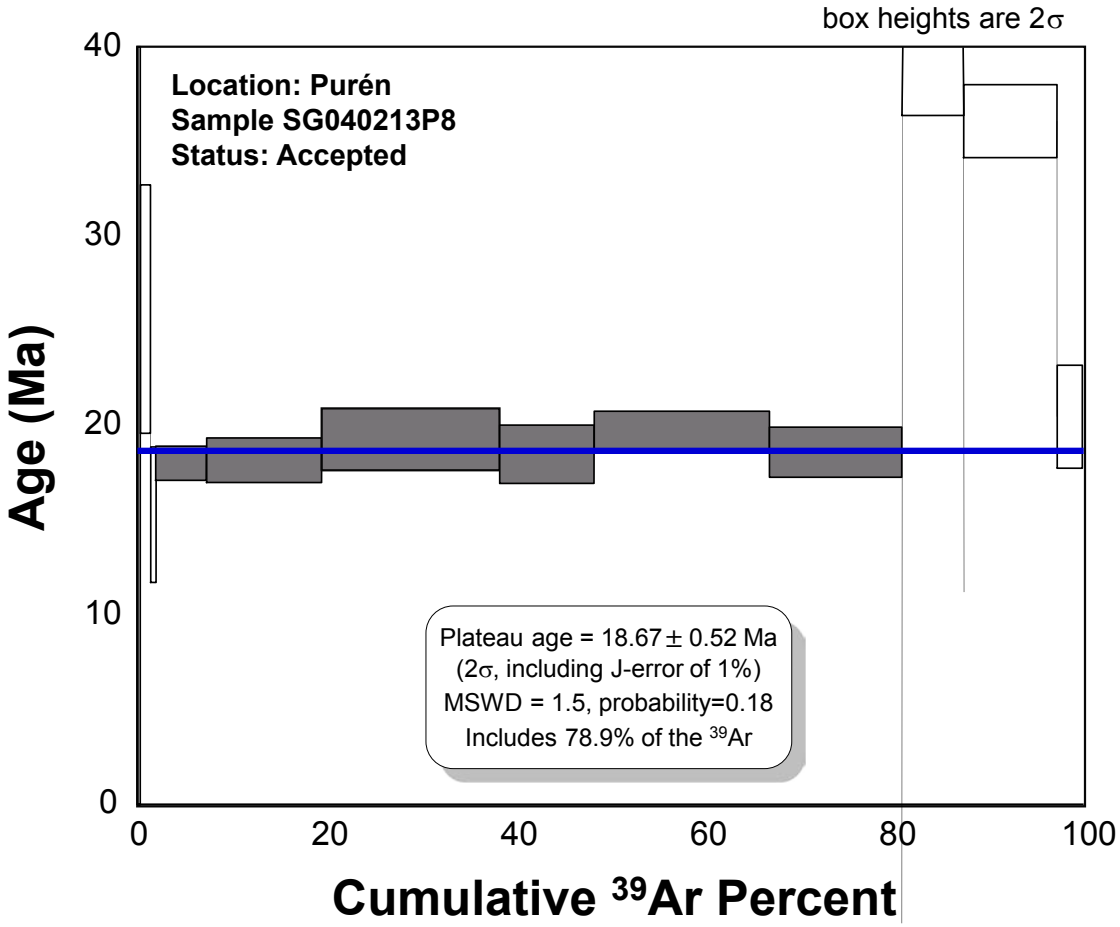
box heights are 2σ
Location: Purén
Sample SG040213P8
Status: Accepted
Plateau age = 18.67 ± 0.52 Ma
(2σ, including J-error of 1%)
MSWD = 1.5, probability=0.18
Includes 78.9% of the 39Ar
Age (Ma)
Cumulative 39Ar Percent
0
10
20
30
40
0
20
40
60
80
100

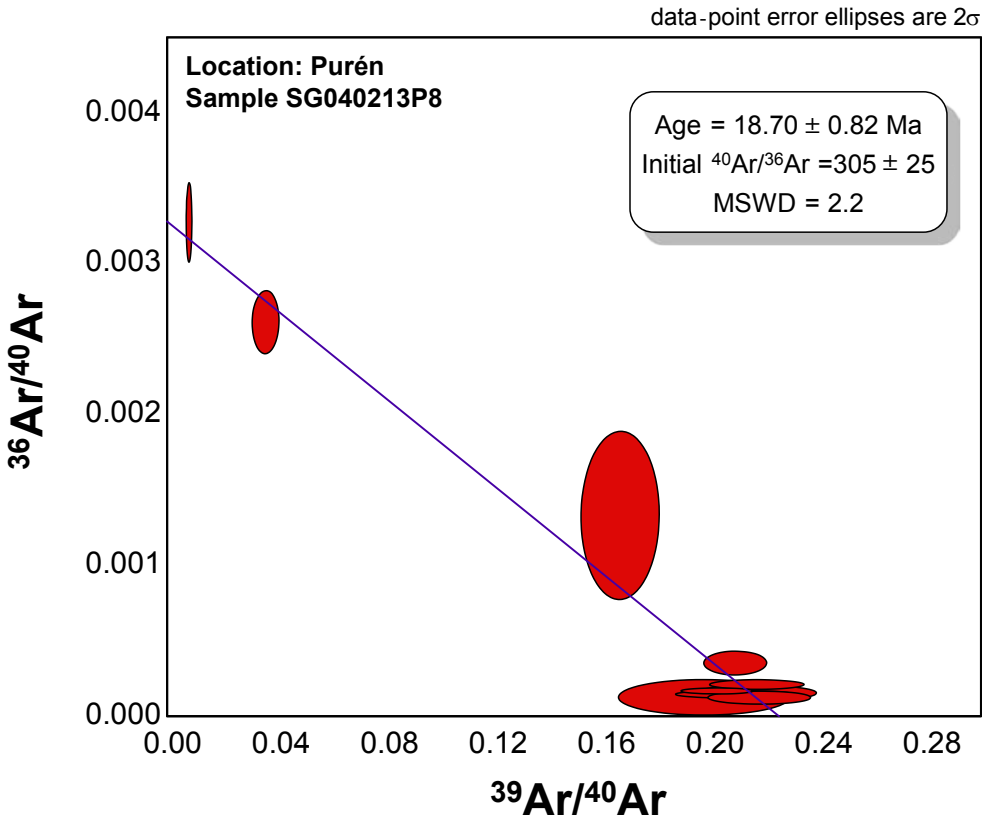
data-point error ellipses are 2σ
Location: Purén
Sample SG040213P8
Age = 18.70 ± 0.82 Ma
Initial 40Ar/36Ar =305 ± 25
MSWD = 2.2
36Ar/40Ar
39Ar/40Ar
0.000
0.001
0.002
0.003
0.004
0.00
0.04
0.08
0.12
0.16
0.20
0.24
0.28

Appendix A5. $^{40}Ar/^{39}Ar$ Biotite, Sample SG16294

SG16294 Biotite

Laser *Isotope Ratios*

Power(%)	$^{40}Ar/^{39}Ar$	2σ	$^{36}Ar/^{40}Ar$	2σ	r.i.	Ca/K	$\%^{40}Ar$ atm	$f^{39}Ar$	$^{40}Ar^*/^{39}ArK$	Age	2σ
2.30	112.52	5.58	0.38	0.02	0.011	0.29	88.60	0.44	12.826	53.66	± 40.57
2.80	24.84	1.05	0.06	0.00	0.008	0.05	67.45	1.76	8.086	34.01	± 7.24
3.20	9.71	0.33	0.00	0.00	0.001	0.01	12.19	4.98	8.523	35.83	± 2.74
3.50	9.13	0.34	0.00	0.00	0.001	0.03	5.63	1.72	8.613	36.20	± 3.00
4.50	9.28	0.21	0.00	0.00	0.007	0.00	3.30	35.28	8.972	37.70	± 1.73
5.00	9.34	0.39	0.00	0.00	0.001	0.01	2.40	32.47	9.117	38.30	± 3.16
5.50	10.56	1.18	0.00	0.00	0.000	0.00	2.62	15.28	10.286	43.15	± 9.57
6.50	7.68	0.42	0.00	0.00	0.004	0.00	10.93	8.08	6.842	28.82	± 3.17

J = 0.00234800 ± 0.00001174 Volume 39ArK = 0.051 x E-13 cm3 NPT

Integrated Date = 36.16 ± 1.11 Ma

Plateau age = 37.2 ± 1.2 Ma (2s, including J-error of 1%) MSWD = 0.87, probability=0.51 Includes 91.9% of the 39A steps 1 through 7

Inverse isochron (correlation age) results, plateau steps: Model 1 Solution (±95%-conf.) on 6 points

Age = 37.0 ± 1.2 Ma Initial 40Ar/36Ar =265 ± 15 MSWD = 1.09 Probability = 0.36

Analysis by Janet Gabites
Pacific Centre for Isotopic and Geochemical Research,
Dept Earth and Ocean Sciences,
The University of British Columbia,
Vancouver, BC., Canada

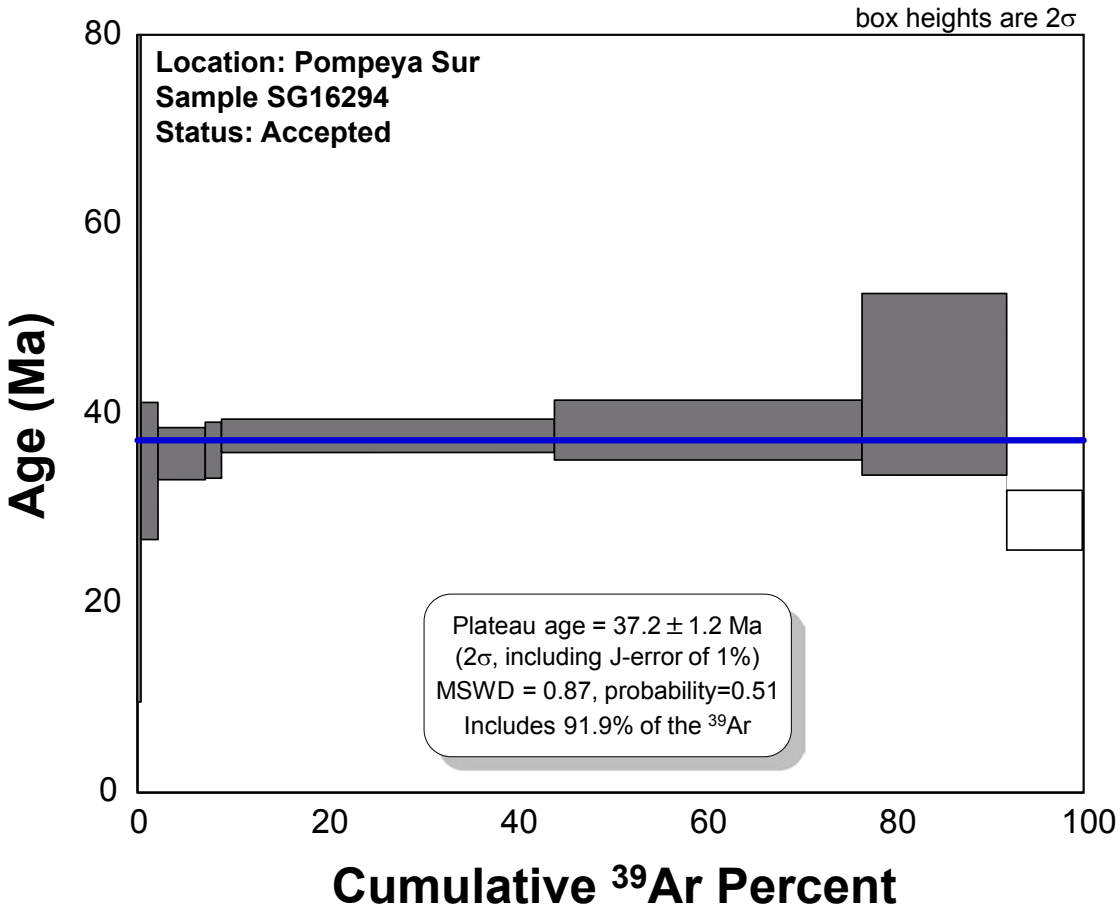
box heights are 2σ
Location: Pompeya Sur
Sample SG16294
Status: Accepted
Plateau age = 37.2 ± 1.2 Ma
(2σ, including J-error of 1%)
MSWD = 0.87, probability=0.51
Includes 91.9% of the 39Ar
Age (Ma)
Cumulative 39Ar Percent
0
20
40
60
80
100

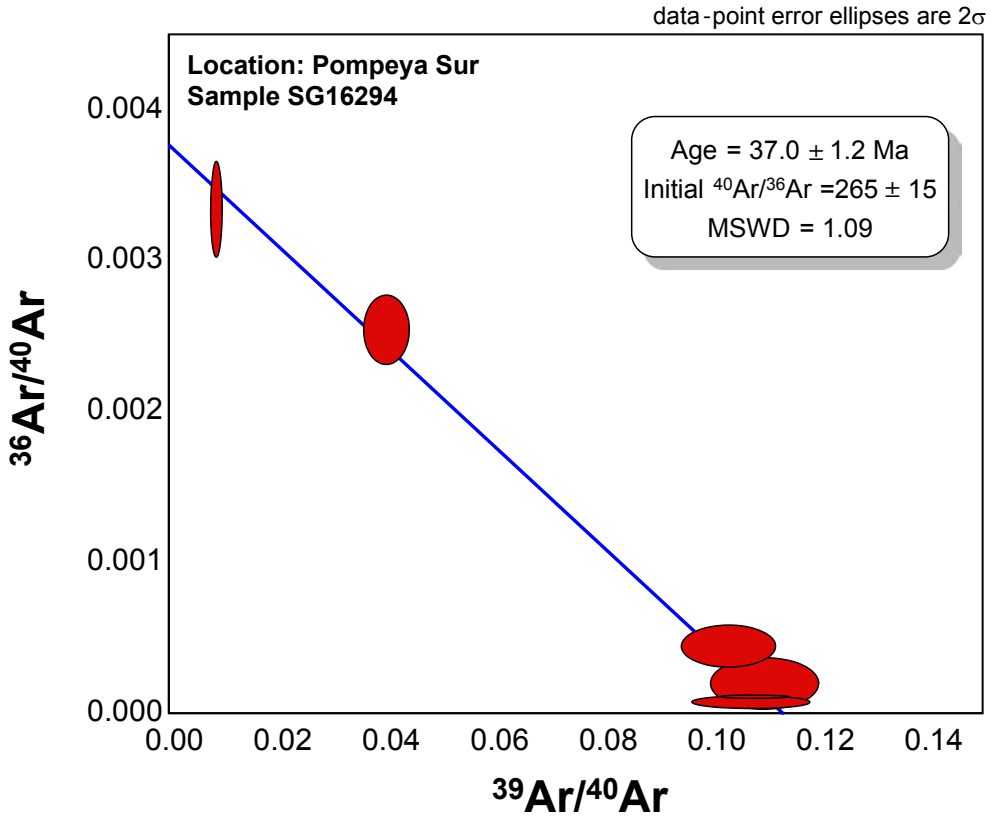
data-point error ellipses are 2σ
Location: Pompeya Sur
Sample SG16294
Age = 37.0 ± 1.2 Ma
Initial 40Ar/36Ar =265 ± 15
MSWD = 1.09
36Ar/40Ar
39Ar/40Ar
0.000
0.001
0.002
0.003
0.004
0.00
0.02
0.04
0.06
0.08
0.10
0.12
0.14

Appendix A6. $^{40}Ar/^{39}Ar$ Alunite Geochronology

Appendix A6. $^{40}Ar/^{39}Ar$ Alunite, Sample SG090313P3

SG090313P3 Alunite

Laser *Isotope Ratios*

Power(%)	*$^{40}Ar/^{39}Ar$*	*2 σ*	*$^{36}Ar/^{40}Ar$*	*2σ*	*r.i.*	*Ca/K*	*% ^{40}Ar atm*	*f ^{39}Ar*	*$^{40}Ar^*/^{39}ArK$*	*Age*	*2σ*
2.20	1302.83	30.76	4.27	0.13	0.010	0.01	80.34	0.06	256.175	928.35	± 131.23
2.50	564.44	33.21	2.30	0.30	0.105	0.00	99.93	1.57	0.406	1.92	± 646.01
2.70	129.80	0.81	0.51	0.01	0.029	0.00	96.63	4.45	4.371	20.58	± 24.19
2.80	53.84	0.35	0.21	0.00	0.022	0.00	94.62	11.09	2.898	13.67	± 9.77
2.90	36.25	0.23	0.14	0.00	0.036	0.00	93.45	18.76	2.372	11.20	± 6.52
3.00	32.70	0.24	0.12	0.00	0.024	0.00	92.81	24.18	2.351	11.10	± 5.86
3.10	61.09	0.37	0.24	0.00	0.063	0.00	95.83	11.20	2.548	12.03	± 11.28
3.20	63.35	0.68	0.25	0.01	0.214	0.00	95.59	10.25	2.792	13.17	± 12.57
3.30	56.06	0.32	0.21	0.01	0.016	0.00	93.72	13.75	3.521	16.60	± 13.32
3.40	205.47	1.53	0.83	0.02	0.015	0.00	98.53	3.51	3.024	14.26	± 38.75
3.50	684.89	6.04	2.80	0.06	0.017	0.00	100.01	1.17	0.088	-0.42	± 132.72

J = 0.00261900 ± 0.00001310 Volume 39ArK = 0.663 x E-13 cm3 NPT

Integrated Date = 12.87 ± 3.42 Ma

Plateau age = 12.3 ± 3.4 Ma (2s, including J-error of 1%) MSWD = 0.15, probability=0.998 Includes 99.94% of the 3 steps 2 through 11

Inverse isochron (correlation age) results, plateau steps: Model 1 Solution (±95%-conf.) on 10 points

Age = 10.8 ± 6.2 Ma Initial 40Ar/36Ar =246.6 ± 6.2 MSWD = 0.14 Probability = 0.99

Analysis by Janet Gabites
Pacific Centre for Isotopic and Geochemical Research,
Dept Earth and Ocean Sciences,
The University of British Columbia,
Vancouver, BC., Canada

Appendix A6. $^{40}Ar/^{39}Ar$ Alunite, Sample SG090313P4

SG090313P4 Alunite

Laser *Isotope Ratios*

Power(%)	*$^{40}Ar/^{39}Ar$*	*2 σ*	*$^{36}Ar/^{40}Ar$*	*2σ*	*r.i.*	*Ca/K*	*% ^{40}Ar atm*	*f ^{39}Ar*	*$^{40}Ar^*/^{39}ArK$*	*Age*	*2σ*
2.20	9749.27	1443.44	0.17	0.22	0.004	0.00	-0.53	0.07	9800.541	5928.86	± 515.69
2.40	4007.72	205.29	13.63	0.75	0.018	0.00	100.48	0.20	19.191	-92.78	± 836.73
2.50	98.26	16.03	0.31	0.07	0.547	0.01	92.74	0.22	7.129	33.29	± 237.07
2.80	18.36	0.26	0.05	0.00	0.264	0.00	83.44	17.98	3.040	14.27	± 4.37
3.10	3.62	0.06	0.00	0.00	0.072	0.00	11.42	67.63	3.210	15.06	± 0.83
3.20	4.93	0.25	0.01	0.00	0.246	0.00	34.78	13.44	3.214	15.08	± 3.92
3.30	16.19	2.17	0.04	0.00	0.722	0.01	79.42	0.32	3.331	15.63	± 22.36
3.50	10.54	4.19	0.03	0.07	0.157	0.02	81.72	0.13	1.926	9.06	± 194.44

J = 0.00260600 ± 0.00001303 Volume 39ArK = 0.139 x E-13 cm3 NPT

Integrated Date = 15.05 ± 0.80 Ma

Plateau age = 15.04 ± 0.81 Ma (2s, including J-error of 1%) MSWD = 0.037, probability=1.000 Includes 99.93% of the 3$ steps 2 through 8

Inverse isochron (correlation age) results, plateau steps: Model 1 Solution (±95%-conf.) on 6 points

Age = 15.03 ± 0.80 Ma Initial 40Ar/36Ar =293 ± 10 MSWD = 0.017 Probability = 0.999

Analysis by Janet Gabites
Pacific Centre for Isotopic and Geochemical Research,
Dept Earth and Ocean Sciences,
The University of British Columbia,
Vancouver, BC., Canada

Appendix A6. $^{40}Ar/^{39}Ar$ Alunite, Sample SG090313P4 (Repeat)

SG090313P4 Alunite

Laser	*Isotope Ratios*										
Power(%)	*$^{40}Ar/^{39}Ar$*	*2 σ*	*$^{36}Ar/^{40}Ar$*	*2σ*	*r.i.*	*Ca/K*	*% ^{40}Ar atm*	*f ^{39}Ar*	*$^{40}Ar^*/^{39}ArK$*	*Age*	*2σ*
2.20	62185.61	30417.72	217.29	106.38	0.000	0.90	103.26	0.01	2025.308	0.00	± 3644.53
2.50	5437.86	183.65	23.82	1.13	0.158	-0.01	129.43	0.33	1600.542	0.00	± 812.03
2.60	98.97	0.56	0.34	0.01	0.005	0.00	102.25	4.30	2.223	-10.51	± 18.94
2.70	59.13	0.39	0.19	0.01	0.040	0.00	96.58	1.34	2.021	9.50	± 13.70
3.00	16.09	0.13	0.05	0.00	0.085	0.00	86.89	28.03	2.110	9.92	± 2.79
3.10	4.49	0.03	0.00	0.00	0.086	0.00	31.61	36.43	3.068	14.40	± 0.45
3.30	5.49	0.07	0.01	0.00	0.300	0.00	42.31	17.27	3.169	14.87	± 0.78
3.40	7.08	0.04	0.01	0.00	0.027	0.00	55.95	4.91	3.119	14.64	± 1.08
3.50	6.60	0.04	0.01	0.00	0.051	0.00	50.73	7.39	3.251	15.26	± 0.98

J = 0.00260600 ± 0.00001303 Volume 39ArK = 0.265 x E-13 cm3 NPT

Integrated Date = 14.54 ± 0.34 Ma

Plateau age = 14.62 ± 0.37 Ma (2s, including J-error of 1%) MSWD = 1.03, probability=0.38 Includes 66% of the 39Ar steps 6 through 9

Inverse isochron (correlation age) results, plateau steps: Model 1 Solution (±95%-conf.) on 7 points

Age = 14.96 ± 0.84 Ma Initial 40Ar/36Ar =283 ± 14 MSWD = 2.3 Probability = 0.042

Analysis by Janet Gabites
Pacific Centre for Isotopic and Geochemical Research,
Dept Earth and Ocean Sciences,
The University of British Columbia,
Vancouver, BC., Canada

Appendix A6. $^{40}Ar/^{39}Ar$ Alunite, Sample SG14161

SG14161Alunite

Laser	*Isotope Ratios*										
Power(%)	*$^{40}Ar/^{39}Ar$*	*2 σ*	*$^{36}Ar/^{40}Ar$*	*2σ*	*r.i.*	*Ca/K*	*% ^{40}Ar atm*	*f ^{39}Ar*	*$^{40}Ar^*/^{39}ArK$*	*Age*	*2σ*
2.30	883.24	19.88	3.45	0.34	0.0058	0.02	115.24	0.16	134.634	-1116.21	± 2215.21
2.50	206.76	1.73	0.87	0.03	0.0143	0.01	124.97	0.61	51.628	-351.43	± 120.52
2.80	14.94	0.10	0.05	0.00	0.0747	0.00	97.42	7.31	0.385	2.38	± 4.67
3.20	8.24	0.06	0.03	0.00	0.0447	0.00	96.42	32.66	0.295	1.82	± 3.58
3.40	7.23	0.05	0.02	0.00	0.0820	0.00	96.38	15.73	0.262	1.62	± 2.87
3.60	8.35	0.05	0.03	0.00	0.0429	0.00	95.56	17.19	0.370	2.29	± 3.06
3.80	7.46	0.05	0.02	0.00	0.0278	0.00	80.30	10.34	1.470	9.07	± 3.43
4.10	7.16	0.05	0.02	0.00	0.1063	0.00	77.21	12.20	1.631	10.06	± 2.12
4.40	5.21	0.03	0.01	0.00	0.0120	0.00	57.90	3.80	2.195	13.53	± 0.98

J = 0.00342100 ± 0.00001711 Volume 39ArK = 0.7965543 x E-13 cm3 NPT

Integrated Date = 10.45 ± 0.77 Ma

Plateau age = 2.0 ± 1.7 Ma (2s, including J-error of 1%) MSWD = 0.047, probability=0.99 Includes 72.9% of the 39A steps 3 through 6

Inverse isochron (correlation age) results, plateau steps: Model 1 Solution (±95%-conf.) on plateau steps

Age = 1.2 ± 6.1 Ma Initial 40Ar/36Ar =300 ± 33 MSWD = 0.042 Probability = 0.96

Inverse isochron (correlation age) results, plateau steps: Model 1 Solution (±95%-conf.) on oldest steps

Age = 17.7 ± 2.2 Ma Initial 40Ar/36Ar =227 ± 28 MSWD = 0.045 Probability = 0.86

Analysis by Janet Gabites
Pacific Centre for Isotopic and Geochemical Research,
Dept Earth and Ocean Sciences,
The University of British Columbia,
Vancouver, BC., Canada

Appendix A6. $^{40}Ar/^{39}Ar$ Alunite, Sample SG14166

SG14166 Alunite

Laser *Isotope Ratios*

Power(%)	*$^{40}Ar/^{39}Ar$*	*2 σ*	*$^{36}Ar/^{40}Ar$*	*2σ*	*r.i.*	*Ca/K*	*% ^{40}Ar atm*	*f ^{39}Ar*	*$^{40}Ar^*/^{39}ArK$*	*Age*	*2σ*
2.30	443.01	28.86	1.42	0.10	0.003	0.12	94.68	0.05	23.553	140.80	± 119.35
2.60	6.57	0.04	0.01	0.00	0.037	0.00	59.42	5.60	2.666	16.50	± 1.50
2.90	3.96	0.04	0.00	0.00	0.046	0.01	34.56	11.91	2.595	16.06	± 0.79
3.20	3.01	0.03	0.00	0.00	0.058	0.00	12.36	45.51	2.636	16.31	± 0.36
3.50	2.95	0.02	0.00	0.00	0.035	0.00	9.25	36.51	2.679	16.58	± 0.30
3.80	22.69	0.83	0.07	0.00	0.197	0.06	85.71	0.43	3.242	20.04	± 15.18

J = 0.00343800 ± 0.00001719 Volume 39ArK = 0.290 x E-13 cm3 NPT

Integrated Date = 16.44 ± 0.22 Ma

Plateau age = 16.44 ± 0.27 Ma (2s, including J-error of 1%) MSWD = 0.64, probability=0.63 Includes 99.95% of the 3(steps 2 through 6

Inverse isochron (correlation age) results, plateau steps: Model 1 Solution (±95%-conf.) on 6 points

Age = 16.34 ± 0.25 Ma Initial 40Ar/36Ar =303 ± 11 MSWD = 1.18 Probability = 0.32

Analysis by Janet Gabites
Pacific Centre for Isotopic and Geochemical Research,
Dept Earth and Ocean Sciences,
The University of British Columbia,
Vancouver, BC., Canada

Appendix A6. $^{40}Ar/^{39}Ar$ Alunite, Sample SG14166 (Lab Control)

SG14166 Alunite

Laser Heating Step	*Isotope Ratios*												
	$^{40}Ar/^{39}Ar$	±1 σ	$^{37}Ar/^{39}Ar$	±1 σ	$^{36}Ar/^{39}Ar$	±1 σ	$^{40}Ar^*/^{39}Ar_K$	±1 σ	^{40}Ar (mol)	$^{40}Ar^*$ (%)	$^{39}Ar_k$ (%)	Age (Ma)	± 2σ
	24.38	0.0534	0.0000	0.0060	0.0694	0.0008	12.4361	0.2227	0.0000	15.9222	15.1363	14.69	1.6783
	7.88	0.0644	0.0228	0.0429	0.0118	0.0034	12.4588	1.0076	0.0000	55.6072	2.8692	16.56	7.5867
	21.97	0.1092	0.0000	0.0180	0.0557	0.0017	12.6910	0.4929	0.0000	25.0876	4.7237	20.82	3.7022
	7.09	0.0303	0.0105	0.0176	0.0085	0.0013	12.6966	0.3733	0.0000	64.4684	7.0545	17.29	2.8092
	6.73	0.0592	0.0252	0.0724	0.0103	0.0063	12.4706	1.8668	0.0000	54.6930	1.6703	13.92	14.0762
	5.35	0.0108	0.0000	0.0014	0.0022	0.0001	12.4809	0.0256	0.0000	87.5683	68.5462	17.71	0.1924

J = 0.002106 ± 0.0000125

Total Fusion Age: 17.78 ± 0.51 Ma

Plateau Age: 17.72 ± 0.2 Ma

Analysis by Richard Spiking
Isotope Geochemistry, Geochronology and Thermochronology Unit
Université de Genève,
Genève, Switzerland.

Appendix A6. $^{40}Ar/^{39}Ar$ Alunite, Sample SG16257

SG16257 Alunite

Laser	*Isotope Ratios*										
Power(%)	*$^{40}Ar/^{39}Ar$*	*2 σ*	*$^{36}Ar/^{40}Ar$*	*2σ*	*r.i.*	*Ca/K*	*% ^{40}Ar atm*	*f ^{39}Ar*	*$^{40}Ar^*/^{39}ArK$*	*Age*	*2σ*
2.40	247.30	4.19	0.87	0.02	0.009	0.02	96.89	0.06	7.693	36.26	± 47.28
2.70	7.63	0.05	0.02	0.00	0.062	0.00	64.70	4.37	2.695	12.79	± 1.07
2.80	5.10	0.15	0.01	0.00	0.455	0.00	43.52	8.05	2.881	13.67	± 1.26
3.00	4.10	0.06	0.00	0.00	0.256	0.00	28.46	17.39	2.930	13.90	± 0.62
3.10	4.12	0.05	0.00	0.00	0.344	0.00	28.96	21.16	2.929	13.89	± 0.46
3.20	4.23	0.04	0.00	0.00	0.016	0.00	32.42	26.05	2.857	13.55	± 0.37
3.30	4.91	0.04	0.01	0.00	0.062	0.00	39.40	13.05	2.978	14.12	± 0.93
3.40	4.95	0.06	0.01	0.00	0.301	0.00	39.34	9.86	3.005	14.25	± 0.72

J = 0.00263300 ± 0.00001317 Volume 39ArK = 0.875 x E-13 cm3 NPT

Integrated Date = 13.76 ± 0.23 Ma

Plateau age = 13.76 ± 0.27 Ma (2s, including J-error of 1%) MSWD = 1.2, probability=0.29 Includes 100% of the 39A steps 1 through 8

Inverse isochron (correlation age) results, plateau steps: Model 1 Solution (±95%-conf.) on 8 points

Age = 13.72 ± 0.34 Ma Initial 40Ar/36Ar =276.3 ± 9.3 MSWD = 1.4 Probability = 0.19

Analysis by Janet Gabites
Pacific Centre for Isotopic and Geochemical Research,
Dept Earth and Ocean Sciences,
The University of British Columbia,
Vancouver, BC., Canada

ndix A6. $^{40}Ar/^{39}Ar$ Alunite, Sample SG16257 (Repeat)

257 Alunite

Isotope Ratios

r(%)	$^{40}Ar/^{39}Ar$	2 σ	$^{36}Ar/^{40}Ar$	2σ	r.i.	Ca/K	% ^{40}Ar atm	f ^{39}Ar	$^{40}Ar^*/^{39}ArK$	Age	2σ
0	936.20	103.91	3.41	0.40	0.008	0.01	100.44	0.03	4.164	-20.16	± 364.96
0	4.29	0.04	0.01	0.00	0.096	0.00	40.79	23.94	2.540	12.19	± 0.68
0	5.35	0.07	0.01	0.00	0.074	0.00	49.17	27.33	2.717	13.04	± 1.45
0	5.47	0.05	0.01	0.00	0.049	0.00	50.28	22.58	2.720	13.05	± 1.21
0	6.48	0.05	0.01	0.00	0.031	0.00	44.78	9.06	3.578	17.15	± 1.65
0	6.15	0.14	0.01	0.00	0.354	0.00	44.71	10.07	3.402	16.31	± 1.39
0	6.00	0.05	0.01	0.00	0.030	0.00	37.14	6.99	3.770	18.06	± 1.07

.00263300 ± 0.00001332	Volume 39ArK =	0.401	x E-13 cm3 NPT	
ted Date =	14.18 ± 0.44	Ma		
u age = 12.49 ± 0.56 Ma	(2s, including J-error of 1%)	MSWD = 0.74, probability=0.53		Includes 73.9% of the 39/ steps 1 through 4
isochron (correlation age) results, plateau steps: Model 1 Solution (±95%-conf.) on 6 points				
12.20 ± 0.91 Ma	Initial 40Ar/36Ar =280 ± 21		MSWD = 1.06	Probability = 0.35

sis by Janet Gabites
e Centre for Isotopic and Geochemical Research

Appendix A6. $^{40}Ar/^{39}Ar$ Alunite, Sample SG16271

SG16271 Alunite

Laser *Isotope Ratios*

Power(%)	*$^{40}Ar/^{39}Ar$*	*2 σ*	*$^{36}Ar/^{40}Ar$*	*2σ*	*r.i.*	*Ca/K*	*% ^{40}Ar atm*	*f ^{39}Ar*	*$^{40}Ar^*/^{39}ArK$*	*Age*	*2σ*
2.30	926.28	148.26	3.73	0.61	0.009	-0.03	110.30	0.03	95.435	-516.64	± 504.46
2.60	175.98	3.83	0.62	0.02	0.062	0.00	97.00	1.03	5.278	24.69	± 37.17
2.80	17.13	0.17	0.05	0.00	0.126	0.00	80.80	10.49	3.290	15.42	± 3.10
2.90	11.12	0.14	0.03	0.00	0.318	0.00	71.83	11.91	3.133	14.70	± 2.30
3.00	10.07	0.11	0.02	0.00	0.178	0.00	65.66	12.92	3.457	16.20	± 1.82
3.10	10.87	0.14	0.03	0.00	0.100	0.00	72.25	12.67	3.017	14.15	± 2.21
3.20	14.02	0.26	0.04	0.00	0.216	0.00	78.12	8.04	3.068	14.39	± 3.26
3.30	9.47	0.10	0.02	0.00	0.045	0.00	67.35	17.19	3.094	14.51	± 1.77
3.40	10.16	0.12	0.03	0.00	0.049	0.00	69.16	10.60	3.133	14.69	± 2.33
3.50	6.81	0.10	0.01	0.00	0.321	0.00	55.98	15.12	2.997	14.06	± 1.19

J = 0.00260400 ± 0.00001302 Volume 39ArK = 0.312 x E-13 cm3 NPT

Integrated Date = 14.64 ± 0.69 Ma

Plateau age = 14.64 ± 0.70 Ma (2s, including J-error of 1%) MSWD = 0.59, probability=0.79 Includes 99.97% of the 3$ steps 2 through 10

Inverse isochron (correlation age) results, plateau steps: Model 1 Solution (±95%-conf.) on 9 points

Age = 14.1 ± 1.3 Ma Initial 40Ar/36Ar =279 ± 10 MSWD = 0.55 Probability = 0.80

Analysis by Janet Gabites
Pacific Centre for Isotopic and Geochemical Research,
Dept Earth and Ocean Sciences,
The University of British Columbia,
Vancouver, BC., Canada

Appendix A6. $^{40}Ar/^{39}Ar$ Alunite, Sample SG16274

SG16274 Alunite

Laser	*Isotope Ratios*										
Power(%)	*$^{40}Ar/^{39}Ar$*	*2 σ*	*$^{36}Ar/^{40}Ar$*	*2σ*	*r.i.*	*Ca/K*	*% ^{40}Ar atm*	*f ^{39}Ar*	*$^{40}Ar^*/^{39}ArK$*	*Age*	*2σ*
2.50	1429.49	48.17	4.52	0.18	0.072	0.12	93.47	0.10	93.313	400.52	± 236.55
2.70	44.03	0.41	0.13	0.00	0.069	0.00	87.92	1.91	5.318	25.37	± 8.66
2.80	8.82	0.06	0.02	0.00	0.050	0.00	57.99	9.55	3.705	17.72	± 1.15
2.90	6.09	0.96	0.01	0.00	0.004	0.00	33.37	14.54	4.056	19.38	± 6.21
3.00	4.96	0.05	0.00	0.00	0.067	0.00	25.66	15.34	3.686	17.62	± 0.62
3.10	5.01	0.03	0.00	0.00	0.064	0.00	26.77	28.56	3.670	17.55	± 0.44
3.20	4.58	0.03	0.00	0.00	0.006	0.00	21.15	29.99	3.615	17.28	± 0.42

J = 0.00265700 ± 0.00001329 Volume 39ArK = 0.284 x E-13 cm3 NPT

Integrated Date = 17.48 ± 0.26 Ma

Plateau age = 17.47 ± 0.32 Ma (2s, including J-error of 1%) MSWD = 0.43, probability=0.79 Includes 98% of the 39Ar steps 3 through 7

Inverse isochron (correlation age) results, plateau steps: Model 1 Solution (±95%-conf.) on 7 points

ge = 17.17 ± 0.34 Ma Initial 40Ar/36Ar =310.0 ± 8.9 MSWD = 0.55 Probability = 0.77

Analysis by Janet Gabites
Pacific Centre for Isotopic and Geochemical Research,
Dept Earth and Ocean Sciences,
The University of British Columbia,
Vancouver, BC., Canada

Appendix A6. $^{40}Ar/^{39}Ar$ Alunite, Sample SG16290

SG16290 Alunite

Laser	*Isotope Ratios*										
Power(%)	*$^{40}Ar/^{39}Ar$*	*2 σ*	*$^{36}Ar/^{40}Ar$*	*2σ*	*r.i.*	*Ca/K*	*% ^{40}Ar atm*	*f ^{39}Ar*	*$^{40}Ar^*/^{39}ArK$*	*Age*	*2σ*
2.10	1105.88	35.69	3.50	0.14	0.011	0.03	93.64	0.13	70.284	303.39	± 189.10
2.30	392.35	45.39	1.17	0.11	0.601	0.00	88.27	0.55	46.034	204.36	± 315.43
2.50	191.63	2.47	0.60	0.02	0.037	0.00	92.72	0.57	13.948	64.39	± 35.38
2.70	77.47	0.55	0.26	0.01	0.089	0.00	99.02	2.84	0.756	3.55	± 15.04
2.80	33.76	3.96	0.10	0.01	0.627	0.00	89.48	7.28	3.552	16.62	± 33.30
3.10	4.60	0.49	0.01	0.00	0.490	0.00	33.51	47.42	3.057	14.31	± 5.16
3.10	5.90	0.04	0.01	0.00	0.049	0.00	34.52	14.89	3.861	18.06	± 0.55
3.30	5.39	0.03	0.00	0.00	0.017	0.00	22.11	26.31	4.195	19.61	± 0.39

J = 0.00259900 ± 0.00001300 Volume 39ArK = 0.144 x E-13 cm3 NPT

Integrated Date = 19.06 ± 0.32 Ma

Plateau age = 18.01 ± 0.57 Ma (2s, including J-error of 1%) MSWD = 1.05, probability=0.35 Includes 69.6% of the 39/ steps 5 through 7

Inverse isochron (correlation age) results, plateau steps: Model 1 Solution (±95%-conf.) on 8 points

Age = 18.9 ± 1.2 Ma Initial 40Ar/36Ar =301 ± 24 MSWD = 6.9 Probability = 0

Analysis by Janet Gabites
Pacific Centre for Isotopic and Geochemical Research,
Dept Earth and Ocean Sciences,
The University of British Columbia,
Vancouver, BC., Canada

Appendix A6. $^{40}Ar/^{39}Ar$ Alunite, Sample SG16293

SG16293 Alunite

Laser	*Isotope Ratios*										
Power(%)	*$^{40}Ar/^{39}Ar$*	*2 σ*	*$^{36}Ar/^{40}Ar$*	*2σ*	*r.i.*	*Ca/K*	*% ^{40}Ar atm*	*f ^{39}Ar*	*$^{40}Ar^*/^{39}ArK$*	*Age*	*2σ*
2.10	24300.61	14905.33	81.96	50.31	0.001	50.20	99.66	0.00	84.582	370.46	± 4483.17
2.30	3795.57	245.71	13.16	0.89	0.004	2.38	102.48	0.06	94.358	-529.00	± 1024.42
2.60	32.23	1.85	0.09	0.01	0.007	0.05	83.25	4.00	5.398	26.05	± 6.23
2.80	9.87	0.43	0.01	0.00	0.043	0.01	39.14	23.74	6.004	28.95	± 2.66
2.90	7.83	0.12	0.00	0.00	0.087	0.03	18.70	14.73	6.368	30.69	± 1.06
3.00	8.19	0.20	0.01	0.00	0.062	0.01	21.86	21.74	6.400	30.84	± 1.62
3.10	6.85	0.75	0.00	0.00	0.008	0.03	16.97	25.82	5.684	27.42	± 5.94
3.20	8.63	0.24	0.01	0.00	0.117	0.03	18.31	9.91	7.050	33.95	± 2.02

J = 0.00268800 ± 0.00001344 Volume 39ArK = 0.257 x E-13 cm3 NPT

Integrated Date = 30.92 ± 0.76 Ma

Plateau age = 30.42 ± 0.88 Ma (2s, including J-error of 1%) MSWD = 0.99, probability=0.43 Includes 90.1% of the 39A steps 1 through 7

Inverse isochron (correlation age) results, plateau steps: Model 1 Solution (±95%-conf.) on 8 points

Age = 31.2 ± 1.6 Ma Initial 40Ar/36Ar =289 ± 15 MSWD = 2.5 Probability = 0.02

Analysis by Janet Gabites
Pacific Centre for Isotopic and Geochemical Research,
Dept Earth and Ocean Sciences,
The University of British Columbia,
Vancouver, BC., Canada

Appendix A6. $^{40}Ar/^{39}Ar$ Alunite, Sample SG16293 (Repeat)

SG16293 Alunite

Laser *Isotope Ratios*

Power(%)	$^{40}Ar/^{39}Ar$	2 σ	$^{36}Ar/^{40}Ar$	2σ	r.i.	Ca/K	$\%^{40}Ar$ atm	$f^{39}Ar$	$^{40}Ar^*/^{39}ArK$	Age	2σ
2.50	330.64	5.74	1.14	0.04	0.022	-0.01	101.76	0.53	5.831	-28.57	± 93.10
2.80	16.62	0.15	0.03	0.00	0.153	0.00	61.03	28.12	6.476	31.21	± 2.32
2.90	13.00	0.11	0.02	0.00	0.210	0.01	47.88	24.26	6.777	32.65	± 1.64
3.00	12.47	0.15	0.02	0.00	0.149	0.00	47.98	25.42	6.489	31.27	± 1.73
3.10	10.29	0.07	0.01	0.00	0.025	0.00	37.29	13.43	6.453	31.10	± 0.98
3.20	11.38	0.32	0.02	0.00	0.104	0.00	52.05	5.72	5.459	26.34	± 7.12
3.40	9.70	0.28	0.02	0.00	0.353	0.01	69.78	2.52	2.933	14.20	± 4.44

J = 0.00268800 ± 0.00001344 Volume 39ArK = 0.238 x E-13 cm3 NPT

Integrated Date = 30.94 ± 0.71 Ma

Plateau age = 31.38 ± 0.78 Ma (2s, including J-error of 1%) MSWD = 1.3, probability=0.27 Includes 97.5% of the 39A steps 1 through 6

Inverse isochron (correlation age) results, plateau steps: Model 1 Solution (±95%-conf.) on 6 points

Age = 31.7 ± 1.3 Ma Initial 40Ar/36Ar =291 ± 13 MSWD = 1.5 Probability = 0.20

Analysis by Janet Gabites
Pacific Centre for Isotopic and Geochemical Research,
Dept Earth and Ocean Sciences,
The University of British Columbia,
Vancouver, BC., Canada

Appendix A6. $^{40}Ar/^{39}Ar$ Alunite, Sample SG16303

SG16303 Alunite

Laser *Isotope Ratios*

Power(%)	$^{40}Ar/^{39}Ar$	*2 σ*	$^{36}Ar/^{40}Ar$	*2σ*	*r.i.*	*Ca/K*	*% ^{40}Ar atm*	*f ^{39}Ar*	*$^{40}Ar^*/^{39}ArK$*	*Age*	*2σ*
2.10	1134.99	36.77	3.47	0.14	0.021	0.06	90.47	0.13	108.186	447.91	± 176.46
2.30	456.60	54.68	1.46	0.15	0.531	0.01	94.45	0.44	25.347	115.32	± 372.45
2.50	191.64	2.47	0.59	0.01	0.037	0.00	90.75	0.57	17.723	81.40	± 34.78
2.70	76.41	0.47	0.25	0.01	0.039	0.00	98.63	2.78	1.051	4.93	± 14.28
2.90	31.89	4.06	0.08	0.01	0.594	0.00	74.13	7.64	8.249	38.34	± 29.89
3.10	5.94	0.23	0.01	0.00	0.437	0.00	31.56	47.23	4.068	19.01	± 2.17
3.30	5.95	0.04	0.01	0.00	0.052	0.00	34.22	14.64	3.912	18.28	± 0.54
3.40	5.29	0.03	0.00	0.00	0.015	0.00	22.41	26.56	4.105	19.18	± 0.40

J = 0.00259800 ± 0.00001299 Volume 39ArK = 0.146 x E-13 cm3 NPT

Integrated Date = 18.87 ± 0.32 Ma

Plateau age = 18.33 ± 0.56 Ma (2s, including J-error of 1%) MSWD = 1.11, probability=0.33 Includes 69.5% of the 39A steps 5 through 8

Inverse isochron (correlation age) results, plateau steps: Model 1 Solution (±95%-conf.) on 6 points

Age = 19.09 ± 0.87 Ma Initial 40Ar/36Ar =284 ± 24 MSWD = 2.4 Probability = 0.049

Analysis by Janet Gabites
Pacific Centre for Isotopic and Geochemical Research,
Dept Earth and Ocean Sciences,
The University of British Columbia,
Vancouver, BC., Canada

Appendix A6. $^{40}Ar/^{39}Ar$ Alunite, Sample SG16303 (Repeat)

SG16303 Alunite

Laser	*Isotope Ratios*										
Power(%)	*$^{40}Ar/^{39}Ar$*	*2 σ*	*$^{36}Ar/^{40}Ar$*	*2σ*	*r.i.*	*Ca/K*	*% ^{40}Ar atm*	*f ^{39}Ar*	*$^{40}Ar^*/^{39}ArK$*	*Age*	*2σ*
2.20	4414.06	667.12	14.82	2.27	0.002	-0.03	99.21	0.15	34.939	-172.08	± 1066.72
2.50	5126.20	260.62	18.05	0.99	0.005	-0.16	104.04	0.70	206.978	-1395.30	± 2221.22
2.80	137.10	1.18	0.49	0.01	0.019	0.00	105.14	37.73	7.043	-33.39	± 27.49
2.90	22.56	0.84	0.06	0.01	0.012	0.00	82.10	39.10	4.037	18.87	± 15.83
3.10	20.83	0.27	0.06	0.00	0.119	-0.01	84.30	7.52	3.269	15.29	± 6.48
3.40	16.91	0.15	0.04	0.00	0.060	0.00	76.68	9.45	3.944	18.43	± 5.61
3.80	10.97	0.13	0.02	0.00	0.055	0.00	62.43	5.65	4.122	19.26	± 6.21

J = 0.00259800 ± 0.00001299 Volume 39ArK = 0.022 x E-13 cm3 NPT

Integrated Date = 17.05 ± 3.39 Ma

Plateau age = 17.8 ± 3.4 Ma (2s, including J-error of 1%) MSWD = 0.30, probability=0.83 Includes 61.7% of the 39A steps 4 through 7

Inverse isochron (correlation age) results, plateau steps: Model 1 Solution (±95%-conf.) on 6 points

Age = 20.4 ± 3.5 Ma Initial 40Ar/36Ar =278.0 ± 8.1 MSWD = 0.66 Probability = 0.62

Analysis by Janet Gabites
Pacific Centre for Isotopic and Geochemical Research,
Dept Earth and Ocean Sciences,
The University of British Columbia,
Vancouver, BC., Canada

Appendix A6. $^{40}Ar/^{39}Ar$ Alunite, Sample SG16303 (Lab Control)

SG16303 Alunite

Laser *Isotope Ratios*

Heating Step	$^{40}Ar/^{39}Ar$	±1 σ	$^{37}Ar/^{39}Ar$	±1 σ	$^{36}Ar/^{39}Ar$	±1 σ	$^{40}Ar^*/^{39}Ar_K$	±1 σ	^{40}Ar (mol)	$^{40}Ar^*$ (%)	$^{39}Ar_k$ (%)	Age (Ma)	± 2σ	K/Ca
	162.81	0.3883	0.0000	0.0067	0.5558	0.0048	0.0000	0.0000	1.411E-14	0.0000	5.9132	0.00	0.0000	
	49.31	0.1034	0.0077	0.0036	0.1535	0.0014	3.9383	0.3961	6.422E-15	7.9871	8.8838	14.82	2.9698	56.0465
	56.39	0.1162	0.0000	0.0030	0.1804	0.0016	3.0729	0.4492	1.127E-14	5.4490	13.6315	11.58	3.3740	78.2581
	16.57	0.0340	0.0038	0.0013	0.0390	0.0004	5.0582	0.1074	5.647E-15	30.5209	23.2416	19.02	0.8031	112.8730
	8.84	0.0180	0.0046	0.0023	0.0114	0.0002	5.4780	0.0585	2.378E-15	61.9994	18.3587	20.59	0.4374	94.3754
	7.54	0.0202	0.0110	0.0058	0.0063	0.0006	5.6892	0.1667	5.683E-16	75.4114	5.1382	21.38	1.2452	39.0195
	8.07	0.0232	0.0017	0.0092	0.0089	0.0008	5.4478	0.2373	4.794E-16	67.5376	4.0537	20.47	1.7737	252.5092
	8.54	0.0606	0.0050	0.0020	0.0088	0.0002	5.9397	0.0815	1.802E-15	69.5743	14.3973	22.31	0.6082	85.4463
	7.86	0.0751	0.0138	0.0381	0.0073	0.0033	5.7085	0.9771	1.248E-16	72.6242	1.0828	21.45	7.2987	31.1172
	8.54	0.0596	0.0000	0.0070	0.0087	0.0007	5.9582	0.2037	6.631E-16	69.7992	5.2992	22.38	1.5210	35.1614

J = 0.0020950 ± 0.0000125

Total Fusion Age: 17.66 ± 0.59 Ma

Plateau Age (although strictly speaking it is not a plateau due to the low cumulative 39Ar): 22.03 ± 0.57 Ma

Analysis by Richard Spiking
Isotope Geochemistry, Geochronology and Thermochronology Unit
Université de Genève,
Genève, Switzerland.

Appendix A7. Whole-Rock Geochemistry

APPENDIX A7: Whole-Rock Geochemistry

Sample		16263	200213-P4	200213-P10	16294	13351	13355	050113-P7
Unit		Pzgd	KTgb	TEpa	TEdi	OMlc2	OMlc2	OMlc2
SiO2	wt%	68.6	52.4	69.4	61	65.1	63.1	63.9
Al2O3	wt%	14.83	17.02	14.63	16.9	16.04	16.67	15.86
Fe2O3	wt%	3.02	8.15	1.33	3.26	2.89	3.89	3.04
CaO	wt%	1.07	8.03	3.03	5.07	4.4	4.86	4.15
MgO	wt%	1.25	4.2	0.23	0.77	1.09	1.5	0.97
Na2O	wt%	1.65	2.74	4.41	3.23	4.42	4.36	4.06
K2O	wt%	4.99	2.78	1.46	2.1	2.37	2.21	2.68
MnO	wt%	0.29	0.14	0.01	0.4	0.06	0.05	0.09
TiO2	wt%	0.42	0.94	0.29	0.49	0.47	0.63	0.45
P2O5	wt%	0.11	0.5	0.09	0.17	0.16	0.2	0.17
Cr2O3	wt%	<0.001	0.005	0.005	0.013	<0.001	<0.001	<0.001
Ba	wt%	0.06	0.06	0.11	0.05	0.07	0.07	0.08
LOI	wt%	3.3	2.51	4.44	5.83	2.51	2.45	3.97
Cu	wt%	<0.01	<0.01	<0.01	<0.01	<0.01	<0.01	<0.01
Ni	wt%	<0.01	<0.01	<0.01	0.01	<0.01	<0.01	<0.01
Pb	wt%	<0.01	<0.01	<0.01	<0.01	<0.01	<0.01	<0.01
SO3	wt%	0.546	0.629	0.475	0.472	0.271	0.099	0.55
Sr	wt%	0.005	0.066	0.055	0.075	0.079	0.073	0.066
V2O5	wt%	0.007	0.04	0.005	0.01	0.01	0.014	0.009
Zn	wt%	0.012	0.009	0.005	0.023	0.006	0.007	0.016
Zr	wt%	0.023	0.007	0.013	0.012	0.013	0.012	0.011
SUM_4X03	wt%	100.18	100.26	100.01	99.95	99.96	100.22	100.12
TOT/C	wt%	0.33	0.4	0.54	0.37	0.23	0.2	0.58
TOT/S	wt%	0.62	<0.02	0.08	0.15	0.09	<0.02	0.08
Ba	ppm	561	696	1104	543	675	628	833
Be	ppm	1	<1	1	<1	5	2	<1
Co	ppm	3.6	21	1.8	4.9	5.5	9.4	5
Cs	ppm	15.2	13	1.5	46.4	4	2.6	9
Ga	ppm	18	18.3	20.1	20.2	20.4	21.3	20.2
Hf	ppm	6.5	2.2	4.1	3.7	3.4	3.7	3.7
Nb	ppm	12.5	5.2	2.9	7	7.2	7.8	8.5
Rb	ppm	176	63	48.5	80.5	63.4	59.5	71.7
Sn	ppm	3	<1	<1	<1	<1	<1	1
Sr	ppm	42.5	613.9	437.1	641.7	699.3	713.1	701
Ta	ppm	0.7	0.3	0.2	0.5	0.5	0.5	0.6
Th	ppm	14.4	2.7	9.4	2.7	3.7	3.7	3.7
U	ppm	1.9	0.8	1.9	1	1.4	1.3	1.4
V	ppm	37	208	32	56	67	95	60
W	ppm	1	<0.5	3.6	<0.5	<0.5	<0.5	<0.5
Zr	ppm	239.3	92.5	131.7	136.5	127.6	135.6	137.4

Sample		16263	200213-P4	200213-P10	16294	13351	13355	050113-P7
Unit		Pzgd	KTgb	TEpa	TEdi	OMlc2	OMlc2	OMlc2
Y	ppm	27.4	16.6	3.1	6.9	6.2	7.3	7.3
La	ppm	43.5	14.2	28.2	16.9	18.9	19.5	18
Ce	ppm	89.5	29	50.5	35.5	39.9	41.6	37.5
Pr	ppm	9.61	3.51	5.07	4.02	4.26	4.58	4.17
Nd	ppm	37.9	16.3	18.8	14.8	16.9	17.9	16.9
Sm	ppm	6.38	3.3	2.66	2.76	2.76	3.2	2.81
Eu	ppm	1.32	1.13	0.61	0.82	0.74	0.88	0.76
Gd	ppm	5.78	3.54	1.48	1.95	1.94	2.22	2.06
Tb	ppm	0.87	0.52	0.15	0.25	0.24	0.28	0.29
Dy	ppm	4.94	2.84	0.8	1.27	1.09	1.52	1.5
Ho	ppm	0.91	0.63	0.12	0.23	0.18	0.22	0.3
Er	ppm	2.96	1.93	0.19	0.61	0.54	0.63	0.71
Tm	ppm	0.46	0.28	0.03	0.09	0.07	0.1	0.11
Yb	ppm	3.02	1.74	0.21	0.6	0.5	0.63	0.64
Lu	ppm	0.41	0.26	0.03	0.1	0.07	0.09	0.09
Mo	ppm	0.7	0.6	0.6	0.2	0.1	<0.1	<0.1
Cu	ppm	2	65.9	29.2	3.1	6.2	12.1	1
Pb	ppm	18.1	2.1	18.2	4.7	0.9	0.6	7.8
Zn	ppm	104	55	46	146	54	65	142
Ni	ppm	3.4	8	2.2	2.3	3.9	8.9	3.2
As	ppm	55.2	2.7	8.4	46.6	3.3	4.7	2.6
Cd	ppm	0.1	0.1	<0.1	<0.1	<0.1	<0.1	<0.1
Sb	ppm	0.4	<0.1	<0.1	<0.1	<0.1	<0.1	<0.1
Bi	ppm	<0.1	<0.1	0.3	<0.1	<0.1	<0.1	<0.1
Ag	ppm	0.1	<0.1	<0.1	<0.1	<0.1	<0.1	0.3
Au	ppb	6.2	2.3	1.1	5	1.7	<0.5	3.9
Hg	ppm	0.03	<0.01	0.07	0.01	<0.01	<0.01	0.12
Tl	ppm	0.2	0.1	<0.1	<0.1	<0.1	<0.1	<0.1
Se	ppm	<0.5	1.4	<0.5	<0.5	<0.5	<0.5	<0.5

Sample		050113-P11	190213-P1	190213-P6	13366	16305	050213-P5	190213-P16
Unit		OMlc2	OMlc2	OMlc2	OMlc3	OMlc3	OMlc4	OMlc4
SiO2	wt%	68.1	68.4	67.7	64.7	56.4	64.1	56.3
Al2O3	wt%	15.54	16.66	15.72	16.81	14.56	17.01	21.68
Fe2O3	wt%	2.13	1.88	2.05	3.21	3.38	3.15	1.85
CaO	wt%	2.71	3.12	2.42	4.14	0.08	3.82	0.55
MgO	wt%	0.71	0.44	0.66	1.42	0.04	0.55	0.09
Na2O	wt%	2.84	4.21	2.78	4.7	1.52	4.78	0.68
K2O	wt%	4.6	2.91	3.95	2.27	1.82	1.76	2.52
MnO	wt%	0.02	0.01	0.02	0.06	<0.01	0.14	0.02
TiO2	wt%	0.38	0.46	0.41	0.51	0.47	0.48	0.48
P2O5	wt%	0.16	0.19	0.17	0.18	0.12	0.15	0.24
Cr2O3	wt%	<0.001	0.002	<0.001	0.002	0.002	0.002	<0.001
Ba	wt%	0.13	0.08	0.06	0.07	<0.01	0.06	0.06
LOI	wt%	2.69	1.81	4.27	1.79	20.71	3.51	15.05
Cu	wt%	<0.01	<0.01	<0.01	<0.01	<0.01	<0.01	<0.01
Ni	wt%	<0.01	<0.01	<0.01	<0.01	<0.01	<0.01	<0.01
Pb	wt%	<0.01	<0.01	<0.01	<0.01	<0.01	<0.01	<0.01
SO3	wt%	0.074	0.022	0.035	0.013	0.557	0.065	0.266
Sr	wt%	0.06	0.075	0.04	0.075	0.043	0.083	0.139
V2O5	wt%	0.008	0.009	0.009	0.013	0.01	0.01	0.012
Zn	wt%	0.044	0.033	0.009	0.007	0.019	0.055	0.013
Zr	wt%	0.011	0.016	0.011	0.012	0.012	0.013	0.012
SUM_4X03	wt%	100.19	100.32	100.3	100	99.74	99.79	99.96
TOT/C	wt%	0.02	<0.02	0.02	<0.02	<0.02	0.06	<0.02
TOT/S	wt%	0.05	0.08	0.44	<0.02	8.26	0.13	2.19
Ba	ppm	1263	706	530	709	58	630	634
Be	ppm	4	5	<1	<1	<1	<1	4
Co	ppm	2.8	2.6	2.6	5.9	7.8	7	1
Cs	ppm	100.6	13.2	25.2	2.5	2.8	8.1	51.8
Ga	ppm	19	20.9	19.5	19.9	23.5	22.9	17.8
Hf	ppm	3.4	3.8	2.9	3.8	4.3	3.3	3.1
Nb	ppm	7.7	8.6	8.5	7.2	7.2	6.3	5.7
Rb	ppm	137.1	96.1	140.9	57	18.3	37.7	62.7
Sn	ppm	<1	1	<1	1	<1	1	<1
Sr	ppm	558.2	661.7	363.7	767.9	342.6	829.4	1303.3
Ta	ppm	0.6	0.7	0.7	0.4	0.5	0.3	0.4
Th	ppm	3.4	4.4	3.7	3.6	2.8	3.7	2.7
U	ppm	1.2	1.4	1.3	1.3	1.7	1.1	1.4
V	ppm	43	50	47	68	52	61	72
W	ppm	<0.5	0.7	0.6	<0.5	1.5	<0.5	<0.5
Zr	ppm	125.4	128.5	122.2	138.9	142.6	143.5	114.4

Sample		050113-P11	190213-P1	190213-P6	13366	16305	050213-P5	190213-P16
Unit		OMlc2	OMlc2	OMlc2	OMlc3	OMlc3	OMlc4	OMlc4
Y	ppm	7.2	7.7	6.1	7.5	5.2	5.4	2.7
La	ppm	15.5	19.4	17.4	21.2	17.9	19	24.9
Ce	ppm	32.9	39	35.7	43.1	38.4	37.7	55.2
Pr	ppm	3.73	4.44	4.04	4.85	4.27	4.26	6.2
Nd	ppm	13.9	16.1	14.8	18.5	16.9	16	25.1
Sm	ppm	2.55	2.89	2.79	2.99	2.65	2.75	3.5
Eu	ppm	0.8	0.69	0.71	0.79	0.74	0.8	0.78
Gd	ppm	2.11	1.91	1.73	2.11	1.71	1.85	2.09
Tb	ppm	0.27	0.25	0.25	0.27	0.19	0.23	0.21
Dy	ppm	1.19	1.38	1.1	1.4	1.05	1.07	0.79
Ho	ppm	0.24	0.22	0.21	0.25	0.14	0.19	0.12
Er	ppm	0.64	0.57	0.59	0.68	0.55	0.58	0.35
Tm	ppm	0.09	0.1	0.09	0.08	0.08	0.07	0.04
Yb	ppm	0.56	0.59	0.44	0.66	0.48	0.53	0.25
Lu	ppm	0.08	0.08	0.08	0.08	0.08	0.08	0.06
Mo	ppm	<0.1	<0.1	0.1	<0.1	0.2	<0.1	<0.1
Cu	ppm	1.2	1.8	1.7	7.7	5.4	4.9	7.9
Pb	ppm	4	2.7	3.1	0.4	3.5	0.7	1.4
Zn	ppm	214	209	45	23	195	380	31
Ni	ppm	1.3	1.4	1.2	1.6	5.2	2.1	0.3
As	ppm	1.5	21.1	30.3	<0.5	55.4	3.2	228.6
Cd	ppm	<0.1	<0.1	<0.1	<0.1	1.2	1.9	<0.1
Sb	ppm	0.4	2.5	1.2	<0.1	0.6	0.3	<0.1
Bi	ppm	<0.1	<0.1	<0.1	<0.1	1.9	<0.1	<0.1
Ag	ppm	<0.1	<0.1	<0.1	<0.1	<0.1	<0.1	<0.1
Au	ppb	<0.5	<0.5	6.3	<0.5	8.3	1.1	17.7
Hg	ppm	0.06	<0.01	0.07	<0.01	0.06	<0.01	0.13
Tl	ppm	0.1	<0.1	<0.1	<0.1	<0.1	<0.1	0.1
Se	ppm	1	<0.5	0.7	<0.5	1.3	<0.5	1.1

Sample		210213-P5	040213-P8	13356	13358	13359	13363	13364
Unit		Mcd2	Mcd3	Mcd4	Mcd4	Mcd4	Mcd4	Mcd4
SiO2	wt%	65.5	62.5	65.7	63.6	67.9	65.9	64.3
Al2O3	wt%	18.19	19.27	16.61	17.14	16.35	15.99	16.8
Fe2O3	wt%	3.52	3.35	3.75	3.92	2.74	2.6	3.29
CaO	wt%	4.72	2.96	3.35	4.35	3.37	4.06	3.15
MgO	wt%	0.84	0.45	0.66	1.73	0.62	1.09	0.62
Na2O	wt%	4.99	3.63	4.07	4.26	4.67	4.31	3.85
K2O	wt%	1.97	1.81	3.45	3.09	2.75	2.84	4.06
MnO	wt%	0.07	0.03	0.05	0.05	0.06	0.06	0.03
TiO2	wt%	0.52	0.47	0.53	0.63	0.44	0.44	0.56
P2O5	wt%	0.21	0.04	0.18	0.21	0.16	0.15	0.2
Cr2O3	wt%	<0.001	<0.001	0.002	<0.001	<0.001	0.016	<0.001
Ba	wt%	0.07	0.06	0.08	0.07	0.09	0.08	0.07
LOI	wt%	0.39	5.15	2.61	0.9	1.01	3.46	2.7
Cu	wt%	<0.01	<0.01	<0.01	<0.01	<0.01	<0.01	<0.01
Ni	wt%	<0.01	<0.01	<0.01	<0.01	<0.01	0.01	<0.01
Pb	wt%	<0.01	<0.01	<0.01	<0.01	<0.01	<0.01	<0.01
SO3	wt%	0.004	<0.002	0.084	0.022	0.033	0.034	0.063
Sr	wt%	0.081	0.067	0.059	0.075	0.066	0.068	0.055
V2O5	wt%	0.007	0.007	0.01	0.014	0.011	0.01	0.013
Zn	wt%	0.007	0.006	0.021	0.021	0.008	0.007	0.113
Zr	wt%	0.014	0.013	0.013	0.013	0.011	0.012	0.012
SUM_4X03	wt%	101.17	99.8	101.28	100.11	100.31	101.16	99.97
TOT/C	wt%	<0.02	<0.02	0.02	<0.02	<0.02	<0.02	0.02
TOT/S	wt%	<0.02	0.03	0.08	<0.02	0.03	0.34	0.02
Ba	ppm	702	615	765	699	807	757	733
Be	ppm	3	<1	<1	1	2	2	4
Co	ppm	5.4	3.6	6.5	8.4	4.1	4.6	5.2
Cs	ppm	1.2	9	38.9	3	4	3.5	9.6
Ga	ppm	21.8	20.1	21.4	21.2	21.4	19.9	21.3
Hf	ppm	3.7	3.5	3.6	4.3	3.4	3.2	4.1
Nb	ppm	7.2	7.4	6	6.4	4.7	5.9	6.1
Rb	ppm	48	44.4	133	93.5	72	75.8	134.9
Sn	ppm	<1	<1	1	<1	1	<1	1
Sr	ppm	813.8	684.7	567.6	654.5	646.5	643.3	528.7
Ta	ppm	0.4	0.6	0.4	0.4	0.4	0.3	0.4
Th	ppm	3	3	3.5	2.9	3.1	3.2	3.2
U	ppm	0.8	0.9	0.9	0.7	1	1.2	0.9
V	ppm	43	42	61	93	57	60	83
W	ppm	<0.5	<0.5	<0.5	<0.5	<0.5	0.5	<0.5
Zr	ppm	157.5	124.8	135.7	139.6	125.5	118.1	145.2

Sample		210213-P5	040213-P8	13356	13358	13359	13363	13364
Unit		Mcd2	Mcd3	Mcd4	Mcd4	Mcd4	Mcd4	Mcd4
Y	ppm	8.6	3.2	5.2	8.2	4.6	5.5	12.2
La	ppm	22.3	11.5	20.1	20.2	18.4	17.7	21.4
Ce	ppm	44.2	20.3	42.3	41.8	38.7	35.9	45.3
Pr	ppm	4.99	1.98	4.56	4.77	4.33	3.93	5.32
Nd	ppm	20.1	8.2	18.2	19.8	16.2	15.5	23.1
Sm	ppm	3.29	1.08	2.87	3.53	2.9	2.49	4.51
Eu	ppm	0.83	0.58	0.77	0.96	0.76	0.72	1.43
Gd	ppm	2.4	0.9	1.99	2.68	1.82	1.8	4.54
Tb	ppm	0.3	0.12	0.24	0.33	0.2	0.22	0.59
Dy	ppm	1.5	0.61	1.09	1.77	1.04	0.95	2.52
Ho	ppm	0.27	0.12	0.19	0.28	0.17	0.16	0.41
Er	ppm	0.75	0.35	0.43	0.64	0.38	0.52	1.04
Tm	ppm	0.12	0.06	0.06	0.1	0.06	0.08	0.13
Yb	ppm	0.75	0.45	0.45	0.65	0.36	0.47	0.83
Lu	ppm	0.11	0.05	0.06	0.09	0.06	0.08	0.13
Mo	ppm	<0.1	<0.1	0.5	0.3	<0.1	<0.1	0.3
Cu	ppm	4.5	3.8	11.6	33.8	6.4	31	56.7
Pb	ppm	0.6	0.5	22.3	2.9	3	0.4	5.9
Zn	ppm	25	28	76	185	49	28	1107
Ni	ppm	0.8	1.5	1.6	2.5	1.1	1.4	2.6
As	ppm	0.5	4.4	96.9	3.1	6.1	1.9	17.1
Cd	ppm	<0.1	<0.1	<0.1	0.3	<0.1	<0.1	4
Sb	ppm	0.1	<0.1	1.9	0.2	0.3	<0.1	0.3
Bi	ppm	<0.1	<0.1	<0.1	<0.1	<0.1	<0.1	<0.1
Ag	ppm	<0.1	<0.1	<0.1	<0.1	<0.1	<0.1	<0.1
Au	ppb	<0.5	1.3	1.8	<0.5	3.7	<0.5	1.6
Hg	ppm	0.01	<0.01	0.04	<0.01	0.02	0.1	0.04
Tl	ppm	<0.1	<0.1	<0.1	<0.1	<0.1	<0.1	<0.1
Se	ppm	<0.5	<0.5	0.7	<0.5	<0.5	<0.5	0.5

Sample		13365
Unit		Mcd4
SiO2	wt%	66.3
Al2O3	wt%	16.12
Fe2O3	wt%	2.75
CaO	wt%	3.55
MgO	wt%	1.13
Na2O	wt%	4.52
K2O	wt%	2.7
MnO	wt%	0.05
TiO2	wt%	0.45
P2O5	wt%	0.15
Cr2O3	wt%	0.003
Ba	wt%	0.08
LOI	wt%	1.88
Cu	wt%	<0.01
Ni	wt%	<0.01
Pb	wt%	0.01
SO3	wt%	0.009
Sr	wt%	0.072
V2O5	wt%	0.012
Zn	wt%	0.008
Zr	wt%	0.01
SUM_4X03	wt%	99.88
TOT/C	wt%	<0.02
TOT/S	wt%	<0.02
Ba	ppm	744
Be	ppm	<1
Co	ppm	5.5
Cs	ppm	3.6
Ga	ppm	21.2
Hf	ppm	3.5
Nb	ppm	5.7
Rb	ppm	74.9
Sn	ppm	<1
Sr	ppm	650.1
Ta	ppm	0.4
Th	ppm	3.3
U	ppm	1.2
V	ppm	63
W	ppm	<0.5
Zr	ppm	126.3

Sample		13365
Unit		Mcd4
Y	ppm	5.8
La	ppm	18
Ce	ppm	36.1
Pr	ppm	4.1
Nd	ppm	15.7
Sm	ppm	2.56
Eu	ppm	0.74
Gd	ppm	1.82
Tb	ppm	0.24
Dy	ppm	1.26
Ho	ppm	0.19
Er	ppm	0.62
Tm	ppm	0.08
Yb	ppm	0.52
Lu	ppm	0.07
Mo	ppm	<0.1
Cu	ppm	5.8
Pb	ppm	0.4
Zn	ppm	32
Ni	ppm	1.3
As	ppm	1.1
Cd	ppm	0.1
Sb	ppm	<0.1
Bi	ppm	<0.1
Ag	ppm	<0.1
Au	ppb	5.8
Hg	ppm	<0.01
Tl	ppm	<0.1
Se	ppm	0.6

Appendix A8. QA/QC of whole-rock geochemistry: Precision

APPENDIX A8: QA/QC of whole-Rock geochemical analysis: Precision

Group	Element	Unit	Method	Sample SG13356 Orig	Dup	%RSD	Quality	Sample SG190213P1 Orig	Dup	%RSD	Quality	Sample SG210213P5 Orig	Dup	%RSD	Quality	Sample SG190213P16 Orig	Dup	%RSD	Quality
Major Oxides	SiO_2	wt%	XRF	65.7	64.8	1.0	Exc	68.4	68.1	0.3	Exc	65.5	64.8	0.8	Exc				
	Al_2O_3	wt%	XRF	16.61	16.33	1.2	Exc	16.66	16.63	0.1	Exc	18.19	18	0.7	Exc				
	TiO_2	wt%	XRF	0.53	0.52	1.3	Exc	0.46	0.45	1.6	Exc	0.52	0.51	1.4	Exc				
	Fe_2O_3	wt%	XRF	3.75	3.74	0.2	Exc	1.88	1.91	1.1	Exc	3.52	3.48	0.8	Exc				
	CaO	wt%	XRF	3.35	3.16	4.1	VG	3.12	3.14	0.5	Exc	4.72	4.67	0.8	Exc				
	MgO	wt%	XRF	0.66	0.7	4.2	VG	0.44	0.45	1.6	Exc	0.84	0.84	0.0	Exc				
	Na_2O	wt%	XRF	4.07	3.98	1.6	Exc	4.21	4.23	0.3	Exc	4.99	4.92	1.0	Exc				
	K_2O	wt%	XRF	3.45	3.45	0.0	Exc	2.91	2.9	0.2	Exc	1.97	1.92	1.8	Exc				
	MnO	wt%	XRF	0.05	0.05	0.0	Exc	0.01	0.01	0.0	Exc	0.07	0.07	0.0	Exc				
	P_2O_5	wt%	XRF	0.18	0.19	3.8	VG	0.19	0.18	3.8	VG	0.21	0.21	0.0	Exc				
	Cr_2O_3	wt%	XRF	0.002	0.002	0.0	Exc	0.002	<0.001	nv	-	<0.001	<0.001	nv	-				
	Ba	wt%	XRF	0.08	0.08	0.0	Exc	0.08	0.08	0.0	Exc	0.07	0.08	9.4	G				
	SO_3	wt%	XRF	0.084	0.096	9.4	G	0.022	0.022	0.0	Exc	0.004	0.004	0.0	Exc				
	V_2O_5	wt%	XRF	0.01	0.011	6.7	VG	0.009	0.01	7.4	VG	0.007	0.009	17.7	NP				
	LOI	wt%	XRF	2.61	2.68	1.9	Exc	1.81	1.84	1.2	Exc	0.39	0.4	1.8	Exc				
REE	La	ppm	4B	20.1	19.5	2.1	Exc	19.4	19.7	1.1	Exc	22.3							
	Ce	ppm	4B	42.3	40.1	3.8	VG	39	41	3.5	VG	44.2							
	Pr	ppm	4B	4.56	4.51	0.8	Exc	4.44	4.68	3.7	VG	4.99							
	Nd	ppm	4B	18.2	17.2	4.0	VG	16.1	17	3.8	VG	20.1							
	Sm	ppm	4B	2.87	2.9	0.7	Exc	2.89	2.96	1.7	Exc	3.29							
	Eu	ppm	4B	0.77	0.71	5.7	VG	0.69	0.77	7.7	G	0.83							
	Gd	ppm	4B	1.99	2.01	0.7	Exc	1.91	2.03	4.3	VG	2.4							
	Tb	ppm	4B	0.24	0.23	3.0	Exc	0.25	0.26	2.8	Exc	0.3							
	Dy	ppm	4B	1.09	1.13	2.5	Exc	1.38	1.31	3.7	VG	1.5							
	Ho	ppm	4B	0.19	0.17	7.9	G	0.22	0.23	3.1	VG	0.27							
	Er	ppm	4B	0.43	0.59	22.2	NP	0.57	0.59	2.4	Exc	0.75							
	Tm	ppm	4B	0.06	0.07	10.9	NP	0.1	0.09	7.4	G	0.12							
	Yb	ppm	4B	0.45	0.48	4.6	VG	0.59	0.52	8.9	G	0.75							
	Lu	ppm	4B	0.06	0.07	10.9	NP	0.08	0.07	9.4	G	0.11							

% RSD = percent relative standard deviation

RSD < 3% Excellent (Exc)

3 < RSD < 7% Very Good (VG)

7 < RSD < 10% Good (G)

RSD > 10% Not Precise (NP)

NV Not Valid (NV)

Orig = Original

Dup = Duplicate

* Field duplicate for sample SG13356 and pulp duplicates for samples SG190213P1, SG210213P5, and SG190213P16

Group	Element	Unit	Method	Sample SG13356 Orig	Dup	%RSD	Quality	Sample SG190213P1 Orig	Dup	%RSD	Quality	Sample SG210213P5 Orig	Dup	%RSD	Quality	Sample SG190213P16 Orig	Dup	%RSD	Quality
Transition Metals	V	ppm	4B	61	54	8.6	G	50	50	0.0	Exc	43							
	Co	ppm	4B	6.5	6.6	1.1	Exc	2.6	2.4	5.7	VG	5.4							
	Ni	wt%	XRF	<0.01	<0.01	nv	-	<0.01	<0.01	nv	-	<0.01	<0.01	nv	-				
	Ni	ppm	1DX	1.6	1.5	4.6	VG	1.4	1.6	9.4	G	0.8				0.3	0.2	28.3	NP
	Cu	wt%	XRF	<0.01	<0.01	nv	-	<0.01	<0.01	nv	-	<0.01	<0.01	nv	-	<0.01			
	Cu	ppm	1DX	11.6	15.2	19.0	NP	1.8	2	7.4	G	4.5				7.9	8.7	6.8	VG
	Zn	wt%	XRF	0.021	0.023	6.4	VG	0.033	0.033	0.0	Exc	0.007	0.007	0.0	Exc	0.013			
	Zn	ppm	1DX	76	81	4.5	VG	209	203	2.1	Exc	25				31	31	0.0	Exc
	Y	ppm	4B	5.2	5.6	5.2	VG	7.7	7.3	3.8	VG	8.6				2.7			
	Zr	wt%	XRF	0.013	0.012	5.7	VG	0.016	0.013	14.6	NP	0.014	0.016	9.4	G	0.012			
	Zr	ppm	4B	135.7	134.7	0.5	Exc	128.5	130.4	1.0	Exc	157.5				114.4			
	Nb	ppm	4B	6	5.1	11.5	NP	8.6	8.7	0.8	Exc	7.2				5.7			
	Mo	ppm	1DX	0.5	0.5	0.0	Exc	<0.1	0.1	70.7	NV	<0.1				<0.1	<0.1	nv	-
	Ag	ppm	1DX	<0.1	<0.1	nv	-	<0.1	<0.1	nv	-	<0.1				<0.1	<0.1	nv	-
	Cd	ppm	1DX	<0.1	<0.1	nv	-	<0.1	<0.1	nv	-	<0.1				<0.1	<0.1	nv	-
	Hf	ppm	4B	3.6	3.5	2.0	Exc	3.8	3.6	3.8	VG	3.7				3.1			
	Ta	ppm	4B	0.4	0.2	47.1	NP	0.7	0.6	10.9	NP	0.4				0.4			
	W	ppm	4B	<0.5	<0.5	nv	-	0.7	<0.5	70.7	NV	<0.5				<0.5			
	Au	ppm	1DX	1.8	2.9	33.1	NP	<0.5	2.3	70.7	NV	<0.5				17.7	11.1	32.4	NP
	Hg	ppm	1DX	0.04	0.05	15.7	NP	<0.01	0.03	70.7	NV	0.01				0.13	0.15	10.1	NP
Basic Metals	Ga	ppm	4B	21.4	20	4.8	VG	20.9	20.9	0.0	Exc	21.8				17.8			
	Sn	ppm	4B	1	<1	70.7	NV	1	<1	70.7	NV	<1				<1			
	Tl	ppm	1DX	<0.1	<0.1	nv	-	<0.1	<0.1	nv	-	<0.1				0.1	0.1	0.0	Exc
	Pb	wt%	XRF	<0.01	0.03	70.7	NV	<0.01	<0.01	nv	-	<0.01	<0.01	nv	-	<0.01			
	Pb	ppm	1DX	22.3	23.6	4.0	VG	2.7	2.8	2.6	Exc	0.6				1.4	1.3	5.2	VG
	Bi	ppm	1DX	<0.1	<0.1	nv	-	<0.1	<0.1	nv	-	<0.1				<0.1	<0.1	nv	-

% RSD = percent relative standard deviation

RSD < 3% Excellent (Exc)

3 < RSD < 7% Very Good (VG)

7 < RSD < 10% Good (G)

RSD > 10% Not Precise (NP)

NV Not Valid (NV)

Orig = Original

Dup = Duplicate

* Field duplicate for sample SG13356 and pulp duplicates for samples SG190213P1, SG210213P5, and SG190213P16

				Sample SG13356				Sample SG190213P1				Sample SG210213P5				Sample SG190213P16			
Group	Element	Unit	Method	Orig	Dup	%RSD	Quality	Orig	Dup	%RSD	Quality	Orig	Dup	%RSD	Quality	Orig	Dup	%RSD	Quality
Alkali Metals/Earths	Be	ppm	4B	<1	<1	nv	-	5	1	94.3	NP	3				4			
	Rb	ppm	4B	133	133.3	0.2	Exc	96.1	94.8	1.0	Exc	48				62.7			
	Sr	wt%	XRF	0.059	0.056	3.7	VG	0.075	0.068	6.9	VG	0.081	0.09	7.4	G	0.139			
	Sr	ppm	4B	567.6	558	1.2	Exc	661.7	636.2	2.8	Exc	813.8				1303.3			
	Cs	ppm	4B	38.9	39.2	0.5	Exc	13.2	13.1	0.5	Exc	1.2				51.8			
	Ba	ppm	4B	765	699	6.4	VG	706	707	0.1	Exc	702				634			
Semimetals	As	ppm	1DX	96.9	89	6.0	VG	21.1	19.8	4.5	VG	0.5				228.6	225.3	1.0	Exc
	Sb	ppm	1DX	1.9	1.9	0.0	Exc	2.5	3	12.9	NP	0.1				<0.1	<0.1	nv	-
Actinides	Th	ppm	4B	3.5	3.1	8.6	G	4.4	3.9	8.5	G	3				2.7			
	U	ppm	4B	0.9	0.9	0.0	Exc	1.4	1.4	0.0	Exc	0.8				1.4			
Nonmetals	Se	ppm	1DX	0.7	<0.5	70.7	NV	<0.5	<0.5	nv	-	<0.5				1.1	1.1	0.0	Exc

% RSD = percent relative standard deviation

RSD < 3% Excellent (Exc)

3 < RSD < 7% Very Good (VG)

7 < RSD < 10% Good (G)

RSD > 10% Not Precise (NP)

NV Not Valid (NV)

Orig = Original

Dup = Duplicate

* Field duplicate for sample SG13356 and pulp duplicates for samples SG190213P1, SG210213P5, and SG190213P16

Appendix A9. QA/QC of whole-rock geochemistry: Accuracy

APPENDIX A9: QA/QC of whole-Rock geochemical analysis: Accuracy

				Standard WP-1 (UBC)					Standard SY-4(D) (ACME)					Standard OREAS72B (ACME)				
Group	Element	Unit	Method	This study	Expected	± Tolerance	%RSD	Quality	This study	Mean	± Tolerance	%RSD	Quality	This study	Mean	± Tolerance	%RSD	Quality
Major Oxides	SiO_2	wt%	XRF	64.6	64.79	1.40	0.30	Exc	50.1	49.9	0.1	0.40	Exc	51.5	51.16	0.12	0.7	Exc
	Al_2O_3	wt%	XRF	16.43	16.52	0.42	0.52	Exc	20.56	20.69	0.08	0.63	Exc	8.94	8.97	0.06	0.4	Exc
	TiO_2	wt%	XRF	0.49	0.51	0.02	3.09	VG	0.3	0.287	0.003	4.33	VG	0.35	0.36	0.004	1.5	Exc
	Fe_2O_3	wt%	XRF	4.4	4.52	0.29	2.74	Exc	6.09	6.21	0.03	1.97	Exc	9.79	9.72	0.09	0.7	Exc
	CaO	wt%	XRF	4.89	4.98	0.14	1.83	Exc	7.89	8.05	0.04	2.03	Exc	3.94	3.96	0.02	0.5	Exc
	MgO	wt%	XRF	2.64	2.68	0.13	1.44	Exc	0.51	0.54	0.01	5.88	VG	16.12	15.93	0.09	1.2	Exc
	Na_2O	wt%	XRF	4.35	4.25	0.44	2.18	Exc	7.25	7.1	0.05	2.07	Exc	1.35	1.29	0.025	4.6	VG
	K_2O	wt%	XRF	1.6	1.62	0.09	1.16	Exc	1.66	1.66	0.02	0.00	Exc	1.32	1.31	0.02	0.5	Exc
	MnO	wt%	XRF	0.08	0.08	0.01	2.61	Exc	0.11	0.108	0.001	1.82	Exc	0.13	0.13	0.0006	0.3	Exc
	P_2O_5	wt%	XRF	0.17	0.16	0.02	3.02	VG	0.13	0.131	0.004	0.77	Exc	0.06	0.06	0.0005	1.9	Exc
	Cr_2O_3	wt%	XRF															
	Ba	wt%	XRF	0.06	0.08	0.00	33.4	NA										
	SO_3	wt%	XRF															
	V_2O_5	wt%	XRF															
	LOI	wt%	XRF	0.13	0.17	0.21	27.4	NA	4.56	4.56	0.07	0.00	Exc					

% RSD = percent relative standard deviation

RSD < 3%	Excellent (Exc)
3 < RSD < 7%	Very Good (VG)
7 < RSD < 10%	Good (G)
RSD > 10%	Not Accurate (NA)

				Standard WP-1 (UBC)					Standard SO-18 (ACME)					Standard SO-18 (ACME)				
Group	Element	Unit	Method	This study	Expected	± Tolerance	%RSD	Quality	This study	Mean	± Tolerance	%RSD	Quality	This study	Mean	± Tolerance	%RSD	Quality
REE	La	ppm	4B	12.7	13.23	1.25	4.13	VG	12.2	12.3	1.8	0.8	Exc	12.7	12.3	1.8	3.1	VG
	Ce	ppm	4B	28.5	28.18	2.73	1.14	Exc	26.1	27.1	2.7	3.8	VG	27.8	27.1	2.7	2.5	Exc
	Pr	ppm	4B	3.23	3.60	0.27	11.4	NA	3.16	3.45	0.35	9.2	G	3.13	3.45	0.35	10.2	NA
	Nd	ppm	4B	13.7	14.55	1.04	6.20	VG	13.3	14	1.4	5.3	VG	13.6	14	1.4	2.9	Exc
	Sm	ppm	4B	2.85	2.95	0.92	3.55	VG	2.8	3	0.4	7.1	G	2.53	3	0.4	18.6	NA
	Eu	ppm	4B	0.82	0.87	0.11	5.95	VG	0.78	0.89	0.09	14.1	NA	0.84	0.89	0.09	6.0	VG
	Gd	ppm	4B	2.66	2.82	0.42	6.02	VG	2.81	2.93	0.29	4.3	VG	2.9	2.93	0.29	1.0	Exc
	Tb	ppm	4B	0.38	0.43	0.04	12.4	NA	0.46	0.53	0.05	15.2	NA	0.46	0.53	0.05	15.2	NA
	Dy	ppm	4B	2.2	2.33	0.24	5.80	VG	2.73	3	0.3	9.9	G	2.71	3	0.3	10.7	NA
	Ho	ppm	4B	0.42	0.47	0.07	12.2	NA	0.61	0.62	0.06	1.6	Exc	0.61	0.62	0.06	1.6	Exc
	Er	ppm	4B	1.15	1.37	0.26	19.1	NA	1.8	1.84	0.18	2.2	Exc	1.69	1.84	0.18	8.9	G
	Tm	ppm	4B	0.21	0.19	0.42	11.3	NA	0.25	0.29	0.03	16.0	NA	0.28	0.29	0.03	3.6	VG
	Yb	ppm	4B	1.08	1.37	0.21	27.2	NA	1.65	1.79	0.18	8.5	G	1.62	1.79	0.18	10.5	NA
	Lu	ppm	4B	0.19	0.21	0.03	12.5	NA	0.26	0.27	0.03	3.8	VG	0.26	0.27	0.03	3.8	VG

% RSD = percent relative standard deviation

RSD < 3%	Excellent (Exc)
3 < RSD < 7%	Very Good (VG)
7 < RSD < 10%	Good (G)
RSD > 10%	Not Accurate (NA)

				Standard WP-1 (UBC)					Standard SO-18 (ACME)					Standard SO-18 (ACME)				
Group	Element	Unit	Method	This study	Expected	± Tolerance	%RSD	Quality	This study	Mean	± Tolerance	%RSD	Quality	This study	Mean	± Tolerance	%RSD	Quality
Transition Metals	V	ppm	4B	91	84.57	10.38	7.06	G	205	200	20	2.4	Exc	205	200	20	2.4	Exc
	Co	ppm	4B	11.9	12.23	1.33	2.73	Exc	24.7	26.2	2.6	6.1	VG	25.5	26.2	2.6	2.7	Exc
	Ni	ppm	1DX	7.1														
	Cu	ppm	1DX	11.2	16.14	8.83	44.1	NA										
	Zn	ppm	1DX	119.3	123.12	12.45	3.20	VG										
	Y	ppm	4B	11.5	13.51	1.43	17.5	NA	29.6	33	3.3	11.5	NA	29.5	33	3.3	11.9	NA
	Zr	ppm	4B	0.008					287.3	280	28	2.5	Exc	280.4	280	28	0.1	Exc
	Nb	ppm	4B	3.5	3.99	0.95	14.1	NA	19.8	20.9	2.1	5.6	VG	19.8	20.9	2.1	5.6	VG
	Mo	ppm	1DX	0.4	1.06	1.19	166	NA										
	Ag	ppm	1DX	<0.1	0.32	0.77	--											
	Cd	ppm	1DX	<0.1	BDL	--	--											
	Hf	ppm	4B	2.8	3.26	0.34	16.5	NA	10.5	9.8	1	6.7	VG	8.1	9.8	1	21.0	NA
	Ta	ppm	4B	0.2	0.23	0.05	16.7	NA	6.9	7.4	0.7	7.2	G	6.6	7.4	0.7	12.1	NA
	W	ppm	4B	<0.5	BDL	2.07	--		14.9	15.1	2.3	1.3	Exc	14.5	15.1	2.3	4.1	VG
	Au	ppm	1DX	<0.5	BDL	0.00	--											
	Hg	ppm	1DX	<0.01	BDL	0.01	--											

				Standard OREAS45EA (ACME)					Standard DS10 (ACME)				
Group	Element	Unit	Method	This study	Mean	± Tolerance	%RSD	Quality	This study	Mean	± Tolerance	%RSD	Quality
Transition Metals	Ni	ppm	1DX	382.3	381	76.2	0.3	Exc	72.2	74.6	11.19	3.3	VG
	Cu	ppm	1DX	670.7	709	141.8	5.7	VG	152.5	154.61	23.1915	1.4	Exc
	Zn	ppm	1DX	30	30.6	7.65	2.0	Exc	357	370	55.5	3.6	VG
	Mo	ppm	1DX	1.5	1.39	0.417	7.3	G	12.7	14.69	3.6725	15.7	NA
	Ag	ppm	1DX	0.2	0.26	0.104	30.0	NA	2.4	2.02	0.606	15.8	NA
	Cd	ppm	1DX	<0.1	0.02	0.076			2.8	2.49	0.6225	11.1	NA
	Au	ppm	1DX	39	53	31.8	35.9	NA	503.4				
	Hg	ppm	1DX	0.02	0.01	DL	50.0	NA	0.25	0.3	0.09	20.0	NA

% RSD = percent relative standard deviation

RSD < 3% Excellent (Exc)

3 < RSD < 7% Very Good (VG)

7 < RSD < 10% Good (G)

RSD > 10% Not Accurate (NA)

				Standard WP-1 (UBC)					Standard SO-18 (ACME)					Standard SO-18 (ACME)				
Group	Element	Unit	Method	This study	Expected	± Tolerance	%RSD	Quality	This study	Mean	± Tolerance	%RSD	Quality	This study	Mean	± Tolerance	%RSD	Quality
Basic Metals	Ga	ppm	4B	17.2	18.27	0.94	6.20	VG	16.7	17.6	1.8	5.4	VG	17	17.6	1.8	3.5	VG
	Sn	ppm	4B	<1	1.40	0.63	--		15	15	5	0.0	Exc	14	15	5	7.1	G
	Tl	ppm	1DX	<0.1	0.19	0.05	--											
	Pb	wt%	XRF															
	Pb	ppm	1DX	3.6	6.37	4.66	76.9	NA										
	Bi	ppm	1DX	<0.1		0.00	--											
Alkali Metals/Earths	Be	ppm	4B	<1		0.09	--		<1	1	2			<1	1	2		
	Rb	ppm	4B	21	23.42	3.34	11.5	NA	25.7	28.7	2.9	11.7	NA	26.2	28.7	2.9	9.5	G
	Sr	wt%	XRF															
	Sr	ppm	4B	745.4	721.54	103.10	3.20	VG	422.8	407.4	40.7	3.6	VG	406.5	407.4	40.7	0.2	Exc
	Cs	ppm	4B	0.4	0.44	0.07	9.06	G	6.8	7.1	0.8	4.4	VG	6.8	7.1	0.8	4.4	VG
	Ba	ppm	4B	600	624.50	54.61	4.08	VG	511	514	51.4	0.6	Exc	526	514	51.4	2.3	Exc

				Standard OREAS45EA (ACME)					Standard DS10 (ACME)				
Group	Element	Unit	Method	This study	Mean	± Tolerance	%RSD	Quality	This study	Mean	± Tolerance	%RSD	Quality
Basic Metals	Tl	ppm	1DX	<0.1	0.072	BDL			5.1	5.1	1.02	0.0	Exc
	Pb	ppm	1DX	13.4	14.3	4.29	6.7	VG	148.8	150.55	30.11	1.2	Exc
	Bi	ppm	1DX	0.3	0.26	0.234	13.3	NA	11.5	11.65	3.495	1.3	Exc

% RSD = percent relative standard deviation

RSD < 3%	Excellent (Exc)
3 < RSD < 7%	Very Good (VG)
7 < RSD < 10%	Good (G)
RSD > 10%	Not Accurate (NA)

				Standard WP-1 (UBC)					Standard SO-18 (ACME)					Standard SO-18 (ACME)				
Group	Element	Unit	Method	This study	Expected	± Tolerance	%RSD	Quality	This study	Mean	± Tolerance	%RSD	Quality	This study	Mean	± Tolerance	%RSD	Quality
Semimetals	As	ppm	1DX	0.6	--	--												
Semimetals	Sb	ppm	1DX	<0.1		0.00												
Actinides	Th	ppm	4B	1.8	2.03	0.10	12.7	NA	9.6	9.9	1	3.1	VG	9.4	9.9	1	5.3	VG
Actinides	U	ppm	4B	0.7	0.80	0.04	14.5	NA	16.2	16.4	1.6	1.2	Exc	15.7	16.4	1.6	4.5	VG
Nonmetals	Se	ppm	1DX	0.7	--	--												

				Standard OREAS45EA (ACME)					Standard DS10 (ACME)				
Group	Element	Unit	Method	This study	Mean	± Tolerance	%RSD	Quality	This study	Mean	± Tolerance	%RSD	Quality
Semimetals	As	ppm	1DX	10.3	9.1	4.095	11.7	NA	48.1	43.7	8.74	9.1	G
Semimetals	Sb	ppm	1DX	0.2	0.2	0.4	0.0	Exc	8.1	8.23	3.292	1.6	Exc
Nonmetals	Se	ppm	1DX	1.5	0.63	1.26	58.0	NA	1.6	2.3	1.38	43.8	NA

RSD < 3%	Excellent (Exc)
3 < RSD < 7%	Very Good (VG)
7 < RSD < 10%	Good (G)
RSD > 10%	Not Accurate (NA)

Appendix A10. Electron probe microanalysis (EPMA) of alunite samples

Appendix A10: Electron probe microanalysis (EPMA) of alunite samples

	Measured wt% Element										Calculated Cations Per Formula Unit									
Sample	**Na_2O**	**K_2O**	**CaO**	**Al_2O_3**	**Fe_2O_3**	**P_2O_5**	**SO_3**	**SrO**	**BaO**	**Sum**	**Na**	**K**	**Ca**	**Al**	**Fe**	**P**	**S**	**Sr**	**Ba**	**Sum**
060113P1-1	0.40	10.37	0.02	36.30	0.18	0.20	37.10	0.11	0.29	84.96	0.07	1.19	0.00	3.85	0.01	0.02	2.51	0.01	0.01	7.66
060113P1-2	0.39	10.86	0.01	37.47	0.00	0.05	36.27	0.07	0.04	85.17	0.07	1.25	0.00	3.98	0.00	0.00	2.45	0.00	0.00	7.76
060113P1-3	0.39	10.48	0.00	36.12	0.40	0.29	36.22	0.08	0.71	84.68	0.07	1.22	0.00	3.87	0.03	0.02	2.47	0.00	0.03	7.71
060113P1-4	0.35	10.77	0.00	35.38	0.25	0.27	36.78	0.10	0.68	84.57	0.06	1.25	0.00	3.80	0.02	0.02	2.51	0.01	0.02	7.69
060113P1-5	0.46	10.30	0.00	36.59	0.29	0.17	35.99	0.10	0.09	83.98	0.08	1.20	0.00	3.93	0.02	0.01	2.46	0.01	0.00	7.72
250113P4-1	2.08	7.70	0.03	36.70	0.03	0.03	37.20	0.26	0.19	84.22	0.36	0.88	0.00	3.88	0.00	0.00	2.51	0.01	0.01	7.66
250113P4-2	2.32	7.06	0.03	36.62	0.05	0.08	36.78	0.30	0.19	83.43	0.41	0.81	0.00	3.90	0.00	0.01	2.50	0.02	0.01	7.66
250113P4-3	0.43	10.29	0.00	36.04	0.01	0.21	36.92	0.13	0.14	84.17	0.08	1.19	0.00	3.85	0.00	0.02	2.51	0.01	0.00	7.66
250113P4-4	0.26	10.86	0.00	36.49	0.12	0.00	36.72	0.13	0.10	84.67	0.05	1.25	0.00	3.89	0.01	0.00	2.50	0.01	0.00	7.71
SG14166-1	1.22	9.40	0.03	37.33	0.03	0.20	37.09	0.10	0.06	85.46	0.21	1.07	0.00	3.92	0.00	0.01	2.48	0.01	0.00	7.70
SG14166-2	1.78	8.10	0.00	37.40	0.00	0.05	36.54	0.18	0.15	84.21	0.31	0.93	0.00	3.97	0.00	0.00	2.47	0.01	0.01	7.69
SG14166-3	1.87	8.15	0.00	37.19	0.03	0.06	37.44	0.04	0.29	85.06	0.32	0.92	0.00	3.90	0.00	0.00	2.50	0.00	0.01	7.67
SG14166-4	1.61	8.67	0.00	37.64	0.00	0.06	36.85	0.13	0.03	84.98	0.28	0.99	0.00	3.96	0.00	0.00	2.47	0.01	0.00	7.71
SG14166-5	1.37	9.17	0.00	36.73	0.00	0.02	36.05	0.27	0.20	83.81	0.24	1.07	0.00	3.95	0.00	0.00	2.47	0.01	0.01	7.75
SG14166-6	1.05	9.62	0.00	37.35	0.04	0.08	36.78	0.14	0.00	85.07	0.18	1.10	0.00	3.94	0.00	0.01	2.47	0.01	0.00	7.71
SG16257-1	2.32	7.88	0.01	37.65	0.08	0.00	37.01	0.06	0.14	85.15	0.40	0.89	0.00	3.95	0.01	0.00	2.47	0.00	0.00	7.73
SG16257-2	2.06	8.22	0.01	37.53	0.02	0.00	36.45	0.10	0.21	84.59	0.36	0.94	0.00	3.97	0.00	0.00	2.46	0.01	0.01	7.75
SG16257-3	1.88	8.38	0.00	37.58	0.03	0.00	36.12	0.16	0.28	84.42	0.33	0.96	0.00	4.00	0.00	0.00	2.45	0.01	0.01	7.76
SG16257-4	1.99	8.51	0.02	37.99	0.01	0.03	36.37	0.08	0.08	85.07	0.35	0.97	0.00	4.00	0.00	0.00	2.44	0.00	0.00	7.77
SG16257-5	2.27	7.84	0.02	37.65	0.15	0.10	37.73	0.06	0.08	85.89	0.39	0.88	0.00	3.90	0.01	0.01	2.49	0.00	0.00	7.69
SG16257-6	2.24	7.71	0.01	38.61	0.04	0.12	37.47	0.12	0.17	86.48	0.38	0.86	0.00	3.98	0.00	0.01	2.46	0.01	0.01	7.70
SG16257-7	4.11	4.08	0.09	36.74	0.00	0.09	37.19	0.15	0.00	82.45	0.72	0.47	0.01	3.89	0.00	0.01	2.51	0.01	0.00	7.61
SG16257-8	4.96	3.63	0.11	37.99	0.00	0.20	37.11	0.06	0.14	84.20	0.85	0.41	0.01	3.96	0.00	0.01	2.46	0.00	0.00	7.71
SG16257-9	1.48	8.46	0.01	36.30	0.00	0.33	36.06	0.16	0.00	82.80	0.26	0.99	0.00	3.92	0.00	0.03	2.48	0.01	0.00	7.68
SG16257-10	4.77	3.56	0.02	38.66	0.02	0.06	37.91	0.00	0.02	85.02	0.80	0.40	0.00	3.97	0.00	0.00	2.48	0.00	0.00	7.65
SG16257-11	5.80	2.04	0.04	39.49	0.00	0.00	38.55	0.00	0.06	85.99	0.96	0.22	0.00	3.98	0.00	0.00	2.48	0.00	0.00	7.65
SG16271-1	1.82	8.51	0.02	37.31	0.00	0.08	37.82	0.06	0.30	85.92	0.31	0.96	0.00	3.88	0.00	0.01	2.51	0.00	0.01	7.68
SG16271-2	1.72	8.66	0.02	37.51	0.01	0.05	36.71	0.01	0.18	84.86	0.30	0.99	0.00	3.96	0.00	0.00	2.47	0.00	0.01	7.73
SG16271-3	1.63	8.58	0.04	37.36	0.01	0.03	36.64	0.08	0.48	84.84	0.28	0.98	0.00	3.95	0.00	0.00	2.47	0.00	0.02	7.72
SG16271-4	1.78	8.47	0.02	37.31	0.05	0.07	37.09	0.08	0.25	85.13	0.31	0.96	0.00	3.92	0.00	0.01	2.48	0.00	0.01	7.70

	Measured wt% Element										Calculated Cations Per Formula Unit									
Sample	**Na_2O**	**K_2O**	**CaO**	**Al_2O_3**	**Fe_2O_3**	**P_2O_5**	**SO_3**	**SrO**	**BaO**	**Sum**	**Na**	**K**	**Ca**	**Al**	**Fe**	**P**	**S**	**Sr**	**Ba**	**Sum**
SG16274-1	0.55	10.21	0.01	36.56	0.25	0.02	36.19	0.19	0.04	84.03	0.10	1.19	0.00	3.93	0.02	0.00	2.48	0.01	0.00	7.72
SG16274-2	0.30	10.26	0.02	36.70	0.26	0.05	36.08	0.17	0.00	83.84	0.05	1.19	0.00	3.95	0.02	0.00	2.47	0.01	0.00	7.70
SG16274-3	0.42	10.57	0.00	36.68	0.21	0.06	36.26	0.20	0.00	84.40	0.07	1.23	0.00	3.93	0.01	0.00	2.47	0.01	0.00	7.73
SG16274-4	0.25	10.40	0.04	36.56	0.27	0.00	35.93	0.13	0.00	83.58	0.04	1.22	0.00	3.95	0.02	0.00	2.47	0.01	0.00	7.71
SG16274-5	0.35	10.11	0.02	36.57	0.32	0.00	35.87	0.18	0.05	83.46	0.06	1.18	0.00	3.95	0.02	0.00	2.47	0.01	0.00	7.70
SG16274-6	0.16	10.70	0.03	36.67	0.04	0.05	35.56	0.25	0.01	83.46	0.03	1.26	0.00	3.98	0.00	0.00	2.45	0.01	0.00	7.74
SG16293-1	2.59	7.28	0.00	37.11	0.01	0.32	37.61	0.36	0.11	85.39	0.44	0.82	0.00	3.87	0.00	0.02	2.50	0.02	0.00	7.67
SG16293-2	2.98	6.55	0.05	37.82	0.05	0.15	36.94	0.49	0.09	85.12	0.51	0.74	0.00	3.95	0.00	0.01	2.46	0.03	0.00	7.71
SG16293-3	2.78	6.57	0.03	37.49	0.00	0.46	36.17	0.26	0.48	84.24	0.48	0.75	0.00	3.97	0.00	0.03	2.44	0.01	0.02	7.71
SG16293-4	1.30	9.43	0.00	37.06	0.00	0.19	36.61	0.16	0.00	84.75	0.23	1.08	0.00	3.93	0.00	0.01	2.47	0.01	0.00	7.73
SG16293-5	1.59	7.89	0.43	36.99	0.05	1.58	35.65	0.80	0.31	85.30	0.28	0.90	0.04	3.90	0.00	0.12	2.39	0.04	0.01	7.68
SG16293-6	2.94	6.39	0.06	37.93	0.05	0.87	37.01	0.87	0.16	86.29	0.50	0.71	0.01	3.92	0.00	0.06	2.43	0.04	0.01	7.68
SG16303-1	3.74	5.82	0.06	37.33	0.03	0.15	37.68	0.12	0.12	85.06	0.64	0.65	0.01	3.88	0.00	0.01	2.49	0.01	0.00	7.70
SG16303-2	2.41	7.45	0.01	36.83	0.05	0.64	36.29	0.33	0.01	84.02	0.42	0.86	0.00	3.91	0.00	0.05	2.45	0.02	0.00	7.71
SG16303-3	2.42	7.19	0.01	36.46	0.09	0.97	35.92	0.38	0.05	83.50	0.42	0.83	0.00	3.89	0.01	0.07	2.44	0.02	0.00	7.69
SG16303-4	1.86	8.35	0.00	36.79	0.09	0.87	37.03	0.42	0.17	85.58	0.32	0.94	0.00	3.85	0.01	0.07	2.47	0.02	0.01	7.68
SG16303-5	4.88	3.11	0.17	37.85	0.02	0.89	37.18	0.45	0.42	84.98	0.83	0.35	0.02	3.91	0.00	0.07	2.44	0.02	0.01	7.65
SG16303-6	4.78	3.38	0.12	37.91	0.00	0.88	36.66	0.36	0.34	84.42	0.82	0.38	0.01	3.94	0.00	0.07	2.43	0.02	0.01	7.67
090313P3-1	0.66	8.44	0.08	30.36	0.16	0.41	29.66	0.71	0.22	70.70	0.14	1.18	0.01	3.91	0.01	0.04	2.43	0.05	0.01	7.77
090313P3-2	0.51	7.54	0.08	28.55	0.21	0.31	27.41	0.46	0.14	65.19	0.12	1.13	0.01	3.97	0.02	0.03	2.42	0.03	0.01	7.74
090313P3-3	0.71	9.65	0.05	35.84	0.08	0.51	34.64	0.50	0.08	82.07	0.13	1.15	0.01	3.95	0.01	0.04	2.43	0.03	0.00	7.74
090313P3-4	0.98	9.52	0.08	35.49	0.27	0.28	35.96	0.60	0.16	83.33	0.17	1.12	0.01	3.85	0.02	0.02	2.48	0.03	0.01	7.71
090313P3-5	0.73	8.14	0.08	31.47	0.23	0.32	30.30	0.64	0.14	72.06	0.15	1.11	0.01	3.96	0.02	0.03	2.43	0.04	0.01	7.75
090313P3-6	0.77	8.85	0.08	34.36	0.35	0.47	32.85	0.55	0.17	78.45	0.15	1.11	0.01	3.97	0.03	0.04	2.41	0.03	0.01	7.74
090313P3-7	0.94	9.46	0.10	35.55	0.21	0.28	34.96	0.75	0.05	82.31	0.17	1.13	0.01	3.91	0.01	0.02	2.45	0.04	0.00	7.75
090313P4-1	0.20	10.27	0.08	34.79	0.13	0.24	33.81	0.00	0.41	79.93	0.04	1.26	0.01	3.95	0.01	0.02	2.45	0.00	0.02	7.75
090313P4-2	0.17	10.91	0.03	37.05	0.01	0.11	37.56	0.00	0.24	86.08	0.03	1.24	0.00	3.88	0.00	0.01	2.50	0.00	0.01	7.67
090313P4-3	0.28	10.03	0.03	35.13	0.11	0.20	34.66	0.04	0.32	80.79	0.05	1.21	0.00	3.93	0.01	0.02	2.47	0.00	0.01	7.70

	Measured wt% Element										Calculated Cations Per Formula Unit									
Sample	**Na_2O**	**K_2O**	**CaO**	**Al_2O_3**	**Fe_2O_3**	**P_2O_5**	**SO_3**	**SrO**	**BaO**	**Sum**	**Na**	**K**	**Ca**	**Al**	**Fe**	**P**	**S**	**Sr**	**Ba**	**Sum**
090313P4-4	0.15	10.60	0.03	36.08	0.07	0.03	35.35	0.03	0.19	82.54	0.03	1.26	0.00	3.95	0.01	0.00	2.47	0.00	0.01	7.72
090313P4-5	0.37	10.89	0.03	37.09	0.04	0.15	36.42	0.10	0.04	85.14	0.06	1.25	0.00	3.94	0.00	0.01	2.46	0.01	0.00	7.74
090313P4-6	0.26	10.68	0.00	36.71	0.23	0.00	37.19	0.07	0.03	85.17	0.05	1.22	0.00	3.88	0.02	0.00	2.50	0.00	0.00	7.68
SG16290-1	2.02	2.02	0.20	31.94	0.32	0.06	16.77	0.00	0.18	53.51	0.56	0.37	0.03	5.36	0.03	0.01	1.79	0.00	0.01	8.17
SG16290-2	2.90	3.04	0.21	33.93	0.28	0.35	26.24	0.00	0.17	67.11	0.63	0.43	0.02	4.47	0.02	0.03	2.20	0.00	0.01	7.83
SG16290-3	2.36	2.49	0.23	32.26	0.32	0.16	20.29	0.00	0.06	58.17	0.59	0.41	0.03	4.95	0.03	0.02	1.98	0.00	0.00	8.02